

## Program

### Monday (National Holiday) 19<sup>th</sup> September 2011

17:00	<i>Registration (Hotel Centraza Hakata 3F Lobby)</i>
18:00	<i>Welcome Reception</i> Hotel Centraza Hakata 3F

### Tuesday 20<sup>th</sup> September 2011

	Room A	Room B	Room C
8:30	<i>Registration (C-Cube 1F Lobby)</i>		
9:30	<i>Opening Ceremony (Room A)</i>		
9:45	<b>PL01 (Room A)</b> Chihaya Adachi (Kyushu Univ., Japan)		
10:30	<i>Break</i>		
10:45	<b>1A01IL / D. Y. Ryu</b>	<b>1B01IL / L. Wu</b>	<b>1C01IL / S. Lim</b>
11:15	<b>1A02 / H. Tsuruta</b>	<b>1B02 / H. Wu</b>	<b>1C02 / S. Kyushin</b>
11:30	<b>1A03 / Y. Harada</b>	<b>1B03 / S. S. Park</b>	<b>1C03 / M.-R. Kim</b>
11:45	<b>1A04 / K. Hori</b>	<b>1B04 / T. Imae</b>	<b>1C04 / O. Sato</b>
12:00	<b>1A05 / D. Mangindaan</b>	<b>1B05 / F. Zhang</b>	<b>1C05 / M. R. Berber</b>
12:15	<i>Lunch Break &amp; Poster Presentation 1P01-58</i> (C-Cube 3F Gallery) Obligation Time (Odd Numbers 12:35-13:25 / Even Numbers 13:25-14:15)		
14:15	<i>Break</i>		
14:30	<b>1A06IL / Y. Tsujii</b>	<b>1B06 / S. A. Sarin</b>	<b>1C06IL / T. Kato</b>
14:45		<b>1B07 / J. Nishida</b>	
15:00	<b>1A07IL / K. Okumura</b>	<b>1B08 / A. Kakugo</b>	<b>1C07IL / E. Woo</b>
15:15		<b>1B09 / A. Md. R. Kabir</b>	
15:30	<b>1A08 / C. Urata</b>	<b>1B10IL / A. J. Crosby</b>	<b>1C08 / M.Santha Moorthy</b>
15:45	<b>1A09 / D. Murakami</b>		<b>1C09 / M. Sohmiya</b>
16:00	<b>1A10 / T. Hirata</b>	<b>1B11IL / N. Hosoda</b>	<b>1C10 / S. Nagappan</b>
16:15	<b>1A11 / A. Horinouchi</b>		<b>1C11 / Md. J. Alam</b>
16:30	<b>1A12 / A. S. Gnedenkov</b>	<b>1B12 / J. P. Gong</b>	<b>1C12 / A. V. Zdravkov</b>
16:45	<i>Coffee Break</i>		
17:00	<b>PL02 (Room A)</b> Hung-Jue Sue (Texas A&M Univ., USA)		

**Wednesday 21<sup>st</sup> September 2011**

	<b>Room A</b>	<b>Room B</b>	<b>Room C</b>
9:15	<b>PL03 (Room A)</b> Sung Chul Kim (KAIST, Korea)		
10:00	<i>Break</i>		
10:15	<b>2A01IL</b> / R.-M. Ho	<b>2B01IL</b> / I. Chung	<b>2C01IL</b> / M. Sato
10:45	<b>2A02IL</b> / M. Maeda	<b>2B02IL</b> / J.-S. Lee	<b>2C02IL</b> / M. Ree
11:15	<b>2A03</b> / Y. Miura	<b>2B03</b> / T.-Y. Lo	<b>2C03</b> / K. Sakurai
11:30	<b>2A04</b> / S. Shimomura	<b>2B04</b> / T. Higuchi	<b>2C04</b> / E. Mylonas
11:45	<b>2A05</b> / W.-K. Lee	<b>2B05</b> / C.-S. Ha	<b>2C05</b> / Y. Sanada
12:00	<b>2A06</b> / T. Ohzono	<b>2B06</b> / H. Watanabe	<b>2C06</b> / I. Akiba
12:15	<i>Lunch Break &amp; Poster Presentation 2P01-57</i> (C-Cube 3F Gallery) Obligation Time (Odd Numbers 12:35-13:25 / Even Numbers 13:25-14:15)		
14:15	<i>Break</i>		
14:30	<b>2A07IL</b> / A. Vedyagin	<b>2B07IL</b> / M. Kobayashi	<b>2C07IL</b> / O. Ishitani
14:45			
15:00	<b>2A08IL</b> / N. Nakashima	<b>2B08IL</b> / M. Geoghegan	<b>2C08IL</b> / H.-Z. Kou
15:15			
15:30	<b>2A09</b> / T. Fujigaya	<b>2B09</b> / S. Kidoaki	<b>2C09</b> / K. Okamoto
15:45	<b>2A10</b> / X. Zhu	<b>2B10</b> / M. Yanagisawa	<b>2C10</b> / L. Jiang
16:00	<b>2A11</b> / S. M. Lyth	<b>2B11</b> / Y. Hirai	<b>2C11</b> / D. Wang
16:15	<b>2A12</b> / K. Liu	<b>2B12</b> / Y. Hoshino	<b>2C12</b> / T. Ueno
16:30	<b>2A13</b> / H. Yang	<b>2B13</b> / P. Xie	<b>2C13</b> / A. Staykov
16:45	<i>Coffee Break</i>		
17:00	<b>PL04 (Room A)</b> Dongyuan Zhao (Fudan Univ., China)		

	<i>Move by train to Hotel Centraza Hakata nearby JR Hakata Station</i>		
19:00	<i>Banquet</i> Hotel Centraza Hakata 3F		

**Thursday 22<sup>nd</sup> September 2011**

	<b>Room A</b>	<b>Room B</b>	<b>Room C</b>
9:15	<b>PL05 (Room A)</b> Bruno Ameduri (ENSCM, France)		
10:00	<i>Break</i>		
10:15	<b>3A01IL / K. Char</b>	<b>3B01IL / M. Han</b>	<b>3C01IL / S. V. Gnedenkov</b>
10:45	<b>3A02IL / S. K. Sinha</b>	<b>3B02IL / Y. Shchipunov</b>	<b>3C02IL / I. Krossing</b>
11:15	<b>3A03 / K. Kojio</b>	<b>3B03 / K. Matsuura</b>	<b>3C03 / A. Hayashi</b>
11:30	<i>Break</i>		
11:45	<b>PL06 (Room A)</b> Masatsugu Shimomura (Tohoku Univ., Japan)		
12:30	<i>Closing &amp; Award Ceremony (Room A)</i>		

12:45	<i>Lunch for Participants to Saga Tour (Room 303)</i>
13:30	<i>Saga Light Source and Medicine Museum Visits by bus</i> <i>(Pre-registered participants only)</i> Return to Fukuoka Airport at around 17:45 and JR Hakata Station at around 18:15

## Nearly zero-gap formation between singlet and triplet excited states and their application for organic electroluminescence

Keigo Sato, Kenichi Goushi and Chihaya Adachi

Organic Photonics and Electronics Research (OPERA), Kyushu University, Japan

Recently, in order to improve the exciton production efficiency at a singlet excited level ( $S_1$ ) in organic light emitting diodes (OLEDs), we employed the mechanism of thermally activated delayed fluorescence (TADF)<sup>1,2</sup>. To realize high TADF efficiency, we need materials that have a small energy gap between  $S_1$  and a triplet excited ( $T_1$ ) levels ( $\Delta E_{ST}$ ).  $\Delta E_{ST}$  can be a small value when the exchange energy that is overlapping between the highest occupied molecular orbital (HOMO) and the lowest unoccupied molecular orbital (LUMO) is small. Therefore, the separation of the HOMO from the LUMO is crucial to enhance the up-conversion from  $T_1$  to  $S_1$  (Reverse ISC). More recently, based on this conception, we developed a triazin derivative (PIC-TRZ) that realizes a small  $\Delta E_{ST}$  of 0.1 eV and the OLED using PIC-TRZ for an emitting layer achieved a high external EL quantum efficiency of  $\eta_{ext}=5.3\%$  that exceeds the theoretical limitation of  $\eta_{ext}$  in conventional fluorescence based OLEDs. In this study, in order to achieve higher  $\eta_{ext}$  using TADF, we developed a novel triazin derivative (PIC-TRZ2) having a nearly zero energy gap between  $S_1$  and  $T_1$ , which was confirmed by the fact that fluorescence and phosphorescence spectra of PIC-TRZ2 shows exactly same 0-0 transition peak (T=5 K). Furthermore, intense delayed fluorescence is confirmed in both the neat and a 6 wt%-PIC-TRZ2:1,3-bis(9-carbazolyl)benzene (m-CP) co-deposited film under photo-excitation at room temperature. In addition, the OLED using PIC-TRZ2 shows a high external quantum efficiency of  $\eta_{ext}=7.9\%$  at 0.01 mA/cm<sup>2</sup> with intense delayed fluorescence.

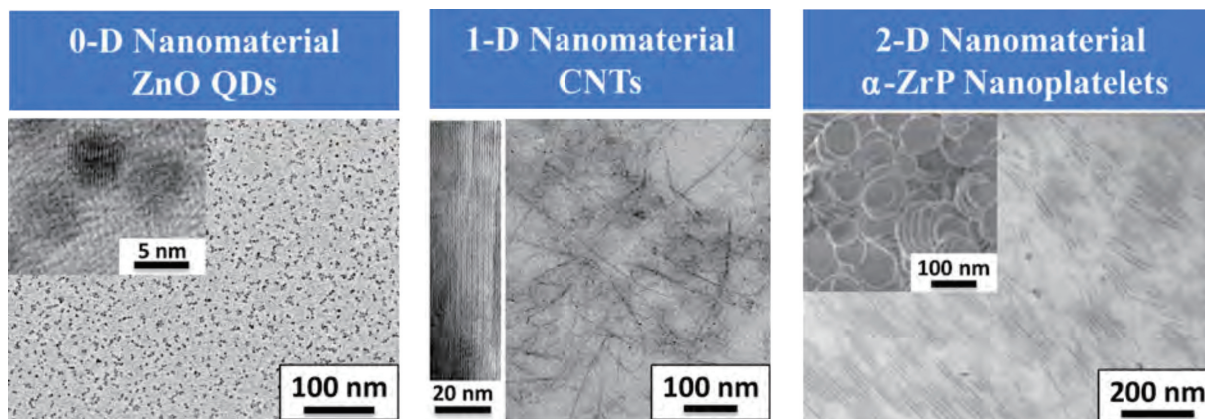
[1] A. Endo, M. Ogasawara, A. Takahashi, D. Yokoyama, Y. Kato and C. Adachi, *Adv. Mater.*, **21**, 4802 (2009)

[2] A. Endo, K. Sato, K. Yoshimura, T. Kai, A. Kawada, H. Miyazaki and C. Adachi, *Appl. Phys. Lett.*, **98**, 083302 (2011)

## Dispersion and Assembly of Nano-materials in Organic Media and Their Nano-scaled Phenomena

K. L. White, X. Zhang, M. Wong, P. Liu, D. Sun, C.-C. Chu, and H.-J. Sue  
Polymer Technology Center, Department of Mechanical Engineering, Texas A&M University,  
College Station, TX 77843-3123, USA

The ability of a material to interact with its environment depends on the characteristic length scale of its structural building blocks. As this length scale reduces, the material begins to be greatly influenced by the immediate surrounding environment and can exhibit unique size and shape dependent behaviors, such as size-dependent optoelectronic properties of quantum dots. Nanomaterials also exhibit large surface to volume ratios which are essential for gas storage, efficient energy conversion, and barrier property enhancement. These nanomaterials can be utilized at various length scales ranging from nanotools or sensors to multi-functional composites. However, these benefits are significantly diminished by the random aggregation of nanoparticles. In order to develop true nanocomposite materials, the individual characteristics of the nanoparticles must be preserved at adequate concentration to modify the bulk response of the material. We have recently developed approaches to fully exfoliate and disperse model nanomaterials which are stable in various solvents and can be transferred to polymer matrices without aggregation.



Nanomaterials used in our research: (Left) Monodisperse semi-conducting zinc oxide quantum dots prepared with simple colloidal method. (Middle) Recently achieved successful exfoliation of carbon nanotubes in various solvents and polymer matrices. (Right) zirconium phosphate nanoplatelets with tunable aspect ratio and exfoliation state.

Zinc oxide is an important semi-conductor with large bandgap and exciton binding energy suitable for short wavelength optoelectronic devices. We developed a simple colloidal method to prepare monodisperse 5-nm ZnO quantum dots (ZnO QDs) with high purity [1]. These materials exhibit unusual optoelectronic and thermal properties if their particle size remains in 5 nm range [2-5]. We have also been able to transfer the ZnO QDs

into various polymer matrices by either grafting ZnO QDs with polymers to make melt-processable nanocomposites, or utilizing zirconium phosphate nanoplatelets (ZrP NPs) to assist in nanoparticle dispersion and stabilization in epoxy and PMMA [3, 4, 6]. The above approaches have enabled realization of commercial potential of nanomaterials for various engineering and microelectronic applications. Recent work has also demonstrated that surfactant-free ZnO QDs exhibit unusual phase transitions for nanoparticles and can self-assemble into transparent macro-scale colloidal crystal with impressive UV-shielding ability [7].

Carbon nanotubes (CNTs) are immensely strong, high modulus cylindrical nanomaterials which can be metallic or semi-conducting and exhibit extremely high thermal conductivity. Individual exfoliation of CNTs is challenging because immediately following synthesis, single-walled CNTs rapidly self-assemble into parallel bundles or ropes due to strong inter-tube van der Waals (vdW) interaction and  $\pi$ -stacking [8, 9]. We developed the first robust and innocuous method to completely debundle nanotube aggregates into an individually dispersed state using a colloidal approach based on reversible electrostatic coupling of ZrP NPs to oxidized CNTs [8, 10]. The ZrP NPs act to absorb and localize sonication energy at tube-tube interfaces, thereby overcoming short-range vdW interactions and physically de-bundling the CNTs. The individually exfoliated CNTs can then be isolated in solution by inducing precipitation of ZrP NPs with either acid or salt addition [11]. Efforts are currently focused on the development of structure-property relationships to identify the mechanisms associated with individual CNTs and whether bundling is preferable in certain conditions. Recently, we demonstrated that sparse networks of individual CNTs behave as an ideal 2-dimensional network of isotropic random resistors using an ink printing method [9]. When a low level of CNT is dispersed in polypropylene matrix, significant improvements in electrical conductivity, thermal stability, and mechanical properties are observed [12].

ZrP NPs have been extensively studied in our group as a means of developing structure-property relationships for the broader class of layered silicates. ZrP NPs are a synthetic analog to naturally occurring layered silicates such as montmorillonite and bentonite, and can be produced with high purity, controlled size, tailored degree of exfoliation, and are easily dispersible in various solvents by proper selection of functional groups [13-16]. We have recently demonstrated that the exfoliation state of other nanoparticles can be effectively tailored using ZrP NPs [4, 8-11]. Investigations regarding the explicit mechanism(s) responsible for this unique effect are currently being pursued.

## References

1. D. Sun, M. Wong, L. Sun, Y. Li, N. Miyatake and H.-J. Sue, "Purification and Stabilization of Colloidal ZnO Nanoparticles in Methanol", *J. Sol-Gel Sci. Tech.*, **43**, 237-243(2007).

2. D. Sun, N. Miyatake and H.-J. Sue, "Transparent PMMA/ZnO Nanocomposite Films Based on Colloidal ZnO Quantum Dots", *Nanotechnology*, 18, 215606(2007).
3. D. Sun and H.-J. Sue, "Tunable Ultraviolet Emission of ZnO Quantum Dots in Transparent Poly(methyl methacrylate)", *Appl. Phys. Lett.*, 94, 253106(2009).
4. D. Sun, W.N. Everett, and H.-J. Sue, "Tuning Dispersion State of Ligand-Free ZnO Quantum Dots in Polymers *via* Exfoliated Nanoplatelets", *Macromolecules*, 42, 1665-1671(2009).
5. T.-H. Lee, H.-J. Sue and X. Cheng, "Solid-State Dye-Sensitized Solar Cells Based on ZnO Nanoparticle and Nanorod Array Hybrid Photoanodes", *Nanoscaled Res. Lett.*, Accepted.
6. M. Wong, R. Tsuji, S. Nutt, and H.-J. Sue, "Glass Transition Temperature Changes of Polymer Nanocomposites Comprised of Finely Dispersed ZnO Quantum Dots", *Soft Matter*, 6, 4482-4490(2010).
7. X. Zhang, D. Sun, H.-J. Sue and R. Nishimura, "Colloidal Crystallization of Surfactant-Free ZnO Quantum Dots", *ChemPhysChem*, July 2011, Submitted.
8. D. Sun, W.N. Everett, C.-C. Chu, and H.-J. Sue, "Single-walled Carbon Nanotube Dispersion with Electrostatically Tethered Nanoplatelets", *Small*, 5, 2692-2697(2009).
9. K. L. White, M. Shuai, X. Zhang, H.-J. Sue, and R. Nishimura, "Electrical Conductivity of Well-Exfoliated Single-Walled Carbon Nanotubes," *Carbon*, Article in Press, Accepted Manuscript.
10. H.-J. Sue, X. Cheng, D. Sun, H. Li, and C.-C. Chu, "Dispersion, Alignment, and Deposition of Nanotubes," US Patent 20100/197832, 2008.
11. X. Zhang, H.-J. Sue, and R. Nishimura, "Dispersion and Retrieval of De-bundled Nanotubes," US Patent 61297986 (in filing), 2010.
12. H.-J. Sue, C.-C. Chu, M. Wong, Y. Ryousho, and T. Zanka, "Dispersion of Nanotubes/or Nanoplatelets in Polyolefins", 61/290,465, Utility Patent Filed, 12/28/2010.
13. L. Sun, W.J. Boo, D. Kong, J.Y. O'Reilly, J.Y. Su, H.-J. Sue, and A. Clearfield, "Effect of Molecular Structure on the Intercalation of  $\alpha$ -Zirconium Phosphate", *J. Colloid. & Interface Sci.*, 333, 503-509(2009).
14. L. Sun, W.J. Boo, A. Clearfield, and H.-J. Sue, "Preparation of  $\alpha$ -Zirconium Phosphate Nanoplatelets With Wide Variations of Aspect Ratios", *New J. Chem.*, 31, 39-43(2007).
15. L. Sun, W.J. Boo, R. Browning, H.-J. Sue, and A. Clearfield, "Effect of Crystallinity on the Intercalation of Monoamine In  $\alpha$ -Zirconium Phosphate Layer Structure", *Chem. Mater.*, 17, 5606-5609(2005).
16. D. Sun, H.-J. Sue, Z.-D. Cheng, Yuri Martinez-Raton, and Enrique Velasco, "Stable Smectic Phase in Suspensions of Polydisperse Colloidal Platelets with Identical Thickness", *Phys. Rev. Lett. E*, 80, 041704(2009).

## Multi-component Polymer Membranes for Direct Methanol Fuel Cell

Sung Chul Kim<sup>1</sup>, Dong Hwee Kim<sup>1</sup>, Yo Han Kwon<sup>1</sup>, Soon Yong So<sup>1</sup>, Sang Young Lee<sup>2</sup>  
<sup>1</sup>KAIST, Korea

<sup>2</sup> Kangwon National University, Korea

Nafion is currently used for the development of the Direct Methanol Fuel Cell (DMFC). Nafion membranes exhibit good chemical, thermal and mechanical stability. But the methanol permeability through the membrane is relatively high and this causes the fuel loss and the reduction of the efficiency of the fuel cell. It is believed that the methanol permeates through the water channel formed in the Nafion membrane and if we reduce the size of the water channel, the methanol permeability will be reduced while maintaining the proton conductivity. Polymer blends of sulfonated poly(aryl ether sulfone) copolymer(60 mole% sulfonation) with hydrophobic poly(ether sulfone) copolymer (RH-2000, Solvay) having the co-continuous morphology were prepared. The degree of phase separation was controlled by freezing the morphology at early stage of spinodal phase separation through controlling the drying temperature and the concentration of the casting solution. The water channel size in the fully hydrated state of the polymer blend membrane was reduced up to 13nm, which resulted in the reduction of the methanol permeability by 50%. Moreover the presence of the continuous and glassy hydrophobic phase of the poly(ether sulfone) copolymer restricted the swelling of the water channel at elevated temperature, which increased the selectivity of the membrane (proton conductivity/methanol permeability).

Another approach to restrict the phase separation is the use of the low molecular weight, highly conductive 100% sulfonated poly(aryl ether sulfone) oligomer instead of the 60 mole% sulfonated polysulfone copolymer used in the previous polymer blend membranes. 100% polysulfone is water soluble and can not be used in the linear form. So the sulfonated oligomer was later crosslinked after the formation of the co-continuous morphology by blending with the hydrophobic polysulfone, thus forming semi-IPN's. Hydroxyl terminated oligomers of the 100% sulfonated polysulfone was synthesized by using excess biphenol. The hydroxyl terminal group was converted to acrylic group by reacting with acryloyl chloride. The acrylic terminated sulfonated polysulfone was blended with commercial polyether sulfone(RH-2000, Solvay) and the acrylic terminal group was photo crosslinked during the solvent evaporation process. The semi-IPN membranes composed of 70% sulfonated polysulfone with 30% RH-2000 showed spinodal morphology. The proton conductivity was somewhat reduced compared to Nafion membranes but the methanol permeability was reduced drastically thus increasing the selectivity and the efficiency of the membranes for the direct methanol fuel cell application.



The other approach to reduce the methanol permeability is to introduce inorganic phases in the water channel. Organic-inorganic hybrid membranes were prepared using sulfonated poly(aryl ether sulfone) copolymer(60 mole% sulfonatin) as templates for the sol-gel reaction of silanes proceeded in water channels.. Silicates synthesized in water channels are believed to effectively act as a barrier to methanol transport. Diethoxydimethylsilane (DEDMS) was employed as an inorganic precursor. DEDMS is known to have hydrophobic nature, therefore is expected to effectively adjust hydrophilicity of the resultant hybrid membranes. Depending on DEDMS uptake into SPAES-60, three different hybrids were prepared, which are designated as H4 (4 wt.% of DEMS), H8 (8 wt.%), H12 (12 wt.%), respectively. An increase of DEDMS uptake allows water uptake to decrease and water channels to become more narrowed and tortuous, which verifies successful development of hydrophobic silicates in water channels. Another noticeable observation is that higher uptake of DEDMS shows better performance in suppressing methanol crossover with slightly deteriorating proton conductivity, resulting in superior selectivity. This improvement in transport properties was discussed in terms of water channel structure and state of water.

- [1] D. H. Kim, J. S. Choi, Y. T. Hong, S. C. Kim, *J. Membr. Sci.*, **2007**, 299, 1
- [2] Y. H. Kwon, S. Y. Lee, S. C. Kim, *Macromolecules.*, **2009**, 42, 14.
- [3] S. Y. So, Y. T. Hong, S. Y. Lee, S. C. Kim, *J. Membr. Sci.*, **2010**. 346, 1

## Hydrothermal Synthesis of Ordered Mesoporous Carbon Materials for Applications

Dongyuan Zhao

Department of Chemistry, Fudan University, Shanghai 200433, P. R. China

Ordered mesoporous carbon materials have attracted a lot of attention because of their unique structures and chemical properties, wide applications for super-capacitor, hydrogen storage, adsorption and separation. Normally the hard-templating method is utilized to fabricate ordered mesoporous carbons, but it is fuss, high-cost, and difficult to realize industrial production. Here, we demonstrate a surfactant-templating approach to synthesize ordered mesoporous phenolic resin polymers and a direct transformation to homologous carbon frameworks [1]. A family of ordered mesoporous organic polymers and carbons are simply achieved by using commercial available cheap phenol and formaldehyde as precursors, triblock followed with a carbonization process. The mesoporous carbons have a large uniform mesopore (2 ~ 20 nm), high surface areas (800 ~ 2400 m<sup>2</sup>/g) and large pore volume (0.8 ~ 2.4 cm<sup>3</sup>/g). The mesostructures can be easily tuned from hexagonal (space group *p6mm*) and cubic (*Im3m*, *Ia3d*, *Fd3m*, *Fm3m*). It is interesting that by using this hydrothermal method, single crystals, nanospheres, vesicles and monoliths can be easily synthesized. For example, mesoporous carbon nanospheres with uniform diameter of 20 ~ 140 nm are fabricated through a low-concentration route (Fig. 1). All the mesopores (~ 2.6 nm) are open and accessible. It shows no cytotoxicity and easily penetrates into living cells. The derived carbons with thick walls are first example of molecular sieves which have ultra high stability. We also show here

large-scale synthesis approach based on the hydrothermal cooperative assembly. Kilogrammes of ordered mesoporous carbons are easily obtained for applications in catalysis, electrochemical supercapacitors and water-treatment.

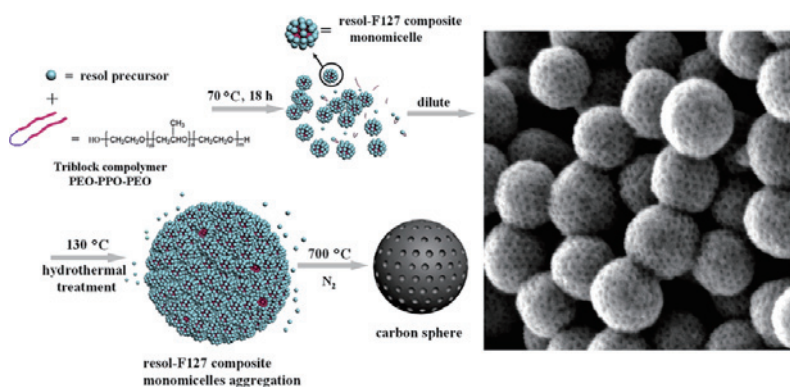


Fig. 1. The scheme for the formation process (left) and representative SEM image of the uniform ordered mesoporous carbon nanospheres.

- [1] F. Q. Zhang, Y. Meng, D. Gu, Y. Yan, C. Z. Yu, B. Tu, D. Y. Zhao, *J. Am. Chem. Soc.*, **127**, 13508 (2005); *J. Am. Chem. Soc.*, **129**, 7746 (2007); *Chem. Mater.*, **18**, 5279 (2006);  
 [2] Y. Huang, *et al*; *Chem. Commun.*, 2641 (2008);  
 [3] Y. Wan, Y. F. Shi, D. Y. Zhao, *Chem. Mater.*, **20**, 933 (2008); D. Gu, *et al*, *Adv. Mater.*, **22**, 833 (2010); Y. Fang, *et al*, *Angew. Chem. Int. Ed.*, 49(43), 7987–7991 (2010).

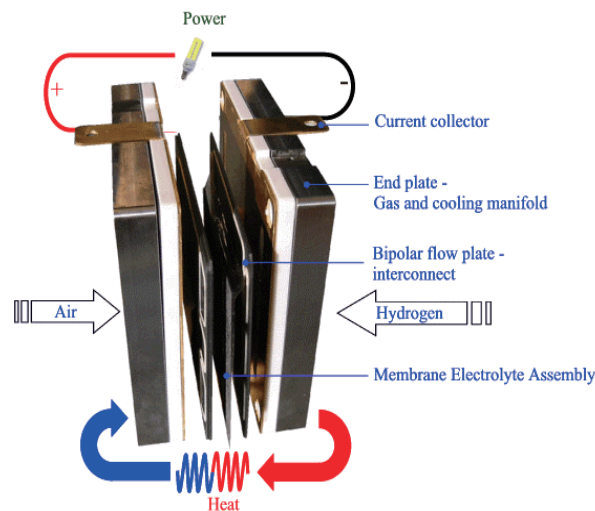
## Fluoromembranes for Fuel Cell: myth or reality?

Ghislain DAVID and Bruno AMEDURI

Institut Charles Gerhardt, Ingénierie & Architectures Macromoléculaires

Ecole Nat. Sup. Chimie de Montpellier, France

Fuel cell can be regarded as potential future alternative source of green Energy. Polymer electrolyte membrane fuel cell (PEMFC) is composed of an electrolyte (usually a membrane which must be an ionic conductor) located between with anode and the cathode, as follows:



The membrane is a functional polymer which bears protonic, cationic or anionic groups depending on the choice of use and must fulfill drastic requirements: high ionic conductivity and stability to HO<sup>•</sup> radicals, and to withstand their properties at 120 °C for about 5000 h. Fluorinated polymers[1] that possess protogen groups are suitable candidates from various strategies:

**-either by « direct » radical copolymerization of fluoroolefins bearing protogen groups, [1,2]**

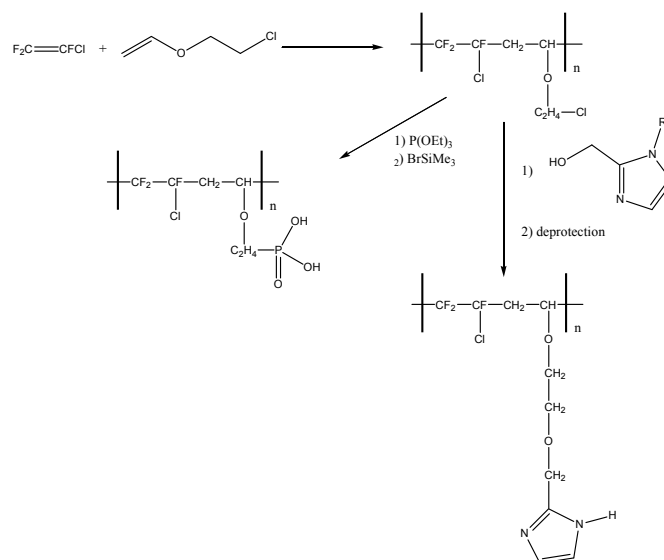
**-or by chemical modifications fluoropolymers [1,2]**

The first strategy has already led to various commercially available products such as Nafion<sup>®</sup>, Flemion<sup>®</sup>, 3M<sup>®</sup> Membrane, Hyflon<sup>®</sup> Ion, Aciplex<sup>®</sup> and others.[1,2]

But, these perfluorosulfonic membranes are quite dependant of a high hydration [3] and, consequently are limited: high temperature (> 90°C) and low relative humidity (HR < 30 %) [4] regarded as real challenges for the development of protonic PEMFCs.

Our recent objectives were to find out new fluorinated membranes bearing either nitrogenous heterocycles such as (benz)imidazoles. or phosphonic acids (though less acidic than sulfonic ones but more dependant of the relative humidity [4]). The key strategy to enable a suitable compromise for both a high amount fluoromonomers and of functions that

insure the conductivity is to carry out an *alternating copolymerization* of chlorotrifluoroethylene and a monomer which bears such a function. Hence, the radical copolymerization du CTFE with 2-chloroethyl vinyl ether (CEVE) to obtain poly(CTFE-*alt*-CEVE) copolymers was first achieved for further chemical modifications to synthesize original copolymers that containing (benz)imidazole [5] or phosphonic acid,[6] as follows:



Fluoropolymers bearing imidazole functions require the obtaining of blend membranes involving sulfonated PEEK (which brings the protonic conductivity at low temperature) and led to conductivities values (ca.  $10 \text{ mS}\cdot\text{cm}^{-1}$ ) but stable up to  $150 \text{ }^\circ\text{C}$ . [5]

Phosphonic acids are interesting conductors (especially for the first acidity) and are rather thermal stable, and this enables them to behave intermediately between sulfonic acids and benzimidazoles. Our first results are encouraging since a conductivity of  $20 \text{ mS cm}^{-1}$  at 95 % relative humidity and results at low HR and high T will also be presented. [6]

Acknowledgments : the authors thank Prof B. Boutevin, Dr D. Jones; Prof J. Roziere, R. Tayouo, A. Soulès and G. Frutsaert for their input and CEA, Peugeot Citroën PSA, and ANR for financial supports.

- [1] B. Ameduri, B. Boutevin, *Well Architected Fluoropolymers: Synthesis, Properties and Applications*; 2004, Elsevier, Amsterdam; Chapter 5; pp 314-327.
- [2] a) R. Souzy, B. Ameduri, *Prog Polym Sci.*, **30**, 644 (2005); b) M. Yoshitake, A. Watakabe, *Adv Polym Sci.*, **215**, 127 (2008).
- [3] C. Wieser, *Fuel Cells*, **4**, 245 (2004).
- [4] K. D. Kreuer, *Solid State Ionics*, **97**, 1 (1997).
- [5] G. Frutseart, G. David, B. Ameduri, D. Jones, J. Roziere, *J. Membr. Sci.*, **367**, 127 (2011).
- [6] R. Tayouo, G. David, B. Ameduri, J. Roziere, S. Roualdes, *Macromolecules*, **43**, 5269 (2010).

**Engineering Biomimetics:  
Biomimetic Surface Materials Prepared by Self-organization**

Yuji Hirai<sup>1,5</sup>, Daisuke Ishii<sup>2,5</sup>, Hiroshi Yabu<sup>1,5</sup>, Hiroko Horiguchi<sup>3,5</sup>, Takahiko Hariyama<sup>3,5</sup>, Yasutaka Matsuo<sup>4,5</sup>, Kuniharu Ijiro<sup>4,5</sup>, Tateo Shimosawa<sup>5</sup>, Kaoru Tsujii<sup>5</sup>, and Masatsugu Shimomura<sup>1,2,5</sup>,

<sup>1</sup>IMRAM, Tohoku University, Japan, <sup>2</sup> WPI-AIMR, Tohoku University, Japan, <sup>3</sup> Hamamatsu Medical University, Japan, <sup>4</sup> RIES, Hokkaido University, Japan, <sup>5</sup> CREST-JST, Japan

Patterns generate functions. In the world of insects, plants, and animals, simply repeated structures sometimes generate functions. For example, the moth-eye, whose surface is covered by regularly arranged sub-cellular size dots pattern, is a “micro device” that enables high-speed night flight of its owner. “Biomimetic surface materials” have now attracted worldwide attentions because of their unique surface properties. In this report, anti-reflective silicon surfaces have been simply prepared by using self-organized honeycomb-patterned polymer films as masks for dry etching process. Simple casting of polymer solutions under highly humid condition can provide “honeycomb patterned” polymer films. Self-packed surface monolayer of mono-dispersed water droplets formed by evaporation cooling on the solution surface acts as a temporary template of micro-pores<sup>1)</sup>.

The “honeycomb-patterned” film has a double-layered structure with pillars supporting the two porous layers on each vertex of the hexagons. Regular arrayed pillar-structure, like a “pincushion”, was formed when the “honeycomb-patterned” film was cleaved into halves by peeling with an adhesive tape. After UV-ozone treatment of the polystyrene honeycomb-patterned film, the film was fixed up side down on silicon substrate with poly vinyl alcohol as adhesive. After peeling of the bottom layer of the honeycomb-patterned film, pincushion-structured porous mask was formed on the silicon substrate.

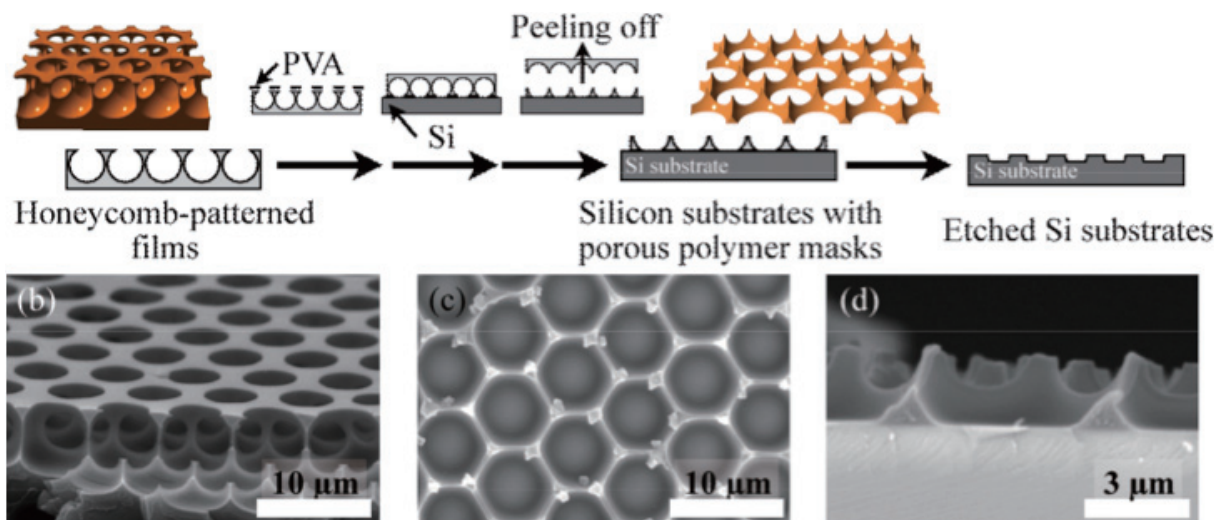


Fig.1 Preparation procedure of Si etching by using honeycomb-patterned polymer mask.

After reactive ion etching of the silicon substrate through the mask, the nano-structured

silicon surface was obtained. Pincushion-like silicon structures with hierarchic spike structures from nano meter to micrometer were formed. The surface showed very small light reflectance and super-hydrophobic nature because a small amount of fluorinated compounds were remained on the silicon surface. The super-hydrophobic surface was turned to a super-hydrophilic surface after UV-ozone treatment for removing fluorinated compounds.

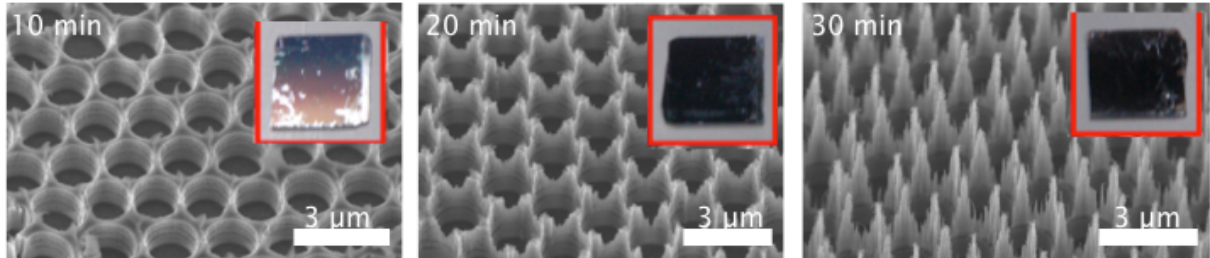


Fig.2 Surface morphology of the etched Si substrates. Deep etching provides “Moth-eye”.

“*Ligia exotica*” is one species of isopods living at waterfront of sea. Hariyama have found that *Ligia exotica* uptakes water from wet ground to its abdomen by using two pairs of legs for branchial respiration. Long-distance water transport was achieved by using open capillary structures formed at the outer surface of the legs<sup>2)</sup>.

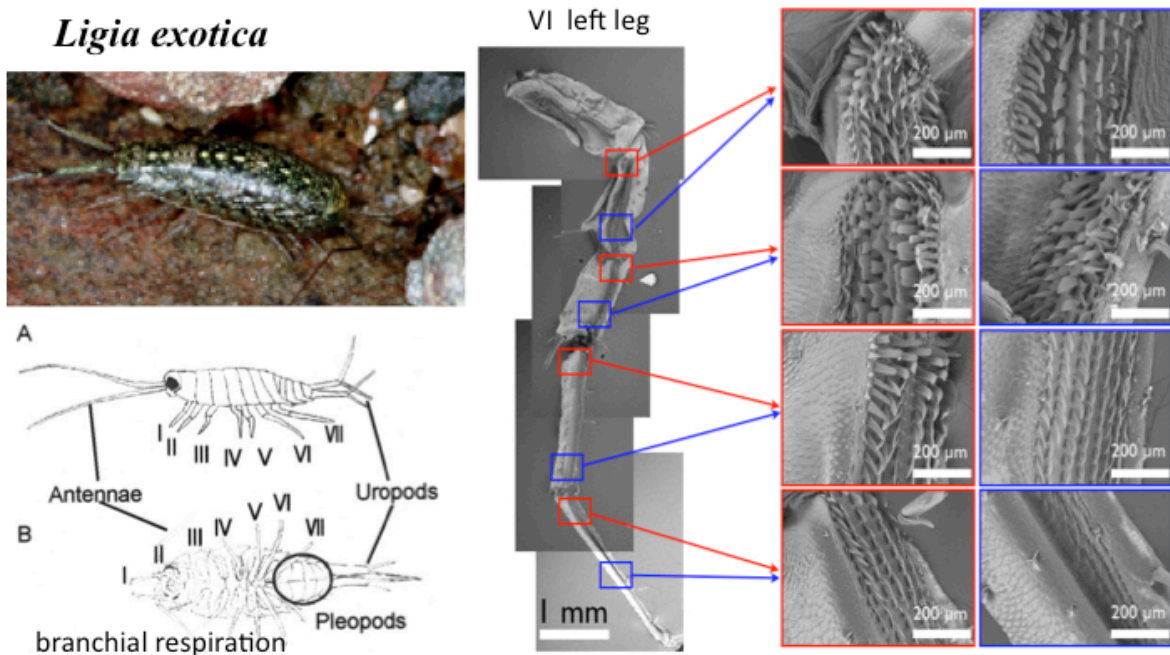


Fig.3 Open capillary structures formed at the outer surface of the legs of *Ligia exoyica*.

Biomimetic water transport surface is designed and prepared by using the patterned Si substrate having both super-hydrophobic and super-hydrophilic properties.

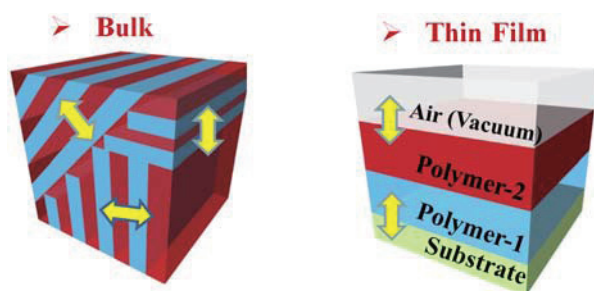
- [1] M. Shimomura, in “Nanocrystals Forming Mesoscopic Structures” pp.157-171. ed. by M. P. Pileni, Wiley-VCHJ (2006).  
 [2] T.Hariyama, et al., *Biol. Bull.*, 213, 196-203 (2007).

## Transition Behavior and Microdomain Orientation in Block Copolymer Films

Du Yeol Ryu,\* Eunhye Kim, Seunghoon Choi, Jinsam Gong, and Hyungju Ahn

Department of Chemical and Biological Engineering, Yonsei University, Seoul 120-749, Korea

The phase behavior of block copolymer (BCP) self-assembly in a film geometry that confines polymer chains to the interfaces will be influenced by the interfacial interactions at substrate/polymer and polymer/air and the commensurability between the equilibrium period ( $L_0$ ) of the BCP and the total film thickness. Particularly on the modified surface, the phase transitions for the films of block copolymers (BCPs), like the order-to-disorder transition (ODT), have been studied by in-situ grazing incidence small angle x-ray scattering (GISAXS) and transmission electron microscopy (TEM).



For films of a lamella-forming polystyrene-*b*-polyisoprene (PS-*b*-PI) on PS grafted substrates, the thickness dependence of the ODT showed a plateau in the value of the ODT for films over 12  $L_0$ , which is still higher than that observed in the bulk PS-*b*-PI.

The ODT was found to increase rapidly with decreasing film thickness. In contrast, the plateau value of the ODT for films on bare Si wafers was nearly identical to that found in the bulk, due to the weak interactions between the BCP and substrate at the oxide/polymer interface. For films of polystyrene-*b*-poly(methyl methacrylate) (PS-*b*-PMMA) on PS grafted substrates, a gradual increase in ODT rather than a plateau value of the ODT, was observed with decreasing film thickness, which can be correlated to the weak temperature dependence of  $\chi$  between PS and PMMA in comparison to that of PS and PI. In contrast, the ODT behavior in thin films of PS-*b*-PMMA on a random copolymer (P(S-*r*-MMA)) substrate indicates a rapid decrease with decreasing film thickness less than 25  $L_0$ . This result can be attributed to a surface-induced compatibilization toward two block components.

### References

- [1] Kim et al., *Polymer*, **51**, 6313-6318 (2010)
- [2] Shin et al., *Macromolecules*, **41**, 9140-9145 (2008)
- [3] Kim et al., *Macromolecules*, **42**, 8385-8391 (2009)

## Novel Tribomaterials Newly Designed/Synthesized by Living Radical Polymerization

Yoshinobu Tsuji<sup>1,2</sup>, Ryo Nakahara<sup>1</sup>, Akihiro Nomura<sup>1</sup>, Atsushi Goto<sup>1</sup>, Kohji Ohno<sup>1</sup>

<sup>1</sup>Institute for Chemical Research, Kyoto University, Japan

<sup>2</sup>JST, CREST, Japan

Successful application of living radical polymerization made it possible to graft low-polydispersity polymers with exceptionally high graft densities, fabricating well-defined “concentrated” polymer brushes (CPBs). In thus prepared CPBs, graft chains in a good solvent are highly stretched, nearly to their full length, giving properties quite different and unpredictable from those of semi-dilute polymer brushes (SDPB) [1]. One of most interesting properties was super lubrication of confronted CPBs in solvents [2,3], which was reasonably ascribed to CPBs never mixing with each other at any high compressions for the conformational entropic reason of highly extended CPB chains. Such fundamental/mechanistic studies motivated us to develop new soft materials with excellent properties similar to the CPB.

Here, we synthesized, as new soft materials, a novel graft-type of gels by cross-linking between graft-chain ends of bottle brushes (prepared by atom transfer radical polymerization with a multi-functional initiator, see Fig. 1) and measured its frictional property using the colloidal-probe AFM technique. Fig. 2 shows the frictional coefficient  $\mu$  as a function of shear rate  $\dot{\gamma}$  for the crosslinked bottle brushes of different side-chain molecular weights  $M_p$  as well

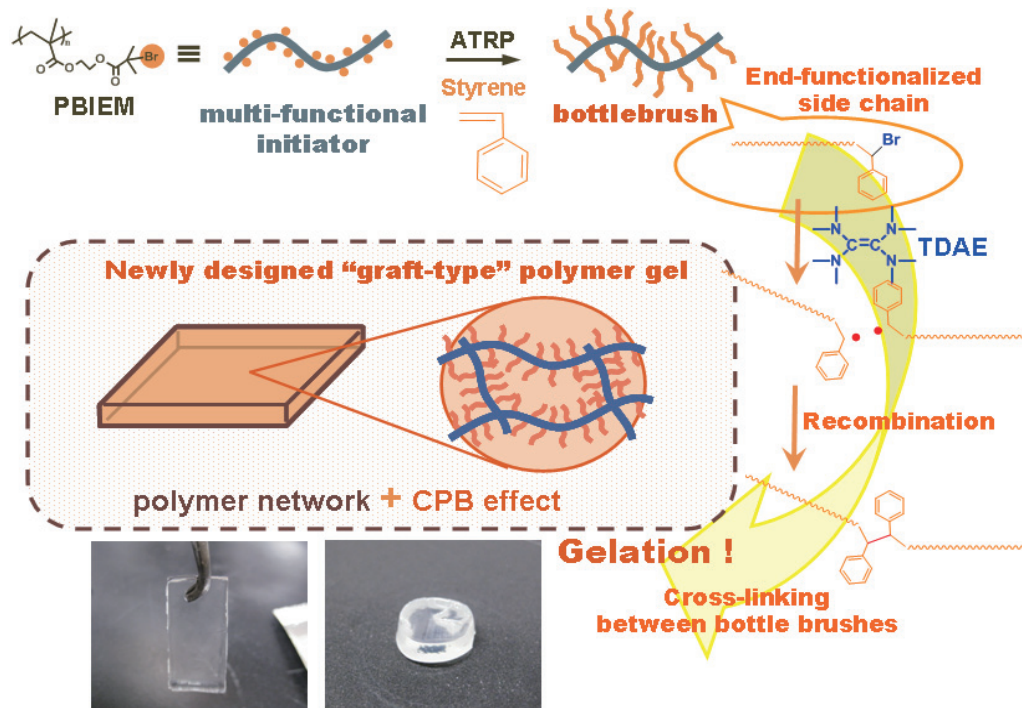
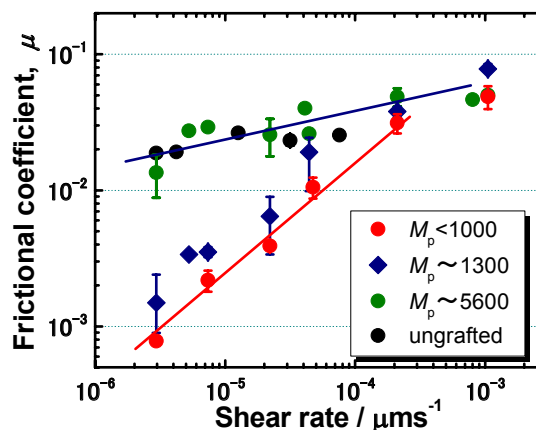


Fig. 1 Controlled synthesis of bottle-brush gels.



as an ungrafted gel. The sample of  $M_p = 5600$  gave the  $\mu$  value in the range of  $10^{-2}$ , similarly to the ungrafted gel. Interestingly, the frictional coefficient was drastically decreased when the side chain of the bottle brush was short enough so that its outermost surface was in the CPB regime in a swollen state ( $M_p \sim 1000$ ).

From another viewpoint of tribomaterials, one can find a good example in a human joint, in which a SDPB-like assembly of proteoglycan reinforced by a collagen fiber plays an important role for lubrication. This bottle brush has charged groups, and thereby electrostatic interaction achieves ultralow friction. We fabricated a composite of the above-mentioned CPB-type of bottle brushes with cellulose nanofiber (CNF). **Fig. 3** shows the scanning electron micrograph of the CNF sheet before and after incorporating the bottle brush. The AFM tribological study demonstrated that the composite sheet gave the excellent lubrication (without any help of charge effect) in addition to improved mechanical strength. We believe that these studies will open up a new route to novel tribomaterials.



**Fig. 2** Plot of frictional coefficient  $\mu$  vs shear rate  $\nu$  for bottle-brush type of gels in toluene.

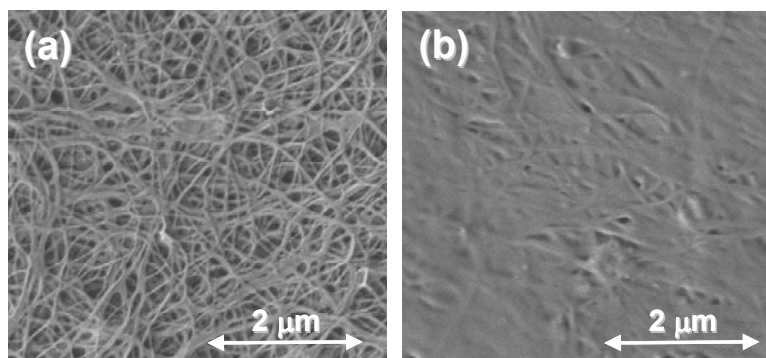


**Fig. 3** Scanning electron micrographs of (a) original CNF sheet and (b) its composite with bottle brush.

## References

- [1] Y. Tsuji, K. Ohno, S. Yamamoto, A. Goto, T. Fukuda, *Adv. Polym. Sci.*, **197**, 1-45 (2006).
- [2] Y. Tsujii, A. Nomura, K. Okayasu, W. Gao, K. Ohno, T. Fukuda, *J. Phys: Conf. Ser.*, **184**, no. 012031 (2009).
- [3] A. Nomura, K. Okayasu, K. Ohno, T. Fukuda, Y. Tsujii, *Macromolecules*, **44**, 5013-5019 (2011).

## Wetting on textured surfaces and simple mechanics of spider webs

Ko Okumura

Physics Department, Graduate school of Ochanomizu University, Japan

Micropatterns created on solid substrates enhance the original wetting property: if the original flat substrates are hydrophobic the patterns make the substrates more hydrophobic while if they are hydrophilic more hydrophilic. As an application of the hydrophobic case we discuss simple two scenarios for the transition of the contact state of a liquid drop placed on such substrates, which is often called the Cassie- Wenzel transition [1-3]. As an example of hydrophilic case we discuss the dynamics of imbibition of such substrates [4-6]. As a digression we briefly discuss simple dynamics of bubbles and drops enclosed in a pseudo two-dimensional cell (Hele-Shaw cell) [7-8]. We also talk on mechanical adaptability of spider webs and clarify how the combination of soft spiral threads and hard radial threads contributes the adaptability [9], emphasizing some similarity to nacre, which is a natural strong material found inside certain sea shells [10].

[1] C. Ishino, K. Okumura and D. Quéré, Wetting transitions on rough surfaces, *Europhys. Lett.* **68** (2004) 419.

[2] C. Ishino and K. Okumura, Nucleation scenarios for wetting transition on textured surfaces: the effect of contact angle hysteresis, *Europhys. Lett.* **76** (2006) 464.

[3] C. Ishino and K. Okumura, Wetting transitions on textured hydrophilic surfaces, *Eur. Phys. J. E* **25** (2008) 415.

[4] Chieko Ishino, Mathilde Reyssat, Etienne Reyssat, Ko Okumura and David Quere, Wicking in a forest of micro-pillars, *Europhys. Lett.* **79** (2007) 56005.

[5] Minako HAMAMOTO-KUROSAKI and Ko OKUMURA, On a moving liquid film and its instability on textured surfaces, *Eur. Phys. J. E* **30**, 283–290 (2009).

[6] Noriko Obara and Ko Okumura, Another scenario for rational scaling exponents from the Navier-Stokes equation: beyond competition of two terms, submitted.

[7] Ayako ERI and Ko OKUMURA, Viscous drag friction acting on a fluid drop confined in between two plates, *Soft Matter*, **7**, 5648 (2011); highlighted on <http://blogs.rsc.org/sm/> (May 25, 2011) and made access-free for 4 weeks after publication.

[8] Maria YOKOTA and Ko OKUMURA, Dimensional crossover in the coalescence dynamics of viscous drops confined in between two plates, *Proc. Nat. Acad. Sci. (USA)*, **108** (2011) 6395–6398; featured in In this issue (This week in PNAS), *PNAS*, **108** (2011) 6337.

[9] Yuko AOYANAGI and Ko OKUMURA, A simple model for the mechanics of spider webs, *Phys. Rev. Lett.* **104**, 038102 (2010); featured in, Philip Ball, Web designers, *Nature Materials* **9**, 190 (2010).

[10] Ko Okumura and Pierre-Gilles de Gennes, Why is nacre strong? : Elastic theory and fracture mechanics for biocomposites with stratified structures, *Eur. Phys. J. E* **4** (2001) 121.

# PREPARATION AND PROPERTIES OF HOLLOW INORGANIC SPHERES

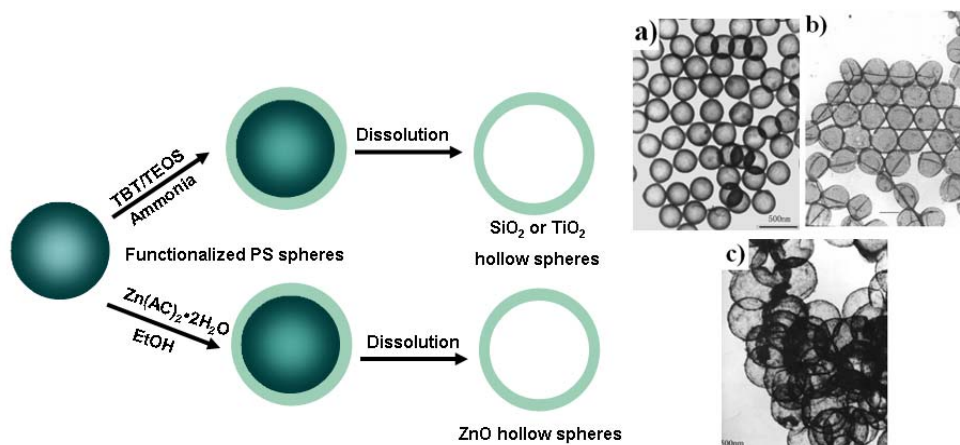
Min Chen, Limin Wu

Department of Materials Science, Advanced Materials Laboratory, Fudan University,  
Shanghai 200433, China. E-mail: Lmw@fudan.edu.cn

Monodisperse hollow spheres have attracted considerable interests in the past decades due to their well-defined morphology, uniform size, low density, high surface areas, and a lot of potential applications. For instance, the large fraction of void space in hollow structures has been usually used to load and control releasing system of some special materials such as drugs, genes, peptides, spiceries and biologic molecules.<sup>1</sup> And it can also be used to modulate refractive index, lower density, increase active area for catalysis and adsorption,<sup>2</sup> improve the particles' ability to withstand cyclic changes in volume, and to expand the array of imaging markers suitable for early detection of cancer.<sup>3</sup>

In contrast to organic polymer hollow spheres, inorganic hollow spheres have special optical, optoelectronic, magnetic, electrical, thermal, electrochemical, photoelectrochemical, mechanical and catalytic properties, herby represent the more common, more diverse, and probably richer class of materials.<sup>4</sup> Since the pioneering works done by Kowalski and colleagues at Rohm and Haas.<sup>5,6</sup> especially in recent ten years, a variety of chemical and physicochemical strategies, including heterophase polymerization/combined with a sol-gel process,<sup>7</sup> emulsion/interfacial polymerization methods,<sup>8-10</sup> self-assembly techniques,<sup>11,12</sup> and surface living polymerization process<sup>13-15</sup> have been employed to prepare inorganic hollow spheres. In particular, template method is the most widely used strategy. In this method, at least two steps are usually indispensable. Firstly, the templates should be modified to confer certain ability to coax inorganic precursor (salt or alkoxide) onto the surface layer of template cores. Then, after the inorganic shell is decorated outside the scaffold, the templates are eliminated, leaving behind a hollow shell. Generally, the templates being used could be divided into hard and soft templates. When hard templates are employed, the structure of hollow product is similar to the templates, with well-defined and monodisperse morphology. But removal of the templates by either thermal (sintering) or chemical (etching) ways is very complicated and energy-consuming. As for soft templates, though, it is relatively easier to remove the templates, the morphology and monodispersity of the as-prepared hollow products are usually poor due to the deformability of soft templates. However, although these drawbacks of template strategies seem to be inherent and insurmountable, some novel techniques such as sacrificial templates, modified soft templates, etc., are emerging to work out these problems. Another important development on the preparation of inorganic hollow spheres are called template-free method such as Ostwald ripening process, which not only combines the advantages of hard- and soft-templates methods, but also escapes from the demerits of these approaches.

In this talk, we will present a one-pot method to synthesize a series of hollow inorganic spheres such as SiO<sub>2</sub>, TiO<sub>2</sub>, ZnO, Ag, Ag/SiO, hybrid, Fe<sub>3</sub>O<sub>4</sub>/ZnS hybrid, as well as PNIPAM/Ag, PS/SiO<sub>2</sub> organic-inorganic hybrid hollow spheres, and further demonstrate their some properties such as catalyst, loading and delivering, photovoltaic properties.<sup>16-22</sup>



**Scheme 1.** Schematic representation for the formation of hollow inorganic spheres.

### References:

- [1] Y. Zhu, J. Shi, W. Shen, X. Dong, J. Feng, M. Ruan and Y. Li, *Angew. Chem. Int. Ed.*, 2005, 44, 5083.
- [2] J. Yuan, K. Laubernds, Q. Zhang and S. L. Suib, *J. Am. Chem. Soc.*, 2003, 125, 4966.
- [3] Y. Zhu, Y. Fang and S. Kaskel, *J. Phys. Chem. C*, 2010, 114, 16382.
- [4] J. Liu, F. Liu, J. Wu and D. Xue, *J. Mater. Chem.*, 2009, 19, 6073.
- [5] A. Kowalski, M. Vogel, R. M. Blankenship, *U. S. Patent* 1884, 4,427,836
- [6] R. M. Blankenship, *U. S. Patent* 1996, 5, 494, 971
- [7] A. Imhof, *Langmuir*, 2001, 17, 3579.
- [8] C. E. Fowler, D. Khushalani and S. Mann, *Chem. Commun.*, 2001, 2028.
- [9] R. K. Rana, Y. Mastai and A. Gedanken, *Adv. Mater.*, 2002, 14, 1414.
- [10] L. Song, X. Ge, M. Wang, Z. Zhang and S. Li, *J. Polym. Sci. Part A: Polym. Chem.*, 2006, 44, 2533.
- [11] C. Chen, S. F. Abbas, A. Morey, S. Sithambaram, L. Xu, H. F. Garces, W. A. Hines and S. L. Suib, *Adv. Mater.*, 2008, 20, 1205.
- [12] M. Zhao, L. Sun and R. M. Crooks, *J. Am. Chem. Soc.*, 1998, 120, 4877.
- [13] Q. Zhou, S. Wang, X. Fan and R. C. Advincula, *Langmuir*, 2002, 18, 3324.
- [14] C. Perruchot, M. A. Khan, A. Kamitsi, S. P. Armes and T. von Werne, *Langmuir*, 2001, 17, 4479.
- [15] T. von Werne and T. E. Patten, *J. Am. Chem. Soc.*, 2001, 123, 7497.
- [16] M. Chen, L. M. Wu, S. X. Zhou, B. You, *Adv. Mater.*, 2006, 18, 801
- [17] Z. X. Wang, S. X. Zhou, L. M. Wu, *Adv. Funct. Mater.*, 2007, 17, 1790
- [18] Z. X. Wang, M. Chen, L. M. Wu, *Chem. Mater.* 2008, 20, 3251
- [19] Z. X. Wang, L. M. Wu, M. Chen, S. X. Zhou, *J. Am. Chem. Soc.*, 2009, 131, 11276
- [20] L. F. Hu, L. M. Wu, X. S. Fang, *Adv. Mater.*, 2011, 23, 1988
- [21] D. Hu, M. Chen, Y. Gao, F. Y. Li, L. M. Wu, *J. Mater. Chem.* 2011, DOI:10.1039/C1JM11172H
- [22] M. Chen, L. F. Hu, J. X. Xu, L. M. Wu, X. S. Fang, *Small.*, 2011, in press

## Non-traditional Bio-inspired Adhesion and Synthetic Morphogenesis

Michael Bartlett<sup>1</sup>, Andrew B. Croll<sup>2</sup>, Daniel King<sup>1</sup>, Beth Paret<sup>1</sup>, Derek Breid<sup>1</sup>, Chelsea Davis<sup>1</sup>,  
Duncan Irschick<sup>3</sup>, Alfred J. Crosby<sup>1</sup>

<sup>1</sup>Polymer Science & Engineering, University of Massachusetts Amherst, USA

<sup>2</sup>Department of Physics, North Dakota State University, USA

<sup>3</sup>Department of Biology, University of Massachusetts Amherst, USA

Nature provides awe-inspiring lessons in designing materials structures from simple building blocks to achieve necessary performance. In this paper, we will summarize two current projects that represent broader efforts within our research group to learn from Nature not only in the design of materials but also in concepts that lead to fundamental understanding of materials properties. The first project focuses on the challenge of developing scalable adhesive interfaces that have the ability to sustain high loads, yet release with minimal energy loss. The second project explores the possibility of adapting shape-forming strategies found in the development of biological tissues into scalable manufacturing processes for fabricating advanced surface structures at small length scales.

Over the past decade or more, a concerted international effort among academic, government, and industrial research laboratories has focused on developing adhesives that display similar attributes to those presented by biological organisms that use adhesion in the process of locomotion. The best known example in Nature is the gecko, yet numerous organisms ranging from beetles to spiders to lizards display similar impressive capabilities. A unifying feature among these examples is the presentation of fibrillar features, which are primarily made from keratin, a rigid protein material. Although significant progress has been made in developing synthetic analogs to these fibrillar surface features, the ability to produce materials that can be scaled to macroscopic sizes while maintaining “gecko-like” attributes has not been demonstrated convincingly. This difficulty suggests that other key lessons must be learned from Nature.

We have experimentally and analytically investigated the fundamental mechanisms of adhesion that link organisms that range in mass over five orders of magnitude. We have developed a scaling theory to link the maximum sustainable force for an adhesive interface as a function of three continuum-level parameters: 1) the interfacial adhesion energy; 2) the interfacial area; and 3) the compliance of the system. The principles of this scaling relationship will be presented, as well as our ability to quantitatively link the maximum sustainable interfacial force for components in Nature from spatula (~100nm) to whole body organisms (~10cm).

Similar to the inspiration provided by high performing adhesive examples in Nature, we also take inspiration from Nature in developing methods to fabricate complicated hierarchical structures, both surface and near-surface, in a scalable manner. One intriguing example is

the process of fingerprint formation in mammals.[1] Fingerprints form due to a differential growth rate between two cell layers of the skin during the first twenty weeks of development. This difference in growth rates between neighboring layers leads to the development of a compressive stress near the interface. Upon reaching a critical stress level, related to the onset of an elastic buckling instability, the skin layers wrinkle to form the fingerprint. The dimensions of the fingerprint patterns can be related to the dimensions and properties of the cell layers.

In our research [2-5], we have focused on understanding the relationship between materials properties, geometry, and stress state in controlling the formation of wrinkle-based patterns in soft synthetic materials. We present here experiments on composite materials comprised of a thin stiff film attached to a soft elastomeric substrate. Due to differential swelling, a compressive stress develops at the film/substrate interface and wrinkling develops at a critical stress level, defined by the elastic modulus mismatch. We can systematically change the morphology of the wrinkle patterns, as shown in Fig. 1. The change in morphology is quantitatively linked to two control parameters: 1) the ratio of applied stress to the critical stress for elastic instability; 2) the ratio of the primary in-plane stresses. We have performed experiments on similarly wrinkled systems to quantify the impact and mechanism for controlling adhesion through the use of wrinkles.[6-8]

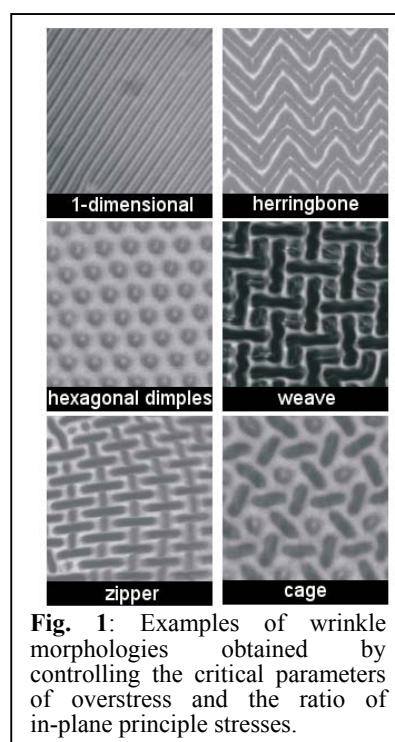


**Fig. 1:** Examples of wrinkle morphologies obtained by controlling the critical parameters of overstress and the ratio of in-plane principle stresses.

- [1] Kucken M., & Newell, A. (2005). Fingerprint formation. *Journal of Theoretical Biology*, 235(1), 71-83.
- [2] Chan, E. P., & Crosby, Alfred J. (2006). Spontaneous formation of stable aligned wrinkling patterns. *Soft Matter*, 2(4), 324-328.
- [3] Chan, E. P., & Crosby, A.J. (2006). Fabricating Microlens Arrays by Surface Wrinkling. *Advanced Materials*, 18(24), 3238-3242.
- [4] Breid, Derek, & Crosby, Alfred J. (2009). Surface wrinkling behavior of finite circular plates. *Soft Matter*, 5(2), 425.
- [5] Breid, Derek, & Crosby, Alfred J. (2011). Effect of Stress State on Wrinkle Morphology. *Soft Matter*, 7(9), 4490-4496.
- [6] Chan, E. P., Smith, E. J., Hayward, R. C., & Crosby, A.J. (2008). Surface Wrinkles for Smart Adhesion. *Advanced Materials*, 20(4), 711-716.
- [7] Kundu, S., Davis, C. S., Long, T., Sharma, R., & Crosby, Alfred J. (2011). Adhesion of nonplanar wrinkled surfaces. *J. Polymer Science Part B: Polymer Physics*, 49(3), 179-185.
- [8] Davis, C. S., & Crosby, Alfred J. (2011). Mechanics of Wrinkled Surface Adhesion. *Soft Matter*, 7(11), 5373-5381.

## Bio-inspired bonding technologies

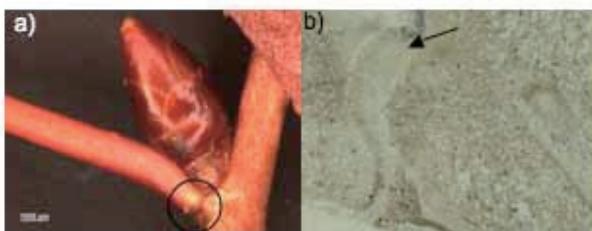
Naoe Hosoda

Hybrid Materials Unit, National Institute for Materials Science, Japan

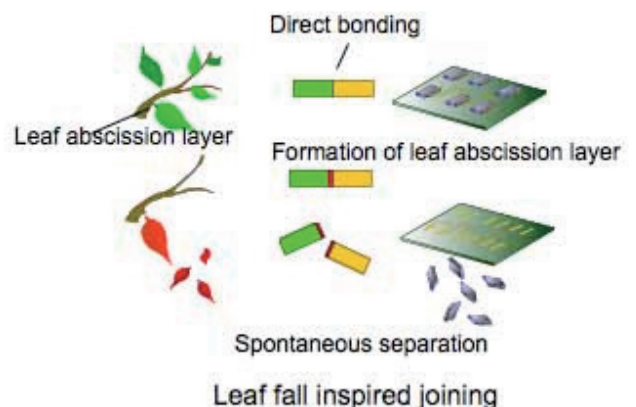
Designing for separation at the interface of a joint is an essential problem for realizing the recycle smoothly. If joints are separated easily at the interface, the recycle of materials is performed with energy-saving. However, it is difficult to separate the parts joined by a conventional bonding method. On the other hand, there are excellent structures of attachment and detachment in the natural world.

Flies, spiders, leaf beetles and lizards have the ability to attach and detach easily to the various surfaces and ceilings and even smooth window glass. Deciduous trees possess a excellent design for easy disassembly, in which they spontaneously shed their leaves and fruits. Deciduous tree leaf developed a special layer at a base of leaf petiole, called by abscission layer, for shedding leaves. The aim of our research is to develop technologies which enable easy attachment/detachment by researching these kinds of natural mechanisms.

We present our research subject about an adhesive attachment system of animals, abscission of leaves and its mimetic joining technologies. The falling leaf inspired joining technology was developed by making an abscission layer at the bonding interface. The abscission layer is controlled using a field such as magnetic field, electric field, gravitation field, microwave, ambient atmosphere of gases and temperatures. Under the field, the abscission layer becomes brittle. In consequence the joint separates spontaneously. We present three methods for reversible interconnections by 1) growing a brittle abscission layer by a heat treatment, 2) using hydrogen atmosphere to be brittle the abscission layer, and 3) by liquid metal embrittlement of the abscission layer using gallium.



a) A base of leaf petiole of *Prunus jamasakura*.  
 b) The cross section of the encircled position in a). The arrow shows an abscission layer.



## Effect of Silica Particles on the Electrical Conductivity of Silver Nanoparticle/epoxy Conductive Adhesives

Seungwoong NAM<sup>2</sup>, Daeheum KIM<sup>2</sup>, Heesuk KIM<sup>1</sup>, Soonho LIM<sup>1\*</sup>

<sup>1</sup> Nanohybrid Research Center, Korea Institute of Science & Technology, Seoul 136-791, Korea

<sup>2</sup> Department of Chemical Engineering, Kwang Woon University, Seoul 139-701, Korea

\* [lim41357@gmail.com](mailto:lim41357@gmail.com)

Isotropic conductive adhesives (ICAs) have numerous advantages over traditional Sn/Pb solder as they require fewer processing steps and lower processing temperature, allowing the preparation of heat-sensitive and low-cost chip carriers with fine-pitch capability.<sup>1</sup> However, their high electrical resistivity and poor mechanical properties have hindered development.<sup>2</sup>

A novel method of improving the electrical conductivity of epoxy/silver nanocomposites by adding silica particles was explored experimentally and theoretically. Silica particles significantly decreased both the electrical percolation threshold concentration of silver nanoparticles and the electrical resistivity of the composite. They also enhanced thermomechanical properties, such as CTE. Molecular simulations demonstrated that effective intermolecular interactions between silver nanoparticles become more attractive with increasing the content of silica particles, aiding the formation of electrical percolation networks.

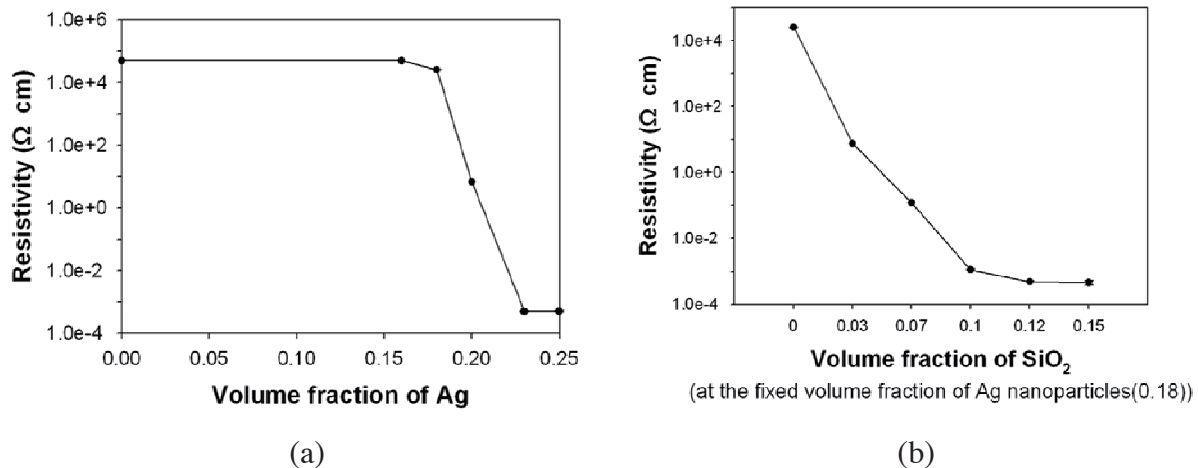


FIGURE. Electrical resistivity as a function of the volume fractions of (a) silver nanoparticles and (b) additional silica particles at the fixed volume fraction of silver nanoparticles (0.18) in nanocomposites

### References

1. C. M. L. Wu, R. K. Y. Li, and N. H. Yeung, *Journal of Electronic Packaging* **124** (4), 374 (2002).
2. M. Zwolinski, J. Hickman, H. Rubin, Y. Zaks, S. McCarthy, T. Hanlon, P. Arrowsmith, A. Chaudhuri, R. Hermansen, S. Lan, and D. Napp, *Components, Packaging, and Manufacturing Technology, Part C, IEEE Transactions on* **19** (4), 241 (1996).



## Development of Self-Organized Inorganic/Organic Hybrid Materials

Takashi Kato

Department of Chemistry and Biotechnology, School of Engineering,

The University of Tokyo, Japan

Biomaterials are inorganic/organic hybrids exhibiting a variety of functions.[1] The hierarchical structures and formation processes of biomaterials have inspired researchers to develop functional hybrid materials processed through mild conditions. The interactions between organic and inorganic components play key roles to form the hybrids.[1,2] Here we report on our recent approaches to the development of new inorganic/organic hybrid materials. Thin-film hybrids with flat surfaces comprising  $\text{CaCO}_3$  crystals are obtained by using macromolecular templates by solution processes. The hybrids of  $\text{CaCO}_3$  and organic polymers form the thin films having a wide variety of morphologies.[2] Oriented  $\text{CaCO}_3$  crystals are obtained by employing an acidic natural peptide isolated from the exoskeleton of a crayfish,[3] or in a liquid crystalline chitin matrix.[4] Patterned thin-film and 3D complex structures of hybrids can be formed in hydrogel matrices (Fig. 1).[5] The amorphous transparent hybrids of  $\text{CaCO}_3$  and acidic macromolecules are also formed under mild conditions.[6] These approaches can be applied to the preparation of the hybrid materials of a variety of inorganic crystals and organic functional macromolecules.[7] In these bioinspired self-organization processes, the control of macromolecular structures and their interactions is essential. These self-organized hybrid materials have great potential in a wide variety of fields of advanced technologies.

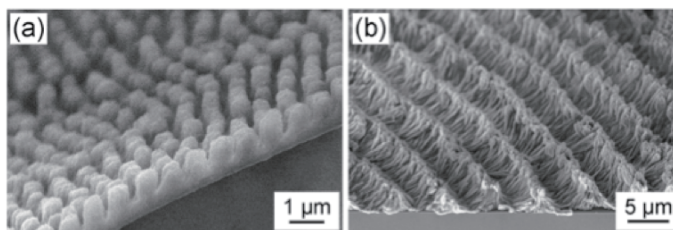


Fig. 1. SEM images of self-organized  $\text{CaCO}_3$ -based hybrid materials with (a) patterned structures[5b] and (b) 3D complex assemblies[5c] of needle-like nanocrystals obtained on functional polymer gel matrices.

[1] E. Bäuerlein, P. Behrens, M. Epple, Eds. *Handbook of Biomineralization*, Wiley-VCH, Weinheim, 2007.

[2] a) T. Kato, T. Sakamoto, T. Nishimura, *MRS Bulletin*, **35**, 127 (2010); b) T. Kato, A. Sugawara, N. Hosoda, *Adv. Mater.*, **14**, 869 (2002); c) T. Kato, *Adv. Mater.*, **12**, 1543 (2000).

[3] a) A. Sugawara, T. Nishimura, Y. Yamamoto, H. Inoue, H. Nagasawa, T. Kato, *Angew. Chem. Int. Ed.*, **45**, 2876 (2006); b) Y. Yamamoto, T. Nishimura, A. Sugawara, H. Inoue, H. Nagasawa, T. Kato, *Cryst. Growth Des.*, **8**, 4062 (2008).

[4] a) T. Nishimura, T. Ito, Y. Yamamoto, M. Yoshio, T. Kato, *Angew. Chem. Int. Ed.*, **47**, 2800 (2008); b) Y. Yamamoto, T. Nishimura, T. Saito, T. Kato, *Polym. J.*, **42**, 583 (2010).

[5] a) T. Sakamoto, Y. Nishimura, T. Nishimura, T. Kato, *Angew. Chem. Int. Ed.*, **50**, 5856 (2011); b) A. Sugawara, T. Ishii, T. Kato, *Angew. Chem. Int. Ed.*, **42**, 5299 (2003); c) T. Sakamoto, A. Oichi, Y. Oaki, T. Nishimura, A. Sugawara, T. Kato, *Cryst. Growth Des.*, **9**, 622 (2009).

[6] Y. Oaki, S. Kajiyama, T. Nishimura, H. Imai, T. Kato, *Adv. Mater.*, **20**, 3633 (2008).

[7] Y. Oaki, S. Kajiyama, T. Nishimura, T. Kato, *J. Mater. Chem.*, **18**, 4140 (2008).

## Stereocomplexed Poly(L-lactic acid)/Poly(D-lactic acid) as Morphology and Crystallization Modifier for Biodegradable Polymers

Eamor M. Woo\*, Ling Chang, Siti Nurkhamidah

Department of Chemical Engineering, National Cheng Kung University, Tainan, 701-01,  
Taiwan [emwoo@mail.ncku.edu.tw](mailto:emwoo@mail.ncku.edu.tw)

ASAM-3, Fukuoka, Japan, Sept. 19-22, 2011

Crystallization kinetics, morphology and crack tendency in stereocomplexing poly(L- and D-lactic acid) (PLLA and PDLA) mixtures crystallized in presence of amorphous molten poly(hydroxyl butyrate) (PHB) or pre-crystallized sc-PLA complex as crystalline templates were studied by differential scanning calorimetry (DSC), polarizing-light optical microscopy (POM), atomic force microscopy (AFM) and wide-angle X-ray diffraction (WAXD). The PHB/sc-PLA blend system shows a single composition-dependent  $T_g$  in all composition, indicating miscibility and interactions between PHB and sc-PLA. This mutual interaction leads to that crystallization growth of sc-PLA in blends is hindered by presence of molten PHB at  $T_c$  and the final morphology of the sc-PLA complexes is significantly altered. When crystallized at high  $T_c$  (130°C or above), morphology transition of stereocomplexed PLA (sc-PLA) occurs from original well-rounded Maltese-cross spherulites to dendritic form in blends of high PHB contents (50 wt% or higher), where PHB acts as an amorphous species. Microscopy characterizations show that morphology sc-PLA in PHB/sc-PLA blends crystallized at  $T_c=170^\circ\text{C}$  no longer retain original complexed Maltese-cross well-rounded spherulites; instead, the spherulites are disintegrated and restructured into two types of dendrites: (1) edge-on feather-like dendrites (early growth) and (2) flat-on wedge-like crystal plates (later growth) by growing along different directions and exhibiting different optical brightness. The concentration and/or distribution of amorphous PHB at the crystal growth front, corresponding to variation of the slopes of spherulitic growth rates, is a factor resulting in alteration and restructuring of the sc-PLA spherulites in the blends. Despite of spherulite alteration, WAXD result shows that these two PHB-induced dendrites still retain the original unit cells of complexes, and thus these two new dendrites are sc-PLA. Interestingly, growth of the flat-on wedge-like dendrites is much slower than edge-on feather-like dendrites. These results indicate that the concentration and/or distribution of the PHB (amorphous diluents) at the crystal growth front corresponding to variation of the slopes of spherulitic growth rates is a factor which results in the different orientation of sc-PLA lamellae in blends. **[Figures 1,2]**

Complex morphology was found to be influenced by presence of excess constituent in mixtures of PLLA and PDLA. Non-equimolar PLLA/PDLA compositions lead to co-crystallization of homo-PLLA and sc-PLA crystals. Introduction of stereocomplex poly(lactic acid) (sc-PLA) crystals either as small nuclei or large sc-PLA spherulites has great influence on patterning the inter-phase boundaries and reducing the cracks in crystallized poly(L-lactic acid) (PLLA) in mixtures with poly(D-lactic acid) (PDLA). It was found that unmelted sc-PLA crystals as small nuclei induce interlamellar cracks in the later-crystallized PLLA crystals tending to develop dendritic spherulites. On the other hand, crystallization of PLLA on pre-crystallized stable well-rounded sc-PLA spherulites as templates lead to overlapped spherulites with no cracks at all. Effects of the sc-PLA crystals on the crystal lamellar inter-phases for reducing the cracks are to be discussed, as time permits.

Crystallization kinetics behavior and morphology of poly(3-hydroxybutyrate) (PHB) blended with of 2-10 wt% loadings of poly(L- and D-lactic acid) (PLLA and PDLA) stereocomplex crystallites, as biodegradable nucleating agents, were studied. **[Figure 3]** Blending PLLA with PDLA at 1:1 weight ratio led to formation of stereocomplexed PLA (sc-

PLA), which was incorporated as small crystalline nuclei into PHB for investigating melt-crystallization kinetics. The Avrami equation was employed to analyze the isothermal crystallization of PHB. The stereocomplexed crystallites acted as nucleation sites in blends, and accelerated the crystallization rates of PHB by increasing the crystallization rate constant  $k$  and decreasing the half-time ( $t_{1/2}$ ). The PHB crystallization was nucleated most effectively with 10 wt% stereocomplexed crystallites, as evidenced by POM results. The sc-PLA complex nucleated PHB crystals exhibit much small spherulite sizes but possess the same crystal cell morphology as that of neat PHB based on the WAXD result.

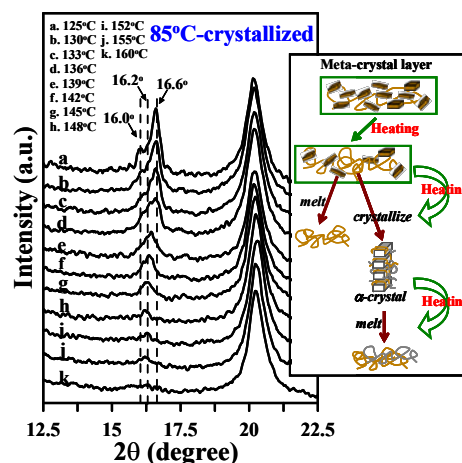
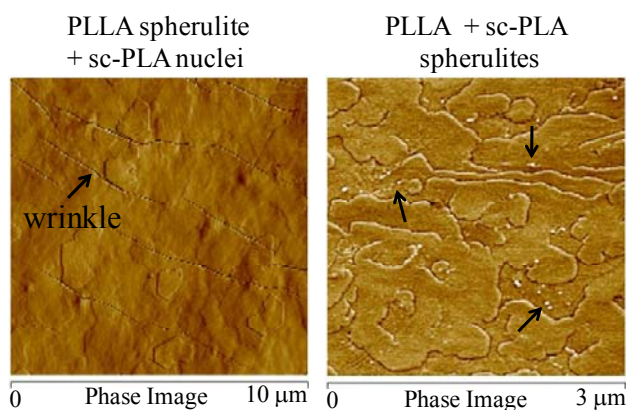


**Figure 1.** AFM phase morphology showing PLLA crystallizing with: (Left) small sc-PLA nuclei, (Right) spherulitic sc-PLA as thin template.

**Figure 2.** Temperature-dependent WAXD profiles for 85°C-crystallized PLLA/LM<sub>w</sub>-PLLA blend.

L. Chang and E. M. Woo, *Macromol. Chem. Phys.*, published on web (2011). DOI: 10.1002/macp.201000375.

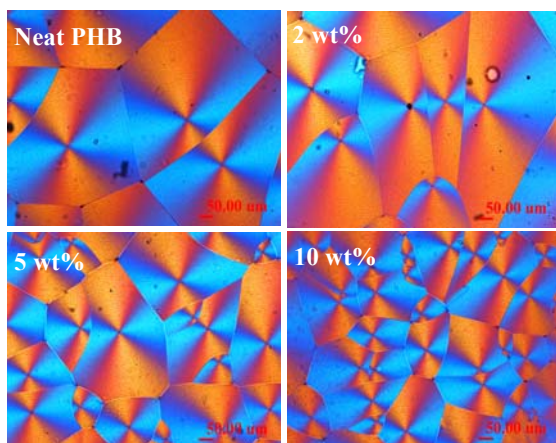


**Figure 3.** POM graphs of spherulites of neat PHB and blends with 2-10 wt% sc-PLA contents isothermally melt-crystallized at 80°C.

## Nanoporous and Nanohybrid Materials from Chiral Block Copolymer Templating

Rong-Ming Ho

Department of Chemical Engineering, National Tsing Hua University, Hsinchu, Taiwan

Block copolymers comprising chiral entities, denoted as chiral block copolymers (BCP\*s), were designed to fabricate helical architectures from self-assembly.[1] A helical phase (denoted H\* to distinguish its P622 symmetry from that of the normal hexagonally packed cylinder phase) was discovered in the self-assembly of poly(styrene)-*b*-poly(L-lactide) (PS-PLLA) BCPs\*.[2] The phase behavior of the PS-PLLA BCPs\* was systematically examined. Moreover, by taking advantage of the degradable character of the PLLA blocks, well-defined nanoporous polymeric materials having various nanostructures including cylinder, H\* and double gyroid lamellae can be fabricated by hydrolysis, and treated as templates. Reactions such as sol-gel reaction and electroless plating can be carried out within the templates for the manufacturing of various nanostructured hybrids. As demonstrated, well-defined nanohybrids with hexagonally packed SiO<sub>2</sub> nanohelices embedded in a PS matrix can be fabricated through templated sol-gel reaction.[3] Also, nanoporous gyroid SiO<sub>2</sub> network materials can be prepared through BCP templating with porosity over 60% after removal of the PS template so as to create extremely low-n materials for antireflection structure.[4] Similar approach can also be carried out for the fabrication of nanoporous metallic materials.[5] As a result, a platform technology to fabricate various well-defined nanohybrids and nanostructured porous materials having control of feature shape and size can be established. A variety of well-defined nanostructures with different constituted components, such as polymer/metals, and polymer/ceramics can be created to give a “Materials Library” for practical applications in nanotechnologies.

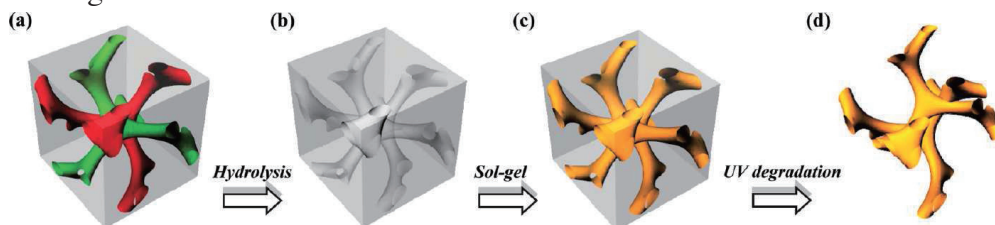


Fig. 1. Schematic illustration for the creation of well-defined nanoporous gyroid SiO<sub>2</sub> from BCP templating. (a) PS-PLLA gyroid morphology (skeleton of double gyroid structure with two identical networks (green and red)). (b) Gyroid-forming nanoporous PS template after the removal of minority PLLA network. (c) PS/SiO<sub>2</sub> gyroid nanohybrids via the templated sol-gel process. (d) Nanoporous gyroid SiO<sub>2</sub> after the UV removal of PS template.

- [1] R.-M. Ho, Y.-W. Chiang, S.-C. Lin, C.-K. Chen *Prog. Polym. Sci.*, **36**, 376 (2011).
- [2] R. -M. Ho, Y. -W. Chiang, C. -K. Chen, H. -W. Wang, H. Hasegawa, S. Akasaka, E. -L. Thomas, C. Burger, B. -S. Hsiao *J. Am. Chem. Soc.*, **131**, 18533 (2009)
- [3] W. -H. Tseng, C. -K. Chen, Y. -W. Chiang, R. -M. Ho, Akasaka S, Hasegawa H *J. Am. Chem. Soc.*, **131**, 1356 (2009)
- [4] H. -Y. Hsueh, H. -Y. Chen, C. -K. Chen, R. -M. Ho, S. Gwo, S. Akasaka, H. Hasegawa *Nano Letters*, **10**, 4994 (2010).
- [5] H.-Y. Hsueh, Y.-C. Huang, R.-M. Ho, C.-H. Lai, T. Makida, H. Hasegawa *Adv. Mater.*, in press (2011).

## DNA-based Soft Interface for Biosensing

Mizuo Maeda<sup>1</sup>

<sup>1</sup>Bioengineering Laboratory, RIKEN Advanced Science Institute, RIKEN, Hirosawa 2-1, Wako, Saitama 351-0198, Japan

DNA-modified nanoparticles disperse in an aqueous medium due to electrostatic repulsion between anionic phosphate groups in the DNA backbone. Interestingly, when complementary single-stranded DNA, whose base number is identical to that of the DNA on the surface, is added to the dispersion of DNA nanoparticles to form the fully matched double helix on the surface, the DNA nanoparticles become unstable and spontaneously form aggregates in a non-crosslinking manner [1].

Furthermore, we have found that the double-stranded DNA-carrying nanoparticles acquire high colloidal stability to disperse in an aqueous medium when a terminal single-base mismatch exists at the interface between the DNA corona and the disperse medium. Exploiting the unique colloidal behavior of the DNA nanoparticles, we have devised a facile single-nucleotide polymorphism genotyping method [2-4].

We applied the SPR imaging technique on our original, power-free microfluidic devices to the detection of the nanoparticles aggregation [5, 6]. Through a combination of non-crosslinking aggregation of DNA nanoparticles and molecular recognition by aptamers or aptazymes, we have also developed analytical systems for detecting cGMP, ATP, FMN, theophyllin [7, 8], and Hg(II) [9]. These analytical functions are designed based on unique properties of soft interface made from relatively-dense assembly of DNA strands.

- [1] K. Sato, K. Hosokawa, M. Maeda, *J. Am. Chem. Soc.*, 125, 8102-8103 (2003).
- [2] K. Sato, K. Hosokawa, M. Maeda, *Nucleic Acids Research*, 33, e4 (2005).
- [3] K. Sato, M. Onoguchi, Y. Sato, K. Hosokawa, M. Maeda, *Anal. Biochem.*, 350, 162-164, (2006).
- [4] K. Hosokawa, K. Sato, N. Ichikawa, M. Maeda, *Lab Chip*, 4, 181-185 (2004).
- [5] Y. Sato, K. Sato, K. Hosokawa, M. Maeda; *Anal. Biochem.*, 355, 125-131 (2006).
- [6] Y. Sato, K. Hosokawa, M. Maeda, *Colloids Surf., B*, 62, 71-76 (2008).
- [7] A. Ogawa, M. Maeda, *Bioorg. Med. Chem. Lett.*, 18, 6517-6520 (2008).
- [8] A. Ogawa, M. Maeda, *Chem. Commun.*, 4666-4668 (2009)
- [9] N. Kanayama, T. Takarada, M. Maeda, *Chem. Commun.*, 47, 2077-2079 (2011).

## Synthesis of Aerogel Nanooxides with Unique Adsorptive and Catalytic Properties

Aleksey Vedyagin<sup>1,2</sup>, Alexander Bedilo<sup>1</sup>, Ilya Mishakov<sup>1,2</sup>, Ekaterina Ilyina<sup>1</sup>

<sup>1</sup>Boreskov Institute of Catalysis SB RAS, Russia

<sup>2</sup>Novosibirsk State Technical University, Russia

Aerogels are materials synthesized by drying of gels in supercritical conditions, i.e. in the absence of the superficial tension, so that the collapse of the pore structure can be avoided. This technology yields materials with small particles size, very high surface area, along with a considerable quantity of superficial defects and low density. This makes them very promising for application as adsorbents and catalysts. It is well known that physicochemical properties of very small oxide crystals substantially depend on their size. Various nanocrystalline oxides synthesized by aerogel technique have been widely investigated as destructive sorbents for decomposition of harmful organic substances [1-4], neutralizations of bacteria [5], as well as in various catalytic processes [6-9].

In the most general understanding, a sol-gel process implies the formation of disordered and branched network of particles (gel) from a precursor solution via a system of colloidal particles (sol) [10]. As a rule, aerogels are synthesized by a widely spread technique based on the use of such organometallic reagents as alkoxides,  $\beta$ -ketonates and carboxylates of metals. Alkoxides are applied most often for synthesis of nanocrystalline oxides. In this case it is possible to avoid using water as the solvent leaving the whole set of parameters free to be controlled. These parameters can be varied to tune the desired properties of resulting gels.

Reagents used for modifying metal alkoxides in sol-gel processes can play two roles. They are often applied to control the reaction rates, influencing thereby the microstructure as well as the homogeneity degree of the obtained gels. In this case modifiers are to be completely removed at the following calcination, leading to synthesis of the corresponding oxides. However, they can be used also for preparation of materials containing functional groups or any other tailored phase.

The described method can be also applied for preparation of nanoscale oxide particles with carbon coating on their surface. The main advantage of such approach is that in this case organic groups are already anchored to the surface of the oxide nanocrystals. Their rather homogeneous distribution can lead to higher number of nuclei during pyrolysis, leading to the formation of extremely small carbon nanoparticles. According to high resolution TEM data (Fig. 1 left), calcined alumina aerogels consist of thin roundish plates about 2 nm thick and ~ 10 nm in diameter.

Sulfated alumina aerogels were synthesized by a similar procedure with sulfuric acid used as a modifying agent. The introduction of sulfuric acid to the solution before gelation results in a substantial decrease of the pore volume, whereas the high surface area of the  $\text{Al}_2\text{O}_3$  aerogels is preserved. The surface areas of the sulfated alumina aerogels after calcination at 600°C usually required to make active acid catalysts was about 600 m<sup>2</sup>/g. This value appears to the highest ever reported for sulfated alumina catalysts and is 2-3 times higher than those reported in the literature.

The synthesized sulfated alumina aerogels showed excellent catalytic activity in dehydrochlorination of 1-chlorobutane, substantially exceeding those of conventionally prepared materials. Also they showed outstanding performance in the destructive sorption in destructive adsorption of (2-chloroethyl)ethyl sulfide that is a mustard gas mimic. 2-CEES conversion rate in pentane solution at room temperature over sulfated aerogel alumina was 3 times higher than on  $\text{Al}_2\text{O}_3$  aerogel and 8 times higher than on MgO aerogel.

The aerogel technique can be successfully applied for synthesis of mixed nanocrystalline

oxide systems. For example, it allowed us to prepare VO<sub>x</sub>/MgO materials possessing exceptionally uniform distribution of vanadium in the MgO structure at a wide range of V/Mg ratios [11]. The synthesized samples of corresponding aerogel hydroxides VMg(OH)<sub>x</sub> are characterized by very high specific surface area (~ 1200 m<sup>2</sup>/g). Dehydration of aerogel VMg(OH)<sub>x</sub> hydroxides in mild conditions results in the formation of VO<sub>x</sub>/MgO samples with high surface area (~ 450 m<sup>2</sup>/g) consisting of cubic crystals with the size below 5 nm (Fig. 1 right). The synthesized mixed aerogels showed superior performance in oxidative dehydrogenation of propane substantially exceeding that of similar materials prepared by impregnation.

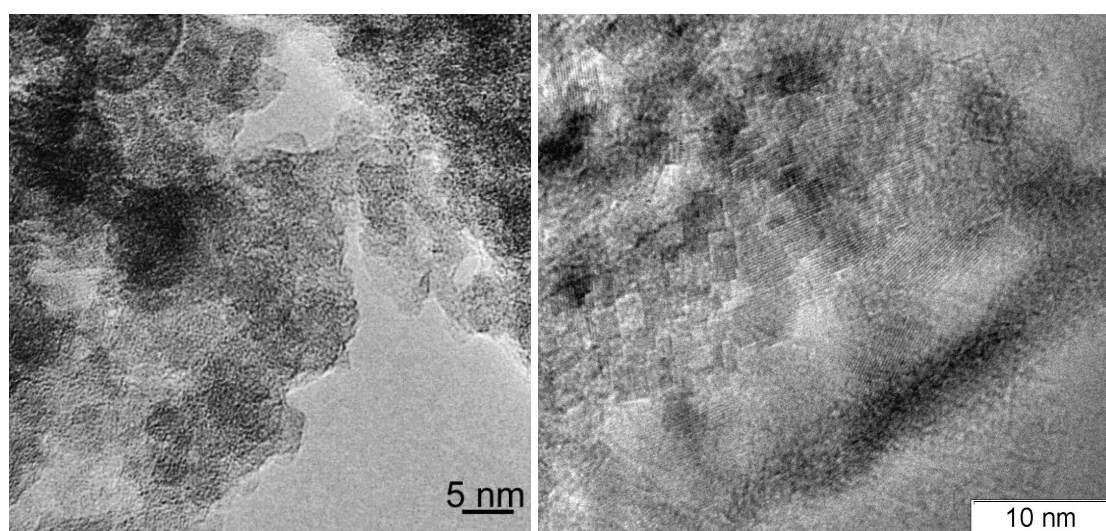


Figure 1. TEM images of aerogel alumina (left) and aerogel 15 wt.% VO<sub>x</sub>/MgO (right).

In the present work the general approach for the preparation of different oxide systems (MgO, Al<sub>2</sub>O<sub>3</sub> etc.) using aerogel technique has been briefly described. Investigation of the effect of reaction conditions on the properties of nanocrystalline oxides allowed us to control better their properties and to synthesize materials with higher surface area and smaller particle size.

- [1] K. J. Klabunde, J. Stark, O. Koper, C. Mohs, D. G. Park, S. Decker, Y. Jiang, I. Lagadic, D. J. Zhang, *J. Phys. Chem.*, **100**, 12142 (1996).
- [2] A. Khaleel, P. N. Kapoor, K. J. Klabunde, *Nanostruct. Mater.*, **11**, 459 (1999).
- [3] R. Richards, W. F. Li, S. Decker, C. Davidson, O. Koper, V. Zaikovski, A. Volodin, T. Rieker, K. J. Klabunde, *J. Am. Chem. Soc.*, **122**, 4921 (2000).
- [4] A. F. Bedilo, M. J. Sigel, O. B. Koper, M. S. Melgunov, K. J. Klabunde, *J. Mater. Chem.*, **12**, 3599 (2002).
- [5] P. K. Stoimenov, R. L. Klinger, G. L. Marchin, K. J. Klabunde, *Langmuir*, **18**, 6679 (2002).
- [6] A. F. Bedilo, K. J. Klabunde, *Nanostruct. Mater.*, **8**, 119 (1997).
- [7] V. V. Chesnokov, A. F. Bedilo, D. S. Heroux, I. V. Mishakov, K. J. Klabunde, *J. Catal.*, **218**, 438 (2003).
- [8] I. V. Mishakov, A. F. Bedilo, R. M. Richards, V. V. Chesnokov, A. M. Volodin, V. I. Zaikovskii, R. A. Buyanov, K. J. Klabunde, *J. Catal.*, **206**, 40 (2002).
- [9] I. V. Mishakov, A. A. Vedyagin, A. F. Bedilo, V. I. Zailovskii, K. J. Klabunde, *Catal. Today*, **144**, 278 (2009).
- [10] S.J. Teichner, *Chemtech* 372, 1991.
- [11] E. V. Ilyina, I. V. Mishakov, A. A. Vedyagin, *Inorg. Mater.*, **45**, 1267 (2009).

## Design of Novel Advanced Materials Based on Soluble Carbon Nanotubes

Naotoshi Nakashima

Department of Applied Chemistry, Graduate School of Engineering & WPI-I2CNER, Kyushu University, Fukuoka 819-0395, Japan  
Japan Science and Technology Agency, CREST

Carbon nanotubes (CNTs) are made of rolled-up graphene sheets with one-dimensional extended p-conjugated structures and have been central materials in the field of nano-materials science and nanotechnology because of their remarkable electronic, mechanical and thermal properties that far exceed existing materials. One of the key issues in the utilization of such a seminal materials for basic researches together with their potential applications is to develop a methodology to solubilize/disperse them in solvents.[1]

After brief description about the strategy to solubilize CNTs in solution, we report our recent study on the design and fabrication of novel CNT/polymer nanohybrids and their applications. The topics are the following.

- i) Determination of precise electronic states of individually dissolved single-walled carbon nanotubes (SWNTs) [2,3]
- ii) SWNT chirality recognition/extraction by polymers[4]
- iii) High conductive transparent SWNT ultrathin films[5]
- iv) CNTs/polymer gel-near IR responsive materials [6]
- v) Electrocatalyst for fuel cell using soluble CNTs[7]

[1] N. Nakashima, Y. Tanaka, T. Fujigaya, "Solubilized Carbon Nanotubes and Their Redox Chemistry", in *Carbon Nanomaterials*, Ed. by F. D'Souza and K. M. Kadish, World Scientific, pp. 245-269, 2011.

[2] Y. Tanaka, Y. Hirana, Y. Niidome, K. Kato, S. Saito, N. Nakashima, *Angew. Chem. Int. Ed.* **48**, 7655-7659 (2009) .

[3] Y. Tanaka, Y. Hirana, Y. Niidome, K. Kato, S. Saito, N. Nakashima, *Angew. Chem. Int. Ed.* **48**, 7655-7659 (2009) .

[4] a) Y. Kato, Y. Niidome, and N. Nakashima, *Angew. Chem. Int. Ed.*, **48**, 5435-5438 (2009); b) H. Ozawa, T. Fujigaya, Y. Niidome, N. Hotta, M. Fujiki, N. Nakashima, *J. Am. Chem. Soc.*, **133** (8), 2651-2657 (2011).

[5] Q. Liu, T.Fujigaya, H.-M. Cheng, and N. Nakashima, *J. Am. Chem. Soc.*, **132**, 16581-16586 (2010).

[6] a) T. Fujigaya, T.Morimoto, N. Nakashima, *Soft Matter*, **7**, 2647-2652 (2011). b) T. Sada, T. Fujigaya, Y. Niidome, K. Nakazawa, Kohji, N. Nakashima, *ACS Nano*, in press.

[7] a) K. Matsumoto, T. Fujigaya, H. Yanagi and N. Nakashima", *Adv. Functional Mater.*, **21**, 1089-1094 (2011). b) K. Matsumoto, T. Fujigaya, K. Sasaki and N Nakashima, *J. Mater. Chem.*, **21**, 1187-1190 (2011).



## Well-defined Stimuli Responsive Polymers

Miseon Jung, Taeyoon Kim, Ildoo Chung  
 Department of Polymer Science and Engineering,  
 Pusan National University, Busan 609-735, Korea

Among the techniques that allow the synthesis of well-defined homopolymers and copolymers, atom transfer radical polymerization (ATRP) is one of the most useful systems, due to its tolerance of impurities, the ready availability of many kinds of initiators, catalysts and monomers, its mild reaction conditions, and its ability to produce polymers with predetermined molecular weights and narrow polydispersities.

This paper describes the successful polymerization of well-defined stimuli responsive di- and tri-block copolymers based on amino acid or poly(ε-caprolactone), which were synthesized from cyclodextrin and polyether glycol via ATRP under near physiological conditions using various water soluble initiators with high yield and narrow molecular weight distributions.

Their lower critical solution temperatures (LCST) were determined by cloud point measurements over a range of pH environments. <sup>1</sup>H NMR spectroscopy, static light scattering, and gel permeation chromatography were used to determine polymer molecular weight and polydispersities.

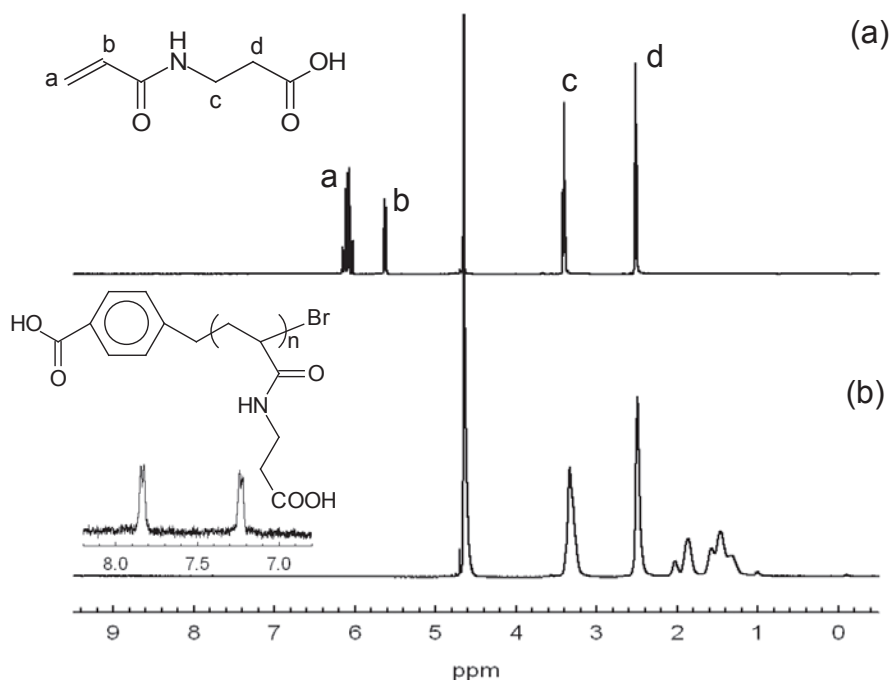


Fig. 1. <sup>1</sup>H NMR spectra of (a) ABA monomer and (b) its homopolymer synthesized by ATRP at ambient temperature (D<sub>2</sub>O).

## Nano Fabrication using Block Copolymers: Nanoparticles, Nano-composites, and Nano-porous Materials

Jae-Suk Lee

Department of Nanobio Materials and Electronics and School of Material Science and Engineering, Program for Integrated Molecular System (PIMS), Gwangju Institute of Science and Technology (GIST), 261 Cheomdan-gwagiro (Oryong-dong), Buk-gu, Gwangju 500-712, Republic of Korea

The bottom-up nanofabrication approaches are biologically inspired which include building up functional nanostructures starting from basic atoms or molecules. In this regard polymeric systems have played important roles for nanofabrication since they can offer nano-reservoir/ templates with different morphologies and tunable sizes. The reservoir/ template can be easily removed after reactions, and can be further modified with different functional groups to enhance the interactions. Due to presence of lone pair of electron on hetero nitrogen atom, pyridine based polymers shows great potential in nano science and technology [1-5].

For more than 10 years, our group has successfully controlled the anionic polymerization of *n*-hexyl isocyanate (HIC) and other similar monomers by adding either NaBPh<sub>4</sub> or 15-crown-5 to the anionic initiators or by developing novel initiator systems to suppress back-biting [6-15]. PICs have many potential applications, such as chiral recognition, optical switches, and liquid crystals. Furthermore, the block copolymers composed of rigid and helical PIC segments are of particular interest for fundamental studies of polymer behavior in solution and in bulk. This presentation covers coil-coil and rod-coil block copolymer based on P2VP, PS, and PHIC blocks (Fig.1 and Fig. 2) assisted fabrication of nano-materials with emphasis on ordered polymeric nanostructures as reservoir/templates to fabricate inorganic, organic/inorganic composites and polymeric materials with nano-scale modifications [16-19].

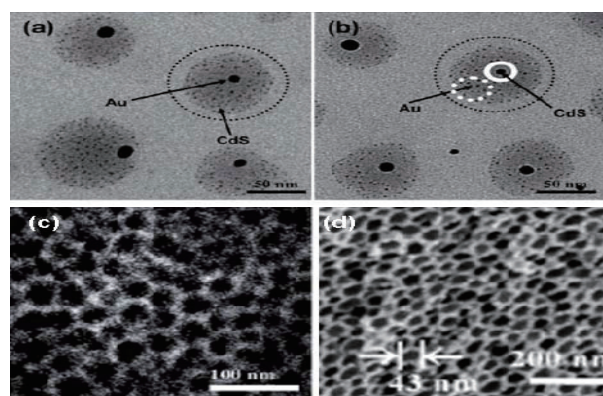


Fig. 1. (a) TEM image of one bigger core-embedded Au NP surrounded by smaller CdS NPs (Au-CdS) in P2VP-*b*-PS ( $f_{P2VP} = 0.75$ ) micelles, (b) bigger core-embedded CdS NP surrounded by smaller Au NPs (CdS-Au) in P2VP-*b*-PS ( $f_{P2VP} = 0.75$ ) micelles [16], (c) SiO<sub>2</sub> nano-composite film from Q-PS-*b*-P2VP ( $f_{P2VP}=0.75$ ), and (d) SiO<sub>2</sub> nano-porous film from Q-PS-*b*-P2VP ( $f_{P2VP} = 0.75$ ) after sintering SiO<sub>2</sub> [17].

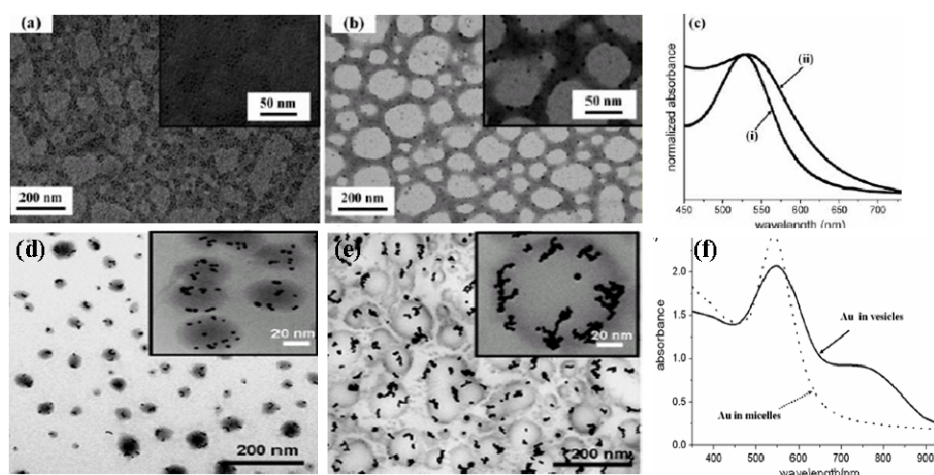


Fig. 2. TEM images of Au NPs embedded in (a) intermicellar-chained network chain of PHIC<sub>189</sub>-*b*-P2VP<sub>228</sub> in CHCl<sub>3</sub>/THF (7/3, v/v), (b) cylindrical micelle network of PHIC<sub>189</sub>-*b*-P2VP<sub>228</sub> in CHCl<sub>3</sub>/THF (3/7, v/v), (c) UV-vis absorption spectra of Au NPs embedded in network nanostructures [18], (d) PHIC<sub>189</sub>-*b*-P2VP<sub>228</sub> micelles in toluene at 3 mg/ml concentration, (e) PHIC<sub>189</sub>-*b*-P2VP<sub>228</sub> vesicles at toluene at 6 mg/ml concentration, and (f) absorption spectra of Au NPs embedded in micelles and vesicles [19].

## References

- [1] J.-S. Lee *et al*, *Adv. Mater.*, **16**, 1814 (2004).
- [2] J.-S. Lee *et al*, *Reactive and Functional Polymers*, **69**, 470 (2009).
- [3] J.-S. Lee *et al*, *Macromolecular Rapid Communications*, **30**, 976 (2009).
- [4] J.-S. Lee *et al*, *Langmuir*, **26**, 9981 (2010).
- [5] J.-S. Lee *et al*, *small*, **6**, 63 (2010).
- [6] J.-S. Lee *et al*, *Macromolecules*, **32**, 2085 (1999).
- [7] J.-S. Lee *et al*, *Macromolecules*, **34**, 2408 (2001).
- [8] J.-S. Lee *et al*, *J. Am. Chem. Soc.*, **127**, 4132 (2005).
- [9] J.-S. Lee *et al*, *Macromolecules*, **39**, 5009 (2006).
- [10] J.-S. Lee *et al*, *Macromolecules*, **39**, 5965 (2006).
- [11] J.-S. Lee *et al*, *Macromolecules*, **40**, 9279 (2007).
- [12] J.-S. Lee *et al*, *Macromolecules*, **41**, 7029 (2008).
- [13] J.-S. Lee *et al*, *Macromolecules*, **42**, 3927 (2009).
- [14] J.-S. Lee *et al*, *Macromolecules*, **44**, 3211 (2011).
- [15] J.-S. Lee *et al*, *Polymer*, **52**, 1925 (2011).
- [16] J.-S. Lee *et al*, *Langmuir*, **23**, 11425 (2007).
- [17] J.-S. Lee *et al*, *J. Mater. Chem.*, **19**, 7322 (2009).
- [18] J.-S. Lee *et al*, *Langmuir*, **25**, 7188 (2009).
- [19] J.-S. Lee *et al*, *Chem. Commun.*, 4824 (2009).

## Reversible Adhesion of Ionic Polymer Brushes Prepared by Controlled Radical Polymerization

Motoyasu Kobayashi<sup>1</sup>, Masami Terada<sup>1</sup>, Atsushi Takahara<sup>1,2</sup>

<sup>1</sup>JST ERATO Takahara Soft Interfaces Project, Japan

<sup>2</sup>Institute for Materials Chemistry and Engineering, Kyushu University, Japan

The ionic interaction between oppositely charged polyelectrolytes is an attractive and promising adhesion force. In this study, the debonding and reversible adhesion of the ionic polymer brush substrates were demonstrated using an aqueous salt solution and deionized water.[1] Surface-initiated atom transfer radical polymerization of 2-(methacryloyloxy)ethyl tri methylammonium chloride (MTAC),[2] 3-sulfopropyl methacrylate potassium salt (SPMK), and 3-(*N*-2-methacryloyloxyethyl-*N,N*-dimethyl)ammonatopropanesulfonate (MAPS)[3] were carried out on the silicon wafers to fabricate ionic polymer brushes with 100 nm thick. As shown in Figure 1(a), 2  $\mu\text{L}$  of deionized water was placed on a brush-immobilized silicon substrate and then another substrate was pressed onto it under a constant load of 4.9 N at 298 K. The contact area of the substrates was maintained at  $5 \times 10 \text{ mm}^2$ . After 2 h of drying time, the adhesion strength was determined by measuring the lap shear adhesion force with a tensile tester in an ambient atmosphere.

The PSPMK and PMTAC brushes adhered strongly with the average adhesion strength of 1.52 MPa. Interestingly, the bonded substrates did not separate even in deionized water hanging a 100-g weight for over 24 h. On the other hand, spontaneous detachment took place within 60 min in 0.5 M NaCl salt aqueous solution, because the hydrated salt ions permeated the adhesion interface to screen the electrostatic

interaction between brushes. After the debonded substrates were washed with deionized water to remove the salt, they readily adhered each other again. The reversible adhesion was also demonstrated by zwitterionic PMAPS brushes.

[1] M. Kobayashi, M. Terada, A. Takahara, *Soft Matter*, **7**, 5717 (2011).

[2] M. Kobayashi, M. Terada, Y. Terayama, M. Kikuchi, A. Takahara, *Macromolecules*, **43**, 8409 (2010).

[3] Y. Terayama, M. Kikuchi, M. Kobayashi, A. Takahara, *Macromolecules*, **44**, 104 (2011).

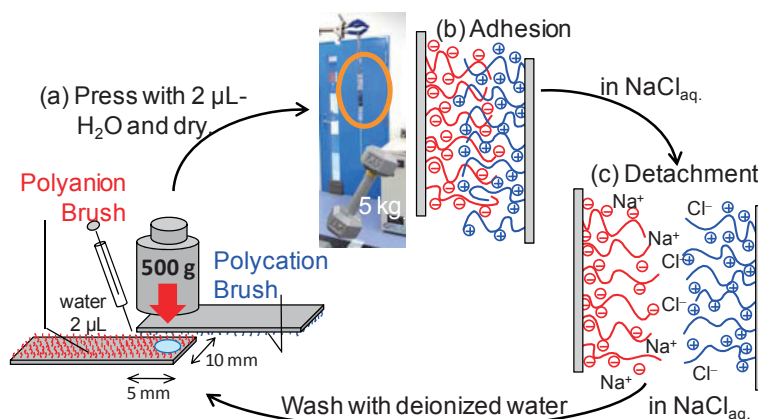


Figure 1. Schematic view of (a) adhesion process of cationic PMTAC and anionic PSPMK brushes, (b) the bonded substrate hanging a 5 kg dumbbell, and (c) detachment of oppositely charged polyelectrolyte brushes in 0.5 M NaCl aqueous solution.

## **Polyelectrolyte brushes: Friction, adhesion, and lubrication.**

Mark Geoghegan<sup>1</sup>, Maryam Raftari,<sup>1</sup> Rita La Spina,<sup>1</sup> Michael J Tomlinson,<sup>1</sup> Zhang Zhenyu,<sup>1,2</sup> Graham J Leggett,<sup>2</sup> Steven P Armes<sup>2</sup>

<sup>1</sup>Department of Physics and Astronomy, University of Sheffield, Sheffield S3 7RH, UK

<sup>2</sup>Department of Chemistry, University of Sheffield, Sheffield S3 7HF, UK

Polyelectrolytes are known for their responsive nature; they change shape with pH or salt, and sometimes with temperature. In aqueous solution they might change from hydrophilic to hydrophobic, but when chemically tethered by one end (brushes) to a substrate, control of their behavior becomes subtler. One aspect of this, is that counterions can be trapped within the brush (osmotic behavior) or above it (double-layer), depending on parameters such as the grafting density of brushes on the surface. A rich phase diagram arises with chemically grafted brushes, and much work has been applied to understanding their behavior. Hydrophilic brushes are well solvated, and are thus lubricious, whereas brushes in their hydrophobic state will exhibit frictional behavior. Also, the charged nature of brushes, coupled with their capacity to hydrogen bond, is important in their adhesive behavior.

In this presentation, the frictional and adhesive nature of polyelectrolyte brushes will be discussed. Frictional behavior will be discussed in the context of the pH and salt-dependent interaction of polyelectrolytes and polyzwitterions with a single-asperity point, i.e. the tip of an atomic force microscope, which may be plain (i.e. silicon nitride), gold-coated, or coated with a hydrophobic or hydrophilic self-assembled monolayer. The adhesion between a polyelectrolyte brush and an oppositely charged hydrogel is also discussed. The pH-dependent nature of the adhesion gives rise to switchable behavior.

Friction force microscopy (FFM) studies on the frictional properties of poly[2-(dimethyl amino)ethyl methacrylate] (PDMAEMA) polybase brushes were made as a function of pH. Here, we observe a transition between different contact mechanics; we observe that the contact mechanics is a strong function of pH, with regions whereby both single asperity contact mechanics behavior (both Johnson-Kendall-Roberts (JKR) and Derjaguin-Müller-Toporov (DMT) models) and multiple contact mechanics (Amontons' law) observed, depending on the pH. Generally, Amontons' law fitted the data best in the extreme pH regions (1, 2, and 12). Between these values at high and low pH, DMT behavior was appropriate, whereas the observation of JKR behavior depended on the surface in contact with the brush, but generally at relatively neutral pH values.

Brushes of the polyzwitterion, poly[2-(methacryloyloxy)ethylphosphorylcholine] (PMPC) was also studied. PMPC is known to exhibit co-nonsolvency in water and ethanol mixtures,

and this is highlighted by an increase in the friction coefficient due to loss of hydration of the brush chains and hence substantially reduced lubrication [1]. It was also found that the friction coefficient of PMPC brushes decreases by the addition of salt in surrounding medium. It is believed that cations or anions could associate with the phosphorylcholine group to different degrees, hinder the inter- and intramolecular interactions, which increase the lubricity of PMPC brushes. The salt-dependent behavior of the PMPC brushes is in contrast to neutron reflectometry results, which hint at an independence of brush conformation with increased added salt [2].

The interaction between (polybase) PDMAEMA brushes and a polyacid presents an intriguing pH-dependent adhesion problem. Oppositely charged polyelectrolytes present an intuitively appealing means of creating a switchable adhesive because pH-induced conformational transitions mean that when one polymer is extended due to osmotic pressure in its counter-ions, another is more collapsed. Changing pH can therefore change the nature of the interactions between the two polymers and therefore provides a means of controlling adhesion. Early experiments show that the adhesion between a grafted layer of polybase and a polyacid hydrogel adhere very strongly in aqueous environment, with a thermodynamic work of adhesion of  $> 0.4$  N/m, but detach at  $\text{pH} \sim 1$  [3,4]. Experiments are described to reveal the dominant factors in this adhesion. Mechanical testing was performed by comparing the adhesion between polyelectrolytes and neutral polymers in order to determine whether hydrogen bonding or electrostatic attraction dominated the adhesion process. These experiments suggest that electrostatic interactions dominate. We also note that using more rigid (more crosslinked) hydrogels, there is a decrease in adhesion, indicating that real-world adhesion (total work of adhesion) has a strong dependence on viscoelastic dissipation within the hydrogel.

[1] Z. Zhang, A. J. Morse, S. P. Armes, A. L. Lewis, M. Geoghegan, and G. J. Leggett, *Langmuir*, **27**, 2514-21 (2011).

[2] M. Kobayashi, K. Mitamura, M. Terada, N. L. Yamada, and A. Takahara, *J. Phys.: Conf. Ser.*, **272**, 012019 (2011).

[3] R. La Spina, M. R. Tomlinson, L. Ruiz-Pérez, A. Chiche, S. Langridge, and M. Geoghegan *Angew. Chem. Int. Ed.*, **46**, 6460-3 (2007).

[4] R. La Spina, A. Chiche, M. R. Tomlinson, and M. Geoghegan, *Eur. Coat. J.*, 22-8 (2011).

## SAXS to Investigate Protein Flexibility and Intrinsic Disorder in Solution

Mamoru Sato

Graduate School of Nanobioscience, Yokohama City University, Japan

Recent development of protein crystallography allows us to understand protein function at atomic level. However, protein is always in motion in solution, which is of great importance to the function. Knowledge of protein dynamics in solution is therefore a prerequisite of understanding how proteins function in cell. Small-angle X-ray scattering (SAXS) and all-atom molecular dynamics (MD) simulation can provide us with such knowledge. MD simulation can provide detailed protein motions in solution at an atomic resolution, but structural ensembles obtained by MD simulation should be assessed by a comparison with experimental data. SAXS data are suitable experimental data for this purpose, although structural data obtained from SAXS experiments are averaged over the structural ensembles in protein solution. In view of this consideration, we have developed a novel method, named MD-SAXS of the combined use of SAXS and MD simulation dedicated to analyze protein dynamics in solution of multi-subunit protein complexes, multi-domain proteins, and so on. In this symposium, we show our recent results on protein dynamics investigated by MD-SAXS.

In the first result [1], we investigated the intrinsic dynamics of a type II restriction endonuclease, EcoO109I by using a 150-ns MD simulation, in which the enzyme fluctuated largely. The SAXS profile calculated from the simulation, considering scattering from explicit hydration water molecule, was in good agreement with the experimentally obtained SAXS profile. The detailed analyses of protein motions have revealed that EcoO109I is intrinsically flexible in the functional movement that cleaves ds-DNA specifically.

In the second result, we studied the intrinsic dynamics of the thermophilic F<sub>1</sub>-ATPase  $\epsilon$  subunit, in which ATP regulates arm motion of its C-terminal domain in F<sub>1</sub>. To determine the overall structures of the ATP-bound and ATP-free forms of the enzyme, we measured SAXS intensities and showed that the overall structure of the ATP-bound form is consistent with the crystal structure, whereas that of the ATP-free form differs significantly from that of ATP-bound form. The ATP-free form was therefore subjected to MD-SAXS and has been shown to be largely fluctuated around at a structure that differs significantly from the ATP-bound crystal structure.

We also show the extension of MD-SAXS to intrinsically disordered proteins (IDPs) or multi-domain proteins that include ID regions between the domains. IDPs are characterized by lack of stable tertiary structure when the protein exists as an isolated polypeptide chain under physiological conditions [2]. They adopt well-defined structures upon binding to their targets. IDPs are mostly found in eukaryotes and generally interact with several target molecules, thus playing important roles as protein hubs in intracellular protein networks.

[1] T. Oroguchi *et al.*, *Biophys. J.* **96**, 2808-2822 (2009)

[2] <http://www.tsurumi.yokohama-cu.ac.jp/IDP/index.html>

## Roles of Functional Groups and Nanostructures in Programmable Digital Nonvolatile Electrical Memory Polymer Systems

Moonhor Ree\*, Suk Gyu Hahm, Dong Min Kim, Kyungtae Kim, Wonsang Kwon,  
Yong-Ki Ko, Yecheol Rho, and Byungcheol Ahn  
Pohang Accelerator Laboratory, Department of Chemistry, Division of Advanced Materials  
Science, Center for Electro-Photo Behaviors in Advanced Molecular Systems, BK School of  
Molecular Science, and Polymer Research Institute, Pohang University of Science &  
Technology (POSTECH), Pohang 790-784, Republic of Korea  
E-mail: ree@postech.edu; <http://www.postech.ac.kr/chem/mree>

Several series of functional polymers bearing charge trapping sites were designed and synthesized for programmable digital electrical memories [1-13]. They were soluble in common solvents and thus their nanoscale thin films easily fabricated by solution coating and subsequent drying process. The functional polymers in devices revealed various types of nonvolatile memory behaviors as well as volatile memory characteristics, depending on the chemical structure, morphological structure, film thickness and temperature. In general, their memory performance was superior, compared to the traditional metal oxide based flash memory devices. Namely, the functional polymers showed excellent nonvolatile or volatile memory performance with low power consumption: unipolarity or bipolarity, high ON/OFF current ratio, long retention time even in ambient air, rapid switching time, and excellent long reliability. Their electro-optical properties were investigated and then correlated to the observed memory behaviors. All the observed memory characteristics were attempted to understand with the chemical composition and morphological nanostructure. Furthermore, their memory mechanism was tried to understand. Overall, our study demonstrated that the selected functional polymers are a very suitable active material for the mass production at low cost of high performance, programmable, digital nonvolatile and volatile memory devices that can be operated with very low power consumption in excellent unipolar or bipolar switching modes with a high ON/OFF current ratio. Moreover, they ensure their properties performance for application in the fabrication of -dimensional multi-stack structure memory devices.

- [1] S. Baek, et al. *Adv. Funct. Mater.* **17**, 2637 (2007).
- [2] S.-H. Hong, et al. *Appl. Phys. Letters* **91**, 093517 (2007).
- [3] J. Kim, et al. *Langmuir* **23**, 9024 (2007).
- [4] Choi, et al. *Adv. Mater.* **20**, 1766 (2008).
- [5] S. G. Hahm, et al. *Adv. Funct. Mater.* **18**, 3276 (2008).
- [6] D. Lee, et al. *IEEE Electron Device Lett.* **29**, 694 (2008).
- [7] S. G. Hahm, et al. *J. Mater. Chem.* **19**, 2207 (2009).
- [8] K. Kim, et al. *J. Phys. Chem. B* **113**, 9143 (2009).
- [9] D. M. Kim, et al. *Langmuir* **25**, 11713 (2009).
- [10] T. J. Lee, et al. *Nanotechnology* **20**, 135204 (2009).
- [11] S. Park, et al. *J. Phys. Chem. B* **114**, 10294 (2010).
- [12] S. Park, et al. *Polymer* **52**, 2170 (2011).
- [13] S. Park, et al. *ACS Appl. Mater. Interf.* **3**, 765 (2011).



## Artificial Multi-Step Light Harvesting Systems

Osamu Ishitani

Department of Chemistry, Tokyo Institute of Technology, Japan

One of the magnificent functions of the photosynthesis is efficient light harvesting. molecules as a light absorber and then efficiently transfer the absorbed photon into the reaction center (RC) of which number is much smaller than that of chlorophylls in the antenna. For example, purple bacteria has a simultaneous two-step accumulation system of light-energy, i.e. LH2  $\rightarrow$  LH1  $\rightarrow$  RC. The photosynthetic light harvesting systems have been widely interested not only in the biology field but also as solar energy conversion systems. Although many artificial systems have been reported, multi-step light accumulation systems constructed of both many light absorbers and a much smaller number of energy-relay units together with final energy acceptors have been rare.

We have recently reported that a linear-shaped rhenium(I) tetranuclear complex connected with a Ru(II) trisdiimine complex (**Ru-Re5**) can work as a light harvesting system in which about 90 % of photons absorbed by the Re(I) chain are intramolecularly gathered into the Ru unit (Fig. 1). Inagaki et al. have reported periodic mesoporous organosilicas (PMOs) as light harvesting antenna, in which many organic chromophores are densely and orderly embedded within

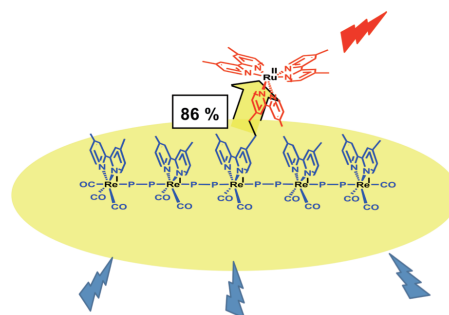


Fig. 1. **Ru-Re5** (p-p = bis(diphenylphosphino)acetylene)

a silica framework. If the two structurally different light harvesting systems could be emergently merged, a novel type of multi-step light accumulation systems might be developed. In this presentation, a successive example of such systems will be reported.

We synthesized a hybrid system of **Ru-Re5** with biphenyl-bearing PMO (Fig. 2), where photons absorbed by about 700 biphenyl groups (the role of LH2) in the framework of BPPMO can be stepwise concentrated to the five Re units (LH1) and then to only one Ru unit (RC) which strongly emits, i.e. two-step light harvesting BPPMO  $\rightarrow$  Re5 unit  $\rightarrow$  Ru unit.

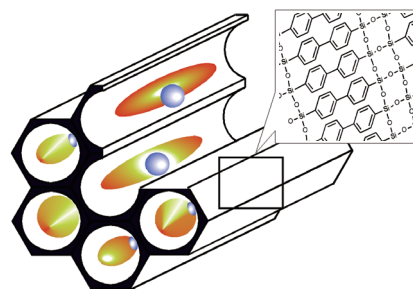


Fig. 2. **Ru-Re-PMO** :**Ru-Re5** is held in the mesopore.

[1] Y. Yamamoto, Y. Tamaki, T. Yui, K. Koike, O. Ishitani, *J. Am. Chem. Soc.*, 132, 11743 (2010).

[2] S. Inagaki, O. Ohtani, Y. Goto, K. Okamoto, M. Ikai, K. Yamanaka, T. Tani, T. Okada, *Angew. Chem.-Intern. Edit.*, 48, 4042 (2009).

## Construction of polymetallic complexes as molecular magnets

Hui-Zhong Kou<sup>1</sup>, Ai-Li Cui<sup>1</sup>

<sup>1</sup>Department of Chemistry, Tsinghua University, Beijing 100084, P. R. China

Molecule-based magnets have been one of the focuses of research in the field of coordination chemistry. The molecular magnets include high- $T_c$  magnets, single-molecule or single-chain magnets and spin crossover magnets, which can be potentially used in magnetic recording. We have been interested in cyanide-bridged bimetallic complexes,<sup>[1-6]</sup> some of which display high- $T_c$  molecular magnetic, single-molecule or single-chain magnet behavior. By way of molecular design, we could construct mixed ligand-bridged hetero-trimetallic complexes.<sup>[2-4]</sup> Bifunctional molecular materials are expected.

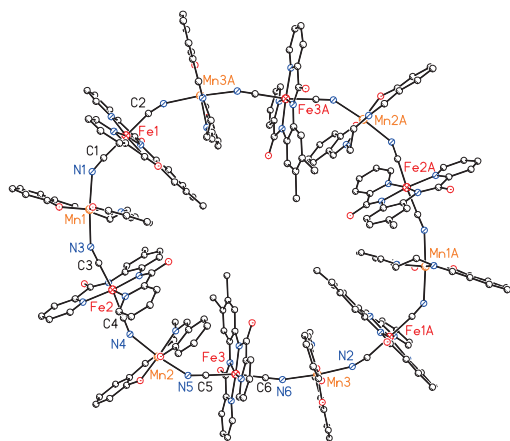


Fig. 1. Structure of a cyanide-bridged  $Mn_6Fe_6$  molecular wheel

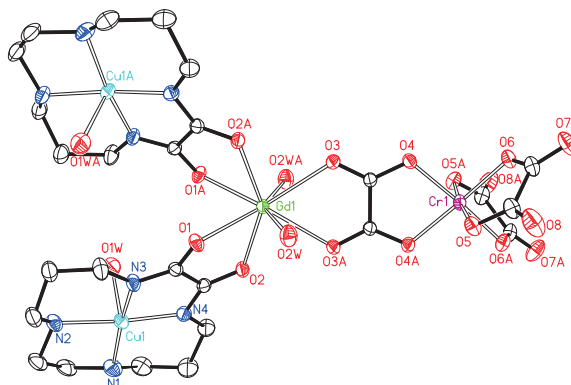


Fig. 2. Structure of an oxamidato- and oxalato-bridged  $Cu_2GdCr$  molecule

- [1] Z.-H. Ni, H.-Z. Kou, L.-F. Zhang, C. Ge, A.-L. Cui, R.-J. Wang, Y. Li, and O. Sato, *Angew. Chem. Int. Ed.*, **44**, 7742 (2005).
- [2] H.-Z. Kou, B. C. Zhou, S. Gao, and R.-J. Wang, *Angew. Chem. Int. Ed.*, **42**, 3288 (2003).
- [3] H.-Z. Kou, K.-Q. Hu, H.-Y. Zhao, J. Tang and A.-L. Cui, *Chem. Commun.*, **46**, 6553 (2010).
- [4] H.-Z. Kou, and O. Sato, *Inorg. Chem.*, **46**, 9513 (2007).
- [5] Z.-H. Ni, J. Tao, W. Wernsdorfer, A.-L. Cui and H.-Z. Kou, *Dalton Trans.*, 2788 (2009).
- [6] H.-Z. Kou, Z.-H. Ni, C.-M. Liu, D.-Q. Zhang and A.-L. Cui, *New J. Chem.*, **33**, 2296 (2009).

## **Formation of Multilayer Thin Films and Complexes Based on Molecular Interactions of Polyelectrolytes**

Kookheon Char

The National Creative Research Initiative Center for Intelligent Hybrids

School of Chemical and Biological Engineering

The WCU Program of Chemical Convergence for Energy & Environment

Seoul National University, Seoul 151-744, Korea

Functionalized polymeric platforms including multilayer films and complexes have been explored for many years based on polyelectrolytes (PEs), which molecular interactions strongly depend on external environments. In particular, layer-by-layer (LbL) deposition has received great attention for the fabrication of functional multilayer films due to many advantages such as inserting functionalities at desired nanoscale positions within the films. The LbL assembled multilayer films containing diverse functional materials (i.e., quantum dots, micelles, graphenes, and proteins) and their unique properties will be reviewed in this presentation. Moreover, external stimuli-driven changes on multilayer films have been investigated by adjusting of the molecular interactions between PEs. In addition to multilayer films based on charged polymers, the formation and morphological transition of charged micelle complexes has also been studied at various solution pH conditions, with a control of specific interactions between two charged micelles. These assorted polymeric platforms based on the molecular interactions between charged functional objects offer great potential applied to many applications ranging from optoelectronics to nanobiomedicine.

## Chemically-attached soft organic interlayers on Si substrate for boundary lubrication: Linear polymers and dendrimer with PFPE overcoat

Myo Minn, N. Satyanarayana and Sujeet K. Sinha<sup>†</sup>

Department of Mechanical Engineering

National University of Singapore

<sup>†</sup> corresponding author (E-mail: mpesks@nus.edu.sg)

Tribological properties such as friction, wear and adhesion are some of the reliability issues limiting the applicability of micro-electro mechanical systems (MEMS) components which are generally made of Si. Ultra-thin organic films such as self-assembled monolayers (SAMs), physically-attached polymer films and ionic liquid films are some solutions for improving the tribological properties of Si surface. However, further research in this area is essential to provide very reliable lubrication solution to the MEMS components. In this presentation, we explore the concept of ultra-thin polymer layer as a soft lubricating interface between Si and a top perfluoropolyether (PFPE) lubricant film. In our first approach, we chemically attached functionalized polyethylene (polyethylene-graft-maleic anhydride) (fPE) molecules to Si via an intermediate molecule of benzophenone ( $\text{Ph}_2\text{CO}$ ). This layer is further overcoated with an ultra-thin layer of PFPE (Figure 1). Figure 2 presents the wear life of the modified layer and compares this with the wear lives of bare Si or Si/fPE [1]. The Si/ $\text{Ph}_2\text{CO}$ /fPE/PFPE film provides extremely high wear life and did not fail under the present set of experimental conditions.

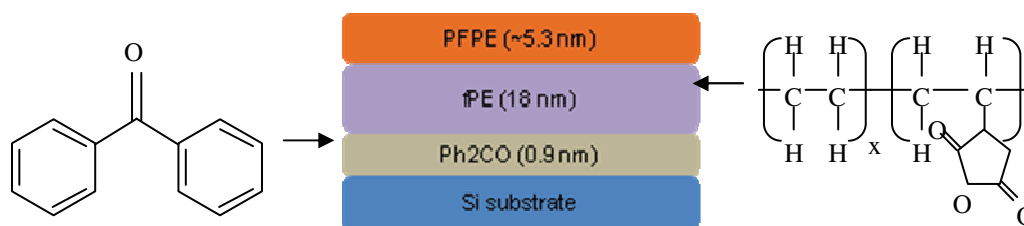


**Figure 1** A schematic diagram of Si substrate with different modified layers (not to scale).

Our second approach is on the use of dendrimer layer (amine-terminated poly (amidoamine) with ethylenediamine core) as an intermediate layer between PFPE films and Si surface. The dendrimer films have molecules in the form of branched-structure and hence the overcoated PFPE molecules are expected to either penetrate into the empty spaces between various arms of dendrimer molecules or chemisorb on to the dendrimer molecules and both these

conditions have shown excellent effects on the coefficient of friction and wear durability of the Si substrate. Table 1 presents the wear durability data for three generations of the dendrimers [2]. It is concluded that a soft and wear resistant polymeric layer overcoated with a nano-lubricant such as PFPE can provide robust protection to Si or similar materials against wear even under sever contact conditions than what would be encountered in a microsystem device.

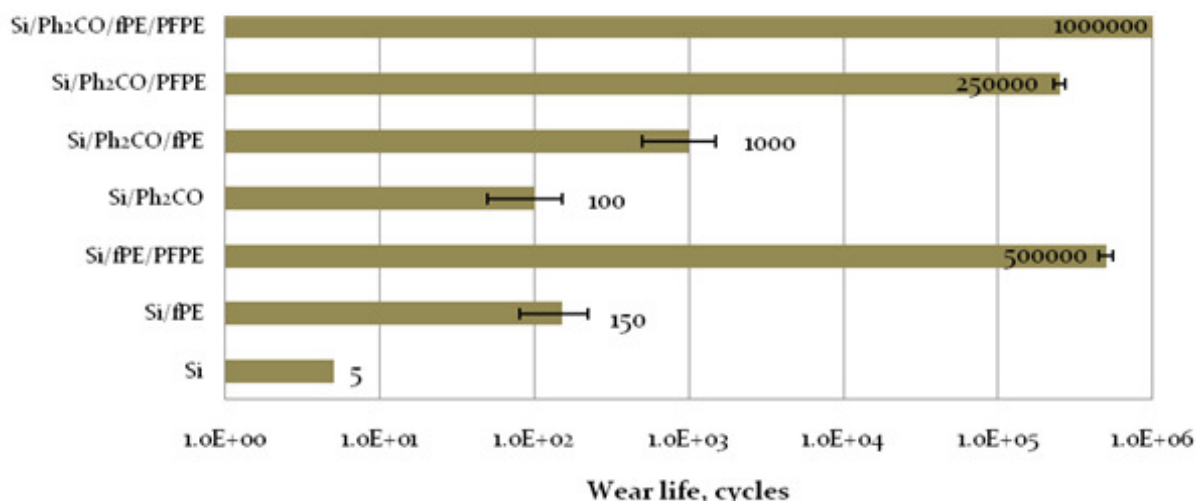


**Figure 2:** The wear durability of Si with different surface modifications. The wear durability tests were conducted on a custom built ball-on-disc tribometer with a silicon nitride ( $\text{Si}_3\text{N}_4$ ) ball of 4 mm diameter as the counterface. The normal load used was 40 mN. The wear durability was determined at a fixed disc rotational speed of 500 rpm (relative linear speed was 0.052 m/s). The wear durability was defined as the number of cycles completed when either the coefficient of friction exceeded 0.3 or large fluctuations in the coefficient of friction (indicative of film failure) or a clear wear track occurred.

**Table 1:** Wear durability data of different modifications obtained from a microtribotester using the ball-on-disc sliding tests (counterface material:  $\text{Si}_3\text{N}_4$  ball of 4 mm diameter). The GPTMS SAM (glycidoxypropyltrimethoxy silane self-assembled monolayer) and the dendrimer layers of different generations were formed on Si using self-assembly process. PFPE (Zdol 4000) was dip-coated onto different substrates using a custom-built dip-coating machine (dip-coating time: 1 min; withdrawal speed: 2.1 mm/sec and concentration: 0.5 wt%).

Sample	Testing conditions (Normal load and rotational speed)	Wear life (number of sliding cycles)
Si	10 g, 200 rpm	<100
Si/PFPE	“	2,000
Si/GPTMS*/PFPE	15 g, 200 rpm	8,000
Si/GPTMS/Dendrimer,	20 g, 200 rpm	40,000

Generation2/PFPE		
Si/GPTMS/Dendrimer, Generation6/PFPE	“	>1,000,000
Si/GPTMS/Dendrimer, Generation8/PFPE	“	280,000

[1] Myo Minn, Y. S. G. Soentanto, S. K. Sinha, Tribology Letters, 41, 217 (2011)

[2] N. Satyanarayana, M. Minn and S. K. Sinha, Data to be submitted to a journal.

## Self-Healing Effects of Halloysite Nanotubes on Corrosion Protection of Multi-Functional Hybrid Coatings

Mijeong Han

Advanced Materials Division, Korea Research Institute of Chemical Technology,  
South Korea

Protection of metals against corrosion is one of the most challenging problems in materials science and the corrosion of metals causes huge losses in the areas of aerospace, automotive, bridges, and shipbuilding industries [1]. The ways to protect the metal surface from the corrosion include cathodic protection, sacrificial anodes, conversion coatings, and protective coatings, etc. Organic-inorganic hybrid coatings have been utilized to provide the protection layers for metal surfaces and shown effective results, but could not be expected further protection after the coating layer started to be damaged.

Halloysite nanotubes are aluminum-silicate hollow cylinder with length of 1~3 $\mu\text{m}$  and a diameter of 30~70nm. These materials have nanocontainers which can be used for loading and releasing corrosion inhibitors [2]. The release of the corrosion inhibitor loaded inside halloysite nanotubes can be controlled by pH [3], which provide self-healing effects when the corrosion occurs.

We loaded benzotriazole as a corrosion inhibitor into halloysite nanotubes in acetone by vacuum/release cycles and the inhibitor loaded halloysite nanotubes embedded in zirconia-organosilane sol-gel coating solution. The coating solutions was coated on aluminum substrates by dip-coating then thermally cured. The corrosion protection properties of the samples were analyzed by electrochemical impedance spectroscopy (EIS) and salt-spray chamber test. Fig.1 presents the results of EIS of sol-gel coating on aluminum without halloysite nanotubes and the impedance and phase angle of the sol-gel coating were dramatically decreased after 336h exposure to 0.1 M NaCl electrolyte. NaCl electrolyte diffused through the coating and lowered the coating's resistance.

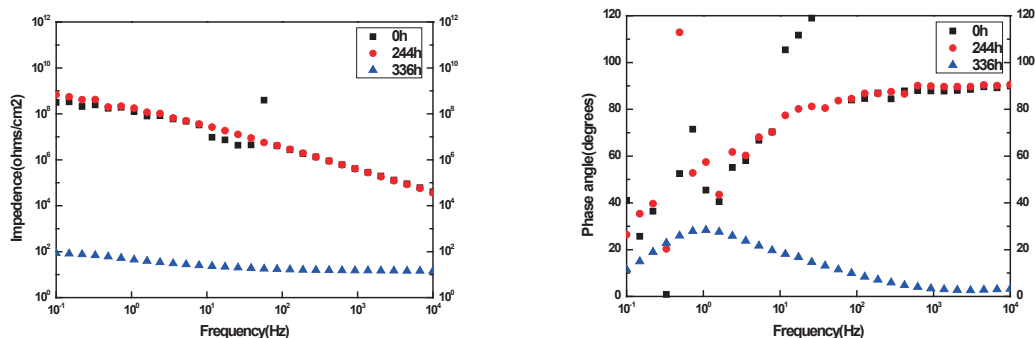


Fig. 1. EIS results of sol-gel coating on aluminum without halloysite nanotubes

A new peak was appeared in the phase angle curves at low frequency range and this indicates the delamination between the sol-gel coating and the aluminum surface.

However, sol-gel coatings with halloysite nanotubes showed different behavior after exposure to the electrolyte as shown in Fig. 2, maintaining the initial impedance and phase angle over a wide range of frequencies. Even after 1176 h exposure to 0.1 M NaCl electrolyte, sol-gel coating with halloysite nanotubes showed almost same impedance and phase angle. It could be explained that halloysite nanotubes played very important role in enhancing the corrosion protection of the surface of aluminum by releasing corrosion inhibitor, which was consistent with the results of salt spray chamber tests.

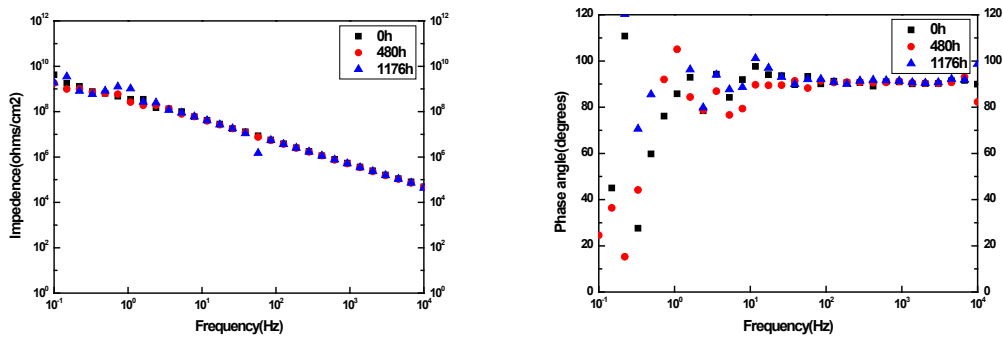


Fig. 2. EIS results of sol-gel coating on aluminum with halloysite nanotubes

- [1] J. Y. Seo, M. Han, *Nanotechnology*, **22**, 025601 (2011).
- [2] E. Abdullayev, R. Price, D. Shchukin, Y. Lvov, *Applied Materials & Interfaces*, **1**, 1437 (2009).
- [3] D. Fix, D. V. Andreeva, T. M. Lvov, D. G. Shchukin, H. Mohwald, *Advanced Functional Materials*, **19**, 1720 (2009).



## Mineralization of Biopolymers as a Route for Functional Materials Preparation

Yury Shchipunov<sup>1,2</sup>

<sup>1</sup>Affiliation Institute of Chemistry, Far East Department, Russian Academy of Sciences, 690022 Vladivostok, Russia,

<sup>2</sup>The WCU Center for Synthetic Polymer Bioconjugate Hybrid Materials, Department of Polymer Science and Engineering, Pusan National University, Busan, Korea

There are numerous examples of hierarchically structured and highly efficient functional materials from mineralized organics in the living nature. Their synthesis and structural organization are genetically predetermined and regulated from molecular up to macroscopic level. The development of biomimicking methods is an area of tremendous activity for engineering advanced materials with regulated structural organization and functionalities through easier processability without using an acid or alkali and organic solvents. By applying recently developed general approach to biomimicking mineralization [1-3], we could fabricate hybrid organic-silica bionanocomposites ranging from hydrogels and adsorbent to biocatalysts and photonic materials at mild conditions that closely resemble that of biomineralization.

The key aspect of our approach is in the silica precursor. The generally applied tetraethoxysilane is poor water soluble and incompatible with biopolymers owing to the alcohol separation after its hydrolysis. We exchanged it for a novel precursor with ethylene glycol residues that gave tetrakis(2-hydroxyethyl) orthosilicate (THEOS). The exchange of ethanol in tetraethoxysilane makes the precursor completely water soluble, while the ethylene glycol separated after the hydrolysis is compatible with biopolymers [1-3]. Its mixing with biopolymers does not course the denaturation of proteins and the precipitation of polysaccharides. There is also a difference in the mechanism of processes. The silica precursor and products of its hydrolysis nucleate on biomacromolecules [3,4]. This leads to their mineralization and following encasement in the inorganic matrix. Synthesis is performed in one stage at needed pH without recourse to a catalyst. Hybrid nanocomposites thus prepared are homogeneous, having mesoporous structure. Their structure and functionality are regulated by biopolymers that biomimic the biomineralization processes of living cells.

Examples are presented by preparation of hydrogels of polysaccharides, which cannot jelly aqueous solutions, mesoporous nanocomposites, biocatalysts and photonic materials.

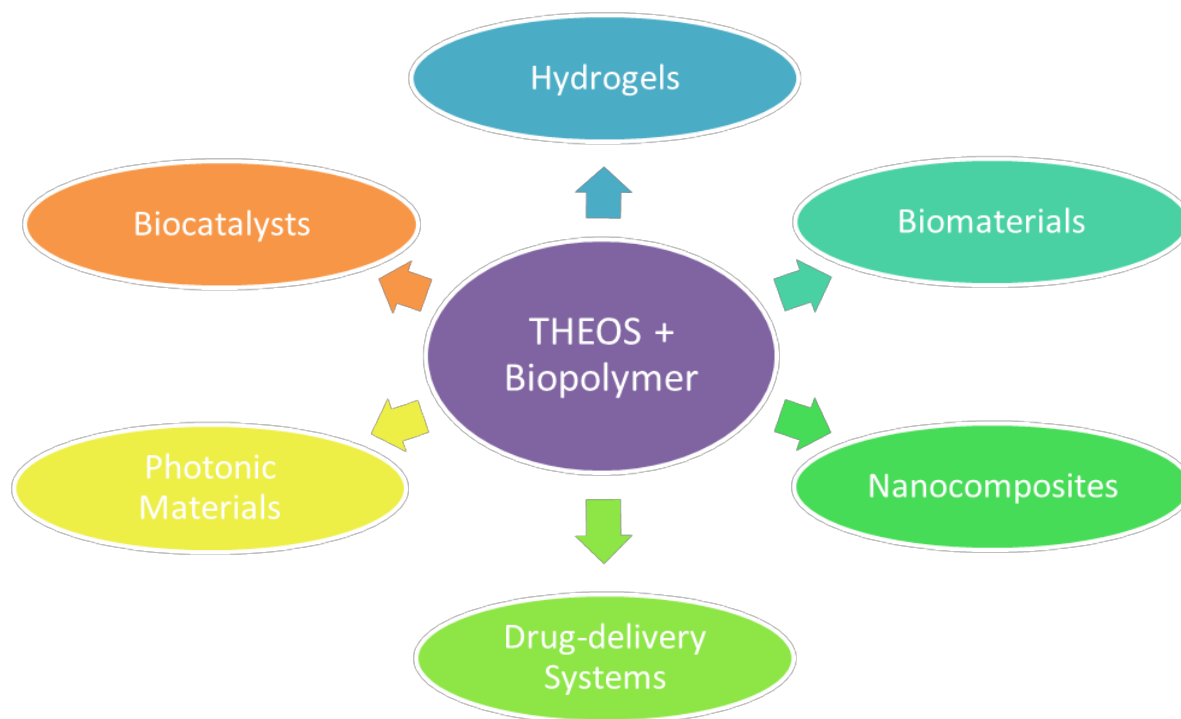


Fig. 1. Main functional materials prepared through the mineralization of biopolymers.

**Hydrogels.** There is a challenge to provide the jellification of solutions of such practically important polysaccharides as chitosan, hyaluronate and cyclodextrin. The mineralization results in the formation of cross-linked silica shells surrounding the biomacromolecules [5]. Owing to the biocompatibility of components used, the hydrogels thus prepared are promising for applications in biomedicine and pharmacology.

**Biocatalysts.** Enzymes are encased into inorganic matrix by the same mineralization. The developed method is ideally suited for the fabrication of biocatalysts. Its main advantage over current techniques lies in that the entrapment conditions are dictated by an enzyme, but not the processing [6]. We could immobilize very labile proteins that lose their activity after the separation even at the appropriate conditions within few hours [7]. The entrapment into the inorganic matrix resulted in a sharp increase of their lifetime.

**Photonic materials.** The transparency of some hybrid biopolymer-silica nanocomposites makes them appropriate for optics. Their doping by additives, e. g. dyes and nanoparticles of noble metals, enables one to functionalize further the optical properties. It was found by examining under the action of ultrashort (femtosecond) laser pulses that some tailored hybrids demonstrated high third-order nonlinear susceptibility and high-speed optical response. Their nonlinear refractive index was about three orders of magnitude greater than that of fused silica,

which at present is widely used to fabricate nonlinear photonic materials. Easy preparation in one stage and low price make these biopolymer-silica nanocomposites are promising for developing novel type of photonic materials.

- [1] Y. Shchipunov, *J. Colloid Interface Sci.*, **268**, 68 (2003).
- [2] Y. A. Shchipunov, T. Y. Karpenko, *Langmuir*, **20**, 3882 (2004).
- [3] Y. A. Shchipunov, in *Bio-Inorganic Hybrid Nanomaterials*, Eds. E. Ruiz-Hitzky, K. Ariga, Yu. M. Lvov, Wiley-VCH, Weinheim, p. 75, 2007.
- [4] Y. A. Shchipunov, A. Kojima, T. Imae, *J. Colloid Interface Sci.*, **285**, 574 (2005).
- [5] Y. A. Shchipunov, T. Y. Karpenko, A. V. Krekoten, I. V. Postnova, *J. Colloid Interface Sci.*, **287**, 373 (2005).
- [6] Y. A. Shchipunov, T. Y. Karpenko, I. Y. Bakunina, Y. V. Burtseva, T. N. Zvyagintseva, *J. Biochem. Biophys. Methods*, **58**, 25 (2004).
- [7] Y. A. Shchipunov, Y. V. Burtseva, T. Y. Karpenko, N. M. Shevchenko, T. N. Zvyagintseva, *J. Mol. Catal. B. Enzymes*, **40**, 16 (2006).

## New Scientific Approaches for Formation of Multifunction Nanocomposite PEO-Coatings at the Surface of Various Metals and Alloys

S.V. Gnedenkov<sup>1</sup>, S.L. Sinebryukhov<sup>1</sup>

<sup>1</sup>Institute of Chemistry Far Eastern Branch, Russian Academy of Sciences, Russia

New scientific approaches to purposeful formation of the composite protective layers at the surface of various metals and alloys and corrosion process taken place at their surface in the corrosion active media have being considered in the relationship with charge transfer mechanism realized at the heterooxide/electrolyte interface. The multifunctional composite coatings which possess the practically important properties (anticorrosive, antiscale, bioinert/bioactive and etc.) were obtained on titanium, aluminium, magnesium alloys as well at the steel and nickel-titanium alloy surfaces by means of the unipolar or bipolar modes of the plasma electrolytic oxidation (PEO) in different water electrolytes [1-6]. The application of the nanosizable polymer and inorganic compounds in the coatings composition allows increasing their stability in corrosion active media (Fig.1).

The chemical composition of the heterooxide coatings, their morphology, electrochemical properties and protection against corrosion in the sea water were investigated by different modern physical-chemical methods.

The study of the PEO-coatings and composite layers with using the impedance spectroscopy method allowed determining their

morphology structure, homogeneity and to research the charge transfer mechanism, which is realized at the oxide heterostructure/electrolyte interface. Application of the local electrochemical impedance spectroscopy (LEIS) method enable one to research the kinetics of the development of the defect zones in the PEO-coating obtaining at the surface of the magnesium alloy during the sample exposure in the corrosion-active solution. The developmental stages of the corrosion-active process have been established. The equivalent electrical circuits, which adequately describes the mechanism of the corrosion process of the protective PEO-coatings has been suggested.

By the analysis of wetting it was found that joint action of PEO treatment and adsorption of hydrophobic agent leads to the inhibition of the corrosion reaction and provides the anticorrosive behavior of metallic sample. The decrease in contact angle for the

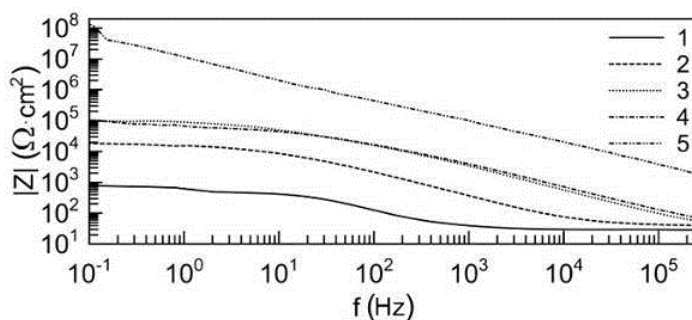


Fig. 1 Impedance modulus versus frequency for the investigated samples: 1 – without coating; 2 – formed in the silicate electrolyte under monopolar mode; 3 – formed in the silicate and fluoride containing electrolyte under monopolar mode; 4 – formed in the silicate and fluoride containing electrolyte under bipolar mode; 5 – formed as sample # 4 followed by SPTFE treatment

nanocomposite superhydrophobic coating during 50 h does not exceed 1–3° at different points along the sample, indicating the extremely high anticorrosion protective action of the nanocomposite superhydrophobic coating (Fig. 2).

The analysis of potentiodynamic polarization data in conjunction with EIS spectra and appropriate equivalent circuit models enabled us to conclude that corrosion processes with nanocomposite superhydrophobic coating is inhibited much more effectively.

The mechanisms of inhibition for nanocomposite superhydrophobic coatings, as follows from electrochemical and wettability data, is related to very low portion of coating area (less than 3% of real surface) being in a real contact with electrolyte solution, the higher ohmic barrier for corrosion reaction, and the shift of free corrosion potential towards positive values, generated by the hydrophobic or the superhydrophobic layers.

Moreover, the bioactive composite coatings containing hydroxyapatite had been developed for implant surgery.

Thus, the results of analysis of presented experimental data enable one to conclude: the composite coatings formed on the base of PEO with using of polymer and inorganic nanosized powders significantly enlarge a practical application of different constructional materials.

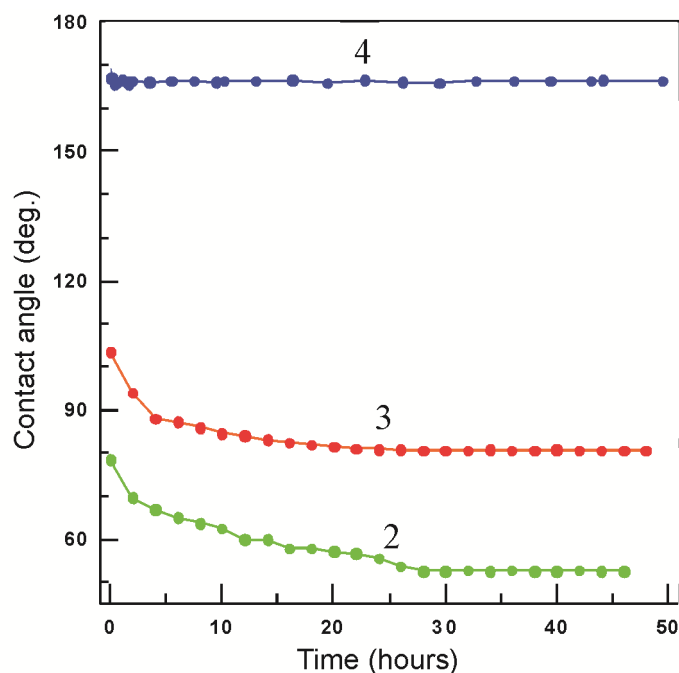


Fig. 2 The evolution of contact angle with time after drop of brine deposition. 2 – PEO-coating; 3 – composite hydrophobic coating; 4 – nanocomposite superhydrophobic coating. Solid lines are used to guide the eye [6].

- [1] S. V. Gnedenkov, S. L. Sinebryukhov, *Compos. Interfaces* **16**, 387 (2009).
- [2] S. L. Sinebryukhov, A. S. Gnedenkov, O. A. Khrisanfova, S. V. Gnedenkov, *Surf. Eng.* **25**(8), 565 (2009).
- [3] S. V. Gnedenkov, O. A. Khrisanfova, S. L. Sinebryukhov, A. V. Puz', A. S. Gnedenkov, *Mater. Manuf. Processes* **23**, 879 (2008).
- [4] S. V. Gnedenkov, O. A. Khrisanfova, A. G. Zavidnaya, S. L. Sinebryukhov, V. S. Egorkin, M. V. Nistratova, A. Yerokhin, A. Matthews, *Surf. Coat. Technol.*, **204**, 2316 (2010).
- [5] S. L. Sinebryukhov, A. S. Gnedenkov, D. V. Mashtalyar, S. V. Gnedenkov, *Surf. Coat. Technol.* **205**, 1697 (2010).
- [6] S. V. Gnedenkov, S. L. Sinebryukhov, V. S. Egorkin, D. V. Mashtalyar, D. A. Alpysbaeva, L. B. Boinovich *Colloids Surf., A*, **383**, 61(2011).

**Novel highly fluorinated Ionic Liquids Cat[M(OR<sup>F</sup>)<sub>4</sub>] (M = Al, B):  
Synthesis, Properties and Basis for the development of quantum chemical  
prediction schemes for physical properties.**

I. Krossing

Freiburg Institute of Advanced Studies (FRIAS), Material Research Center (FMF) and  
Institute of Inorganic Chemistry, University of Freiburg, Freiburg, Germany.

In recent years we have been working in the field of synthesis<sup>[1]</sup> and physical characterisation<sup>[2]</sup> of Ionic liquids (ILs), the investigation of speciation in ILs<sup>3</sup> and the *in silico* prediction of the physical properties of ILs.<sup>[4,5,6]</sup>

The ASAM lecture will focus on synthesis, application and properties of novel ionic liquids on the basis of the [M(Ohfip)<sub>4</sub>]<sup>-</sup> anion (Ohfip = OC(H)(CF<sub>3</sub>)<sub>2</sub>, M = Al,<sup>[7]</sup> B) with very low viscosities (down to 33 mPa s<sup>-1</sup> at 24°C), high conductivities and high thermal and electrochemical stability. These model ILs with almost no ion-specific anion-cation interaction were the basis for new developments, i.e. a robust model to predict the melting point of potential ILs with a validity range from -50 to +300°C.<sup>[8]</sup> If time permits, a revised approach to predict temperature dependent IL-viscosities and -densities will be presented.<sup>[9]</sup>

**References:**

<sup>1</sup> I. Raabe, K. Wagner, K. Guttsche, M. Wang, M. Graetzel, G. Santiso-Quinones and I. Krossing, *Chem. Eur. J.* **2009**, *15*, 1966-1976.

<sup>2</sup> a) H. Weingärtner, P. Sasisanker, C. Daguene, P. J. Dyson, I. Krossing, J. M. Slattery and T. Schubert, *J. Phys. Chem. B* **2007**, *111*, 4775-4780; b) C. Daguene, P. J. Dyson, I. Krossing, A. Oleinikova, J. Slattery, C. Wakai and H. Weingärtner, *J. Phys. Chem. B* **2006**, *110*, 12682-12688.

<sup>3</sup> P. Eiden, Q. Liu, S. Zein El Abedin, F. Endres and I. Krossing, *Chem. Eur. J.* **2009**, *15*, 3426-3434.

<sup>4</sup> a) I. Krossing, J. M. Slattery, *Z. Phys. Chem.* **2006**, *220*, 1343; b) J. Slattery, C. Daguene, P. J. Dyson, T. Schubert, I. Krossing, *Angew. Chem. Int. Ed.* **2007**, *46*, 5384–5388.

<sup>5</sup> U. P. R. M. Preiss, J. M. Slattery and I. Krossing, *Ind. Eng. Chem. Res.* **2009**, *48*, 2290-2296.

<sup>6</sup> a) I. Krossing, J. M. Slattery, C. Daguene, P. J. Dyson, A. Oleinikova and H. Weingärtner, *J. Am. Chem. Soc.* **2006**, *128*, 13427-13434; b) I. Krossing, J. M. Slattery, C. Daguene, P. J. Dyson, A. Oleinikova and H. Weingärtner, *J. Am. Chem. Soc.* **2007**, *129*, 11296.

<sup>7</sup> a) S. Bulut, P. Klose, M.-M. Huang, H. Weingaertner, P. J. Dyson, G. Laurenczy, C. Friedrich, J. Menz, K. Kuemmerer, I. Krossing, *Chem. Eur. J.* **2010**, *16*, 13139-13154; b) I. Raabe, K. Wagner, K. Guttsche, M. Wang, M. Gratzel, G. Santiso-Quinones, I. Krossing, *Chem. Eur. J.* **2009**, *15*, 1966-1976.

<sup>8</sup> U. Preiss, S. Bulut and I. Krossing, *Journal of Physical Chemistry B*, **2010**, *114*, 11133-11140.

<sup>9</sup> P. Eiden, S. Bulut, T. Köchner, C. Friedrich, T. Schubert and I. Krossing, *Journal of Physical Chemistry B*, **2011**, *115*, 300-309.

## Surface Modification of Rubber by Preferential Segregation of Inorganic Materials

Hirofumi Tsuruta, Yoshihisa Fujii, Keiji Tanaka

Department of Applied Chemistry, Kyushu University, Japan

**Introduction:** Recently, the construction of highly-functionalized polymer surfaces has been desired for applications in variety of fields. Various chemical or physical processes such as plasma and corona treatments, graft-polymerization, sputtering, or metal coating are popular to modify, or improve, properties and functions at polymer surfaces [1]. Although these methods have a tremendous potential, they also possess the drawbacks of fabrication cost. Thus, an alternative cost-effective method to realize the surface modification of polymers should be established. We here present a simple and easy method to construct a weatherproof surface for polymers based on the voluntary segregation of inorganic material.

**Experiments:** As matrix polymer and surface modifier, polyisoprene (PI) and tetraethoxysilane (TEOS) were used. A number-average molecular weight of monodisperse PI was 392k. In order to promote hydrolysis of TEOS, ethanol, H<sub>2</sub>O, and hydrochloric acid (HCl) were mixed with TEOS. A ratio of ethanol, H<sub>2</sub>O, and

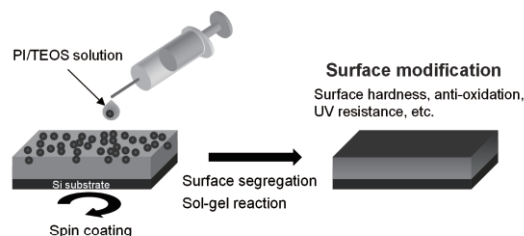


Fig. 1. Schematic illustration for sample preparation.

TEOS was equimolar. HCl was used as a catalyst at a fixed molar ratio of 0.05 to H<sub>2</sub>O. The solution was stirred for 2 hours at 333 K under ambient atmosphere. The mixture of PI and TEOS were prepared by mixing tetrahydrofuran solution of PI and hydrolyzed TEOS solution, and the mixing ratio of PI and TEOS was fixed to be (95/5) in weight. The PI/TEOS blend films were spin-coated from a mixed solution onto hydrogen-passivated silicon wafers. The films were annealed for 24 h at 333 K under ambient atmosphere. Fig. 1 shows the schematic illustration for sample preparation. The chemical composition in the vicinity of the PI/TEOS blend film surface was examined by angular-dependent X-ray photoelectron spectroscopy (ADXPS) over a range of take-off-angle for photoelectrons from 15 to 90 °. Anti-oxidant property for the films was judged on the basis of the surface roughness after the O<sub>2</sub> plasma treatment. Surface morphology of the films was observed by atomic force microscopy (AFM).

**Results and discussion:** Fig. 2 shows the  $\sin \theta$  dependence of integral intensity ratio of Si<sub>2p</sub> to C<sub>1s</sub> ( $I_{\text{Si}2p}/I_{\text{C}1s}$ ) for a PI/TEOS blend film. Closed circles are the experimental data, and the solid curve denotes the best-fit one. The  $I_{\text{Si}2p}/I_{\text{C}1s}$  value increased with decreasing  $\sin \theta$ , corresponding to the analytical depth. Assuming that the concentration of TEOS component exponentially decays with increasing depth [2], the relationship between real depth and the atomic ratio of silicon to carbon ( $n_{\text{Si}}$ ) was extracted. The inset of Fig. 2 shows the result. It

is clear that the TEOS component was gradually enriched toward the surface. This implies that the cross-linked Si–O–Si bonds were formed at the surface through the sol-gel process of TEOS. Thus, it is expected that the inorganic network vests mechanical strength to the surface of the rubber films.

In general, plasma irradiation induces morphological changes in the surface of polymer materials due to the chain scission. Hence, the surface morphology for the films was observed before and after plasma irradiation, leading to discussion about anti-oxidant property for the sample. Fig. 3 shows the surface morphology and cross-section profiles of untreated and treated films for the PI and PI/TEOS blend. Root-mean square (RMS) roughness is given below the surface morphology in Fig. 3. The surface of the PI film became rougher after the plasma treatment. On the other hand, no significant change was observed at the surface in the PI/TEOS blend film. This means that the anti-oxidant property of the PI film was remarkably improved due to the surface segregation of TEOS via the formation of the inorganic network.

In conclusion, we have succeeded in the construction of PI film with the stiff surface layer based on the surface segregation of TEOS. We believe that this technique greatly simplifies the preparation of highly-functionalized polymer surface and possesses a certain potentiality for industrial applications.

## References

- [1] Stamm, M. *Polymer Surfaces and Interfaces: Characterization, Modification and Applications*, Springer: Verlag, Part 1, 2008.
- [2] D. Kawaguchi, K. Tanaka, T. Kajiyama, A. Takahara, and S. Tasaki, *Macromolecules*, **36**, 6824 (2003).

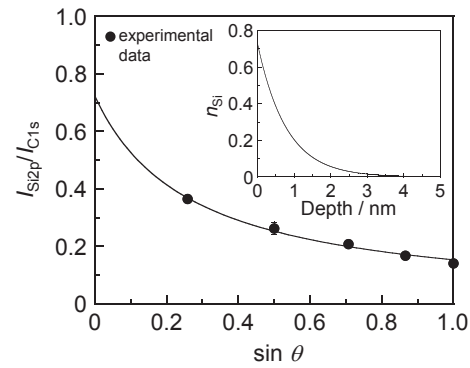


Fig. 2.  $\sin \theta$  dependence of integral intensity ratio of  $Si_{2p}$  to  $C_{1s}$  ( $I_{Si2p}/I_{C1s}$ ) for a PI/TEOS blend film. The solid curve denotes the best-fit one. The inset shows the depth profile of atomic ratio of silicon to carbon ( $n_{Si}$ ).

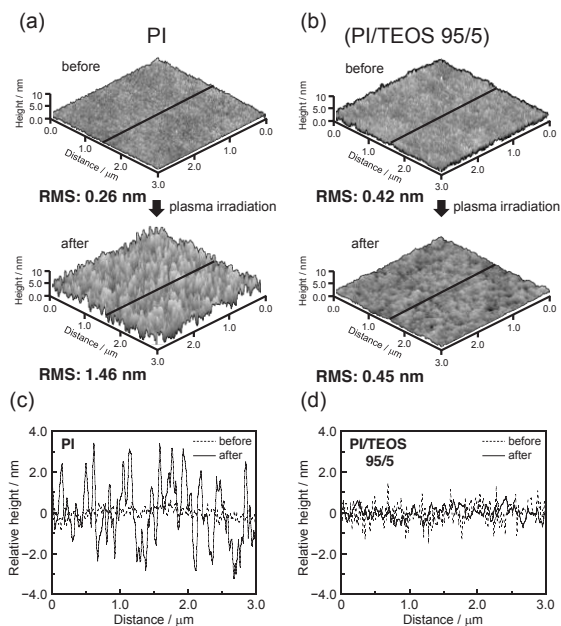


Fig. 3. Surface morphology (a, b) and cross-section profiles (c, d) along lines in (a) and (b) for a PI film (a, c) and a PI/TEOS blend film (b, d).



## Study of adhesion between self-assembled monolayers and poly(dimethyl siloxane)

Yoshiko Harada, Saburo Yamamoto, Hiroshi Jinnai, Atsushi Takahara  
Takahara Soft Interfaces Project, ERATO, JST, Japan

We report here a study on adhesion between self-assembled monolayers (SAMs) of alkylsiloxane on solid substrates and poly(dimethyl siloxane), PDMS. Our experiments utilize the JKR (Johnson-Kendall-Roberts) theory of contact mechanics and instrumentation [1], which allowed us to determine the work of adhesion and elastic constants of solid samples. Fig. 1a shows the home-built adhesion tester set on an inverted microscope, along with the images of contact area. A hemispherical PDMS probe, flat PDMS sample, and a scheme for SAMs are shown in Fig. 1b, c, and d, respectively. Although the chemical make up of PDMS (methyl terminated siloxane network) and methyl-terminated alkylsiloxane SAMs are similar, work of adhesion at thermodynamic equilibrium for PDMS-PDMS was  $\sim 41.7 \text{ mJ/m}^2$ , and that for PDMS-SAMs was  $\sim 35.6 \text{ mJ/m}^2$ . It is plausible that the lower work of adhesion between SAMs and PDMS stems from the less mobile alkyl chains of the SAMs that allow less interaction with PDMS. We are currently carrying out more detailed investigation on the cause of this difference.

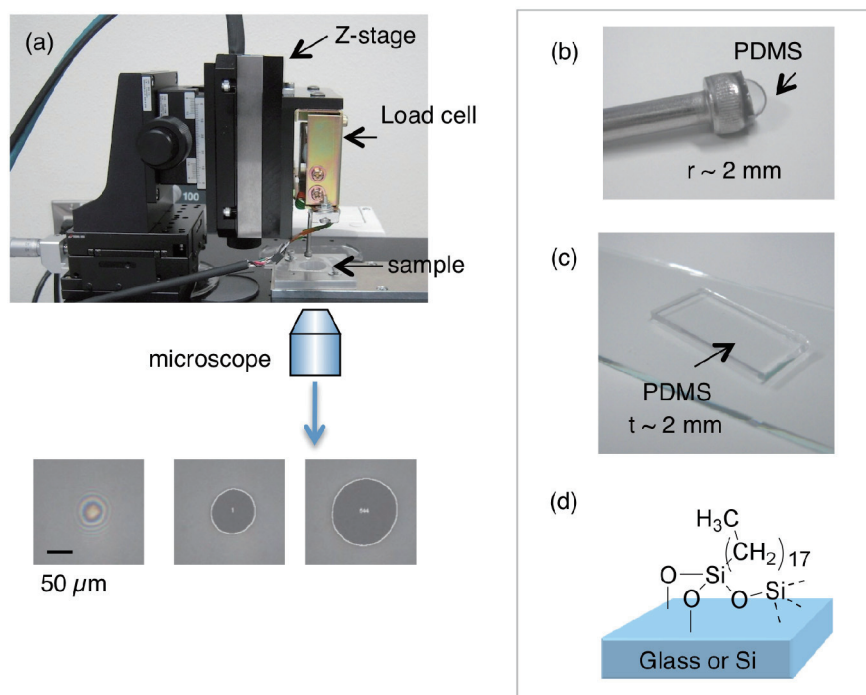


Figure 1: (a) adhesion tester on an inverted microscope, and images of contact area, (b) through (d) are representative samples used in experiments. (b) hemispherical PDMS probe, (c) PDMS flat, (d) scheme of SAMs.

[1] K. L. Johnson, K. Kendall, A. D. Roberts, *Proc. R. Soc. London* **A324**, 301 (1971).

## Microscopic Heterogeneity in Local Viscoelastic Properties of Aqueous Solution of Worm-like Micelles by Optical Tweezers

Koichiro Hori, Atsuomi Shundo, Keiji Tanaka

Department of Applied Chemistry, Kyushu University, Japan

**Introduction:** Dynamics of soft materials such as polymers and micelles are quite complicated because of their hierarchical structure. Thus, to give a better understanding of the dynamics in soft materials, various time- and space-resolved rheological measurements should be made. However, experimental technique to examine the viscoelastic properties at microscopic scale has been limited. Recently, optical tweezers have been applied to examine the viscoelastic properties at the micrometer scale in polymer solutions, biological gels and so forth. In this method, a probe particle which is dispersed in a medium to be measured is trapped and sinusoidally oscillated by a laser beam. The response movement of the particle reflects the viscoelastic properties of the surrounding medium [1]. In this study, we report on local viscoelastic properties in an aqueous solution of worm-like micelles, which are composed of cetyl trimethyl ammonium bromide (CTAB) and sodium salicylate (SalNa).

**Experiments:** The worm-like micelle solution was prepared by mixing the solutions of CTAB and SalNa and successive aging the mixture at 298 K for 3 hours. Concentration of CTAB was kept to be 20 mM for all experiments. The micelle structure was controlled by changing molar ratio of CTAB and SalNa: 1/0, 1/0.5 and 1/1. Polystyrene particles with the radius ( $r$ ) of 0.23 and 0.54  $\mu\text{m}$  were used as a probe to examine the local viscoelastic properties.

**Results and discussion:** Fig. 1(a) shows an optical microscopic image of a probe particle dispersed into the worm-like micelle solution. Infrared laser with a wavelength of 1064 nm was focused on a particle and then was sinusoidally oscillated with an amplitude in the range of 0.07 - 2.6  $\mu\text{m}$  at 1.0 Hz. A plot of particle position against time could be well fitted by a sinusoidal equation, which gave an amplitude value. The amplitude measured in the worm-like micelle solution was smaller than those of the laser amplitude. This is probably because a network structure based

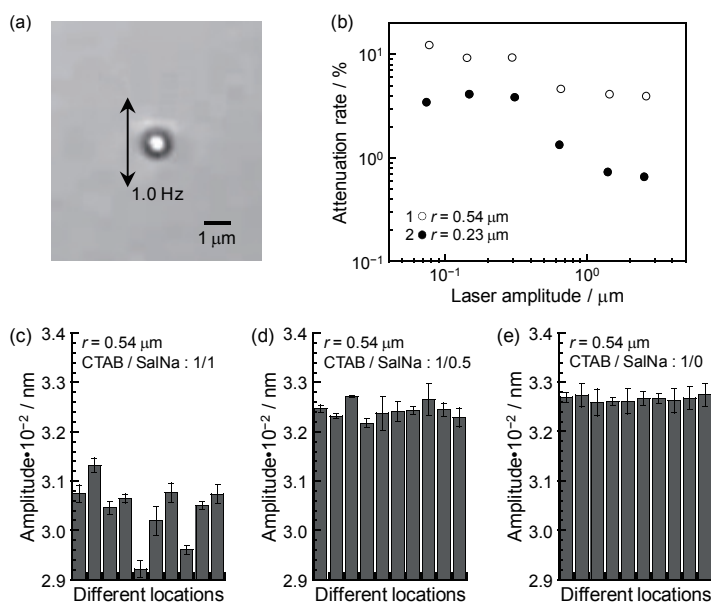


Fig. 1. Optical microscopic image of a probe particle dispersed into an worm-like micelle solution (a), laser amplitude dependence of the amplitude difference between laser and particle movements (b), correlation between amplitudes and locations of the particle in the micelle solutions with the CTAB/SalNa ratio of 1/1 (c), 1/0.5 (d) and 1/0 (e).

on the entanglements of worm-like micelles suppressed the particle motion. Fig. 1(b) shows the amplitude difference between laser and particle movements as a function of the laser amplitude. Each value was normalized by the corresponding laser amplitude. As the laser amplitude went through  $0.4 \mu\text{m}$ , the difference started to decrease. This indicates that the aggregation states of worm-like micelles were in part broken by the particle movement and the extent of the destruction became more significant with increasing laser amplitude. Thus, the amplitude of  $0.33 \mu\text{m}$ , at which the structural destruction was trivial if any, was adopted for further study.

Fig. 1(c-e) summarizes the particle amplitude measured at different 10 locations in the worm-like micelle solutions with the CTAB and SalNa ratio of 1/1, 1/0.5 and 1/0. The average amplitude was smaller in the order of 1/1, 1/0.5 and 1/0 ( $0.33$ ,  $0.32$  and  $0.30 \mu\text{m}$ ). This result is good accordance with the fact that larger amount of SalNa in CTAB solution gives longer worm-like micelles and longer micelles are generally effective for stronger mechanical properties due to the entanglements [2]. Importantly, the value of the amplitude widely varied in the worm-like micelle solution, depending on the location of the particles. The coefficient of variation (CV) for the amplitudes were 2.0, 0.50, and 0.16 % for CTAB/SalNa = 1/1, 1/0.5 and 1/0, respectively. Thus, it is plausible that there exists heterogeneity in the network structure of worm-like micelles and the extent became more striking for longer micelles.

These results motivated us to examine dynamic viscoelastic moduli for the worm-like micelle solution. Fig. 2 shows storage and loss moduli ( $G'$  and  $G''$ ) measured at different 10 locations in the worm-like micelle solutions with the CTAB/SalNa ratio of 1/1 and

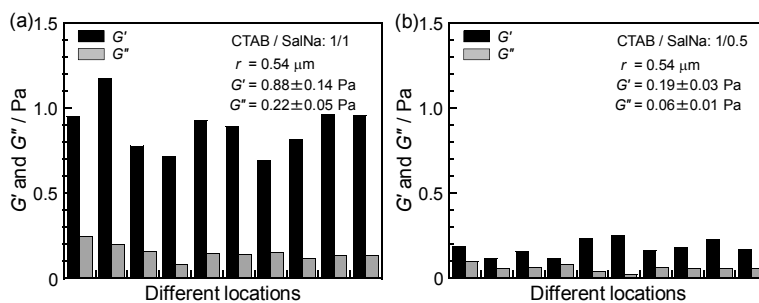


Fig. 2. Storage ( $G'$ , black bars) and loss ( $G''$ , gray bars) moduli measured at different locations in the worm-like micelle solutions with the CTAB/SalNa ratio of 1/0.5 (a) and 1/1 (b).

1/0.5. In both cases,  $G'$  was larger than  $G''$ , meaning that the media are elastic. An important fact is that the location-dependent variation of  $G'$  and  $G''$  was more striking for the CTAB/SalNa ratio of 1/1 (CV = 16 % for  $G'$ , 30 % for  $G''$ ) than that of 1/0.5 (CV = 13 % for  $G'$ , 20 % for  $G''$ ). This does not only indicates heterogeneity in the network structure but also that in viscoelastic properties. The characteristic length scale of the heterogeneity should be on the order of the particle size, namely micrometer scale. Detail discussion on the characteristic length and time scale of viscoelastic heterogeneity will be given in the talk.

## References

- [1] A. Shundo, K. Mizuguchi, M. Miyamoto, M. Goto, and K. Tanaka, *Chem. Commun.*, DOI: 10.1039/c1cc12733k.
- [2] Z. Lin, J. J. Cai, L. E. Scriven, and H. T. Davis, *J. Phys. Chem.*, **98**, 598 (1994).

## Kinetics and Physicochemical Properties of Biofunctional Amine-containing Plasma Polymer Thin Films

Dave Mangindaan, Ching-Chuan Chang, Meng-Jiy Wang\*

Department of Chemical Engineering, National Taiwan University of Science and Technology, Taiwan

43, Keelung Rd., Sec. 4, Taipei 106, Taiwan

\*Corresponding author e-mail: mjwang@mail.ntust.edu.tw

### Abstract

Biofunctional plasma-polymerized thin films prepared from amine-containing saturated (propylamine) and unsaturated precursors (allylamine and propargylamine, respectively) were investigated in terms of the deposition rate, polymerization kinetics and thin film morphology as function of the applied power. On the other hand, surface chemistry (N/C ratio and imine content) was believed to govern the growth of L-929 fibroblast cells on the prepared amine-functionalized surfaces. The obtained results allow the relationships between the deposition kinetics, the physicochemical and biological response of the amine plasma polymers to be quantitatively elucidated.

### 1. Introduction

Materials contain amine functionality attract great interests for their wide-range applications in membranes for wastewater treatments [1-2], functionalization of carbon nanotubes or microspheres [3], biocompatibility improvement in biomedical materials [4-5], microfluidics [6], and in sensor fabrications [7-9]. The creation of amine functions by using plasma polymerization provided great advantages including single-step, solvent-free and rapid fabrication for the deposition of pinhole-free thin films [10]. The precursors employed to integrate amine functionalization by plasma polymerization was extensively reviewed [11]. However, it was observed that allylamine, a C<sub>3</sub> amine (amine conjugated with three carbons) with double bond of =CH<sub>2</sub> group, is extensively studied, with examples in application as coating layer on biomaterials such as polyethyleneterephthalate [12], polystyrene and polyethylene powder [13], stainless steel stents or on aluminum [14], in the fields of sensor technology [15], as well as for DNA immobilization [16]. The mechanism of allylamine plasma polymerization has been reported and reviewed by different research groups [11,17]. Nevertheless, the comparisons among plasma polymerizations with other C<sub>3</sub> amine molecules, i.e. propylamine [18-19] and propargylamine [18], were less reported. Moreover, due to the highly complex course of plasma polymerization, the supporting literature detailed the relationships between the deposition kinetics with the physical-chemical properties of plasma polymers were less reported [20-22].

In this study, we prepared amine-containing plasma polymers from C<sub>3</sub> amine monomers with different conjugation degree. The variance in saturation degree led to different deposition kinetics. Furthermore, we found that the created amine plasma polymers showed direct effects on the growth of L-929 fibroblast cells where the higher N/C ratio and imine content promoted higher cell density on plasma polymers. The results, integrating experimental data and mathematical calculations, have detailed how greatly the chemical structure of monomers influenced the physical-chemical properties of the prepared plasma polymers and their application as biofunctional soft materials.

### 2. Experimental

#### 2.1 Materials

Propylamine (99%, boiling point 48 °C), allylamine (99%, b.p. 53 °C), and propargylamine

(98%, b.p. 84 °C) were purchased from Acros and utilized as received without further purification. Quartz substrate (intrinsic frequency 10 MHz) was purchased from Taitien Electronics Co., Taiwan. Si wafer substrate (100, n-type, Wafer Works Corp, Taiwan) was prepared and cleaned by applying Kern's method [23]. In brief, Si wafer was cleaned by immersing in ethanol-acetone mixture (1:1) to remove organic and inorganic residues. The cleaning was assisted by ultrasonic cleaner for 15 min.

## 2.2 Plasma polymerization

The polymerization of C<sub>3</sub> amines was conducted in a plasma system which was modified from the previous work [24]. The system is consisted of three main parts: (i) a reaction chamber; (ii) a radio-frequency generator (Huttinger, model PFG 300 RF, Germany); and (iii) a vacuum system. In brief, the deposition of all monomers was set at 100 mTorr, 20 sccm, heating temperature at 40 °C, for 60 min. The vaporized monomer was introduced into the chamber and was polymerized with different applied power (5, 10, 30, 50 W) on quartz and Si wafer. Due to overheating issue in our plasma apparatus, applied power more than 50 W is not possible at the moment.

## 2.3 Cell culture

The cell culture of L-929 fibroblast cells were performed in a humidified incubator with temperature 37 °C and 5% CO<sub>2</sub> control. All culture media were purchased from Sigma: Dulbecco's modified eagle medium (DMEM-high glucose); trypsin, lyophilized powder; EDTA; fetal bovine serum; sodium bicarbonate; sodium pyruvate; and l-glutamine. The L-929 cells were cultivated for 24 h, with the initial cell density of 20,000 cells/mL. Cell fixation prior to SEM analyses was carried out by immersing cells in 0.2% (10 min, 4°C) and 2.5% (60 min, 4°C, twice) glutaraldehyde, respectively. For SEM imaging, the L-929 fibroblast cells were dehydrated by applying a gradient of ethanol concentrations from 30 to 90%, (30, 40, 50, 70, 80 and 90 %, 10 min for each concentration) and 99.5 % (10 min, 3 times) sequentially, at room temperature. The drying process was completed by critical point drying (Tousimis<sup>®</sup> Samdri<sup>®</sup> PVT-3B).

## 2.4 Thin film characterizations

The amount of the deposited polymers on quartz substrate was quantified by quartz crystal microbalance (ANT Technologies Co., model ANTQ3000, Taiwan). The wettability of the surface was evaluated by measuring the static contact angles (Sindatek) with deionized water. At least five droplets were measured for each position, with 1 mL droplet volume. The cell morphology of L-929 fibroblasts on different surfaces was observed by using scanning electron microscopy (SEM, JEOL JSM-6300). The chemical composition of the plasma polymerized thin films was determined by electron spectroscopy for chemical analysis (ESCA). Thermo VG Scientific Theta Probe Instrument with monochromatic source of Al-K $\alpha$  (1,486.6 eV), with other details were described in our previous work [24]. The surface concentration of primary (NH<sub>2</sub>) and secondary (NH) amine groups was determined by the derivatization technique employing trifluoromethyl benzaldehyde (TFBA) and trifluoroacetic anhydride (TFAA), with the derivatization mechanism reported elsewhere [17]. The derivatization was performed by exposing the plasma polymer films 30 and 10 min with TFBA and TFAA vapor, respectively, in a sealed container at ambient condition [25]. The primary and secondary amine concentrations were obtained from surface fluorine and carbon concentrations analyzed by ESCA on the derived samples.

## 3. Results

Plasma polymerizations by using three different C<sub>3</sub> amine monomers were carried out and

the prepared thin polymer films were characterized by ESCA. The deposition rate was evaluated by QCM measurement. The stability of the deposited thin films was examined by ESCA analyses by immersing the samples in PBS for 48 h. Cell-surface interactions were studied by culturing L-929 fibroblast cells directly on surfaces prepared from the three C<sub>3</sub> amine plasma polymers.

### 3.1 The deposition of the C<sub>3</sub> amine plasma polymers

The plasma polymerization was performed under 100 mTorr with power ranged from 0-50 W, in a relatively low deposition rate (ng/s). For all the three C<sub>3</sub> amine monomers, the deposition rate revealed a nearly linear relationship as function of the applied power (Fig. 1).

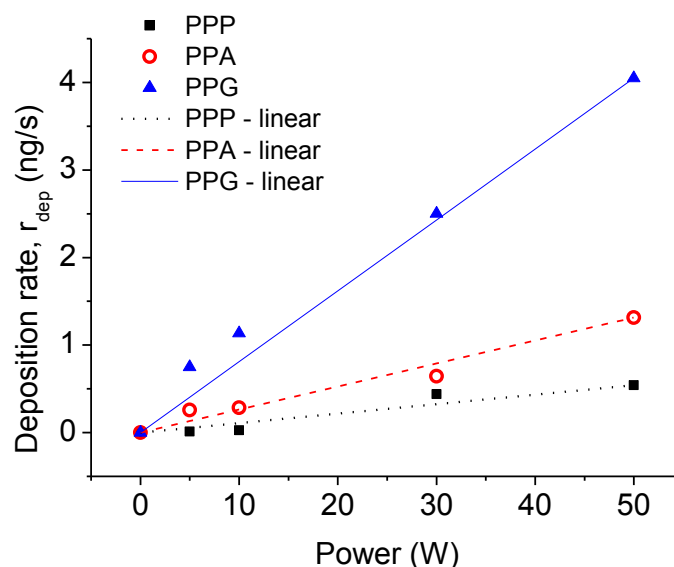


Fig. 1. Deposition rate of C<sub>3</sub> amine monomers by plasma polymerization as function of applied power.

A set of linear fittings was applied to show the linearity and indicate the deposition rate, as tabulated in Table 1. It is noted that as the degree of unsaturation in monomers increased (monomers containing double- or triple- bonds), the deposition rate ratio was increased to 1.92 folds and 6.32 folds for allylamine (PPA) and propargylamine (PPG) relative to that of propylamine (PPP, 1.00). At the highest applied power utilized (50 W), the deposition rate was 0.61, 1.30, and 4.04 ng/s for plasma polymers deposited from propylamine, allylamine, and propargylamine, respectively.

Table 1. The kinetic parameter for the deposition rate of plasma polymers.

Parameters	PPP	PPA	PPG
Deposition rate constant $K_{dep}$ ( $10^{-14}$ s <sup>2</sup> /m <sup>2</sup> )	1.314	2.520	8.301
$K_{dep}/(K_{dep} \text{ PPP})$ ratio	1.000	1.917	6.317
$R^2$	0.937	0.971	0.991

### 3.2 ESCA surface characterizations

The chemical composition of the plasma polymerized C<sub>3</sub> amines (50 W, 60 min) was examined by ESCA. The wide-scan spectra exhibited three peaks corresponding to carbon (C1s, 284.6 eV), nitrogen (N1s, 398 eV), and oxygen (O1s, 533 eV) (data not shown), as summarized in Table 2. The existence of oxygen is probably due to the oxidation originated from oxygen residue in reactor during the plasma polymerization or caused by atmospheric exposure after the deposition [17]. More than 15% of nitrogen was successfully incorporated

by using all the C<sub>3</sub> amine monomers where the deposition of PPA incorporated a higher nitrogen content (16.4 %, N/C ratio = 0.219) than that of PPP (15.6 %, N/C = 0.198) and PPG (15.0 %, N/C = 0.189).

Table 2. The chemical composition and the ESCA high-resolution C1s peak deconvolution of plasma polymerized C<sub>3</sub> amines.

Plasma polymer		PPP	PPA	PPG
Covalent bonds		1	2	3
C (%)		78.7	74.7	80.8
O (%)		5.7	8.9	4.2
N (%)		15.6	16.4	15
N/C (%)		19.8	21.9	18.9
C <sub>I</sub> (284.6 eV)	C-C (%)	72.0	68.5	64.8
C <sub>II</sub> (285.5 eV)	C-N (%)	9.2	8.7	13.9
C <sub>III</sub> (286.1 eV)	C=N, C-O, C-C≡N (%)	16.5	17.1	14.2
C <sub>IV</sub> (287.6 eV)	CO-NH, C=O (%)	2.3	5.7	7.1
<i>R</i> <sup>2</sup>		0.99	0.99	0.99

The ESCA high resolution spectra of the plasma polymers were normalized to 284.6 eV (C<sub>I</sub> for C-C binding), the main carbonaceous backbone structure. The nitrogen-containing C-N bindings were deconvoluted to C<sub>II</sub> (C-N, at 285.5 eV), C<sub>III</sub> (C=N; C-O; and C-C≡N, at 286.1 eV) and C<sub>IV</sub> (CO-NH; C=O, at 287.6 eV), (Fig. 2, and Table 1).

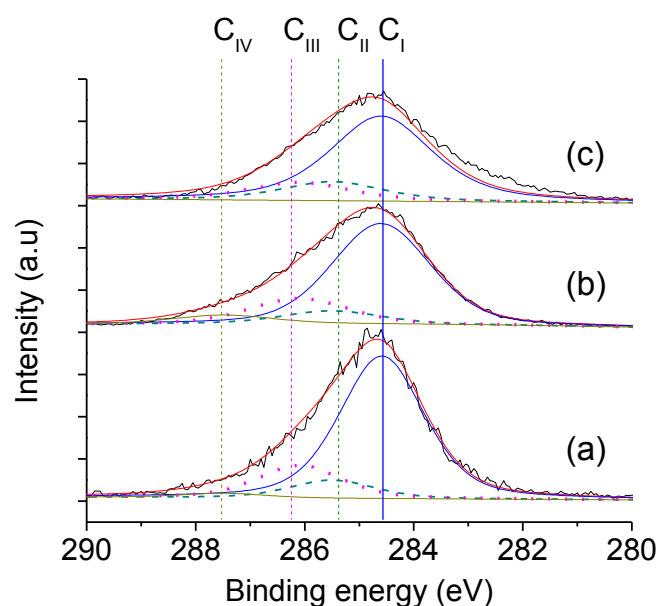


Fig. 2. ESCA high-resolution C1s spectra of PPP (a), PPA (b), and PPG (c), deposited at 20 sccm flowrate, 100 mTorr pressure, 50W for 60 min.

The ESCA results showed clearly that PPA possessed the highest nitrogen content, in particular C<sub>III</sub> (17.1 %), than that of PPP and PPG (16.5 and 14.2 %, respectively). Furthermore, some studies demonstrated that nitrile (C-C≡N) or alcohol (C-O) was found to be minor constituent in the C<sub>III</sub> peak [26], with imine (-C=N) as the dominant functional groups (more than 50% proportion) [18]. The N/C ratio from the wide scan corresponded proportionally to the C<sub>III</sub> content, suggesting that the deposition of PPA introduced

significantly higher imine functionalities than that of PPP and PPG.

Furthermore, the primary and secondary amine obtained by TFBA and TFAA derivatization of each plasma polymer were investigated by ESCA and profiled in Table 3. It was demonstrated that the PPA incorporated the most amount of primary and secondary amines onto the surface compared to PPP and PPG. Moreover, the secondary amine dominated the surface by more than five folds to that of primary amines.

Table 3. Primary and secondary amine content of plasma polymers.

Amines	PPP	PPA	PPG
Primary [NH <sub>2</sub> ]	0.61	0.71	0.44
Secondary [NH+OH]	4.07	6.73	2.39
Total amines	4.68	7.44	2.83

### 3.3 Stability of plasma polymerized C<sub>3</sub> amine thin films

For a stability test, two sets of plasma polymers from the three monomers were independently prepared (20 sccm, 10 W, 60 min). After immersing the plasma deposited amine-containing specimens in PBS for 48 h, dissolution and swelling were not observed for the deposited films. Moreover, ESCA characterizations tabulated in Table 4 also confirmed that there is no significant change in chemical composition of the films after the immersion. Thus, it can be concluded that the fabricated films are stable after immersion in PBS, even for films produced in low power.

Table 4. Atomic composition of amine-containing plasma polymers before and after immersion in PBS for 48 h.

Plasma polymer	Condition	C (%)	N (%)	O (%)
PPP	Before	77.9 ± 0.7	17.1 ± 1.8	5.1 ± 1.1
	After	75.0 ± 2.3	14.2 ± 0.5	10.9 ± 2.8
PPA	Before	78.8 ± 0.9	17.2 ± 1.3	4.2 ± 0.5
	After	75.6 ± 2.3	13.5 ± 0.1	11.0 ± 2.3
PPG	Before	79.5 ± 0.8	15.5 ± 0.1	5.1 ± 0.6
	After	75.4 ± 0.2	12.0 ± 0.4	12.7 ± 0.1

For all the three plasma polymers, more than 95 % of carbon and nitrogen content were preserved and only slight oxidation was detected by about 5 % for PPP, and 7% for PPA and PPG which is presumably due to the sample immersion in oxidative condition. It is therefore reasonable to conclude that all of the prepared amine-containing plasma polymers were exceptionally stable that the superior properties can assist further the applications in surface coatings and surface functionalization of biomedical devices.

### 3.4 Cell responses of L-929 fibroblasts on C<sub>3</sub> amine plasma polymers

L-929 fibroblast cells were directly cultivated on the plasma deposited amine-containing thin films (20 sccm, 50 W, 60 min) to investigate the interactions between cells and plasma polymers (Fig. 3). On the bare Si wafer, L-929 cells showed spherical morphology with limited cell number, close to the initial cell seeding density (20,000 cells/mL on samples with 1 cm<sup>2</sup> surface area), as shown in Fig. 3a). The round shaped cells represented their dormant phase under the limited niche for cell growth on Si wafer. On the other hand, the fibroblasts showed highly extended pseudopodia on all C<sub>3</sub> amine plasma polymerized surfaces (Fig. 3b-3d).



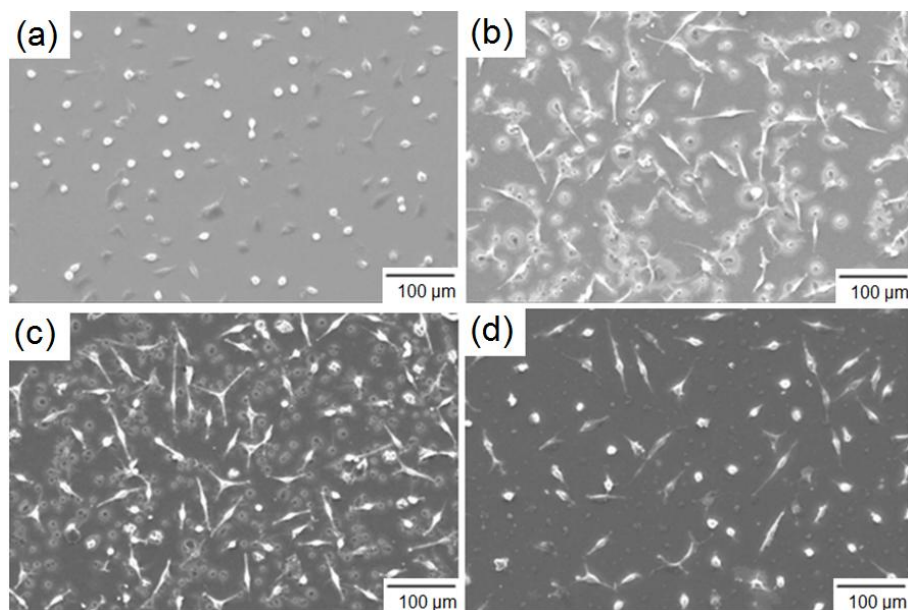


Fig. 3. L-929 fibroblasts cell behavior on surfaces of bare Si wafer (a), PPP (b), PPA (c), and PPG (d).

Quantitatively, on PPP and PPG surfaces, the cell density increased to nearly 1.5 folds of the initial seeding density to be about 34,000 and 32,000 cells/cm<sup>2</sup>, respectively (Fig. 3b and 3d). Moreover, a greater than two folds of the initial cell density was observed (~40,000 cells/cm<sup>2</sup>) exclusively on PPA surface (Fig. 3c). The well spread of L-929 cells verified the nitrogen-containing functions promoted effectively the cell attachment on the plasma polymers.

## 4. Discussion

### 4.1 The correlations between molecular structure and kinetics

The result of the plasma polymerization kinetics of PPP, PPA, and PPG showed that the difference of the rate constants was not directed by the operational parameters because only one set of plasma parameters (i.e. fixed flowrate, temperature, and pressure) was employed. In this case, the well known Yasuda parameter for plasma polymerization,  $W/FM$  [10], was not employed to discuss the mechanism for the deposition rate. The results in this study reported that the higher rate constant was obtained for the C<sub>3</sub> amine monomer possessed more covalent bonds (i.e., for propargylamine plasma polymer). Therefore, the structure of monomers might provide the better elucidation on the deposition mechanism for plasma polymerization.

Fally et al. have demonstrated that plasma polymerization of PPP, PPA and PPG monomers showed the deposition rates with ration of 1.0: 2.0: 5.1 (normalized to the  $K_{dep}$  of PPP) [18], resembled to the  $K_{dep}$  calculated in this work (1.0: 1.9: 6.3) (Table 5). We therefore analyzed and discussed the roles of (i) covalent bond number, (ii) bond length, and (iii) amine bond dissociation energy (NH<sub>2</sub> BDE), on the deposition rate constant for the three C<sub>3</sub> amine monomers used in this study (Table 5).

Table 5. The relationship between the molecular structure of precursors and  $K_{dep}$  of  $C_3$  amines plasma polymers.

Properties	Unit	PPP	PPA	PPG	$R^2$ for $K_{dep}$
Covalent bond	-	1	2	3	0.875
Bond length <sup>a</sup> [27]	Å	1.501	1.337	1.195	0.846
NH <sub>2</sub> BDE	kcal/mol	85.7 <sup>[28]</sup>	69.3 <sup>[29]</sup>	38.3 <sup>b</sup>	0.967
W/FM <sup>[10]</sup>	10 <sup>5</sup> kJ/kg	1.222	1.179	1.139	0.860

Notes: <sup>a</sup> Bond length [27] is defined as the distance of -C-C (corresponding to bond number= 1), -C=C (bond number= 2), and -C≡C (bond number= 3), for propylamine, allylamine, and propargylamine, respectively.

<sup>b</sup> The bond dissociation energy (BDE) of X-NH<sub>2</sub> to be X + NH<sub>2</sub> for example of propargylamine plasma polymer (PPG) is calculated by:

$$\Delta H_{f,298}^0 X_{(g)} + \Delta H_{f,298}^0 NH_{2(g)} - \Delta H_{f,298}^0 XNH_{2(g)} \quad (1)$$

$\Delta H_{f,298}^0 X = 49.0$  kcal/mol [30];  $\Delta H_{f,298}^0 NH_{2(g)} = 45.4$  kcal/mol [31]; while  $\Delta H_{f,298}^0 XNH_{2(g)} = 56.1$  kcal/mol [32]. From eq. 1, the BDE of X-NH<sub>2</sub> for PPG is calculated to be 38.3 kcal/mol.

A poor correlation was found for the deposition rate constant  $K_{dep}$  versus the number of the covalent bonds and the bond length ( $R^2 < 0.95$ ). On the other hand, a linear relationship was clearly shown for  $K_{dep}$  and NH<sub>2</sub> BDEs for  $C_3$  amine monomers ( $R^2 = 0.967 > 0.95$ ). It is therefore clear that the factor governing the deposition rate constant is *principally* the dissociation energy for the amine bond (NH<sub>2</sub> BDE) of the monomers under plasma polymerization process.

#### 4.2 Cell response related to surface chemistry of $C_3$ amines plasma polymers

Previously, we suspected that the wettability of the plasma-polymerized surface is also govern the cell attachment. However, the almost identical wettability of PPA and PPG (with water contact angle of  $53.2 \pm 1.9^\circ$  and  $55.8 \pm 2.8^\circ$ , respectively, taken with  $n=5$ ) could not explain the enhancement of cell density on PPA by  $\sim 8000$  cells/cm<sup>2</sup> compared to PPG. Moreover, the concept of wettability still could not describe the similar cell density trend on PPP and PPG although the wettability of PPP is very different ( $38.6 \pm 1.4^\circ$ ) with that of PPG ( $55.8 \pm 2.8^\circ$ ). For that reason, we deduced that the cell density on amine-containing plasma polymers is not related with the wettability, and therefore investigated the effect of the surface chemistry of the films toward the cell response.

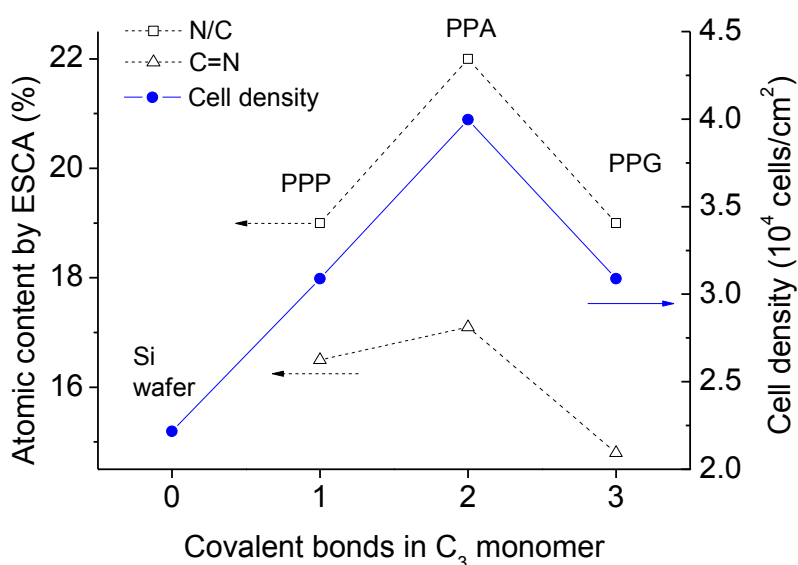


Fig. 4. Relationship between surface chemistry of  $C_3$  amines plasma polymers towards L-929 fibroblast cell density.

The plasma polymerization results revealed that the deposition rate of PPG was about three to six times higher than that of PPA and PPP. However, the cell adhesion, commonly known as a direct reflection of the amount of amine/imine functionalities on the surface of materials, did not correspond to the higher deposition rate (thicker plasma polymerized thin film). For the deposited PPA, although the amounts of imines (C=N) and nitrogen content (described by N/C ratio) were only slightly higher than that of PPP and PPG, the cell density of L-929 increased significantly (Fig. 4). With 2% difference in N/C ratio and 0.6-2.3% difference in imine content, the cell density was improved by 25% (from 32,000 to 40,000 cells/cm<sup>2</sup>) on PPA surfaces.

The higher nitrogen content incorporated in PPA than that of PPP and PPG under the same experimental conditions was also observed in literature [18]. A study of amine derivatization reaction by using 2,2,2-trichloroethanol (TCE) showed that 3N/Cl atomic ratio for PPA is the highest (47.6) compared to that of PPP (28.6) and PPG (12.5) [18]. The ratio describes the amount of N captured by Cl from TCE, indicating the availability of nitrogen content on the surface. Furthermore, as exhibited Table 3 and described in Section 3.3, the surface amine concentration (especially the secondary amine) is also supposed to have an important role in promotion of L-929 growth. The most incorporation of primary and secondary amines in PPA (among other plasma polymers prepared in this study) confirmed the trend of prosper L-929 cells growth on PPA weighed against PPP and PPG. Therefore, both the literature and the experimental results from this study suggested that PPA incorporated higher imine and surface amine than its analogs (PPP and PPG) and that the imine groups and surface amine concentration promoted the growth of L-929 cells significantly.

## 5. Conclusion

Amine-containing plasma polymer thin films were successfully prepared from three types of C<sub>3</sub> amine precursors with different saturation degree. Notable difference in deposition rates of about two and six folds was observed from allylamine and propargylamine compared to that of propylamine precursors. ESCA characterization identified the increase of the intensity of amine functionalities as function of the applied power for the three C<sub>3</sub> amine monomers.

Further analyses on the three C<sub>3</sub> amine precursors revealed that the amine bond dissociation energy of precursor governed the polymerization kinetics by showing a linear relationship with the deposition constant  $K_{dep}$ . Moreover, the cell responses on the C<sub>3</sub> amine polymerized thin films demonstrated that the imine content and N/C ratio played pivotal role in promoting cell adhesion. With the exceptional stability, controllability, and biocompatibility, the amine-containing plasma polymers possess vast potential for the application in surface coating and the surface modifications for biofunctional materials.

## Acknowledgement

The authors express great appreciation to the National Science Council for their financial supports (NSC 99-2621-M-011-003)

## References

- [1] I. Gancarz, G. Pozniak, M. Bryjak, and W. Tylus. *Eur. Polym. J.* **38**, 1937 (2002).
- [2] G. Pozniak, I. Gancarz, M. Bryjak, and W. Tylus. *Desalination* **146**, 293 (2002).
- [3] A. Denizli, B. Salih, and E. Piskin. *J. Chromatogr. A* **773**, 169 (1997).
- [4] L. Dai, H. A. W. St.John, P. Z. Jingjing Bi, R. C. Chatelier, and H. J. Griesser. *Surf. Interface Anal.* **29**, 46 (2000).
- [5] F. Truica-Marasescu, and M. R. Wertheimer. *Plasma Process. Polym.* **5**, 44 (2008).
- [6] J. Xu, and K. K. Gleason. *Chem. Mater.* **22**, 1732 (2010).
- [7] A. Hiratsuka, H. Muguruma, S. Sasaki, K. Ikebukuro, and I. Karube. *Electroanalysis*

- 11**, 1098 (1999).
- [8] R. Nakamura, H. Muguruma, K. Ikebukuro, S. Sasaki, R. Nagata, I. Karube, and H. Pedersen. *Anal. Chem.* **69**, 4649 (1997).
- [9] K. Nakanishi, H. Muguruma, and I. Karube. *Anal. Chem.* **68**, 1695 (1996).
- [10] N. Inagaki. *Plasma Surface Modification and Plasma Polymerization*. Technomic Publishing Company, Inc., Basel, Switzerland 1996.
- [11] K. S. Siow, L. Britcher, S. Kumar, and H. J. Griesser. *Plasma Process. Polym.* **3**, 392 (2006).
- [12] P. Hamerli, T. Weigel, T. Groth, and D. Paul. *Biomaterials* **24**, 3989 (2003).
- [13] M. Tatoulian, F. Bretagnol, F. Arefi-Khonsari, J. Amouroux, O. Bouloussa, F. Rondelez, A. J. Paul, and R. Mitchell. *Plasma Process. Polym.* **2**, 38 (2005).
- [14] J. F. Friedrich, R. Mix, and G. Kuhn. *Surf. Coat. Technol.* **174–175**, 811 (2003).
- [15] H. Yatsuda, M. Nara, T. Kogai, H. Aizawa, and S. Kurosawa. *Thin Solid Films* **515**, 4105 (2007).
- [16] Z. Zhang, W. Knoll, and R. Förch. *Surf. Coat. Technol.* **200**, 993 (2005).
- [17] A. Choukourov, H. Biederman, D. Slavinska, L. Hanley, A. Grinevich, H. Boldyryeva, and A. Mackova. *J. Phys. Chem. B* **109**, 23086 (2005).
- [18] F. Fally, C. Doneux, J. Riga, and J. J. Verbist. *J. Appl. Polym. Sci.* **56**, 597 (1995).
- [19] A. G. Shard, J. D. Whittle, A. J. Beck, P. N. Brookes, N. A. Bullet, R. A. Talib, A. Mistry, D. Barton, and S. L. McArthur. *J. Phys. Chem. B* **108**, 12472 (2004).
- [20] D. Hegemann, M. M. Hossain, E. Korner, and D. J. Balazs. *Plasma Process. Polym.* **4**, 229 (2007).
- [21] L. Denis, D. Cossement, T. Godfroid, F. Renaux, C. Bittencourt, R. Snyders, and M. Hecq. *Plasma Process. Polym.* **6**, 199 (2009).
- [22] L. Denis, P. Marsal, Y. Olivier, T. Godfroid, R. Lazzaroni, M. Hecq, J. Cornil, and R. Snyder. *Plasma Process. Polym.* **7**, 172 (2010).
- [23] W. Kern. *J. Electrochem. Soc.* **137**, 1887 (1990).
- [24] D. Mangindaan, W.-H. Kuo, Y.-L. Wang, and M.-J. Wang. *Plasma Process. Polym.* **7**, 754 (2010).
- [25] A. Choukourov, H. Biederman, I. Kholodkov, D. Slavinska, M. Trchova, and A. Hollander. *J. Appl. Polym. Sci.* **92**, 979 (2004).
- [26] Z.-F. Li, and A. N. Netravali. *J. Appl. Polym. Sci.* **44**, 319 (1992).
- [27] K. Kuchitsu. *Landolt-Bornstein: Numerical Data and Functional Relationships in Science and Technology*. Vol. II/25C Springer-Verlag, Berlin, Heidelberg, Germany. 2000.
- [28] Y. Luo. *Handbook of Bond Dissociation Energies in Organic Compounds*. CRC Press, Boca Raton, Florida, USA 2003.
- [29] Y. Ma, W. Guo, L. Zhao, S. Hu, J. Zhang, Q. Fu, and X. Chen. *J. Phys. Chem. A* **111**, 6208 (2007).
- [30] D. R. Lide. *CRC Handbook of Chemistry and Physics*. CRC Press, Boca Raton, Florida, USA 2005.
- [31] P. J. Linstrom, and W. G. Mallard. *NIST Chemistry WebBook*. National Institute of Standards and Technology, Gaithersburg, Maryland, USA 2001.
- [32] J. L. Holmes, F. P. Lossing, and P. M. Mayer. *Chem. Phys. Lett.* **198**, 211 (1992).

## DYNAMIC WATER/OIL REPELLENT PROPERTIES OF TRANSPARENT MULTILAYERED SILOXANE-ORGANIC HYBRID FILMS

Chihiro Urata, Dalton F. Cheng, Atsushi Hozumi

National Institute of Advanced Industrial Science and Technology (AIST)

2266-98 Anagahora, Shimoshidami, Nagoya 463-8560, Japan

Improvement of the water/oil repellent properties of various kinds of solid surfaces, such as metals, ceramics, resins, woods, and fabrics, has been greatly demanded in a wide variety of engineering fields. Among the numerous approaches toward this purpose, the use of liquid-like thin organic layers, such as less-densely packed monolayers, umbrella/ring-shaped monomeric layers, and polymer brush films, is one of the most promising.<sup>[1]</sup> These organic layers exhibit very low energy barriers between metastable states of liquid droplets on the surface, leading to the formation of nonhysteretic surfaces (increase in the ease of mobility of liquid drops).

In this study, we propose a novel coating system for improvement of the water/oil repellent properties of solid surfaces using multilayered siloxane-organic hybrids (MSHs). MSHs, derived from co-hydrolysis and polycondensation of an alkylalkoxysilane (in the present case, decyltriethoxysilane [DTES]) and a tetraalkoxysilane (in this case, tetramethoxysilane [TMOS]) mixture, are composed of alternating hydrophobic alkyl and siloxane layers with nanometer-scale interval distance between the layers.<sup>[2]</sup> Use of such hybrid materials as coatings offers the advantage that with less densely packed alkyl chains due to the presence of condensed silica species between alkylsilyl groups, the monolayer is expected to be flexible and to exhibit a liquid-like property.

MSH film contains decyl (C10) moieties was coated on a glass substrate (MSH-C10-glass) according to the previous reports.<sup>[2]</sup> For comparison, a C10-terminated glass substrate (C10-glass) was prepared using DTES vapor. Dynamic water/oil repellency was evaluated by contact angle (CA) hysteresis analysis using water and hexadecane as probe liquids.<sup>[1]</sup>

As shown in Fig. 1-b, our MSH-C10-glass is transparent. The XRD pattern indicates the formation of multilayered structure with an interlayer distance of about 3.6 nm. (Fig. 1-a and c) The CA hysteresis of MSH-C10-glass for water and hexadecane was 2° (advancing /receding contact angles ( $\theta_A/\theta_R$ ) = 110°/108°) and 1° (39°/38°), respectively, and droplets of both liquids on this surface rolled easily at low tilt angles. On the other hand, in the case of the C10-glass, water and

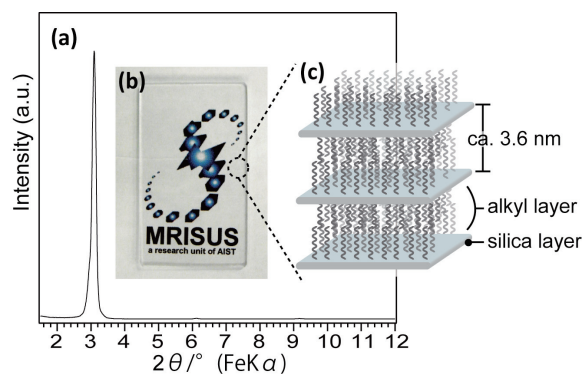


Fig.1 (a) Typical XRD pattern, (b) transparency, and (c) structural model of MSH-C10-glass.

oil droplets pinned to the surface because of the large CA hysteresis (water had a CA hysteresis of  $33^\circ$  ( $\theta_A/\theta_R=110^\circ/77^\circ$ ) and hexadecane formed a thin film on the surface ( $\theta_A/\theta_R=<10^\circ/<5^\circ$ ). The C10 chains of the MSH-C10-glass are expected to be loosely packed and/or considerably more disordered than those on the glass surface. Such a surface likely shows liquid-like properties, resulting in the enhancement of dynamic water/oil repellency. Our multilayered siloxane-organic hybrid films showing extremely low CA hysteresis may undoubtedly show great potential for transparent water/oil repellent coatings.

[1] (a) A. Y. Fadeev et al, *Langmuir*, **15**, 3759 (1999); (b) A. Y. Fadeev et al, *Langmuir*, **16**, 7268 (2000); (b) A. Hozumi et al., *Langmuir*, **26**, 2567 (2010); (c) D. F. Cheng et al, *submitted*.

[2] (a) A. Shimojima et al., *J. Am. Chem. Soc.*, **120**, 4528 (1998); (b) A. Shimojima et al., *Langmuir*, **18**, 1144 (2002); (c) C. Urata, et al., *J. Mater. Chem.*, **21**, 3711 (2011).

## DYNAMICS OF CASSIE BAXTER-WENZEL WETTING TRANSITION ON TEXTURED POLYMER SURFACES

Daiki Murakami<sup>1</sup>, Hiroshi Jinnai<sup>1</sup>, Atsushi Takahara<sup>1,2</sup>

<sup>1</sup> Japan Science and Technology Agency (JST), ERATO, Takahara Soft Interfaces Project, CE80, Kyushu University, 744 Motooka, Nishi-ku, Fukuoka 819-0395, Japan

<sup>2</sup> Institute for Materials Chemistry and Engineering, Kyushu University, Japan

Liquids on textured solid surface exhibit either one of the two types of wetting, *i.e.*, Cassie-Baxter and Wenzel states. In the former, air that is trapped in the groove forms the composite (solid/air) hydrophobic surface, while the liquid penetrate into the groove and thus the surface wettability is emphasized due to the increase of contact area in the latter. Although the static behaviors of those two types of wetting are well understood both experimentally and theoretically, dynamical aspects in the wetting phenomena, *i.e.*, the switching or transition between those two states, remains an open question.

In the present study, we focused the dynamics of wetting transition from Cassie-Baxter to Wenzel states. The wetting behavior of water and ionic liquids on a fluorinated cycloolefin polymer, CYTOP™ (AGC, Japan) was investigated. The nano-scale pillar-patterned on CYTOP was prepared by the nano-imprint lithography. The contact angles of water droplet on the pillar-patterned surfaces changed between theoretical values of the Cassie-Baxter and Wenzel states, whereas ionic liquids (ILs) were clearly in Wenzel wetting state (**Figure 1**). Furthermore, the optical microscopic views of water droplet from the bottom of the textured surface revealed that the wetting transition proceeded with drastically different time scale depending on the aspect ratio of fabricated patterns (**Figure 2**). Simple models representing the surface energies in Cassie-Baxter, Wenzel, and transient states demonstrated that the wetting dynamics, *e.g.*, the progression rate and stability of wetting state, was dominated by the energy barrier between Cassie-Baxter and Wenzel states.

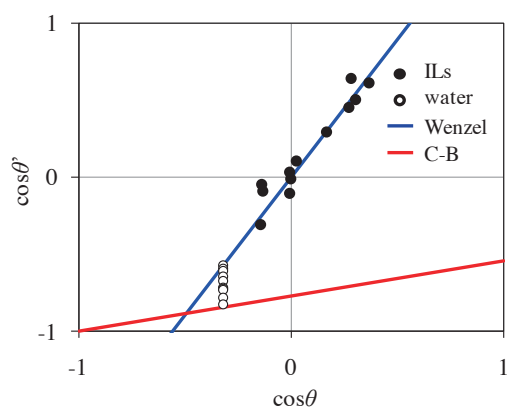
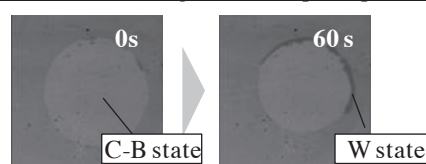


**Figure 1.** Contact angle of water and various ionic liquids on 230nm pillar patterned CYTOP surface.

width:230 nm,height: 200 nm pillar pattern



width:2 μm,height: 1 μm pillar pattern



**Figure 2.** Optical microscopic observations of Cassie-Baxter to Wenzel wetting transition on the patterned CYTOP surfaces.

## Aggregation Structure of Poly(2-methoxyethyl acrylate)/Poly(methyl methacrylate) Blend Films at the Water Interface

Toyoaki Hirata<sup>1</sup>, Hisao Matsuno<sup>1</sup>, Masaru Tanaka<sup>2</sup>, Keiji Tanaka<sup>1</sup>

<sup>1</sup>Department of Applied Chemistry, Kyushu University, Japan

<sup>2</sup>Department of Biochemical Engineering, Yamagata University, Japan

**Introduction:** An aggregation structure and thermal motion of polymers at the water interface have a huge effect on surface functions such as adhesion, wettability, biocompatibility, and so on. Poly(2-methoxyethyl acrylate) (PMEA) is well known as a blood-compatible material.[1] However, it is still open why PMEA exhibits such an excellent property. Thus, the first trial to solve this problem is to understand the aggregation structure and thermal molecular motion of PMEA at the water interface. We have previously succeeded to construct the stable and flat PMEA surface in air by mixing poly(methyl methacrylate) (PMMA) into it and successive annealing under an appropriate condition.[2] In this study, the aggregation structure of the blend films at the water interface was investigated.

**Experiments:** PMEA with the number-average molecular weight ( $M_n$ ) of 26 k and the molecular weight distribution ( $M_w/M_n$ ) of 3.23, and PMMA with the  $M_n$  of 85 k and  $M_w/M_n$  of 1.09 were used. PMEA/PMMA blend films with various blend ratios were prepared by a spin-coating method onto silicon wafers. For comparison, PMMA homopolymer and PMEA/PMMA bilayer films were also prepared in the same manner. These films were annealed at appropriate temperatures for 6 hours, respectively. Then, the aggregation structure of the blend films was investigated by atomic force microscopic (AFM) observation, contact angle measurement, and sum frequency generation (SFG) vibrational spectroscopy.

**Results and discussion:** Fig. 1 shows immersion time dependence of the root-mean-square surface roughness (RMS) for the PMEA/PMMA blend and PMMA homopolymer films obtained by AFM. The RMS value for all films in water did not change within 24 hours. AFM phase images revealed that the blend surfaces kept being in a homogeneous state even after 24 hours in water. Fig. 2 shows immersion time dependence of the contact angle for the air bubble on the PMEA/PMMA blend, PMMA homopolymer, and PMEA homopolymer films, respectively. Although the contact angle values decreased with increasing the immersion time in water for all films, the decaying behavior was different for one another. Since the blend film surfaces were stable even in water observed by AFM, the time course of

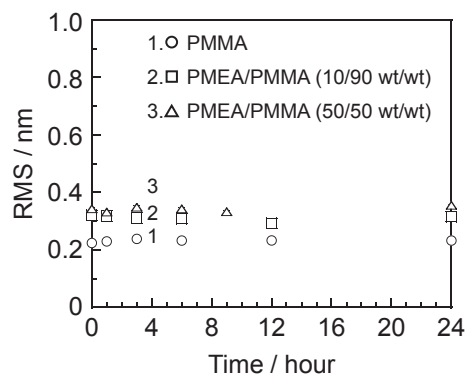


Fig. 1. Immersion time dependence of the RMS for the PMEA/PMMA (10/90, 50/50 wt/wt) blend and PMMA film surfaces in water. The value at 0 hour means the RMS obtained at air interface (surface).



contact angle should not be related to the surface roughness. When the surrounding environment of the polymer surface was changed from air to water, the structural rearrangement occurs at the outermost surface of the films. Interestingly, in the case of PMEAs/PMMA (10/90, 50/50) blend and PMEA homopolymer films, the measurement must be truncated after a time because an air bubble could not be contacted with the surfaces. On the other hand, the bubble could attach to PMMA homopolymer films even after 24 hours. These results indicate that the surface of the PMEAs/PMMA blend films constructed the similar molecular aggregation states to the PMEA homopolymer films surface. According to our previous research, the PMEA fraction at the outermost surface of the PMEAs/PMMA (50/50) blend film was 100 vol%.[2] However, a time, at which an air bubble could not adhere to the PMEAs/PMMA blend film, was longer than that for the PMEA homopolymer film. This means that polymer chain rearrangement should be occurred not only at the outermost surface but also at the near surface of the blend films in order that the aggregation state at the outermost surface reaches the quasi-equilibrium state of the system. In order to clarify the hydration structure of the blend films at the water interface, the local conformations of PMEA and water molecule analyzed by SFG spectroscopic measurement will be discussed.

### References

- [1] M. Tanaka, T. Motomura, M. Kawada, T. Anzai, Y. Kasori, T. Shiroya, K. Shimura, M. Onishi, A. Mochizuki, *Biomaterials*, **21**, 1471 (2000).
- [2] T. Hirata, H. Matsuno, M. Tanaka, K. Tanaka, *Phys. Chem. Chem. Phys.*, **13**, 4928 (2011).

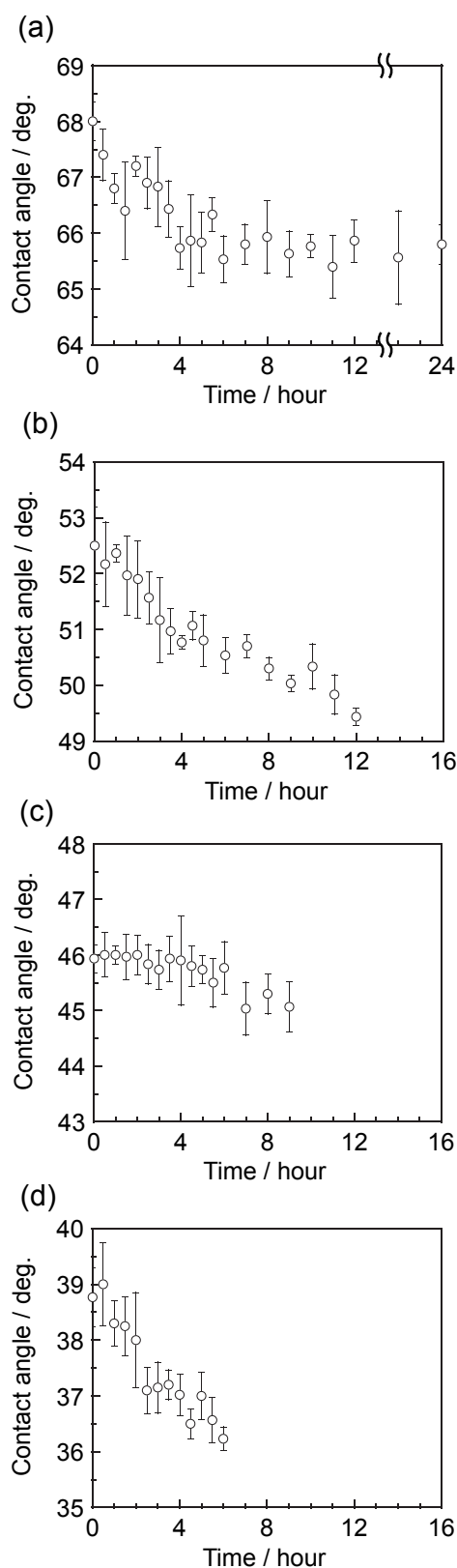


Fig. 2. Immersion time dependence of contact angle for the air bubble on (a) PMMA, PMEAs/PMMA (b) 10/90, (c) 50/50 wt/wt blend, and (d) PMEA films in water.

## Surface Reorganization in Polymer Film during Contact Angle Measurement

Ayanobu Horinouchi, Yoshihisa Fujii, Keiji Tanaka  
Department of Applied Chemistry, Kyushu University, Japan

**Introduction:** Static contact angle measurement has been widely used to characterize the surface of materials in various fields. The usual definition of “static” is that a probe liquid is gently put on the surface of a material which is parallel to the ground. The surface of a soft material reorganizes in response to the surrounding circumstances to minimize the interfacial free energy [1]. Such a surface reorganization can sometimes take place even at a temperature at which polymers existed in the internal bulk phase are frozen [1]. Thus, it can be expected that even for a static measurement, the region beneath a probe liquid structurally reorganizes. In this study, we report the time dependence of the static contact angle on poly(methyl methacrylate) (PMMA) using water as a probe liquid.

**Experiments:** Monodisperse PMMA with the number-average molecular weight of 300k was used. The bulk glass transition temperature ( $T_g^b$ ) of PMMA used here was 405 K. Films of PMMA were spin-coated from a toluene solution onto silicon wafers. The PMMA films were annealed under vacuum at various temperatures for 24 h, respectively. Then, time dependence of water contact angle on each film was measured.

**Results and discussion:** Fig. 1 shows the time ( $t$ ) dependence of contact angle ( $\theta(t)$ ) for PMMA films. There are two regimes, exponential and linear, for the  $t$ - $\theta$  relation. The  $\theta$  value for the film annealed at 433 K was higher than that for the as-spun film at a given time. This result indicates that the hydrophobicity at the PMMA surface increased after the thermal annealing above  $T_g^b$ . After the initial stage,  $\theta$  monotonically decreased with increasing time. Although the decrement of  $\theta$  after 10 s, due to the water evaporation, was comparable with each other, it was discernibly different between them at the initial stage. Sum-frequency generation vibrational spectroscopy revealed that the initial  $\theta$  decrease reflects the surface reorganization caused by the presence of a water droplet and that the extent was dependent on the annealing.

In conclusion, we measured the contact angle of a water droplet on the flat surface of PMMA. This way to measure the contact angle has been regarded as “static”. Nevertheless, water induces structural changes of the chains existing in the outermost region of the film. Thus, a static contact angle measurement is not truly “static” if the substance to be characterized is a soft material, such as a polymer.

### Reference

[1] K. Tanaka *et al.* *Langmuir*, **24**, 296 (2008).

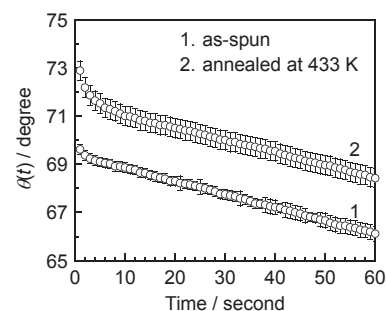


**Fig. 1.** Time dependence of water contact angle for the PMMA films.

## Morphology and Properties of the Surface Heterostructure Investigated by Scanning Electrochemical Techniques

A. S. Gnedenkov<sup>1</sup>, S. L. Sinebryukhov<sup>1</sup>, D. V. Mashtalyar<sup>1</sup>, S. V. Gnedenkov<sup>1</sup>

<sup>1</sup>Institute of Chemistry, Far Eastern Branch, Russian Academy of Sciences, Vladivostok, Russia

Features of the kinetics and the mechanism of the corrosion process in the local heterogeneous parts of the magnesium alloy's surface have been investigated by means of the localized electrochemical techniques. The stages of the corrosion process in the artificial defect in the coating obtained by plasma electrolytic oxidation (PEO) method at the surface of the magnesium alloy have been investigated as well. The plasma electrolytic oxidation method is used for production of multifunctional practically significant coatings that improve the surface properties of various metals and alloys [1-4]. Morphology peculiarities, the electrode potential and current distribution in the defect zone and neighboring surface area were investigated using Localized Electrochemical Impedance Spectroscopy (LEIS), Scanning Kelvin Probe (SKP) and Scanning Vibrating Probe (SVP) techniques along with Non-Contact Optical Surface Profiler (OSP) technique. The analysis of the experimental data enabled us to suggest that the corrosion process in the defect zone develops predominantly at the magnesium/coating interface. The data processing shows us a good correlation between the results obtained by a group of methods at all stages of the corrosion process.

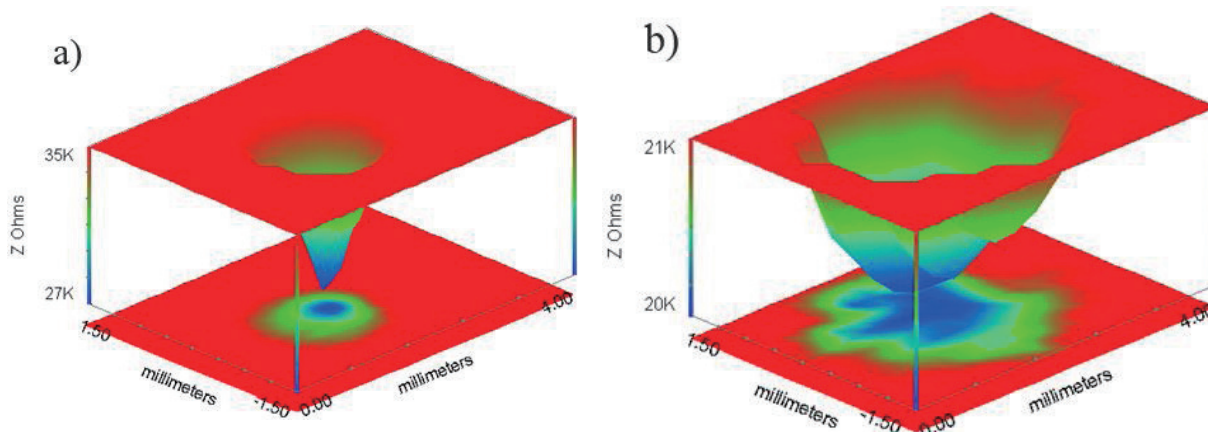


Fig. 1. LEIS mapping on the area around the artificial defect in the PEO-coating on the Mg alloy sample. Impedance modulus: a) before immersion in the 3% NaCl solution, and b) after a 15-hour immersion in the 3% NaCl solution.

Kinetics and the mechanism of the corrosion process on the magnesium alloy in the local part of the heterogeneous area – the artificial defect zone at the surface of the PEO-coating were also investigated by combination of the localized scanning methods (LEIS, SVP, SKP, OSP). This study enables one to establish the stages of the corrosion-active process. The experimental impedance spectra measured in the defect zone after sample's immersion in a corrosion media were fitted using the Randles equivalent circuit [5]. LEIS data (Fig. 1)

enabled one to conclude that the corrosion process in the defect zone develops predominantly at the magnesium/coating interface.

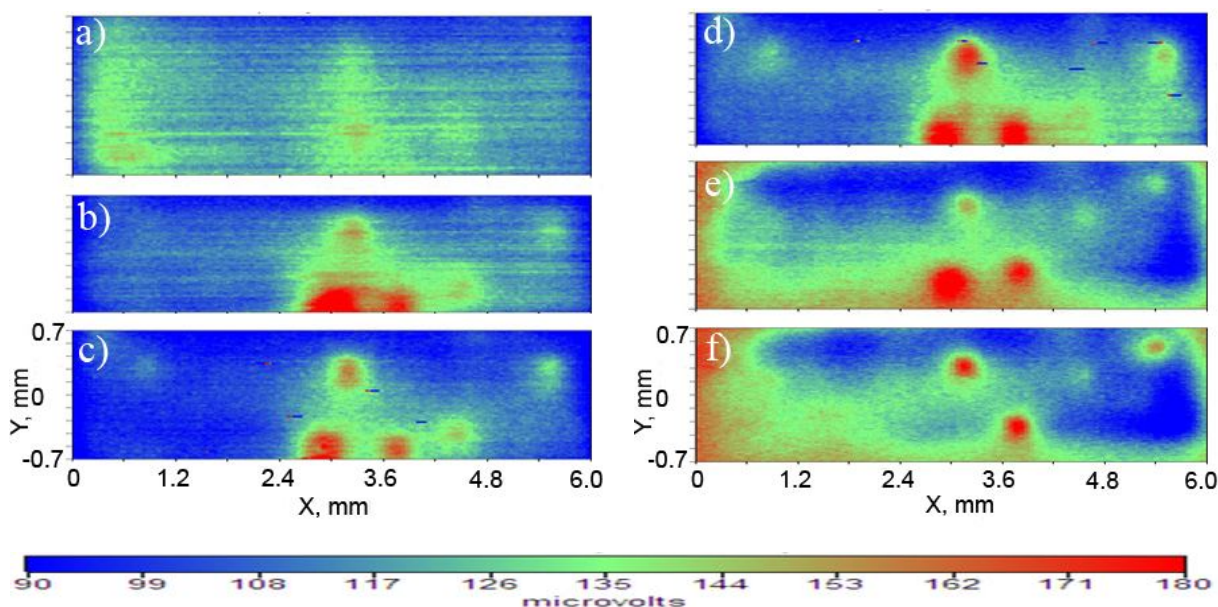


Fig. 2. SVP mapping on the area of the Mg alloy sample without coating. After immersion in the water solution: a) 4-h, b) 16-h, c) 32-h, d) 37-h, e) 49-h, and f) 60-h.

For the purpose of the evaluation of the intensity of corrosion process at the surface of the magnesium alloy the SVP method was also used. As a result of sample's immersion in the water the intensive corrosion process by means of formation of the local anodic and cathodic regions (blue and red areas, respectively at the Fig. 2a, b, c) have appeared at the surface. Red areas (Fig. 2) were a parts of the MA8 sample with more positive values of the potential, blue ones- less positive (anodic regions). Appearance of cathodic areas may be caused by existence of the intermetallic phase in the magnesium alloy's composition. These areas during immersion time have reduced in size and then turned into anodic ones (Fig. 2d, e, f) under influence of the corrosion process. Changing of the potential gradient along the surface could be observed during the increasing of time of immersion of the sample in the electrolyte. SVP-results testify about of the intensive corrosion process even in the almost pure water and, therefore, enable one to emphasize that magnesium alloys need in the reliable anticorrosion protection.

- [1] A. L. Yerokhin, X. Nie, A. Leyland, A. Matthews, *Surf. Coat. Technol.*, **122**, 73 (1999).
- [2] T. H. Teh, A. Berkani, S. Mato, P. Skeldon, G. E. Thompson, H. Habazaki, K. Shimizu, *Corros. Sci.*, **45**, 2757 (2003).
- [3] A. Ghasemi, V. S. Raja, C. Blawert, W. Dietzel, K. U. Kainer, *Surf. Coat. Technol.*, **202**, 3513 (2008).
- [4] S. V. Gnedenkov, S. L. Sinebryukhov, *Compos. Interfaces*, **16**, 387 (2009).
- [5] S. L. Sinebryukhov, A. S. Gnedenkov, D. V. Mashtalyar, S. V. Gnedenkov, *Surf. Coat. Technol.*, **205**, 1697 (2010).

## One-Dimensional Polymer Blend Nanorods with Gradient Composition and Gradient Crystallite Distribution

Hui Wu<sup>1</sup>, Zhaohui Su<sup>2</sup>, Atsushi Takahara<sup>1\*</sup>

<sup>1</sup> Institute for Materials Chemistry and Engineering, Kyushu University, Japan

<sup>2</sup> Changchun Institute of Applied Chemistry, Chinese Academy of Sciences, China

One-dimensional (1-D) polymeric nanomaterials have drawn significant attention due to their unusual properties for the potential applications in mechanical, chemical, optical, and electronic devices.[1,2] Novel 1-D nanostructures with specific orientation, polymorphism, phase-separated morphology, anisotropic surface, and gradient composition distribution were demonstrated.[2-4] Generally, the produced 1-D nanomaterials are considered as uniform nanoobjects and its structures along the length direction are identical due to the same processes that the whole nanomaterial experienced. However, the high aspect ratio (length/diameter) of 1-D nanomaterials opens opportunities to fabricate nanomaterials with anisotropic structure and properties, such as gradient refractive index, improved strength against thermal stress, gradient mechanical modulus and extraordinary plasticity, for the application in functional optical and mechanical nanodevices.

To explore these kinds of novel nanomaterials, using isotactic polystyrene /poly(2,6-dimethylphenylene oxide (iPS/PPO) blends as an example, the polymer blend nanorods with diameter of 35 nm were generated by melt-wetting nanoporous anodic aluminum oxide (AAO) templates with polymer melts. To assess the composition distribution along the nanorod length, the composition, crystallinity and orientation of iPS at different positions of nanorods were investigated by micro-Fourier transform infrared spectroscopy (micro-FTIR), which makes the structural information in small sections of nanorods from the top to the bottom to be spatially resolved. The iPS content in nanorods decreased, while the iPS crystallites with perpendicular orientation increased from top to bottom. The 1-D polymer nanorods having gradient composition and gradient crystallite distribution were demonstrated in the study.

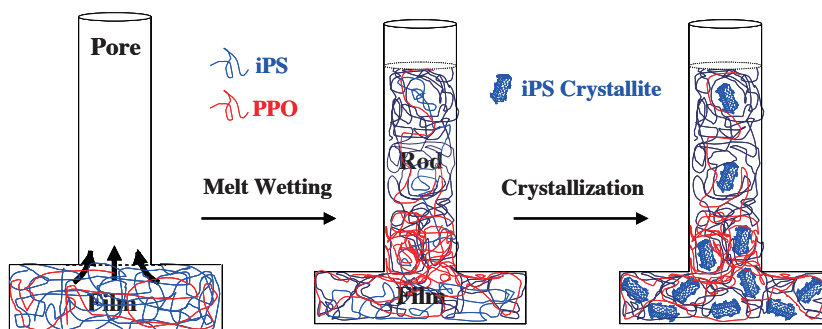


Fig. 1. Schematic illustration of the formation of iPS/PPO blend nanorods with gradient composition and gradient crystallite distribution.

[1] C. R. Martin, *Science*, **266**, 1961 (1994).

[2] M. Steinhart, *Adv. Polym. Sci.*, **220**, 123 (2008).

[3] H. Wu, W. Wang, H. Yang and Z. Su, *Macromolecules*, **40**, 4244 (2007).

[4] H. Wu, Z. Su and A. Takahara, *Soft Matter*, **7**, 1868 (2011).

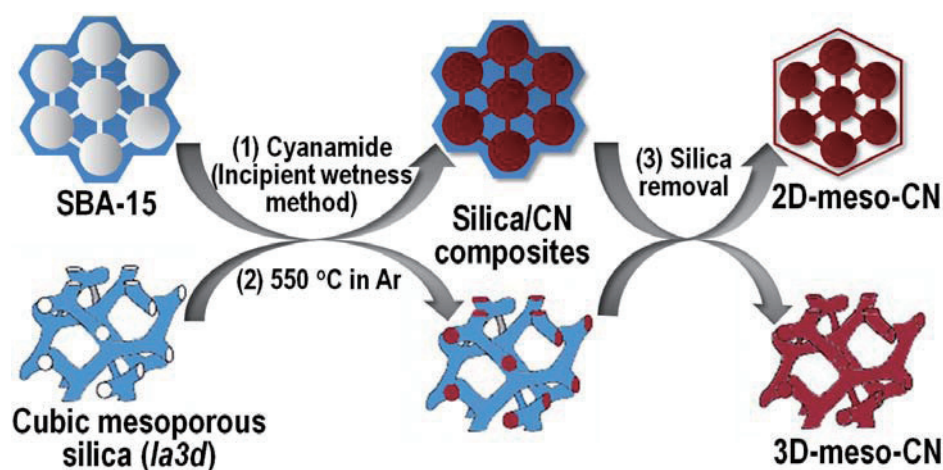
## Facile Synthesis of Mesoporous Carbon Nitrides Using Incipient Wetness Method and The Application as Hydrogen Adsorbent

Sung Soo Park,<sup>1</sup> Sang-Wook Chu,<sup>1</sup> Chunfeng Xue,<sup>2</sup> Dongyuan Zhao,<sup>2</sup> Chang-Sik Ha<sup>1</sup>

<sup>1</sup>Department of Polymer Science and Engineering, Pusan National University, Korea

<sup>2</sup>Department of Chemistry, Advanced Materials Laboratory, Fudan University P. R. China

Highly nitrogen-enriched mesoporous carbon nitride materials with 2-dimensional (2-D) (2D-meso-CN) and 3-dimensional (3-D) mesostructures (3D-meso-CN) were synthesized using mesoporous silica as a hard template and cyanamide as a precursor *via* incipient wetness process without using any solvent. The materials were characterized by small-angle X-ray scattering (SAXS), X-ray diffraction (XRD), and transmission electron microscopy (TEM) for the mesostructure analysis, N<sub>2</sub> adsorption-desorption isotherms for surface area and pore size distribution, and X-ray photoelectron spectroscopy (XPS) and Fourier-transform infrared red (FT-IR) spectroscopy for the composition analysis of frameworks. The mesoporous carbon nitride replicas have graphitic-like stacking of carbon nitride sheets in mesopore walls. The N/C ratio of the mesoporous carbon nitride replicas is 1.13 after the carbonization at 550 °C for 3 h. 2D-meso-CN and 3D-meso-CN have the BET surface area of 361 and 343 m<sup>2</sup>g<sup>-1</sup>, large pore volume of 0.50 and 0.67 cm<sup>3</sup>g<sup>-1</sup>, and pore diameter of 27.8 Å (for 2D-meso-CN), 24.5 and 80.3 Å (for 3D-meso-CN), respectively.



Scheme 1. Illustration for the synthesis process of the mesoporous carbon nitrides 2D- and 3D-meso-CN using incipient wetness method without any solvent.

Experiments on hydrogen storage were carried out for the application of the nitrogen-enriched mesoporous carbon synthesized in this work.

Fig. 1 shows hydrogen uptakes of 2D-meso-CN and 3D-meso-CN at 77 K (a, b) and 2D-meso-CN, 3D-meso-CN and FDU-15 at 298 K (c, d, and e) under various pressures. The capacity of hydrogen uptake of 2D-meso-CN (1.71 wt%) and 3D-meso-CN (1.56 wt%) have higher values at 77 K than at 298 K (0.28 wt% for 2D-meso-CN, 0.25 wt% for 3D-meso-CN). And the capacity of hydrogen uptake of 2D-meso-CN was some higher than 3D-meso-CN at

77 K and at 298 K under 50 bar. The result may be due to the higher surface area of 2D-meso-CN ( $361 \text{ m}^2\text{g}^{-1}$ ) than 3D-meso-CN ( $343 \text{ m}^2\text{g}^{-1}$ ). On the other hand, under lower pressure (below about 25 bar at 77 K and below about 9 bar at 298 K), the capacity of hydrogen uptake of 3D-meso-CN was some higher than 2D-meso-CN at both temperature of 77 K and 298 K (Fig. 1 and inset in Fig. 1). The result may be contributed to the 3D-dimensional mesostructure with bimodal mesopores which can generate the easy diffusion of hydrogen molecules in mesopores.

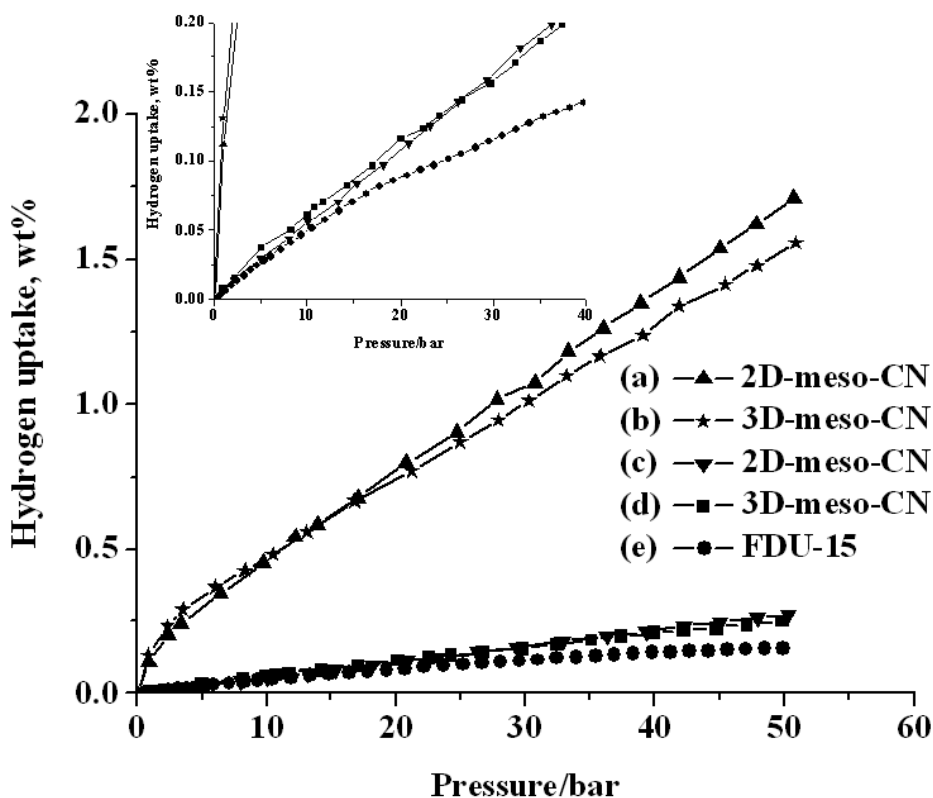


Fig. 1 Hydrogen uptake of (a) 2D-meso-CN and (b) 3D-meso-CN at 77 K and (c) 2D-meso-CN, (d) 3D-meso-CN and (e) FDU-15 at 298 K under various pressures. Inset shows the hydrogen uptake in the range of 0-40 bar.

The mesoporous carbon nitride materials may have potential applications in the area of not only gas-uptake such as hydrogen and carbon dioxide but also methanol fuel cells, catalysis, photocatalysis, and electron emission devices.

#### References

- [1] S. S. Park, S.-W. Chu, C. Xue, D. Zhao, C.-S. Ha, *J. Mater. Chem.*, **21**, 10801 (2011).
- [2] Q. Li, J. Yang, D. Feng, Z. Wu, Q. Wu, S. S. Park, C.-S. Ha, D. Zhao, *Nano Res.*, **3**, 632 (2010).
- [3] Z. Yang, Y. Xia, R. Mokaya, *J. Am. Chem. Soc.*, **129**, 1673 (2007).

## Fabrication and Functionalization of Confeito-like Au Nanoparticles

Toyoko Imae and Masaki Ujihara

Graduate Institute of Engineering, National Taiwan University of Science and Technology,

Taipei, Taiwan ROC

In this study, we aimed to develop a simple and versatile method to prepare anisotropic nanoparticles without seeds or templates. Additionally we considered the method from a viewpoint of green chemistry. To accomplish these objectives, a catalytic behavior of Au nanoparticles (AuNPs) to decompose peroxides was focused. Hydrogen peroxide was selected as a convenient reducing agent in an aqueous system, and effects of protecting agents were examined on the synthesis of confeito-like AuNPs. Moreover, surface-enhancing effects on Raman spectra were evaluated for obtained nanoparticles. These results are useful to design anisotropic nanoparticles, which have desirable plasmonic properties for sensors, optoelectronic devices, medical therapies and the other applications.

The synthesis of AuNPs was performed by one pot process at ambient temperature. Briefly, an aqueous solution of  $\text{NaAuCl}_4$  was mixed with a protecting agent (citrate, poly(ethylene oxide)-poly(propylene oxide) block copolymer and poly(vinyl pyrrolidone)). An aqueous solution of  $\text{H}_2\text{O}_2$  was added into the solution, and an aqueous solution of NaOH was poured there with vigorous stirring. The reaction solution was left overnight at rest to accomplish the reaction, and thus the dispersions of AuNPs were obtained.

In an alkaline condition,  $\text{NaAuCl}_4$  is reduced by  $\text{H}_2\text{O}_2$  and results confeito-like AuNPs with diameters of several tens to a few hundred nano-meters. The growth mechanism of these AuNPs could be attributed to an autocatalytic reduction by the AuNPs for decomposition of  $\text{H}_2\text{O}_2$ . The detailed structures of AuNPs were different according to the protecting agents because of the selective adsorption of the agents onto the crystal faces of Au.

The AuNPs were also characterized in terms of optical properties. The confeito-like AuNPs were purple to blue and indicated broad plasmon absorption in the range from 500 to near-infrared region, while the conventional-AuNP has its plasmon absorption only around 520 nm. The confeito-like AuNPs which were prepared in an aqueous solution of citric acid resulted in  $\sim 4$  times stronger surface enhanced Raman spectra (SERS) than that from the conventional-AuNP, although SERS effects of the other confeito-like AuNPs were not necessarily strong. The order of enhancement factors corresponded to that of plasmon absorption bands. These results mean that the plasmon absorption band is tunable with the structures of confeito-like AuNPs to obtain better surface-enhancing effect.

In this study, it was demonstrated that a one-pot synthesis method could quickly provide confeito-like AuNPs with different structures and optical properties. These results would be useful to design plasmonic devices.



## Fluorescence Upconversion Microbarcodes for Multiplexed Biological Detection

Fan Zhang, Dongyuan Zhao

*Department of Chemistry, and Laboratory of Advanced Materials, Fudan*

*University, Shanghai 200433, P. R. China*

Multiplexed suspension arrays of encoded microspheres offer several advantages over planar arrays such as flexibility in target selection, fast binding kinetics, and well controlled binding conditions.<sup>[1,2]</sup> For multiplexed detection a reporter dye is required and the region of the spectrum that is occupied by its emission profile is not available for encoding. But for dye and Quantum dots encoding materials described above, the interfering with organic reporter tags that have excitations in the visible or UV is still a major problem.<sup>[3]</sup> In the present work, we show that this problem could be resolved by the development of upconversion optically encoded microbeads. This encoded bead technology is based on the optical properties of RE ions doped upconversion nanoparticles (UCNPs), which are excited in the infrared region instead of the UV and visible region to give emission in the visible domain. These UCNPs show a high photostability, low toxicity, and their multicolor optical properties can be tuned by variation of lanthanide dopants and the host matrix. In particular, it is extremely important to note that there is no optical cross talk between the upconversion optical code and any reporter dyes. The single wavelength 980-nm continuous wave (CW) laser used to excite the upconversion materials does not excite dyes which absorb in the visible and UV region and, conversely, the upconversion materials are not excited by the visible lasers used to excite the organic dyes. All these favorable properties have indicated the great potential of UCNPs in the multiplexed detection.

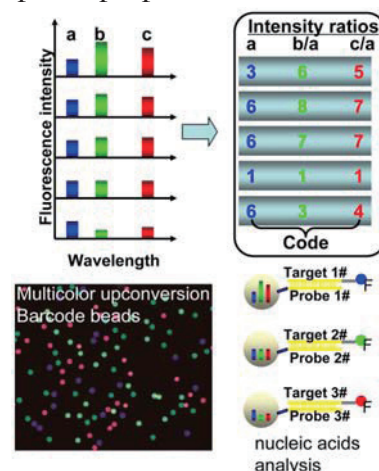


Fig. 1. Fluorescence upconversion microbarcodes for multiplexed biological detection

- [1] R. Wilson, A. R. Cossins, D. G. Spiller, *Angew. Chem. Int. Ed.* **2006**, *45*, 6104.
- [2] N. H. Finkel, X. H. Lou, C. Y. Wang, L. He, *Anal. Chem.* **2004**, *46*, 353A.
- [3] M. J. Dejneka, A. Streltsov, S. Pal, A. G. Frutos, K. Yost, P. K. Yuen, U. Muller, J. Lahiri, *Proc. Natl. Acad. Sci. USA* **2003**, *100*, 389.

## BIONANOCOMPOSITE FILMS FORMED BY CHITOSAN WITH CLAY NANOPARTICLES VIA SELF-ORGANIZATION

Sergey Sarin<sup>1</sup>, Irina Postnova<sup>2</sup>, Yury Shchipunov<sup>1</sup>

<sup>1</sup>Institute of Chemistry, Far East Department, Russian Academy of Sciences, 690022, Vladivostok, Russia

<sup>2</sup>Far Eastern Federal University, the School of Natural Sciences, Vladivostok, Russia

Films of chitosan with clay nanoparticles have been prepared by means of an adopted method that was suggested for the jellification of aqueous solutions of this polysaccharide in [1-3]. Their self-organization is based on regulated electrostatic interactions. As clay nanoparticles, synthetic saponite was taken. It belongs to smectite type of 2:1 phyllosilicates that consist of an octahedral sheet located between two tetrahedral sheets. The thickness of these plates is ca. 1 nm and lateral dimensions are 20-40 nm. Negative charges are located on their surface. Chitosan macromolecule charge is caused by amino groups of which the pK value is equal to ca. 6.3. This means that they are in charged state in slightly acidic or acidic media, whereas are uncharged in neutral and alkaline media. This property is used to regulate the electrostatic interactions of chitosan macromolecules with clay nanoparticles by progressive charging through the gradual acidification of an aqueous solution [1]. By following the suggested approach, one can exclude common phase separation, attaining to the homogeneous distribution of components.

A study of the bionanocomposites films placed in water revealed that their swelling is dependable on the concentration ratio of chitosan to saponate. The minimal water absorption was related to the stoichiometric ratio of oppositely charged groups in the polysaccharide and clay nanoparticle surface.

The properties and structure of bionanocomposites films were examined by the dynamic thermo-mechanical analysis, small-angle X-ray scattering and scanning electron microscopy. It was found that they had the stratified morphology. There were plates of up to 10  $\mu$ m long and 20-30 nm thick at the chitosan-saponate stoichiometric ratio. Small-angle X-ray scattering examination revealed the presence uniformly distributed heterogeneities. When mechanical and thermal properties of bionanocomposite films were studied, a glass state was found. The mentioned features led us to the conclusion that there is the self-organization of chitosan and saponite nanoparticles into an ordered structure in the course of progressive charging of polysaccharide.

### References

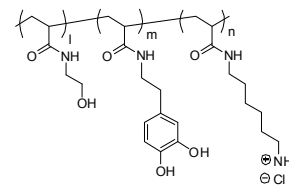
- [1]. Y. Shchipunov, N. Ivanova, V. Silant'ev. *Green Chem.* 11, 1758, 2009.
- [2]. Y. Shchipunov, N. Ivanova, S. Sarin, *Mendeleev Commun.* 19, 149, 2009.
- [3]. Y. Shchipunov, S. Sarin, I. Kim, C.-S. Ha. *Green Chem.* 12, 1187, 2010

## Adhesion of Metal Oxide by Gelation of Mussel Adhesive Protein Mimetic Polymer

Jin Nishida, Motoyasu Kobayashi, Atsushi Takahara  
JST, ERATO, Takahara Soft Interfaces Project, Japan

The mussel adheres to various surfaces (even polyethylene or teflon surface) in water through marine adhesive protein (MAP). It is well known that mussel MAP specifically contains “nonstandard” amino acid 3,4-dihydroxyphenylalanine, which works as a cross-linking point and interact with surface to give strong adhesion. We synthesized a water soluble poly(acrylamide) derivatives having dihydroxyphenyl groups and amino groups as a mussel MAP mimetic, and transformed to an adhesive hydrogel by aerobic oxidation. The resulting MAP mimetic hydrogel was used as adhesive for aluminum plates.

Two types of acrylamide derivatives containing Boc protected amino group and triethylsilyl protected dihydroxyphenyl group were copolymerized with hydroxyethylacrylamide by AIBN initiator. Protective groups in the resulting copolymer were removed by acid hydrolysis to give water-soluble MAPs mimetic polymer (Scheme 1).



Scheme 1. MAP mimetic polymer

The obtained MAP mimetic polymer was dissolved in phosphate buffer solution (pH=8.0) to proceed cross-linking reaction. The solution gradually became viscous under ambient air atmosphere to give a gel within 2 hours (Fig 1), while no gelation occurred under argon atmosphere. Addition of tyrosinase (catechol oxydase) to the copolymer aqueous solution enhanced the gelation rate. The gel was formed within 20 minutes. These results indicated that the cross-linking reaction of the synthesized MAP mimetic polymer was triggered by oxidation of dihydroxyphenyl moieties, which are similar to the cross-linking mechanism of natural MAP.



Fig 1. A gel prepared from phosphate buffer solution of synthesized polymer.

Two aluminum substrates were put together with the MAP mimetic polymer solution in a lapped joint under humid air for 24 hours, forming a rigid gel layer between the aluminum substrates. Lap shear adhesive strength of the adhered specimen was 0.46 MPa, which was almost same strength as the synthesized MAP with native sequence reported by Yamamoto.[1] The cohesive failure of the adhesive polymer layer took place when the bonded two aluminum plates were mechanically deformed in the lap shear test. In this case, the polymer gel failed prior to the peeling off from the aluminum plates because 3,4-dihydroxyphenyl group in the polymer strongly interacted with metal oxide surfaces through chelate bond formation

[1] H. Yamamoto, *J. Chem. Soc. Perkin Trans. I*, 613 (1987)

## Controlled CW-CCW Motion of the Ring-shaped Microtubules Assembly

Akira KAKUGO<sup>1,3</sup>, Jian Ping GONG<sup>2</sup>

(<sup>1</sup>Graduate School of Science, <sup>2</sup>Faculty of Advanced Life Science, Hokkaido University, <sup>3</sup>JST-Presto)

Tel&Fax: +81-11-706-2635, E-mail: kakugo@sci.hokudai.ac.jp

**[Introduction]** Recently, a method was established for the formation of microtubule (MT) assemblies by an active self-organization (AcSO) process, in which MTs were crosslinked during sliding motion on a kinesin-coated surface, and this was coupled with adenosine triphosphate (ATP) hydrolysis. Streptavidin (ST) was the glue used to crosslink biotin-labeled MTs. So far we have revealed that MTs were self-organized into various structures such as bundle, ring and

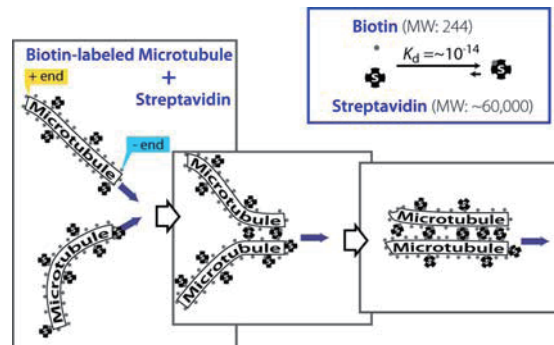


Fig.1 Schematic illustration of AcSO of MTs.

network depending on the initial condition of the AcSO process. It was also reported that ring-shaped MT assemblies obtained through the AcSO showed preferential counterclockwise (CCW) rotation [Ref. 1]. These ring shaped MTs assemblies might be a promising candidate for further development towards artificial bio-actuators, where free tuning of CCW rotation to clockwise (CW) rotation is an important underlying issue to be addressed. In this paper, we report on our findings that the preferential rotation of ring shaped MTs assembly obtained through AcSO process is significantly affected by the incubation time for MTs preparation.

### [Result and Discussion]

MT was polymerized at 37°C in the presence of 33.6μM tubulin and 0.64M DMSO. Then, MT was incubated for each incubation time (30min, 3h, 6h, 9h, 24h). After 3h of the AcSO, preferential rotation of the obtained ring shaped MTs assembly was evaluated under a fluorescent microscope. Fig.2 shows the result. Drastic transition of the preferential rotation of the ring shaped MT assemblies from CCW direction to CW direction was observed with the prolongation of incubation time for MT polymerization. In this paper we will also discuss this transition in terms of a change in PFs number.

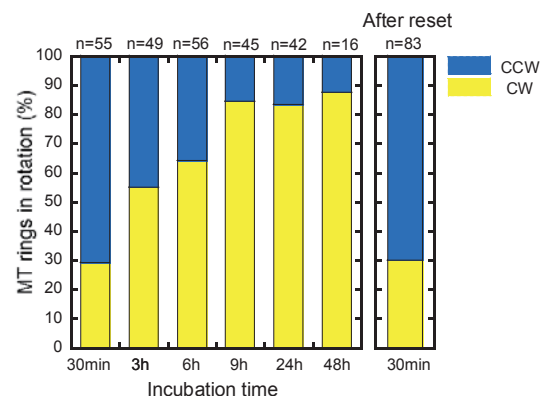


Fig.2 Effect of incubation time on the preferential rotation of MTs ring formed by AcSO on kinesin-fixed surface.

**[Reference]** Ref. 1, Kawamura, R.; Kakugo, A.; Osada, Y.; J.P. Gong. *Biomacromolecules* 2008, 9, 2277-2282

## Formation of the Ring-shaped Assembly of Microtubules at the Air-buffer Interface

Arif Md. Rashedul Kabir,<sup>1</sup> Akira Kakugo,<sup>2,3</sup> Yoshiki Tamura,<sup>4</sup> Tamaki Kajihara,<sup>4</sup>  
Inoue Daisuke,<sup>4</sup> Jian Ping Gong,<sup>2</sup> and Hiroyuki Mayama<sup>5</sup>

<sup>1</sup>Division of Biological Sciences, Graduate school of Science, Hokkaido University, JAPAN;

<sup>2</sup>Faculty of Advanced Life Science, Hokkaido University, JAPAN; <sup>3</sup>PRESTO, Japan Science and Technology Agency (JST); <sup>4</sup>Graduate School of Life Science, Hokkaido University,

JAPAN; <sup>5</sup>Nanotechnology Research Center, Research Institute for Electronic Science, Hokkaido University, JAPAN

Biopolymers such as actin, microtubule and DNA are well known for their fascinating *in vivo* self-organization phenomena. Considerable efforts have been devoted to mimic their organization process *in vitro* that produced ring shaped or toroid structures. However, understandings of the factors that lead to such assembled structures deserve much more investigation to achieve a unified insight of the assembly process, particularly of the microtubules. Additionally, the direct *in situ* observation of the assembly process has not been possible yet to demonstrate. We report on the assembly process of microtubules at the air-buffer interface that resulted in ring-shaped structures with a uniform size distribution and high yield. Using an ‘air-buffer interface control system’ combined with the newly developed ‘inert chamber system (ICS)’ we have also successfully observed the fast ring formation process of microtubules at the interface. This is the ever first direct *in situ* observation of such assembly process and probably provides with a valuable discernment in understanding the *in vivo* organizational behavior of biopolymers.

## Lamellar Bilayers as Reversible Sacrificial Bonds to Toughen Hydrogel

Md. Anamul Haque<sup>a</sup>, Takayuki Kurokawa<sup>b</sup>, and Jian Ping Gong<sup>b</sup>

<sup>a</sup> Graduate School of Science, Hokkaido University, Sapporo 060-0810, Japan

<sup>b</sup> Faculty of Advanced Life Science, Hokkaido University, Sapporo 060-0810, Japan

A novel anisotropic hydrogel with a unidirectionally aligned membrane-like lamellar bilayer structure of macroscopic size is synthesized in a one-pot polymerization reaction from a polymerizable surfactant (dodecylglyceryl itaconate:DGI) and acrylamide in presence of a crosslinker. Prior to the polymerization, by applying shear flow to the precursor solution, thousands of lamellar bilayers of self-assembled DGI are aligned in one direction parallel to the substrate surface. Polymerized lamellar bilayers are stacked periodically and entrapped in the polyacrylamide network. This hydrogel shows one-dimensional swelling, strong anisotropy in the elastic modulus, and beautiful structural color. Owing to the softness and large deformability of the gel, the color of the gel can be reversibly tuned by the compressive strain over a wide wavelength range, which might be used as a soft tactile sensor, that is able to detect a complicated force field, and deformation based color display.

The stratified lamellar bilayers not only diffract light to exhibit magnificent structural color, but also serve as a reversible sacrificial bond that dissociate upon deformation and give rise to the excellent mechanical functions such as high toughness, self-recovery, and persisting fatigue resistance. Both the molecular dissociation and lipid-like mobile nature of bilayers dramatically enhance the resistance to crack propagation by suppressing the stress concentration at the crack tip with the formation of extra-ordinary blunting. The unique toughening phenomena might allow deep insight into the toughening mechanism of the hydrogel-like soft materials such as biological soft tissues.

### Reference

Md. A. Haque, G. Kamita, T. Kurokawa, K. Tsujii, J. P. Gong, *Advanced Materials*, 22(45), 5110-5114(2010).

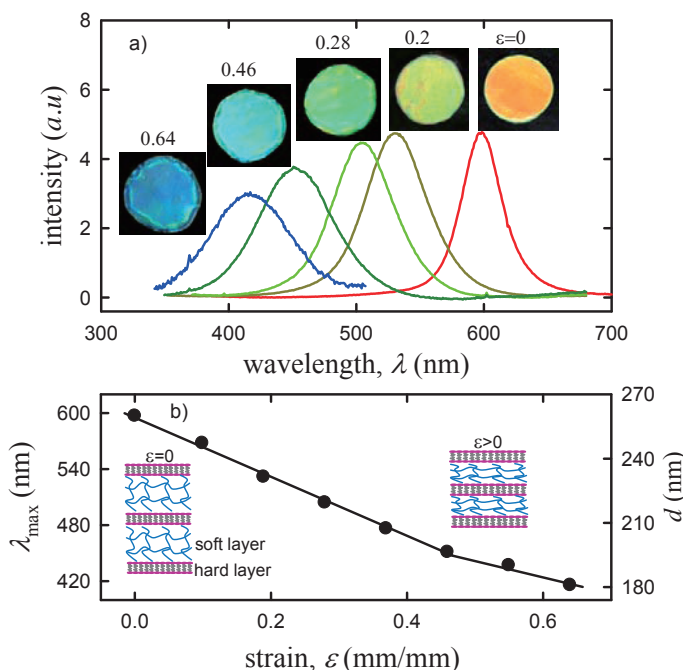


Figure 1. a) Shift of the gel color from red to blue upon gradual increasing of compressive strain (right to left) perpendicular to the lamellar layer and their corresponding reflection spectrum. b) Compressive strain dependence of the wavelength maximum ( $\lambda_{\max}$ ) and lamellar distance ( $d$ ).

## Silyl Groups as Substituents of Novel Amorphous Compounds

Soichiro Kyushin<sup>1</sup>, Kyohei Otsuka<sup>1</sup>, Yuma Negishi<sup>1</sup>, Shintaro Ishida<sup>2</sup>

<sup>1</sup>Department of Chemistry and Chemical Biology, Graduate School of Engineering,  
Gunma University, Japan

<sup>2</sup>Department of Chemistry, Graduate School of Science, Tohoku University, Japan

Amorphous substances such as amorphous metals, metallic glasses, low-temperature glass matrices, and starburst-shaped molecules are formed by cooling their liquid or gas states. We report novel organosilicon amorphous compounds which show amorphous phases as mesophases between solid and liquid phases in both heating and cooling processes.

*p*-Terphenyl derivatives containing an alkyldimethylsilyl group (e.g. compound **1**) were synthesized. The measurement of differential scanning calorimetry (DSC) showed that these compounds exhibit mesophases between solid and liquid phases (Fig. 1). The mesophases showed no reflections in X-ray diffraction, and only dark fields were observed by a polarizing microscope. These results show that the mesophases lack structural regularity of molecular arrangement and are amorphous phases. We discuss the thermodynamic behavior of these compounds on the basis of the effects of substituents on the silicon atom, theoretical calculations, and phase diagrams.

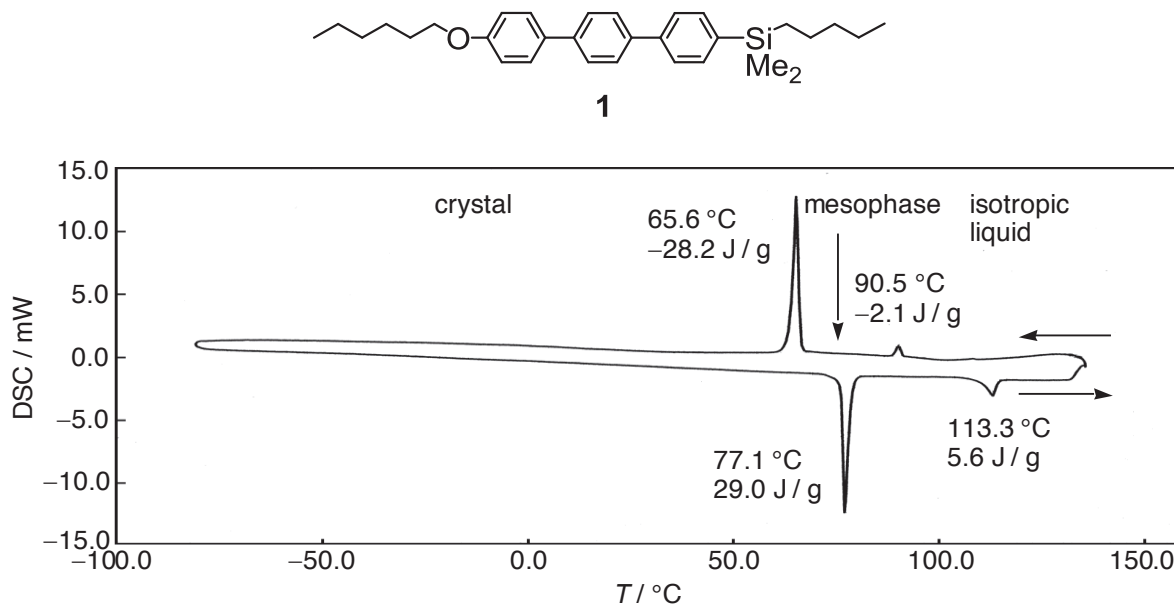


Fig. 1. DSC trace of compound **1**.

## Preparations and Long-Term Stability Testing of Iodine Free Polymer Electrolytes for Dye-Sensitized Solar Cells

Mi-Ra Kim<sup>1</sup>, Sang-Eun Cho<sup>1</sup>, Young-Keun Kim<sup>1,2</sup>, Won-Pill Hwang<sup>1</sup>, Min-Hye Seo<sup>1</sup>, and Jin-Kook Lee<sup>1,\*</sup>

<sup>1</sup>Department of Polymer Science & Engineering, Pusan National University, South Korea

<sup>2</sup>SOLCHEM Co., LTD, South Korea

Dye-sensitized solar cells (DSSCs) has been considered a promising photovoltaic device, which was first reported by Grätzel in 1991.[1] The solar cell is constituted by photo-anode nanocrystalline TiO<sub>2</sub>, a molecular dye, an electrolyte containing a typically iodide/triiodide (I<sup>-</sup>/I<sub>3</sub><sup>-</sup>) redox couple and counter electrode.[2] However, liquid electrolytes have many problems. First, these electrolytes contain volatile solvents which lead leakage and volatilization of the electrolyte. Second, there are possibility desorption and photo-degradation of the attached dyes, and the corrosion of the Pt counter electrode.[3] Third, iodine (I<sub>2</sub>) which addition to make redox couple (I<sup>-</sup>/I<sub>3</sub><sup>-</sup>) is colored and sublimated in air. Therefore iodine absorbs lights of visible range and would escape from the cell unless it is hermetically sealed.[4] In order to replace liquid electrolyte, many attempts have been made such as a polymer matrix in gel electrolytes or polymer electrolytes with poly(vinylidene fluoride), poly(vinylidene fluoride-co-hexafluoropropylene), poly(ethylene glycol), and poly(ethylene oxide).[5-7]

In this study, we were applied nonyl phenol ethoxylate (NPE) which had low molecular weight as a new matrix in solid type electrolytes for iodine free DSSCs. Four different kinds of electrolytes based on NPE were prepared for DSSCs. Their photovoltaic performance and long-term stabilities were measured by using a Solar Simulator. In Figure 1, the DSSC devices using iodine free NPE electrolyte have maintained over 72 % of its initial the overall power conversion efficiency ( $\eta$ ) after 1000 hours aging at 80 °C. The open circuit voltage (Voc) was maintained 100 % after stability test for 1000 hours. The DSSCs using iodine free NPE electrolyte possessed a better long-term stability than that of DSSCs containing iodine NPE electrolyte.

In order to characterize solid type electrolytes, charge transfer resistance (R<sub>ct</sub>) of electrolytes was examined by Electrochemical Impedance Spectroscopy (EIS) and visible light absorption of electrolytes was estimated by UV-visible absorption spectra. In addition, on these devices using the solid type electrolyte the nanopore-filled electrolytes into the nanocrystalline TiO<sub>2</sub> film were investigated by using a Scanning Electron Microscope (SEM).



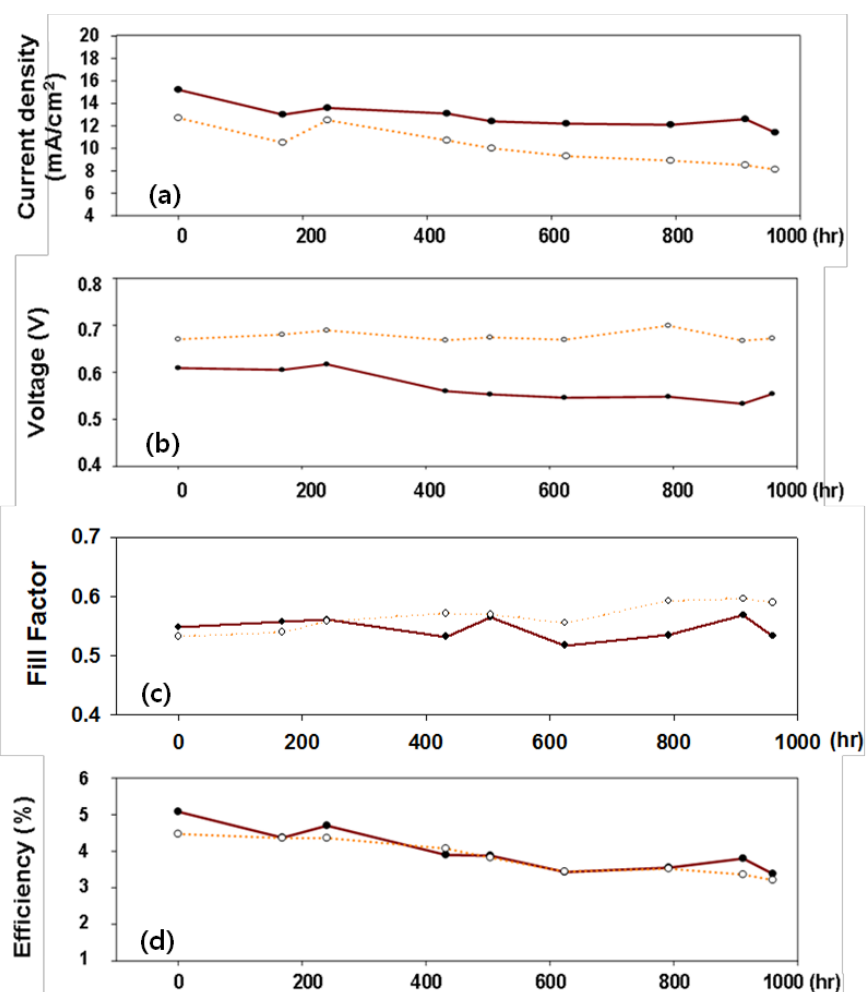


Figure 1. Detailed photovoltaic parameters of a device using polymer electrolyte with iodine (solid line) and a device using polymer electrolyte without iodine (dotted line) during stored in the dark and air at 80°C. Current density,  $J_{sc}$  (a); Voltage,  $V_{oc}$  (b); Fill Factor (c); Efficiency,  $\eta$  (d).

- [1] B. O. Regan and M. Grätzel, *Nature* **353**, 737 (1991).
- [2] A. Hagfeldt and M. Grätzel, *Chem. Rev.* **95**, 49 (1995).
- [3] J. Wu, S. Hao, Z. Lan, J. Lin, M. Haung, Y. Haung, L. Fang, S. Yin and T. Sato, *Adv. Funct. Mater.* **17**, 2645 (2007).
- [4] Y.L. Lee, Y.J. Shen and Y.M. Yang, *Nanotechnology* **19**, 455201 (2008).
- [5] Y. Yang, J. Zhang, C. Zhou, S. Wu, S. Xu, W. Liu, H. Han, B. Chen and X.Z. Zhao, *J. Phys. Chem. B* **112**, 6594 (2008).
- [6] E. Stathatos, P. Lianos and C. Krontiras, *J. Phys. Chem. B* **105**, 3486 (2001).
- [7] J.K. Lee, S.I. Jang, Y.G. Kim, Y.W. Jang, B.H. Jeong, J.U. Kim, K.S. Jung and M.R. Kim, *Molecular Crystals and Liquid Crystals* **491**, 307 (2008).

## Control of Magnetic Properties by Light in a Single Chain Magnet

Osamu Sato, Shinji Kanegawa, Tao Liu

Institute for Materials Chemistry and Engineering, Kyushu University, Japan

We aimed at creating tunable single chain magnets through light- or heat-induced metal-to-metal charge transfers (MMCTs). The reaction of  $\text{Li}[\text{Fe}(\text{bpy})(\text{CN})_4]$  (bpy = 2,2'-bipyridine),  $\text{Co}(\text{ClO}_4)_2 \cdot 6\text{H}_2\text{O}$ , and 4,4'-bipyridine in water produced block-shaped crystals of  $\{[\text{Fe}(\text{bpy})(\text{CN})_4]_2\text{Co}(4,4'\text{-bipyridine})\} \cdot 4\text{H}_2\text{O}$  (**1**). The crystal structure comprising neutral bimetallic  $[\text{Fe}(\text{bpy})(\text{CN})_4]_2\text{Co}(4,4'\text{-bipyridine})$  layers with uncoordinated water molecules located between the layers. Magnetic measurements show that the  $\chi T$  product was  $4.20 \text{ cm}^3 \text{ mol}^{-1} \text{ K}$  per  $\text{Fe}_2\text{Co}$  unit at room temperature, corresponding to the presence of one  $\text{Co}^{\text{II}}_{\text{HS}}$  and two  $\text{Fe}^{\text{III}}_{\text{LS}}$  with significant orbital contributions. On cooling, the  $\chi T$  values remained nearly constant between 300 and 250 K. However, slowly decreasing the temperature ( $0.5 \text{ K min}^{-1}$ ) from 250 to 200 K afforded a steep decrease in the  $\chi T$  products, reaching  $1.70 \text{ cm}^3 \text{ mol}^{-1} \text{ K}$  at 200 K. In contrast, on heating ( $0.5 \text{ K min}^{-1}$ ), the  $\chi T$  values increased and returned to the initial value with a small thermal hysteresis loop. Such a magnetic feature confirmed a reversible charge-transfer process that involved transformation between the high-temperature (HT) phase with  $\text{Fe}^{\text{III}}_{\text{LS}}$  ( $S = 1/2$ ) and  $\text{Co}^{\text{II}}_{\text{HS}}$  ( $S = 3/2$ ) metal ions and the low-temperature (LT) phase with diamagnetic  $\text{Fe}^{\text{II}}_{\text{LS}}$  ( $S = 0$ ) and  $\text{Co}^{\text{III}}_{\text{LS}}$  ( $S = 0$ ) centers.

Irradiation with a 532 nm laser light induced a valence state change from the  $\text{Fe}^{\text{II}}_{\text{LS}}\text{-Co}^{\text{III}}_{\text{LS}}$  state to the  $\text{Fe}^{\text{III}}_{\text{LS}}\text{-Co}^{\text{II}}_{\text{HS}}$  state. After irradiation, the spin topology changed from discrete clusters to one dimensional, and SCM behavior would be expected considering the negative anisotropy constant  $D$  of  $\text{Co}^{\text{II}}$ , strong intrachain magnetic interaction transmitted via the cyanide bridge, and weak interchain magnetic interaction transmitted via 4,4'-bipyridine and hydrogen bonding. Upon light irradiation at 5 K for more than 12 h, a significant increase in  $\chi T$  values was observed because of the photoinduced transformation from diamagnetic  $\text{Fe}^{\text{II}}_{\text{LS}}(\mu\text{-CN})\text{Co}^{\text{III}}_{\text{LS}}$  to metastable paramagnetic  $\text{Fe}^{\text{III}}_{\text{LS}}(\mu\text{-CN})\text{Co}^{\text{II}}_{\text{HS}}$  units. To investigate the dynamics of the magnetization, the alternative current (ac) magnetic susceptibility was studied as a function of both temperature and frequency. Variable-temperature ac susceptibility measurements revealed a strong frequency dependence of both in-phase ( $\chi'$ ) and out-of-phase components ( $\chi''$ ), as observed in other SCMs. The in-phase ac susceptibility showed a frequency independent peak at 3.8 K, which might be due to the weak interchain antiferromagnetic interactions, as suggested by the fact that the maximum of  $\chi''$  decreased with decreasing frequency. A semicircular Cole-Cole diagram ( $\chi''$  versus  $\chi'$ ) was constructed from the variable-frequency data collected at 1.85 K, and was fit to a generalized Debye model, giving an  $\alpha$  value of 0.34. This analysis demonstrated that the state of **1** after irradiation is an antiferromagnetic ordered phase of SCMs.

## Design of high Performance Polymer Electrolyte Membrane Fuel Cell Based on Multi-Walled Carbon Nanotube-Conductive Polymer Composites

Mohamed R. Berber<sup>1</sup>, Tsuyohiko Fujigaya<sup>1,2</sup> and Naotoshi Nakashima<sup>1,2,3</sup>

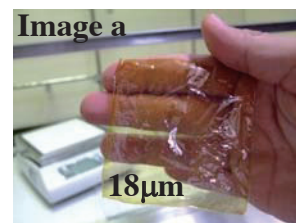
<sup>1</sup>Department of Applied Chemistry, Graduate School of Engineering, Kyushu University, Japan

<sup>2</sup>World Premier International (WPI) Research Center, International Institute for Carbon-Neutral Energy Research (I2CNER), Kyushu University, Fukuoka 819-0395, Japan

<sup>3</sup>JST-CREST, 5 Sanbancho, Chiyoda-ku, Tokyo, 102-0075, Japan

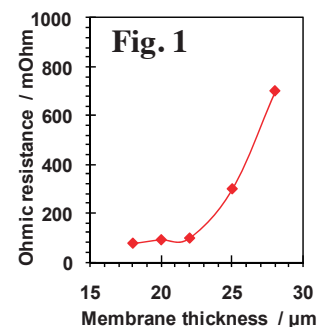
Energy shortages and environmental pollution are serious challenges that humanity will face for the long-term. Hence, we are encouraged as researchers to find an alternative source of energy. Fuel cells (FCs) are electrochemical devices with high energy conversion efficiency, minimized pollutant emission and other advanced features, and are receiving a great deal of attention. Polymer electrolyte membrane fuel cell (PEMFC) is a type of FCs in which conductive polymers are used as electrolytes and carbon-supported dual-layer catalyst are used as electrodes. Most of the present PEMFC are using Nafion polymer as a proton conducting membrane, however it functions only in a highly hydrated condition which limits its operation at low temperature. On the other hand, carbon black/platinum (CB/Pt) is typically used as a catalyst to accelerate the speed of the electrochemical reactions at the electrode sides. This composite has also unfavorable interfacial structure for FCs durability and performance. Accordingly, understanding how membrane structures and porous electrodes influence the FC performance has a scientific and industrial interest.

Recently, polybenzimidazole (PBI) was recognized as a high temperature conducting polymer, overcoming several challenges for PEMFC technology. Our group [1] tested a FC containing PBI as membrane and carbon nanotube composites (CNT/PyPBI/Pt) at the electrode sites. Successfully, we found promising FC properties.



Here, we tried to modify and optimize the measurement conditions of our FC by controlling the ionic transport which represents a significant voltage loss and strongly reduces the FC performance, in addition to designate highly conductive polymer composite electrodes.

By assembling a thin polymer electrolyte membrane of PBI (18  $\mu\text{m}$ ; image a), the performance of the cell was enhanced due to the decrease of ionic resistance (Figure 1). The open circuit voltage was recorded to be 1.0 V. The limiting current density became 1800  $\text{mA}/\text{cm}^2$ . The cell power density was highly improved and reached around 250  $\text{mW}/\text{cm}^2$ , comparing to 110  $\text{mW}/\text{cm}^2$  [1].



[1] K. Matsumoto, T. Fujigaya, K. Sasaki, N. Nakashima, *J. Mater. Chem.* **21**, 1187 (2011).

## Periodic Mesoporous Organosilicas with Amphoteric Ligand Functionalized Framework for Drug Delivery

M. Santha Moorthy, Sung Soo Park, Chang-Sik Ha\*

Department of Polymer Science and Engineering, Pusan National University, Republic of Korea

Periodic mesoporous organosilicas (PMOs) are a novel branch of ordered hybrid mesoporous materials in which the organic fragments are regularly distributed within the framework. The introduction of ligand functionality in the framework of the mesoporous silica materials is potentially advantageous for the various types of applications including catalyst, adsorption of metal ions and drugs. It is possible to control the properties such as adsorption capacity, surface hydrophobicity and thermal as well as mechanical properties by changing the nature and distribution of functional groups in the hybrid mesoporous silica.

In the present work, we have successfully synthesized well ordered hexagonal PMOs through co-condensation of bissilylated diaminomaleonitrile ligand (BSDAMN) and tetraethylorthosilicate (TEOS) as a silica source, using a triblock copolymer (Pluronic P123) as a structure directing agent in acidic medium with various BSDAMN to TEOS ratios. The surfactant was removed by solvent extraction method using 1% HCl-ethanol solution at 60 °C. The diaminomaleonitrile siloxane precursor was characterized by  $^1\text{H}$  and  $^{13}\text{C}$ -NMR spectroscopic techniques. The bridged functionality was incorporated into the material as a bridge-bonded group, and the nitrile group of the ligand was chemically modified into amidoxime with hydroxylamine reagent.

Silica materials were characterized by powder X-ray diffraction, Transmission electron microscopy (TEM), Fourier-transform infrared (FT-IR) spectroscopy,  $\text{N}_2$  sorption isotherm,  $^{29}\text{Si}$  and  $^{13}\text{C}$  CP MAS NMR spectroscopic analyses, and thermogravimetric analysis (TGA). The morphologies of the materials were identified by scanning electron microscopic analysis.

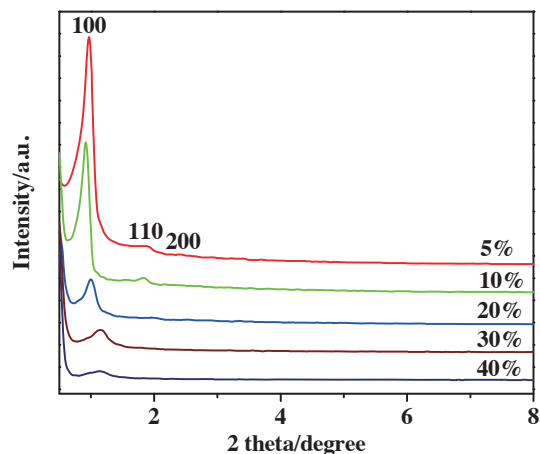


Fig. 1. XRD patterns of PMO materials with the different content of BSDAMN.

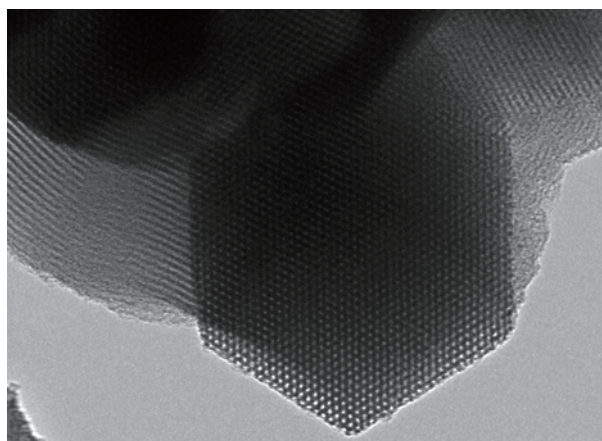


Fig. 2. TEM image of PMO with 5 % of BSDAMN.

### References

1. S. Matsumoto, T. Kobayashi, T. Aoyama, T. Wada, *Chem. Commun.*, 1910 (2003).
2. S. H. Kim, S. Matsumoto, *Dyes and Pigments*, **72**, 406 (2007).

## Unique behavior of poly (vinyl pyrrolidone) confined in the two dimensional nanospace

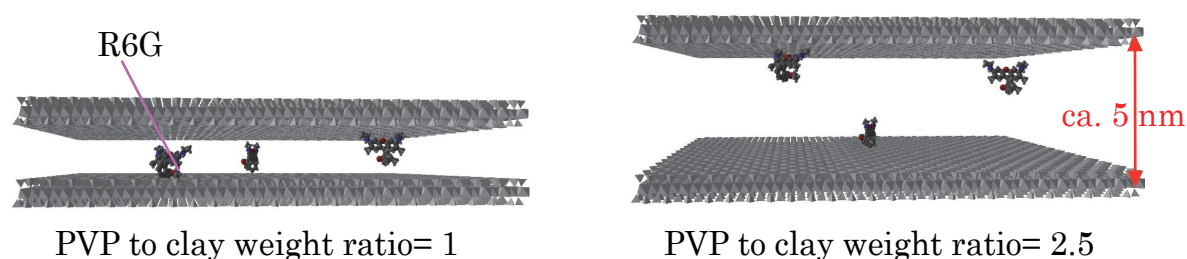
Minoru Sohmiya,<sup>1,2</sup> Shingo Omata,<sup>1</sup> Makoto Ogawa<sup>1,2</sup>

<sup>1</sup>Department of Earth Sciences, Waseda University, Japan

<sup>2</sup>Graduate school of Creative Science and Engineering, Waseda University, Japan

Polymer based nanocomposite materials have been investigated due to the possible and versatile modification of the materials performance (mechanical strength, thermal stability, gas barrier or flammability) by the incorporation of small amounts of nanosized inorganic particles. The confinement of polymers in nanospaces has also been investigated for long time, for example water soluble polymers are known to be intercalated into clay.[1] The polymer content directly correlates the interlayer expansion of clay, meaning the two dimensional nanospace with designable gap (distance between the adjacent layer) can be created[2] to be used for the guest immobilization.[3] In the present study, we prepared dye and polymer co-intercalated clay hybrid to show the height of the interlayer 2-dimensional nanospace is varied by the polymer content and how the interlayer expansion affects the photoinduced event of the intercalated dye.

For this purpose, a synthetic saponite (Sumecton SA) was used as the host material, water soluble polymer, poly(vinyl pyrrolidone) (PVP), was used as the guest polymer to be intercalated and Small amount (0.1-1% of cation exchange capacity of Sumecton SA) of rhodamine 6G (R6G), which is a useful photoluminescent dye, was intercalated into the synthetic saponite before the intercalation of polymer. In addition, the photostability of R6G in clay polymer intercalation compounds was examined.



Scheme 1. Schematic drawings of R6G-PVP-SA films.

R6G and PVP co-intercalated smectite (R6G-PVP-SA) films were prepared by cation exchange of SA (2 g) in aqueous solutions of R6G (200 mL) at r.t. for 1 day. Then, PVP was added to the R6G-SA intercalation compound and the mixture was allowed to react at r.t. for 1 day. The loading amount of R6G varied from 0.1 to 1 % of the cation exchange capacity of SA (71 meq. / 100 g of clay). The suspension (2 mL) was cast on a flat glass

plate (30x30 mm) and dried under air at r.t. The amount of the added PVP was 1: 0-5 (the weight ratio of R6G-SA intercalation compound: PVP).

Fig. 1 shows the XRD patterns of the R6G-PVP-SA films to show the interlayer expansion varied depending on the polymer contents. In order to investigate the effect of the interlayer nanospace expansion on the excited state behavior of the co-intercalated R6G, luminescence self-quenching efficiency was examined as a function of PVP content by applying Stern-Volmer plot, where X-axis was the calculated concentration based on the interlayer volume and the adsorbed R6G amount. The plots shows effective self-quenching with the increase of the R6G loading and the self-quenching efficiency (gradient of the plots) was increased with the increase of PVP content (the interlayer spacing). This suggests that the distance

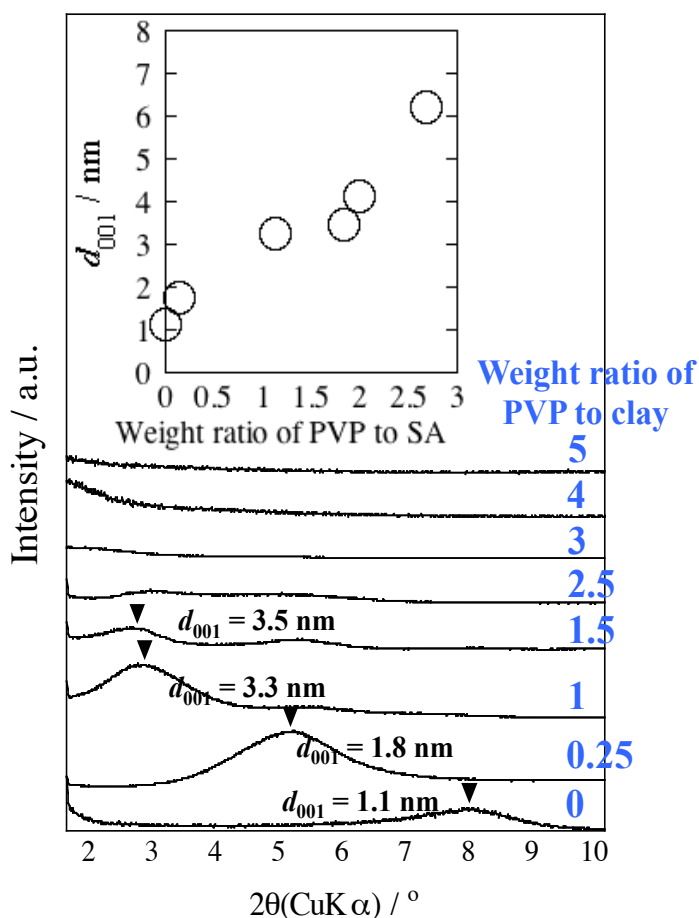


Figure 1. Representative XRD patterns of the R6G-PVP-SA films; R6G amount is 1% of CEC of SA and the weight ratio of the added PVP amounts to SA are 0-5. The inset shows the relationship between  $d_{001}$  values and the weight ratio of PVP amount to SA.

between adjacent R6G was varied by changing the PVP contents.

The stability of R6G in R6G-PVP-SA film under artificial sunlight was examined to find the degradation of R6G in R6G-PVP-SA film was suppressed dramatically. This suggests that the R6G was stabilized by the intercalation into clays with PVP possibly due to the suppressed oxygen diffusion through the film as well as the difference in the relaxation processes.

## References

- [1] B.K.G. Theng, *Formation and Properties of Clay-Polymer Complexes*. Elsevier: Amsterdam, 1979.
- [2] C. M. Koo, *et al.*, *Polymer*, **44**, 681-689 (2003).
- [3] M. Ogawa and K. Kuroda, *Bull. Chem. Soc. Jpn.* **70**, 2593-2618 (1997).

## Effect of Solvents on the Synthesis and Characterization of Hydrophilic to Hydrophobic Organic-Inorganic Hybrids for Coatings

Saravanan Nagappan, Jin-Joo Park, Chang-Sik Ha\*

Department of Polymer Science and Engineering, Pusan National University, Republic of Korea

The hydrophilic to hydrophobic organic-inorganic hybrids have been synthesized by sol-gel technique using polymethylhydrosiloxane (PMHS), 2,2,3,4,4,4 hexafluorobutylmethacrylate (HFBMA), and tetraethyl orthosilicate (TEOS). Initially PMHS was reacted with HFBMA using toluene as a solvent by hydrosilylation process under the conditions of 120 °C in N<sub>2</sub> atmosphere to 24 hours using Pt catalyst. This produces an elastomeric fluorinated polymethylhydrosiloxane (FPMHS) precursor by the complete evaporation of solvent using a rotary evaporator. The fluorinated polymethylsiloxane/silica (FPMS/Silica) hybrids have been synthesized by the reaction of the precursor and TEOS with equivalent amount of water and different quantities of ethanol solvent at 70-80 °C for 24 hours. The dispersed hybrids in ethanol were spin-coated on glass substrates and thermally baked at 80 °C. The functional groups, chemical structures and compositions, surface morphology and their properties of the hybrids have been analyzed by FTIR, <sup>1</sup>H-NMR, <sup>29</sup>Si MAS-NMR, XPS and SEM with EDAX, AFM, XRD and TGA. The dynamic contact angles (DCA) to water and ethylene glycol on the coated samples were also measured by drop shape analysis system. The prepared hybrid thin films have exhibited good transparency and hydrophilic to stable hydrophobic nature by the increase of ethanol amounts.

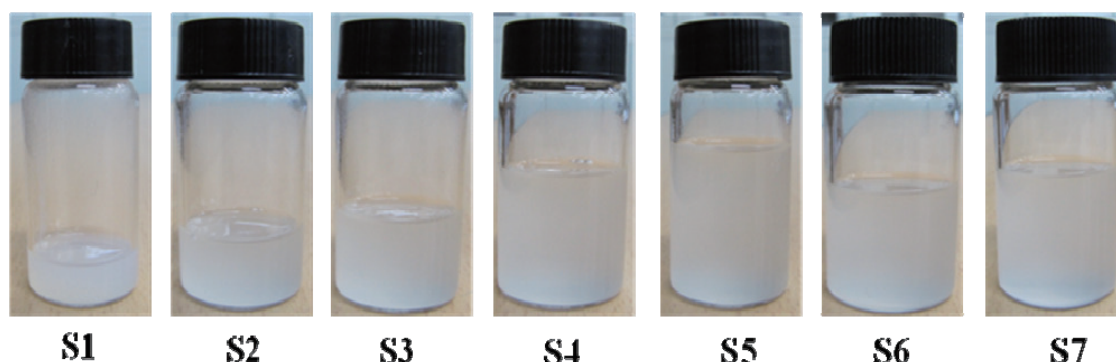


Fig. 1. Dispersed solution of FPMS/Silica hybrids with different amounts of ethanol in range from 1 to 10 of EtOH/TEOS ratio.

### References

- [1] C. Tang, W. Liu, S. Ma, Z. Wang, C. Hu, *Prog. Org. Coat.*, **69**, 359 (2010).
- [2] G. De, B. Karmakar, D. Ganguli, *J. Mater. Chem.*, **10**, 2289 (2000).
- [3] Y. Kim, W. K. Lee, W. J. Cho, C.-S. Ha, M. Ree, T. Chang, *Polym. Int.*, **43**, 129 (1997).

## Shape Changes in Gold/Silver Bimetallic Systems including Polygonal Gold Seeds under Oil-Bath Heating at 150 °C

Md. Jahangir Alam<sup>1</sup>, Mika Matsunaga<sup>2</sup>, and Masaharu Tsuji\*<sup>1,2</sup>

<sup>1</sup>Graduate School of Engineering Sciences, Kyushu University, Kasuga 816-8580, Japan

<sup>2</sup>Institute for Materials Chemistry and Engineering, Kyushu University, Kasuga 816-8580

Shape changes in Au/Ag bimetallic nanoparticles have been studied under continuous oil bath heating at 150 °C in ethylene glycol (EG) on the basis of TEM, TEM-EDS, and UV-Vis spectral data of products. When a mixture of polygonal Au and spherical Ag particles was heated for 10-60 min, they melted each other and became spherical Au/Ag alloys with an average diameter of 207±35 nm. When polygonal Au seeds were added to AgNO<sub>3</sub>/EG/PVP solution heated at 150 °C for 10-60 min, a significant shape changes in products were observed. After continuous heating for 30 min, Au@Ag core shell particles attached to Ag rich Ag/Au alloy nanowires and after 60 min heating they are turned to excentered Au@Ag/Au nanoparticles with an average diameter of 414±92nm. The new type excentered Au@Ag/Au nanoparticles consist of a small spherical Au component and Ag rich Ag/Au alloy component.

### 1. Introduction

We have recently found that polygonal Au nanoparticles with average diameters of ≈40 nm could be converted to monodispersed spherical particles with an average diameter of ≈290 nm under continuous oil-bath heating for 10-60 min in EG [1]. The rate of shape conversion depends on gas dissolved in solvent and it was strongly enhanced in the presence of O<sub>2</sub> in ethylene glycol (EG). We discussed the transformation of Au nanostructures in terms of gas bubbling induced Ostwald ripening, shape-selective oxidative etching by O<sub>2</sub>/Cl<sup>-</sup>, and grain-rotation-induced grain coalescence (GRIGC) and fusion mechanisms. However, more definite evidence was necessary whether gold nanoparticles really melt or they are etched under various conditions. In order to study shape changes in polygonal Au nanoparticles under oil-bath heating at 150 °C in more detail, Ag nanoparticles are either added or produced by the addition of AgNO<sub>3</sub> in this work. Then shape and component changes in Au nanoparticles are observed under continuous heating at 150 °C for 10-60 min by TEM, TEM-EDS, and UV-Vis spectral data of products.

We have made two kinds of experiments in this study [2]. One is the shape and component changes in mixtures of polygonal Au particles and small Ag nanoparticles during oil-bath heating for 10-60 min. We could obtain definite evidence that whether polygonal Au particles really melt and alloys are formed from mixtures of Au/Ag particles. The second experiment was addition of polygonal Au seeds to AgNO<sub>3</sub>/PVP/EG solution heated at 150 °C for 10-60 min. These results demonstrated that drastic changes in products occur from Au@Ag core shell and Ag rich Ag/Au nanowires to the excentered Au@Ag/Au particles.



## 2. Experimental

**Preparation of polygonal Au seeds:** 15 mL of EG solution was preheated at 150 °C for 60 min under Ar gas bubbling. Then a mixture of HAuCl<sub>4</sub>.4H<sub>2</sub>O and PVP (M<sub>w</sub> = 40 k) as a polymer surfactant in 5 mL of EG was added and further heated at 150 °C for 10 min with Ar gas bubbling. After 10 min heating yellow coloured gold solution is turned to brownish red. The products were collected by centrifugal separation to remove all by-products produced in the supernatant.

**Preparation of Ag seeds:** A mixture of 2.4 mM AgNO<sub>3</sub>, 1 M PVP (M<sub>w</sub> =10,000 in term of monomer units) in 20mL of EG was heated at 150 °C for 4 min with Ar gas bubbling. After 4 min heating the colourless solution was changed to yellow colour. It was cooled at room temperature.

**Mixing and heating:** A new fresh EG solution containing 250 mM PVP and polygonal Au seeds was mixed with 30% Ag nanoparticle enriched solution or AgNO<sub>3</sub> (24 mM) solution. The total volume of solution was 20 mL. The mixture was heated from room temperature to 150 °C for 60 min with sampling 10, 30, and 60 min.

## 3. Result and discussion

### 3.1 Shape and component changes in mixtures of polygonal Au and spherical Ag particles

Polygonal Au seeds consist of octahedral, triangular-plate like, decahedral particles, as shown in Fig. 1(a). Octahedral particles are single crystal, triangular-plate like particles are single-twin particles, and decahedral particles are multiple-twin particles. Fig. 1(b) shows TEM images of monodispersed spherical Ag nanoparticles with average size of 15 nm. Fig. 1(c) shows the typical images of mixture of polygonal Au and monodispersed spherical Ag particles without any heating condition. In this case Au and Ag nanoparticles are located side by side without any shape change. In continuous heating process they melted each other and became spherical Au/Ag alloys with an average diameter of 207±35 nm for 10, 30, and 60 min in Fig. 1(d), (e), (f), respectively.

### 3.2 Shape and component changes in products by the addition of polygonal Au particles to AgNO<sub>3</sub>/PVP/EG solution

When polygonal Au seeds (Fig. 2a) were added to AgNO<sub>3</sub>/EG/PVP solution heated at 150°C for 10-60 min, significant shape changes in products were observed. After continuous heating for 10 min, Au@Ag core shell particles marked with red circles in Fig. 2(b) are produced. On the other hand, after 30 min heating larger Au@Ag particles, and Ag rich Ag/Au alloy nanowires are produced as shown in TEM-EDS data (Fig. 2c). It should be noted that after heating for 60 min, they turned to excentered Au@Ag/Au particles as shown in TEM-EDS data (Fig. 2d). The excentered Au@Ag/Au particles are composed of small Au

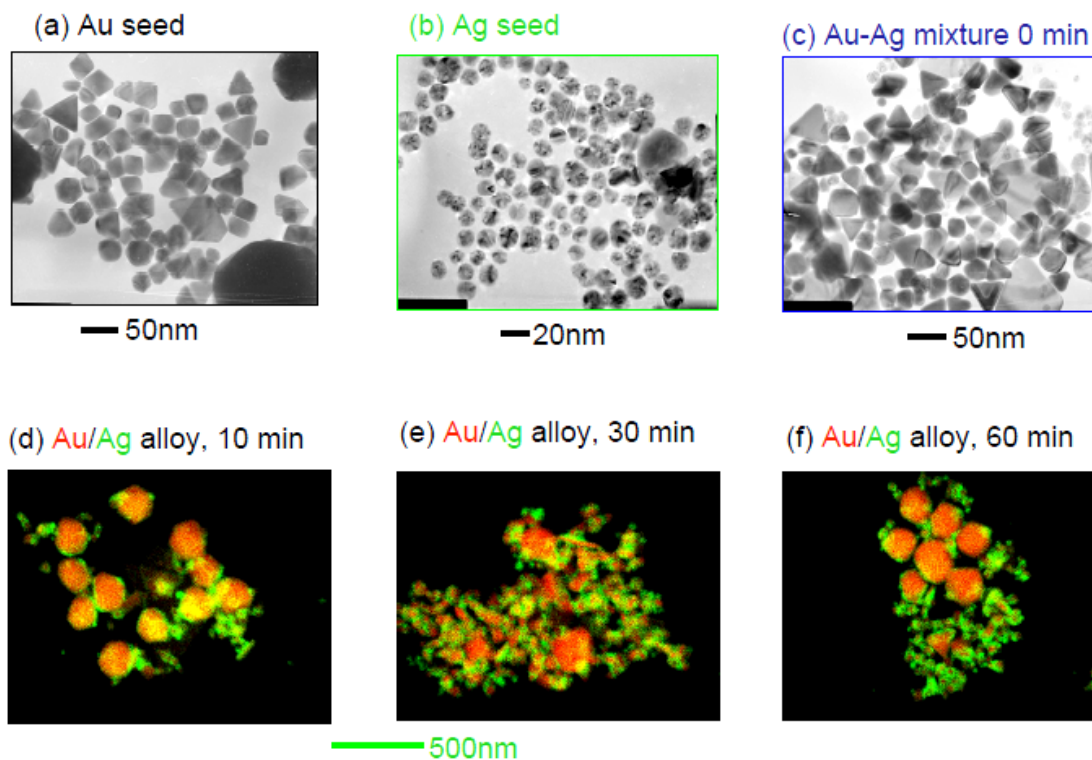


Fig. 1. Typical TEM images of (a) Au polygonal seeds, (b) spherical shapes of Ag particles, (c) mixture of Au and Ag seeds before heating, (d) spherical and elongated shapes of Au/Ag particles for 10 min heating, (e) Au/Ag particles are prepared for 30 min, (f) Au/Ag alloy particles for 60 min.

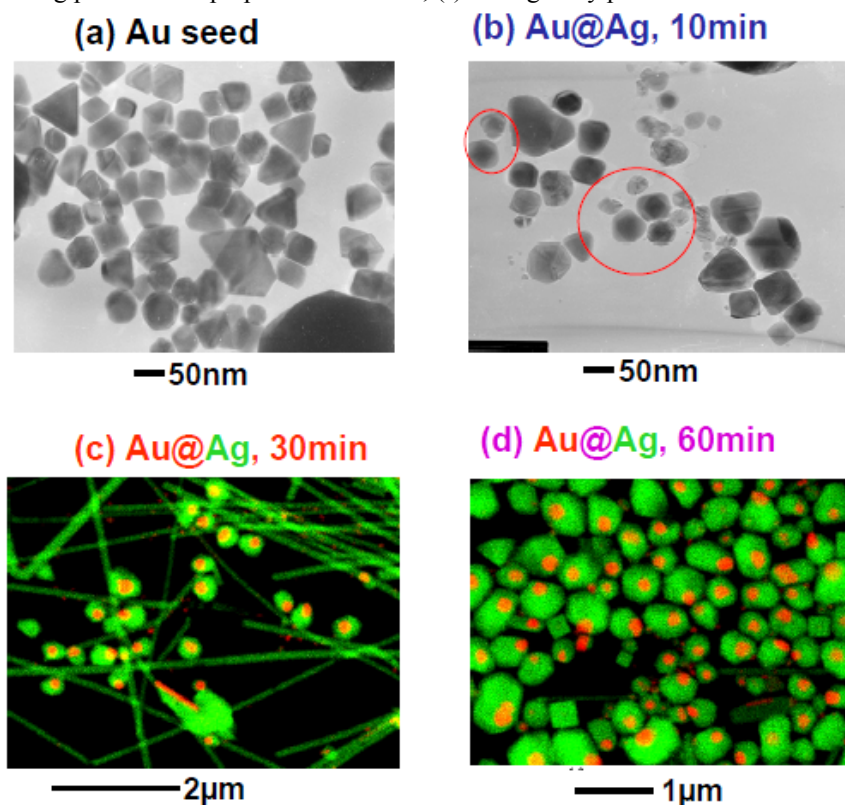


Fig. 2. Typical TEM images of (a) Au polygonal seeds (b) shapes of Au@Ag core shell for 10 min (c) Au/Ag alloy nanowires and spheres for 30 min, (d) monodisperse excentered Au@Ag/Au particles are prepared for 60 min heating. Red=Au, green=Ag.

parts with an average diameter of  $166\pm 42$  nm and Ag rich Ag/Au alloy particles with an average diameter of  $414\pm 92$ nm. The atomic ratio of Ag: Au in alloy parts were  $98.6\pm 0.5:1.4\pm 0.5\%$ , respectively.

### 3.3 Mechanisms of shape transformation

Fig. 3 shows the grain-rotation-induced grain coalescence (GRIGC) and fusion mechanism. According to this model, polygonal Au single and twin particles having well-defined faces were lost after the formation of large spherical Au/Ag alloy particles by fusion with spherical Ag particles. Fig. 4 shows a schematic process for shapes conversion of polygonal Au particles to excentered Au@Ag/Au nanoparticles by the addition of AgNO<sub>3</sub>/PVP/EG solution. After heating for 10 min Au@Ag core-shell particles are formed. After heating for 30 min, Ag rich Ag/Au nanowires (Au content: about 0.5-1%) become dominant products and Au@Ag particles are attached to Ag/Au nanowires due to Ostwald ripening. A small amount of Au component in Ag/Au wires arises from thermal dissolution of Au seeds by HNO<sub>3</sub>. Au@Ag particles act as catalyst for dissolution of Ag/Au alloy nanowires via  $Au^{3+} + Ag \rightarrow 2Ag^{+} + Au^{+}$  reaction, where  $Au^{3+}$  arises from dissolution of Au@Ag particles. Ag/Au nanowires are fused and dissolved thermally during aging at 150 °C for 60 min. The formation of excentered

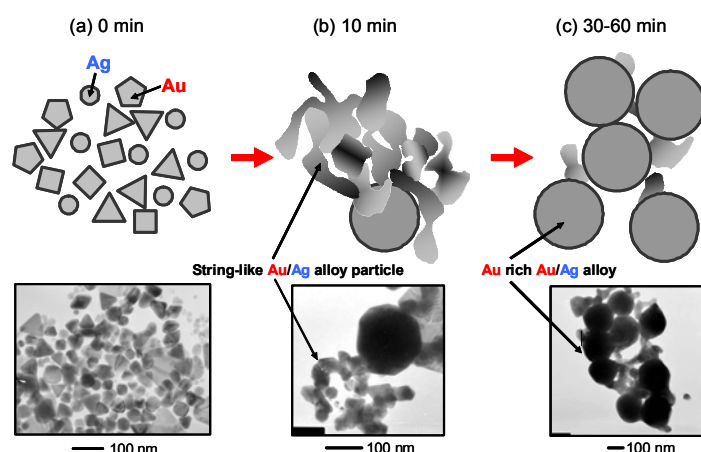


Fig. 3. Melting process of polygonal Au and spherical Ag particles to sphere Au/Ag alloy particles.

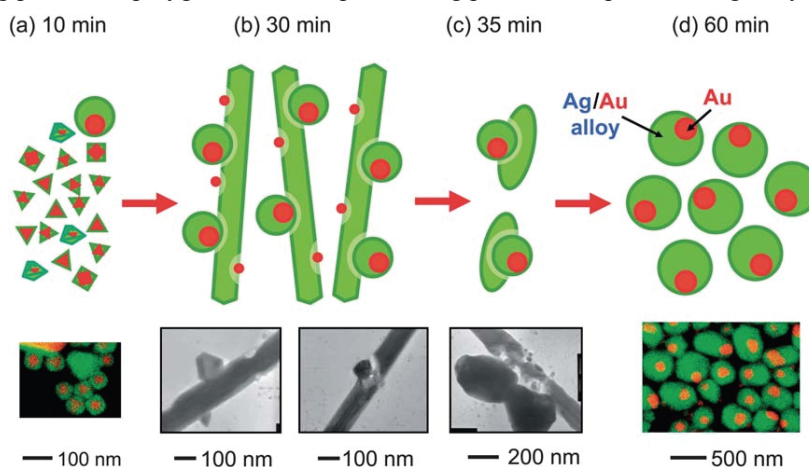


Fig. 4. A schematic process for shapes conversion to excentered Au@Ag/Au particles.

Au@Ag/Au particles indicates that excentered Au@Ag/Au structure is more stable than complete random Au/Ag alloy structure in our conditions.

#### **4. Conclusion**

Shape changes in Au/Ag bimetallic nanoparticles were studied under oil-bath heating at 150 °C in EG. When a mixture of Au and Ag particles was heated for 60 min, spherical Au/Ag alloys with an average diameter of 207±35 nm were produced. When polygonal Au seeds were added to AgNO<sub>3</sub>/EG/PVP solution heated at 150 °C for 10-60 min, excentered Au@Ag/Au particles with small Au parts and Ag rich Ag/Au alloy particles were formed via Ag rich Ag/Au nanowires.

#### **5. References**

- [1] Md. J. Alam, M. Tsuji, and M. Matsunaga, *Bull. Chem. Soc. Jpn.*, **83**, 92 (2010).
- [2] Md. J. Alam, M. Tsuji, M. Matsunaga, and D. Yamaguchi, *CrystEngComm*, **13**, 2984 (2011).

#### **ACKNOWLEDGEMENTS**

This work was supported by a Grant-in-Aid for Scientific Research (B) from the Ministry of Education, Culture, Sports, Science, and Technology of Japan (MEXT, No. 22310060) and by the Management Expenses Grants for National Universities Corporations from the MEXT.

## New Approaches to Solvothermal Synthesis of Cobalt Ferrite Nanocrystals

A.V. Zdravkov, J.S. Kadulina, N.N. Khimich

Grebenshchikov Institute of Silicate Chemistry, Russian Academy of Sciences,  
Makarova emb. 2, St. Petersburg 199034, Russia

Preparation techniques of spinel-type cobalt ferrite nanoparticles have been investigated intensively in recent years because of their potential applications in high-density magnetic recording, microwave devices and magnetic fluids. Several processes to produce ferrite nanoparticles have been proposed, such as sol-gel method, citrate precursor technique, chemical precipitation, electrochemical synthesis, complexometric synthesis, combustion method and solid-state reaction. However in most of these methods long reaction time or the subsequent heat treatment procedure for improvement of the crystallinity is needed which requires the energy consume. The promising method for cobalt ferrite production is the hydrothermal synthesis but it requires special equipment. In addition, there are a lot of organic solvents boiling at high temperatures which allow carrying out a synthesis of different metal oxides at atmospheric pressure without using of autoclaves. We believe that in this case the process will strongly depend on structure of solvent (polarity, presence or absence of labile proton etc).

Thus the main goal of this work was to investigate synthetic procedure leading to cobalt ferrite with the use of inorganic precursors (obtained by co-precipitation of  $\text{Co}(\text{OH})_2$  and  $\text{Fe}(\text{OH})_3$  from aqueous solution) treated in high-boiling (b.p. 250–400 °C) organic solvents containing different functional groups – in glycerol, diphenyloxide, oleic acid, butyl oleate and oleylamine. It's necessary to note that despite on amorphous character of precursors obtained we have no a simple mixture of hydroxides but a structured system cobalt(II) hydroxide – iron(III) hydroxide, i.e. we can talk about formation of the gel “cobalt(II) hydroxide – iron(III) hydroxide” during the sol-gel synthesis. We can make such conclusion because of the fact that the separate precipitation of cobalt(II) and iron(III) hydroxides in analogues conditions leads to a formation of amorphous iron(III) hydroxide and crystalline cobalt(II) hydroxide.

The synthesis in anhydrous media at high temperatures differs considerably from such process in hydrothermal conditions. It leads to the formation of unknown adducts of solvents with forming spinel-type structures and to unusual behavior of ensembles of nanoparticles during synthesis – in some cases the particle size became less with increasing of reaction time which was varied between 3 and 72 hours. The resulting precipitates were dried, calcined at 400–800 °C and characterized by XRD, TEM, FTIR, elemental analysis and magnetic measurements. In addition, we observed some interesting effects during thermal analysis of

the precipitates.

The XRD patterns (Co  $K_{\alpha}$  radiation) of the samples is shown in Fig. 1. All peaks are characteristic for  $CoFe_2O_4$  cubic spinel-type structure. The absence of foreign diffraction lines suggests the phase purity. Using Scherrer equation and TEM microscopy data (Fig. 2) we obtained an average grain size of about 10–70 nm (in the case of butyl oleate, glycerol, diphenyloxide and oleylamine), and about several micrometers in case of oleic acid.

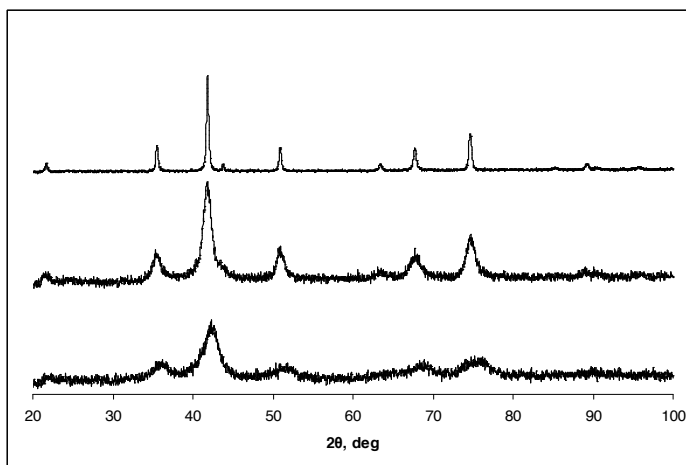


Fig. 1. XRD patterns of samples prepared in oleic acid (top), in oleylamine (centre) and in diphenyloxide (bottom) (Co  $K_{\alpha}$ ).

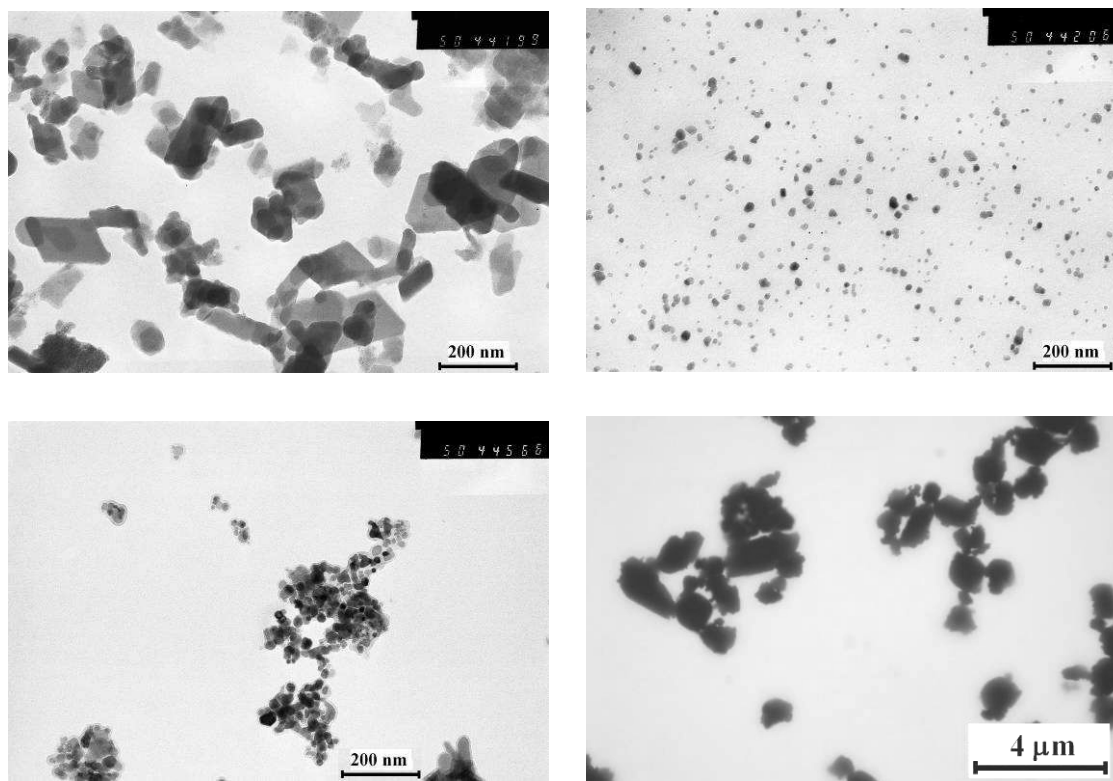


Fig. 2. TEM micrographs of samples prepared in glycerol (top left), butyl oleate (top right), oleylamine (bottom left) and oleic acid (bottom right)

The magnetic behavior of prepared powders strongly depends on the synthetic conditions and in particular on size of obtained particles. Their properties varied from diamagnetic (prepared in glycerol) to superparamagnetic (prepared in diphenyloxide and butyl oleate) and ferrimagnetic (prepared in oleic acid and oleylamine).

## Glycopolymer Substituted Biomaterials via RAFT Living Radical Polymerization

Yoshiko Miura,<sup>1,2</sup> Masayuki Toyoshima,<sup>2</sup> Masami Takara,<sup>1</sup> Yu Hoshino<sup>1</sup>

<sup>1</sup>Department of Chemical Engineering, Kyushu University, Japan

<sup>2</sup>Japan Advanced Institute of Science and Technology, Japan

Saccharides on the cell surfaces play important roles in a living system. Basically, protein-saccharide interaction is weak, but it can be amplified by multivalency. The glycopolymers, which has pendant saccharides, are known to exhibit the large saccharide-protein interaction based on the saccharide assembled structure along the polymer backbone. We have investigated the synthesis of glycopolymers using radical initiator.

In this investigation, the glycopolymers via living radical polymerization was investigate by Reversible Addition-Fragment chain Transfer (RAFT) reagent, and the hybrid biomaterials were prepared. In this investigation, the acrylamide derivatives with saccharides such as p-acrylamidephenyl  $\alpha$ -mannose were used as monomers. The glycopolymers were prepared with RAFT reagents, and the polydispersities of the obtained glycopolymers were below 1.5. Then the glycopolymers were reduced to yield thiol-terminated polymer, which was conjugated to gold nanoparticles and gold substrate.

The glycopolymer modified gold nanoparticles showed the specific biological recognition to lectins. For example, the glycopolymer modified nanoparticle with  $\alpha$ -mannose showed the colorimetric change with addition of lectins. The addition of concanavalinA (ConA, mannose recognition protein) induced the red shift, though other proteins didn't induce the color change. The shifts of the UV spectra were fitted by Langmuir plot, and the dissociation constant of  $K_d$  was  $1.89 \times 10^{-9}$  (M), meaning the strong molecular recognition ability. The glycopolymer modified nanoparticles were also applied to biosensor of lateral flow assay. The lateral flow assay was conducted with the target protein of ConA. The color of nanoparticle was observed with addition of ConA. The glycopolymer via RAFT living radical polymerization showed strong protein-saccharide interaction, and was applied as biosensing.

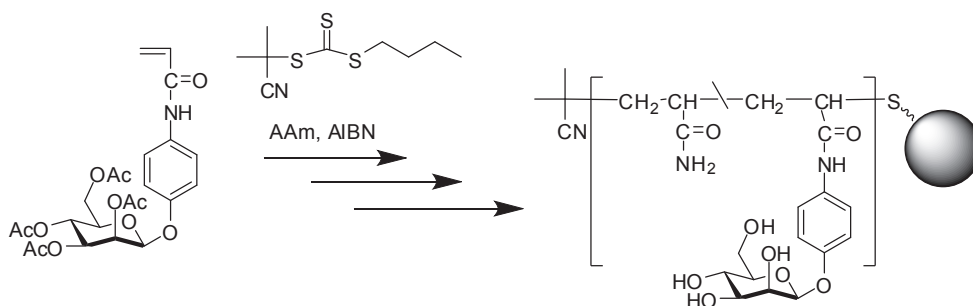


Figure 1 The synthetic scheme of glycopolymer modified gold nanoparticle via RAFT living radical polymerization.

## An Effect of Polymer Surface Stiffness on Fibroblast Adhesion

Shinichiro Shimomura, Hisao Matsuno, Keiji Tanaka

Department of Applied Chemistry, Kyushu University, Japan

**Introduction:** Cell behaviors such as adhesion, spreading, proliferation, and differentiation strongly depend on their culture environments. Recently, it has been revealed that various adhesive cells could feel physical properties such as stiffness of polymer materials as a scaffold.[1] These cells preferentially adhere to harder surfaces compared to softer ones. However a detail mechanism of stiffness recognition by cells has not been well understood. In general, thermal molecular motion at the polymer surfaces is enhanced in comparison with that in the internal bulk region. Furthermore, such an activated polymer mobility is a function of the distance from the outermost region.[2] In this study, we investigate an effect of surface molecular motion at the polystyrene (PS) film surfaces on cell adhesion.

**Experiments:** PS homolayer films with various number-average molecular weights ( $M_n$ ) on cover glasses were prepared by a spin-coating method. The film thickness of PS ( $d_{PS}$ ) was regulated to be approximately 200 nm. And also, PS/polyisoprene (PI) bilayer films with various  $d_{PS}$  and constant PI-thickness were prepared in the same manner. In this case,  $d_{PS}$  ranged from 17 to 200 nm and PI-thickness was constant. Mouse L929 fibroblast cells were cultured on these films at 310 K (37 °C) under a humidified atmosphere of 5 % CO<sub>2</sub>, and then initial cell adhesion and spreading behaviors were evaluated by microscopic observations.

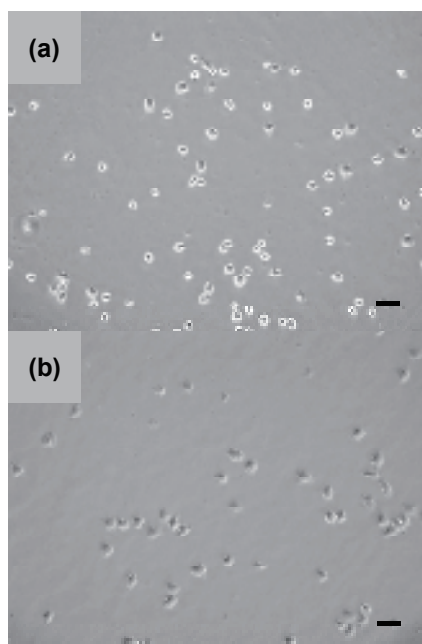


Fig. 1. L929 fibroblasts adhered on PS homolayer films with  $M_n$  of (a) 6k and (b) 75k, respectively. Scale bars correspond to 50  $\mu\text{m}$ .

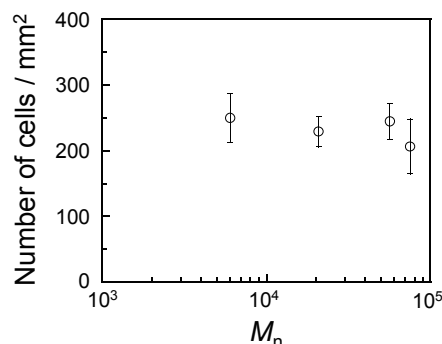


Fig. 2.  $M_n$  dependence of the number for L929 fibroblasts adhered on the PS homolayer films.



**Results and discussion:** The film surfaces of PS with lower  $M_n$  were in a rubbery state at room temperature, and the ones of PS with higher  $M_n$  were in a glassy state.[2] Fig. 1 shows the phase contrast images of L929 cells adhered on PS homolayer films. The number of adherent cells on the films was insensitive to  $M_n$ , as shown in Fig. 2.

These results indicate that cell behaviors might be independent of the thermal molecular motion at the outermost surface of the PS films. The molecular motion is extremely activated with a depth region of approximately 10 nm from the outermost surface. Thus, glassy PS/rubbery PI bilayer films were prepared as scaffolds. This system enables us to gain access to the characteristic depth scale for the surface stiffness of the cell recognition. Fig. 3 shows the phase contrast images of L929 cells on PS/PI bilayers. The number of cells ( $N$ ) on these films remarkably decreased with decreasing thickness when  $d_{PS}$  went beyond approximately 25 nm, as shown in Fig. 4. Furthermore, the spreading ratio of the cells also decreased with the same region. In our previous study, we evaluated surface storage modulus ( $E'$ ) for PS/PI bilayer films and revealed that the surface  $E'$  strongly depended on the  $d_{PS}$ . [3] Interestingly, the  $d_{PS}$  dependence of cell adhesion on PS/PI bilayer films observed here are very similar with that of surface  $E'$ . These results imply that L929 fibroblast could recognize the surface stiffness with a depth region of approximately 25 nm.

### References

- [1] D. E. Discher, P. Janmey, and Y. L. Wang, *Science*, **310**, 1139 (2005).
- [2] K. Tanaka, A. Takahara, and T. Kajiyama, *Macromolecules*, **33**, 7588 (2000).
- [3] N. Satomi, K. Tanaka, A. Takahara, and T. Kajiyama, *Macromolecules*, **34**, 6420 (2001).

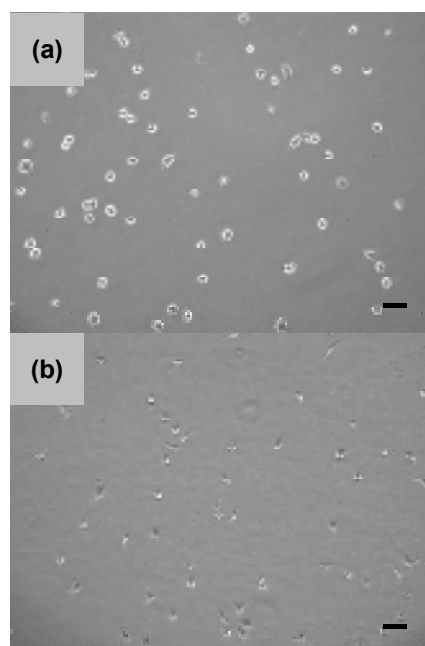


Fig. 3. L929 fibroblasts adhered on PS/PI bilayer films with (a) 25 nm- and (b) 200 nm- $d_{PS}$ , respectively. Scale bars correspond to 50  $\mu\text{m}$ .

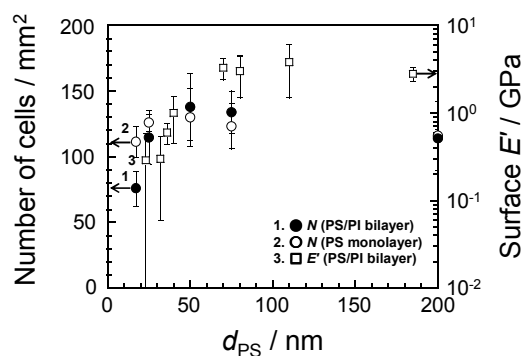


Fig. 4. Relation of the number for adhered L929 fibroblasts to  $d_{PS}$ . Closed and open circles show the number of cells on PS/PI bilayer and PS homolayer films, respectively. Open square shows  $d_{PS}$  dependence of surface  $E'$  of PS/PI films.[3]

## Surface Analysis and Degradation Behavior of Poly(l-lactide) by End-group Modifications

Won-Ki Lee

Department of Polymer Engineering, Pukyong National University, Busan 608-739, Korea

In order to control the initial rate of enzymatic degradation, a biodegradable poly(l-lactide) (PLLA) was modified by the incorporation of small amount of poly(dimethyl siloxane) (PDMS) or fluorocarbons, both of which are hydrophobic and thus inactive to enzymatic degradation. The surface properties of modified PLLAs were investigated by contact angle and x-ray photoelectron spectroscopy (XPS) measurements. From the XPS results, the surface layer of both modified PLLA films was dominated by the modifiers, PDMS and fluorocarbons which have lower surface energies than that of PLLA. The enzymatic degradation was carried out in a 0.1 M potassium phosphate buffer (pH 8.5) in the presence of proteinase K. The results indicate a significant retardation of the initial enzymatic degradation of the modified PLLA films, presumably due to the increased hydrophobicity and decreased enzyme susceptibility of the modified surface layers.

## Shape-Tunable Microwrinkles

Takuya Ohzono<sup>1</sup> and Hirosato Monobe<sup>2</sup>

<sup>1</sup>Nanosystem Research Institute (NRI), AIST, Japan

<sup>2</sup>UBIQEN (Kansai), AIST, Japan

Microwrinkles are mechanically self-organized surface undulations with an intrinsic wavelength, showing various stripe patterns (Figure 1). The average orientation of the stripes is repeatedly altered by changing, for example, the direction of uniaxial compression applied to the sample; thus, the surface is shape-tunable (ref. 1) as is the skins and biological membranes. As one possible application, we use the unique property for shaping and manipulating liquids, because such method are important for micro-patterning, microfluidics and biosensing, and may provide fundamental insights into phenomena in confined small spaces.

Here, we report a simple technique for shaping liquids into micrometer-scale filaments. Microgrooves on microwrinkles can function as open channel capillaries for various liquids with appropriate wettabilities. Tuning the groove depth of the microwrinkles by modulating strain, we explore the capillary action of liquids in microgrooves, which form liquid filaments emanating from a large reservoir (Figure 2, ref. 4). Based on this concept, a

regular array of liquid filaments can be formed over a large area by a simple coating method, and these filaments can be further reshaped by exploiting nonlinear changes in microwrinkle topography (Figure 3, ref. 3). The liquid micropatterns are also used for template for forming Au nanoribbons (ref. 2). This technology shows promise for applications in micro-patterning, nano- and micro-reactors, and microfluidics.

We thank New Energy and Industrial Technology Development Organization (NEDO) of Japan for their supports.

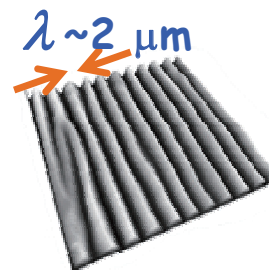


**Figure 1.** AFM image of mechanically self-organized microwrinkles.

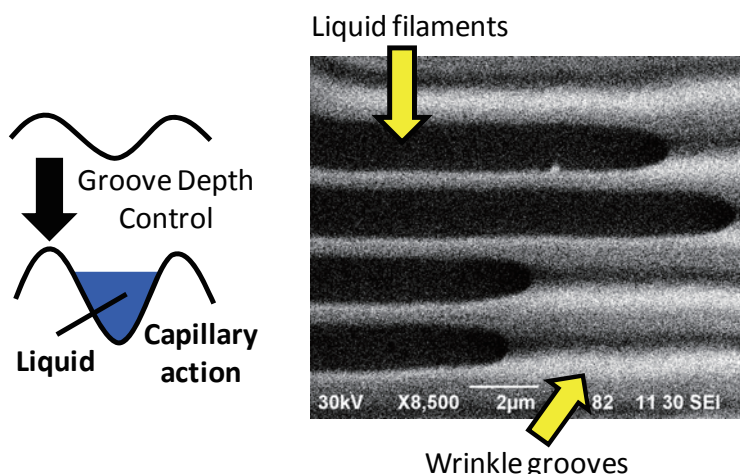


**Figure 2.** Tuning the groove depth of the microwrinkles by modulating strain, we explore the capillary action of various liquids in microgrooves, which form liquid filaments emanating from a large reservoir.

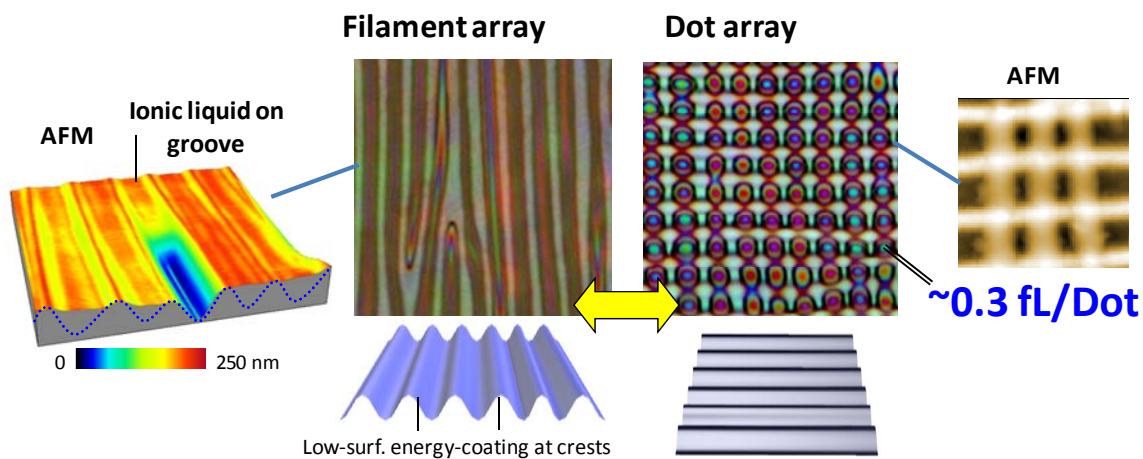


**Figure 3** Using the dynamical and non-linear micro-topological change of microwrinkles, we demonstrate that the morphology of an array of liquid filaments formed on microwrinkle grooves are dramatically and reversibly transformed into a regular array of micro-droplets, “dots”, depending on the predefined contact angle.

### Related Publications

- [1] T. Ohzono, M. Shimomura, *Phys. Rev. B* 69, 132202, 2004.
- [2] T. Ohzono, H. Monobe, *Small*, 7, 506, 2011.
- [3] T. Ohzono, H. Monobe, *Langmuir*, 26, 6127, 2010.
- [4] N. Uchida, T. Ohzono, *Soft Matter*, 6, 5929, 2010.
- [5] T. Ohzono, et al., *Soft Matter*, 5, 4658, 2009.
- [6] T. Ohzono, et al., *Applied Physics Letters*, 95, 014101, 2009.
- [7] T. Ohzono, *Chaos*, 19, 033104, 2009.

## Collection of Single Cell from Carbon Nanotube-Coated Substrate by Photo-irradiation

Tsuyohiko Fujigaya<sup>1,2</sup>, Takao Sada<sup>1</sup>, Naotoshi Nakashima<sup>1,2,3</sup>

<sup>1</sup>Department of Applied Chemistry, Graduate School of Engineering, Kyushu University, Fukuoka 819-0395, Japan

<sup>2</sup>WPI-I<sup>2</sup>CNER, Kyushu University, Fukuoka 819-0395, Japan

<sup>3</sup>JST-CREST, Tokyo, 102-0075, Japan

Single-walled carbon nanotubes (SWNTs) are nanomaterials that possess remarkable electrical, mechanical, and thermal properties and have been explored for biological applications. One of the applications of SWNTs in biology is the cell culture substrate, where the unique one-dimensional high aspect structure and hydrophobic nature of SWNTs gave better substrate to culture the cells.[1] In addition, SWNTs have unique near-IR (NIR) responsive properties such as strong photoabsorption, photothermal conversion and photoacoustic generation. In this report, we describe development and application of photo responsive SWNT substrate for the cell collection and the cell patterning. These techniques is of interest especially for basic study of cells, stem cell research, organ culture, or tissue engineering.

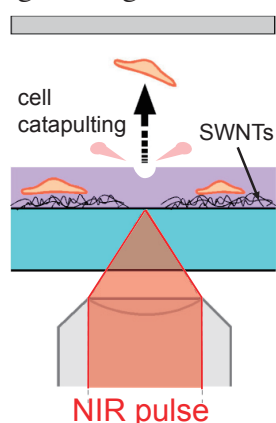


Fig. 1. Mechanism of the cell collection upon NIR irradiation.

We have developed SWNT-coated cell culture substrate, which enables a single cell collection by irradiating a near-IR laser pulse (1064 nm) to the cell of interest (Fig. 1). The mechanism of the cell collection is the shock wave generation triggered by the photoacoustic effect of the irradiated SWNTs. The captured cells showed the red fluorescent, which clearly indicate the cell membrane of the removed cells was disturbed.

As a functional analysis for the catapulted single cell, we carried out an RNA analysis using the real-time reverse transcription polymerase chain reaction (RT-PCR) technique. We observed an increase in the fluorescent intensity corresponding to the gene amplification which is extracted from the collected single cell (Fig. 2, solid line). Based on the control experiment carried out in the absence of the catapulted cell that shows a very weak fluorescent (Fig. 2, dotted line), it is obvious that the signal originated from the genetic information of the catapulted single cell and the catapulted cell retains the genetic information. It is worth emphasizing that a functional analysis using the captured single cell is possible [2].

We have developed SWNT-coated cell culture substrate, which enables a single cell collection by irradiating a near-IR laser pulse (1064 nm) to the cell of interest (Fig. 1). The mechanism of the cell collection is the shock wave generation triggered by the photoacoustic effect of the irradiated SWNTs. The captured cells showed the red fluorescent, which clearly indicate the cell membrane of the removed cells was disturbed.

As a functional analysis for the catapulted single cell, we carried out an RNA analysis using the

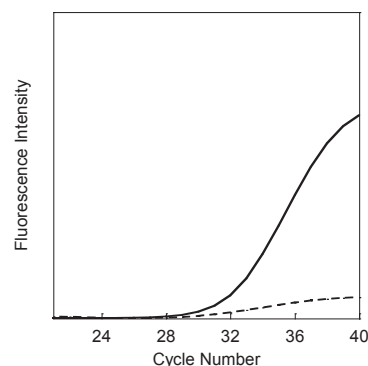


Fig. 2. Monitoring the fluorescence on the PCR cycles in the presence (solid line) and absence (black line) of the catapulted cell.

[1] N. Aoki, T. Akasaka, F. Watari and A. Yokoyama, *Dent. Mater. J.* **2007**, 26, 178.

[2] T. Sada, T. Fujigaya, Y. Niidome, K. Nakazawa and N. Nakashima, *ACS Nano*, **2011**, 5, 4414.

## Organic Ferromagnetic Materials Design with High-spin Stability Index by Quantum Chemical Approach

Xun Zhu<sup>1</sup>, Feng Long Gu<sup>3,4</sup>, and Yuriko Aoki<sup>2,4</sup>

<sup>1</sup>Department of Molecular and Material Sciences, Interdisciplinary Graduate School of Engineering Sciences, Kyushu University, 6-1 Kasuga-Park, Fukuoka 816-8580, Japan

<sup>2</sup>Department of Material Sciences, Faculty of Engineering Sciences, Kyushu University, 6-1 Kasuga-Park, Fukuoka 816-8580, Japan

<sup>3</sup>Center for Computational Quantum Chemistry, South China Normal University, Guangzhou 510631 China

<sup>4</sup>Japan Science and Technology Agency, CREST, 4-1-8 Hon-chou, Kawaguchi, Saitama 332-0012, Japan

### 1. Introduction

Organic ferromagnets have attracted much attention during the last several decades as their possible properties such as low density and good solubility. However, direct calculation for such high-spin systems becomes difficult because of the big size of the molecule. Linear scaling *ab initio* approaches are required for efficient electronic states calculations of large systems. The elongation method [1] developed in our group is designed for large systems and is analogous to the real synthesis of polymers. This treatment [2] now is applicable for theoretical prediction of their ferromagnetism. Our high-spin index  $L_{ij}^{\min}$  ( $L_{\min}$ ) [3], an index used to represent the magnitude of non-disjoint quality and high-spin stability, is incorporated into open-shell elongation method and then it's applied to ferromagnetic material design.

### 2. Method

#### 2.1. Open-shell elongation method

The open-shell calculation of elongation method is implemented in the same way as that in closed-shell elongation method. Suppose that each unit has an unpaired electron with up-spin during the calculation and the size of starting cluster ( $N_{st}$ ) is two units. In the beginning, the eigenvalue problem of A+B part with triplet states is solved with conventional method to initiate the elongation method. After that, a localization method is applied to the molecular orbitals (MOs) of A+B part, which is then localized into two different sets of MOs. One is mainly localized on A part including a lone pair electron, and the other is mainly localized on B part including another lone pair electron. In the next step, the A part is frozen and only B part is taken into account with the attacking monomer C part with a lone pair electron, as shown in Figure 1. After solving the eigenvalue problem of B+C with triplet state, the MOs of B+C are localized again in a similar way as those in A+B, and then new attacking monomer approaches one by one to the chain. In such a way, we treat the interaction as triplet state by solving the constant size Fock matrix based on the RLMO. This treatment is repeated until the size of the chain reaches our desired length and finally the obtained chain has the highest spin state.

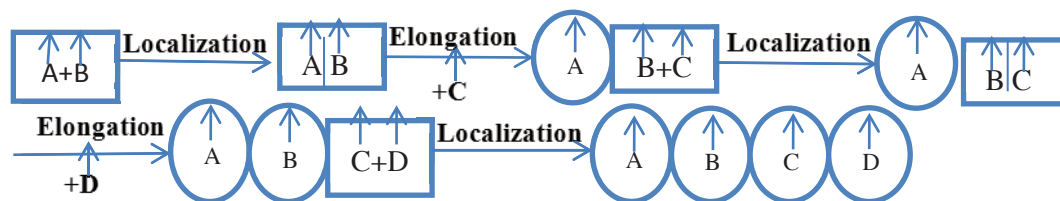


Figure 1. Schematic flow chart of the open-shell elongation method, where up-arrows are up-spin.

#### 2.2. High-spin stability index $L_{\min}$

##### (1) Method to evaluate $L_{\min}$

Given two sets of NBMOs,

$$\psi_i = \sum_r C_{ir} \chi_r, \psi_j = \sum_r C_{jr} \chi_r \quad (1)$$

$$L_{ij} = \sum_r (C_{ir} C_{jr})^2 \quad (2)$$

can be defined as the mixing between NBMOs, where  $C_{ir}$  is the coefficient of  $r$ -th atomic orbital (AO) in the  $i$ -th NBMO[3].

The smallest  $L_{ij}$  value, i.e., the  $L_{ij}^{\min}$  value after the unitary transformation must correspond to exchange integrals between  $i$ -th and  $j$ -th NBMOs, e.g., in the case of combination of two allyl radicals as shown in Figure 2. In general, we can change the MO coefficients of degenerate NBMOs by using a unitary transformation.

$$\begin{pmatrix} \psi'_i \\ \psi'_j \end{pmatrix} = \begin{pmatrix} \sin \theta & \cos \theta \\ -\cos \theta & \sin \theta \end{pmatrix} \begin{pmatrix} \psi_i \\ \psi_j \end{pmatrix}, \quad (3)$$

where

$$\psi'_i = \sum_r C'_{ir} \chi_r, \quad \psi'_j = \sum_r C'_{jr} \chi_r. \quad (4)$$

Then we use the new coefficients to calculate  $L_{\min}$  as

$$L_{\min} = \sum_{i=1}^N \sum_{j>i}^N \sum_r (C'_{ir} C'_{jr})^2, \quad (5)$$

and repeat the above procedure in iterative way until convergence criterion is fulfilled. The stability of the triplet state of “non-disjoint” type systems can be predicted by the index  $L_{\min}$  by which main part of exchange integrals can be expressed.

## (2) Analytical prediction (AP) method

We can define  $L_{AP}$  searching analytically for  $L_{\min}$  [4] as

$$L_{AP} = \sum_{j=1}^N \sum_{k>j}^N \sum_r (c_{jr})^2 (c_{kr})^2 = \sum_{j=1}^N \sum_{k>j}^N \sum_r (n_{jr} c_j)^2 (n_{kr} c_k)^2 = \sum_{j=1}^N \sum_{k>j}^N n_{jk} c_j^2 c_k^2, \quad (6)$$

where  $c_j$  and  $c_k$  are the coefficients of  $j$ -th NBMO and  $k$ -th NBMO, respectively,  $n_{jk}$  is the number of  $c_j^2 c_k^2$ ,  $N$  is the number of unpaired electrons of the system. Using “zero sum rule” and normalization condition to get  $c_j^2$  and  $c_k^2$ ,  $L_{AP}$  can be calculated for non-disjoint closed-type,

$$L_{AP} = \sum_{j=1}^N \sum_{k>j}^N n_{jk} c_j^2 c_k^2 = aN + b, \quad (7)$$

where  $a$  and  $b$  are undetermined coefficients.

## 3. Results and discussion

The relationship between  $L_{\min}$  and  $\Delta E(L-H)$  is investigated for the following six models.

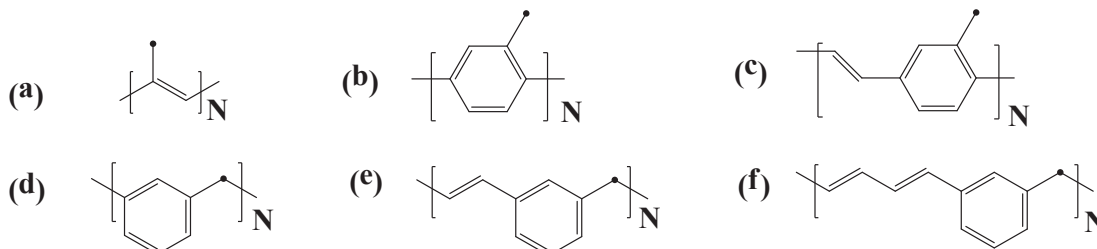


Figure 3. Models used for calculation of  $L_{\min}$

(1) First, the open-shell elongation method has been tested on the model (b) (see Figure 3) at the level of ROHF/STO-3G. The total energy errors between elongation method and conventional method are  $\sim 10^{-8}$  a.u. and the values of  $L_{\min}$  calculated from elongation method

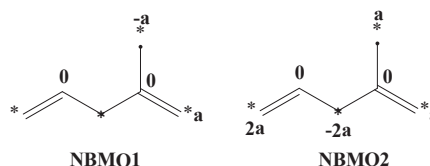


Figure 2. Two NBMOs of allyl radical

and conventional method are same as shown in Figure 4(a) and 4(b), respectively. Therefore, the validity of the open-shell elongation method at this level is confirmed.

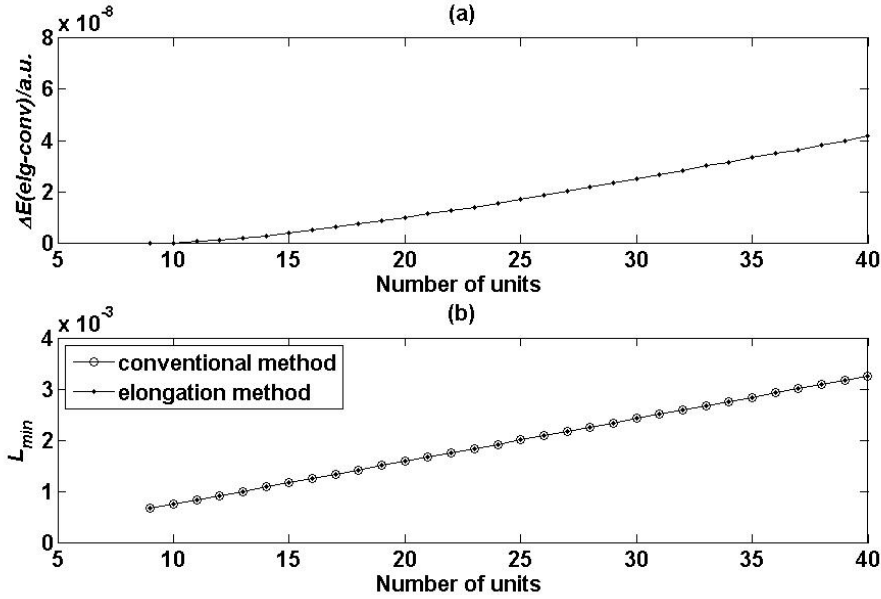


Figure 4. (a) Total energy difference between elongation method and conventional method (b)  $L_{\min}$  of elongation method and conventional method. (a) and (b) are calculated for model (b) at the level of ROHF/STO-3G,  $N_{\text{st}} = 9$ .

(2) Next,  $L_{AP}$  was derived for the six models given in Figure 3 as the following equations.

$$L_{AP}(a) = \frac{1}{2} \sum_{j=1}^N \sum_{k>j}^N \frac{\sum_{i=0}^{j-1} 16^i}{\sum_{i=0}^{j-1} 4^i \sum_{i=0}^{k-1} 4^i} \quad (N=2,3,\dots) \quad (8)$$

$$L_{AP}(b) = 3 \sum_{j=1}^N \sum_{k>j}^N \frac{\sum_{i=0}^{j-1} 16^i}{(3 \sum_{i=0}^{j-1} 4^i + 4^j)(3 \sum_{i=0}^{k-1} 4^i + 4^k)} \quad (N=2,3,\dots) \quad (9)$$

$$L_{AP}(c) = \sum_{j=1}^N \sum_{k>j}^N \frac{4 \sum_{i=0}^{j-1} 16^i - 1}{49 \sum_{i=0}^{j-1} 4^i \sum_{i=0}^{k-1} 4^i} \quad (N=2,3,\dots) \quad (10)$$

$$L_{AP}(d) = \frac{3}{100} N - \frac{3}{175} \quad (N=2,3,\dots) \quad (11)$$

$$L_{AP}(e) = \frac{3}{196} N \quad (N=2,3,\dots) \quad (12)$$

$$L_{AP}(f) = \frac{1}{108} N + \frac{1}{189} \quad (N=2,3,\dots) \quad (13)$$

On the other hand,  $L_{\min}$  values were also calculated by Hückel method, ROHF/PM3, and ROB3LYP/3-21G methods as shown in Table 1. The values of  $L_{\min}$  obtained for  $N = 6$  are



very close to those calculated at Hückel level for the models.  $L_{\min} > 0 \Rightarrow \Delta E(L-H) > 0$  for all models, where  $\Delta E(L-H)$  is the energy difference between the lowest spin state and highest spin state, i.e.  $\Delta E(L-H) = E(L) - E(H)$ .

Models	Lmin				$\Delta E(L-H)/\text{a.u.}$
	$L_{\text{AP}}$	Hückel	ROHF/PM3	ROB3LYP/3-21G	
(a)	0.5083	0.4822	0.00667	0.03680	0.038
(b)	0.0802	0.0783	0.00043	0.00203	0.096
(c)	0.0773	0.0745	0.00005	0.00049	0.147
(d)	0.1629	0.1651	0.01120	0.01950	0.109
(e)	0.0918	0.0925	0.00133	0.00662	0.103
(f)	0.0608	0.0611	0.00017	0.00261	0.101

Table 1.  $L_{\text{AP}}$  is calculated with AP method, other values of  $L_{\min}$  are calculated by combined methods shown in 2.2 with Hückel method and elongation method at the levels of ROHF/PM3 and ROB3LYP/3-21G at  $N = 6$  from starting cluster,  $N_{\text{st}} = 4$ .  $\Delta E(L-H)$  is calculated at the ROB3LYP/3-21G level with conventional method.

When systems enlarge,  $c_j^2$  and  $L_{\min}$  decrease. For closed-type systems, the number of overlap between each pair of  $L_{ij}^{\min}$  ( $j>i$ ) is same, the longer the distance between spin-containing sites, the smaller the exchange interaction between them, which leads to smaller  $\Delta E$ . For open-type systems, the number of overlap between each pair of  $L_{ij}^{\min}$  ( $j>i$ ) increases, thus the exchange interaction between spin-containing sites increases, which leads to bigger  $\Delta E$ .

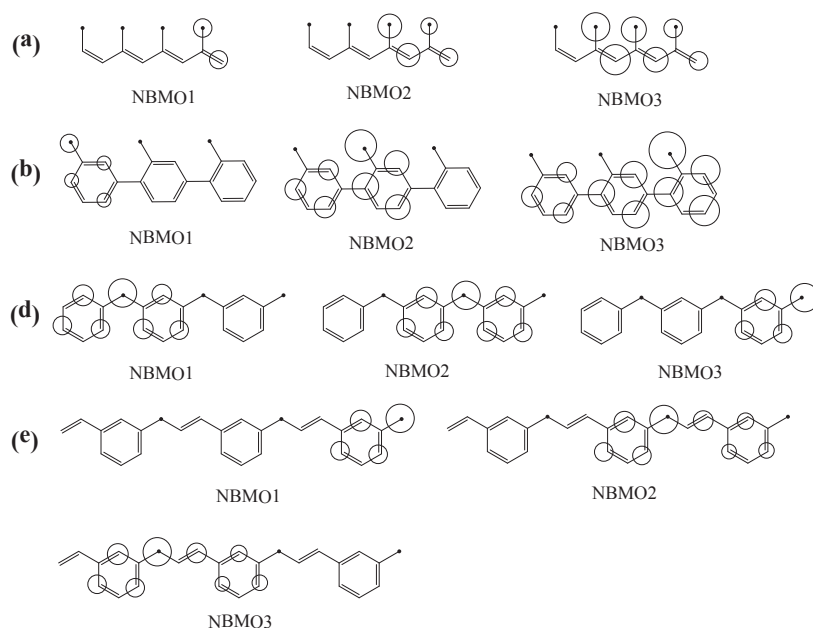


Figure 4. NBMOs of models (a), (b), (d) and (e)

- [1] A. Imamura, Y. Aoki, K. Maekawa, *J. Chem. Phys.*, **95**, 5419 (1991).  
 [2] Y. Aoki, *et al.*, *Computational Methods in Science and Engineering*, **963**, 120 (2007).  
 [3] Y. Aoki, A. Imamura, *Int. J. Quant. Chem.*, **74**, 491 (1999).  
 [4] Y. Orimoto, Y. Aoki, *J. Chem. Theory Comput.*, **2**, 786 (2006).

## Nitrogen-doped graphene synthesized by solvothermal chemistry

Stephen M. Lyth<sup>1</sup>, Yuta Nabae<sup>2</sup>, Nazrul Islam<sup>2</sup>, Terauki Hayakawa<sup>2</sup>, Shigeki Kuroki<sup>2</sup>,  
Masa-aki Kakimoto<sup>2</sup>, Seizo Miyata<sup>2</sup>

<sup>1</sup>International Institute for Carbon-Neutral Energy Research, Kyushu University, Japan

<sup>2</sup>Department of Organic and Polymeric Materials, Tokyo Institute of Technology, Japan

Graphene has recently taken the scientific world by storm. It is an atomic layer of carbon, peeled from graphite using sticky tape in 2004, leading a Nobel Prize in 2010 [1]. It has a dazzling array of properties, including high strength, surface area, flexibility and conductivity. Graphene sheets up to 70 cm in size have been fabricated [2]. Potential applications include solar cells, sensors, transistors, displays, touch-screens, and energy storage devices.

It is crucial to be able to tailor the properties of graphene. One method is to include heteroatoms such as nitrogen in the structure (Fig. 1a). Nitrogen inclusion has been predicted to induce spin polarization, negative differential resistance, ferromagnetism, semiconductor behavior, enhanced gas adsorption, and to increased conductivity. Nitrogen-containing graphene has been synthesized by various methods [3], including reduction of graphene oxide, arc discharge in ammonia, chemical vapor deposition in ammonia, and N<sub>2</sub> plasma irradiation.

Here, we present a novel method of producing nitrogen-doped graphene by solvothermal reaction between sodium and ethanolamine, followed by flash pyrolysis in air. Fig. 1b shows transmission electron microscopy (TEM) of the resulting macroporous foam-like graphene. The nitrogen content was measured by CHN elemental analysis to be ~15 wt.%, and was readily tailored by pyrolysis. X-ray photoelectron spectroscopy showed mainly pyridinic and quaternary nitrogen bonding, suggesting inclusion both the edges and in the basal-plane. Atomic force microscopy reveals a thickness of 1.7 nm, corresponding to bilayer graphene, or functionalized single-layer graphene. The surface area measured by BET nitrogen adsorption was up to 170 m<sup>2</sup>/g. The electrochemical oxygen reduction activity current density was high, despite this being a metal-free catalyst system, showing great promise for use in fuel cells.

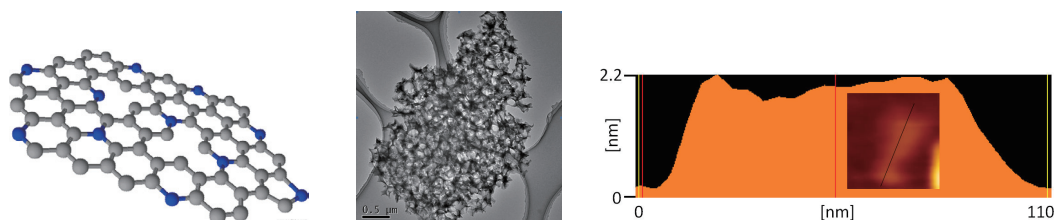


Figure 1. Structure (carbon/grey, nitrogen/blue), TEM, and AFM of nitrogen-containing graphene.

[1] K. S. Novoselov, A. K. Geim, et al. *Science*, **306**, 666 (2004)

[2] S. Bae, H. Kim, Y. Lee, X. Xu, et al., *Nature Nanotechnology*, **5**, 574 (2010)

[3] X. Li, H. Wang, J. Robinson et al, *J. of the American Chemical Society*, **131**, 15939 (2009)

## Development of Elongation Geometry Optimization Method

Liu Kai<sup>1</sup>, Feng Long Gu<sup>2,3</sup>, and Yuriko Aoki<sup>3,4</sup>

<sup>1</sup>Department of Molecular and Material Sciences, Interdisciplinary Graduate School of Engineering Sciences, Kyushu University, 6-1 Kasuga-Park, Fukuoka 816-8580, Japan

<sup>2</sup>Center for Computational Quantum Chemistry, South China Normal University, Guangzhou 510631, China

<sup>3</sup>Department of Material Sciences, Faculty of Engineering Sciences, Kyushu University, 6-1 Kasuga-Park, Fukuoka 816-8580, Japan

<sup>4</sup>Japan Science and Technology Agency, CREST, 4-1-8 Hon-chou, Kawaguchi, Saitama 332-0012, Japan

### 1. Introduction

Since Kohn and Pople won the Nobel prize in 1998 [1], computational chemistry became a more and more powerful method to understand, design and control the properties of materials [2]. As the computer science development, it's possible and convenient for us to predict and design novel functional materials by variety of chemical software, like: Gaussian [3], Gamess [4], ADF [5], and so on. Unfortunately, theoretical chemistry describes the chemical structures and properties at the level of atom and molecular of first principle, whereas functional materials are always in bulk state. It's too expensive to calculate the properties of materials by first principle. Nowadays, many famous methods, such as Divide and conquer [6], fragment molecular orbital [7] and local space approximation [8], have been proposed to demonstrate the electronic structure of materials with high accuracy and efficiency. Elongation method [9], originally proposed by Imamura in the early 1990s for quasi-one dimension polymers, is also a kind of linear scaling approach with high accuracy and efficiency to calculate the electronic states. Currently elongation method has been implemented into Gamess software, and can be employed to predict novel molecular properties both by *ab initio* and DFT method. Here we extend the elongation method to be available for molecular geometry optimization.

### 2. Method and result

Elongation method is solving the Fock equation at region local molecular orbital (RLMO) basis instead of conventional canonical molecular orbital (CMO) basis [10]. Therefore, the gradient calculation of geometry optimization is a bit different from conventional method (Eq. 1). The derivative of the total energy (E) dependences on the nuclear coordinate  $X_A$ , can be written as:

$$\frac{\partial E}{\partial X_A} = \sum_{\mu\nu} \mathbf{D}_{\nu\mu} \frac{\partial \mathbf{H}_{\mu\nu}^{\text{core}}}{\partial X_A} + \frac{1}{2} \sum_{\mu\nu\lambda\sigma} \mathbf{D}_{\nu\mu} \mathbf{D}_{\lambda\sigma} \frac{\partial (\mu\nu|\lambda\sigma)}{\partial X_A} + \frac{\partial V_{\text{NN}}}{\partial X_A} - \sum_{\mu\nu} \mathbf{Q}_{\nu\mu} \frac{\partial \mathbf{S}_{\mu\nu}}{\partial X_A} \quad (1)$$

where  $\mathbf{D}$  is the density matrix,  $\mathbf{H}$  and  $\mathbf{S}$  means the Hamiltonian and overlap of system,

respectively. The nuclear-nuclear repulsion is defined by  $V$ . The  $Q$  matrix of conventional method is defined as:

$$Q_{\nu\mu} = \sum_i n_i \varepsilon_i C_{\mu i} C_{\nu i} \quad (2)$$

Whereas, during SCF iteration, elongation method only calculates the activate region, important part of local orbital. Therefore, the  $Q$  matrix is rewritten as:

$$Q_{\nu\mu} = \sum_{i,j} n_i C_{\nu i}^{SCF} \varepsilon_{ij} C_{\mu j}^{SCF} \quad (3)$$

Some model systems have been optimized by elongation method compared to conventional results. As shown in Fig. 1, the difference of bond length of linear  $(HF)_{n=20}$  system is about  $10^{-4}$  of magnitude, and 6-31G could not represent accurate intermolecular hydrogen bond.

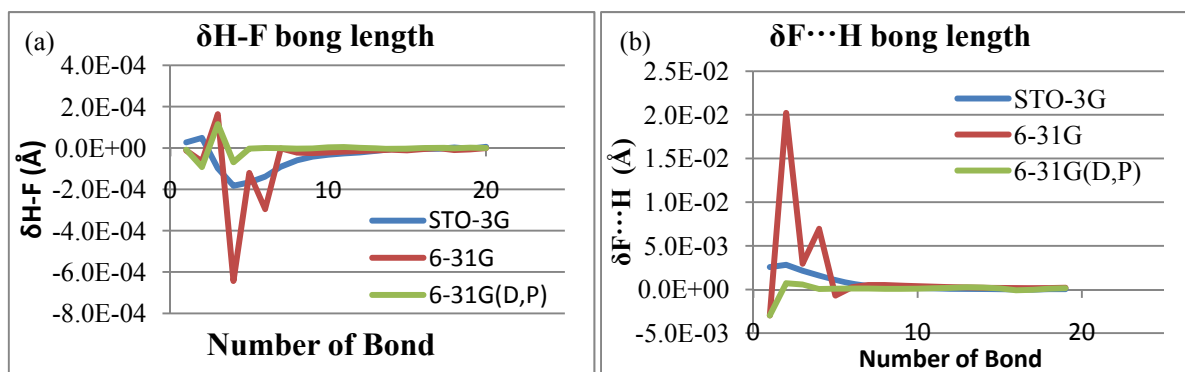


Fig. 1 The difference of bond length  $R_{H-F}$  (a) and hydrogen bond  $R_{F...H}$  (b) of  $(HF)_{n=20}$  between elongation and conventional methods at STO-3G, 6-31G and 6-31G(D,P) basis sets.

For bonding model system, planar polyacetylene is also optimized at STO-3G. The difference in bond length and bond angle between the two methods has been shown in Fig. 2.

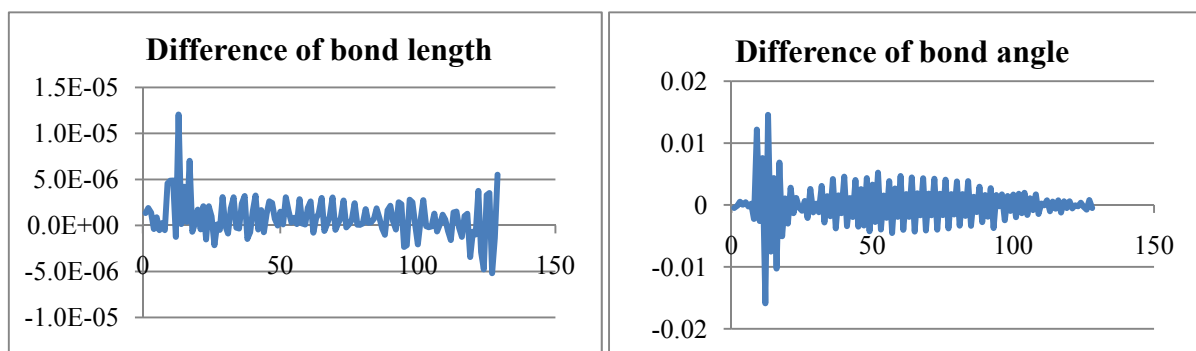


Fig.2 The difference of bond length and bond angle of polyacetylene at STO-3G basis set.

Finally, a kind of ATPase (PDB code: 2kz9) has been optimized at STO-3G basis set by elongation geometry optimization method. As shown in Fig 3, elongation optimization structure (blue one) was well matched to that by conventional optimization structure (red one) and the root mean square deviations between them was found to be 0.11.

### 3. Conclusion

Elongation geometry optimization has been implemented into Gamess software. Compared with conventional method, it has successfully located the equilibrium structures of model system with small error. The following work is to optimize three dimensions systems and improve its efficiency for general use.

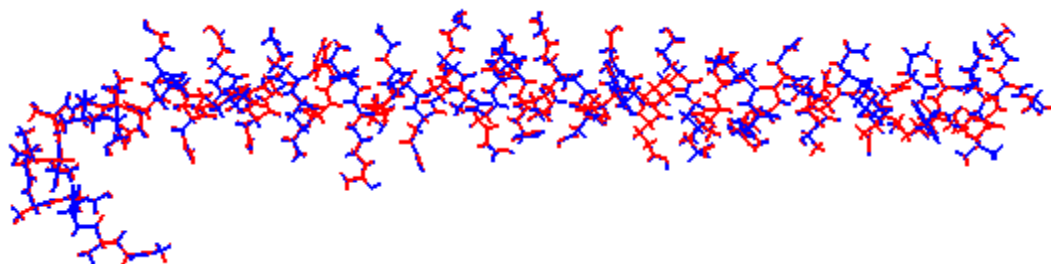


Fig.3 Optimized structures by conventional method (red) and elongation method (blue).

#### 4. References

- [1] [http://nobelprize.org/nobel\\_prizes/chemistry/laureates/1998/](http://nobelprize.org/nobel_prizes/chemistry/laureates/1998/)
- [2] E. A. Carter, P. J. Rossky, *Acc. Chem. Res.*, **39**, 71(2006).
- [3] Gaussian 03, Revision B.05, M. J. Frisch, G. W. Trucks, H. B. Schlegel, G. E. Scuseria, M. A. Robb, J. R. Cheeseman, J. A. Montgomery, Jr., T. Vreven, K. N. Kudin, J. C. Burant, J. M. Millam, S. S. Iyengar, J. Tomasi, V. Barone, B. Mennucci, M. Cossi, G. Scalmani, N. Rega, G. A. Petersson, H. Nakatsuji, M. Hada, M. Ehara, K. Toyota, R. Fukuda, J. Hasegawa, M. Ishida, T. Nakajima, Y. Honda, O. Kitao, H. Nakai, M. Klene, X. Li, J. E. Knox, H. P. Hratchian, J. B. Cross, C. Adamo, J. Jaramillo, R. Gomperts, R. E. Stratmann, O. Yazyev, A. J. Austin, R. Cammi, C. Pomelli, J. W. Ochterski, P. Y. Ayala, K. Morokuma, G. A. Voth, P. Salvador, J. J. Dannenberg, V. G. Zakrzewski, S. Dapprich, A. D. Daniels, M. C. Strain, O. Farkas, D. K. Malick, A. D. Rabuck, K. Raghavachari, J. B. Foresman, J. V. Ortiz, Q. Cui, A. G. Baboul, S. Clifford, J. Cioslowski, B. B. Stefanov, G. Liu, A. Liashenko, P. Piskorz, I. Komaromi, R. L. Martin, D. J. Fox, T. Keith, M. A. Al-Laham, C. Y. Peng, A. Nanayakkara, M. Challacombe, P. M. W. Gill, B. Johnson, W. Chen, M. W. Wong, C. Gonzalez, and J. A. Pople, Gaussian, Inc., Pittsburgh PA, 2003.
- [4] M.W.Schmidt, K.K.Baldrige, J.A.Boatz, S.T.Elbert, M.S.Gordon, J.H.Jensen, S.Koseki, N.Matsunaga, K.A.Nguyen, S.Su, T.L.Windus, M.Dupuis, J.A.Montgomery, *J. Comput. Chem.*, **14**, 1347 (1993).
- [5] G. te Velde, F.M. Bickelhaupt, E.J. Baerends, C. Fonseca Guerra, S.J.A. van Gisbergen, J.G. Snijders, T. Ziegler, *J. Comput. Chem.*, **22**, 931 (2001).
- [6] W. T. Yang, *Phys. Rev. Lett.*, **66**, 1438(1991).
- [7] K. Kitaura, E. Ikeo, T. Asada, T. Nakano, M. Uebayasi, *Chem. Phys. Lett.*, **313**, 701(1999).
- [8] B. Kirtman, C. P. de Melo, *J. Chem. Phys.*, **75**, 4592 (1981).
- [9] A. Imamura, Y. Aoki, K. Maekawa, *J. Chem. Phys.*, **95**, 5419 (1991).
- [10] F. L. Gu, Y. Aoki, J. Korchowiec, A. Imamura, B. Kirtman. *J. Chem. Phys.*, **121**, 10385 (2004).

**MOLECULAR DESIGN FOR DONOR-NANOWIRE-ACCEPTOR  
PHOTOELECTRIC CONVERSION MATERIALS  
BY USING ELONGATION METHOD**

Huaqing Yang<sup>1</sup>, Oleksandr Lododa<sup>2</sup>, Feng Long Gu<sup>3,4</sup>, and Yuriko Aoki<sup>2,4</sup>

<sup>1</sup>Department of Molecular and Material Sciences, Interdisciplinary Graduate School of  
Engineering Sciences, Kyushu University, Japan

<sup>2</sup>Department of Molecular and Material Sciences, Interdisciplinary Graduate School of  
Engineering Sciences, Kyushu University, Japan

<sup>3</sup>Center for Computational Quantum Chemistry, South China Normal University, Guangzhou,  
510631, China

<sup>4</sup>Japan Science and Technology Agency, CREST, 4-1-8 Hon-chou, Kawaguchi, Saitama  
332-0012, Japan

In last decade, more and more conjugated fullerene-oligothiophene-porphyrin linked triads have been investigated [for example, refs.1-2]. Now it is widely applied to photovoltaic cells, nonlinear optical, electronic conductor, and so on. I introduce a new method of molecular design, namely, elongation method that proposed by Prof Imamura [ref.3] and hereafter developed in our laboratory for 20 years [for example, refs.4-6]. It is considered to be a feasible and an efficient approach to compute electronic states of large polymer system at Hartree-Fock and post Hartree-Fock levels. It is being developed to compute three-dimensional periodic and nonperiodic systems. The efficiency and accuracy is very high, even for the systems with strongly delocalized  $\pi$  electrons. The aim of this abstract is to apply this method to design a Donor-Nanowire-Acceptor linked triads. to be more specific, namely, (C<sub>60</sub>)-oligo(3-ethyl-2,5-thienylene-ethylne)(OTE)-tetraphenylporphyrin(TPP).

## 1. Method

The basic principle of this method and the advantage of this treatment are shown in Figures 1 and 2. The principle of elongation method is: first a starting cluster is chosen. It is divided into two parts, namely A part and B part. After localization, A part is frozen, and a monomer C will attack the B part, and then localization again. After several repetitions, we can get the required elongated system. The advantage of this treatment is that we only calculate the parts located on both sides, while the centered will be saved after elongation calculation as shown in Figure 2. So compared with conventional calculation, it will save much time by using this method.

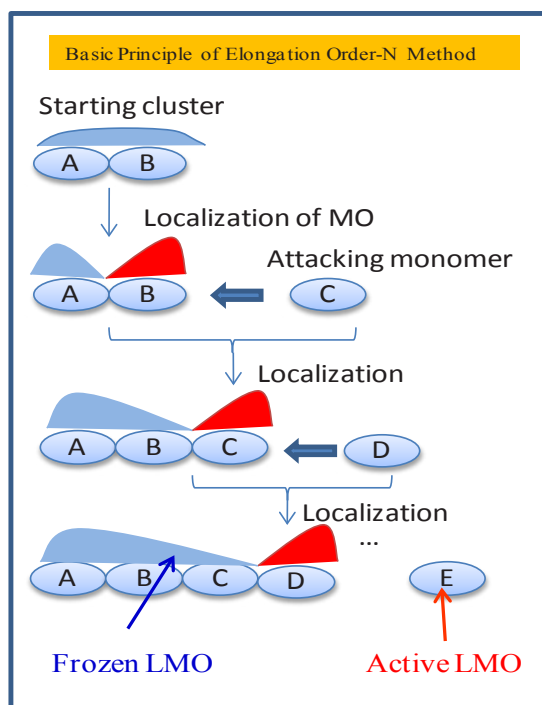


Figure 1

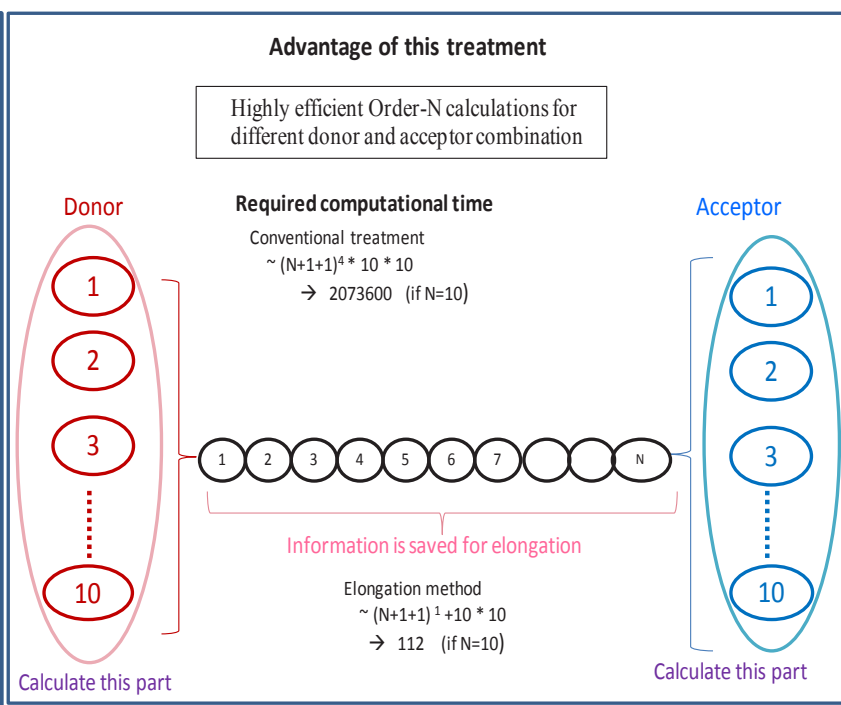


Figure 2

The model adopted here is shown in Figure 3, where the role of TPP is donor and C60 is acceptor. The charge transfer will be expected from TPP to C60 through OTE. The elongation process is described in Figure 4.

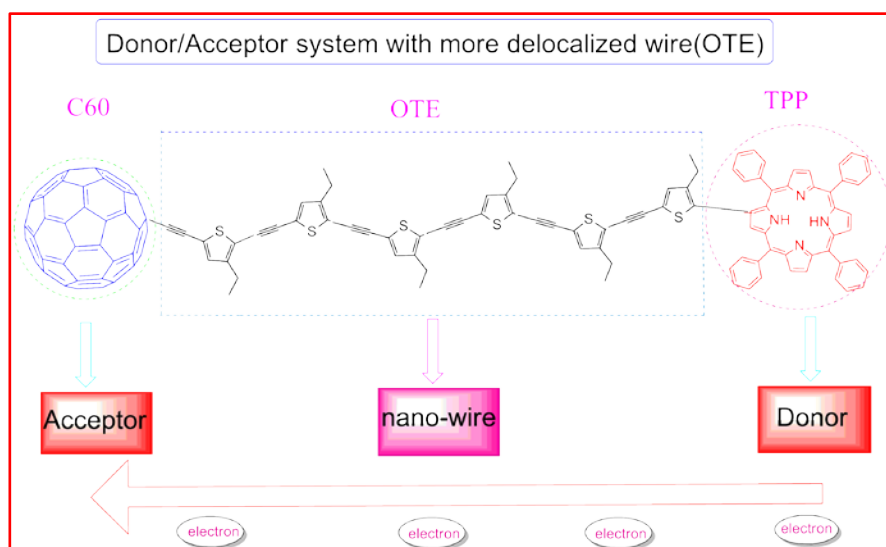


Figure 3

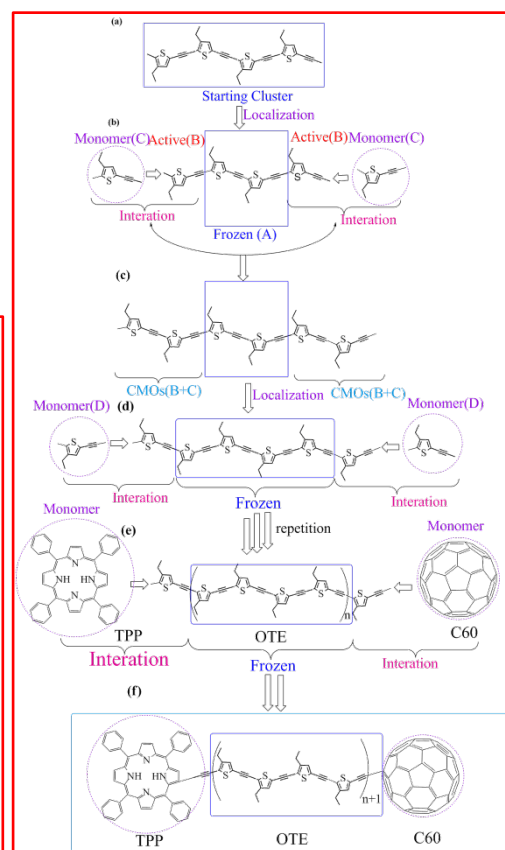


Figure 4

## 2. Results

The total energy and energy difference between conventional and elongation calculations are shown in Table 1 where energy errors  $\Delta E/\text{atom}$  is shown as  $\sim 10^{-8}$  a.u./atom, very high

accuracy even for such delocalized systems. We investigate now the relationship between donor and acceptor species and their electronic structures by orbital interaction analysis for designing highly efficient photoelectric conversion materials.

Table 1. Total energies and energy differences between elongation and conventional calculations.

step	Conventional(a.u)	Elongation(a.u)	$\Delta E^{(elg)} - \Delta E^{(cnv)}$ (a.u)	$\Delta E/atom$ (a.u)
1	-2709.83053845	-2709.830538454	0	0
2	-4101.56739654	-4101.567395539	1.00210E-06	1.11344E-08
3	-5493.30422752	-5493.304224101	3.42360E-06	2.85300E-08
4	-6885.04108746	-6885.041080727	6.73130E-06	4.48753E-08
5	-8276.77791481	-8276.777904278	1.05366E-05	5.85367E-08
6	-9668.51480107	-9668.514786489	1.45857E-05	6.94557E-08
7	-11060.2517615	-11060.25174273	1.87756E-05	7.82317E-08
8	-12451.9894943	-12451.98947122	2.30549E-05	8.53885E-08
9	-13843.7317328	-13843.73170509	2.76985E-05	9.23283E-08
10	-17964.8300848	-17964.83006068	2.41334E-05	5.53518E-08

#### Reference:

- [1] J.Ikemoto, K.Takimiya, Y.Aso, T.Otsubo, M.Fujitsuka and O.Ito, *Organic Letters*, **4**,3(2002)
- [2] T.Nakamura, M.Fujitsuka, Y.Araki, O.Ito, J.Ikemoto, K.Takimiya, Y.Aso and T.Otsubo, *J. Phys. Chem.B.*, **108**, 10700 (2004).
- [3] A.Imamura, Y.Aoki and K.Maekawa, *J.Chem.Phys.*, **95**, 5419 (1991).
- [4] F.L.Gu, Y.Aoki, J.Korchowiec, A.Imamura and B.Kirtman, *J.Chem.Phys.*, **121**, 10385(2004)
- [5] J.Korchowiec, F.L.Gu, A.Imamura, B.Kirtman and Y.Aoki, *Int.J.Quantum Chem.Phys.*, **102**, 785 (2005).
- [6] F.L.Gu, B.Kirtman and Y.Aoki, *Challenges and Advances in Computational Chemistry and physics.*, **13**,175(2011)



## Solvent Swelling Induced Self-assembly of Silicon-containing Block Copolymers

Ting-Ya Lo<sup>1</sup>, Chia-Cheng Chao, Rong-Ming Ho<sup>1</sup>

<sup>1</sup>Department of Chemical Engineering, National Tsing-Hua University, Hsinchu 30013,  
Taiwan

Block copolymers (BCPs) can self-assemble into a variety of ordered nanostructures through microphase separation for BCPs with different volume fractions. To acquire a variety of nanostructure would require the synthesis of a series of BCPs with different volume fractions. In this study, a simple method to create various nanostructures resulting from the self-assembly of one-composition block copolymer (BCP) was developed. By using selective solvents for PS-PDMS self-assembly, the phase behavior of intrinsic BCP system can be enriched due to the variation in constituted fraction through preferential swelling the microdomain by selective solvent. Most interestingly, the equilibrium phase of PS-PDMS/solvent mixtures can be successfully preserved after solvent evaporation. We speculate that the preservation is attributed to the high segregation strength of PS-PDMS. In contrast to the intrinsic phase of BCP (that is lamellae phase), these kinetically trapped phases are classified as metastable phases. Also, stable lamellae phase can be reformed by thermal annealing those metastable phases, further demonstrating the feasibility to control the metastability of the microphase-separated morphologies.

## Three-dimensional observation of micro-phase separated structure in 3D confinement

Takeshi Higuchi<sup>1</sup>, Hiroshi Yabu<sup>2,3</sup>, Masatsugu Shimomura<sup>2,4</sup>, Hiroshi Jinnai<sup>1,4,5</sup>

<sup>1</sup>Institute for Materials Chemistry and Engineering, Kyushu University, Japan

<sup>2</sup>Institute of Multidisciplinary Research for Advanced Materials, Tohoku University, Japan

<sup>3</sup>Precursory Research for Embryonic Science and Technology (PRESTO), Japan Science and Technology Agency (JST), Japan

<sup>4</sup>WPI Research Center: Advanced Institute for Materials Research (WPI-AIMR), Tohoku University, Japan

<sup>5</sup>Exploratory Research for Advanced Technology (ERATO), JST, Japan

Block copolymers have been received much attention for novel building blocks to fabricate nano-scale structures because they form various kinds of micro-phase separation structures (e.g., cylindrical, lamellar, bicontinuous, and others) depending on their segment ratios and molecular weights. The micro-phase separation structures have been investigated in bulk films from both theoretical and experimental aspects. It was found that the frustrated micro-phase separation structures were formed in nano-sized confined geometries. For example, the block copolymers form helical structures in the cylinders (2D confinement system) even though the block copolymer has no chirality [1]. Basis on the theory, nanoparticles made of block copolymers are candidates of such a 3D confinement system.

In recent years, we have reported that various kinds of polymer particles can be prepared by a simple solvent evaporation process, that is, the evaporation of a good solvent from a polymer solution containing poor and good solvents; the Self-Organized Precipitation (SORP) method as shown in Fig. 1 [2]. This method can be applied to versatile polymers by selecting suitable solvent combinations for the polymers. By the SORP method, the nanoparticles with micro-phase separation structures (e.g., cylindrical, unidirectionally stacked lamellar, and onion-like structures) can be prepared [3, 4].

Recently, we have reported that the frustrated micro-phase separation structures (i.e., tennis ball, screw-like structures) of block copolymers having high molecular weight were formed in the nanoparticles as a 3D confinement system [5]. In this talk, the 3D structural observations of the block copolymer nanoparticles were carried out by transmission electron tomography (TEM) [6].

The nanoparticles were prepared from poly(styrene-*b*-isoprene) ( $Mn_{(PSt)}$ : 318,000,  $Mn_{(PI)}$ : 512,000,  $Mw/Mn$ : 1.15,  $f_{PI}$ : 0.65) by using the SORP method. Fig. 2 shows the

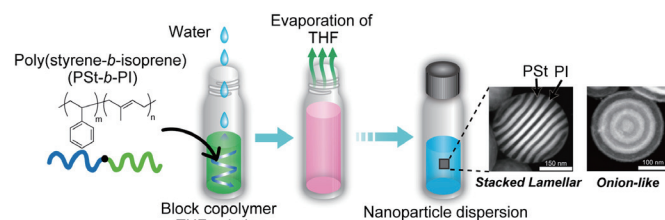


Fig. 1. Preparation method of block copolymer nanoparticles. Symmetrical block copolymer formed stacked lamellar and onion-like structures in nanoparticles.

TEM and 3D reconstructed images of the nanoparticles with different particle diameters. The green and blue coloured 3D images correspond to PI and PSt phases of the nanoparticles, respectively. TEM images of the block copolymer nanoparticles with different particle diameters are shown in Fig. 2-(a1-a7). In these TEM images, the bright and dark regions of the nanoparticles are respectively attributed to the nonstained PSt and the PI moieties stained with OsO<sub>4</sub>. To determine the 3D structures of micro-phase separated structures in the nanoparticles, detailed structural analysis was carried out by TEMT. The reconstructed 3D images of PI phases (Fig. 2-(b1-b7)) and PSt phases (Fig. 2-(c1-c7)) are shown along with  $D/L_0$ , where  $D$  is the particle diameter (measured from the 3D structure of particle) and  $L_0$  is the equilibrium periodic length of the lamellar structure in its bulk film. The black arrows in Fig. 2-(a1, a3) indicate the same particles observed by TEMT. TEMT observations revealed that a wide variety of micro-phase separated structures were formed in the nanoparticles depending on  $D/L_0$ . By focusing on the structures of PSt phases at the surface of nanoparticles (Fig. 2-(c1-c7)), micro-phase separated structures can be categorized into three types: ring, helix, and branched helix. In contrast, in the central region of the nanoparticles with  $D/L_0 > 1.17$ , PSt spherical domain were formed, whose size increased with particle diameter. These micro-phase separated structures formed in nanoparticles have never been observed not only in the bulk film but also in other (1D and 2D) confinement geometries.

From the 3D structural data of the nanoparticles, the volume fraction of the PI phase ( $f_{PI}$ ) in each nanoparticle was calculated, which is shown in Fig. 2 (a1-a7). The smallest nanoparticle ( $D/L_0 = 0.66$ ) has  $f_{PI} = 0.55$  and the other nanoparticles have  $f_{PI} \sim 0.60$ . The block copolymer should have  $f_{PI} = 0.65$ , at least in the bulk state. The  $f_{PI}$  of the nanoparticles decreased in comparison with its known intrinsic value, implying that the molecular conformation of block copolymers in the nanoparticles is different from that in the bulk, owing to the 3D

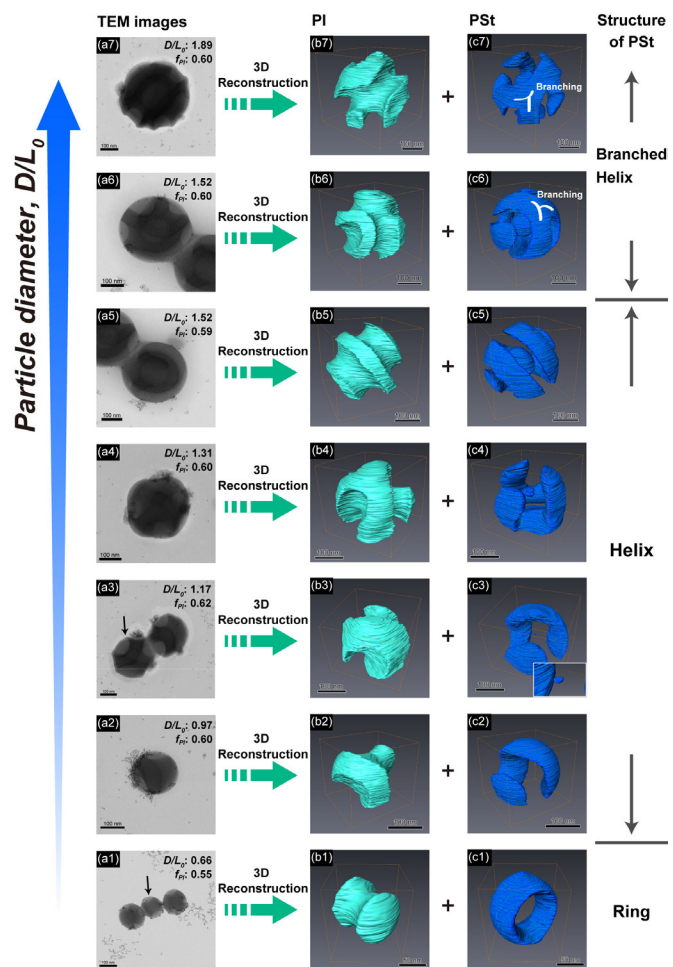


Fig. 2 (a1-a7) TEM images of block copolymer nanoparticles observed by TEMT. The 3D structures of PI (b1-b7) and PSt (c1-c7) phases of the nanoparticles were shown separately.

confinement effect of the nanoparticles. Further details of structural analysis will be discussed at conference time.

[1] P. Dobriyal, H. Xiang, K. Matsunaga, J. -T. Chen, H. Jinnai, T. P. Russell, *Macromolecules*, **42** (22), 9082 (2009).

[2] H. Yabu, T. Higuchi, K. Ijio, M. Shimomura, *Chaos*, **15**(4), 047505 (2005).

[3] H. Yabu, T. Higuchi, M. Shimomura, *Adv. Mater.*, **17**(17), 2062 (2005).

[4] T. Higuchi, A. Tajima, H. Yabu, M. Shimomura, *Soft Matter*, **4**, 1302 (2008).

[5] T. Higuchi, A. Tajima, K. Motoyoshi, H. Yabu, M. Shimomura, *Angew. Chem. Int. Ed.*, **47**(42), 8044 (2008).

[6] T. Higuchi, K. Motoyoshi, H. Sugimori, H. Jinnai, H. Yabu, M. Shimomura, *Macromol. Rapid. Commun.*, **31**(20), 1773 (2010).

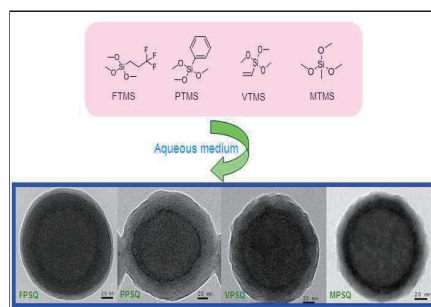
## Polysilsesquioxane Hollow Nanospheres via Polymer Templating

Puping Dong and Chang-Sik Ha

Department of Polymer Science and Engineering, Pusan National University, Busan 609-735, Korea

A series of organofunctional polysilsesquioxane (PSQ) hollow nanospheres were prepared by an environment friendly method. The use of this simple and reproducible synthetic approach resulted in highly uniform and monodisperse hollow nanospheres with high coverage of functional groups, namely, fluoroalkyl, phenyl, vinyl and methyl groups. By adjusting the precursor concentration, the particle size and shell thickness could be precisely controlled. The structure and functionality of these hollow nanospheres were characterized by field-emission scanning electron microscopy, transmission electron microscopy, Fourier transform infrared spectroscopy, solid-state NMR spectroscopy, X-ray diffraction and nitrogen adsorption–desorption studies. These materials were used as drug delivery carriers and adsorbents to treat the benzophenone-containing wastewater. In particular, it was found that the hydrophobic contaminants could be effectively removed. The hydrophobic surface property of the polysilsesquioxane hollow nanospheres was found to be an important factor that influences the adsorption capacity[1,2].

All organoalkoxysilane precursors used for the polycondensation reactions contained a common trimethoxysilyl terminal group and different organic functional groups, as depicted in Scheme 1, where the precursors were trifluoropropyltrimethoxysilane (FTMS), phenyltrimethoxysilane (PTMS), vinyltrimethoxysilane (VTMS) and methyltrimethoxysilane (MTMS).



Scheme 1. Molecular structures of the organosilane precursors and the corresponding PSQ hollow spheres prepared from aqueous medium.

- [1] F. P. Dong, W. P. Guo, S. W. Chu and C. S. Ha, *Chem. Commun.*, 7498 (2010).  
 [2] F. P. Dong, W. P. Guo, S. S. Park, and C.S. Ha, *J. Mater. Chem.*, in print.

## Manipulation of surface properties: attachment of nanometer-thick sticker on versatile substrates

Hirohmi Watanabe<sup>1</sup>, Aya Fujimoto<sup>1</sup>, and Atsushi Takahara

<sup>1</sup>JST, ERATO Takahara Soft Interfaces Project, Japan

Surfaces and interfaces have a strong influence on material properties such as adhesion, friction, electrical properties, and biocompatibilities [1]. Therefore, precise control of surfaces and interfaces is indispensable for the promotion of innovation in future science and technology. We report here a simple, efficient method to introduce specific functionalities on versatile substrates [2]. The key of the concept is the use of nanomembrane as a nanometer-thick sticker. Because nanomembrane layer is formed on a substrate coated with a sacrificial polymer layer, dissolution of the sacrificial polymer leads to detachment of the nanomembrane from the substrate. The detached nanomembrane may be re-attached to a second substrate like a sticker (Fig. 1).

When a nanomembrane retaining the surface properties is transferred to another surface, functional surface can be easily obtained in a similar manner to conventional, direct modification methods. Attachment of nanomembrane does not affect physical properties of the materials except surface properties because of the extremely thin geometry of nanomembrane. This sticker-like application of nanomembrane is a simple and yet efficient for the fabrication of functional surface on variety of substrates. In this presentation, we fabricated an anti-fouling surface on various substrates as an example. The fabricated nanomembranes were transferred to various other substrates, including Si, polymer film, and metal (Fig. 2).

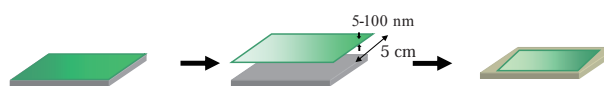


Fig. 1. Schematic illustration of manipulation of

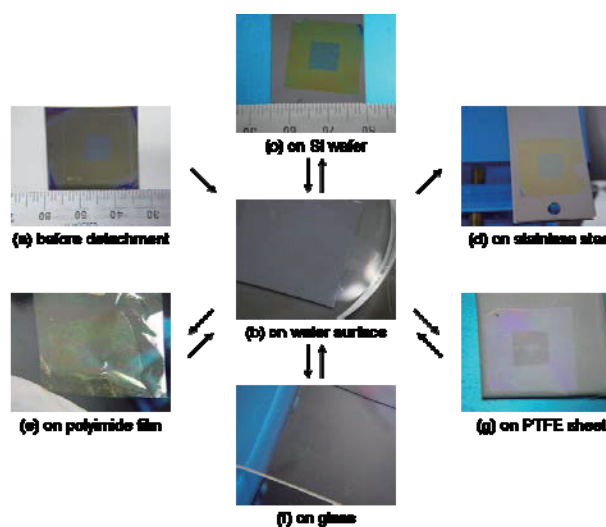


Fig. 2. Digital camera images of a nanomembrane on different substrates. The nanomembrane repeatedly transferred onto different substrates.

[1] P. G. De Gennes, in *Soft Interfaces*, Cambridge Univ. Press, Cambridge United Kingdom 1994.

[2] H. Watanabe, Aya Fujimoto, A. Takahara, *Soft Mat.*, **2011**, 7, 1856–1860

## “Mechanobio-materials”: design of micropatterned elastic gels to control cell mechanotaxis and motility-related functions

Satoru Kidoaki

*Institute for Materials Science and Engineering, Kyushu University, Fukuoka 819-0395, Japan*

*E-mail: kidoaki@ms.ifoc.kyushu-u.ac.jp*

### INTRODUCTION

Recently, mechanobiology-based cell manipulation technology has drawn much attention in bioengineering field. As the advanced trends in the biomaterial researches that intend to control the mechanobiology of cells based on the design of micro-mechanical extracellular milieu, mechanical cell manipulation employing the elastic substrates for cell culture is focused in this paper. Control of cell motility on the well-designed elasticity gradient materials, i.e., control of mechanotaxis, and correlated stem cell lineage specification on the elasticity-micropatterned gels were investigated. For the first, we are focusing on the understanding and control of cell mechanotaxis, which might provide a basis for designing mechanobio-materials to manipulate cell motility. To establish the condition to induce cell mechanotaxis, we have developed the photolithographic surface microelasticity patterning method for fabricating a cell-adhesive hydrogel with a microelasticity-gradient (MEG) surface using photocurable styrenated gelatin. On the well-designed micropatterned elastic field, mechanotaxis was successfully controlled. Concept and perspective of the biomaterials that manipulate cell mechanobiology, i.e., mechanobio-materials, are discussed.

### EXPERIMENTAL METHODS

Cell-adhesive MEG gels were prepared by photocurable styrenated gelatin using a custom-designed reduction projection photolithography systems. Patterned MEG gels were prepared by regulating the photoirradiation power, periods, and positions. Surface elasticity and its two-dimensional distribution were characterized by microindentation tests using atomic force microscopy. On the prepared MEG gel, movement trajectories of 3T3 fibroblast were observed by time-lapse microscopy.

### RESULTS AND DISCUSSION

To investigate the condition to induce and control mechanotaxis, patterned MEG gels with different absolute surface elasticities in soft and hard regions, elasticity jumps between them, and sharpness of elasticity boundary. Three critical criteria of the elasticity jump and the absolute elasticity to induce mechanotaxis have been identified<sup>1-3</sup>: 1) a high elasticity ratio between the hard region and the soft one, 2) elasticity of the softer region to provide medium motility, and 3) sharpness of the elasticity boundary. Especially, concerning the characterization of the effect of sharpness of elastic boundary on the induction efficiency of mechanotaxis, MEG gels with the different sharpness of elastic boundary and the same magnitude of elasticity jump between softer and stiffer regions were fabricated. While on the diffuse elastic boundary cells did not exhibit any directional movements, marked enhancement of mechanotaxis was observed on the discrete elastic boundary of ca. 30 kPa jump within 50  $\mu\text{m}$ -wide boundary. Essential condition to induce mechanotaxis was found to be enough sharp elasticity jump in the region where a single cell can adhere and sense it. Based on these design criteria, localization of stem cells on hard and soft regions could be successfully controlled, suggesting an possible dynamic control of input of mechano-signals from elastic substrate in the moving process of cells.

### CONCLUSION

Essential condition to induce cell mechanotaxis, i.e., sharpness of the elasticity boundary, has been established based on the photolithographic micropatterned gelation techniques, and applied for regulation of motility-related mechano-signal input.

### REFERENCES

1. S. Kidoaki and T. Matsuda., *J. Biotech.*, 133, 225-230 (2008).
2. S. Kidoaki and T. Matsuda, *IEEE Int. Symp. Micro-Nanomechatro Human Sci.* 469-474 (2008)
3. T. Kawano and S. Kidoaki, *Biomaterials*, 32, 2725-2733 (2011).

## Controlling the Orientation and Localization of a Biomacromolecule in a Model Cell System: Experimental Demonstration with DNA and the Potassium Channel KcsA

Miho Yanagisawa<sup>1</sup>, Ayako Kato<sup>2</sup> and Kenichi Yoshikawa<sup>2</sup>

<sup>1</sup>Department of Physics, Faculty of Science, Kyushu University, Japan

<sup>2</sup>Department of Physics, Graduate School of Science, Kyoto University, Japan

In cellular membranes, the distribution and orientation of biomacromolecules, such as proteins or DNA molecules, are regulated according to their functions. To study the mechanism, the biomacromolecules have been reconstituted in cell-sized vesicles ( $> 5 \mu\text{m}$ ). However, the interaction between the biomacromolecules and lipids is still unclear, and their orientation cannot be adequately controlled. Here, we report two topics, i.e., a successful reconstitution of a membrane protein with desired orientation in a cell-sized vesicle using droplet-transfer technique [1], and a characteristic localization of DNA accompanied with the structural transition upon phase separation of a lipid membrane [2].

First, we report the orientation control of KcsA potassium channel with either an outside-out or inside-out orientation in giant vesicles, using droplet-transfer technique (Fig. 1). We prepared water-in-oil droplets lined with a lipid monolayer. When solubilized KcsA was encapsulated in the droplet, it accumulated at monolayers of phosphatidylglycerol (PG) and phosphatidylethanolamine (PE), but not at a monolayer of phosphatidylcholine (PC). The droplet was then transferred through an oil/water interface having a preformed monolayer. The interface monolayer covered the droplet so as to generate a bilayer vesicle. By creating chemically different lipid-layers at the droplet and oil/water interface, we obtained vesicles with asymmetric lipid compositions in the outer and inner leaflets. KcsA was spontaneously inserted into vesicles from the inside or outside, and this was accelerated in vesicles that contained PE or PG. Integrated insertion into the vesicle membrane and the KcsA orientation was examined by functional assay, exploiting the pH sensitivity of the opening of the KcsA when the pH-sensitive cytoplasmic domain (CPD) faces toward acidic media. KcsA loaded from the inside of the PG-containing vesicles becomes permeable only when the

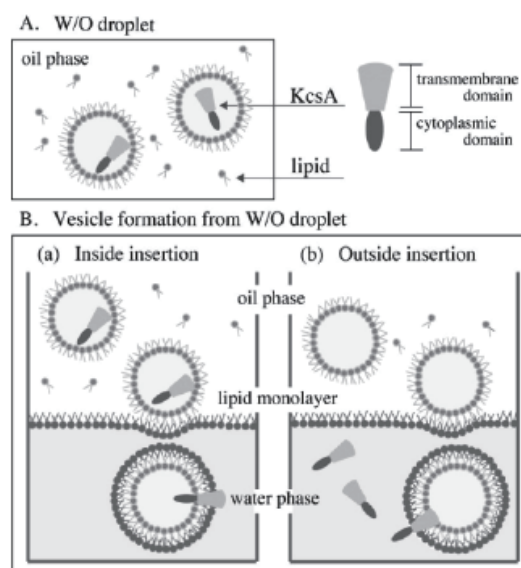


**Figure 1.** Orientation control of KcsA in a cell-sized vesicle using droplet transfer method. (A) Water in oil (W/O) droplets covered by a lipid layer. (B) KcsA insertion into vesicles from (a) the inside or (b) outside.



intra-vesicular pH is acidic, and the KcsA loaded from the outside becomes permeable when the extravesicular pH is acidic (Fig. 2). Therefore, the internal or external insertion of KcsA leads to an outside-out or inside-out configuration so as to retain its hydrophilic CPD in the added aqueous side [1].

Second, we report the coupling of phase separation on a phospholipid membrane with a structural transition of giant DNA. We performed single-DNA measurements in the presence of cell-sized giant unilamellar vesicles (GUV) composed of dioleoylphosphatidylcholine (DOPC), PE, and cholesterol. We observed the effect of phase separation of the lipid membrane by changing PE from dioleoylphosphatidylethanolamine (DOPE) to dipalmitoylethanolamine (DPPE), which corresponds to a change from a homogeneous phase to two segregated phases of liquid-ordered and liquid-disordered states on the membrane. In the homogeneous membrane, DNA molecules exhibited a compact conformation in aqueous solution containing a physiological concentration of  $Mg^{2+}$  and polyamine, without attaching to the membrane surface. In contrast, in the membrane that was segregated into two domains, DNA molecules were adsorbed onto the liquid-ordered phase that was rich in DPPE by taking an elongated conformation [2].

The coupling with this method of orientation control with phase separation of lipids in vesicles containing the preferred lipids [3], it should be possible to control the spatial distribution of membrane proteins in the desired orientation.

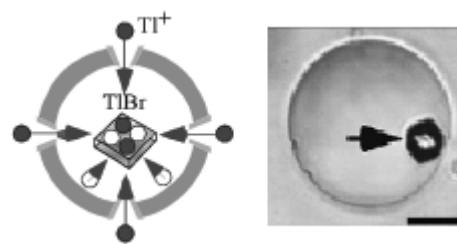


**Figure 2.** Gating of oriented KcsA allows  $Tl^+$  ion flux into the vesicle, and forms crystals with the intracellular  $Br^-$ . Scale bar  $10\mu m$ .

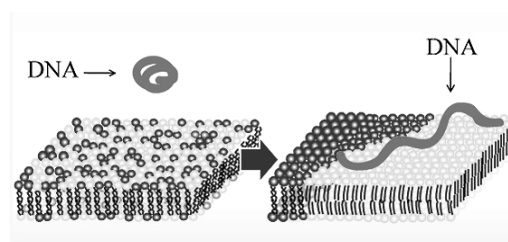


**Figure 3.** Interaction of DNA with a (left) homogeneous or (right) phase-separated membrane. DNA is localized in PE-rich phase (white).

[1] M. Yanagisawa, M. Iwamoto, A. Kato, K. Yoshikawa and S. Oiki. “Oriented reconstitution of a membrane protein in a giant unilamellar vesicle: Experimental verification with the potassium channel KcsA”, *J. Am. Chem. Soc.*, **133**, 11774 (2011).

[2] A. Kato, A. Tsuji, M. Yanagisawa, D. Saeki, K. Juni, Y. Morimoto and K. Yoshikawa. “Phase Separation on a Phospholipid Membrane Inducing a Characteristic Localization of DNA Accompanied by Its Structural Transition”, *J. Phys. Chem. Lett.*, **1**, 3391 (2010).

[3] M. Yanagisawa, M. Imai and T. Taniguchi. “Shape deformation of ternary vesicles coupled with phase separation”, *Phys. Rev. Lett.*, **100**, 148102 (2008).

## Fabrication of Biomimetic Wettability Patterned Silicon Surfaces by using Self-organized Honeycomb masks

Yuji Hirai<sup>1,4</sup>, Hiroshi Yabu<sup>1</sup>, Yasutaka Matsuo<sup>2,4</sup>, Kuniharu Ijio<sup>2,4</sup>,  
Masatsugu Shimomura<sup>1,2,4</sup>,

<sup>1</sup> IMRAM, Tohoku University, Japan

<sup>2</sup> RIES, Hokkaido University, Japan

<sup>3</sup> WPI-AIMR, Tohoku University, Japan

<sup>4</sup> CREST, JST, Japan

In nature, there are many functional water-controlling surfaces, such as a water repellency surface of a lotus leaf, a superhydrophobic water adhesion surface of a rose petal, a water harvest surface of a beetle's back, and so on. We have reported that honeycomb-patterned porous polymer films can be prepared by casting a solution of hydrophobic polymer and amphiphilic polymer on a solid substrate by using condensed water droplet arrays as templates[1]. The superhydrophobic pincushion film was easily formed by simple peeling off the top-layer of the honeycomb-patterned film with an adhesive tape[2]. In this report, we show the preparation of the biomimetic wettability patterned silicon nano-structured surface by dry etching process with self-organized honeycomb-patterned films as etching masks.

We prepared honeycomb-patterned films from polystyrene and amphiphilic polymer by casting their chloroform solution. After UV-O<sub>3</sub> treatment, honeycomb-patterned films were fixed on silicon substrates up side down with poly(vinyl alcohol) solution as adhesive. After peeling off the bottom layer of the honeycomb-patterned films, porous polymer masks were formed. After reactive ion etching of the silicon substrate through the mask, the silicon nanopike-array structure was obtained. We measured water contact angles (CAs) on the silicon nanopike-array structures, and the maximum CA was over 170 degree. From the results of X-ray photoelectron spectrum of the silicon nanopike-structures, fluorine was detected after dry etching. The result suggests that superhydrophobicity is realized due to fluorocarbon absorbed on the surface and their surface structures. After UV-O<sub>3</sub> treatment with photo-masks, fluorine was removed at irradiation area, and the area shows superhydrophilicity. These results suggest that we can easily design superhydrophobic and superhydrophilic patterned surfaces by UV-O<sub>3</sub> treatment through photo-masks.

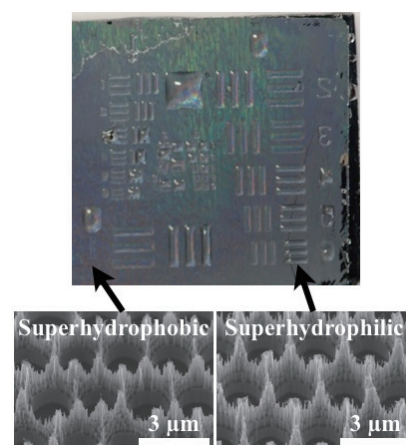


Fig. 1. A photograph and FE-SEM images of wettability patterned silicon nanopike-array structures

[1] N. Maruyama, et al., *Supramol. Sci.*, **5**, 331-336 (1998)

[2] H.Yabu, M. Takebayashi, M. Tanaka, M.Shimomura, *Langmuir*, **21**(8), 3235(2005)

## Plastic Antibodies: Development and Applications

Yu Hoshino<sup>1</sup>, Kenneth J. Shea<sup>2</sup>

<sup>1</sup>Kyushu University, Japan

<sup>2</sup>University of California, Irvine, USA

Synthetic polymer nanoparticles that are capable of recognizing specific biomacromolecules are of significant interest as “Plastic Antibodies”; stable and inexpensive alternatives for antibodies. However, the design of synthetic NPs capable of capturing target biomacromolecules is a formidable challenge. In nature, interactions between biomacromolecules arise from multiple weak interactions comprised of electrostatic, hydrophobic and hydrogen bonding interactions on complementary three-dimensional binding surfaces. In an effort to mimic these interactions, bulk polymer materials that capture target molecules by multipoint-interactions have been synthesized by incorporating functional monomers that interact with target molecules by electrostatic interactions [ref.1]. Nano-size materials with affinity for a target peptide/protein have also been synthesized by optimizing the composition and/or ratio of functional groups on the surface of the synthetic NPs [ref.2,3]. Linear polymers that are functionalized with small arginine receptors have also been shown to interact with arginine-rich proteins [ref. 4].

We have been developing general procedures to create plastic antibodies using toxic peptide (melittin) as a model target antigen . As a first step, procedures to create multifunctional polyacrylamide nanoparticles consisting of combinations of functional monomers were developed. In vitro toxin neutralization tests revealed that polymer NPs synthesized with an optimized combination of functional monomers could capture target molecules via multipoint hydrophobic and electrostatic interactions and neutralize its function [ref.5].

Although, the binding capacity of the optimized particles were enormous, binding affinity of the particles were not strong enough to be used as plastic antibodies *in vivo*. To achieve nanoparticles with greater affinity for the target peptide, we applied molecular imprinting strategy. By polymerizing the optimized multifunctional polymers in the presence of target peptides, nanoparticles with strong affinity for the target peptides that were comparable to the natural antibodies were obtained [ref.6,7]. Since, the particles are inert and nontoxic to the animal model, we further tested the efficacy of the imprinted particles in the bloodstream of living mice. The results demonstrated that the imprinted polymer nanoparticles efficiently capture the cytotoxic peptide melittin in the bloodstream. The strong and specific affinity of the imprinted NPs enabled the sequestration of the target peptide in the blood. The melittin•MIPNP complexes are then cleared from the blood by the mononuclear phagocytic system in the liver. As a result of binding and removal of melittin by the particles *in vivo*, mortality and peripheral toxic symptoms of melittin were significantly diminished [ref.8].

One definite drawback of the molecular imprinting strategy is the cost of expendable template peptide. Affinity purification strategy is proposed to redeem the drawback of molecular imprinting strategy. In the affinity purification process, randomly copolymerized multifunctional polymers are purified by the target peptides that are immobilized on the surface of the solid state such as agarose beads. In the first demonstration of the affinity purification experiment, it has been revealed that the “randomly” copolymerized multifunctional nanoparticles are mixture of the particles that has high and low affinity binding sites. Furthermore, the purified nanoparticles showed much stronger affinity to the peptide than the average of the particles before purification process [ref.9].

- [1] Oya T, *et al.* (1999) *Science* 286:1543-1545.
- [2] De M, You C-C, Srivastava S, Rotello VM (2007) *J Am Chem Soc* 129:10747-10753.
- [3] Dervede J, *et al.* (2010) *Proc Natl Acad Sci USA* 107:19679-19684.
- [4] Koch SJ, Renner C, Xie X, Schrader T (2006) Tuning linear copolymers into protein-specific hosts. *Angew Chem Int Ed* 45:6352-6355.
- [5] Y. Hoshino, T. Urakami, T. Kodama, H. Koide, N. Oku, Y. Okahata, K. J. Shea, *Small*, **5**, 1562-1568 (2009)
- [6] Y. Hoshino, T. Kodama, Y. Okahata, K. J. Shea, *J. Am. Chem. Soc.*, **130**, 15242-15243 (2008).
- [7] Zhiyang Zeng, Yu Hoshino, Andy Rodriguez, Hoseong Yoo, Kenneth J. Shea, *ACS nano*, **4**, 199-204 (2010).
- [8] Y. Hoshino, *et al.*, *J. Am. Chem. Soc.*, **132**, 6644-6645 (2010).
- [9] Y. Hoshino, *et al.*, *J. Am. Chem. Soc.*, **132**, 13648-13650 (2010).

# Conductivity Analysis of DNA

Xie Peng<sup>1</sup>, Feng Long Gu<sup>3,4</sup>, and Yuriko Aoki<sup>2,4</sup>

<sup>1</sup>Department of Molecular and Material Sciences, Interdisciplinary Graduate School of Engineering Sciences, Kyushu University, 6-1 Kasuga-Park, Fukuoka 816-8580, Japan

<sup>2</sup>Department of Material Sciences, Faculty of Engineering Sciences, Kyushu University, 6-1 Kasuga-Park, Fukuoka 816-8580, Japan

<sup>3</sup>Center for Computational Quantum Chemistry, South China Normal University, Guangzhou 510631 China

<sup>4</sup>Japan Science and Technology Agency, CREST, 4-1-8 Hon-chou, Kawaguchi, Saitama 332-0012, Japan

## 1. Introduction

DNA molecules, well known for containing the genetic code of all living species, has a potential for use as a molecular wire for its special one-dimensional layered  $\pi$ - $\pi$  electrons stacking structure of base pairs in double-stranded DNA [1]. It has the possibility of electronic conduction. There are many factors that influence on DNA conductivity such as: base sequences, counter-ion effect, environment of DNA (humidity), length of DNA molecule, structure of DNA, doping effect, etc. In this report, we investigated the influences of counter-ion and base sequences.

## Part I Counter-ion effect

### 2.1 Model molecules

To investigate the influence of the counter-ion on the electronic states of DNA, we performed local density states (LDOS) calculations [2] for eight types of DNA molecules (Fig.1) such as: A- & B- type poly(dA)·poly(dT) & poly(dG)·poly(dC) neutralized by  $H^+$  and  $Na^+$  respectively. A, T, G, C denote adenine, thymine, guanine, cytosine respectively.

### 2.2 Calculation methods and results

We have examined the LDOS figures of key fragments for each model such as: adenine, guanine and  $Na^+$ . From Fig.2 (a) and (b) we found that the valence bands were formed by base adenine/guanine's HOMO, even if we replaced  $H^+$  with  $Na^+$ , the valence band were still formed by adenine/guanine's HOMO. However a new conduction band near 0 eV lied in between valence band and conduction bands were formed by  $Na^+$ . This implies that the through-space electron transfers between stacking base

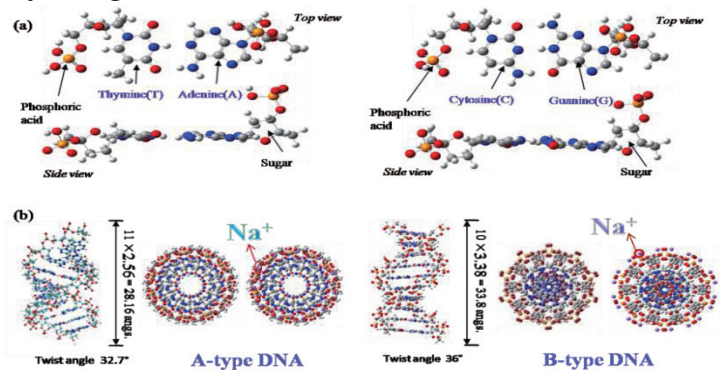


Fig.1 DNA molecules

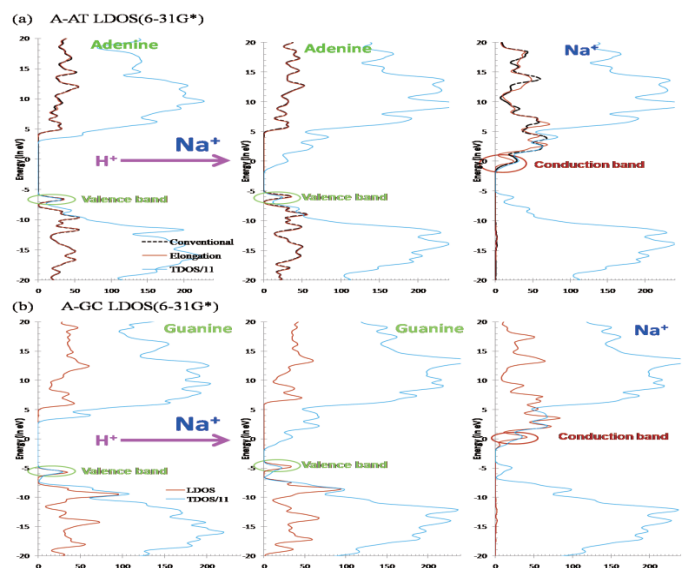


Fig.2 LDOS for A- poly(dA) · poly(dT) and poly(dG) · poly(dC)

adenine/guanine and  $\text{Na}^+$  occur more easily than that between stacking base pairs.

## Part II Base sequences effect

### 3.1 Model molecules

DNA usually has A, B and C forms depending on base sequence, relative humidity, type and concentration of counter-ions. B form can be observed in most various base composition and base sequences [3]. We selected one polymononucleotide, four polydinucleotides and six polytrinucleotides in B form neutralized by  $\text{Na}^+$  as our model molecules as shown in Table 1.

### 3.2 Calculation methods and results

We analyzed the valence band and the energy gap of the LDOS figures for each DNA model. It is found that the valence band of DNA containing guanine comes from guanine's HOMO, but the valence band of DNA containing no guanine comes from adenine's HOMO (shown in Fig.3), all conduction bands come from  $\text{Na}^+$ .

We compared the LUMO-HOMO energy gap ( $\Delta E_g$ ) of each polynucleotide in Table 1. We found that  $\Delta E_g$  of the polynucleotide containing guanine is lower than that of the polynucleotide containing no guanine. The value of  $\Delta E_g$  depends on the base composition of DNA, that is, the base composition will affect the conductivity of DNA.

## 4. Conclusions

Based on the above results, we can conclude that the conductivity of poly(dG)·poly(dC) neutralized by  $\text{Na}^+$  is the best conductor of all DNA models. The through-space electron transfers between stacking base guanine and  $\text{Na}^+$  would be more important for the conductivity of DNA compared to other bases. By comparing the energy gap of each B-type DNA model with different base composition, the effect for DNA conductivity related to base composition is in the order of: G-G > G-C > G-A > G-T > A-T where comes from Table 1.

As a next step, we are going to analysis the relationship between bioactivity and sequence alignment in various types of DNA.

## References

- [1] R.G. Endres, D.L. Cox, R.R.P. Singh, *Rev. Mod. Phys.* **76**, 195 (2004).
- [2] Y. Aoki, A. Imamura, *J. Chem. Phys.* **97**, 8432 (1992).
- [3] A.G.W. Leslie, S. Arnott, R. Chandrasekaran, R.L. Ratliff, *J. Mol. Biol.* **143**, 49(1980).

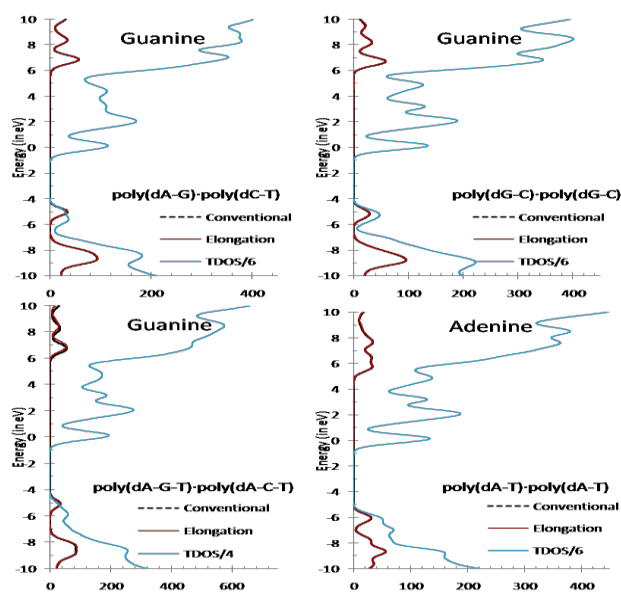


Fig.3 The LDOS of guanine/adenine for 4 DNA models

Table 1 The LUMO-HOMO energy gap

B-DNA	$E_{\text{LUMO}}(\text{au})$	$E_{\text{HOMO}}(\text{au})$	$\Delta E_g(\text{au})$	$\Delta E_g(\text{ev})$
poly(dA-T)·poly(dA-T)	-0.0067	-0.2127	0.206	5.605
poly(dA-A-C)·poly(dG-T-T)	-0.0073	-0.1893	0.182	4.952
poly(dA-C)·poly(dG-T)	-0.0051	-0.1868	0.1817	4.944
poly(dA-G-T)·poly(dA-C-T)	-0.0086	-0.1861	0.1775	4.830
poly(dG-A-T)·poly(dA-T-C)	-0.0083	-0.1841	0.1758	4.784
poly(dA-G-C)·poly(dG-C-T)	-0.0075	-0.182	0.1745	4.748
poly(dG-C)·poly(dG-C)	-0.005	-0.1789	0.1739	4.732
poly(dG-G-T)·poly(dA-C-C)	-0.0086	-0.1793	0.1707	4.645
poly(dA-G)·poly(dC-T)	-0.0122	-0.1782	0.166	4.517
poly(dG)·poly(dC)	-0.012	-0.1686	0.1566	4.261

## Shape-Persistent Micelles Bearing Calix[4]arene Building Block

Kazuo Sakurai<sup>1</sup>, Shota Fujii<sup>1</sup>, Naoto Yagi<sup>2</sup> and Storatos Mylonas<sup>2</sup>

<sup>1</sup>Department of Chemistry and Biochemistry, University of Kitakyushu,  
Hibikino, Kitakyushu 808-0135, Japan.

<sup>2</sup>Japan Synchrotron Radiation Research Institute (JASRI/SPring-8), 1-1-1 Kouto, Sayo  
679-5198, Japan.

A series of cationic calix[4]arene-based lipids with alkyl chains of varying length were newly synthesized and found to form spherical micelles at low pH (protonated state of the amine headgroup) for propyl and hexyl tails, denoted by CaL[4]C3 and C6, respectively. Upon deprotonation with increasing pH, CaL[4]C3 showed a sphere-to-cylinder transition, while CaL[4]C6 changed from sphere to cylinder to monolayer vesicle. Synchrotron small-angle X-ray scattering (SAXS) patterns from both spherical and cylindrical CaL[4]C3 micelles exhibited a sharp intensity dump, indicating high symmetry and shape monodispersity. The size monodispersity of the CaL[4]C3 spherical micelles was confirmed with analytical ultracentrifugation, whereas CaL[4]C6 showed polydispersity. This is the first observation that the shape persistency is maintained upon the structural transition. From SAXS, static light scattering, and analytical ultracentrifugation, the aggregation numbers for the CaL[4]C3 and CaL[4]C6 spherical micelles were evaluated at 6 and 12, respectively. When the number of carbons of the alkyl chain was increased to 9 (CaL[4]C9), monolayer vesicles formed at low pH while at high pH no clear morphology could be observed. The present results indicate that a suitable combination of tail length, head volume, and rigidity of the building block is necessary to attain the shape persistency. With a shape determination program of Dummy, the micellar architecture was determined to have a regular hexahedron like form.

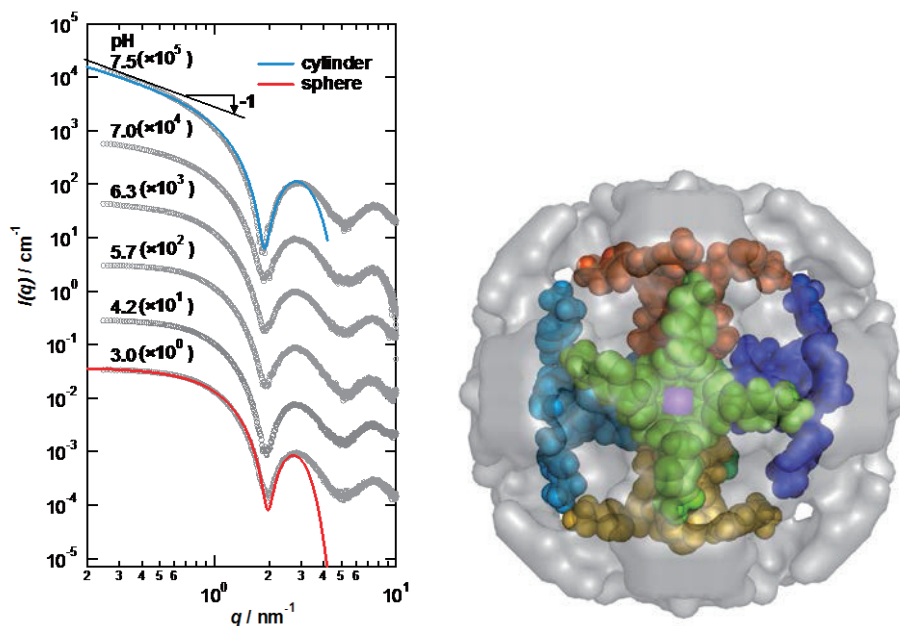


**Figure 1.** SAXS profile changes upon pH change for CaL[4]C3 (left) and the result of the dummy bead model.

## Structure of the monodisperse micelles of an amphiphilic calixarene molecule

Efstratios Mylonas<sup>1</sup>, Shota Fujii<sup>2</sup>, Tadashi Okobira<sup>2</sup>, Kazuya Uezu<sup>2</sup>, Naoto Yagi<sup>1</sup>, Kazuo Sakurai<sup>2</sup>

<sup>1</sup>Research and Utilization Division, JASRI, Japan

<sup>2</sup>Department of Chemistry & Biochemistry, The University of Kitakyushu, Japan

Suitable cationic surfactants as carriers of genetic material are of paramount importance for future applications of gene therapy. We have synthesized a cationic amphiphilic molecule containing a calix[4]arene ring group, propyl chains on the lower rim and 1,2,3-triazole and amine groups on the upper rim (Fig. 1). In aqueous solution of low ionic strength and low pH the amine group is positively charged and the molecules form monodisperse micelles with an aggregation number of 6, as evidenced by Small Angle X-ray Scattering (SAXS), analytical ultracentrifugation and Atomic Force Microscopy.



**Fig. 1** Cationic Calix[4]arene monomer

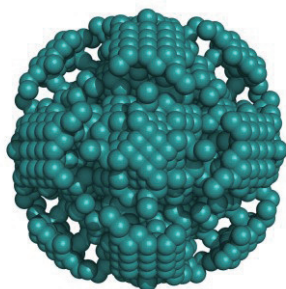


**Fig. 2** Dummy atom model

To visualize the overall shape of the molecule we created dummy atom models from the SAXS data [1]. The beads in a dummy atom model do not represent any specific atom or chemical group but rather they are placeholders with identical electron density for the space occupied by the molecule. A representative model of the low pH micelles with an imposed octahedral symmetry is shown in Fig. 2. The model has a roughly spherical shape and a maximum size of 45nm. The model is also hollow which indicates that the alkyl chains have

electron density similar to that of water.

To produce a more detailed model and to reduce the inherent ambiguity of SAXS data we used atomic coordinates of the monomer with optimized geometry [2] to construct the supramolecular assembly. We assumed a cubic symmetry for the starting model with one molecule at each face of the cube, the propyl chains on the lower rim pointing to the centre of the micelle and the charged amine groups on the upper rim pointing outside. The initial crude placement of the molecules was optimized with molecular dynamics (MD) simulations in explicit water solvent, employing the general AMBER force field [3]. A preliminary model of the simulation and the corresponding fit to the experimental SAXS data is shown in Fig. 3. Though this model does not retain the original symmetry, as expected, it adopts a micellar structure with the hydrophobic alkyl "tails" bundled together and the hydrophilic nitrogen-rich "heads" on the periphery of the assembly. The fit to the SAXS data, while not perfect,



illustrates that the produced model is similar to the structure of the assembly in solution. Our goal is to generate models that completely reproduce the experimental SAXS data in a quantitative way.

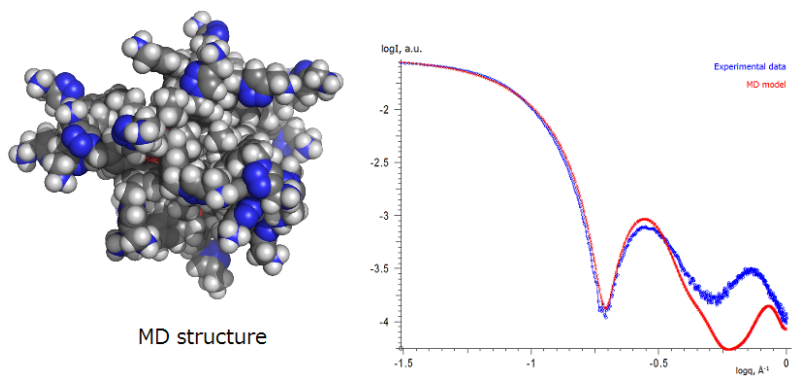


**Fig. 3** MD model and fit to experimental SAXS data

- [1] D. I. Svergun (1999) *Biophys J.* 76(6) 2879-2886.
- [2] Gaussian 09, Revision A.1, M. J. Frisch et al., Gaussian, Inc., Wallingford CT, 2009.
- [3] J. Wang et al. (2004) *Journal of Computational Chemistry* 25, 1157-1174.

## Distribution of Br-Bearing Hydrophobic Molecules in the Polymeric Micelle Core Studied with ASAXS

Yusuke Sanada<sup>1</sup>, Kouichi Shiraishi<sup>2</sup>, Masayuki Yokoyama<sup>2</sup>, Kazuo Sakurai<sup>1,3</sup>

<sup>1</sup>Faculty of Environmental Engineering, The University of Kitakyushu, Japan

<sup>2</sup>Research Center for Medical Science, Jikei University School of Medicine, Japan

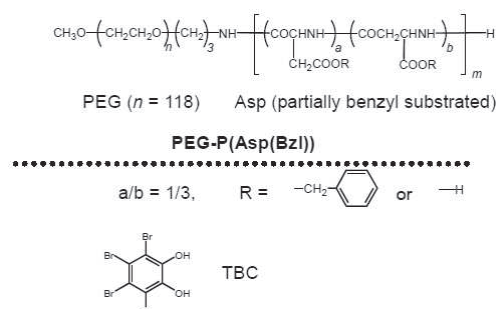
<sup>3</sup>JST-CREST, Japan

Anomalous small-angle X-ray scattering (ASAXS) can provide the information of how the probe atoms are distributed by measuring scattering near the X-ray absorption edge. In this study, we tried to clarify the location and/or state of a bromine compound TBC, as a probe, included in the block copolymer micelle (shown in scheme 1).

Measurements were carried out with the SPring-8 BL40B2 for a light source, and wavelengths were selected some points near absorption edge wavelength priori determined.

Obtained SAXS data was corrected with structural factor  $S(c)$  calculated (Fig. 1A). SAXS result of the polymer micelle itself can fitted with a theoretical curve of a core-shell model (Fig. 1B lower), but the results of the ASAXS can not explained with core-shell model (Fig. 1B upper). The experimental data points of  $q < 0.8 \text{ nm}^{-1}$  can be fitted with the solid sphere with radius of 6.6 nm. On the other hand, experimental the points of  $q < 0.8 \text{ nm}^{-1}$  the curve shapes

horizontal and this wider horizontal region fitted with small particle with the radius of less than 0.2 nm. Combined with these two kinds of spherical particles the experimental curve successfully explained.



**Scheme 1.** Chemical structure of block copolymer and bromine compound.

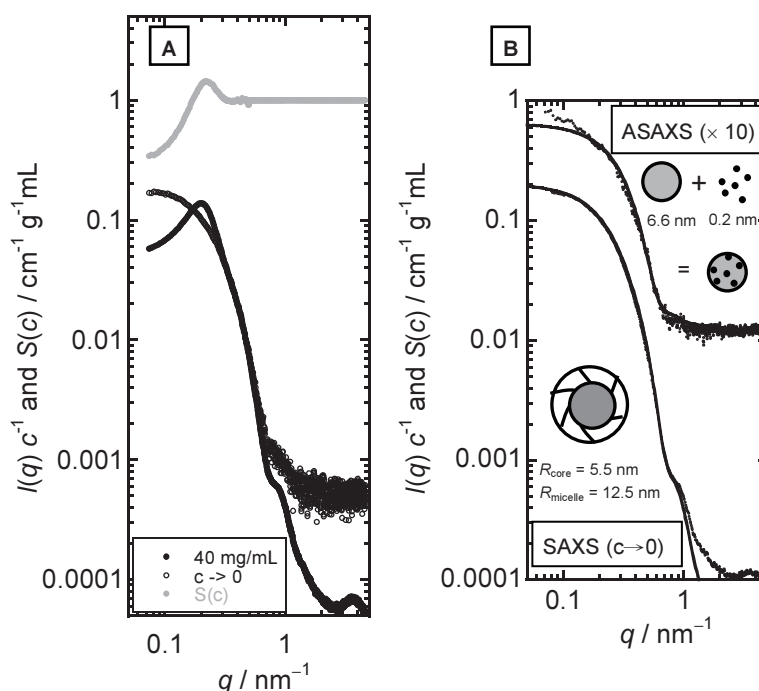


**Fig. 1.** (A) SAXS profiles of micellar solutions ( $c = 40 \text{ mg/mL}$  and  $c \rightarrow 0$ ) and calculated  $S(c)$  of the solution. (B) SAXS and ASAXS profiles of micellar solutions with theoretical curves of core-shell model (for SAXS) and combination of two kinds of spheres (for ASAXS).

## Structural Characterization of Polymer Micelles with Anomalous Small-angle X-ray scattering near Bromine *K*-edge

Isamu Akiba<sup>1,2</sup>, Atsuro Takechi<sup>1</sup>, Megumi Sakou<sup>1</sup>, and Kazuo Sakurai<sup>1,2</sup>

<sup>1</sup>Department of Chemistry & Biochemistry, The University of Kitakyushu, Japan

<sup>2</sup>JST-CREST, Japan

Polymeric micelles composed of amphiphilic block copolymers are expected to play important roles in the future drug delivery system (DDS). The internal structure of polymer micelle should have a marked effect on the drug-loading rate and the drug-release profile of DDS carriers. Therefore, detail analyses of the internal structures of polymer micelles are highly desired. Anomalous small-angle X-ray scattering (ASAXS) near the *K*-edge of Br is expected to be a powerful tool for detail analyses of organic materials because Br can be introduced organic molecules with a covalent bond [1]. Thus, in this study, we examined ASAXS near the Br *K*-edge for analysis of the structure of polymeric micelle composed of poly(ethylene glycol) (PEG) and poly(4-bromostyrene) (PBrS).

PBrS-*block*-PEG-*block*-PBrS (PBrS-PEG-PBrS) was synthesized by NMRP technique using PEG having TEMPO units at both chain ends. The hydrodynamic radius and aggregation number ( $N_{agg}$ ) of the PBrS-PEG-PBrS micelle were determined to 32.3 nm and  $8.2 \times 10^2$ , respectively. For the micelle solution, ASAXS measurements were performed at BL-40B2 station of SPring-8, Japan. The *K*-edge of Br is determined to 13.483 keV from absorption spectrum. Then, the incident X-ray beam in SAXS measurements was varied between 13.28 and 13.473 keV.

SAXS intensity of the PBrS-PEG-PBrS micelle decreases as the energy of incident X-ray approaches the *K*-edge of Br. Fig. 1 shows the resonant term obtained from the energy dependence of SAXS profile of PBrS-PEG-PBrS micelle with various energies of incident X-ray. The resonant term in this study is attributed to hydrophobic core. The resonant term sufficiently agree with the SAXS profile calculated for hard sphere with 10.2 nm radius. The  $N_{agg}$  estimated from the core volume ( $8.4 \times 10^2$ ) agrees very closely with that obtained by FFF/MALS. Therefore, ASAXS analysis can reveal internal structure of polymer micelle precisely.

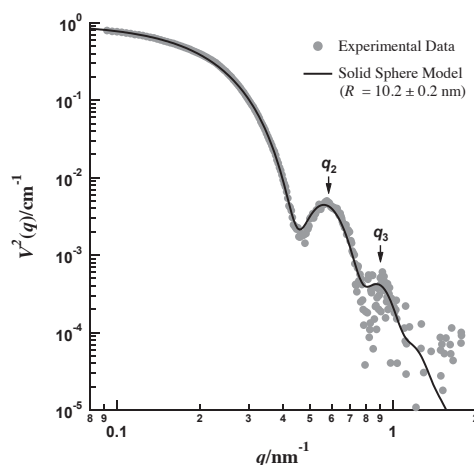


**Fig. 1.** Resonant term from ASAXS result for PBrS-PEG-PBrS micelle.

- [1] M. Sakou, A. Takechi, M. Handa, Y. Shinohara, Y. Amemiya, H. Masunaga, H. Ogawa, N. Yagi, K. Sakurai, and I. Akiba, *J. Phys. Conf. Ser.*, **272**, 012022 (2011).

## Plasmonic Nanostructures Toward Efficient LEDs and Solar Cells

Koichi Okamoto<sup>1,2</sup> and Kaoru Tamada<sup>1</sup>

<sup>1</sup>Institute for Materials Chemistry and Engineering, Kyushu University, Japan

<sup>2</sup>PRESTO, Japan Science and Technology Agency, Japan

The technique of controlling and utilizing the Surface plasmon (SP) is called "plasmonics" and has attracted much attention with the recent rapid advance of nanotechnology. One futuristic application of plasmonics is the development of high-efficiency light-emitting diodes (LEDs). LEDs have been expected to eventually replace traditional fluorescent tubes as new illumination sources, however, their emission efficiencies are still substantially lower than those of fluorescent lights. For the first time, we have reported that the SP coupling is very powerful technique to increase emission efficiencies of InGaN/GaN quantum wells (QWs) and other various materials [1].

Fig. 1 shows the photoluminescence (PL) spectra taken for InGaN/GaN QWs (3nm/10nm) which have various emission wavelength. Ag layers (50 nm) were deposited on top of the surfaces by a high vacuum thermal evaporation. The PL peak intensities of uncoated samples were normalized to 1 and huge enhancements were observed by Ag coating especially at the shorter wavelength region. The obtained PL enhancement should be attributed to the SP coupling effect. The coupling between the electron-hole pairs (excitons) and the SPs at

the metal surface increases the spontaneous emission rate and the internal quantum efficiencies [2]. The SP coupling effect was remarkable when the emission energy was close to the SP frequency described as dotted line in Fig. 1 at 2.84 eV (437 nm). However, it was found that the enhancement effect became lower and lower with increasing of wavelength.

We believe that the observed plasmonic effect should be applicable to the high efficiency LEDs. Fig. 2 shows the energy conversion scheme of the SP coupling and light emission. The SP-exciton and SP-photon coupling processes provide new emission pathways. The high efficiency LEDs should be achievable if the new emission path through the SP coupling is much faster than the original emission path (②+⑪>③、④>⑫ in Fig. 2). By the similar way, plasmonics should be also able to improve high-efficiency solar cells, because the SP-exciton and SP-photon coupling processes are reversible. The sun-light can couple to the SP at the metal/dielectric interface and generate the excitons in the dielectric materials. This process

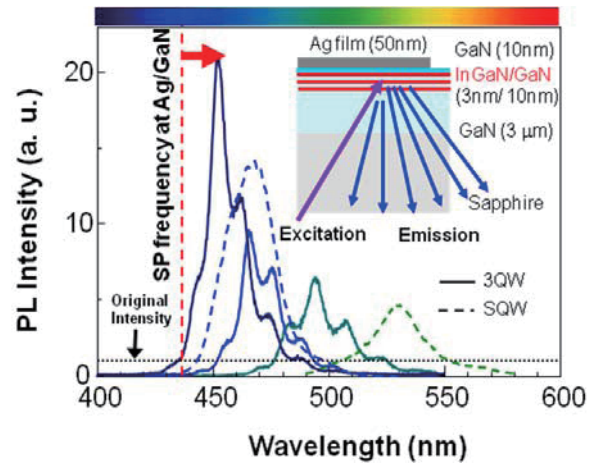


Fig. 1. SP enhanced PL spectra of InGaN/GaN QWs with various emission wavelength.

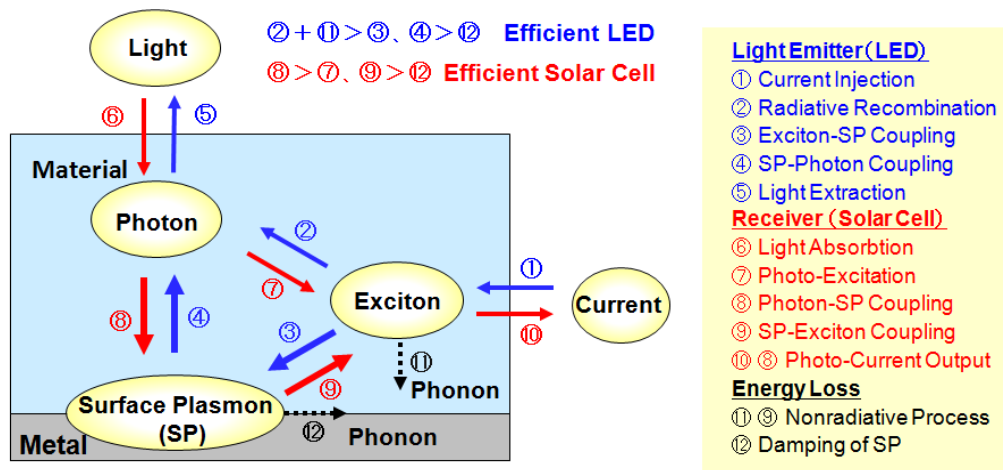


Fig. 2. Energy conversion scheme of the SP enhanced LED and solar cell.

should increase efficiencies of light absorption and photocurrent conversion.

Until now, several types of the plasmonic LEDs and solar cells have been reported, however, these are still far from practical utilizations. Further optimization of the metal nanostructure and tuning of the SP coupling process are required to develop both plasmonic LEDs and solar cells. Therefore we are designing more effective plasmonic nanostructures by using the 3-dimensional finite difference time domain (3D-FDTD) calculations and the nanofabrication processes with several bottom-up techniques. For example, we can control the resonance spectra of localized SP (LSP) mode by using the Ag nanoparticles with various diameters. By optimization of the Ag particle size, we achieved high efficient green emission from InGaN/GaN QWs [3], which has been very difficult to improve the emission efficiency. Moreover we succeeded to control the LSP resonance spectra with much wider wavelength region by employing particle pair and 2D nanosheet structure of Ag nanoparticles with 5nm diameter as shown in Fig. 3 [4]. Based on these plasmonic nanostructures, we propose new type of plasmonic LEDs and solar cells.

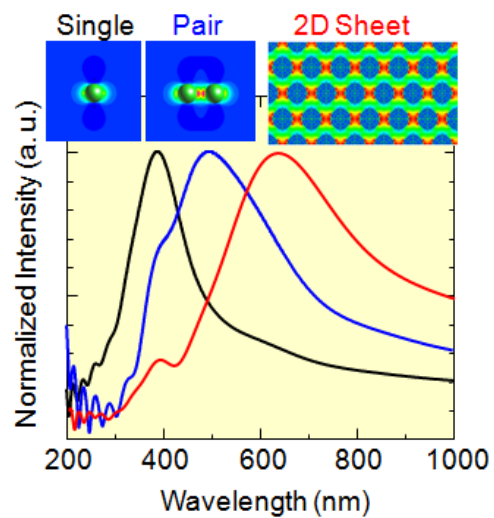


Fig. 3. Resonance spectra of LSP modes calculated by FDTD method for Ag single, pair, and 2D sheet structure.

[1] K. Okamoto, I. Niki, A. Shvarts, Y. Narukawa, T. Mukai, A. Scherer, *Nat. Mater.*, **3**, 601 (2004).  
 [2] K. Okamoto, Y. Kawakami, *IEEE J. Select. Top. Quantum Electron.* **15**, 1190 (2009).  
 [3] K. Okamoto, Y. Kawakami, and K. Tamada, *5th International Conference on Surface Plasmon Photonics*, TuD-3 (2011).  
 [4] M. Toma, K. Toma, K. Michioka, D. Obara, K. Okamoto, K. Tamada, *Phys. Chem. Chem. Phys.* **13**, 7459 (2011).

## Theoretical design of polythiophene derivatives as high performance photovoltaic cell

Lizhi Jiang<sup>1</sup>, Shou Feng<sup>1</sup>, Yuriko Aoki<sup>2,3</sup>

<sup>1</sup>Department of Molecular and Material Sciences, Interdisciplinary Graduate School of Engineering Sciences, Kyushu University, Kasuga, Fukuoka 816-8580, Japan

<sup>2</sup>Department of Material Sciences, Faculty of Engineering Sciences, Kyushu University, 6-1 Kasuga-Park, Fukuoka 816-8580, Japan

<sup>3</sup>Japan Science and Technology Agency, CREST, 4-1-8 Hon-chou, Kawaguchi, Saitama 332-0012, Japan

In these recent years, polythiophene (PT) derivatives [1] have attracted wide attention for their promising prospects in solar cell field [2], mainly because they have electrical conductivity like metals and semiconductors, resulting from their narrow band gaps. The structures of PT derivatives substituted by side chains will change. The interesting result directly induced by this is the suddenly shrinking band gap.

All the geometries of the neutral and charged molecules are optimized at HF/6-31G\*\* level. The optical absorption spectra of polyisopnaphthothiophene (PINT) shown in Fig.1 are calculated using the singly excited configuration interaction states (CIS). Orbital cut analysis, frontier orbital and mulliken charge distribution analysis and local density of states (LDOS) analysis are used in this work.

Chain length effect is observed that the structures of PINT change from aromatic(A) to quinoid(Q) type structures when  $n \geq 8$  (Fig.1). The structural transformation will induce the formation of lone electrons in the ends of quinoid molecules. The approximate degenerate energy of these two lone electrons causes the energy gap to decrease, or even disappear (Fig.2). The curves in the potential figures (Fig.3) indicate that short chain PINT ( $n=3\sim 5$ ) prefers aromatic type and long chain PINT ( $n=10\sim$ ) prefers quinoid type structure. However, the structures of PINT with moderate size ( $n=6\sim 9$ ) are determined by the initial selected geometrical parameters, because there are two local minima in the potential curves for them (Fig.3). In Fig.3,  $\Delta E$  is the relative energy of each structures compared with

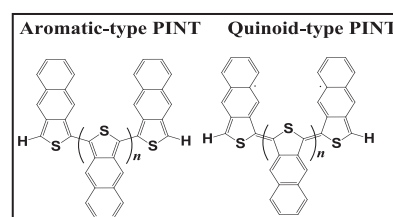


Fig.1 Two kinds structures of PINT

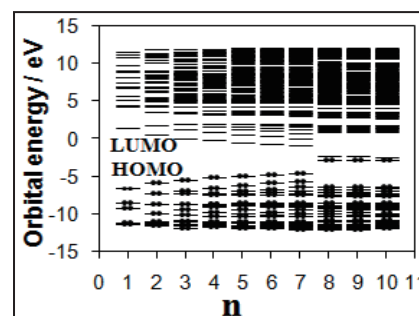


Fig.2 Energy levels of PINT in different sizes

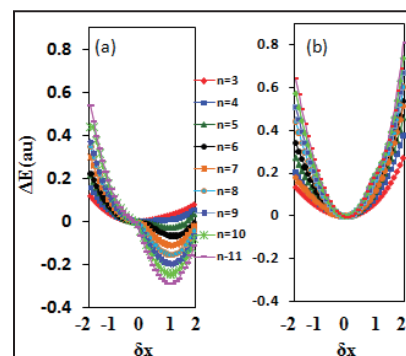
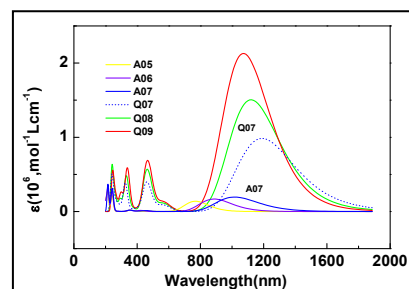


Fig.3 Potentials of PINT before and after orbital deletion

that of aromatic structures.  $\delta\chi = \frac{B_A - B}{B_A - B_Q}$ , in which  $B_A$ ,  $B_Q$  and  $B$  are the inter-units bond length of aromatic, quinoid and other PINT, respectively.

In UV/Vis/NIR spectra shown in Fig.4, a new absorption peak is found in the quinoid type PINT, which is corresponding to  $n \rightarrow \pi^*$  transition. It supports our assumption for the formation of lone pair electrons. This bipolaron is more excited, thus the absorption in NIR region is much stronger than that of aromatic structures.



**Fig.4 UV/Vis/NIR spectra of PINT in different type structures**

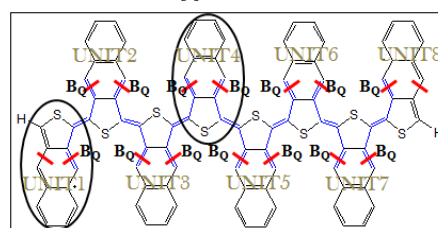


**Fig.5 The specified delocalized  $B_Q$  deleted by orbital cut analysis**

However, the HOMO and its similar LUMO are localized in both ends of quinoid PINT as shown in Fig. 6(a). It is not helpful for conductivity in the central part through the backbone. By orbital cut analysis (Fig.5), quinoid structures disappeared. The localized HOMO changes to delocalized one as shown in Fig.6 (b). It also induces the approximate degenerate energy disappearing. It implies that the delocalized  $\pi$  orbital in position  $B_Q$  is very important for the quinoid PINT formation.

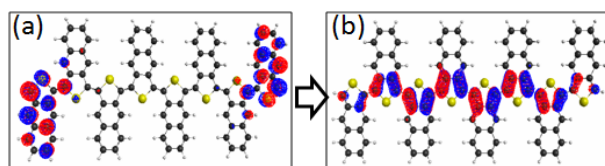


**Fig.6 HOMO of quinoid PINT changes after orbital cut**

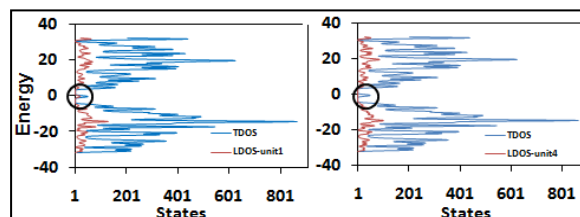


**Fig.7 TDOS and LDOS of PINT with eight units**

Short chain aromatic PINT is examined to be with no conductivity, while the long chain quinoid type PINT is clearly found to act as conductor like metals from the total density of states (TDOS) (Fig.7) analysis. And the conducting properties are mostly contributed by both the ends of the molecules through LDOS analysis [3].

PINT may be a kind of potential polymer conductors. The bipolaron is easier to be obtained if the delocalized  $\pi$  orbital in  $B_Q$  position is strong. The possibility of conduction in the central backbone is very small, when the bipolaron is formed in the structures, for the electron is localized in the ends of the molecule and it is hard to transfer through the backbone. This problem may be another key factor which is needed to be considered.

[1] A. Ramirez-Solis, B. kirtman, R. Bernal-Jaquez, C.M.Zicovich-Wilson, *J. Chem. Phys.* **130**, 164904 (2009).

[2] I. Osaka, T. Abe, S. Shinamura, K.Takimiya, *J. Am. Chem. Soc.* **133**, 6852(2011).

[3] Y. Aoki, A. Imamura, *J. Chem. Phys.* **97**, 8432(1992).

## Performance improvement in Organic Light-emitting Diodes via Modifying ITO Surface by an Au Layer

Dan Wang<sup>1</sup>, Katsuhiko Fujita<sup>1,2</sup>

<sup>1</sup> Department of Applied Science for Electronics and Materials, Kyushu University, Japan

<sup>2</sup> Institute for Materials Chemistry and Engineering, Kyushu University, Japan

Nanoparticles have attracted enormous interest in researching organic electronic devices due to unique features such as high dielectric constant. Here we report that gold nanoparticles dispersed on ITO surface perform good ability to enhance the current density and luminance in organic light emitting diodes (OLED). The hole-only device was also fabricated to verify the function of the gold nanoparticles.

The synthesis of hyper-branched polystyrene (HPS) and HPS-stabilized Au nanoparticles (HPS-Au) has been already reported [1]. The HPS-Au with Au concentration of 4.5wt% (against HPS) dissolved in toluene to form 0.3wt% solution was spin coated on ITO surface at 2000rpm. After being annealed at 80°C for 0.5 h in ambient environment, it was exposed under mercury lamp for 30min, then rinsed in solution for 30min followed by UV-ozone treatment for 30min.

The NPB (50nm), Alq3 (70nm), LiF (0.5nm) and Al (60nm) were evaporated sequentially under the pressure of  $4 \times 10^{-4}$  Pa. The device without Au nanoparticles was also prepared to research the effect of Au nanoparticles on devices. The hole-only device (ITO/HPS Au/NPB/Al) was fabricated by the same procedure without Alq3 and LiF.

From Fig.1, the current density is improved via modifying ITO surface by Au nanoparticles. The value of the device with HPS-Au rises at lower voltage obviously. When the current density is achieved at 100mA/cm<sup>2</sup>, the voltage is about 7V, which is almost 1.5V smaller than the device without HPS-Au.

Fig.2 shows that the luminance property is also improved by HPS-Au. At 8V, the luminance of the device with HPS-Au is achieved at 8875cd/m<sup>2</sup>, however, the value of the device without HPS Au is just 2898cd/m<sup>2</sup>. The maximum luminance is 24580cd/m<sup>2</sup>, which is 9880cd/m<sup>2</sup> higher, comparing with the device of without HPS-Au.

The current density profile of the hole-only devices (Fig. 3) clearly shows that the hole current in device with HPS-Au is much higher, indicating the significantly lower hole injection barrier.

The HPS-Au introduced between ITO surface and NPB can act as an injection layer to enhance the hole injection efficiency and driving voltage of OLEDs.

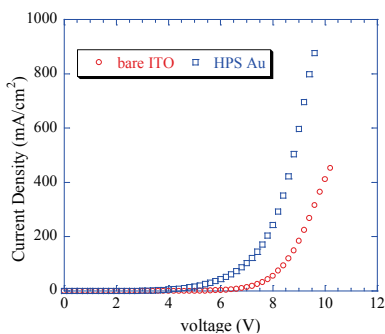


Fig.1 The current-density vs voltage characteristics of OLED devices with and without HPS-Au

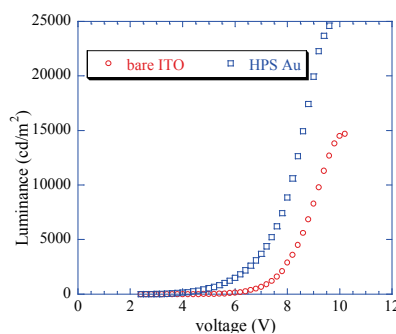


Fig.2 The luminance vs voltage characteristics of the OLED devices with and without HPS-Au

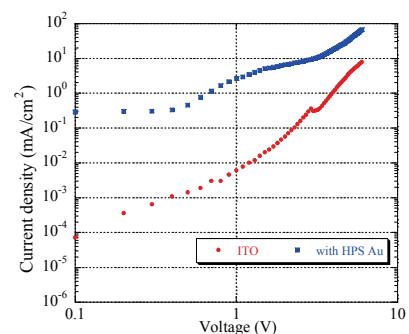


Fig.3 The current density vs voltage characteristics of the hole-only devices with and without HPS-Au

[1] H.Ichikawa, K. Yasui, M. Ozawa, K. Fujita. *Synthetic Metals*, 159, 973(2009).



## Improvement of cycling durability and device yield in the organic resistive memory composed of gold nanoparticles and hyper-branched polymer

Takahiro UENO<sup>1</sup>, Kei YASUI<sup>2</sup>, Masaaki OZAWA<sup>2</sup>, Keisuke ODOI<sup>2</sup>, Katsuhiko FUJITA<sup>1,3</sup>

<sup>1</sup> Graduate School of Engineering Science, Kyushu University, Japan

<sup>2</sup> Nissan Chemical Industries, Ltd., Japan

<sup>3</sup> Institute for Materials Chemistry and Engineering, Kyushu University, Japan

Recently, much attention has been paid to the organic memories for the next-generation nonvolatile memory. However, the driving mechanism has not been clarified yet and the device yield and the durability are poor to practical applications. The devices show two resistive states (ON/OFF states). We have shown that ON state should be caused by the conductive filaments formed by nanoparticles (NPs) in the polymer matrix (filamentary conduction model). Some particle aggregates initially formed at the bottom electrode interface could be the beginning points of filament growth. Therefore, it would be important to form particle aggregate uniformly in the device. In this study, we placed a higher concentrated particle layer on the bottom electrode in order to improve reproducibility of the devices. And we evaluated the cycling durability ON/OFF switching.

We used hyper-branched polystyrene (HPS) as host polymer and Au NPs which is protected by HPS (HPS-Au) as NPs. We fabricated the devices as follows. We spin-coated *o*-dichlorobenzene solution of HPS-Au (30 wt%) and annealed (150 °C, 30 min) in N<sub>2</sub> atmosphere. After UV exposure (30 min), we formed HPS / HPS-Au (4.5 wt%)(3/1 v/v) film under the same conditions. We formed aluminum as bottom/top electrodes by vacuum vapor deposition. And we also fabricated device without a higher concentrated particle layer as reference device.

The device yield was improved from 94 to 100 % by insertion of a higher concentrated particle layer. The cycling durability of ON/OFF switching also improved from about 100 to more than 1000 cycles. According to transmission electron microscopy (TEM) observation, these results would be because conductive filaments should be more uniformly formed and increased by insertion of a higher concentrated particle layer.

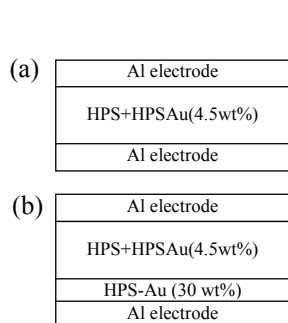


Fig.1 Device structure ;  
(a)Reference,  
(b) Double layer device

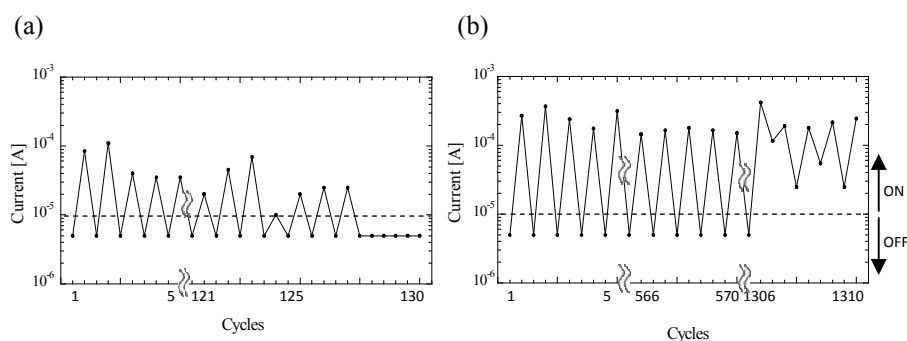


Fig.2 The cycling endurance;  
(a) Reference, (b) Double layer device

## Electrical Current Rectification in Boron, Nitrogen-doped Nanographenes and Cyclophanes

Aleksandar Staykov<sup>1</sup>, Kazunari Yoshizawa<sup>1,2</sup>

<sup>1</sup>International Institute for Carbon-Neutral Energy Research, Kyushu University, Japan

<sup>2</sup>Institute for Materials Chemistry and Engineering, Kyushu University, Japan

The electron-transport properties of boron and nitrogen doped nanographenes and cyclophanes are investigated with the non-equilibrium Green's function method and are compared to the transport properties of the unsubstituted species. Aim of the study is to derive the effect of the heteroatomic defects on the conductance of nanographenes and to suggest new effective ways for current control and design of carbon devices. Of special interest are the electrical current rectifying properties of asymmetrically doped nanographenes and cyclophanes, as well as the rectification mechanism. The mechanisms of donor- $\pi$  bridge-acceptor and donor- $\sigma$  bridge-acceptor rectification are used to explain the diode-like properties of asymmetrically doped nanographenes and cyclophanes. The electron-rich nitrogen and electron-poor boron heteroatoms introduce conductance channels within the HOMO-LUMO gaps of the hydrocarbons and cyclophanes and significantly enhance the conductance. The combination of nitrogen and boron impurities in one polycyclic aromatic hydrocarbon leads to asymmetrical I/V curve with rectification ratio of 2. The rectification is further enhanced in the cyclophanes where the boron impurities are located in one of the layers and the nitrogen impurities in the other. Due to the efficient separation of the donor and acceptor parts, rectification ratio of 7 was estimated. The rectifying properties of the asymmetrically doped carbon materials are analytically derived from the non-equilibrium Green's function theory. Qualitative calculations are performed with the non-equilibrium Green's function method combined with the Hückel theory. Quantitative calculations are performed with the non-equilibrium Green's function method combined with the density functional theory.

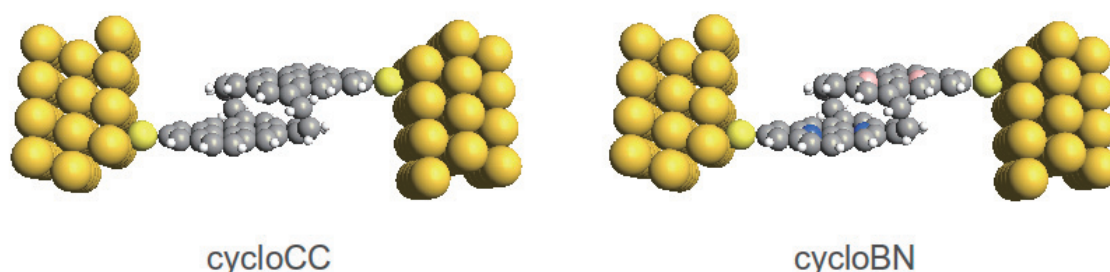


Figure 1: Cyclophane and boron, nitrogen-doped cyclophane junctions. cycloCC denotes the unperturbed cyclophane and cycloBN denotes the boron, nitrogen-doped cyclophane. Nitrogen is shown with blue color and boron is shown with pink color.

## Atomic Force Microscopic Study on the Structure of Cross-linked Polymers

Ken Kojio, Junpei Arata, Suguru Motokucho, Kohji Yoshinaga  
 Division of Chemistry and Materials Science,  
 Graduate School of Engineering, Nagasaki University

Cross-linked polymers are quite important especially for industrial applications. However, the structure-property relationship of these polymers is not clear on account of their complicated molecular structures. Polyurethane (PU) can be given as a good candidate for understanding the relationship because it is relatively easy to control the molecular weight between cross-linking points and the density of dangling chains. In this study, we synthesized the cross-linked PUs based on poly(oxypropylene) glycol (PPG) ( $M_n=1000$  and  $8000$ ) and trifunctional isocyanate (TKA) with various molecular weights between cross-linking points and the density of dangling chains. Then, the effect of these parameters on the phase structure of the cross-linked PU was investigated using atomic force microscope (AFM).

The cross-linked PU was synthesized with PPG and TKA by a one-shot method using dibutyltin diraulylate (DBTL) as a catalyst. To control the network structure of the cross-linked PU, the ratio of  $K=[\text{NCO}]/[\text{OH}]$  was changed from 0.8 to 1.2. Thermal property was investigated by differential scanning calorimetry. The glass transition temperatures were observed at  $-46.0$  and  $-64.0$  °C for PPG1000-TKA-1.04 and PPG8000-TKA-1.07, respectively. This difference can be ascribed to the difference in urethane bond concentration. Discussion in detail will be given below. Figure 1 shows AFM phase images for (a) PPG1000-TKA-1.04 and (b) PPG8000-TKA-1.07. In both images, one can see clear contrast, which might be from differences in interaction between a cantilever tip and the sample surface and viscoelasticity at the top sample surface. These differences could be from urethane bond concentration and density of dangling chain in this study. The size of darker parts in Figure 1 (a) was larger than those in Figure 1 (b). This trend might be due to molecular weight difference in PPG. Figure 2 shows AFM phase images for (a) PPG1000-TKA-0.80 and (b) PPG8000-TKA-1.20. The contrast in Figure 2 (b) was quite clear in comparison with Figure 2 (a). The cross-linked PU with a higher  $K$  value possesses higher cross-linking density, resulting in the formation of a rigid layer at the sample surface. Thus, it was reasonable to conclude from these results that the reason that the contrast in phase images was observed can be attributed to the difference of cross-linking density, which is induced by the difference in the number of molecules forming the closed-network.

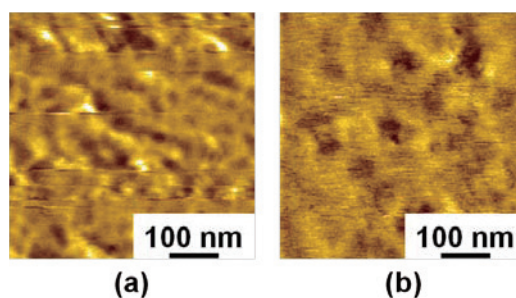


Figure 1 AFM phase images of (a) PPG1000-TKA-1.04-DBTL and (b) PPG8000-TKA-1.07-DBTL.

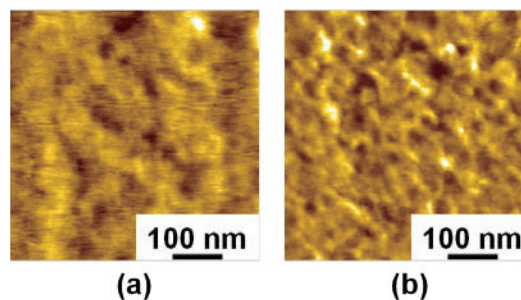


Figure 2 AFM phase images of (a) PPG1000-TKA-0.80 -DBTL and (b) PPG1000-TKA-1.20-DBTL.

## Peptide Nanocapsule Self-assembled from Viral $\beta$ -Annulus Peptide

Kazunori Matsuura,<sup>1,2</sup> Kenta Watanabe,<sup>1</sup> Tomohiro Nakamura,<sup>1</sup> Nobuo Kimizuka<sup>1,2</sup>

<sup>1</sup>Graduate School of Engineering, Kyushu University, Japan.

<sup>2</sup> International Research Center for Molecular Systems, Kyushu University, Japan.

Recently, application of plant viruses to nanotechnology have attracted much attention due to their fascinating nanostructures with discrete nano-space [1]. However, it remains difficult to rationally design artificial viral capsid. Supramolecular protein assemblies in biological system, such as viral capsids and clathrin, provide excellent models for the *de novo* design of artificial peptide nano-assemblies. For example,  $C_3$ -symmetric  $\beta$ -annulus motif peptide of tomato bushy stunt virus participates in the formation of dodecahedral internal skeleton. We have demonstrated that virus-inspired  $C_3$ -symmetric peptide conjugates self-assembled into nanocapsules [2-4].

In this paper, we report that a synthesized viral  $\beta$ -annulus peptide (24 residues) showed spontaneous self-assembly into hollow nanocapsules with the size of 30-50 nm in water (Fig. 1) [5]. The hollow structure was revealed by small angle X-ray scattering measurement. We also report self-assembly of Ni-NTA-modified  $\beta$ -annulus peptide into the stable nanocapsules and their complexation with His-tagged green fluorescent protein (GFP). GPC analyses of Ni-NTA-modified  $\beta$ -annulus peptide and His-tagged GFP revealed that the peptide nanocapsules complexed with His-tagged GFP.

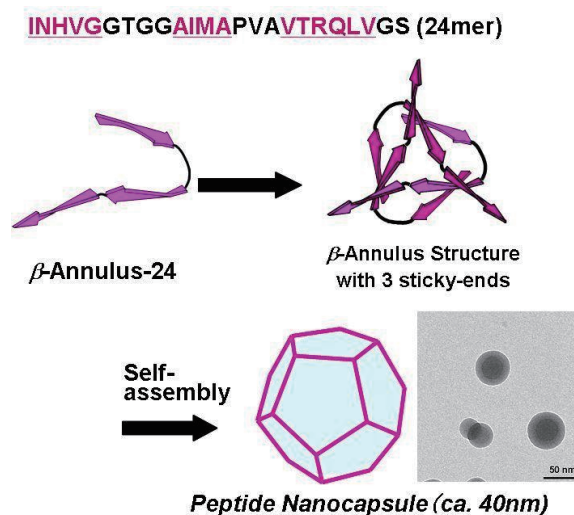


**Figure 1.** Schematic illustration of self-assembly of peptide nanocapsule from viral  $\beta$ -annulus peptide.

- [1] N. F. Steinmetz, D. J. Evans, *Org. Biomol. Chem.*, **5**, 2891 (2007).  
 [2] K. Matsuura, K. Murasato, and N. Kimizuka, *J. Am. Chem. Soc.*, **127**, 10148 (2005).  
 [3] K. Matsuura, H. Matsuyama, T. Fukuda, T. Teramoto, K. Watanabe, K. Murasato and N. Kimizuka, *Soft Matter*, **5**, 2463 (2009).  
 [4] K. Matsuura, H. Hayashi, K. Murasato, and N. Kimizuka, *Chem. Commun.*, **47**, 265 (2011).  
 [5] K. Matsuura, K. Watanabe, K. Sakurai, T. Matsuzaki, and N. Kimizuka, *Angew. Chem. Int. Ed.*, **49**, 9662 (2010).

## Development of Mesoporous Carbon Nanoreactors

Akari Hayashi<sup>1,2</sup>, Patrick Reinhard<sup>1,4</sup>, Katsuya Kato<sup>5</sup>, Kazunari Sasaki<sup>1,2,3</sup>

<sup>1</sup> International Research Center of Hydrogen Energy, Kyushu University, Japan

<sup>2</sup> International Institute for Carbon-Neutral Energy Research (WPI), Kyushu University, Japan

<sup>3</sup> Faculty of Engineering, Department of Mechanical Engineering, Kyushu University, Japan

<sup>4</sup> Swiss Institute of Technology (ETH), Switzerland

<sup>5</sup> National Institute of Advanced Industrial Science and Technology (AIST), Japan

Mesoporous carbon is known as a material with highly ordered pores, and we are particularly interested in such nano-space of mesoporous carbon (Fig. 1). It is very easily prepared through self-organization of carbon precursors (resorcinol, formaldehyde, triethylorthoacetate) and a surfactant (Pluronic F-127), followed by carbonization. The resulting pore structure is hexagonally ordered and three dimensionally extended. Interestingly, those pore size can be controlled by changing the experimental conditions. We treat carbon nano-space as a reaction site and develop carbon nanoreactors by further introduction of catalysts into the pores. A variety of nanoreactors can be developed with diverse catalysts, from metal catalysts to biological enzymes. Furthermore, by making use of high conductivity of mesoporous carbon, those nanoreactors can be applied to electrode materials. Here, we present two examples of such nanoreactors.

For the first example<sup>1-3</sup>, platinum metal catalysts together with ionomers are successfully introduced into nano-space, and electrochemical investigation of such nanoreactor results in a distinctive behavior, which is not observed with platinum on other carbon materials. For example, platinum catalysts inside the nano-space are very stable and able to form well dispersed small particles (1 nm or less) without aggregation. Reaction selectivity is also demonstrated with this nanoreactor. Any water-related electrocatalytic reactions are hindered, but proton-related reactions are promoted. Such a distinctive function is expected owing to hydrophobic nano-environment around platinum catalysts.

The second type of nanoreactors is made through introduction of an enzyme, Laccase, into the pores. Enzymes are known as environmentally friendly catalysts, but its low stability against outer environment is always a problem. In this study, the stability of Laccase is improved, and more interestingly its enzymatic activity is higher than that on regular carbon back even though more enzymes are adsorbed on carbon black. Since inter-particles pores of carbon black is much larger than pores of mesoporous carbon, enzymes are less adsorbed on nano-space of mesoporous carbon, but well aligned in small space. Such nano-environment probably results in high enzymatic reactivity.

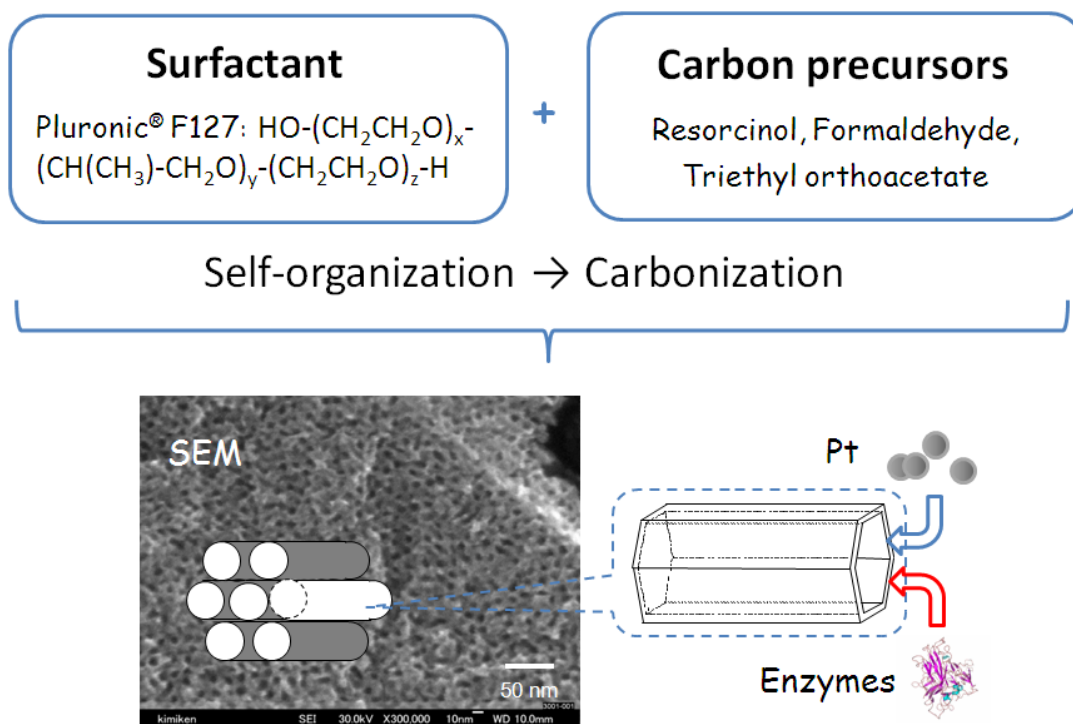


Fig. 1. Synthesis and structure of mesoporous carbon

- [1] A. Hayashi, H. Notsu, K. Kimijima, J. Miyamoto, I. Yagi, *Electrochim. Acta*, **53**(21), 6117 (2008).
- [2] A. Hayashi, K. Kimijima, J. Miyamoto, I. Yagi, *Chem. Lett.*, **38**(4), 346 (2009).
- [3] A. Hayashi, K. Kimijima, J. Miyamoto, I. Yagi, *J. Phys. Chem. C*, **113**(28), 12149 (2009).

## Tunable Domain in Phase-separated Monolayer of Hydrocarbon Guanidinium and Fluorocarbon Carboxylic Acid

Yushi Oishi<sup>1</sup>, Takayuki Narita<sup>1</sup>, Katsuhiko Ariga<sup>2</sup>, Toyoki Kunitake<sup>3</sup>

<sup>1</sup>Department of Chemistry and Applied Chemistry, Saga University, Japan

<sup>2</sup>World Premier International (WPI) Research Center for Materials Nanoarchitectonics (MANA), National Institute for Materials Science (NIMS), Japan

<sup>3</sup>Department of Chemical Processes and Environments, The University of Kitakyushu, Japan

The phase separation of hydrocarbon and fluorocarbon components due to the surface free energy difference is known to produce domains of submicrometer to micrometer. On the other hand, amphiphiles were molecularly miscible in a single phase through the electrostatic and hydrogen bonding interactions. We conceived that these opposing effects of immiscibility between hydrocarbon and fluorocarbon skeletons and attractive interaction, both electrostatic and hydrogen bonding, would be combined in controlling two-dimensional molecular mixing, resulting in the designed construction of nanometer-sized phase-separated surfaces. In this study, the phase separation behavior of (hydrocarbon guanidinium/fluorocarbon carboxylic acid) mixed monolayers at different subphase pHs and ionic strengths was investigated with an atomic force microscope (AFM).

A benzene/ethanol solution of hydrocarbon guanidinium (DG) and fluorocarbon carboxylic acid (DfmA) at a concentration of  $8 \times 10^{-4}$  M was spread on an aqueous solution of HCl, NaOH or NaCl at 293 K. The monolayer was transferred at  $20 \text{ mN m}^{-1}$  by the horizontal drawing-up method onto a freshly cleaved mica. Topographic image of the monolayer surface was obtained with a Seiko SPA 300 AFM which was operated in the constant force mode in air at 293 K by using a  $20 \times 20 \text{ }\mu\text{m}^2$  scan head and silicon nitride tip on a cantilever with a spring constant of  $0.022 \text{ N m}^{-1}$ .

Figure 1 shows an AFM image of the (DG/DfmA : 25/75) mixed monolayer with a scan area of  $60 \text{ nm} \times 60 \text{ nm}$ , where the brighter and darker portions correspond to the higher and lower regions of the monolayer surface, respectively. Round-like domains ca. 15 nm in diameter and 0.4 nm in height were observed above the surrounding surface. The heights from the mica substrate are estimated to be 1.1 and  $0.7 \pm 0.1 \text{ nm}$

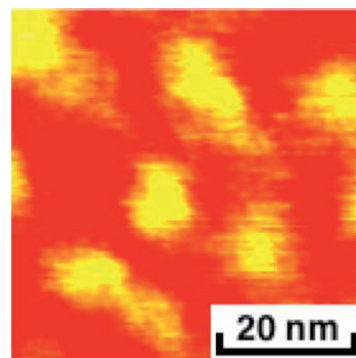


Fig.1 AFM image of (DG/DfmA) mixed monolayer.

for the higher (domain) and lower (surrounding) regions, respectively, by artificially piercing hole through the monolayer with an applied force stronger than  $10^{-9}$  N. These heights are consistent with the thickness of the respective monolayer of DG and DfmA. Therefore, it is clear that a phase separation between DG and DfmA molecules occurred in the mixed monolayer, and also that the higher and

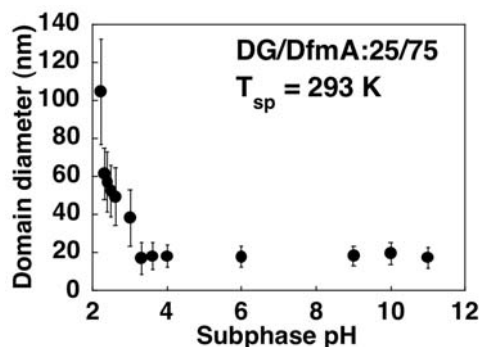


Fig.2 Subphase pH dependence of domain diameter in (DG/DfmA) mixed monolayer.

lower regions in AFM image were assigned to the aggregated regions of DG and that of DfmA, respectively. The subphase pH dependence of domain size in the (DG/DfmA : 25/75) mixed monolayer, evaluated from the AFM images of the monolayer at pH 2.3 – 11.0 is shown in Fig. 2. The domain size in the monolayer below pH 3.3 increased with decreasing pH to  $105 \pm 20$  nm at pH 2.3, whereas that above pH 3.3 was constant of 15 nm. Above pH 3.3 (higher degree of ionic dissociation), the phase separation by the surface free energy difference for hydrocarbon DG chain with cationic hydrophilic part and fluorocarbon DfmA chain with anionic one causes thermodynamic instability by excess repulsive energy among molecules in domain and matrix regions. Hence, the interfacial region between domain and matrix may increase, that is, smaller domain is formed to reduce the repulsive energy. Below pH 3.3 (lower degree of ionic dissociation), the surface free energy difference between hydrophobic parts of DG and DfmA in the mixed monolayer dominates the phase separation behavior, which results in formation of larger domain. Furthermore, the domain became large to be ca. 1  $\mu$ m in diameter at 0.6 M with increasing the concentration of NaCl in subphase.  $\text{Na}^+$  and  $\text{Cl}^-$  ions probably screen electrostatic force between hydrophilic parts of DG and DfmA to increase the immiscibility and promote the phase separation, resulting in formation of a fairly larger domain.

In conclusion, size control of two-dimensional cluster from nano to micrometer in phase-separated monolayer has been achieved by varying pH and ionic strength in subphase corresponding to change in electrostatic interaction between two hydrophilic parts in contribution factors to phase separation of the (DG/DfmA : 25/75) mixed monolayer.



## Morphological Control of Binary Block Copolymer Micelle Complexes by Varying Solution pH

Misook Lee<sup>1</sup>, and Kookheon Char<sup>1\*</sup>

<sup>1</sup> School of Chemical and Biological Engineering  
The National Creative Research Initiative Center for Intelligent Hybrids  
Seoul National University  
Seoul 151-744, Korea

The morphology of charged block copolymer micelle complexes, consisting of poly(styrene-*b*-acrylic acid) (PS-*b*-PAA) and poly(styrene-*b*-4-vinyl pyridine) (PS-*b*-P4VP) micelles, was controlled by pH of aqueous solvent. The charge densities of the corona block (PAA or P4VP blocks) dispersed in water were the sensitive functions of solution pH. The high pH region (pH > 6.5) is particularly interesting in the present case due to the formation of spherical micelle complexes since the degree of ionization of the P4VP blocks is almost negligible. These spherical clusters were then slowly transformed into different morphologies when the solution pH was adjusted to the range allowing both of the corona blocks to be oppositely charged. The morphological transitions of micelle blends were monitored by varying experimental parameters such as initial solution pH, aging time and blending ratio of two micelles when coupled with the effect of final solution pH. The present study demonstrates that the kinetic pathway for the formation and transformation of micelle complexes at various solution pH is significantly important for the control of packing symmetry involving charged polymeric nanoparticles

[1] J. Cho, J. Hong, K. Char and F. Caruso, *J. Am. Chem. Soc.*, **128**, 9935 (2006).

## Thermoresponsive Dispersion Property of Tri-arm Poly(NIPAAm-b-HEAAm) Diblock Copolymers

Md. Ashaduzzaman,<sup>1</sup> Shuhei Kai,<sup>1</sup> Shinobu Uemura,<sup>1</sup> Masashi Kunitake<sup>1,2</sup>

<sup>1</sup>Graduate School of Science and Technology, Kumamoto University, Japan

<sup>2</sup>CREST, JST, Japan

Block copolymers composed of a water-soluble segment and a thermo-responsive segment with the expectations of their emerging intelligent property that includes thermal self-assembles in water have been attracted much attention to the scientific community because of their promising applications such as drug and gene nanocarriers, sensors. In this presentation, we report the dispersion properties of tri-arm poly(NIPAAm-b-HEAAm)<sub>3</sub> (TNH) block copolymers synthesized via successive atomic transfer radical polymerization (ATRP) (Figure 1). ATRP allows us to design the formulation in terms of arms, block position and length of the block.

1,3,5-(2'-bromo-2-methyl-propionato) benzene was used as an initiator for ATRP of NIPAAm in dimethylsulfoxide and isopropanol binary solvent mixture first, then poly(NIPAAm) homopolymer was used as a macro-initiator for ATRP of HEAAm into ethanol and water mixture. Both ATRP were conducted using a suitable ligand/catalyst complex for predetermined reaction time. After purification by dialysis, the polymer products were characterized by <sup>1</sup>H-NMR and elementary analysis. The conformational change of NIPAAm units was also confirmed by <sup>1</sup>H-NMR in D<sub>2</sub>O.

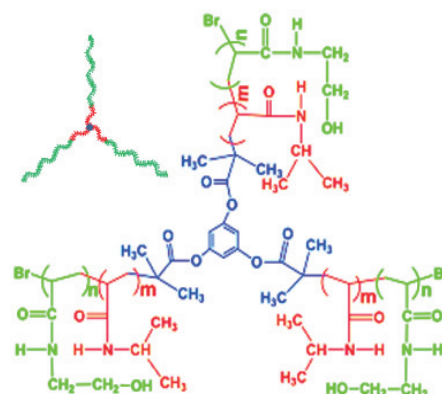


Figure 1. Structure of triarm poly(NIPAAm-b-HEAAm)<sub>3</sub> diblock copolymer.

The thermo-responsive dispersion properties of triarm shaped diblock copolymers of thermo-responsive polyN-isopropylacrylamide (poly-(NIPAAm)) as a core unit and polyN-hydroxy-ethylacrylamide (poly(HEAAm)) as a hydrophilic outer shell were successfully synthesized and characterized with poly(NIPAAm). The core and the outer shell were synthesized by ATRP. The dispersion properties of poly(NIPAAm-b-HEAAm)<sub>3</sub> and poly(NIPAAm) were investigated from two aspects, concentration and temperature dependencies. Various aggregation states from a homogeneous mono-dispersion (unimer) until a soft gel were able to be controlled generally by two factors, temperature and concentration and were investigated by fluorescence measurements, dynamic light scattering measurements (DLS) and turbidity measurements. The block polymer was completely dissolved in water up to 10<sup>-6</sup> M with no turbidity even above lower critical solution

temperature (LCST). Above the LCST (ca. 33.6 °C), poly(NIPAAm-b-HEAAm)<sub>3</sub> polymer (ca. 4 x 10<sup>-7</sup> M) aggregates, in which the NIPAAm moiety was shrunk and formed a hydrophobic core, were monitored by dynamic light scattering measurements, while no signal was observed below the LCST. The size of globular aggregates with diameter in the range 35 to 170 nm was kinetically controlled by incubation in the transition temperature region near the LCST. The size of globular aggregates was stable above that temperature region. The polymer should have potential in the biomedical field for applications such as temperature sensitive drug delivery systems or embolic agents.

#### References

Md. Ashaduzzaman, S. Kai, S. Uemura, M. Kunitake, *Chem. Lett.* **2011**, 40, 165-167.

## Thermo-responsive Soft Materials Prepared by Multi-crosslinking with Silica Nanoparticles

Md. Ashraful Alam<sup>1</sup>, Makoto Takafuji<sup>1,2</sup>, Hirotaka Ihara<sup>1,2</sup>

<sup>1</sup> Department of Applied Chemistry and Biochemistry, Kumamoto University, Japan

<sup>2</sup> Kumamoto Institute for Photo-Electro Organics (Phoenics), Kumamoto, Japan

Poly(*N*-isopropylacrylamide) PNIPAAm hydrogels are the most popular of temperature-sensitive soft materials. Owing to its unique thermosensitivity, PNIPAAm hydrogels have been developed for many applications such as drug delivery [1], tissue engineering [2] and switchable hydrogels [3]. However there are some problems due to the fact that the poor mechanical properties limit their applications. To improve the mechanical strength, several approaches using hybridization with inorganic nanoparticles have been reported: e.g., the surface modification of inorganic materials with organic polymer [4] or the construction of organic polymers with inorganic materials via the sol-gel method [5], or by in situ radical polymerization of a polymerizable monomer in an aqueous or organic dispersion of nanoparticles [6]. However, most of these hybrid hydrogels still have few disadvantages. For example, it takes a considerable amount of time to complete the gelation process, and unreacted monomers and initiators remain inside the resultant hydrogels that may occasionally induce undesirable effects in medical and biological uses.

Here, we introduce a new class of thermo-responsive hybrid soft materials prepared by using inorganic nanoparticles as multi-crosslinkers. The preparation method can be characterized by the fact that the copolymer having reactive anchoring groups was simply mixed with a silica nanoparticle (SiNP) suspension at room temperature. Therefore, impurities such as unreacted monomer and initiator cannot exist in the obtained hydrogel.

Poly(NIPAAm<sub>n</sub>-*co*-MAPTS<sub>m</sub>) was prepared by free radical polymerization of NIPAAm and methacryloylpropyl trimethoxysilane (MAPTS) in methanol at 60 °C using AIBN as an initiator and characterized by <sup>1</sup>H NMR and FTIR spectroscopies and size exclusion chromatography (Table 1). The diameter of silica nanoparticles (Nissan Chemical Industries, Ltd.) was measured by dynamic light scattering (DLS).

Table 1 : Characterization of poly(NIPAAm<sub>n</sub>-*co*-MAPTS<sub>m</sub>) and PNIPAAm

Polymer	NIPAAm/MAPTS		M <sub>w</sub> (x 10 <sup>5</sup> )	M <sub>n</sub> (x 10 <sup>5</sup> )	PDI
	Feed ratio	Real ratio <sup>a</sup>			
poly(NIPAAm <sub>n</sub> - <i>co</i> -MAPTS <sub>m</sub> )	100/1	105.7/1	2.96	1.19	2.48
PNIPAAm	100/0	-	2.15	0.75	2.87

<sup>a</sup> The real ratio of the resultant poly(NIPAAm<sub>n</sub>-*co*-MAPTS<sub>m</sub>)s were calculated from <sup>1</sup>H NMR spectra.

The thermo-responsive organic-inorganic hybrid hydrogels were prepared in a test tube by mixing the aqueous solution of poly(NIPAAm<sub>n</sub>-co-MAPTS<sub>m</sub>) and SiNP suspension. The onsite gelation was materialized by an inversion method at 25 °C. The transparent hybrid hydrogels (Fig. 1) were produced within few minutes to couple of days depending on the concentration and mixing ratio of copolymers and silica nanoparticles. In contrast, no gelation was observed for a

poly(NIPAAm<sub>n</sub>-co-MAPTS<sub>m</sub>) solution without SiNP. Moreover, PNIPAAm without an anchoring trimethoxysilyl group did not show any gelation even in mixing with high concentration of SiNP.

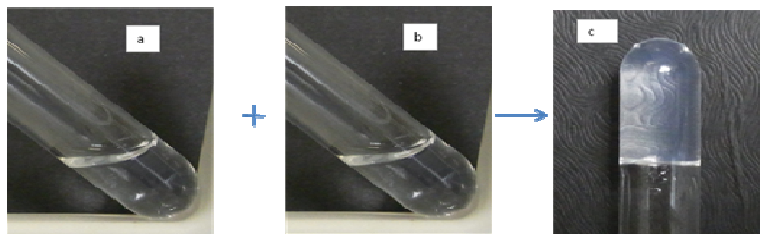


Fig 1. Typical example of hybrid polymer hydrogel from poly(NIPAAm<sub>n</sub>-co-MAPTS<sub>m</sub>) and SiNP.

These observations suggest

that the methoxysilyl groups of poly(NIPAAm<sub>n</sub>-co-MAPTS<sub>m</sub>) react with the silanol groups of SiNP as multiple crosslinker to form hybrid hydrogels. The thermosensitivity of hybrid hydrogels as well as the corresponding copolymers were evaluated by measuring the lower critical solution temperature (LCST). Poly(NIPAAm<sub>n</sub>-co-MAPTS<sub>m</sub>) and its hybrid hydrogel exhibited LCST around 32 °C. No significant influence to LCST was observed by using SiNP crosslinker. The hybrid hydrogel became turbid, shrank with increasing the temperature above LCST, and restored to a transparent hydrogel by lowering the temperature below LCST. The mechanical strength of the hybrid hydrogels was evaluated by a stress-strain test. For example, the compressive strength of the hybrid hydrogel prepared by mixing 5 wt% of poly(NIPAAm<sub>n</sub>-co-MAPTS<sub>m</sub>) with n/m = 106 and 10 wt% SiNP was found to be 177 kPa at 62 % compression.

In conclusion, a new class of thermo-responsive soft materials have been prepared by simply mixing functional copolymer having reactive anchoring groups with inorganic nanoparticles. Regarding the thermo-responsive properties of the hybrid materials, no undesirable perturbation with SiNP on LCST was observed.

- [1] A. Matsumoto, R. Yoshida, K. Kataoka, *Biomacromolecules*, **5**, 1038 (2004).
- [2] M. Yamato and T. Okano, *Mater. Today*, **7**, 42 (2004).
- [3] O. Kretschmann, S. W. Choi, M. Miyauchi, I. Tomatsu, A. Harada, H. Ritter, *Angew. Chem., Int. Ed.*, **45**, 4361 (2006).
- [4] E. Carlier, A. Guyot, A. Revillon, *React. Polym.*, **16**, 115 (1991).
- [5] M. W. Ellsworth, B.M. Novak, *J. Am. Chem. Soc.*, **113**, 2756 (1991).
- [6] K. Haraguchi, T. Takehisa, *Adv. Mater.*, **14**, 1120 (2002).

## Molecular weight dependence of viscoelastic properties for symmetric poly(styrene-block-2-vinylpyridine)

Long Fang<sup>1</sup>, Yoshiaki Takahashi<sup>1</sup>, Atsushi Noro<sup>2</sup>, Atsushi Takano<sup>2</sup>, Yushu Matsushita<sup>2</sup>

<sup>1</sup> Department of Molecular & Material Science, and Institute for Material Chemistry and Engineering, Kyushu University, Kasugakouen 6-1, Kasuga, Fukuoka 816-8580, Japan,

<sup>2</sup> Department of Applied Chemistry, Graduate School of Engineering, Nagoya University, Furo-cho, Chikusa-ku, Nagoya 464-8603, Japan

### Introduction

Block copolymers exhibit a phase transition between ordered (microphase-separated) and disordered (homogeneous) states at a certain critical temperature, commonly referred to order-disorder transition temperature ( $T_{ODT}$ ), which depends on molecular weight, block composition and interaction parameter of block segments [ref.1]. Phase behaviour of block copolymers have been widely investigated, especially for order-disorder transition (ODT) and order-order transition (OOT) [ref.2]. However, few research examined viscoelastic properties of block copolymers at molecular level, since it is very difficult to separate or specify the response at molecular level. If there is a block copolymer with the block components having almost the same physical properties, it will become possible to analyze viscoelastic properties at molecular level. Polystyrene (PS) and poly(2-vinylpyridine) (P2VP) are suitable block components for such study because they have almost the same Kuhn segment length and similar viscoelastic properties in bulk and common good solvents [ref.3]. Hence, in this study we will report the effect of molecular weight on the viscoelastic properties for symmetric poly(styrene-block-2-vinylpyridine) (SP) diblock copolymers in the ordered state.

### Experiment

Symmetric SP diblock copolymers with the molecular weight from  $1.0 \times 10^4$  to about  $40 \times 10^4$  and the corresponding PS homopolymers with almost the same molecular weight were pressed for 5 min at 150 °C to obtain the disc samples with the size of 8 mm diameter and 1.1 mm thickness for rheological measurements. The disc samples were placed into vacuum oven for 10 hrs at 110 °C before the rheological measurements. Rheological measurements were performed on a rheometer (Anton Parr, MCR300) using the parallel plate geometry. Frequency ( $\omega$ ) sweep was conducted from 100 to 0.01 rad/s at a constant strain of 1 % in a temperature range of 220~120 °C under N<sub>2</sub> gas after 10 min duration time before measurements at each temperature.

### Results and discussion

Because of nearly identical properties between PS and P2VP, master curve for SP diblock copolymers can be obtained with time temperature superposition principle by using WLF equation, which is the same as those for components. To examine the viscoelastic properties of ordered block copolymers at molecular level, the response from multi grain structure must be removed from the data, which can be described by the line with the slope of 1/2 as shown

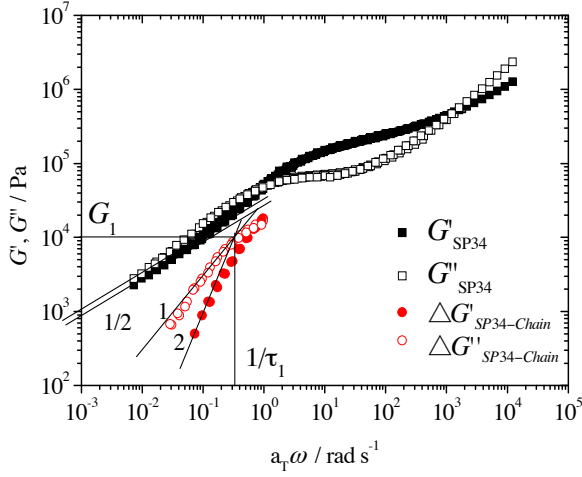


Fig. 1. Double logarithmic plots  $G^*$  and  $\Delta G^*$  against  $a_T \omega$  for SP34 at 160 °C.

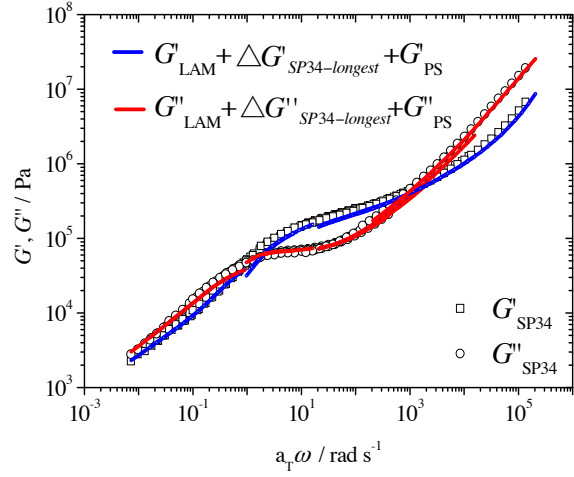


Fig. 2. Comparison of  $G^*$  between SP34 and the sum of three parts

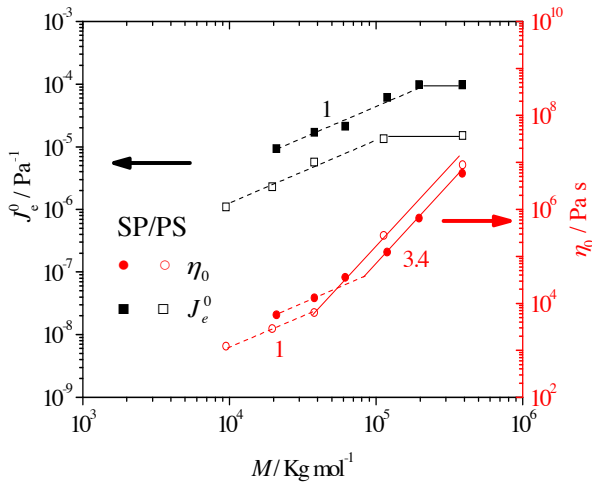


Fig. 3. Double logarithmic plots  $J_e^0$  and  $\eta_0$  against  $M$  for SP and PS at 160 °C.

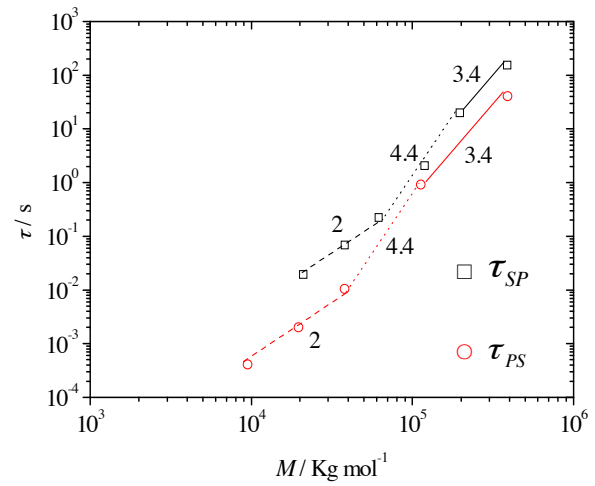


Fig. 4. Double logarithmic plots  $\tau$  against  $M$  for SP and PS at 160 °C.

in Figure 1. We obtained  $\Delta G^*$  by subtracting lamellar response from the raw modulus of SP diblock copolymers, which are also shown in Figure 1. By using  $\Delta G^*$ , which is approximated by the Maxwell model, lamellar response and PS modulus in the high frequency region were combined together and compared with the raw modulus of SP diblock copolymers as shown in Figure 2. It is observed that the modulus composed of three parts are nearly equal to the raw modulus of SP diblock copolymers. Therefore,  $\Delta G^*$  can be regarded as the response from the longest relaxation mechanism of chains in the ordered structure. We obtained  $\Delta G^*$  of other SP diblock copolymers by the same method and calculated zero-shear viscosity ( $\eta_0$ ), zero-shear steady-compliance ( $J_e^0$ ) and the longest relaxation time ( $\tau_{SP}$ ) for SP diblock copolymers from them. Molecular weight dependence

of  $\eta_0$ ,  $J_e^0$  and  $\tau_{SP}$  are shown in Figure 3 and 4. It is observed that the relationship of  $\eta_0$ ,  $J_e^0$ ,  $\tau_{SP}$  with  $M$  for SP diblock copolymers have almost the same scaling law with PS homopolymers, namely,  $\eta_0 \sim M^1$  when  $M < M_{C-SP}$  and  $\eta_0 \sim M^{3.4}$  when  $M > M_{C-SP}$ ,  $J_e^0 \sim M^1$  when  $M < M'_{C-SP}$  and  $J_e^0 \sim M^0$  when  $M > M'_{C-SP}$ ,  $\tau_{SP} \sim M^2$  when  $M < M_{C-SP}$ ,  $\tau_{SP} \sim M^{4.4}$  when  $M_{C-SP} < M < M'_{C-SP}$  and  $\tau_{SP} \sim M^{3.4}$  when  $M > M'_{C-SP}$ , where  $M_{C-SP} = 7.0 \sim 8.0 \times 10^4$  and  $M'_{C-SP} = 19 \sim 20 \times 10^4$ , which are about two times of the critical molecular weights for P2VP homopolymers. Further discussion will be presented at the meeting.

### Reference

- [1] Leibler, L. *Macromolecules*, **13**, 1602 (1980).
- [2] Abetz, V.; Simon, Peter F. W. *Adv. Polym. Sci.*, **189**, 125 (2005).
- [3] Takahashi, Y.; Ochiai, N.; Matsushita, Y.; Noda, I. *Polym. J.*, **28**, 1065 (1996).



## The morphological control of helical structures in mixtures of an ABC-triblock terpolymer and A-homopolymers

Song Hong<sup>1</sup>, Hidekazu Sugimori<sup>2</sup>, Kazuyuki Matsunaga<sup>2</sup>, Takeshi Kaneko<sup>2</sup>, Volker Abetz<sup>3</sup>, and Hiroshi Jinnai<sup>\*4,5</sup>

<sup>1</sup> Institute for Materials Chemistry and Engineering, Kyushu University, Japan

<sup>2</sup> Department of Macromolecular Science and Engineering, Kyoto Institute of Technology, Japan

<sup>3</sup> Institute of Polymer Research, Helmholtz-Zentrum Geesthacht, Germany

<sup>4</sup> JST, ERATO Takahara Soft Interfaces Project, Kyushu University, Japan

<sup>5</sup> WPI Advanced Institute for Materials Research, Tohoku University, Japan

We have previously reported the experimental visualization of the three-dimensional (3D) helical morphology of a polystyrene-*block*-polybutadiene-*block*-poly(methyl methacrylate) triblock terpolymer (SBM) using transmission electron microtomography (TEMT).[1] Our results revealed a double helical structure composed of polybutadiene (PB) helical microdomains around hexagonal-packed polystyrene (PS) cylinder cores in a poly(methyl methacrylate) (PMMA) matrix. By controlling the solvent evaporation rate on the film after solvent annealing, the homogeneous parallel and perpendicular orientations of the hexagonally packed helical structure were achieved in the SBM films with the thickness up to micron level. [2] This helical structure may have great potential as a base soft material for new applications, such as the template for fabricating nanosprings or nanocoils etc, which strongly demand a quantitative adjustment of the structure.

In this work, the morphology in mixtures of the SBM triblock terpolymer [ $M_n$ : 34k(S)-12k(B)-124k(M),  $M_w/M_n = 1.03$ ] and polystyrene homopolymers was observed by Dual-axis TEMT. Two polystyrene homopolymers were used here with different molecular weights, 8.4k and 97k, denoted by hPS<sub>84</sub> and hPS<sub>970</sub>, respectively. The morphology was found vary with the faction of PS-microdomains in the system ( $\Phi_{PS}$ ) and the molecular weight of homopolymer ( $M_{n,homo}$ ).

In hPS<sub>84</sub>/SBM mixture, the diameter of the double helical structure ( $D$ ) and the spacing between adjacent helical structures ( $L$ ) increased with increasing  $\Phi_{PS}$ , while the pith ( $p$ ) decreased simultaneously. When  $\Phi_{PS}$  reached 0.32, the helical structure broke up, and finally turned to spherical microdomains at  $\Phi_{PS} = 0.37$ , in which the PB spherules hexagonally arranged on the PS/PMMA interface. While in hPS<sub>970</sub>/SBM mixture,  $D$  and  $L$  increased more dramatically, compared with the hPS<sub>84</sub>/SBM mixture, while  $p$  kept constant. Moreover, the triple helices and four-stranded helices successively appeared in the hPS<sub>970</sub>/SBM system as  $\Phi_{PS}$  increasing. As  $\Phi_{PS}$  was up to 0.37, macroscopic phase of PS domains can be observed. (Fig. 1)

The morphology dependence on  $M_{n,homo}$  may involve the solubilization behavior of

homopolymers as a function of their molecular weights. [3] Since the PS block chains (bPS) are confined with one end fixed at the interfaces and with their segments restricted in the PS domain space, the mixing of these confined PS chains with hPS chains involves a significant loss of the conformational entropy in both the free chains (hPS) and the confined chains (bPS). Obviously the loss of the conformational entropy increases with increasing  $M_{n,homo}$ . Hence hPS with lower  $M_{n,homo}$  (*i.e.* hPS<sub>84</sub>) tends to uniformly swell the PS microdomain. And the addition of hPS on the interface of a PS microdomain changes the local volume fractions of three components of PS, PB and PMMA near the interface. The relatively decreasing of the volume fraction of PB results to the PB helices break up and eventually turns to spherical microdomains. Meanwhile, hPS with higher  $M_{n,homo}$  (*i.e.* hPS<sub>970</sub>) tends to cause the PS microdomains to swell less uniformly, resulting in hPS segregation toward the middle of the PS microdomains, or segregation out from the microdomain system to form a macroscopic phase. As few hPS chains distribute on the interface of PS microdomain, the local volume fractions of three components keeps a constant approximately. As a consequence, the helical morphology is maintained as the  $\Phi_{PS}$  increasing, while the number of helical strands thus increases to keep equilibrium of helix angle.

Hereby, we realized the quantitative adjustment of the structure parameters, *i.e.*

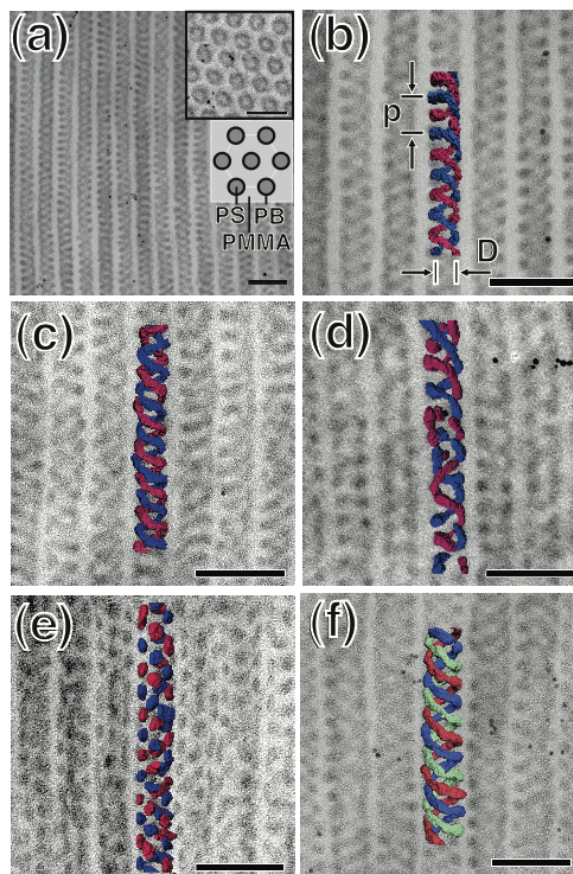


**Fig. 1** (a) TEM image of the neat SBM triblock terpolymer; (b) The 3D reconstructed images obtained in the neat SBM by TEMT; (c~f) TEM image and TEMT 3D reconstructed images in polymer mixtures [(c) SBM/hPS<sub>87</sub> with  $\Phi_{PS} = 0.30$ , (d) 0.32, (e) 0.37, and (f) SBM/hPS<sub>970</sub> with  $\Phi_{PS} = 0.26$ , respectively]. PB microdomains colored blue, red and green. Scale bars represent 100 nm in all images.

the diameter, pitch and spacing of helical structure of the PB microdomains in SBM triblock terpolymer by the means of the mixture of SBM and PS homopolymers. Moreover, the triple helix and four-stranded helix were achieved in this mixture system, which further enhanced the promising applications of the ABC-triblock terpolymer as the template for the synthesis of new materials.

- [1] H. Jinnai, T. Kaneko, K. Matsunaga, C. Abetz, V. Abetz, *Soft Matter.*, **5**, 2042 (2009).
- [2] S. Hong, H. Sugimori, T. Kaneko, V. Abetz, H. Jinnai, manuscript in preparation.
- [3] T. Hashimoto, H. Tanaka, H. Hasegawa, *Macromolecules*, **23**, 4378 (1990).

## Dynamical behavior of polystyrene grafted nanoparticles studied by X-ray photon correlation spectroscopy

Taiki Hoshino<sup>1,2</sup>, Moriya Kikuchi<sup>1,2</sup>, Daiki Murakami<sup>1,2</sup>, Koji Mitamura<sup>1,2</sup>, Yoshiko Harada<sup>1,2</sup>, Yoshihito Tanaka<sup>2</sup>, Sono Sasaki<sup>2,3</sup>, Masaki Takata<sup>2</sup>, Hiroshi Jinnai<sup>1,2</sup>, Atsushi Takahara<sup>1,2</sup>

<sup>1</sup> JST, ERATO Takahara Soft Interfaces Project, Japan

<sup>2</sup> RIKEN SPring-8 Center, Japan

<sup>3</sup> Graduate School of Science and Technology, Kyoto Institute of Technology, Japan

Although the dynamical behavior of nanoparticles in polymer matrix is different from that of the conventional Brownian motion [1], the details of such dynamical behavior are still unknown. Moreover, the dynamical features of polymer-grafted nanoparticles are rarely studied. In the present study, the dynamics of the polystyrene (PS)-grafted nanoparticles dispersed in PS matrix have been studied.

X-ray photon correlation spectroscopy (XPCS) has been installed at BL19LXU beamline of SPring-8 [2]. In an XPCS measurement, samples are coherently illuminated, and the fluctuation of scattered speckle intensity is observed. The time-autocorrelation functions  $g_2(q,t)$  are then acquired from the intensity fluctuation. Here,  $q$  and  $t$  are the wave vector and time, respectively. Representative  $g_2(q,t)$  at  $q \sim 2.56 \times 10^{-2} \text{ nm}^{-1}$  over the temperature,  $T$ , range between 443.15 K and 503.15 K are shown in Fig. 1. The relaxation behavior becomes faster as  $T$  increases, reflecting the decrease of the viscosity of the PS matrix. The temperature dependence of the PS-grafted nanoparticles was studied by the continuous time random walk (CTRW) model [3]. In the CTRW model, the particle motion is expressed by the discrete steps. The mean displacement of a particle after  $N$  steps is expressed by  $N^\alpha \delta$ , where  $\delta$  is the average length of a single jump. The parameter  $\alpha$  takes a value between 0 and 1.  $\alpha = 0.5$  and  $\alpha = 1$  represent the Brownian motion and the ballistic motion, respectively. From the fitting analysis of the measured  $g_2(q,t)$  at each temperature, we obtained  $\alpha \sim 0.8$  at  $T < 473.15$  K and  $\alpha \sim 0.5$  at  $T > 473.15$  K, indicating that the dynamical behavior of the nanoparticles is mostly Brownian in the higher temperature region, while it change to ballistic with decreasing temperature.

[1] V. Ganesan et al., *J. Chem. Phys.* **124**, 221102 (2006).

[2] T. Hoshino et al., *J.Phys: Conf. Ser.*, **272**, 012020 (2011).

[3] A. Duri et al., *Europhys. Lett.*, **76**, 972 (2006).

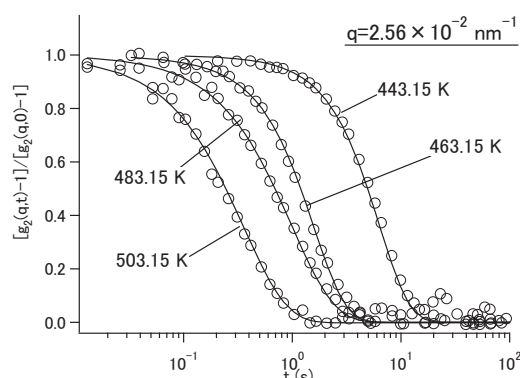


Fig. 1 Representative time-autocorrelation functions of the scattered speckle intensity from polystyrene-grafted nanoparticles in polystyrene matrix at various temperatures above matrix  $T_g$ .

## Self-healing properties of cross-linked polymers with radically exchangeable dynamic covalent bond units

Keiichi Imato<sup>1</sup>, Takeshi Kanehara<sup>1</sup>, Yoshifumi Amamoto<sup>1</sup>, Masamichi Nishihara<sup>2</sup>,  
Atsushi Takahara<sup>1,2</sup>, Hideyuki Otsuka<sup>1,2</sup>

<sup>1</sup> Graduate School of Engineering, Kyushu University, Japan

<sup>2</sup> Institute for Materials Chemistry and Engineering, Kyushu University, Japan

Self-healing materials attract a lot of attention because of their ability to repair the internal and external damage. Thereby, they can extend their lifetimes, lead to reduce the waste, and moreover have the potential to be applied to many applications that we cannot repair easily. Diarylbibenzofuranone (DABBF) which is a novel dynamic covalent bond unit can reach a state of radically thermodynamic equilibrium under air at room temperature without any stimuli. Furthermore, DABBF and radical species formed from cleaved DABBF are tolerant of oxygen [ref. 1]. In this research, we synthesized self-healable gels by introducing DABBF into cross-linked polymers and evaluated their chemical and mechanical properties (Fig. 1) [ref. 2].

Cross-linked polymers with DABBF as a cross-linker were prepared by polyaddition of DABBF **1** and tolylene diisocyanate terminated polypropylene glycol. We confirmed the reaction proceeded successfully because the reaction mixture lost the fluidity.

The cross-linked polymer gels dissolved in a solvent containing excess DABBF **1** at room temperature. This behavior showed that exchange reaction between DABBF **1** and cross-linking sites well proceeded. Furthermore, the gels swollen with DMF can self-heal by contacting samples together after they were cut by a razor (Fig. 2). Self-healing behavior was verified from the complete recovery of mechanical properties and the control experiment.

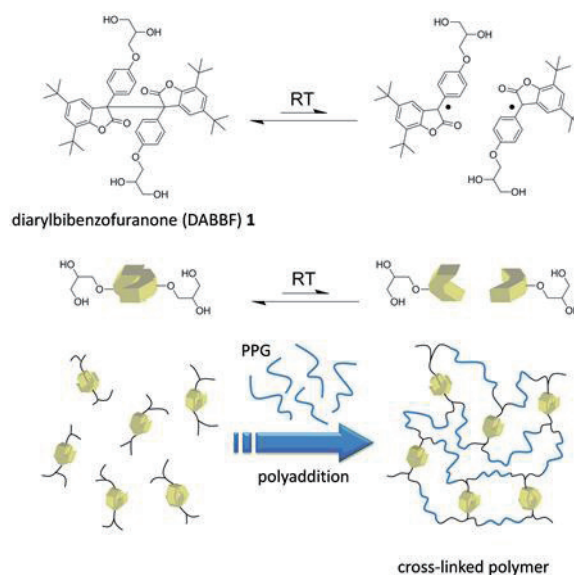


Fig. 1. Chemical structure and equilibrium of DABBF and scheme of synthesis of cross-linked polymer with DABBF.

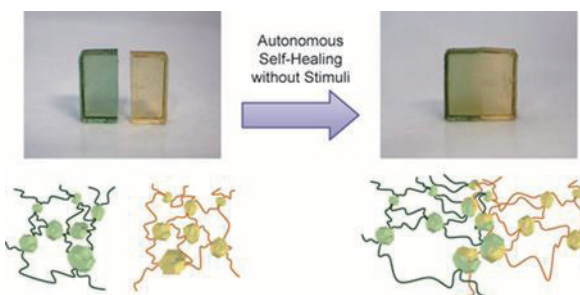


Fig. 2. Photographs and images of chemical gels with DABBF before and after self-healing.

[1] J. C. Scaiano et al., *J. Am. Chem. Soc.* **2006**, *128*, 16432-16433.

[2] K. Imato et al., submitted for publication.

## Layer-by-Layer Self-assembly Containing Drug-encapsulating Nano Particles on Polyanion- modified Stainless Steel Substrate

Mamiko INOUE<sup>1</sup>, Xu HANG<sup>1</sup>, Jin NISHIDA<sup>2,3</sup>, Motoyasu KOBAYASHI<sup>2,3</sup>,  
Kaku NAKANO<sup>4</sup>, Kensuke EGASHIRA<sup>4</sup>, Atsushi TAKAHARA<sup>1,2,3</sup>

<sup>1</sup>Graduate School of Engineering, Kyushu University

<sup>2</sup>JST, ERATO, Takahara Soft Interfaces Project

<sup>3</sup>Institute for Materials Chemistry and Engineering, Kyushu University, Fukuoka, Japan

<sup>4</sup>Graduate School of Medical Sciences, Kyushu University

### Introduction

Catechol group has been widely known as an adhesive functional group due to its strong interaction with metal oxide[1,2]. We synthesized adhesive anionic copolymer (P1) containing the catechol groups to modify a stainless steel (SUS) surface in order to adsorb sufficient amount of cationic nano particles (NP) on this surface by electrostatic interaction.

### Experimental

Conventional free radical polymerization of *N*-(3,4-dihydroxyphenyl) ethylmethacrylamide (DMAm) and 3-sulfopropyl methacrylate, potassium salt (SPMK) was carried out to prepare poly(DMAm)-*ran*-poly(SPMK) (DMAm/SPMK = 0.20/0.80) (P1). A SUS plate was dipped into aqueous solution of P1 or poly(SPMK) for 30 minutes and annealed at 100 °C for 6 hours. The substrates were alternately dipped into the solution of positive-charged poly(lactic-*co*-glycolic acid) NP encapsulating fluorescein isothiocyanate (FITC-NP) and negatively charged heparin (Hep) solution. Multilayer of FITC-NP and Hep denoted as (FITC-NP)<sub>*n*</sub>(Hep)<sub>*k*</sub> was obtained by *n* th and *k* th deposition of FITC-NP and Hep solution. The multilayers-built SUS plate was immersed in Tris buffer solution (pH=7.4) to release FITC-NP at 25 °C. The concentration of released FITC-NP in the solution was estimated by spectrophotofluorometer.

### Results and Discussion

When the homo poly(SPMK) was coated on the SUS substrate, polymer layer was immediately removed from the surface by washing with water, while the P1 remained on the substrate even after the washing or dip-coating process, which were confirmed by XPS and fluorescence microscopy. P1 anchored on SUS surface through the chelation of catechol group with metal oxide to form stable anionic layer, which enhanced the efficient adsorption of cationic NP.

Fig. 2 shows evolution of FITC-NP release from (FITC-NP)<sub>3</sub>(Hep)<sub>3</sub> layer on P1-modified SUS. The concentration of released FITC-NP in the solution began to increase just after the deposition of the substrate in a buffer solution and saturated within 60 min. The release rate and period could be controlled by the multilayer number and the chemical structure of polymers.

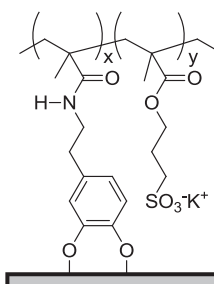


Fig. 1 Chemical structure of P1

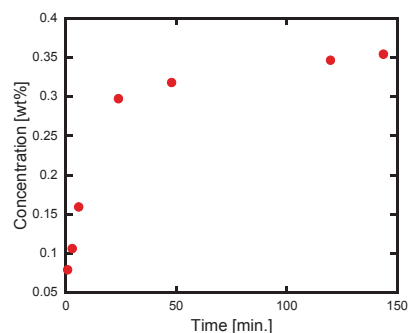


Fig. 2 Cumulative amount release profile of FITC-NP from multilayer film on SUS.

[1] P. B. Messersmith, *et al.*, *PNAS*, **103**, 12999-13003 (2006).

[2] H. J. Butt, *et al.* *Adv. Mater.*, **20**, 3872-3876 (2008).

## Characterization of a Cationic Polymer Brush on Silica Nanoparticle Prepared by Surface-initiated ATRP

Tatsuya Ishikawa<sup>1</sup>, Moriya Kikuchi<sup>2</sup>, Motoyasu Kobayashi<sup>2</sup>, Atsushi Takahara<sup>1,2,3</sup>

<sup>1</sup>Graduate School of Engineering, Kyushu University, Japan

<sup>2</sup>JST, ERATO Takahara Soft Interfaces Project, Japan

<sup>3</sup>Institute for Materials Chemistry and Engineering, Kyushu University, Japan

### Introduction

Chain dimensions of surface-tethered polyelectrolytes on the nanoparticle in the aqueous solution are important for the colloidal stability and dispersion. In this study, well-defined cationic polymer with narrow molecular weight distribution were immobilized on a silica nanoparticle (SiNP) by surface-initiated atom transfer radical polymerization (SI-ATRP) to investigate the influence of the salt concentration on the chain dimensions of a cationic polymer tethered on a surface.

### Experimental

SI-ATRP of 1-(2-methacryloyloxy)ethyl-3-ethylimidazolium chloride (MEImCl) from alkyl bromide-immobilized SiNP with a radius of 54 nm was carried out in 2,2,2-trifluoroethanol for 24 h at 60 °C. Surface-grafted polymer was cleaved by treatment with HF aqueous solution to determine the molecular weights ( $M_n$ ) and  $M_w/M_n$ . Chain dimensions of surface-tethered polymer was characterized in the aqueous NaCl solutions at various salt concentrations by dynamic light scattering (DLS), and small angle X-ray scattering (SAXS) measurements. Radius of gyration of polymer layer was estimated from SAXS profiles using the core-shell model considering interacting excluded-volume chains and assuming Schulz distributed core with the radius of gyration of polymer layer.<sup>1</sup>

### Results and Discussion

The  $M_n$  and  $M_w/M_n$  of cleaved poly(MEImCl) determined by aqueous SEC measurement were 169,000 and 1.13, respectively. The graft density was 0.021 chains/nm<sup>2</sup> estimated from the determined values of  $M_n$ ,  $R_c$  and weight of grafted-polymer. Hydrodynamic radius ( $R_H$ ) of poly(MEImCl)-g-SiNP obtained by DLS was converted to hydrodynamic radius of polymer layer ( $R_{H, brush}$ ) by  $(R_H - R_c)/2$ . As shown in Figure 1,  $R_{H, brush}$  gradually decreased with an increase in salt concentration of sodium chloride from 0 to 1.0 mol/L. Reduction of  $R_{H, brush}$  can be explained by screening of electrostatic repulsion between the monomer units by added salt,<sup>2</sup> resulting in a change in the conformation of polymer chain.

### References

- [1] J. S. Pedersen, et al. *Macromolecules* **2003**, *36*, 416.  
 [2] A. Takahashi, et al. *J. Phys. Chem.* **1970**, *74*, 944–946.

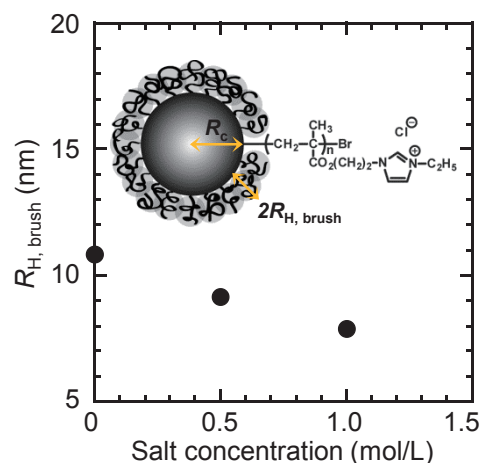


**Figure 1.** Dependence of  $R_H$  on salt concentration for poly(MEImCl)-g-SiNP in aqueous NaCl at 298 K.

## Hybrid Polymer Nano Films Prepared by Interfacial Click Reaction

Shuhei Kai<sup>1</sup>, Md. Ashaduzzaman<sup>1</sup>, Shinobu Uemura<sup>1</sup>, Masashi Kunitake<sup>1,2</sup>

<sup>1</sup>Graduate School of Science and Technology, Kumamoto University

<sup>2</sup>Core Research for Evolutional Science and Technology,  
Japan Science and Technology Corporation (JST-CREST)

Since the introduction of the concept by Sharpless and coworkers<sup>1</sup> in 2001, click reactions have attracted great attention, because of their unique properties such as high selectivity and high efficiency under ambient condition. Various hierarchical nanostructured polymers, such as block polymers, polymer gel networks and modified dendrimers have been synthesized by using click reaction. Recently, the click reaction has been conducted not only in homogeneous media but also on surfaces or at interfaces.

Herein, we report new class of polymer materials, including thin films, soft gels, and hollow capsules, consisting of composite polymer nanofilms which were prepared by the Cu(I)-catalyzed Huisgen click reaction between lipophilic polymers or between lipophilic and hydrophilic polymers (Fig. 1). To confirm the feasibility of interfacial click reaction taking place at an oil-water interface, three lipophilic and one hydrophilic

polymer bearing an alkyne group, poly(2-hydroxy-3-azidopropyl methacrylate) (p-HAzPMA), poly(styrene-co-2-azidoethyl acrylate) (p-Sty-co-AzA), poly[propargyl(2-propynyl) methacrylate] (p-PgMA), and poly(sodium styrenesulfonate-co-propargyl acrylate) (p-NaSS-co-PgA), were synthesized by thermal radical polymerization. As three components, azide polymer, alkyne polymer and copper catalyst, were arranged into aqueous phase and oil phase separately, the polymer-polymer cross-linking reaction is proceeded only at the interface. Figure 2 shows O/W hollow capsules consisting of p-Sty-co-AzA and p-NaSS-co-PgA which were synthesized by interfacial click reaction (Type B). Especially, the combination of lipophilic azide polymers and hydrophilic alkyne polymers allowed us to provide “Janus” nanofilms both with hydrophilic and lipophilic surfaces.

[1] H. C. Kolb, M. G. Finn, and K. B. Sharpless, *Angew. Chem. Int. Ed.*, **40**, 2004 (2001).

[2] S. Kai, M. Ashaduzzaman, S. Uemura, and M. Kunitake, *Chem. Lett.*, **40**, 270 (2011).

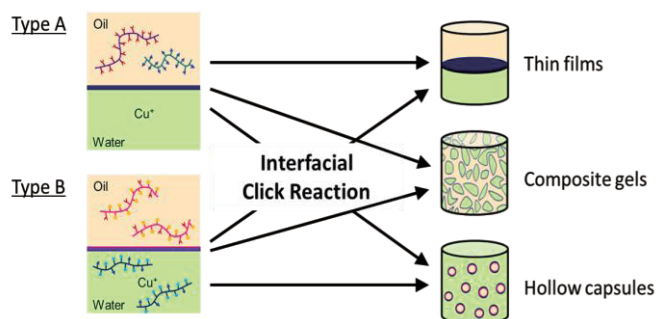


Fig. 1. Schematic representation of homo- and hetero-type liquid-liquid interfacial click reactions and products.

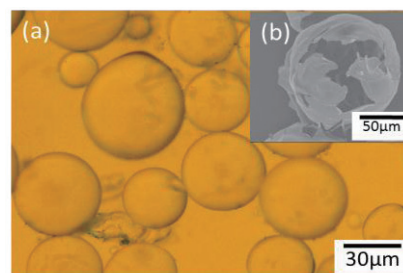


Fig. 2. Optical microscope (a), and SEM (b) images for hetero-crosslinked O/W hollow capsules consisting of p-Sty-co-AzA and p-NaSS-co-PgA.



## Crystallization of calcium carbonate in thermotropic liquid crystalline phases by use of new crown ether complex with calcium cation

Shouta Daiki<sup>1</sup>, Hiroki Higuchi<sup>2</sup>, Yasushi Okumura<sup>2</sup>, and Hirotsugu Kikuchi<sup>2</sup>

<sup>1</sup>Interdisciplinary Graduate School of Engineering Sciences, Kyushu University, Japan

<sup>2</sup>Institute for Materials Chemistry and Engineering, Kyushu University, Japan

Biomimetalization is the process by which living organisms produce minerals such as calcium carbonate. The structures of their biomimetalins are highly controlled from the nano- to the macroscopic level, resulting in complex architectures that provide multifunctional properties. In this study, we investigated the method for crystallization of calcium carbonate in thermotropic liquid crystalline phases with molecular orientational order by use of the new crown ether derivatives as calcium ion carriers (Fig.1) [1].

Samples were prepared by the mixture of 97 wt% 4-cyano-4'-pentylbiphenyl ; 5CB (Aldrich) and 3 wt% calcium cation-complexed crown ether derivatives. The mixture was placed in contact with water in the sandwiched glass cells. The glass cells were then placed in a closed desiccator together with ammonium carbonate for 10 days in 30°C (Fig.2) [2].

The precipitated crystals was observed by polarizing optical microscopy and scanning electron microscopy (SEM). As shown in Fig.3a, The precipitated crystals was observed not only near the interface between liquid crystal and water, but also around the liquid crystal phases. This result could be due to the carbonate ions which was produced by the reaction of small amount of water in liquid crystal phases and CO<sub>2</sub> gas. It was found that the precipitated crystals had the anisotropic shape by SEM observation (Fig.3b). It is suggested that the crystallization was affected by the nematic liquid crystal with orientational order.

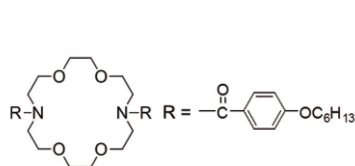


Fig.1 New crown ether derivative

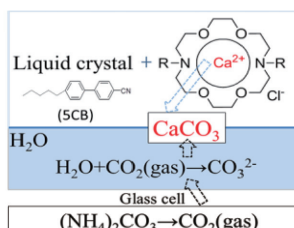


Fig.2 Method of crystallization by use of the carbon dioxide gas

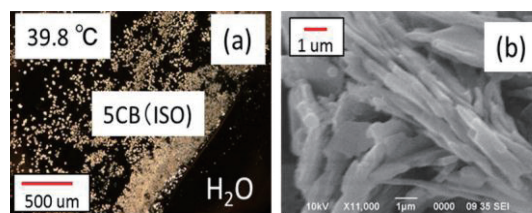


Fig.3 Polarizing optical micrographs near the interface between liquid crystal and water in the sandwiched glass cells (a). SEM images of the precipitated crystals (b).

### [Acknowledement]

This work was supported by Grant-in-Aid for Scientific Research on Innovative Areas of " Fusion Material : Creative Development of Materials and Exploration of Their Function through Molecular Control " (no. 2206) from the Ministry of Education, Culture, Sports, Science and Technology, Japan (MEXT).

[1] C. P. Pedersen, *J. Am. Chem. Soc.*, **1967**, 89, 7017.

[2] T. Nishimura, T. Ito, Y. Yamamoto, M. Yoshio, and T. Kato, *Angew. Chem. Int. Ed.*, **2008**, 120, 2842.

## Stimuli Responsive Triblock Copolymers Based on Polyrotaxane

Miseon Jung, Ildoo Chung

Department of Polymer Science and Engineering,  
Pusan National University, Busan 609-735, Korea

Cyclodextrins(CDs) are well known to form inclusion complexes with various compounds because of their hydrophobic cavity[1]. This inclusion phenomenon leads to significant changes of the solution properties of the guest molecule[2]. Hydrophobic, water-insoluble molecules become water-soluble by treatment with aqueous solution of cyclodextrins without any chemical modification of the guest molecule. A large number of monomers can be homo- or copolymerized under simple conditions but, in general, it does not result in polymers with well-defined structures by conventional free radical polymerization. Using living radical polymerization, it is possible to synthesize well-defined polymers with desired molecular weights and low polydispersities[3]. Here stimuli responsive triblock copolymers were synthesized by the polymerization of n-isopropyl acrylamide(NIPAAm) by ATRP under environmentally friendly conditions with pseudopolyrotaxane initiator, in which many cyclodextrins threaded onto polyether glycol.

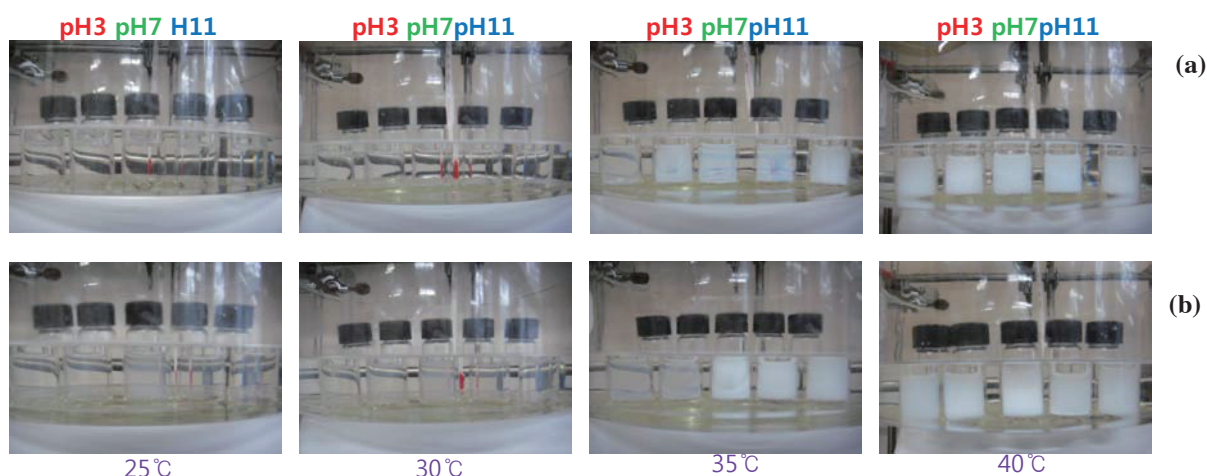


Fig. 1. Stimuli responsive behaviors of (a)PEG and (b)PPG based triblock copolymers.

The synthesized triblock copolymers were also used to evaluate their stimuli responsive behaviors, such as pH and thermal responsivities. As shown in Fig. 1, polyrotaxane based triblock copolymers have different dual responsive behaviors depending on the values of pH and temperature.

[1] H. Ritter, M. Tabatabai, *Prog. Polym. Sci.*, **27**, 1713 (2002).

[2] L. He, J. Huang, Y. Chen, Li. Liu, *Macromolecules*, **38**, 3351 (2005).

[3] J. Storsberg, M. Hartenstein, A. H. E. Muller, H. Ritter, *Macromol. Rapid Commun.*, **21**, 1342 (2000).

## Self Polishing Properties of Antifouling Paint Resins based on Polyurethane Matrices

S.H. Ryu<sup>1</sup>, S.M. Park<sup>1</sup>, H. Park<sup>2</sup>, I.W. Lee<sup>2</sup>, H.H. Chun<sup>2</sup> and N.J. Jo<sup>1\*</sup>

<sup>1</sup>Department of Polymer Science & Engineering, Pusan National University,

<sup>2</sup>Advanced Ship Engineering Research Center, Pusan National University,  
San 30, Jangjeon-dong, Gumjeong-gu, Busan, 609-735, South Korea

\* namjujo@pusan.ac.kr

Antifouling paints have a primary role in the marine industry as protecting the attachment of biofouling in marine environment and reducing the fuel consumption of ships. Since the use of tributyltin(TBT) groups in antifouling paints was banned internationally, the development of new antifouling coating with biocidal effects on the marine organisms and no potential accumulation for the aquatic environment has been required. Polyurethane(PU) coatings are increasingly used instead of traditional coatings because their superior properties and longer lifetimes greatly lengthen the interval between refurbishments. So, in the study, we synthesized the novel self polishing resins by applying PU matrices with different polyols and various quaternary ammonium salts which are effective biocides. The thickness change of the resin by dynamic immersion in artificial seawater was checked to investigate the self polishing property. As shown in Fig. 1, PU(PTAd600)-C09 with poly(tetramethylene dipate) glycol of molecular weight of 600g/mol(PTAd600) and tripropylamine(C09) has had good erosion property. And Fig. 2 shows the fouling rate of each coatings in the seawater for 10 weeks. Consequently, We predict PU(PTAd600)-C09 will be the potential antifouling resin in the near future.

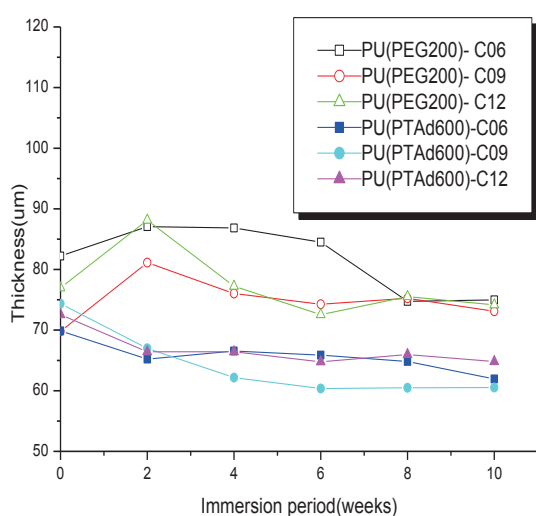


Fig. 1. The thickness change of PU coating by dynamic immersion.

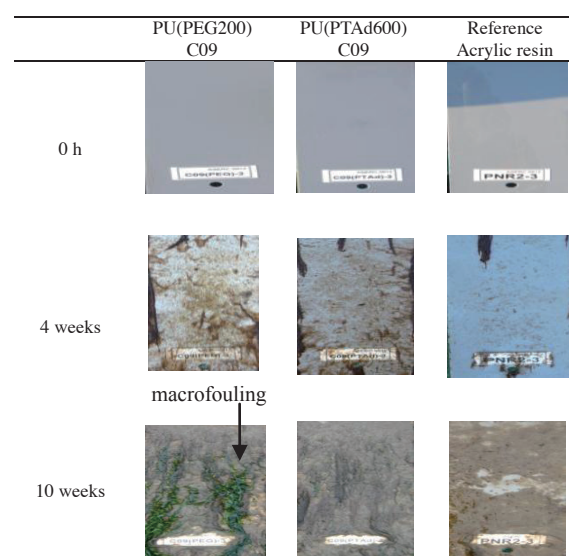


Fig. 2. The fouling rate of each PU coatings during immersion periods.

## Shape Evolution of Flag-type of Silver Nanostructures in DMF Solution

Masaharu Tsuji<sup>1</sup>, Xinling Tang<sup>2</sup>, Keiko Uto<sup>1</sup>, and Mika Matsunaga<sup>1</sup>

<sup>1</sup> Institute for Materials Chemistry and Engineering, Kyushu University, Japan

<sup>2</sup> Graduate School of Engineering Sciences, Kyushu University, Japan

Shape evolution of novel flag types of silver nanostructures has been studied using a two-step reduction method. At low  $\text{AgNO}_3$  concentrations, trapezoid and triangular platelike structures having  $\{111\}$  facets were evolved from long side  $\{100\}$  facets of Ag nanorods. At higher  $\text{AgNO}_3$  concentrations, tetrahedral flags having  $\{111\}$  facets were evolved from equilateral triangular plates. Growth mechanisms of flag-type of silver nanostructures are discussed.

For the past twenty years, extensive studies have been carried out to develop preparation methods of novel shapes of metallic particles and their application. We have recently studied shape evolution of novel flag types of silver nanostructures using a two-step reduction method.<sup>1</sup>

In the first step, pentagonal Ag nanorods were prepared by polyol reduction of  $\text{AgNO}_3$  in ethylene glycol in the presence of PVP. In the second step,  $\text{AgNO}_3$  was reduced in DMF in the presence of Ag nanorod-seeds and PVP. Then trapezoid and triangular platelike structures having  $\{111\}$  facets were evolved from long side  $\{100\}$  facets of Ag nanorods (Figs. 1a-1e). At higher  $\text{AgNO}_3$  concentrations, tetrahedral flags having  $\{111\}$  facets were evolved from equilateral triangular plates (Fig. 1f). The crystal structures of flag types of Ag nanostructures are determined and their growth mechanisms are discussed on the basis of TEM, SEM, SAED, and TEM-EDS data. It was found that tetrahedral flags were grown either through the formation of two equilateral triangular plates connected on a nanorod or through the crystal

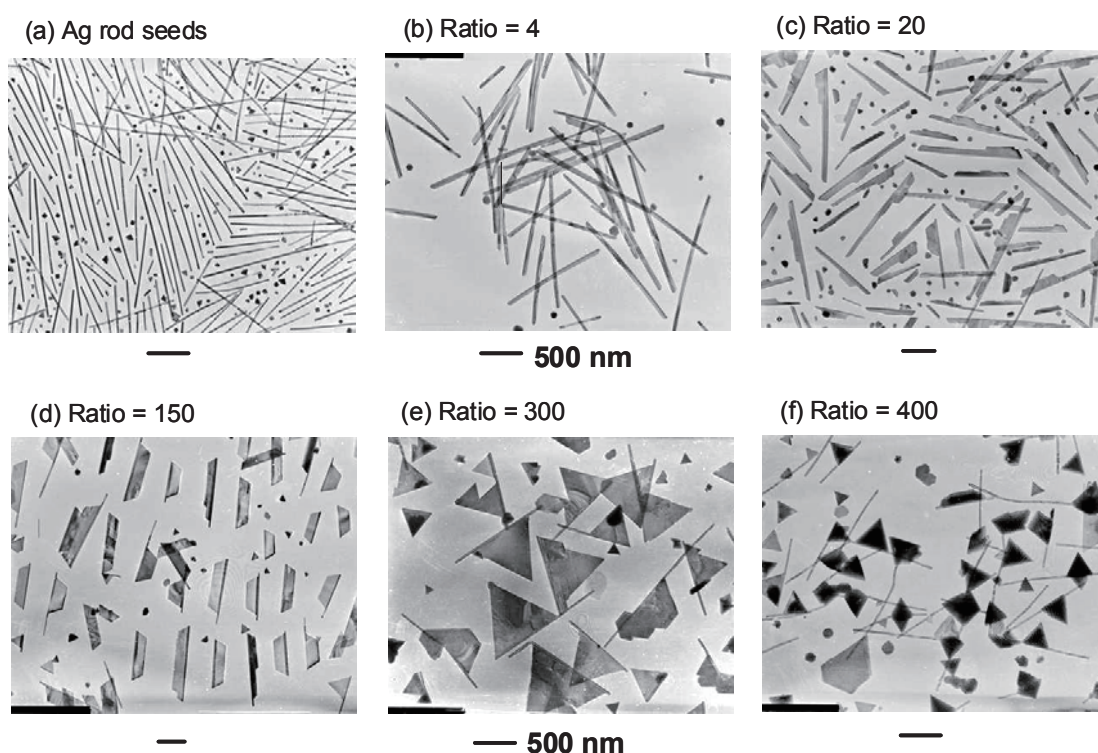


Fig. 1. TEM images of flag types of silver nanostructures prepared at various  $[\text{AgNO}_3]/[\text{Ag in rod seeds}]$  ratios in DMF.

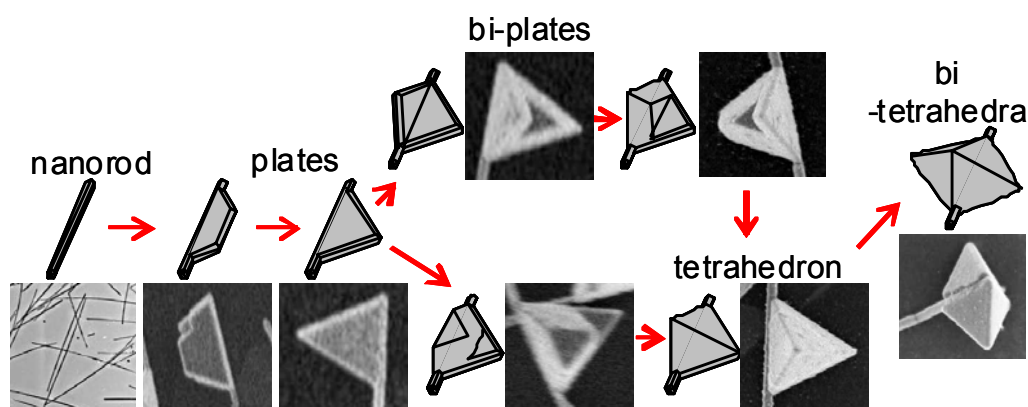


Fig. 2. Crystal structures and growth mechanisms of flag types of silver nanostructures prepared in DMF.

growth of triangular pyramidal structures over triangular plates (Fig. 2). The present results demonstrate that Ag nanorods can be used as new seeds for the unique flag types of Ag nanostructures.

The extinction spectra of Ag seeds and flag type products were measured in the UV-Vis-NIR region (Fig. 3). The surface plasmon resonance (SPR) band of Ag seeds consists of a main peak at ca. 385 nm with a weak shoulder peak at ca. 350 nm. The main peak at ca. 385 nm and the subpeak at ca. 350 nm are ascribed to the out-of-plane dipole and out-of-plane quadrupole resonances of the {100} side walls of the Ag nanowires, respectively. When long Ag nanowires are produced, a long tail band is observed above ca. 450 nm. This tail band can be ascribed to the overlapping of the in-plane quadrupole and dipole resonance modes of the Ag nanowires. It is known that silver plates give the main SPR bands above ca. 500 nm, and they shift to red and become broad with increasing edge lengths. The red shifts of the major SPR peak from 385 to 410 nm and an increase in the intensity of the SPR bands above ca. 450 nm with increasing the  $[\text{AgNO}_3]/[\text{Ag in rod seeds}]$  ratio from 4 to 150 can be explained by the formation of trapezoid and triangular platelike structures. Further increasing the  $[\text{AgNO}_3]/[\text{Ag in rod seeds}]$  ratio to 300, shapes of flags change from platelike flags to tetrahedral flags. The longer wavelength component above 400 nm becomes strong and spectra give rather flat extinction in the 400–1200 nm region with a broad peak at ca. 850 nm, when tetrahedral flags are formed at an  $[\text{AgNO}_3]/[\text{Ag in rod seeds}]$  ratio of 400.

In the present study, we found that platelike and tetrahedral flag types of Ag nanostructures give broader and flatter extinction in the Vis-NIR region than those of known Ag nanostructures. Therefore, flag type Ag nanostructures are promising materials having new optical properties in a wide wavelength range.

[1] M. Tsuji, X. L. Tang, M. Matsunaga, Y. Maeda, M. Watanabe. *Cryst. Growth Des.* **10**, 5238 (2010).

#### ACKNOWLEDGEMENTS

This work was supported by a Grant-in-Aid for Scientific Research (B) from the Ministry of Education, Culture, Sports, Science, and Technology of Japan (MEXT, No. 22310060) and by the Management Expenses Grants for National Universities Corporations from the MEXT.

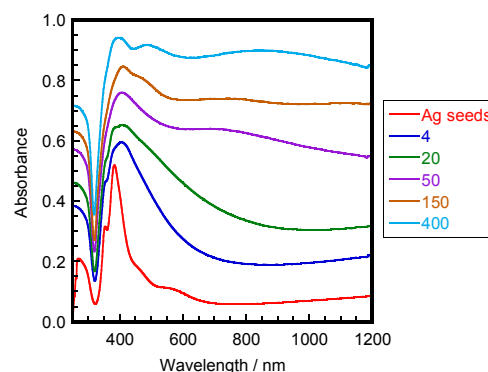


Fig. 3. Extinction spectra of Ag seeds and flag-types of Ag nanostructures obtained at various  $[\text{AgNO}_3]/[\text{Ag in rod seeds}]$  ratios.

## Epitaxial growth of Au@Ni Core-shell Nanocrystals Having a Large Lattice Mismatches of 13.6%

Masaharu Tsuji<sup>1</sup>, Daiki Yamaguchi<sup>2</sup>, Mika Matsunaga<sup>1</sup>, and Koji Ikedo<sup>2</sup>

<sup>1</sup> Institute for Materials Chemistry and Engineering, Kyushu University, Japan

<sup>2</sup> Graduate School of Engineering Sciences, Kyushu University, Japan

Au@Ni core-shell nanocrystals were prepared using a two-step reduction method. First, mixtures of octahedral, triangular and hexagonal plate-like, decahedral, and icosahedral Au core seeds were prepared by reducing  $\text{HAuCl}_4 \cdot 4\text{H}_2\text{O}$  in ethylene glycol (EG) using microwave heating in the presence of polyvinylpyrrolidone (PVP) as a polymer surfactant. Then Ni shells were overgrown on Au core seeds by reducing  $\text{Ni}(\text{NO}_3)_2 \cdot 6\text{H}_2\text{O}$  in EG with NaOH and PVP using oil-bath heating. Resultant crystal structures were characterized using TEM, HR-TEM, TEM-EDS, selected area electron diffraction (SAED), and XRD measurements. Since a very large mismatch (13.6%) exists in lattice constants between Au (0.4079 nm) and Ni (0.3524 nm), the epitaxial growth of Ni shells over Au cores was expected to be difficult. Nevertheless, about 40 monolayers of Ni{111} shells were grown epitaxially on flat planes and sharp corners of Au{111} cores. The SAED patterns showed Ni layers parallel to Au layers.

Recently, Fan et al.<sup>1</sup> investigated syntheses of bimetallic core-shell nanocubes in aqueous solution using a two-step seed-mediated growth method with octahedral Au cores. Their systematic investigation of the growth of core-shell heterogeneous structures of four typical noble metals (i.e., Au, Ag, Pd, and Pt) revealed the relevant growth modes and general criteria for the conformal epitaxial growth or the heterogeneous nucleation and growth of various noble metals. They found that two different forms exist for the growth of heterogeneous metal shells on the gold core: the conformal epitaxial growth for Au@Pd and Au@Ag nanocubes, and the heterogeneous nucleation and island growth for Au@Pt nanospheres. Based on results of their systematic studies, they reported that the lattice constants of two metals are expected to be comparable, with lattice mismatch of less than about 5%. In this study we have examined the epitaxial growth of Au@Ni nanocrystals having a large lattice mismatch (13.6%) using a two-step method to examine effects of lattice mismatch.<sup>2</sup>

Au@Ni core-shell nanocrystals were prepared using a two-step reduction method. As the first step, Au nanocrystal seeds were prepared by MW heating in EG. In the process, 2.4 mM of  $\text{HAuCl}_4 \cdot 4\text{H}_2\text{O}$  was dissolved in 20 mL EG solvent. Then, 1 M of PVP (Mw = 40 k) was added to the solution above. The whole reaction system was heated for 3 min using MW irradiation. In the second step, 14 mL EG solution containing 286 mM of PVP (Mw = 55 k) was bubbled by Ar gas at a flow rate of 150 mL/min for 10 min and preheated at 175°C. Subsequently, Au seeds in 3 mL EG solution were added to the solution described above. Then, 10 mM of  $\text{Ni}(\text{NO}_3)_2 \cdot 6\text{H}_2\text{O}$  and 666.7 mM of NaOH in 3 mL EG solution was injected dropwise to the solution using a syringe pump at an injection rate of 0.3 mL/min. The total heating time after injection of  $\text{Ni}(\text{NO}_3)_2 \cdot 6\text{H}_2\text{O}$  was 120 min. HR-TEM and TEM-EDS data (2100F; JEOL) and XRD data and Extinction spectra of the product solutions were measured to characterize products.

Fig. 1 shows a) TEM, b) SAED, c) TEM-EDS and d) its line analysis data of triangular plate type of Au@Ni nanocrystal. The TEM-EDS data demonstrate more clearly that each Au core is covered by the same shapes of Ni shells, which implies that the favorable facets of Ni shells are {111} as in the case of Au cores. The distributions of Au component in octahedral,

decahedral, and icosahedral Au cores have maxima in the center and decreases greatly on corners or edges, whereas those in triangular and hexagonal-plate like particles are rather flat on the plates (Fig. 1e). The distributions of Ni components have maximum at the

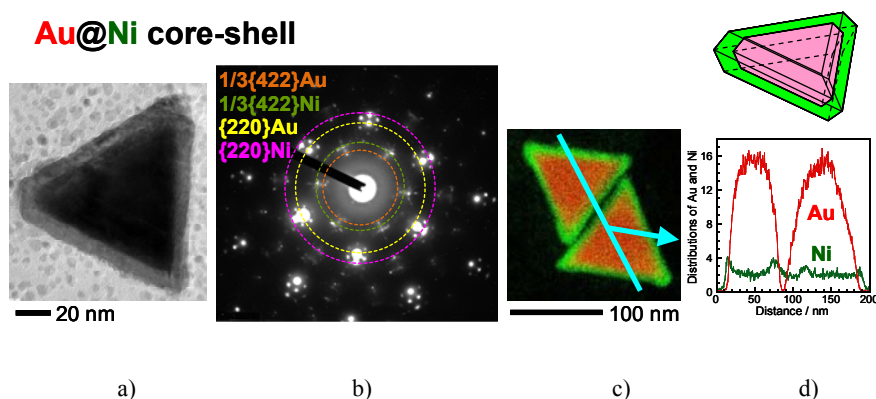


Fig. 1. a) TEM, b) SAED, c) TEM-EDS and d) its line analysis data of triangular plate type of Au@Ni.

corners or side edges and they are rather flat on the plane owing to uniform coverage of Ni shells. On the basis of above EDS analyses of each shape of nanocrystal, Au cores are covered by uniform Ni shells with thickness of about 10 nm.

SAED patterns were measured by focusing the electron beam perpendicularly on the flat surface of a typical triangular nanoplate (Fig. 1b). SAED spots exhibit two sets of hexagonal symmetry patterns in which six heavy white spots corresponding to the  $\{220\}$  reflections of the face-centered-cubic (fcc) Au and Ni single-crystal orientated in the  $[111]$  direction are observed, strongly suggesting that the flat surfaces of the nanoplates are parallel to the  $\{111\}$  plane. Furthermore, a set of weaker spots at the positions of  $1/3\{422\}$  has been found, indicating a twinning boundary within the Au  $\{111\}$  and Ni  $\{111\}$  planes normal to the TEM electron beam. The  $1/3\{422\}$  reflections are forbidden for a perfect fcc single-crystalline structure. In addition to many hexagonal spots, small hexagonal double-diffraction spots of fcc Au and Ni nanocrystals are observed around  $\{220\}$  spots of Au and Ni as shown in Figure 1b, although some of them are partially superimposed with each other. The same SAED patterns attributable to Au and Ni, partially overlapping, are observed on the same lines from the center of diffraction pattern including double-diffraction spots. These results led us to conclude that Ni $\{111\}$  shell layers of  $\approx 10$  nm in thickness are grown epitaxially on Au $\{111\}$  facets despite the presence of a large lattice mismatch between Au (0.4079 nm) and Ni (0.3524 nm). Since the lattice spacing between  $\{110\}$  facets of Ni, about 40 monolayers of Ni $\{111\}$  shells are overgrown on the  $\{111\}$  facets of Au cores. An important finding in this study is that uniform 40 monolayers of Ni shells are epitaxially grown over Au cores, even though the lattice mismatch between Au and Ni (13.6%) is much larger than 5%.

It should be noted that the epitaxial growth rate of Ni shells is essentially independent of shape and position (plain, edge, or corner) of particles for Au@Ni. This implies that there is a case that epitaxial growth rate is independent of shape and position of particles in the formation of Au@Ni nanocrystals. Epitaxial growth of metallic shells over Au crystals is discussed in terms of (i) lattice constants, (ii) electronegativity, and (iii) bond energy.

## ACKNOWLEDGEMENTS

This work was supported by a Grant-in-Aid for Scientific Research (B) from the Ministry of Education, Culture, Sports, Science, and Technology of Japan (MEXT, No. 22310060) and by the Management Expenses Grants for National Universities Corporations from the MEXT.

[1] F. R. Fan, D. Y. Liu, Y. F. Wu, S. Duan, Z. X. Xie, Z. Y. Jiang, Z. Q. Tain, *J. Am. Chem. Soc.*, **130**, 6949 (2008).

[2] M. Tsuji, D. Yamaguchi, M. Matsunaga, K. Ikeda, *Cryst. Growth Des.*, **11**, 1995 (2011).

# PREPARATION AND CHARACTERIZATION OF SEMI-IPN HYBRID HYDRGELS BASED ON IMOGLITE NANOFILLER AND DIAMINE-MODIFIED HYALURONIC ACID

Kyung Lynne PARK<sup>1</sup>, Hideyuki OTSUKA<sup>1,2</sup>, and Atsushi TAKAHARA<sup>1,2\*</sup>

<sup>1</sup> Graduate School of Engineering, Kyushu University, 744 Motooka, Nishi-ku, Fukuoka 819-0385, Japan

<sup>2</sup> Institute for Materials Chemistry and Engineering, Kyushu University, 744 Motooka, Nishi-ku, Fukuoka 819-0385, Japan

\* takahara@cstf.kyushu-u.ac.jp

Hybrid hydrogels with nano-scale clays have been attracted for biomedical technologies such as tissue engineering, biosensor, and controlled drug delivery.<sup>[1]</sup> Among nano-clay materials, imogolite has a unique structure and physical properties. Imogolite is a hydrous aluminosilicate nanotube(Fig 1) which has a high aspect ratio, large specific surface area, and good transparency.<sup>[2]</sup> Here, we evaluated mechanical properties, water uptake, and biostability of a semi-interpenetrating network (semi-IPN) based on fiber-like imogolite nano-filler(IG) and cross-linked hyaluronic acid with hexamethylenediamine (HA-HMDA). The semi-IPN HA-HMDA/IG hydrogels are prepared easily by the addition of HMDA and IG to high concentrated HA activated with 1-ethyl-3-[3-(dimethylaminopropyl]carbodiimide (EDCI) and 1-hydroxybenzotriazole monohydrate(HOBt) under acidic condition(Fig 2).<sup>[3]</sup> FT-IR analysis elucidated that imogolite nano-fillers formed semi-IPN with HA-HMDA phase accompanying hydrogen bonding interaction. Figure 3 shows SEM images of freeze-dried hydrogel which reveal typical morphologies of semi-IPN fibrous hydrogels. Reinforcement of cross-linked hyaluronic acid hydrogel was achieved by the imogolite addition which increases cross-linking density.

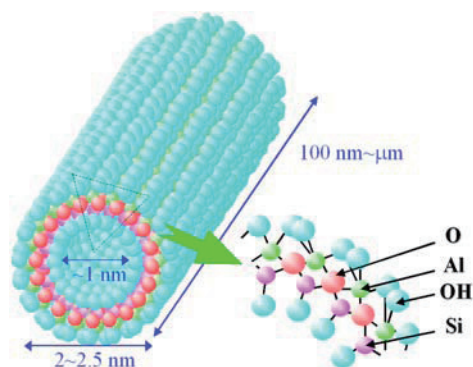


**Figure 1.** Schematic representation of Imogolite nanotube.

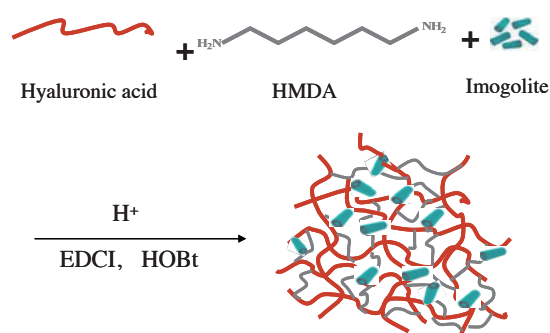


**Figure 2.** Schematic for synthesizing semi-IPN hybrid hydrogels.



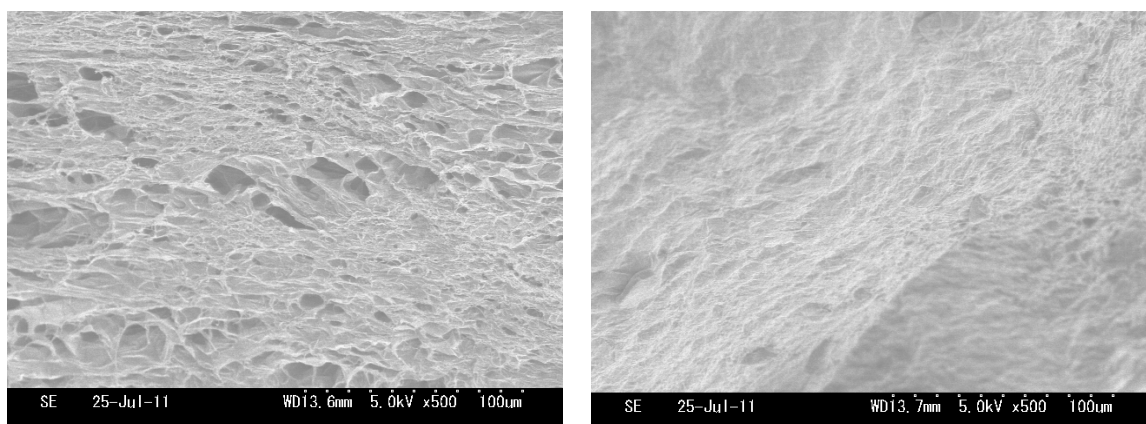


**Figure 3.** SEM images of freeze dried HA-HMDA hydrogel(left) and HA-HMDA/IG hybrid hydrogel(right).

## References

- [1]. Kabiri, K, Mirzadeh, H, Zohuraan-Mehr, M. J, Daliri, M. *Polym Int*, **58**,1252 (2009).
- [2]. K. Yamamoto, H. Otsuka, S. Wada, D. Sohn, and A. Takahara, *Soft Matter*, **1**, 372 (2005).
- [3]. J. S. Yeom, S. H. Bhang, B. S. Kim, M. S. Seo, E. J. Hwang, I. H. Cho, J. K. Park, and S. K. Ahn, *Bioconj. Chem.*, **21**, 240 (2010).

## Preparation and Characterization of Polycarbonate Nanocomposites based on Surface Modified Halloysite Nanotubes

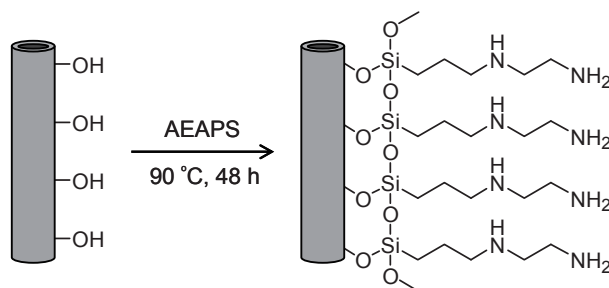
Hui Jing<sup>1</sup>, Weng On Yah<sup>1</sup>, Wei Ma<sup>1</sup>, Yuji Higaki<sup>1,2</sup>, Hideyuki Otsuka<sup>1,2</sup>, Atsushi Takahara<sup>1,2</sup>

<sup>1</sup>Graduate School of Engineering, Kyushu University, Japan

<sup>2</sup>Institute for Materials Chemistry and Engineering, Kyushu University, Japan

Polymer/clay nanocomposites are extensively attracted to research interest due to the very low cost of the clay mineral, relatively simple preparation, and fairly predictable stiffening behavior when introduced into polymers.<sup>[1]</sup> In the present work, halloysite nanotubes (HNTs) were modified with *N*-(2-aminoethyl)-3-aminopropyltrimethoxysilane (AEAPS) by a vapor phase method (Scheme 1), HNTs-based polycarbonate (PC) nanocomposites with a thickness of 110  $\mu\text{m}$  were prepared by compression molding method with a series of surface modified HNTs. The effect of HNTs dispersion state on the morphology, mechanical properties, and thermal stabilities of PC/modified HNTs nanocomposites was investigated.

Typical comparative stress-strain curves of the PC/HNTs composite samples are shown in Figure 1. There was about 72% improvement in PC/unmodified HNTs (0.5%) nanocomposites in tensile modulus compared with neat PC. Moreover, compared with PC/unmodified HNTs composites with 0.5wt% HNTs, the tensile strength, elongation, and transparency of the PC/modified HNTs nanocomposites increased by 17%, 24% and 1.4%, respectively. Such increase can be attributed to the incorporation of the modified HNTs as well as the better dispersion of HNTs in the PC matrix.<sup>[2]</sup> The TGA curves revealed that the temperature at 10% weight loss for the nanocomposite filled with 0.5wt% modified HNTs was 4°C higher than that of the unmodified PC, 21°C higher than that of neat PC. These results revealed that the thermal stability and mechanical properties of PC matrix was improved by the incorporation of modified HNTs.



Scheme 1. modification of HNTs with AEAPS in the vapor phase.

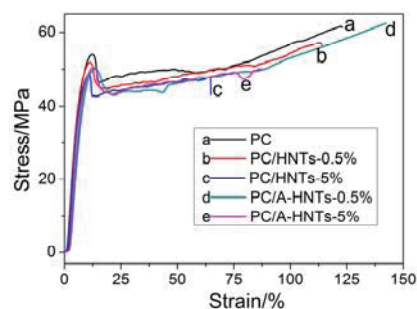


Figure 1. Stress-strain curves of PC/HNTs nanocomposites.

[1] P. Podsiadlo, A. K. Kaushik, E. M. Arruda, A. M. Waas, B. S. Shim, J. Xu, H. Nandivada, B. G. Pumphlin, J. Lahann, A. Ramamoorthy, N. A. Kotov, *Science*. 318, 80 (2007).

[2] N. Hameed, P. A. Sreekumar, V. S. Valsaraj, S. Thomas. *Polym Composite* 30, 7 (2009).

## Well-defined Acrylic 4-Arm Star Polymer by ATRP

Byungjin Jung<sup>1</sup>, Youngsoo Na<sup>2</sup>, Ildoo Chung<sup>1</sup><sup>1</sup>Department of Polymer Science and Engineering,  
Pusan National University, Busan 609-735, Korea<sup>2</sup>Segye Chem company, Yangsan 626-110, Korea

Star polymers are a special kind of branched polymers composed of a central core and different numbers of linear chains with the properties of low solution or melt viscosities, because their molecular structures behave similar to a solution of hard sphere and exhibit limited chain entanglements, which is beneficial to polymer processing. Star polymers with different composition of acrylic monomers such as n-butyl acrylate(n-BA), methyl methacrylate(MMA), 2-hydroxyethyl methacrylate(HEMA) were obtained via atom transfer radical polymerization with multifunctional ATRP initiators as the cores of the stars.[1,2]

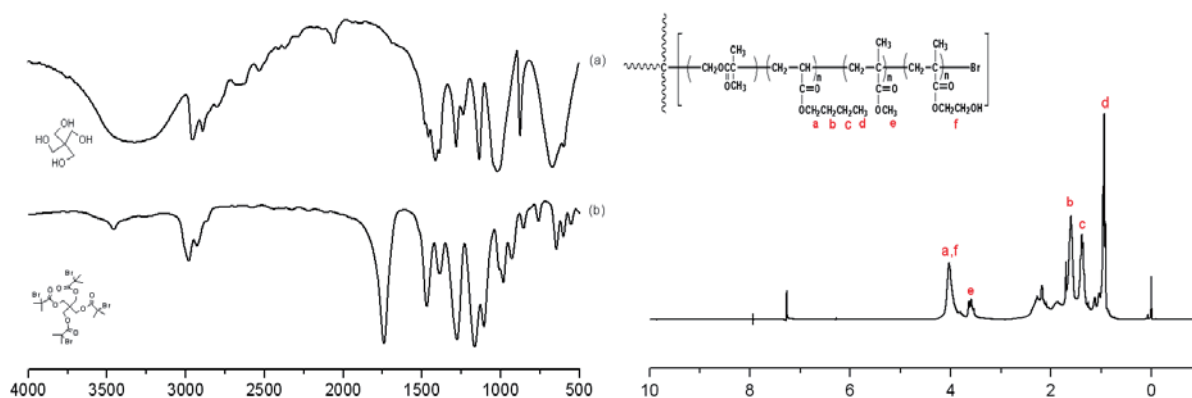


Fig. 1. FT-IR spectra of the synthesized initiator (a) pentaerythritol (b) 4-arm PT-Br.

Fig. 2. <sup>1</sup>H-NMR spectra of copolymer initiated by 4-arm PT-Br.

The synthesized star polymers were characterized by FT-IR, <sup>1</sup>H NMR spectroscopies and GPC with refractive index and evaluated their thermal properties as well as intrinsic viscosities in order to be potentially used in the industrial field. The FT-IR spectrum of the initiator shows characteristic absorption peaks at 1738(C=O stretch), 1271(C-O-C stretch), and 1164(C-Br bending) with concurrent disappearance of -OH stretching of the hydroxyl moiety at 3650~3000 cm<sup>-1</sup>. Fig. 2 showed the chemical shifts of <sup>1</sup>H-NMR spectra of acrylic 4-arm star polymer by ATRP indicating the characteristic peaks at 4.04 ppm (-OCH<sub>2</sub>-), 3.82 ppm (-OCH<sub>3</sub>-), 0.8-2 ppm (polymer backbone) with concurrent disappearance of C=C peaks of double bond around 5.5-6.5 ppm.

[1] K. Matyjaszewski, J. Xie, *Chem. Rev* **101**, 9 (2001).

[2] I. Chung, P. Britt, E. Harth and J. Mays, *Chem. Comm.* **28**, 8 (2005).

## Development of Carbon Nanotube/UV-Curable Polymer Nanocomposites and Evaluation of Their Dispersion State and Thermal Conductivity

Takahiro Fukumaru<sup>1</sup>, Tsuyohiko Fujigaya<sup>1,2</sup>, Naotoshi Nakashima<sup>1,2,3</sup>

<sup>1</sup>Department of Applied Chemistry, Graduate School of Engineering,

Kyushu University, Japan

<sup>2</sup>WPI I<sup>2</sup>CNER, Kyushu University, Japan

<sup>3</sup>Japan Science and Technology Agency, CREST, Japan

The homogeneous dispersion of carbon nanotubes (CNTs) in matrix polymer is essential to maximize the CNT's properties such as mechanical strength, electric conductivity, and thermal conductivity of the composites.

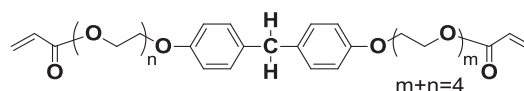


Fig. 1. Chemical structure of 1.

In this presentation, we describe 1) a new CNT/polymer nanocomposite system consisting of a UV-curable monomer (1, Fig. 1) and single-walled carbon nanotubes (SWNTs) that satisfy both the homogeneous dispersion and excellent processability requirements [ref.1], 2) the evaluation of bundled degrees of SWNTs in the SWNT/Polymer nanocomposites based on the intensity changes in the radial breathing mode (RBM) of their Raman spectra at a 785-nm, excitation, and 3) the thermal conductivity measurements of the composite films using the temperature wave analysis method [ref.2]. Our simple mixing dispersion requires no chemical treatments for the SWNT and is expected to achieve a greater enhancement of the thermal conductivity of the CNT/polymer composites.

Fig. 2 shows the plots of the thermal conductivity of the films as a function of the SWNT-loading and it shows that a higher SWNT-loading produces a higher thermal conductivity. The RBM in the SWNT Raman spectra at a 785 nm excitation reflects the degree of aggregation of SWNTs based on the fact that the RBM at around 267 nm of (10,2)SWNTs is absent in the isolated SWNTs but it present in the bundles of the SWNTs. Plot of the peak at 267 nm of the composite as a function of the SWNT-loading shows resemble trend to the plots of the thermal conductivity as a function of the SWNT-loading. This result indicated that the composite films contain bundled SWNTs and degree of debundling varies with the SWNT concentration and bundled SWNTs may effect on the thermal conductivity of the composite films. .

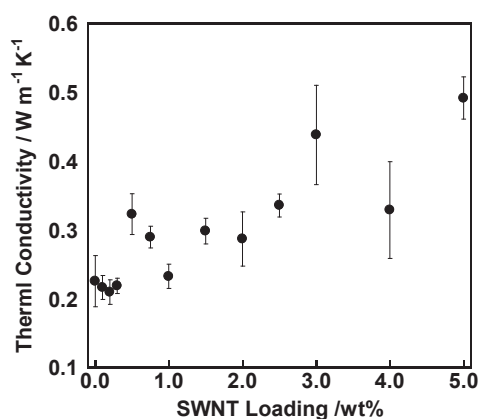


Fig. 2. Plots of the thermal conductivity of the SWNT/1 films as a function of the SWNT loading.

[1] T. Fujigaya, S. Haraguchi, T. Fukumaru, N. Nakashima, *Adv. Mater.* **20**, 2151 (2008).

[2] T. Fujigaya, T. Fukumaru, N. Nakashima, *Synthetic. Metals* **159**, 827 (2009).

## Lipophilic and Anionic Polymer Network based on Tetraphenylborates

Yuki Furukawa<sup>1</sup>, Kenta Kokado<sup>1,2</sup>, Kazuki Sada<sup>1,2</sup>

<sup>1</sup>Graduate School of Chemical Science and Engineering, <sup>2</sup>Graduate School of Science, Hokkaido University, Sapporo 060-0810, Japan

Tetraphenylborates are well-known as weakly-coordinating and lipophilic anions, and their salts with tetraalkylammonium are soluble and dissociated into free ions in non-polar organic solvents such as chloroform ( $\epsilon = 4.8$ ) and THF ( $\epsilon = 7.6$ ). This ion-dissociation prompted us to design and prepare the lipophilic polyelectrolyte gels by incorporation of them as the ionic groups into lipophilic polymer chains such as poly(octadecylacrylate) and polystyrene. We demonstrated that they acted as superabsorbent polymers that swelled largely with the high swelling degrees in less- or non-polar organic solvents.[1] This superior swelling behaviors were caused by osmotic pressure and electrostatic repulsion derived from dissociation of the ionic groups in these media.

Herein, we report preparation of novel anionic, lipophilic and rigid polymer networks based on tetraphenylborates and control of their network structures and morphologies. A formyl group was introduced in each phenyl group of tetraphenylborate anion, and the resulting tetra-functional anion (**C6**) was used as a new monomer for the lipophilic and anionic network polymers (Scheme 1). Then, polymerization and cross-linking by imine formation with the bifunctional amine (**L1**) were carried out in various monomer concentrations and polarity of the media (Table 1).

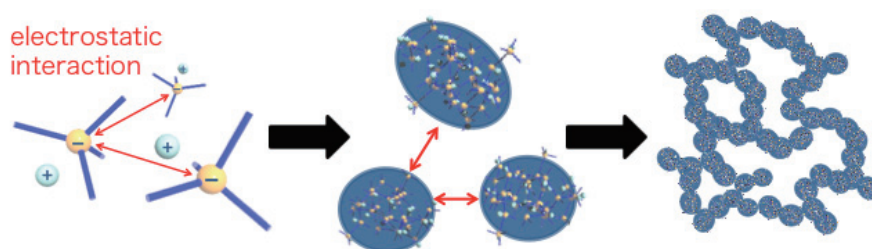


Fig. 1. Schematic illustration of growth mechanism of network polymers

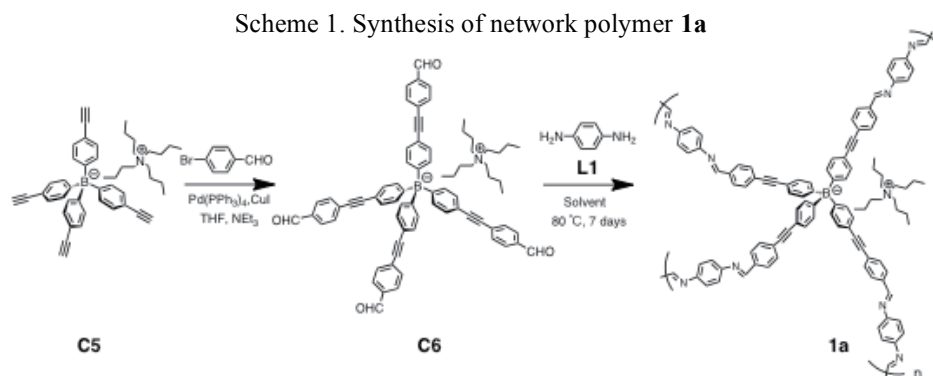


Table 1. Synthesis conditions of network polymer **1a**

Run	C6* (mM)	C6 (mmol)	L1 (mmol)	Solvent	Mixture ratio	Dielectric constant ( $\epsilon$ )
1	10	0.0093	0.019	1,4-Dioxane : DMSO	5 : 1	9.6
2	10	0.0093	0.019	1,4-Dioxane : DMSO	1 : 1	24.3
3	10	0.0093	0.019	1,4-Dioxane : DMSO	1 : 2	31.7
4	200	0.011	0.022	1,1,2,2-Tetrachloroethane		8.2
5	100	0.011	0.022	1,1,2,2-Tetrachloroethane		8.2
6	50	0.011	0.022	1,1,2,2-Tetrachloroethane		8.2
7	10	0.011	0.022	1,1,2,2-Tetrachloroethane		8.2
8	10	0.023	0.054	1,4-Dioxane : DMSO : H <sub>2</sub> O	9 : 2 : 2	29.7
9	10	0.023	0.054	1,4-Dioxane : DMSO : H <sub>2</sub> O	6 : 3 : 1	36.4
10	29	0.023	0.054	1,4-Dioxane : DMSO : H <sub>2</sub> O	2 : 18 : 1	43.8

\* Concentration of monomer C6

After the polymerization for 7 days at 80 °C in a sealed tube, the network polymers were deposited as powder in the low-dielectric media, while they formed gels in the high-dielectric ones. In the presence of water, the reaction mixtures were kept as the solution state. Solubility test, IR and TGA clearly indicated the formations of the network polymers based on tetraphenylborate cores. According to SEM, the network polymers had aggregated structures of small spherical particles in the low-dielectric media (Fig. 2a) and the fibrous network structures in the high-dielectric ones (Fig. 2b, c). In the former media, ion dissociation was suppressed during the polymerization process, and the spherical particles aggregated to each other (Fig. 3). On the other hand, in the latter media, ion dissociation was promoted, and ion repulsion induced to form the expanded network structure (Fig. 3). We further investigated the porosity of the resulting network polymers by TGA. They could absorb a large amount of solvent molecules in their networks.

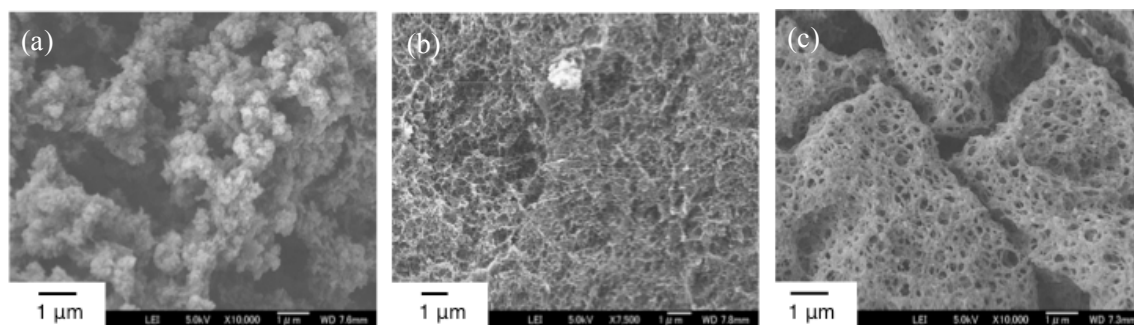
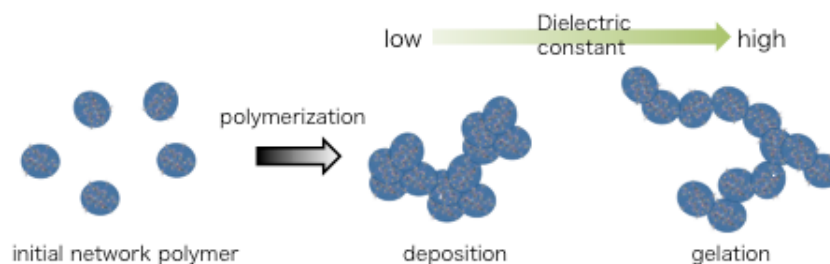
Fig. 2. SEM images of network polymers (a) **Run-1**, (b) **Run-2** and (c) **Run-3**.

Fig. 3. (a) Schematic illustration of growth mechanism of network polymers in low-dielectric media and high-dielectric media

[1] T. Ono, T. Sugimoto, S. Shinkai, K. Sada, *Nat. Mater.* **2007**, 6, 429.

## Structures and Properties of SBA-15 Thin Film with TiO<sub>2</sub> Nanoparticles

Takashi Gondo<sup>1</sup>, Atsushi Kohno<sup>2</sup>, Takayuki Tajiri<sup>2</sup>, Kazuhiro Yamada<sup>1</sup>, Kenji Kaneko<sup>1</sup>

<sup>1</sup> Department of Materials Science and Engineering, Kyushu University, Japan

<sup>2</sup> Department of Applied Physics, Fukuoka University, Japan

### ABSTRACT

Mesoporous SBA-15 thin film was used as a template for fabricating TiO<sub>2</sub> nanoparticles and their microstructures and physical properties were examined.

### INTRODUCTION

Recently, it has been a great interest to fabricate nanoparticles with narrow distribution of particles' size, since their quantum and surface effects are strongly dependent on it [1][2]. It is therefore that the controlling of particle sizes has been of the great importance and desired for a long period. In fact, there have been several attempts to fabricate nanoparticles with narrow size distributions [3], and among them, using mesoporous silica SBA-15 as a template would probably be the best candidate [1].

Structure analysis of SBA-15 thin films with/without incorporation of TiO<sub>2</sub> nanoparticles were examined by X-ray diffraction (XRD) and X-ray reflectivity (XRR), then electrical properties of them were examined by capacitance-voltage (C-V) measurement method.

### EXPERIMENTS

The mesoporous silica thin films (SBA-15) were deposited by spin-coating technique on Si substrate. The coating solution were prepared by the addition of an ethanol solution of ethylene oxide/propylene oxide/ethylene oxide triblock copolymers (EO<sub>20</sub>PO<sub>70</sub>EO<sub>20</sub>, P123, Aldrich) to silica sol-gel prepared by heating mixture of tetraethoxysilan (TEOS), ethanol (EtOH), H<sub>2</sub>O and HCl. SBA-15 thin films were then prepared by annealing the coated thin films. TiO<sub>2</sub> nanoparticles were fabricated by soaking SBA-15 thin films in an acetate-diluted TiO<sub>2</sub> precursor solution and heating process. Structural analysis of SBA-15 thin films with/without TiO<sub>2</sub> nanoparticles were characterized by XRD and XRR. Furthermore, electrical properties of SBA-15 thin film with/without TiO<sub>2</sub> nanoparticles were examined by C-V measurements with metal-insulator-semiconductor (MIS) structure.

### RESULT AND DISSCUTION

Thickness of the films was measured as ~330 nm with its mean density as ~1.2 g/cm<sup>3</sup> by XRR measurement (Fig.1). According to the XRD patterns, the pore channels of SBA-15 were found parallel to the substrate with its unit cell parameter as 6.7 nm, in which the size of pores and the thickness of the silica walls were estimated as ~4.7 nm and ~2.0 nm

respectively by following equation,

When  $\text{TiO}_2$  nanoparticles were fabricated by annealing of soaked SBA-15 thin film into acetate-diluted  $\text{TiO}_2$  precursor solution, the oscillation amplitude of XRR was increased without changing the thickness and the pore size, namely there was not structural change but increase of the density, which suggests the formation of the  $\text{TiO}_2$  nanoparticles within SBA-15. It was therefore confirmed that the  $\text{TiO}_2$  nanoparticles with narrow distribution of particle size could be fabricated via SBA-15 as the template.

Fig.2 shows C-V characteristic of Metal-Insulator-Semiconductor (MIS) structure with  $\text{TiO}_2$  nanoparticles fabricated using SBA-15 template. The presences of counter clockwise hysteresis and that of a shoulder around 1.0 V were confirmed, when voltage was swept from positive to negative. Electrons were injected and trapped into electron level of SBA-15/Si interface and/or in SBA-15 thin films, since counter clockwise hysteresis and curve of in C-V characteristics was arisen due to the charge injection and retention characteristic into Si quantum dots. Subsequently, these results indicated that electrons were tunnel injected into nanoparticles under positive voltage, in which parts of electrons were discharged with decrease gate voltage. This MIS structure therefore would have strong prospective of the memory effect.

#### Reference

- [1]. T. Tajiri, *et al.*, J. Phys. Soc. Jpn. 75, 113704(2006)
- [2]. N. Satoh, *et al.*, Nature Nanotechnology 3, 106 - 111 (2008)
- [3]. D. Zhao, *et al.*, Chem. Mater. 2000, 12, 275-279
- [4]. M. Kruk, *et al.*, Chem. Mater. 12, 1961-1968 (2000)

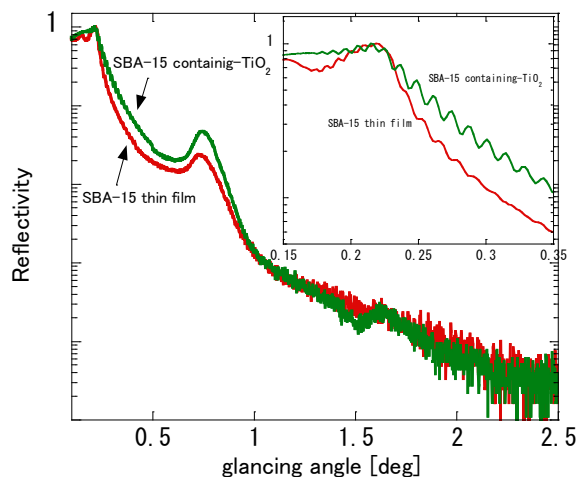


Fig.1 X-ray reflectivity of SBA-15 thin film and  $\text{TiO}_2$ -containing SBA-15 thin film.

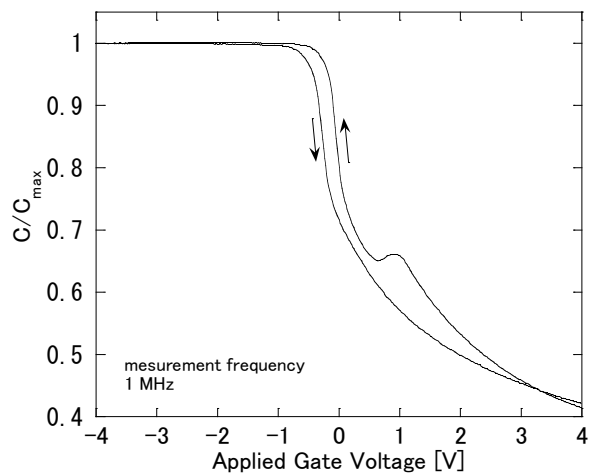


Fig.2 C-V characteristic of MIS structure with  $\text{TiO}_2$  nanoparticles.



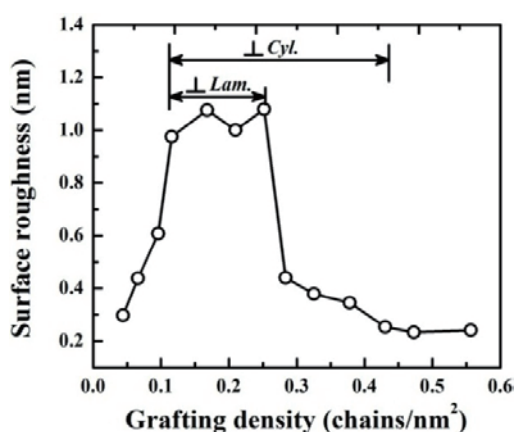
## Microdomain Orientation in PS-*b*-PMMA Thin Films on PS Grafted Substrates

Jinsam Gong, Rui Guo, Eunhye Kim, Seunghoon Choi, Sujin Ham, and Du Yeol Ryu\*

Department of Chemical and Biological Engineering, Yonsei University, Seoul 120-749, Korea

Block copolymer (BCP) self-assembly, due to its ability to spontaneously form well-organized structures (typically 10–100 nm), has been an attracting candidate for a variety of applications with nanoscale periodic patterns. In a film geometry that confines polymer chains to the interfaces, the microdomain orientation of cylinder- or lamella-forming BCPs can be influenced by the interfacial interactions at substrate/polymer and polymer/air and a commensurability between the total film thickness and the equilibrium period of the BCP. Directing microdomain orientation in the BCP films has attracted considerable attention in recent few decades as a key issue to satisfy the demand for nanolithographic or some specific applications.

A grafting-to or crosslinking approach to surface modification with functional poly(styrene-*r*-methyl methacrylate)s (P(S-*r*-MMA)s) produced the perpendicular orientation of cylindrical or lamellar microdomains in polystyrene-*b*-poly(methyl methacrylate) (PS-*b*-PMMA) films, because the balanced interfacial interactions (or surface neutrality) on substrates were adjusted by the relative composition of random copolymers. Prior studies on the surface neutrality for PS-*b*-PMMA films indicated that the perpendicular orientation of cylindrical and lamellar microdomains can be optimized at 0.64 and 0.55 of PS mole fraction of P(S-*r*-MMA), respectively, on the basis of the perpendicular thickness window.



We observed the microdomain orientation in thin films of cylinder- and lamella-forming PS-*b*-PMMA on the substrates with PS brushed (or grafted) homopolymers, where grafting density of underlying PS layers are controlled by the reaction parameters such as time and temperature during grafting to the substrates. When grafting density range of PS brush is adjusted, such a simple and facile route provides the perpendicular orientation of cylindrical and lamellar microdomains in PS-*b*-PMMA films.

### References

- [1] Ham et al., *Macromolecules*, **41**, 6431-6437 (2008)
- [2] Ryu et al., *Macromolecules*, **42**, 4902-4906 (2009)

## Durable Polyacrylic Adhesives Based on Their Hybrid Organic/Inorganic Nanocomposites with Silica

Kuiseung Hwang<sup>1</sup>, Youngsoo Na<sup>2</sup>, Ildoo Chung<sup>1</sup>

<sup>1</sup>Department of Polymer Science and Engineering,  
Pusan National University, Busan 609-735, Korea

<sup>2</sup>Segye Chem Company, Yangsan 626-110, Korea

The modification of inorganic silica particles with organics leads to the production of organic-inorganic hybrid particles in which the organic components may be chemically bonded to a silica matrix.[1] The mechanical, electrical and optical properties of the resulting organic-inorganic hybrid particles are then governed by the type and concentration of the organics used.[1,2] In this work, hybrid organic/inorganic nanocomposites were synthesized from well-dispersed spherical silica nanoparticles which were prepared from colloidal silica and methyltrimethoxysilane(MTMS), followed by the incorporation into acryl adhesive to improve the mechanical properties and durabilities. The homogeneity and morphology of the resulting nanocomposites were examined by FE-SEM, TEM, and AFM. The thermal properties of nanocomposites were determined by TGA and DSC. The synthesized nanocomposites were also evaluated their adhesion properties such as viscosity, peel strength, weatherability, and thermal endurance test. Durable polyacrylic adhesive nanocomposites showed higher glass transition temperature of  $-26.48^{\circ}\text{C}$  by temperature increment of  $4.9^{\circ}\text{C}$  as compared with that of pure polyacrylic adhesive, demonstrating that interfacial adhesion between organic polyacrylic adhesive and inorganic silica component was prominently improved by the addition of organically modified colloidal silica. This increase in the glass transition temperature for durable polyacrylic adhesive nanocomposites may be attributed to more restricted chain mobility of the durable polyacrylic adhesive nanocomposites by the presence of silica network.

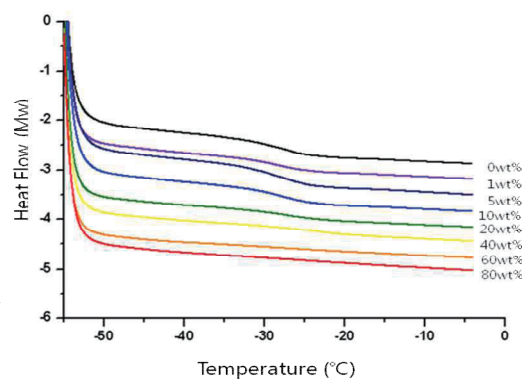


Fig 1. DSC curves of nanocomposites mixed with 0 to 80 wt% MTMS-modified colloidal silica nanoparticles in acryl adhesive.

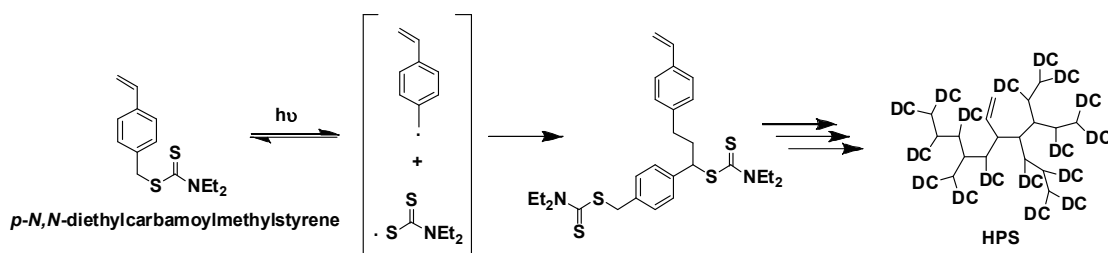
[1] A. Van Blaaderen and A. Vrij, *J. Colloid Interface Sci*, **156**, 1 (1993).

[2] F. Hatakeyama and S. Kanzaki, *J. Am. Ceram. Soc.*, **73**, 2107 (1990).

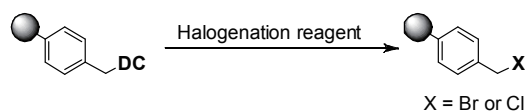
The synthesis of a hyper branched polymer for the application to the dispersing agents of metal particles.

Hideo NAGASHIMA<sup>1</sup>, Takashi NISHIKATA<sup>1</sup>, Takashi Sue<sup>1</sup>, Akihiro TANAKA<sup>2</sup>, and Keisuke KOJIMA<sup>2</sup> (<sup>1</sup>Institute for Materials Chemistry and Engineering Kyushu University, 6-1 Kasugakouen, Kasuga-shi Fukuoka 816-8580, Japan <sup>2</sup>Nissan Chemical Industries, Ltd., 2-10-1 Tsuboinishi, Funabashi-shi Chiba 274-8507, Japan)

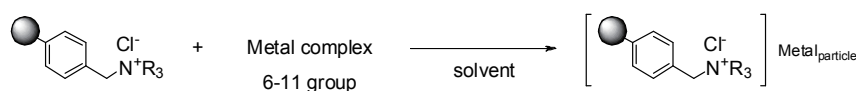
Hyperbranched polymer is a very attractive materials having a variety of properties, high dispersion, low viscosity. Since hyperbranched polymer has a quasi-spherical nano-structures in which a lot of functional groups are located at the surface, the property of derivatives of that are sharply dependent on the terminal functional groups. Ishizu and co-workers reported that *p*-*N,N*-diethylcarbamoylmethylstyrene undergoes radical photo-initiated polymerization to give hyperbranched polystyrene (HPS) bearing diethylcarbamoyl (DC) groups at the terminal position. We have recently established a new polymerization method, which is very advantageous from the industrial point of view.



HPS-X (X=Cl, Br) is a very important intermediate obtained by the halogenation of DC group for the further functionalization.



The ammonium derivatives from HPS-X are very effective for stabilizing a variety of metal particles.



Complexes derived from HPS-ammonium derivatives and metal particle show a high dispersities and stabilities with catalytic properties.

So, they can be used as the catalyst for a variety of reactions.

## Dielectric Environment Effect on the States of $\pi$ -Electrons of $(n,m)$ Single-Walled Carbon Nanotubes

Yasuhiko Hirana<sup>1</sup>, Yasuro Niidome<sup>1,2</sup>, and Naotoshi Nakashima<sup>1,2,3</sup>

<sup>1</sup>Graduate School of Engineering, Kyushu University, 744 Motooka, Nishi-ku Fukuoka 819-0395, Japan

<sup>2</sup>World Premier International (WPI) Research Center International Institute for Carbon-Neutral Energy Research (I<sup>2</sup>CNER), Kyushu University, 744 Motooka, Nishi-ku, Fukuoka 819-0395, Japan

<sup>3</sup>CREST, Japan Science and Technology Agency, 5 Sanbancho, Chiyoda-ku, Tokyo 102-0075, Japan

The redox properties (i.e. electronic densities, the Fermi levels, redox potentials) of single-walled carbon nanotubes (SWNTs) are related to the structures of SWNTs that have a specified diameter and chiral angle uniquely related to a pair of integers  $(n,m)$ ; the so-called chiral index. Electronic structure, one of the most fundamental features of SWNTs, also strongly depends on their diameter and chirality.

Here we report the finding that the electrochemical band gaps ( $E_g^{electr}$ ) of  $(n,m)$ SWNTs are strongly affected by the change in dielectric environments around the isolated SWNTs. In situ photoluminescence (PL) spectroelectrochemistry [1] of the films containing isolated SWNTs cast on ITO electrodes was completed in several organic solvents and then the oxidation and reduction potentials,  $E_g^{elect}$  and Fermi levels of the individual  $(n,m)$ SWNTs in the solvents were determined. We discovered that the  $E_g^{elect}$  of the  $(n,m)$ SWNTs become greater as the solvent dielectric constants decreased, which is in sharp contrast to the optical band gaps that show virtually no solvent dependence [2]. Moreover, the states of the  $\pi$ -electrons in the SWNTs were evaluated from the dependence of the band gaps on the diameter of the SWNTs. The present study provides useful information for a deep understanding of the fundamental electronic properties of isolated  $(n,m)$ SWNTs in solvents.

[1] Y. Tanaka, Y. Hirana, Y. Niidome, K. Kato, S. Saito, N. Nakashima, *Angew. Chem. Int. Ed.* **2009**, *48*, 7655-7659.

[2] Y. Hirana, Y. Tanaka, Y. Niidome, N. Nakashima, *J. Am. Chem. Soc.* **2010**, *132*, 13072-13077.

## Cross-linked Cyclodextrin Beads for Chromatographic Removal of Endotoxin from DNA Solution

Masayo Sakata, Koji Uezono, Kana Yoshimura, Masashi Kunitake

Graduate School of Science and Technology, Kumamoto University  
2-39-1 Kurokami, Kumamoto 860-8555, Japan

Cellular products such as DNA vaccines and proteins, produced by recombinant gene technology, are usually contaminated with endotoxin (lipopolysaccharide; LPS). In this work, using cross-linked cyclodextrin (CyD) beads [1], the selective adsorption of LPS was investigated to separate LPS from DNA. For hydrophobic adsorption of LPS, we expected that the cavities of the  $\beta$ - and  $\gamma$ -CyD tube (diameter: 0.70 and 0.85 nm, respectively) could include the hydrophobic chains of LPS. In this report, we compared the chromatographic LPS-separation activity of the CyD beads with that of cationic polymer beads.

Figs. 1a, b and c, show the effect of the buffer's ionic strength on the selective adsorption of LPS from a DNA solution containing LPS by various adsorbents. As shown in Fig. 1b, Poly( $\epsilon$ -lysine)-immobilized cellulose beads [2] (ETclean-L, Chisso, Japan, commercial LPS adsorbent) had the highest LPS-adsorbing activity (>99%) at  $\mu = 0.05$  to 0.4. However, it adsorbed not only LPS but also DNA at all ionic strengths tested. DEAE-Sepharose had high adsorption activities for both LPS and DNA at a low ionic strength,  $\mu = 0.05$ , and the adsorption activities significantly decreased with increasing ionic strength (Fig.1c). Therefore, ETclean-L and DEAE-Sepharose could not selectively adsorb LPS at any ionic strength. By contrast, the  $\gamma$ -CyD beads selectively adsorbed LPS (77-88%) without adsorption of DNA (<1%) over a wide range of ionic strengths ( $\mu$ ) from 0.05 to 0.8 (Fig. 1a).

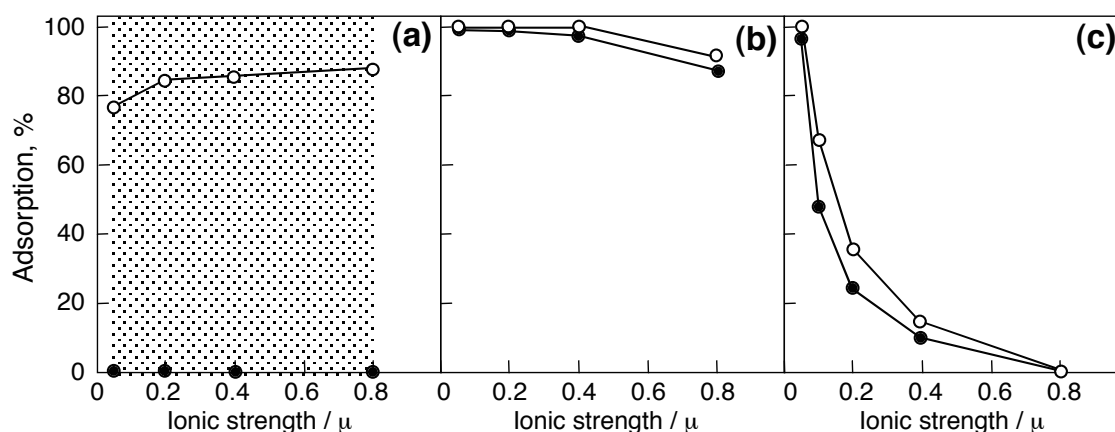


Fig. 1. Effect of buffer's ionic strength on selective adsorption of LPS by  $\gamma$ -CyD polymer beads (a), ETclean-L (b), and DEAE-Sepharose (c). The adsorptions of LPS (○) and DNA (●) were determined by a batch method with 0.1 mL of wet adsorbent and 2 mL of a DNA solution (DNA from salmon sperm,  $M_w$   $3 \times 10^5$ ; 50  $\mu$ g/mL) containing natural LPS (15 EU/mL) at pH 6.0 and ionic strength  $\mu = 0.05$ -0.8.

### References

- [1] T. Kikuchi, F. Hamada, et al. *Jpn. Kokai Tokkyo Koho*, JP-2006143953, 2006.
- [2] M. Todokoro, M. Sakata, et al. *J. Liq. Chromato. Rel. Technol.*, **25**, 601 (2002).

## Functional E-SBR for Fuel-Efficient Tire Tread Compounds

Heejeong Kim<sup>1</sup>, Ki-hyun Kim<sup>2</sup>, Hyuk Soo Kwon<sup>2</sup>, Byeungho Seo<sup>2</sup>, Wonho Kim,<sup>2</sup> Gwang Hoon Kwag,<sup>3</sup> Dong Hyuk Na,<sup>3</sup> Jun Keol Choi,<sup>3</sup> Jong Yeop Lee<sup>3</sup>, Jong Woo Bae<sup>4</sup> and Hyun-jong Paik<sup>1</sup>

<sup>1</sup>Department of Polymer Science & Engineering, Pusan National University, Busan 609-735, Korea

<sup>2</sup>Department of Chemical Engineering, Pusan National University, Busan 609-735, Korea

<sup>3</sup>Kumho Petrochemical R&BD Center 57-1 Hwaam-dong, Yusung-gu Daejeon, South Korea

<sup>4</sup>Rubber Material Research Division, Korea Institute of Footwear & Leather Technology, Busan 614-100, Korea

According to "EU labeling" policy, every tire sold in EU should be marked the label on the surface the tire according to the fuel efficiency from 2012, and laws related to vehicle fuel efficiency and emission gas will be gradually strengthened until on 2020 in the worldwide. Silica has started to be used as a reinforcement agent instead of carbon black for making green tire, but its application is still limited with the low affinity between emulsion polymerized rubber and silica. We report a new copolymer for fuel-efficient tire material. Styrene-Butadiene-Glycidyl methacrylate copolymer (GMA-SBR) was synthesized using emulsion polymerization initiated by p-methane hydroperoxide. After polymerization, the latex was treated with solution of sodium chloride and sulfuric acid. It was possible for GMA-SBR to increase the tensile strength, the dynamic property and the compatibility with silica via the ring-opening reaction of glycidyl methacrylate units. Improved wet traction performance and enhanced rolling resistance were measured by DMA.

## Molecular Design of Thermo-Sensitive Polymers by Utilization of Weak Interaction with Small Organic Molecules

Shogo AMEMORI<sup>1</sup>, Kenta KOKADO<sup>2</sup> and Kazuki Sada<sup>2</sup>

<sup>1</sup>Graduate School of Chemical Sciences and Engineering, <sup>2</sup>Graduate School of Science, Hokkaido University, Japan

Thermo-responsive polymers show reversible drastic changes in their solubilities in solution by heating. The solubility changes of the polymers are generally attributed to changes of interactions among polymer chains and solvent molecules. For examples poly(*N*-isopropylacrylamide), poly(ethylene glycol) or poly(vinyl alcohol) in water show LCST behavior by breaking attractive interaction between the polymer chain and water molecules and inducing changes of the polymer conformations with increasing solution temperature[ref. 1]. However, it is still difficult to design thermo-responsive behaviors in non-aqueous solvents. In this presentation, we demonstrated control of LCST and UCST behaviors of the specially-designed polymer **1** with urea moieties by addition of various small molecules (Fig. 1).

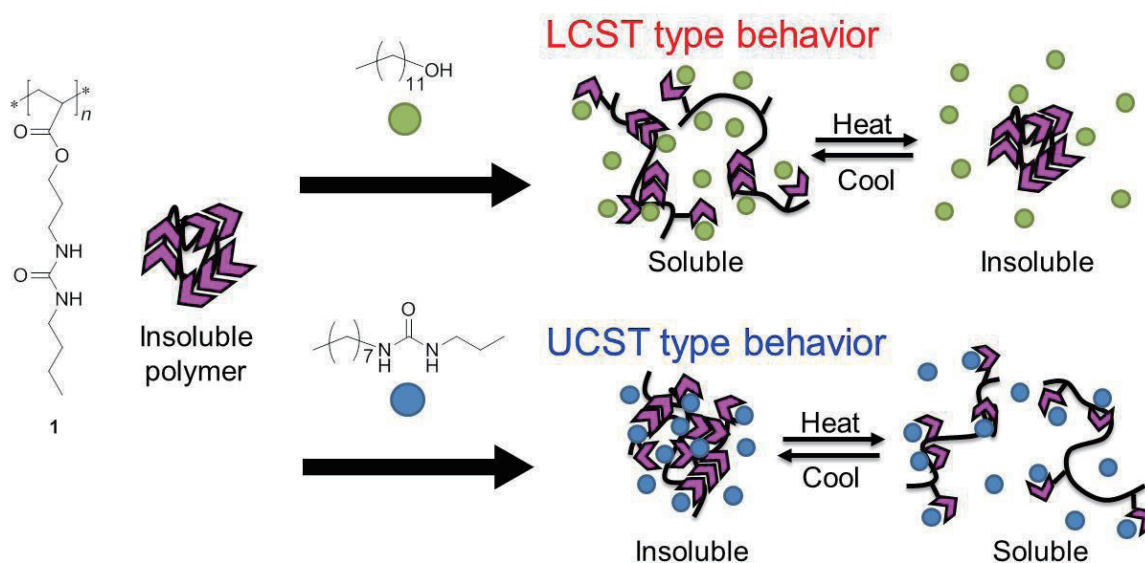


Fig. 1. Concept of the thermo-sensitive polymer controlled LCST type and UCST type by low molecular weight additives.

First, we investigated the solubility of the polymer **1** in various organic solvents. In acetonitrile, THF, 1,2-dichloroethane and hexane, the polymer was practically insoluble because of the strong hydrogen bonds between the urea moieties on the polymer chain. In methanol, ethanol and hexanol, the polymer was soluble because the protic polar solvents can form hydrogen bonds with the urea groups and cleaved association of the urea moieties. This result prompted further us to investigate control of LCST and UCST behaviors of **1** in the presence of additives in non-polar media by perturbation of hydrogen bonds between the

urea groups.

The solubility changes of the polymer **1** was investigated in 1,2-dichloroethane in the presence of various small molecules such as alcohols, amides, ureas and carboxylic acids (Table 1). For example UCST-type phase separation was observed by addition of *N,N*-butylpropylurea, 1-octanoic acid and tetrabutylammonium bromide, and LCST-type phase separation was by addition of 1-octanol, 1-dodecanol, pyrenemethanol and cholesterol, as shown in Fig. 2. For a series of aliphatic amides with different alkyl chain length, shorter and longer alky amides had UCST-type and LCST-type type phase separation, respectively. Moreover, polyhydroxy compounds such as neopentyl glycol and triethanolamine exhibited UCST-type phase separation, indicating that increase of the number of hydroxyl groups changed from LCST-type phase separation to UCST-type. These results show that the hydrogen bonding abilities between the urea groups and the additives play a key role for control of the thermo-sensitivity. The additives that can interact strongly to the urea groups induced UCST-type phase separation and those weakly did LCST-type one.

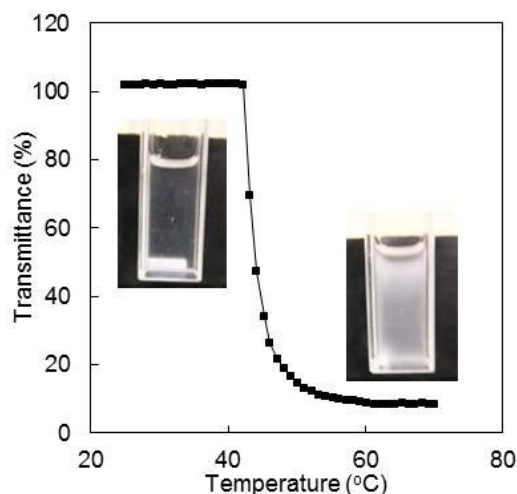
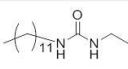
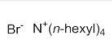
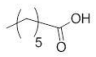
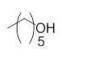
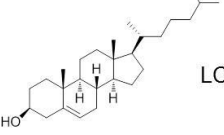
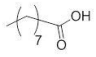
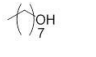
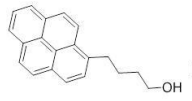
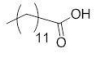
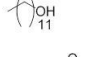
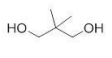
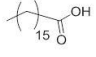
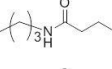
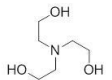
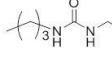
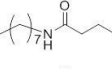
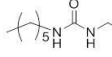
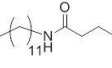
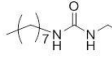
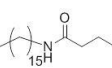


Fig. 2. LCST behavior of **1** (25 mg/mL) in the presence of dodecanol (0.57 M) in 1,2-dichloroethane. Recorded at 700 nm. Heating rate: 1 °C/min.

Table 1. Thermal behavior of Polymer **1** (25 mg/mL, 0.11 M) in the presence of small molecules in 1,2-dichloroethane (Concentration of small molecules and phase transition temperature in parentheses).

additives	Thermo-sensitivity	additives	Thermo-sensitivity	additives	Thermo-sensitivity
None	Insoluble	 UCST (0.26 M, 41 °C)	 Br <sup>-</sup> N <sup>+</sup> (n-hexyl) <sub>4</sub> UCST (0.015 M, 28 °C)		
 UCST (0.18 M, 41 °C)	 LCST (0.71 M, 46 °C)	 LCST (0.52 M, 57 °C)			
 UCST (0.13 M, 40 °C)	 LCST (0.65 M, 43 °C)	 LCST (0.52 M, 35 °C)			
 UCST (0.09 M, 44 °C)	 LCST (0.57 M, 43 °C)	 UCST (0.35 M, 51 °C)			
 UCST (0.07 M, 40 °C)	 UCST (0.93 M, 33 °C)	 UCST (0.31 M, 76 °C)			
 UCST (0.64 M, 32 °C)	 UCST (0.69 M, 63 °C)				
 UCST (0.39 M, 44 °C)	 LCST (0.65 M, 51 °C)				
 UCST (0.34 M, 37 °C)	 LCST (0.65 M, 47 °C)				

[1] H. Feil, Y. H. Bae, J. Feijen, S and W. Kim, *Macromolecules*, **26**, 2496 (1993). R. Liu, M. Fraylich and R. Saunders, *Colloid Polym. Sci.* 2009, **287**, 627. D. Schmaljohann, *Adv. Drug Delivery Rev.*, **58**, 1655 (2006).



## Synthesis and Characterization vinylbenzyl chloride-co-styrene-co hydroxyethyl acrylate(VBC-co-St-co-HEA)anion-exchange membrane for All-vanadium redox flow battery

Young min Baek, Jin Sun Koo, Noh Seok Kwak, Taek Sung Hwang<sup>†</sup>

<sup>†</sup>Department of Applied Chemistry and Biological Engineering, College of Engineering, Chungnam National University, 79 Daehangno, Yuseong-gu, Daejeon 305-764, South Korea

### Abstract

In this study, we have synthesized vinylbenzyl chloride-co-styrene-co hydroxyethyl acrylate(VBC-co-St-co-HEA) copolymer that can be applied to redox flow battery process. The anion exchange membrane was prepared by the amination and crosslinking of VBC-co-St-co-HEA copolymer. The chemical structure and thermal properties of VBC-co-St-co-HEA copolymer and aminated VBC-co-St-co-HEA (AVSH) membrane were characterized by FT-IR, <sup>1</sup>H-NMR, TGA, and GPC analysis. The membrane properties such as ion exchange capacity(IEC), electrical resistance, ion conductivity and efficiency of all-vanadium redox flow battery were measured with the prepared membranes. The IEC value, electrical resistance, and ion conductivity were 1.17 meq/g, 1.9  $\Omega \cdot \text{cm}^2$ , 0.009 S/cm, respectively. The charge-discharge efficiency, voltage efficiency and energy efficiency from result of all-vanadium redox flow battery test were 99.5%, 72.6% and 72.1%, respectively.

### 1. Introduction

The redox flow battery (RFB) is being investigated as one of the most promising electrochemical energy storage devices for a wide range of applications, such as electric vehicles, photovoltaic arrays.[1,2] In the RFB system, ion exchange membrane is served as a separator between anode and cathode electrolytes and also provided proton conduction. The ideal ion exchange membrane should have high ionic conductivity, low ion crossover, high selectivity, durability and low cost. Nafion (Dupont, USA) has excellent properties on the ion exchange membrane. However, it suffers from the vanadium ions crossover through the membrane, which causes decreasing in energy efficiency. Furthermore, it is too expensive for commercial use. Some of other ion exchange membranes such as Selemion, CMV, DMV (Asahi glass Co., Japan) are unsuitable due to their degradation by  $\text{VO}_2^+$  in vanadium RFB.

### 2. Experimental

In this study, the main materials include 4-Vinylbenzyl chloride (VBC), styrene (ST), 2-Hydroxyethyl Acrylate (HEA), trimethylamine (TMA), glutaric dialdehyde, toluene,

Dimethylformamide (DMF) and Azobisisobutyronitrile(AIBN). VBC, ST, HEA, TMA and adipic acid were purchased from Aldrich(Seoul, Korea). Toluene and dimethylformamide were purchased from Samchun. All reagents were used without further purification.

we have synthesized vinylbenzyl chloride-co-styrene-co hydroxyethyl acrylate(VBC-co-St-co-HEA) copolymer. The anion exchange membrane was prepared by the amination and crosslinking of VBC-co-St-co-HEA copolymer.

Table 1. Synthesis conditions of VBC-co-St-co-HEA copolymer

Code No.	Weight ratio			AIBN (wt%)	Toluene (wt%)	Reaction Time (hr)	Reaction Temp. (°C)
	VBC	St	HEA				
VSH-1	2.5	4.5	2.5	1	40	36	70
VSH-2	3.0	4.5	2.5	1	40	36	70
VSH-3	3.5	4.5	2.5	1	40	36	70

### 3. Results and discussion

The charge-discharge efficiency, voltage efficiency and energy efficiency from result of all-vanadium redox flow battery test were 99.5%, 72.6% and 72.1%.

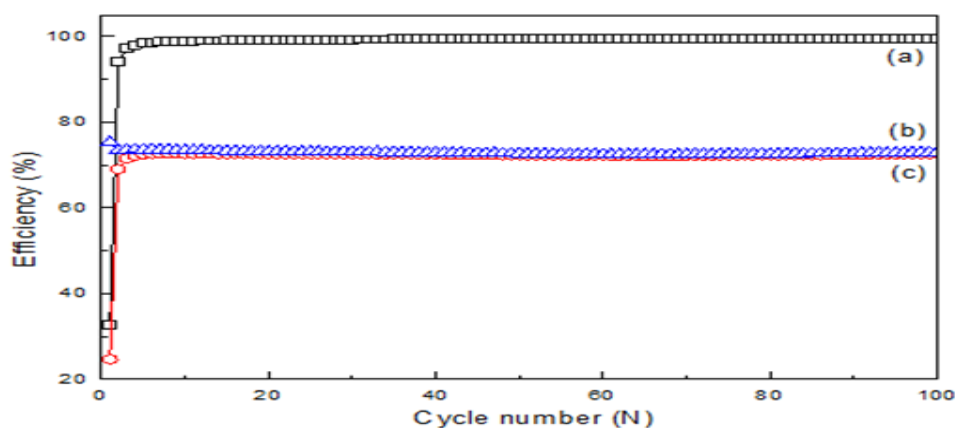


Figure 1. VRB efficiency for AVSH-3(in 6wt %glutaric dialdehyde) anion exchange membrane during cycling (current density :40 mA/cm<sup>2</sup>); (a) charge-discharge efficiency, (b) voltage efficiency, and (c) energy efficiency.

- [1] V. M. Barragan, J. P. G. Villaluenga, M. P. Godino, M. A. Izquierdo-Gil, C. Ruiz-Bauza, B. Seoane, *J. Colloid Interface Sci.*, **333**, 497 (2009).
- [2] J. Qiu, M. Li, J. Ni, M. Zhai, J. Peng, L. Xu, H. Zhou, J. Li, G. Wei, *J. Membrane Sci.*, **297**, 174 (2007).
- [3] Z. Mai, H. Zhang, X. Li, S. Xiao, Hongzhang Zhang, *J. Power sources*, **10**, 1016 (2010).

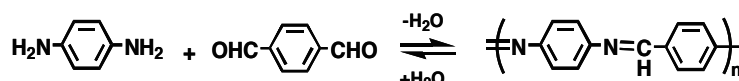
## Aromatic Schiff-base Polymer Films Prepared in Aqueous Solution by On-site Polycondensation

Rintaro Higuchi<sup>1</sup>, Ryota Tanoue<sup>1</sup>, Kazuki Sakaguchi<sup>1</sup>, Shinobu Uemura<sup>1</sup>, Masashi Kunitake<sup>1,2</sup>

<sup>1</sup>Department of Science and Technology, Kumamoto University, Japan

<sup>2</sup>Core Research for Evolutional Science and Technology,  
Japan Science and Technology Agency (JST-CREST)

The deposition of  $\pi$ -conjugated polymer thin films on arbitrary surfaces is crucial for assembling polymer electronic devices such as organic light-emitting diodes, field-effect transistors, and solar cells. Here we introduce a novel chemical liquid deposition (CLD) method to prepare aromatic  $\pi$ -conjugated polymer films based on surface-selective Schiff-base coupling between aromatic amines and aromatic aldehydes, which is a reversible reaction controlled by the pH of the solution (Scheme 1). Spontaneous film deposition of the polymers on hydrophobic substrates selectively was achieved by adequate control both of the reaction and adsorption equilibria.[ref.1]



Scheme 1. Typical Schiff-base coupling reaction between aromatic primary amine and aldehyde

When freshly cleaved highly oriented pyrolytic graphite (HOPG) was immersed in 0.1 mM aqueous solution containing 4,4'-diaminostilbene (ASB) and 2,5-thiophenedicarboxyaldehyde (TCA) adjusted to pH 2.8 for several hours under 303 K, colorful polymer films on the HOPG were obtained by deposition (Fig. 1). The red-shift on the UV-Vis spectra in accordance with deposition time observed would suggest an extension of  $\pi$ -conjugated systems by surface polycondensation. In addition, from many combinations between aromatic amines and aldehydes as building blocks, various  $\pi$ -conjugated aromatic polymer films were successfully prepared. This simple and highly designable CLD methodology to prepare  $\pi$ -conjugated polymer films will promise to explore next-generation organic electronics materials prepared from aqueous solution under ambient conditions without massive equipments.

[1] R. Tanoue *et al.*, *ACS Nano*, **5** (5), 3923 (2011).

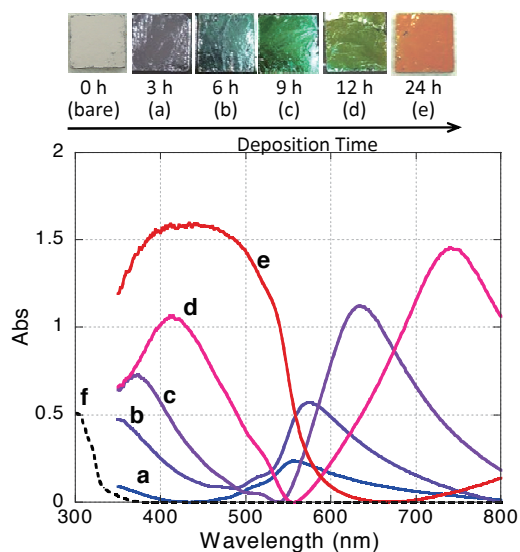


Fig. 1. Typical photos and UV-Vis reflection spectra of ASB-TCA Schiff-base polymer films deposited onto a HOPG. Deposition times are 3 h (a), 6 h (b), 9 h (c), 12 h (d), and 24 h (e). The black dotted line (f) reveals a solution for 24 h after mixing. Each film was deposited under 303 K, pH 2.8.

## The Effect of Inorganic Fillers on Electrospun Nanofibers for Dye-sensitized Solar Cells

Won-Pill Hwang<sup>1</sup>, Min-Hye Seo<sup>1</sup>, Young-Keun Kim<sup>1,2</sup>, Mi-Ra Kim<sup>1</sup>, and Jin-Kook Lee<sup>1\*</sup>

<sup>1</sup>Department of Polymer Science & Engineering, Pusan National University, Republic of Korea

<sup>2</sup>Solchem Co., LTD, Republic of Korea

To obtain the high conversion efficiency DSSC, the use of liquid electrolyte is inevitable and iodine is one of the most important ingredients in electrolyte [1]. However, the liquid electrolyte can easily evaporate and eventually, the leakage may trigger the short of the cell. According to our previous study, electrospun nanofibers have porous structure that could hold liquid from evaporation [2]. With these nanofibers, both high efficiency and long-term stability could be promised when these nanofibers are applied to the electrolyte system. To obtain higher power conversion efficiency and stability, nanofibers were modified with several inorganic materials. The inorganic materials were incorporated into poly-(vinylidene fluoride-co-hexafluoropropylene) (PVDF-HFP). To enhance the ionic conductivity, aluminum oxide (Al<sub>2</sub>O<sub>3</sub>), silicone dioxide (SiO<sub>2</sub>) [3], and titanium isopropoxide (TIP) were used in this experiment. The weight percent of the inorganic materials were varied to confirm the tendency and the parameters for the electrospinning technique had been optimized during the experiment. Electrolyte uptake and the porosity of the nanofibers were measured with eq. 1 and eq. 2 where *m* and *m*<sub>0</sub> are the mass of wet and dry electrospun nanofibers, respectively.

$$U = \left[ \frac{(m-m_0)}{m_0} \right] \times 100\% \quad (1)$$

$$P \text{ (vol\%)} = \left( 1 - \frac{\rho_m}{\rho_p} \right) \quad (2)$$

The porosities (*P*) of the electrospun nanofibers were calculated from the density of each electrospun nanofibers and the density of pure PVDF-HFP. Fig. 1 shows the field emission scanning electron microscopy (FESEM) images of electrospun nanofibers. The images were taken after the removal of the solvent.

And overall power conversion efficiencies of the DSSC device using modified electrospun nanofiber are shown in Table 1.

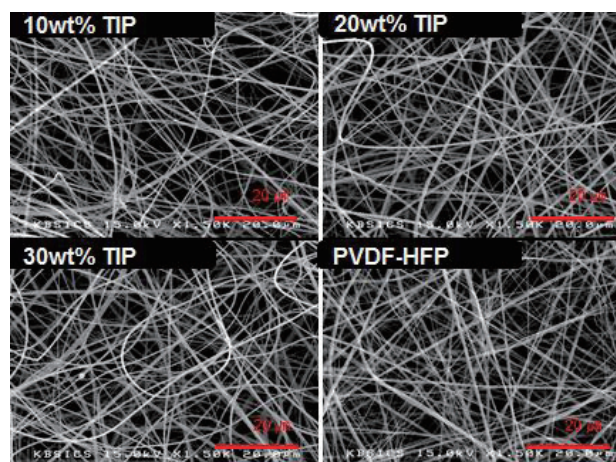


Fig. 1 FESEM images of PVDF-HFP/TIP (10, 20, and 30wt%) and PVDF-HFP nanofibers

Table 1 Photovoltaic properties of DSSC devices using PVDF-HFP/ $\text{Al}_2\text{O}_3$  (0.1, 0.3, and 0.5wt%), PVDF-HFP/ $\text{SiO}_2$  (1, 3, and 5wt%), and PVDF-HFP/TIP (10, 20, and 30wt%), and only PVDF-HFP electrospun nanofibers

Type of Inorganic Fillers (weight %)	$V_{oc}$ (V)	$J_{sc}$ ( $\text{mA}/\text{cm}^2$ )	Fill Factor	Efficiency (%)
$\text{Al}_2\text{O}_3$ (0.1)	0.71	13.2	0.60	5.64
$\text{Al}_2\text{O}_3$ (0.3)	0.71	13.9	0.61	5.99
$\text{Al}_2\text{O}_3$ (0.5)	0.72	12.9	0.61	5.66
$\text{SiO}_2$ (1)	0.73	11.6	0.63	5.33
$\text{SiO}_2$ (3)	0.73	11.6	0.59	5.03
$\text{SiO}_2$ (5)	0.71	11.3	0.62	5.00
TIP (10)	0.73	12.0	0.61	5.42
TIP (20)	0.74	12.7	0.61	5.74
TIP (30)	0.72	13.4	0.59	5.72
Only PVDF-HFP	0.70	10.7	0.62	4.70

[1] M. K. Nazeeruddin, *J. Am. Chem. Soc.*, **127**, 16835(2005)

[2] S. Park, *J. Solmat.*, **95**, 296(2011)

[3] P. Raghavan., *J. Electro. Acta.*, **54**, 228(2008)

## Polypyrrole – Carbon Black Nanocomposite Electrode For Conducting Polymer Actuator

Hyun Ju Bak, Hyun-Ok Lim, and Nam-Ju Jo\*

Department of Polymer Science and Engineering, Pusan National University, South Korea

Upon to oxidation and reduction, conducting polymers(CPs) show a volume change, which is able to be utilized as actuators. Particularly polypyrrole(PPy) is most promising CP actuator materials in a view point of high electrical conductivity and environmental stability. However, the electrical resistance of a free-standing CP actuator film can produce significant IR drop along its length, which can reduce the actuator performance[1,2]. To solve this problem, the construction of CP actuator based on PPy/carbon black(CB) nanocomposite film electrodes and a solid polymer electrolyte(SPE), polyurethane/Mg(ClO<sub>4</sub>)<sub>2</sub>, was accomplished. PPy/CB nanocomposite film was electrochemically polymerized from aqueous dispersions of pyrrole monomer containing carbon black. Polyurethanes as a matrix of SPE were synthesized by using a two-step method based on poly(tetramethylene ether) glycol(PTMG), 4,4'-methylenediphenyl diisocyanate(MDI), and 1,4-butanediol(1,4-BD). SPEs with various Mg(ClO<sub>4</sub>)<sub>2</sub> contents were prepared by solution casting method. Ultimately, we constructed PPy nanocomposite/SPE/PPy nanocomposite tri-layer actuator showing improved electrochemical properties.

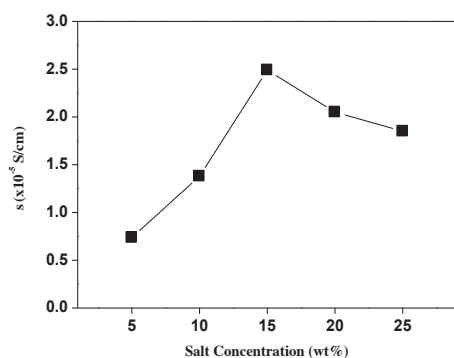


Fig. 1. The ionic conductivity of SPE.

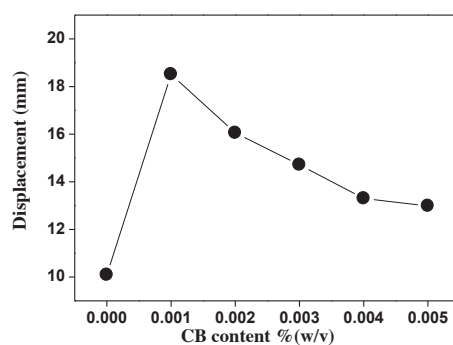


Fig. 2. Displacement of PPy nanocomposite actuator.

Fig. 1 shows the ionic conductivity of SPE as a function of salt concentration. A maximum conductivity of  $2.49 \times 10^{-5}$  S/cm was achieved at room temperature for 15wt% of Mg(ClO<sub>4</sub>)<sub>2</sub> salts. Fig. 2 shows the displacement of PPy nanocomposite actuator. The best displacement appeared when the conductivity of PPy nanocomposite film was the highest. Also we confirmed the feasibility of electrochemical properties for solid-state CP actuator based on PPy nanocomposite film and SPE available in air.

[1] Y. Bar-Cohen, *Journal of spacecraft and rockets*, **39**, 822 (2002)

[2] D.Zhou, G.M. Spinks, G.G. Wallace, C.Tiyapiboonchaiya, D.R. MacFarlane, M. Forsyth, and J. Sun, *Electrochimica Acta*, **48**, 2335 (2003)

## Surface Modification of Dye-sensitized Solar Cells using Poly[(quaternized *N*-Vinyl imidazole)-*co*-poly(*N*-Vinyl amine)]

Changhwan Ju,<sup>1</sup> Sungsu Lim,<sup>2</sup> Jae-Jun Lee,<sup>2</sup> and Hyun-jong Paik<sup>1</sup>

<sup>1</sup>Pusan National University, Department of Polymer Science and Engineering, Busan, Korea

<sup>2</sup>Konkuk University, Department of Applied Chemistry, Chungju, Korea

The dye-sensitized solar cells (DSSCs) has attractive features of high energy conversion and low production cost. [1] The blocking layers play high efficiency in the photovoltaic process of the DSSCs. Poly[(*quaternized N*-vinyl imidazole)-*co*-poly(*N*-vinyl phthalimide)] (pQVIm-*co*-pNVPI) used in DSSCs was synthesized by reversible-addition fragmentation transfer (RAFT) polymerization. Poly[(*quaternized N*-vinyl imidazole)-*co*-poly(*N*-vinyl amine)] (pQVIm-*co*-pVAm) were prepared via hydrazinolysis reaction of pQVIm-*co*-pNVPI. [2] The modified DSSC cells were prepared by carbodiimide-mediated coupling reaction of pQVIm-*co*-pVAm and N3 dye. This reactions show fig. 1. The synthesized copolymers were characterized by FT IR and <sup>1</sup>H-NMR spectroscopy. The modified DSSC cells were characterized by FT IR, XPS to verify the amide bond. Table 1 compared the solar cell characteristics for DSSCs with polymer, and without polymer. The DSSC performance using surface modification cells was 0.77 V, 8.69 mA/cm<sup>2</sup>, 0.68 and 3.55 % under AM 1.5.

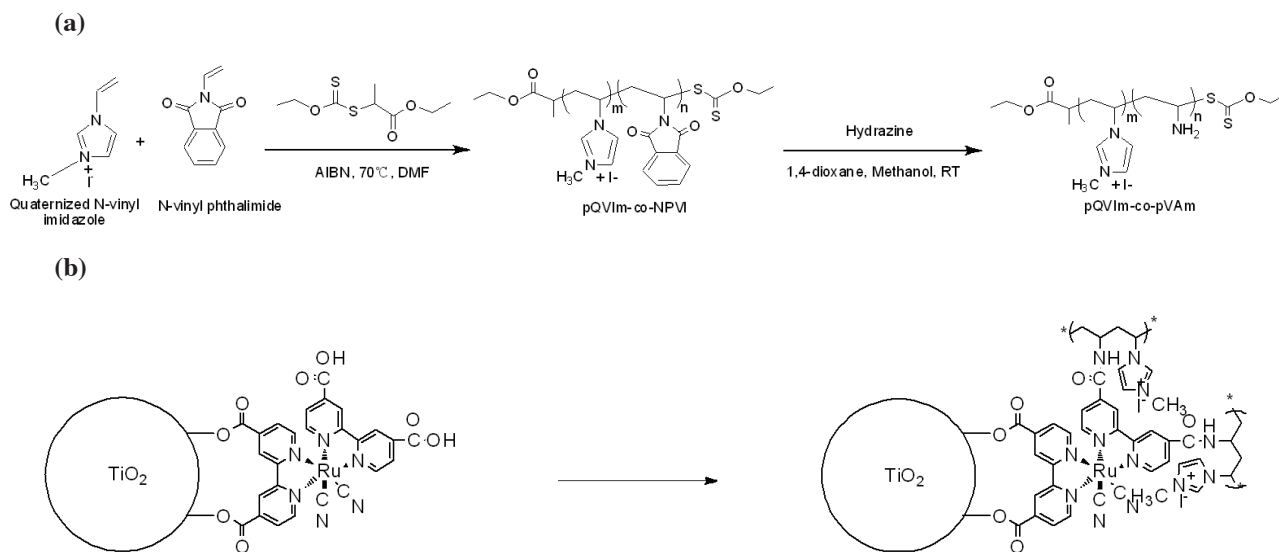


Fig. 1. Scheme of synthesized (a) random copolymer, p(QVIm-*co*-NVPI) via RAFT technique and deprotection of p(QVIm-*co*-NVPI), (b) N3 dye and p(QVIm-*co*-VAm) complex.

Table 1. Solar cell measurements of DSSCs with polymer and without polymer

	Voc (V)	Jsc (mA/Cm <sup>2</sup> )	FF (%)	Eff. (%)
Reference Cell	0.67	7.83	65.12	3.44
Coupling Cell	0.77	6.74	68.34	3.55

- [1]. Gratzel, M., Photoelectrochemical cells. *Nature*, 2001. 414(6861): p. 338-344.
- [2]. Maki, Y., H. Mori, and T. Endo, Controlled RAFT Polymerization of N-Vinylphthalimide and its Hydrazinolysis to Poly(vinyl amine). *Macromolecular Chemistry and Physics*, 2007. 208(24): p. 2589-2599.



## Preparation of IPA-co-HDO-co-(TPA/MA) copolymer anion-exchange membrane using UV crosslinking

Jae Chul Jung, Won Ho Jung, Taek Sung Hwang<sup>†</sup>

*Department of applied chemistry and biological engineering,  
Chungnam National University, Daejeon 305-764, Republic of Korea*

### ABSTRACT

In this study, The IPA-co-HDO-co-(TPA/MA) copolymers for all vanadium redox-flow battery were synthesized by melt condensation polymerization using isophthalic acid(IPA), 1,6-hexandiol(HDO), terephthalic acid(TPA) and maleic anhydride(MA). The amination of chloromethylated IPA-co-HDO-co-(TPA/MA)(CIHTM) copolymer was carried out trimethylamine, and also, the anion exchange membrane was prepared by UV crosslinking reaction. The structure and thermal stability of IHTM copolymers were confirmed by FT-IR, <sup>1</sup>H-NMR, TGA analysis. And also, the anion membrane properties such as water uptake, ion exchange capacity, electric resistance and electrical conductivity, were measured by gravimetry, titration and LCR meter. The efficiency of the all-vanadium redox flow battery was carried out.

### Introduction

In the RFB system, ion exchange membrane is served as a separator between anode and cathode electrolytes and also provided proton conduction. The ideal ion exchange membrane should have high ionic conductivity, low ion crossover, high selectivity, durability and low cost. In this study, we have synthesized an copolymer by two-step melt condensation based on Isophthalic acid (IPA). And we have prepared anion exchange membrane using trimethylamine and pentaerythritol tetraacrylate (PETA) with UV curing system.

### Experimental

#### Synthesis of the copolymer

The synthesis of IPA based copolymer was carried out in a 3 liter capacity 4-neck glass batch reactor equipped with a mechanical stirrer, nitrogen inlet, thermocouple, and bead condenser. This reaction consists of 2-step polycondensation reaction. The synthesis conditions were shown in Table 1.

Table 1. synthesis condition of IPA-co-HDO-co-(TPA/MA) copolymer.

Code No.	1st step		2nd step			Temp. (°C)		Reaction time (hr)	
	IPA (mol/L)	HDO (mol/L)	TPA (mol/L)	MA (mol/L)	HQ (mol/L)	1st	2nd	1st	2nd
IHTM-1	1.0	3.73	0.33	0.67	0.001	220	220	8	8
IHTM-2	1.5	3.73	0.33	0.67	0.001	220	220	8	8
IHTM-3	2.0	3.73	0.33	0.67	0.001	220	220	8	8

## Result

### Ion exchange capacity

One of the important factor on the ion exchange membrane is ion exchange capacity (IEC). The IEC of prepared IHTM membranes was determined by the fisher's titration method. The IEC values of the prepared IHTM membranes were 0.45-1.0 meq/g. The ion exchange capacity of the IHTM membranes increased with Amination time from 1 to 5hr.

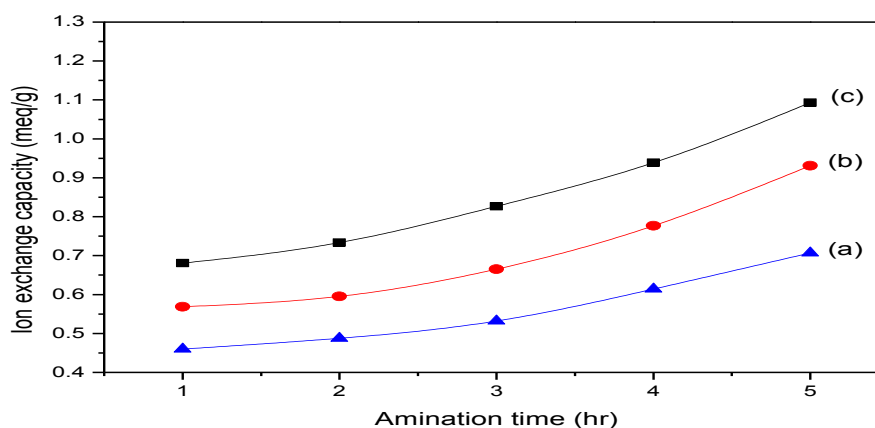


Fig. 1. Ion exchange capacity of IHTM anion exchange membrane; (a) IHTM-1, (b) IHTM-2, (c) IHTM-3

## Conclusions

The membranes of IPA-co-HDO-co-(TPA/MA) were characterized in terms of ion exchange capacity, electrical properties. The ion exchange capacity, electric resistance and electrical conductivity were 1.10 meq/g, 1.98  $\Omega \cdot \text{cm}^2$ , and 0.009 S/cm, respectively. The efficiency of charge-discharge, voltage, and energy for the all-vanadium redox flow battery were 96.5%, 74.6%, 70.0%, respectively.

## References

- [1] . M. Pourbaix, *National Association of Corrsion Engineers*, Houston (1982)
- [2] D.H. Lee, Y. S. Kang, J.H. Kim, *Macromol. Res.* 17, 104-109 (2009)

## Preparation $\text{Li}_{1.33}\text{Mn}_{1.67}\text{O}_4$ sphere bead by calcinations process and $\text{Li}^+$ adsorption properties.

Won Ho Jung, Jae Chul Jung, Noh Seok Kwak, Taek Sung Hwang\*

\*Department of Applied Chemistry and Biological Engineering, College of Engineering, Chungnam National University, 79 Daehangno, Yuseong-gu, Daejeon 305-764, South Korea

Phone: \*+82-42-821-5687, fax: +81-42-822-8995

E-mail: \*[tshwang@cnu.ac.kr](mailto:tshwang@cnu.ac.kr)

### Abstract

$\text{Li}^+$  onto seawater has recovered by various materials and process, because of Lithium is one of rare metal resources. In this study, the  $\text{Li}_{1.33}\text{Mn}_{1.67}\text{O}_4$  sphere bead(LSB) was prepared by suspension polymerization using divinyl benzene (DVB), styrene monomer (Sty) and lithium manganese oxide ( $\text{Li}_{1.33}\text{Mn}_{1.67}\text{O}_4$ ). A sphere bead was synthesis by DVB-Sty polymerization and  $\text{Li}_{1.33}\text{Mn}_{1.67}\text{O}_4$  was added to investigate its adsorption of  $\text{Li}^+$  on the seawater and lithium enrichment water. Addition amount of  $\text{Li}_{1.33}\text{Mn}_{1.67}\text{O}_4$  were carefully carried independently or as in combination to find the optimum condition for amount of  $\text{Li}^+$  adsorption. The thermal decomposition of organic material during the calcinations process certainly increased the surface area of LSB. SEM analysis confirmed that the LSB has diameter range of 100 to 300 nm and according to XRD analysis confirmed that spinel structure of LSB. ICP analysis confirmed that amount of  $\text{Li}^+$  adsorption by LSB in seawater and lithium enrichment water.

### 1. Introduction

The growing concerns about lithium battery and the rising issues of lithium were rare metal resources. Among the rare metal resources, lithium is the one of the most important material for lithium battery. Many researchers are studying Li adsorbent materials for adsorption of  $\text{Li}^+$  in seawater and wastewater. In this study, the LSB for  $\text{Li}^+$  adsorption in seawater and lithium

enrichment water form by suspension polymerization and calcinations process. Suspension polymerization has one of method for produce polymer bead. DVB-Sty suspension polymerization was prepared sphere bead for addition  $\text{Li}_{1.33}\text{Mn}_{1.67}\text{O}_4$ . And according to calcinations process, increase surface area on the LSB.

### 2. Experimental

Divinyl benzene (DVB; 80%), styrene monomer (Sty; 99.50%) were purchased from aldrich and use to monomer of suspension polymerization. LSB was synthesized from suspension polymerization base on DVB and Sty. During polymerization, added  $\text{Li}_{1.33}\text{Mn}_{1.67}\text{O}_4$  for  $\text{Li}^+$  adsorbent. DVB-Sty was supporting to  $\text{Li}_{1.33}\text{Mn}_{1.67}\text{O}_4$  and formation pore from calcinations process. LSB were synthesized in a 1000ml 4-neck round flask with mechanical stirrer, heating mentle. Poly(vinyl alcohol) (PVA) were dissolved in distilled water at 80 °C. Monomers were prepared Mixed DVB, Sty,  $\text{Li}_{1.33}\text{Mn}_{1.67}\text{O}_4$  and 2,20azobisisobutyronitrile (AIBN; 98.0%) in the toluene (99.0%) were used to synthesis initiator and pore-forming agent. Monomer solution was put in the PVA solution with a dropping funnel at 80 °C for 4hr.

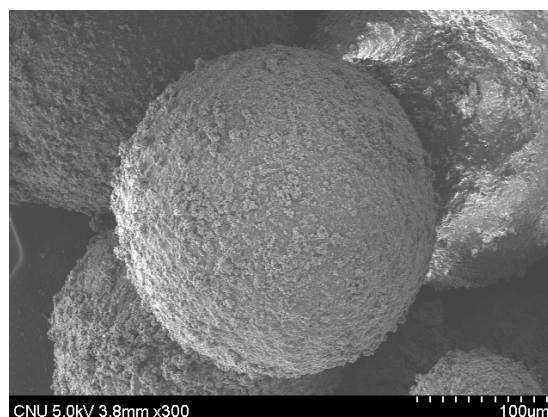
**Table 1.** The condition of LSB synthesis

Monomer		Adsorbent	Pore agent
DVB	Sty	$\text{Li}_{1.33}\text{Mn}_{1.67}\text{O}_4$	Toluene
		1.0 g	
15.0 g	5.0 g	3.0 g	2.0 g
		5.0 g	

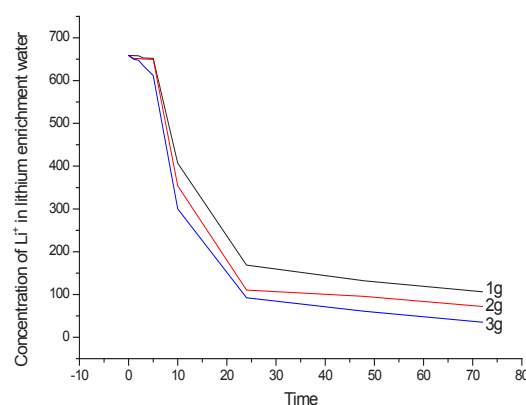
### 3. Results and discussion

Fig. 1. Represents produced LSB surface which was analyzed by SEM. Fig. 1. Shows the LSB has 200nm of diameter and has a rough surface. Fig. 2. Show the amount of

$\text{Li}^+$  adsorption used LSB in lithium enrichment water.



**Fig. 1.** SEM image of LSB.



**Fig. 2.** The  $\text{Li}^+$  adsorption effect by amount of  $\text{Li}_{1.33}\text{Mn}_{1.67}\text{O}_4$ .

### Reference

- [1] H. Pauwels, M. Brach, C. Fouillac, *Physicochemical and Engineering Aspects*, 100, 73 (1995).
- [2] Q. H. Zhang, S. P. Li, *Chemical Engineering Science*, 65, 169 (2010).
- [3] A. H. Hamzaoui, B. Jamoussi, A. M'nif, *Hydrometallurgy*, 90, 1 (2008).

## Structural Transitions and Magnetic Bi-stabilities on Cobalt(II) Nitrate Complexes with Tridentate N-donors Ligands

Shinji Kanegawa<sup>1</sup>, Junichi Nishioka<sup>1</sup>, Motohiro Nakano<sup>2</sup> and Osamu Sato<sup>1</sup>

<sup>1</sup>Institute for Materials Chemistry and Engineering, Kyushu University, 6-1 Kasuga-koen, Kasuga, Fukuoka, 816-8580, Japan

<sup>2</sup>Department of Applied Chemistry, Graduate School of Engineering, Osaka University2-1 Yamadaoka, Suita, Osaka, 565-0871 Japan

Magnetic molecular materials exhibiting magnetic bi-stabilities in response to external stimuli such as heat and light are attracting a great attention because of their potential application in molecular switching devices. The typical examples exhibiting such magnetic bi-stability are spin crossover complexes. This kind of compounds shows magnetic switching behaviors based on the inter-conversion between two states with different spin multiplicity. On the other hand, we are recently focusing on orbital angular momentum to develop new magnetically bi-stable materials. It is well known that origins of magnetic moment are spin magnetic momentum and orbital angular momentum. Hence, controlling of orbital angular momentum offers novel alternative routes to induce magnetic bi-stabilities. Indeed, we have recently reported a Co(II) complex that exhibits magnetic bi-stability based on the change in the orbital angular momentum quenching.[1] In the present work, we investigated the magnetic properties of two mono-nuclear Co(II) complexes with tridentate ligands(L1, L2). We found that they show switchable magnetic properties through single crystal-to-single crystal phase transitions. Additionally, we found that the magnetic behaviors strongly depend on the direction of an applied magnetic field. (Fig. 2)

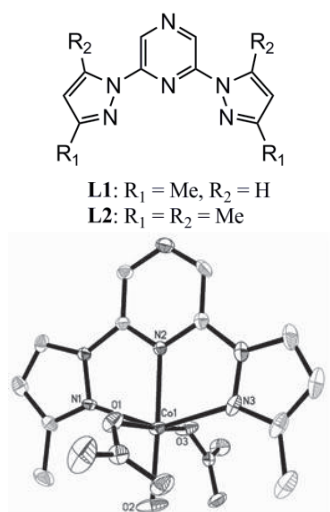


**Figure 1.** Molecular structure of (a) tridentate ligands and (b) Co(II) complex[Co(NO<sub>3</sub>)<sub>2</sub>(H<sub>2</sub>O)(L<sub>1</sub>)]. The structure of the complex was analyzed at 190 K.

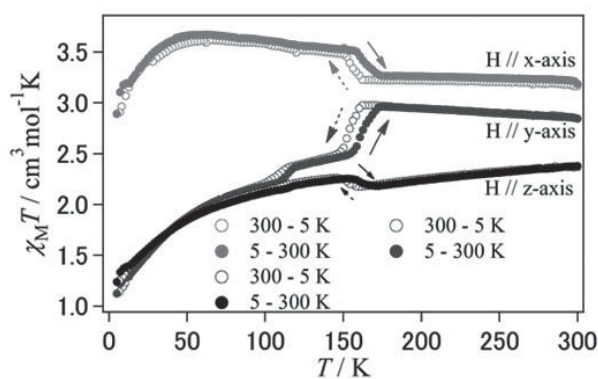


**Figure 2.** Temperature dependence of  $\chi_M T$  ( $\chi_{Mx} T$ ,  $\chi_{My} T$  and  $\chi_{Mz} T$ ) for single-crystal of [Co(NO<sub>3</sub>)<sub>2</sub>(H<sub>2</sub>O)(L1)] in cooling (○) and heating mode (●)

[1] G. Juhász, O. Sato, K. Yoshizawa et al. J. Am. Chem. Soc., 2009, 131, 4560–4561.

## Sphere to Cylinder Transition induced by pH Dependent Conformational Change of Amphiphilic Calix[4]arene

Shota Fujii<sup>1</sup>, Tomoki Nishimura<sup>1</sup>, Yusuke Sanada<sup>1</sup>, Kazuo Sakurai<sup>1,2</sup>

<sup>1</sup>The University of Kitakyushu, Japan

<sup>2</sup>JST-CREST

Controlled self-assembly of amphiphilies is an important field in material science. Amphiphilic molecules consisting of hydrophilic and hydrophobic block segments have been proven to be promising scaffolds for self-assembled structures on the nanometer scale.

Among many functional amphiphilies, calix[4]arene moiety is particular useful as a rigid segment to provide a well-defined nanometer-sized structure. Although many structural studies of self-assembled amphiphilic calix[4]arene derivatives have been reported, the pH-dependent structural change of self-assembled amphiphilic calix[4]arene derivatives remains relatively unexplored field. Here, we reported the synthesis of an amphiphilic calix[4]arene (denoted CaL[4]C3, see Fig.1) and the structural change from sphere to cylinder for amphiphilic CaL[4]C3 induced by pH with SAXS and AFM.

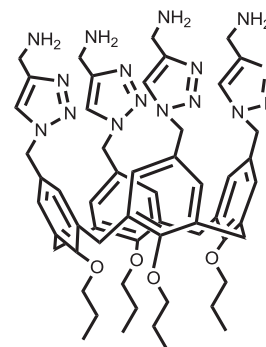


Fig.1 Chemical Structure of CaL[4]C3

Fig.2 shows the SAXS profiles of CaL[4]C3 in aqueous solution at pH 5.7 ~ 7.5. The result revealed that CaL[4]C3 undergoes a clear transition from a sphere with the radius of 2.0 nm to a rigid cylinder with the cross-sectional radius of 1.5 nm, accompany with the pH induced protonation on amine groups of CaL[4]C3 and change the packing parameter. These spherical and cylindrical assemblies are confirmed by AFM.

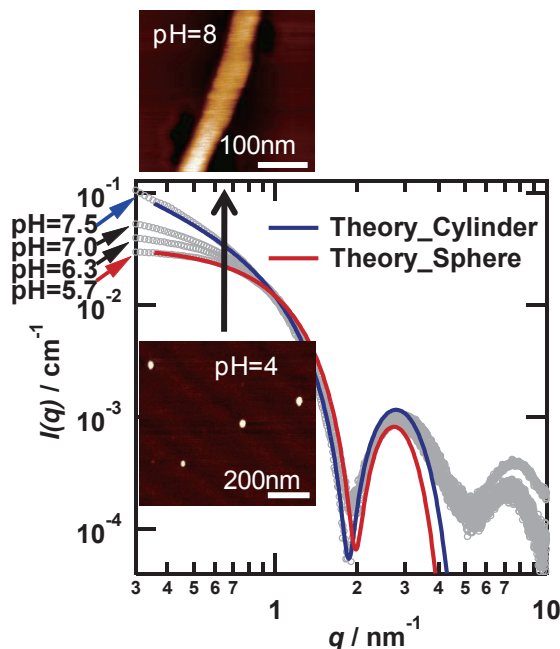


Fig.2 SAXS profiles of CaL[4]C3 in aqueous solution at pH 5.7 ~ 7.5.

## Anomalous Small-Angle X-ray Scattering from the Micelles made of a Br-bearing Lipid

Chie Iino<sup>1</sup>, Hiroyasu Masunaga<sup>2</sup>, Isamu Akiba<sup>1</sup>, Kazuo Sakurai<sup>1,3</sup>

<sup>1</sup>Department of Chemistry and Biochemistry, The University of Kitakyushu, Japan

<sup>2</sup>JASRI/SPring-8

<sup>3</sup>JST-CREST

Amphiphilic compounds are known to form the variety of structures such as the cylinder and the spherical micelles, vesicles or lamellar in aqueous solution and are applied to DDS (Drug Delivery System) particle. One of the problems in DDS is to control drug release precisely. It is necessary to analyze finely the retention form in DDS particles to clean it, but there are no solutions at present. The anomalous small-angle X-ray scattering (ASAXS) can provide the information not only about the electron density but the structure of the nanoparticle. This method gives the description of local structures induced by different elements. In this study, we synthesized a bromine-bearing cationic lipid [Fig.1] and characterized the self-assemblies formed from it.

The result of SAXS profile could fit in the bilayer core-shell theory and specified the existence domain of bromine in lipid micelles by resonant term extracted from SAXS [Fig.2]. Then considering the result of electron density of bromine domain using four layered core-shell theory, we retried to fit SAXS data [Fig.3]. The four layered model was more match with data in wide  $q$  side comparing the fitting results of bilayer with four layered model.

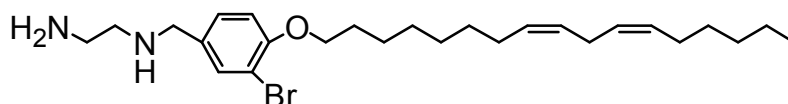


Fig.1 Chemical structure of bromine-bearing cationic lipid

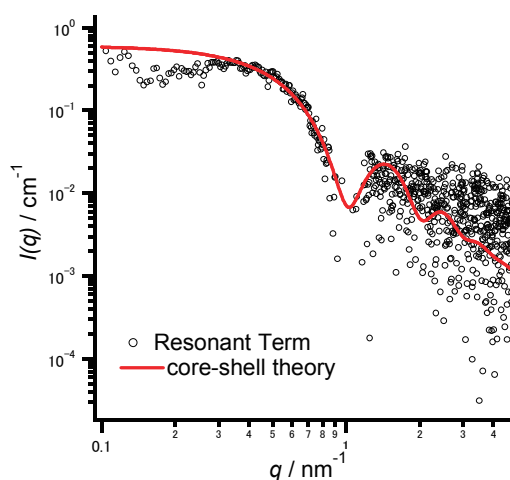


Fig.2 Resonant term(ASAXS data) of micelles

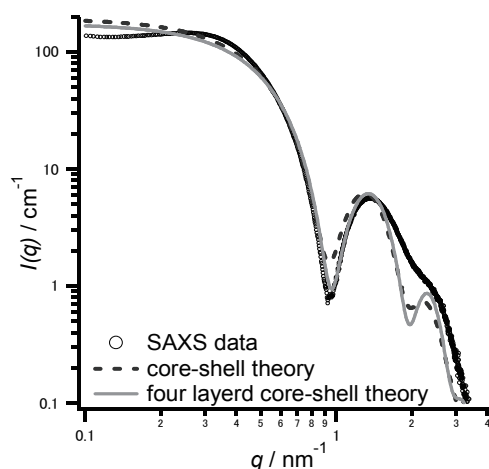


Fig.3 The results of fitting using two type theories

## Static and Dynamic Scattering from Silica Nanoparticle Immobilized Polysulfobetaine in Aqueous NaCl solutions

Moriya Kikuchi<sup>1,2</sup>, Yuki Terayama<sup>3</sup>, Tatsuya Ishikawa<sup>3</sup>, Taiki Hoshino<sup>1,2</sup>,  
Motoyasu Kobayashi<sup>1,2</sup>, Hiroki Ogawa<sup>4</sup>, Hiroyasu Masunaga<sup>4</sup>, Noboru Ohta<sup>4</sup>,  
Jun-ichiro Koike<sup>5</sup>, Misao Horigome<sup>5</sup>, Hiroshi Jinnai<sup>1,2</sup>, and Atsushi Takahara<sup>1,2,3</sup>

<sup>1</sup>Japan Science and Technology Agency, ERATO, Takahara Soft Interfaces Project, Japan

<sup>2</sup>Institute for Materials Chemistry and Engineering, Kyushu University, Japan

<sup>3</sup>Graduate School of Engineering, Kyushu University, Japan

<sup>4</sup>Japan Synchrotron Radiation Research Institute / Spring-8, Japan

<sup>5</sup>DIC Cooperation, Chiba, Japan

### Introduction

It is well known that poly(3-(*N*-2-methacryloyloxyethyl-*N,N*-dimethyl) ammonio-propanesulfonate) (PMAPS) exhibit a unique aqueous solution behavior in contrast with the conventional polyelectrolytes. The PMAPS is insoluble in de-ionized water at room temperature because of the strong attractive inter- and intramolecular electrostatic interaction between ammonium cations and sulfonyl anions [1]. However, experimental works of the PMAPS brush state are limited to the chain dimension of that in an aqueous solution. In this study, we carried out dynamic light scattering (DLS) and synchrotron small-angle X-ray scattering measurements of surface-grafted PMAPS on a silica nanoparticle (SiNP-PMAPS) in aqueous NaCl solutions at various salt concentrations ( $C_s$ ) to investigate the chain dimensions and conformation of surface-grafted polymer chains.

### Experimental

The surface-initiated atom transfer radical polymerization of MAPS was carried out with the initiator-immobilized SiNP with a radius of 55 nm [2]. The number-average molecular weight ( $M_n$ ) and polydispersity index ( $M_w/M_n$ ) of the cleaved graft PMAPS from the SiNP surface with an aqueous HF solution were determined to be  $M_n = 7.21 \times 10^4$  g mol<sup>-1</sup> and  $M_w/M_n = 1.27$  by size exclusion chromatography calibrated with a series of PMAPSs as a standard. The graft density of PMAPS brush on a SiNP surface was estimated to be 0.043 chains nm<sup>-2</sup> using values of weight loss measured by thermogravimetric analysis of SiNP-PMAPS and  $M_n$  of PMAPS.

DLS experiments of SiNP-PMAPS samples in aqueous NaCl solutions at 25 °C were carried out at scattering angle ranging from 30 to 150 ° using a goniometer system purchased from ALV (Langen, Germany) employing a HeNe laser (wavelength  $\lambda = 632.8$  nm) with a power of 22 mW. The scattering vector ( $q$ ) was defined as  $4\pi n_s \sin(\theta/2)/\lambda$ , where  $n_s$  and  $\theta$  are the refractive index of solvent and the scattering angle. To eliminate the effects of polymer concentration and scattering angles, the diffusion coefficient of SiNP-PMAPS at an infinite dilution was determined by extrapolating to  $q = 0$  and  $C = 0$ . The hydrodynamic radius of the surface-grafted polymer layer ( $R_{H,brush}$ ) of SiNP-PMAPS was calculated from  $(R_H - R_c)/2$ ,



where  $R_H$  and  $R_c$  are the hydrodynamic radius of the SiNP-PMAPS and the radius of a SiNP.

SAXS experiments of SiNP-PMAPS samples in aqueous NaCl solutions at room temperature was carried out at the BL40B2 and BL03XU beam lines of SPring-8 using an incident X-ray with a wavelength  $\lambda = 0.1$  nm and sample-to-detector (imaging plate) distance of 2205 and 7994 mm. The scattering vector as defined by  $4\pi\sin(\theta)/\lambda$  was calibrated by the average of 6 peaks of dry collagen. The radius of gyration of the surface-grafted polymer layer ( $s$ ) of SiNP-PMAPS was estimated from the SAXS profile using a core-shell model analysis, taking interacting excluded-volume chains into account [3].

## Results and Discussion

Figure 1 shows the  $C_s$ -dependence of  $R_{H,brush}$  ( $\circ$ ) and  $s$  ( $\square$ ) for SiNP-PMAPS in aqueous NaCl solutions. The values of  $R_{H,brush}$  and  $s$  for SiNP-PMAPS increased with increasing  $C_s$  from 0.050 to 5.0 M. These results clearly implied that the  $C_s$ -dependence of the repulsive interaction between polymer chains for SiNP-PMAPS in an aqueous NaCl solution was similar to that of the free PMAPS[1,4]. The  $M_w$ -dependence of the z-average mean-square radius of gyration ( $\langle S^2 \rangle_z$ ) for the free PMAPS in a theta state in an aqueous NaCl solution at 0.074 M is experimentally given by [4]

$$\langle S^2 \rangle_z^{1/2} = 0.018M_w^{0.5} \text{ (nm)} \quad (1)$$

The thickness of the polymer brush layer for SiNP-PMAPS was estimated be 9.5 nm, which was much larger than the  $\langle S^2 \rangle_z^{1/2} = 5.4$  nm calculated from equation (1) for free PMAPS chains at the same  $C_s$  and  $M_w$ . The ratio of the radius of gyration to the hydrodynamic radius is defined as  $\rho$ , which is a universal constant for free chains almost irrespective of the chemical structure and molecular weight of polymers.  $\rho$  estimated from  $s$  and  $R_{H,brush}$  of the surface-grafted polymer layer of SiNP-PMAPS in aqueous NaCl solutions are approximately 1.17 – 1.38, which

were similar to those (1.2 – 1.5) of typical flexible free polymers in the theta and good solvents [5]. These results indicated that the chain conformation of PMAPS brushes on a SiNP surface behaves like a Gaussian coil. As far as we know, this is the first experimental report on the chain conformation of PMAPS brush state in an aqueous NaCl solution.

## References

- [1] T. Kato et al., *Ber. Bunsenges. Phys. Chem.*, **100**, 784-787 (1996).
- [2] Y. Terayama et al., *Macromolecules*, **44**, 104-111 (2011).
- [3] J. S. Pedersen et al., *Macromolecules*, **36**, 416-433 (2003).
- [4] Y. Terayama et al., *J. Phys.: Conf. Ser.*, **272**, 012010 (2011).
- [5] T. Konishi et al., *Macromolecules* **24**, 5614-5622 (1991).

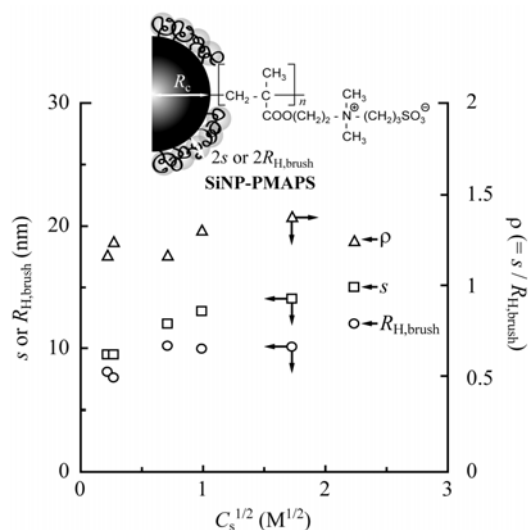


Figure 1.  $C_s$ -Dependence of  $R_{H,brush}$ ,  $s$ , and  $\rho$  of SiNP-PMAPS in aqueous NaCl solutions.

## Supramolecular Complex of Lipopolysaccharide and Cationic Micelles to Control Cytokine Response

Wenjing Li<sup>1</sup>, Tomoki Nishimura<sup>1</sup>, Shinichi Mochizuki<sup>1</sup>, and Kazuo Sakurai<sup>1,2</sup>

<sup>1</sup>The University of Kitakyushu, 1-1 Hibikino, Wakamatsu-ku, Kitakyushu, Fukuoka, 808-0135, Japan;

<sup>2</sup>CREST, Japan Science and Technology Agency, 4-1-8, Honcho, Kawaguchi, Saitama, 332-0012, Japan

Lipopolysaccharide(LPS) is a large molecule consisting of a lipid and a polysaccharide joined by a covalent bond. They are found in the outer membrane of Gram-negative bacteria, act as endotoxins and elicit strong immune responses in animals. Therefore, if it is contained as an impurity in medical device such as an injection cylinder, even small amount, it can cause serious problem.

The origin of the LPS bioactivity is known due to its supramolecular structure and thus addition of cationic lipids (as Fig1) that can bind to phosphoric acid portions can reduce its cytokine secretion. We are presenting our recent results that the addition of various cationic lipids to LPS changes its original cylindrical structure to cylinder, explored with synchrotron small angle X-ray scattering as well as AFM. We found that the LPS bioactivity strongly related to its morphology as well as added lipids.

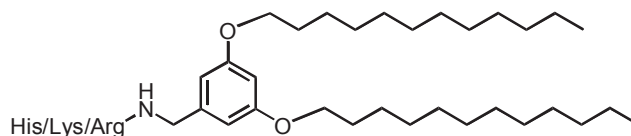


Fig1. Chemical structures of arginine/lysine/histidine lipid

Fig1. Chemical structures of arginine/lysine/histidine lipid

## Optical Shutter Based on Labyrinthine Pattern Formation of Magnetite Nanoparticles

Jushin Bai<sup>1</sup>, Yasushi Okumura<sup>2</sup>, Hiroki Higuchi<sup>2</sup>, Hirotsugu Kikuchi<sup>2</sup>

<sup>1</sup>Interdisciplinary Graduate School of Engineering Sciences, Kyushu University, Japan

<sup>2</sup>Institute for Materials Chemistry and Engineering, Kyushu University, Japan

It is known that when an alternating electric field is applied to the cell composed of two pieces of parallel electrodes which is filled with two types of immiscible liquids, the mutually interpenetrated phase (Labyrinthine pattern) can be induced [1]. However, there are few examples of the research, because high voltage exceeded 1 KV is necessary [2]. In this study, we will report on an optical shutter based on low-voltage labyrinthine pattern formation of magnetite nanoparticles coated with oleic acid which were dispersed in organic solvent.

The magnetite nanoparticles coated with oleic acid were synthesized by coprecipitation method and were dispersed in organic solvent (dodecane) to prepare colloid liquids. The diameter of the magnetite nanoparticles and their hydrodynamic diameter in dodecane were characterized by X-ray diffraction (XRD) and dynamic light scattering (DLS) respectively.

When an alternating electric field is applied to the ITO (Indium-Tin Oxide) cell with 10  $\mu\text{m}$  gap composed of two pieces of parallel electrodes which is filled with the colloid liquid, the nanoparticles were agglomerated and formed labyrinthine pattern or other patterns by changing the voltage and frequency. The images were observed by an optical microscope and recorded by digital CCD camera. The voltage-frequency phase diagram of the pattern formation was prepared and shown in Fig. 1

It was estimated that the diameter of magnetite nanoparticles was 10 nm by XRD, and the hydrodynamic diameter in dodecane was approximated 44 nm by DLS. The cause could be contemplated that dozens of particles condensed to get large. The conditions of pattern formation were confirmed and shown in Fig. 1. Especially when the alternating voltage was 12.9 V/50 Hz, stable pattern was formatted.

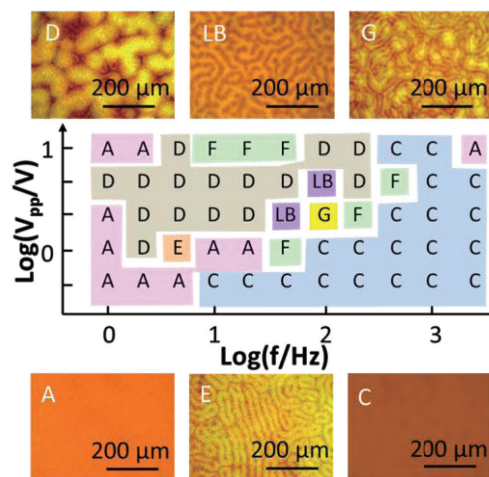


**Figure 1.** Voltage-frequency phase diagram of magnetic nanoparticle suspension and the induced patterns.

[1] M. Zahn, et al. *IEEE Transactions on Industry Applications*, IA-21, no. 1, pp. 53-61, Jan/Feb 1985.

[2] R.E. Rosensweig, et al. *J. Magnetism and Magnetic Materials*, vol. 39, pp. 127-132. Nov. 1983.

## Large electrooptic property in aqueous dispersions of non-organic nanoparticles with high-aspect ratio

Aya Jinnouchi<sup>1</sup>, Yasushi Okumura<sup>2</sup>, Nobuyoshi Miyamoto<sup>3</sup>, Sunao Yamada<sup>4</sup>,  
Hiroki Higuchi<sup>2</sup> and Hirotugu Kikuchi<sup>2</sup>

<sup>1</sup>Interdisciplinary Graduate School of Engineering Sciences, Kyushu University, Japan

<sup>2</sup>Institute for Materials Chemistry and Engineering, Kyushu University, Japan

<sup>3</sup>Faculty of Engineering, Fukuoka Institute of Technology, Japan

<sup>4</sup>Graduate School of Engineering Kyushu University, Japan

The nanoparticles with high-aspect ratio are oriented in the electric field more easily than normal organic molecules, because their induced dipole moments are larger than those of normal organic molecules. In this study, we measured electric field-induced birefringence of aqueous dispersions of inorganic nanosheets and gold nanorods, and found unique electro-optic effects.

We prepared aqueous dispersions of fluorohectorite (FHT,  $\text{Na}_{0.75}\text{Mg}_{2.83}\text{Si}_4\text{O}_{10}\text{F}_{2.13}$ , 350 nm in diameter and 10 nm in thickness) (1.2~1.8 wt%) and gold nanorod with four kinds of aspect ratios, 4.0, 5.0, 8.3, and 8.5 (DAI NIPPON TORYO) (0.015~0.06 wt%). We applied electric fields (100 Hz, 1,000 Hz, and 10,000 Hz) to samples filled in Kerr cell with 10 mm optical path length and 1 mm interelectrode distance, and measured the electric field induced birefringence using lock-in detection system. We found that the inorganic nanosheet aqueous dispersions showed quadratic electro-optic effects with Kerr coefficients ( $10^{-8} \sim 10^{-7}/\text{mV}^{-2}$ ) larger than those of normal organic molecules ( $10^{-14} \sim 10^{-10}/\text{mV}^{-2}$ ). On the other hand, electric field-induced birefringences of the gold nanorod aqueous dispersions are about 10 times larger than those of inorganic nanosheets in our applied electric field range. Different from usual Kerr effect, this birefringence is proportional to the electric field intensity. We will discuss about the mechanism of these effects.

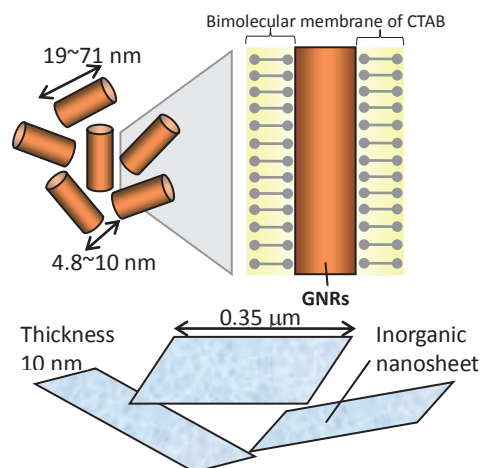


**Figure 1.** Schematic illustrations of gold nanorods and inorganic nanosheets.

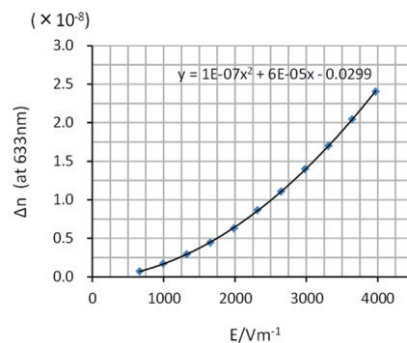


**Figure 2.** Typical plot of birefringence  $\Delta n$  as a function of electric field intensity  $E$  for inorganic nanosheets : Measuring frequency is 10,000Hz.

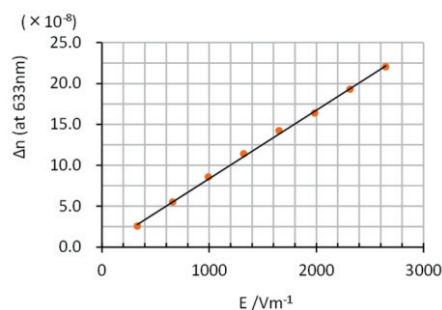


**Figure 3.** Typical plot of birefringence  $\Delta n$  for PSS-modified GNRs aqueous dispersions as a function of electric field (1,000 Hz) intensity  $E$ . Aspect ratio of the GNRs was 5.0.

## CHIRAL LIQUID CRYSTAL PHASES INDUCED BY NOVEL FLUORINATED CHIRAL DOPANT

Kota KAKISAKA<sup>1</sup>, Hiroki HIGUCHI<sup>2</sup>, Yasushi OKUMURA<sup>2</sup>, Hirotsugu KIKUCHI<sup>2</sup>

<sup>1</sup>Department of Applied Science for Electronics and Materials, Kyushu University  
6-1, Kasuga-Koen, Kasuga, Fukuoka, 816-8580, Japan

<sup>2</sup>Institute for Material Chemistry and Engineering, Kyushu University  
6-1, Kasuga-Koen, Kasuga, Fukuoka 816-8580, Japan

### • Abstract

When chiral dopants are added to a nematic liquid crystal (N-LC), a chiral nematic (N\*) phase, which has a helical structure in molecular arrangement, is generally induced. The power to induce the helical twisting molecular arrangement by a chiral dopant is called the helical twisting power (HTP). In the case of the N\* phase having the relatively short helical pitch less than 500nm, blue phases (BPs) appear in a very narrow temperature range between the N\* phase and the isotropic phase<sup>[1]</sup>. Because BPs require a large chirality, chiral dopants having the large HTP are key-materials for BPs. Recently, BPs are expected to be applied to new LC materials because they require no surface treatments of substrates due to an optically isotropy in the voltage off state and possess the high speed response upon an applied electric field. On the other hand, the fluorinated N-LCs prevent a contamination of ionic impurities being mixed into the LCs because the fluorine group has the low polarizability despite the highest electronegativity. In addition, because the fluorinated compounds possess the low cohesive energy and viscosity, fluorinated N-LCs have the fast response time upon an applied electric field. In this study, we designed and synthesised novel fluorine substituted chiral dopants which are expected to indicate high solubility in fluorinated N-LC and high HTP by using a binaphthyl skeleton<sup>[2]</sup> (Figure 1). We investigated HTPs and

solubilities of the chiral dopants in the fluorinated N-LC mixture JC-1041XX (JNC Co. Ltd.) and found that ring-closed chiral dopants showed high HTPs with low temperature dependences. Especially, **Close-F** possessed the highest HTP among the chiral dopants shown in Fig. 1, and showed a high solubility in the host liquid crystal. The high HTP, low temperature dependence and high solubility of **Close-F** could be resulted from the combination of the fluorine groups and the rigid structure by ring-fused moiety. Furthermore, we will report on the electro-optics properties of **Close-F** doped liquid crystals.

[1] H. Kikuchi et al. *Nat. Mater.*, **1**, 64-68 (2002)

[2] G. Proni and G. P. Spada, *J. Org. Chem.*, **65**, 5522-5527 (2000)

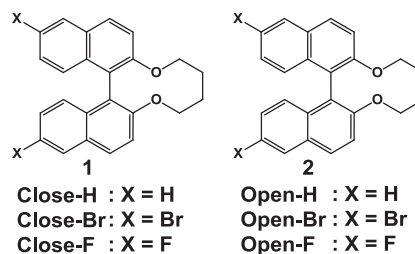


**Figure 1.** Chemical structure of synthesized binaphthyl chiral dopants.

## Elasticity of Sodium Alginate Interpenetrating Gels

Akihiko Takada, Masashi Nakamura, Naru Kawahara, Yoshiaki Takahashi  
 Division of Advanced Device Materials, Institute for Materials Chemistry and Engineering,  
 and Department of Molecular & Material Sciences, IGSES, Kyushu University  
 Kasugakouen 6-1, Kasuga, Fukuoka, 816-8580, Japan

Kesorn Merat, Visit Vao-Soongnern  
 School of Chemistry, Institute of Science, Suranaree University of Technology  
 Nakhon Ratchasima, 30000 Thailand

### Introduction:

Interpenetrating gel, gel of interpenetrating network (IPN) types, is defined as a complex gel formed by a combination of more than two types of polymers, in which each polymer forms network independently and interpenetrates the other network. The interpenetrating network gel is expected to show properties different from those of single network gels such as high impact property and also expected to be used for introducing new functions into a gel network by using the other polymer network. We have studied on interpenetrating network gels formed by gelatin (Glt) and sodium alginate (Alg) in aqueous system. Because Glt is formed by descending temperature and Alg is formed by addition of divalent cations such as  $\text{Ca}^{2+}$ , we can form each network independently, which allows us to control the gel formation. In this paper, we measured intrinsic viscosity to investigate interaction between these two polymers. And we measured moduli also for IPN gels and semi-IPN gels to investigate properties of gel modulus by each gelations, such as whether additivity of the gel moduli is satisfied for this system or not.

Gelatin (Morinaga & Co. Ltd.) and sodium alginate (Nacalai Tesque Inc.) were used without further purification. Deionized water was used as solvent. All solutions prepared was once heated at  $60^\circ\text{C}$  for at least 2hours. Intrinsic viscosity  $[\eta]$  was measured using Ubbelohde type of capillary viscometer.  $[\eta]$  for Glt solutions was measured at temperature higher than  $30^\circ\text{C}$  at which gelation of Glt does not occur.  $[\eta]$  for Alg solutions and mixed solution of Glt and Alg with different Glt/Alg ratio were measured at  $30^\circ\text{C}$ . Elastic modulus of Glt gels, Alg gels, IPN gels, and semi-IPN gels were measured at  $25^\circ\text{C}$  using indentation type of elastometer assembled by ourselves and were estimated using Hertz's equation for sphere. SAXS measurements for these gels were performed by SAGA Light Source, BL06.

Intrinsic viscosity of Alg solutions

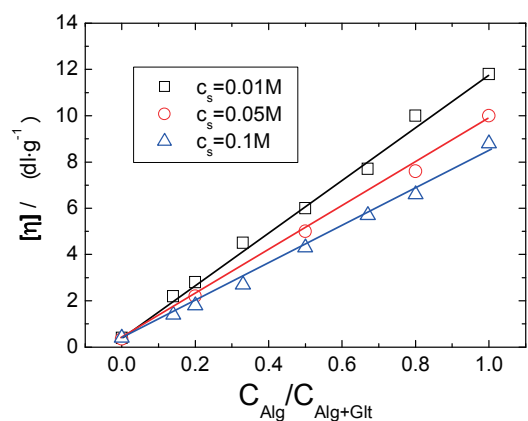


**Fig.1** Intrinsic viscosity  $[\eta]$  for mixed solutions of sodium alginate (Alg) and gelatin (Glt) at  $30^\circ\text{C}$  with three different added salt NaCl concentrations  $C_s$ .

showed dependence on added salt NaCl concentration  $C_s$ , which is a typical behavior of polyelectrolytes. On the other hand, intrinsic viscosity of Glt solutions was independent of the amount of the added salt. In this study, NaCl concentration were set 0.1M as standard condition for solutions and gels. Fig. 1 shows intrinsic viscosity  $[\eta]$  for mixed solutions of Alg and Glt with different Alg contents at 30°C with three different  $C_s$ . For all  $C_s$ ,  $[\eta]$  changed linearly with changing Alg content. This data shows that the chain dimension of each polymer is not changed by existence of the other polymer so that no special interaction between Alg and Glt is present in the aqueous system.

As for gelation of the solutions, at first, we tried to prepare Alg gels by adding  $CaCl_2$  solution into Alg solution. However, the gels were not homogeneous at all and the elastic modulus showed fairly large position dependence. Gelatin semi-IPN (Glt-sIPN) gels were prepared by gelation of Glt by cooling mixed solvents of Glt and Alg. Glt concentration  $C_{Glt}$  dependence of modulus for Glt-sIPN gels is shown in Figure 2, as well as that of Glt gels. The data of Glt-sIPN and Glt gels coincide with each other, which indicates that the galation of Glt is not affected by existence of Alg and also the added salt NaCl.

IPN gels were prepared by immersing the Glt-sIPN gels into  $CaCl_2$  solution. Elastic modulus of the IPN gels is also shown in Figure 2. The elastic modulus shows larger value than that of Glt gel or Glt-sIPN gels. From the IPN gels, we prepared Alg gel by procedure that the IPN gel was immersed in a large amount of NaCl solution at 40°C for about one month with exchanging NaCl solution several times. The gels look uniform unlike the Alg gel which was prepared directly from Alg solution and the elastic modulus did not exhibit position dependence. Figure 3 shows Alg concentration dependence of elastic modulus of the Alg gels. The data are almost located on one line with slope of 2. We used the data of Alg gel modulus and checked additivity of gel moduli of Glt gel and Alg gel. However, the additivity is not satisfied and the elastic modulus of IPN gel is much higher than summation of moduli of Alg and Glt gels.

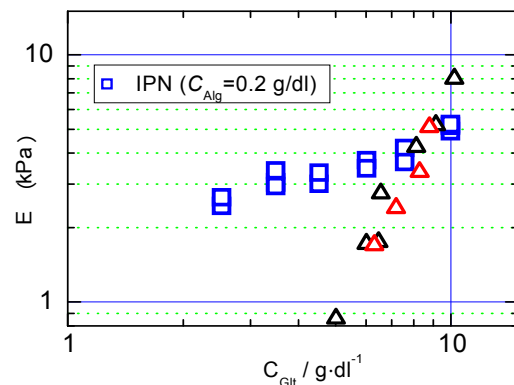


**Fig.2** Double logarithmic plot of elastic modulus  $E$  vs. Glt concentration  $C_{Glt}$  for Glt( $\circ$ ), Glt-sIPN( $\Delta$ ) and IPN( $\square$ ) at 25°C. Alg concentrations  $C_{Alg}$  of s-IPN and IPN gels are 0.2 g/dl

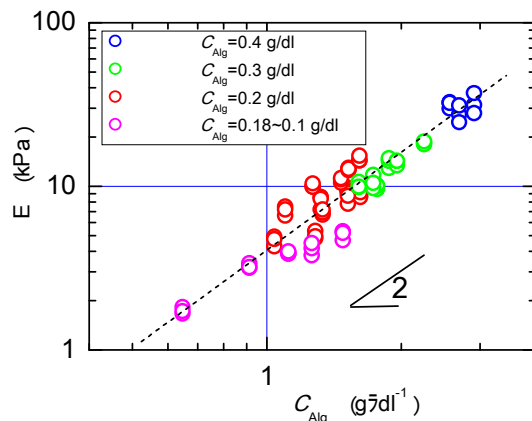


**Fig.3** Alg concentration  $C_{Alg}$  dependence of elastic modulus  $E$  for Alg gels prepared from IPN gels.  $C_{Alg}$  of caption in Figure indicates initial Alg concentration of mixed solution.  $C_{Alg}$  of horizontal axis was calculated by correction of gel volume change.

## Coupled Flexural-Torsional Vibration of Delaminated Beams Subjected to Axial Loads and Static End Moments

Yang Liu<sup>1</sup>, Dongwei Shu<sup>1</sup>,

<sup>1</sup> Nanyang Technological University, Singapore

<sup>1</sup> School of Mechanical and Aerospace Engineering, Nanyang Technological University, 50  
Nanyang Avenue, Singapore 639798, Singapore

For the coupled flexural-torsional vibration of delaminated beams subjected axial load and end moments, analytical solutions are developed solve the both vibration and delamination problems. The Euler-Bernoulli beam theory and the ‘free mode’ assumptions in delamination vibration are adopted. Parametric studies are performed to study the effect of axial load and end moments on natural frequencies of delaminated beams, considering various length of delamination with different thickness-wise location and span-wise location. The effect of delamination on buckling load and end moment for lateral instability is well studied. For mode shapes, the effect of axial load and end moments on the bending displacement mode shape, along with the effect of end moments on the torsional displacement mode shape is presented.

Let  $w_i(x, t)$  and  $\theta(x, t)$  denote the midplane deflection of beam  $i$  and torsional displacement, respectively. The governing equations for the free coupled flexural-torsional vibration of beam  $i$  subjected to axial loads and end moments are ( $i = 1 - 4$ )

$$-EI_t \frac{\partial^4 w_i}{\partial x^4} + P_t \frac{\partial^2 w_i}{\partial x^2} + M_{zz,t} \frac{\partial^2 \theta_i}{\partial x^2} - \rho_t A_t \frac{\partial^2 w_i}{\partial t^2} = 0, \quad (1)$$

$$GJ_t \frac{\partial^2 \theta_i}{\partial x^2} + \left( P_t I_{p,t} / A \right) \frac{\partial^2 \theta_i}{\partial x^2} + M_{zz,t} \frac{\partial^2 w_i}{\partial x^2} - \rho_t I_{p,t} \frac{\partial^2 \theta_i}{\partial t^2} = 0. \quad (2)$$

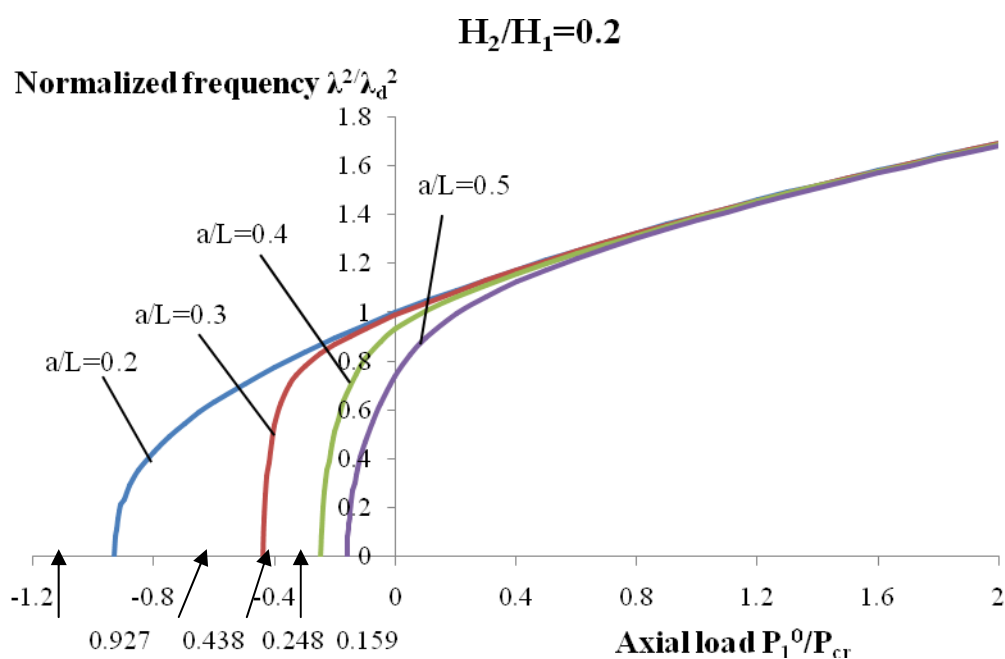
Fig. 1 shows normalized ‘free mode’ frequency  $\lambda^2/\lambda_d^2$  of beams subjected to axial force only, with a midplane single delamination of various lengths. The nondimensional frequency of the delaminated beam  $\lambda^2$  is normalized with respect to that of undelaminated beam  $\lambda_d^2$ . The axial load is normalized with respect to the critical buckling load of an undelaminated beam  $P_{cr}$ .

$$\bar{P}_1^0 = \frac{P_1^0}{P_{cr}} = \frac{F_1^0}{4\pi^2 EI_1} L^2 \quad (4.17)$$

It is tensile load when  $P_1^0/P_{cr}$  is positive, compressive load when  $P_1^0/P_{cr}$  is negative. The natural frequency increases as the tensile load increases or the compressive load



decreases. As shown in Fig. 1, when the beam is subjected to axial compressive load, the differences of natural frequencies between each length of delamination become bigger while the axial compressive load increases. It is also shown in Fig. 1 that the natural frequencies show a more precipitous decline when the delamination moves away from the midplane. The results agree well with the work of Della and Shu [1] (Fig. 2). When the load  $\bar{P}_1^0$  approaches the buckling load the natural frequency vanishes, the buckling load for the beam with a single delamination, it agrees well with the results of Huang and Kardomateas [2] (Table 2). When the load  $\bar{P}_1^0$  is tensile and increases, the differences of natural frequencies with various length of delamination becomes smaller, which coincides with Shu's work [3].



(a)

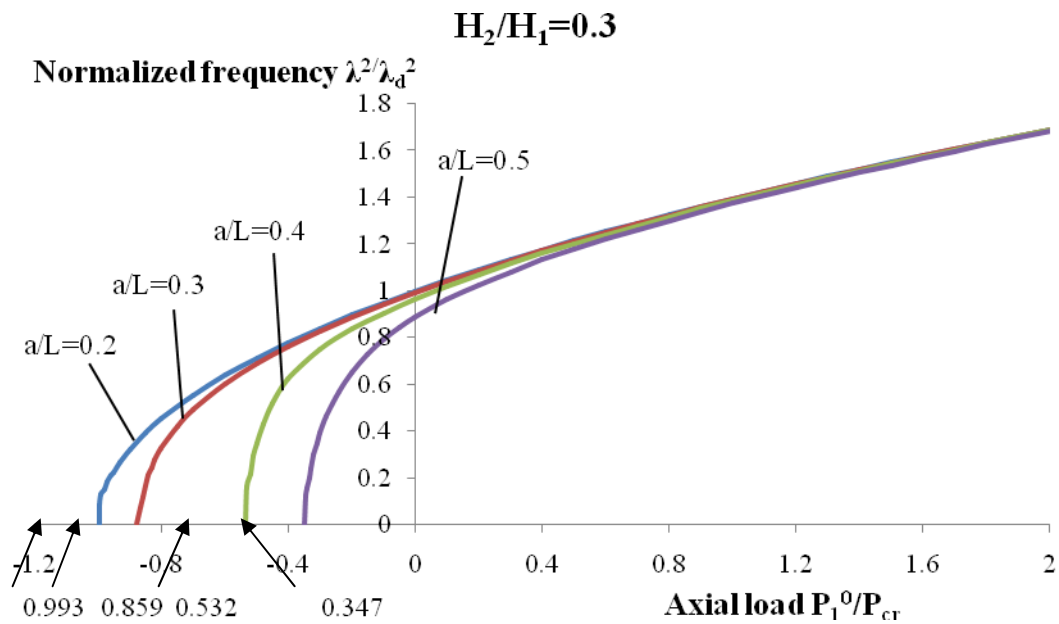


Figure 4.2. Mode 1 ‘free mode’ frequency  $\lambda^2/\lambda_d^2$  versus the axial load  $P_1^0/P_{cr}$  for a homogenous clamped-clamped beam with a single delamination,  $d/L = 0.0$ . When  $\lambda = 0$ ,  $P_1^0/P_{cr}$  is the buckling load: (a)  $H_2/H_1=0.2$ ; (b)  $H_2/H_1=0.3$ .

- [1] C. N. Della and D. Shu. Free vibration analysis of multiple delaminated beams under axial compressive load. *Journal of Reinforced Plastic and Composites*, v 28, n 11, p 1365-81, (2009)
- [2] H. Huang and G. A. Kardomateas. Buckling of Orthotropic Beam-Pates with Multiple Central Delaminations, *International Journal of Solids and Structures*, 35: 355–1362. (1998)
- [3] D. Shu. Vibration of beams with a single delamination under axial loading. *Materials Science Forum*, v 675 677, p 477-480, 2011, *Advanced Material Science and Technology*. (2011)

## Autonomous Main Chain Exchange Reactions of Dynamic Covalent Polymers at Room Temperature

Takeshi Kanahara<sup>1</sup>, Atsushi Irie<sup>1</sup>, Keiichi Imato<sup>1</sup>, Masamichi Nishihara<sup>2</sup>, Atsushi Takahara<sup>1,2</sup>, Hideyuki Otsuka<sup>1,2</sup>

<sup>1</sup> Graduate School of Engineering, Kyushu University, Fukuoka 819-0395, Japan

<sup>2</sup> Institute for Materials Chemistry and Engineering, Kyushu University, Japan

By introducing exchangeable dynamic covalent bonds into the main chains, linear polymers can be hybridized. We have reported polymer scrambling reactions driven by some external stimuli such as heating, UV irradiation, and catalyst.<sup>[1]</sup> In the present study, we employed diarylbibenzofuranone (DABBF) derivatives as the dynamic covalent bond units. DABBF

derivatives do not require special stimuli to reach a state of thermodynamic equilibrium with arylbenzofuranone radical, which formed by cleavage of DABBF (Figure 1).

DABBF-containing polyester (DABBF-PEs) was prepared by polycondensation of DABBF-diol and adipoyl chloride, and also DABBF-containing polyurethane (DABBF-PUr) was synthesized by polyaddition of DABBF diol and diisocyanate-terminated poly(propylene glycol). Since DABBF derivatives can exchange at room temperature

under air, scrambling reaction between DABBF-PEs and DABBF-PUr was carried out by simply mixing the polymers in organic solvent. Differential scanning calorimetric (DSC) measurement revealed that each scrambled polymer has single glass transition temperature ( $T_g$ ) in the region between those for PEs and PUr, indicating that main chain exchange reaction proceeded autonomously. Furthermore, scrambled polymer films showed different mechanical properties by changing the mixing ratios of DABBF-PEs and DABBF-PUr.

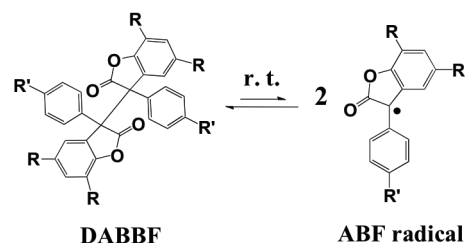


Fig. 1 Reversible reaction of DABBF.

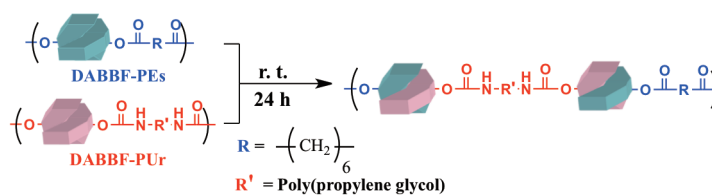


Fig. 2 Autonomous polymer scrambling reaction between PEs and PUr.

Table 1. Young's modulus and glass transition temperature of DABBF-hybrid polymer films.

PEs : PUr (molar ratio)	Young's modulus (MPa)	$T_g$ (°C)
PEs (homo)	—	99.2
3 : 1	86.8 (± 8.1)	11.6
2.5 : 1	18.6 (± 4.4)	-1.7
2 : 1	0.958 (± 0.312)	-9.1
PUr (homo)	—	-26.7

— : Not determined

[1] H. Otsuka, A. Takahara et al., *J. Am. Chem. Soc.*, **125**, 4064 (2003); *Chem. Commun.*, **45**, 1073 (2009); *Prog. Polym. Sci.*, **34**, 581 (2009); *Chem. Commun.*, **46**, 1150(2010).

## NLO analysis of ladder-structure polydiacetylenes derivatives

Ling Zhi Kang<sup>1</sup>, Feng Long Gu<sup>1,2</sup>, and Yuriko Aoki<sup>2,3</sup><sup>1</sup>Center for Computational Quantum Chemistry, South China Normal University, Guangzhou 510631 China<sup>2</sup>Japan Science and Technology Agency, CREST, 4-1-8 Hon-chou, Kawaguchi, Saitama 332-0012, Japan<sup>3</sup>Department of Material Sciences, Faculty of Engineering Sciences, Kyushu University, 6-1 Kasuga-Park, Fukuoka 816-8580, Japan

In recent years, Polydiacetylenes (PDAs) derivatives have drawn much attention due to their nonlinear optical properties and potential utilization in optical and electro-optical devices[1]. Especially, a kind of novel ladder-type PDAs derivatives with two chains has shown their large second hyperpolarizability in experiment[2]. In this work, inter-chain interaction and hydrogen bonding effects on the NLO properties of the ladder-structure PDAs derivatives are investigated by using the elongation finite field method, i.e., Elongation –FF method[3].

Previous study about the effects of arrangements of donors (-NH<sub>2</sub> group) and acceptors (-NO<sub>2</sub> group) on PDAs derivatives's nonlinear optical (NLO) properties have been investigated by Chen et al.[4]. All systems they studied have large (hyper)polarizabilities. It is worth mentioned that the different arrangements of donors and acceptors have different effect on their NLO properties.

In this study, we investigate double chain (Fig.1 (a)), hydrogen bonded double chain by -NH<sub>2</sub> group and acceptors -NO<sub>2</sub> group between two chains (Fig.1 (b)), and ladder chain connected by -C≡C- (Fig.1 (c)) for the case that large phenyl group was attached as a donor. To examine the effect from phenyl group on NLO property, simple chains capped by hydrogen atoms were also calculated for the comparison.

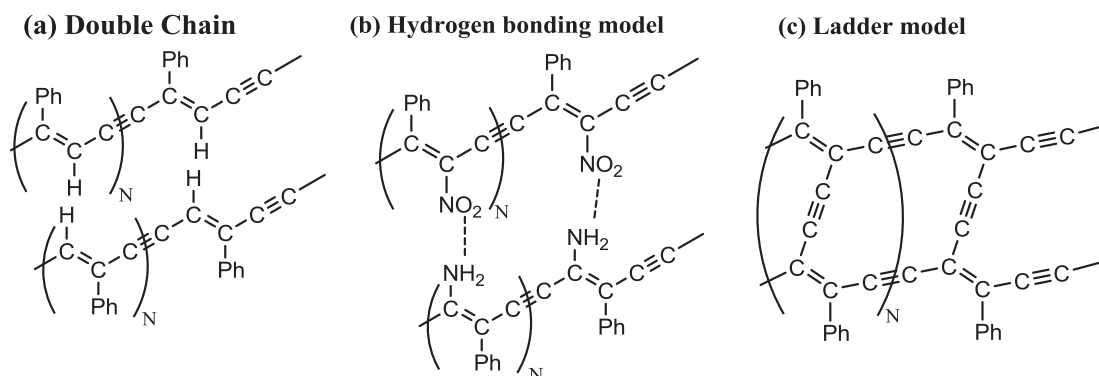


Fig. 1 The structures of PDA and its ladder-type derivatives.

The elongation-FF method[3] illustrated in Fig. 2 is applied to PDA chains for investigating inter-chain interaction and hydrogen bonding effects on NLO properties.

Here, we briefly explain the process according to this figure. Firstly, the delocalized canonical molecular orbitals of a starting cluster are first localized into frozen and active regions in specified parts of the system. Next, a monomer is attacking to this cluster to the active region, and eigenvalue problem is solved by disregarding the regional localized molecular orbitals (RLMOs) which have very weak interaction with the attacking monomer. The frozen region is defined to be far away from an attacking monomer in each elongation step. By repeating this procedure, the polymer chain is elongated step by step to any desired length. The RLMO representation allows one to freeze one part of the system far away from the polymer chain propagation site. The frozen part is disregarded in the elongation self-consistent field procedure. By this method, a significant reduction of the number of variational degrees of freedom as well as two-electron integrals brings a reduction in computation time drastically.

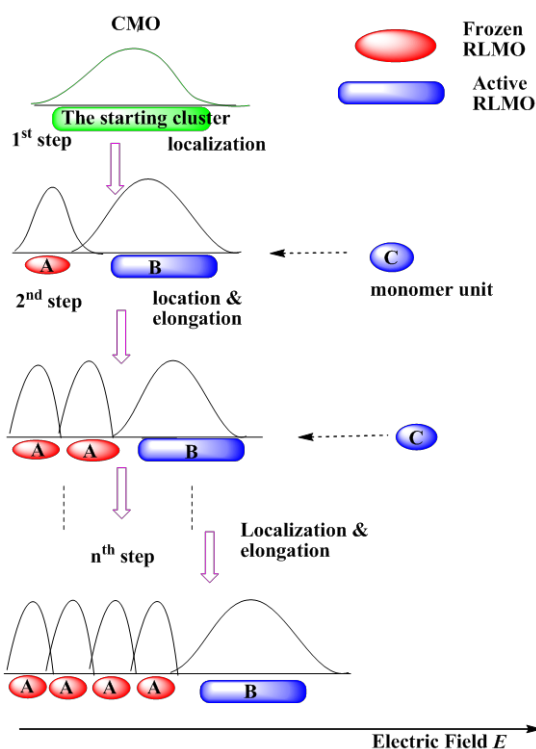


Fig. 2 Schematic outline of the elongation method. The CMO and RLMO indicate a canonical molecular orbital and a regional localized molecular orbital, respectively.

For calculating NLO properties we adopted elongation-FF method. In this approach, molecular (hyper)polarizabilities are obtained by numerically differentiating the total energy with respect to electric fields. We now need to look further to test the (hyper)polarizabilities and concentrate to analyse inter-chain interaction and hydrogen bonding effect between chains to NLO, which are expected to be useful for the design of new NLO materials.

- [1] C. Sauteret, J.-P. Hermann, R. Frey, F. Pradere, J. Ducuing, R. H. Baughman, R. R. Chance, *Phys. Rev. Lett.* **36** (1976) 956.
- [2] S. Okada, K. Hayamizu, H. Matsuda, A. Masaki, N. Minami, H. Nakanishi, *Macromolecule* **27** (1994) 6259.
- [3] F. L. Gu, Y. Aoki, A. Imamura, D. M. Bishop, B. Kirtman, *Mol. Phys.* **101** (2003) 1487.
- [4] W. Chen, G. -T. Yu, F. L. Gu, Y. Aoki, *Chem. Lett.* **474** (2009) 175.

## Preparation of 4-Arm Star Polymer containing Copper-Phthalocyanine Core from Phthalonitrile Functionalized Polystyrene via ATRP

Byoungjae Kim<sup>1</sup>, Jonghwa Jeong<sup>1</sup>, Bohyun Kim<sup>2</sup>, Jin-goo Kim<sup>3</sup>, Ki-suck Jung<sup>3</sup> and Hyun-jong Paik<sup>1</sup>

<sup>1</sup> Department of Polymer Science and Engineering, Pusan National University, Busan 609-735, Korea

<sup>2</sup> Education Program for Samsung Advanced Integrated Circuit, Pusan National University, Busan 609-735, Korea

<sup>3</sup> Department of R&D, Iridos Ltd., Ulsan, 689-892, Korea

Metallophthalocyanines (MPc) have drawn considerable attentions as molecular materials with outstanding electronic and optical properties. In recent years, MPcs were intensively investigated as target molecules for the sensors, light-emitting devices, solar cells, photodynamic therapy. Even with vast applications, it was difficult to synthesize soluble MPcs in molecular level due to their aggregation properties, resulting from their strong  $\pi$ - $\pi$  interaction.

We introduced the well-defined  $\alpha$ -functionalized polystyrene with phthalonitrile group via ATRP to prepare the soluble copper phthalocyanine (CuPc). The 4-arm star polymer was synthesized through the tetracyclization of  $\alpha$ -functionalized polystyrenes with copper chloride.  $\alpha$ -Functionalized polystyrene was characterization by gel permeation chromatography (GPC), <sup>1</sup>H NMR and UV/Vis. spectroscopy. The formation of 4-arm star polymer was verified by UV/Vis. spectroscopy and GPC with UV detector at 350nm.

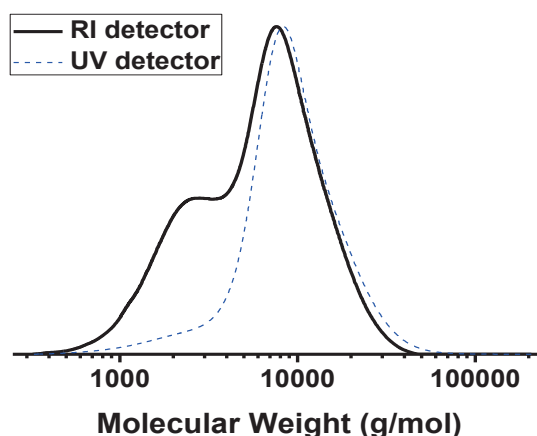
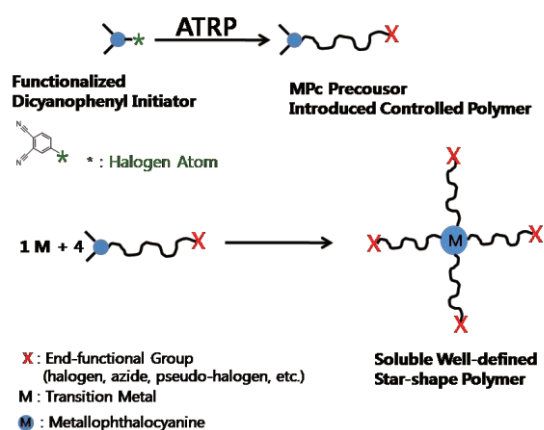


Fig. 1. Overall scheme of Synthesis of 4-arm star polymer containing CuPc core.

Fig. 2. GPC traces of 4-arm star polymer containing CuPc core from RID and VWD (350 nm).

## Fabrication and Spectroscopic Properties of Layer-by-Layer Gold Nanosheet on Gold Thin Film

Akihito Yoshida, Keisuke Imazu, Xinheng Li, Koichi Okamoto, and Kaoru Tamada  
Institute for Materials Chemistry and Engineering, Kyushu University, Japan

There has been growing interest in the ordered structure of noble metal nanoparticles (NPs) such as Au and Ag NPs because of their collective effects caused by electromagnetic coupling of surface plasmon resonance (SPR) [1]. In a previous study, our group fabricated highly ordered 2D array of monodisperse Ag NPs, called Ag nanosheet, and found the spectroscopic property changes (e.g. sharpened absorption band) due to the collective effect [2]. Recently we examined the optical properties of multilayered Ag nanosheet deposited on the Au thin film by layer-by-layer manner and found the layer number dependences of SP band peak energy and SP band width, which probably are signs of the plasmon coupling between the Ag nanosheet and the Au thin film.

In this presentation, we report the spectroscopic properties of multilayered Au NP 2D sheet (Au nanosheet) on Au thin film. Similarly to the multilayered Ag nanosheet, the absorption spectra of the multilayered Au nanosheet (Fig. 1) show the layer number dependences of peak energy and band width, which cannot be observed for the Au nanosheets on quartz substrate, suggesting the presence of an interaction between the Au NPs and Au thin film. We also report the spectroscopic properties of hybrid multilayered assemblies composed of Ag nanosheets and Au nanosheets to examine the intralayer coupling.

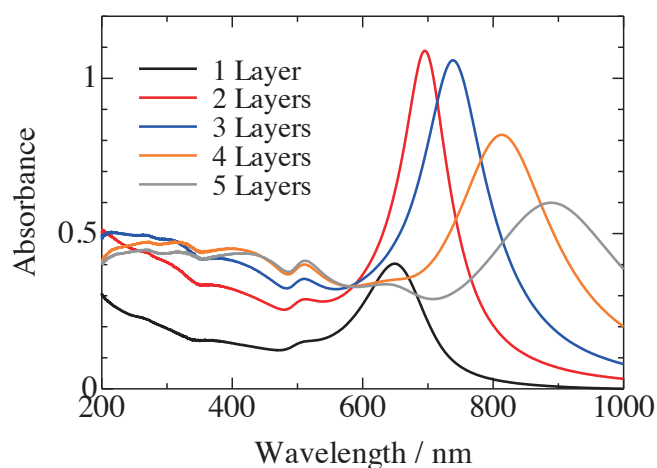


Fig. 1. Absorption spectra of multilayered Au nanosheet on Au thin film. Absorbance values are calculated from reflectance.

[1] C. L. Haynes et al., *J. Phys. Chem. B*, **107**, 7337 (2003).

[2] M. Toma et al., *Phys. Chem. Chem. Phys.*, **12**, 14749 (2011).

## Structural analyses of lattice structure of polymer-stabilized blue phase by confocal laser scanning microscope

Takahiro Ashimine<sup>1</sup>, Hiroki Higuchi<sup>2</sup>, Yasushi Okumura<sup>2</sup>, Hirotsugu Kikuchi<sup>2</sup>

<sup>1</sup>Interdisciplinary Graduate School of Engineering Sciences, Kyushu University, Japan

<sup>2</sup>Institute for Materials Chemistry and Engineering, Kyushu University, Japan

Liquid crystal blue phases (BPs) appear in a narrow temperature range when a nematic liquid crystal is mixed with high concentration of chiral dopants. The lattice structure of BP depends on the concentration of chiral dopants, the lattice size becomes larger with increasing the concentration of them. The three dimensional structure of polymer-stabilized blue phase (PSBP) with the order of optical wavelength can be non-destructively investigated by confocal laser scanning microscope (CLSM) which is a novel imaging technique that allows non-destructive optical observation with high resolution [1]. So far, BP's periodical patterns corresponding to the bcc lattice were observed not only surface but also internal region [2]. In this study, we observed the lattice structure in PSBP with the different concentration of chirality by using confocal laser scanning microscope.

The samples of the PSBP I for CLSM observations were prepared as follows: a mixture solution of a liquid crystal, a chiral dopant, monomers, and a photoinitiator was sandwiched between a slide glass and a thin cover glass and left at the appropriate temperature until a desired BP texture appeared and was irradiated with UV light to polymerize the monomer in a BP.

The blue phases have been identified by reflection spectrometry and observed by a polarizing optical microscope observation. Figure 1 shows CLSM observation photograph of PSBPI. Hexagonal and square dot sequences were observed in PSBPI. The dot sequence spacing gave close agreement with the lattice spacing expected from the cross-sectional surface of the lattice structure of BPI. The lattice distortion was conformed near the interface between different orientational domains. The regular or irregular interval of contrasting density of dot sequences were also observed near there.

[1] Nakamura, O; Kawata, S. *J. Opt. Soc. Am. A* **1990**, 7, 522-526.

[2] K. Higashiguchi, K. Yasui, and H. Kikuchi, *J. Am. Chem. Soc.*, **2008**, 130, 6326.

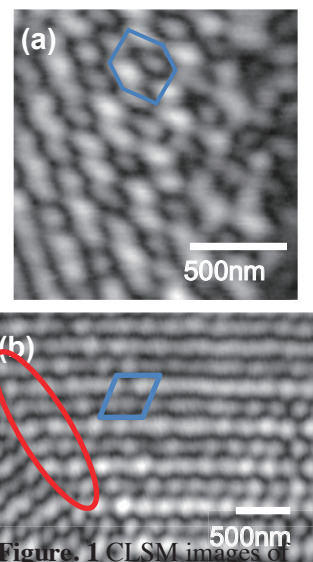


Figure. 1 CLSM images of PSBPI. The scale bars correspond to about 500 nm.



## Thermo- and Photo-Responsive Water-Soluble Polymer

Ryusuke Enomoto, Shin-ichi Yusa

Department of Materials Science and Chemistry, University of Hyogo, Japan

### Introduction

Stimuli-responsive polymers, whose structure and properties change in response to external stimuli such as temperature, pH, ionic strength, and light have recently received much attention. Temperature and light are the most attractive stimuli. Poly(*N*-isopropylacrylamide) (pNIPAM) has received significant attention because of its interesting thermo-responsive properties in water. An aqueous solution of pNIPAM undergoes a thermally reversible phase separation [1]. pNIPAM dissolves in water at room temperature, but separates from the aqueous phase above 31-32 °C, which is called the lower critical solution temperature (LCST). Malachite green (MG) is known as a photochromic molecule, which reversibly changes the intensely green colored cation from the clear neutral molecule under UV-irradiation because of dissociation of the hydroxide counter anion [2]. The cationic MG recombines with the hydroxide counter anion by heating in the dark (Fig. 1). In this study, we have prepared random copolymers (p(NIPAM/MG)) composed of NIPAM and a small amount of a vinyl monomer bearing MG [3] via conventional free radical polymerization. The LCST of p(NIPAM/MG) can be changed by UV-irradiation due to photo-induced ionization of the MG groups.

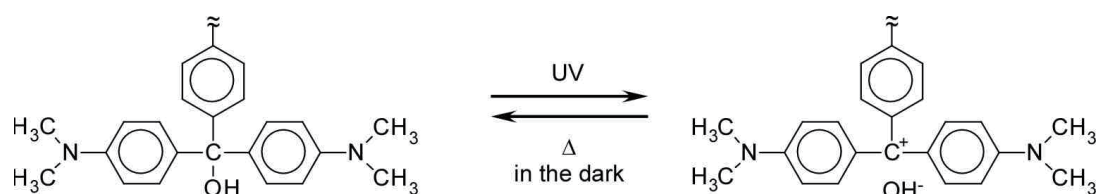


Fig. 1. The chemical structure of the malachite green (MG) derivatives before and after UV-irradiation.

### Experiment

p(NIPAM/MG) was prepared via conventional free radical polymerization as follows: NIPAM, MG monomer, and polymerization initiator (AIBN) were dissolved in methanol. The mixture was degassed by purging with argon for 30 min. Free radical polymerization was carried out at 60 °C for 24 h (Fig. 2). The reaction mixture was dialyzed against methanol for 2 days and then against pure water for 1 day by using a dialysis membrane with a molecular weight cutoff of 14 kDa. The polymer was recovered by freeze-drying.  $^1\text{H}$  NMR spectra were measured using  $\text{DMSO-}d_6$ . The quantitative conversion was confirmed by  $^1\text{H}$  NMR focusing on the intensity ratio of the vinyl groups. The number-average molecular weight ( $M_n$ ) and polydispersity index ( $M_w/M_n$ ) were determined by gel-permeation chromatography (GPC) using DMF as an eluent at a flow rate of 0.6 mL/min. The absorbance for aqueous solutions of

p(NIPAM/MG) was measured ranging from 500 - 800 nm. The change of the percent transmittance (%T) at 800 nm of the aqueous polymer solutions was measured under UV-irradiation (= 275 nm) and in the dark with increasing temperature. The temperature was raised from 20 to 60 °C at a heating rate of 1.0 °C/min.

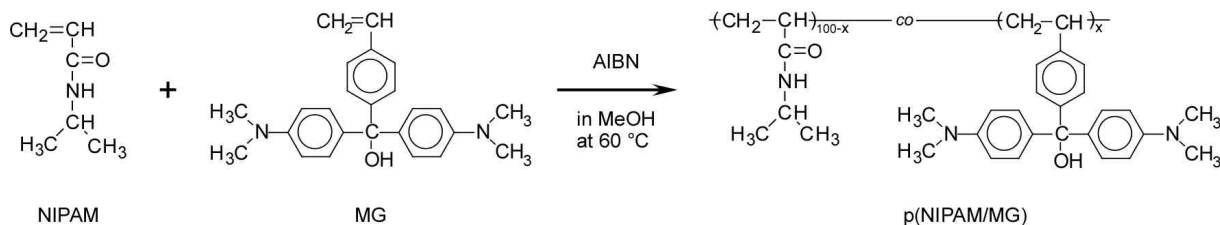


Fig. 2. Radical polymerization of NIPAM and MG containing monomer in methanol at 60 °C.

## Results and Discussion

The quantitative conversion of p(NIPAM/MG) was 95.6 %, estimated with  $^1\text{H}$  NMR.  $M_n$  and  $M_w/M_n$  for p(NIPAM/MG) were  $1.09 \times 10^5$  and 2.09, respectively. p(NIPAM/MG) in the deionized water at pH = 12 indicated absorption maximum at 620 nm due to the MG units (Fig. 3). The introduction of MG groups in the polymer was also confirmed by  $^1\text{H}$  NMR. The MG content in p(NIPAM/MG) was calculated from UV-vis absorption to be 0.35 mol%. The LCST for the aqueous solution of p(NIPAM/MG) was measured under UV-irradiation and in the dark (Fig. 4). The LCST for p(NIPAM/MG) in the dark was 33.5 °C, which increased to 34.5 °C under UV-irradiation. The polarity of p(NIPAM/MG) can be changed by photo-induced ionization of the MG groups. PNIPAM containing polar groups such as cationic MG was induced to increase the LCST. Therefore, we could control the LCST of p(NIPAM/MG) by UV-irradiation.

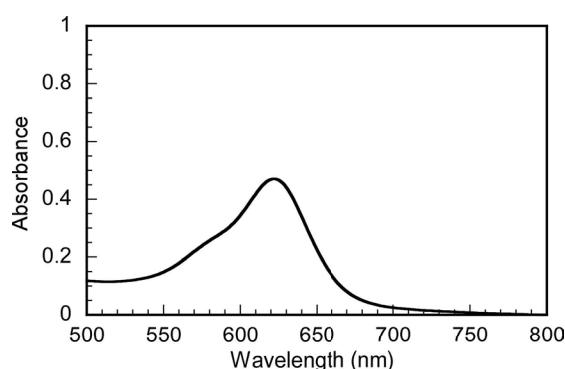


Fig. 3. UV-vis absorption spectrum for the aqueous solution of p(NIPAM/MG) at pH = 12, where the polymer concentration is 0.5 g/L.

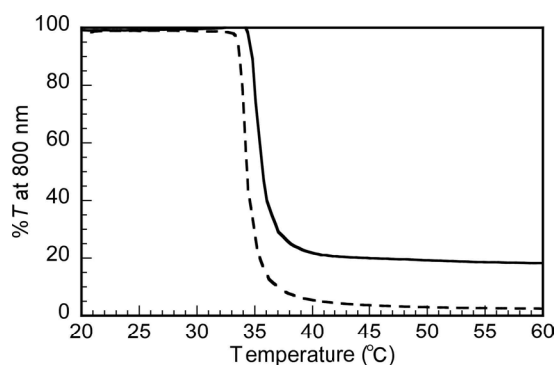


Fig. 4. Percent transmittance (%T) at 800 nm for the aqueous solutions of p(NIPAM/MG) under UV-irradiation (—) and in the dark (---) as a function of temperature.

## References

- [1] S. Fujishige, K. Kubota, I. Ando, *J. Phys. Chem.*, **93**, 3311 (1989).
- [2] R. M. Uda, M. Oue, K. Kimura, *Chem. Lett.*, **33**, 586 (2004).
- [3] W. Itamar, R. Shai, S. Ronith, Z. Tsaffir, *J. Am. Chem. Soc.*, **115**, 8690 (1993).

## Comparison of viscoelasticity of a few natural polymers in ionic liquid

Hao Hu<sup>1</sup>, Akihiko Takada<sup>2</sup>, Yoshiaki Takahashi<sup>2</sup>

<sup>1</sup> Interdisciplinary Graduate School of Engineering Sciences, Kyushu University, Japan

<sup>2</sup> Institute for Materials Chemistry and Engineering, Kyushu University, Japan

### Introduction:

It has been reported that the ionic liquid, 1-butyl-3-methylimidazolium chloride (BmimCl) can dissolve the insoluble polysaccharides such as cellulose. However, there are few reports on the solution properties of polymers using ionic liquids as solvents. In this study, a polysaccharide, pullulan, which is used as a standard polymer for aqueous solution is successfully dissolved into the ionic liquid, BmimCl without degradation via aqueous solution. Comparison of viscoelasticity of pullulan, and a few other natural polymers in dilute ionic liquid solutions are discussed.

### Experiments:

Preparation of pullulan solutions: The solutions were prepared by mixing BmimCl and aqueous solution of pullulan followed by evaporation of water. Molecular weight ( $M_w$ ) of pullulan was  $M_w = 40.4 \times 10^4$ ,  $M_w = 21.2 \times 10^4$  with  $M_w / M_n = 1.13$ .

Preparation of cellulose solution: Dried cotton was dissolved to BmimCl by maintaining it in a vacuum oven at 130°C for 2 hours. With the same method, silk fibroin BmimCl solution was preparation.

Viscoelastic measurement: The viscoelasticity of the solution was measured by MCR-300 Rheometer.

### Results and discussion

In the dilute region, the viscoelastic properties of pullulan solution changed from Zimm-like behavior to the Rouse-like behavior with increasing pullulan concentration. In Fig. 1 and Fig. 2, the experimental data agreed with the calculated values by using the Rouse-Zimm model with added long-time term. (eq. 1~5) [ref. 1]

$$G'(\omega) = \frac{CRT}{M} \sum_{p=1}^N \frac{\omega^2 \tau_p^2}{1 + \omega^2 \tau_p^2} + G_{LT} \frac{\tau_{LT}^2 \omega^2}{1 + \tau_{LT}^2 \omega^2} \quad (1)$$

$$G''(\omega) = \frac{CRT}{M} \sum_{p=1}^N \frac{\omega \tau_p}{1 + \omega^2 \tau_p^2} + G''(\text{solvent}) \quad (2)$$

$$G_{LT} = Qc[\eta] \frac{cRT}{M} \quad (3)$$

$$\tau_p = \frac{\tau_1}{p^\alpha} \quad (4) \quad \tau_{LT} = p\tau_1 \quad (5)$$

For the cellulose solution, the viscoelastic property in the dilute region was similar to the

solution of pullulan. By fitting the calculation to the experimental data (Fig. 3), the molecular weight ( $M_w$ ) of cotton was determined with  $M_w = 2 \times 10^5$ .

The viscoelastic property of silk fibroin in the dilute region was shown by Fig. 4. The experimental data agreed with the calculated values by using the Rouse-Zimm model with added long-time term. However the viscoelastic behavior was Zimm-like, and Rouse-like behavior was not observed even at higher concentration. This viscoelastic behavior is different from general linear macromolecules. One of the reasons is considered to be the branching structure of silk fibroin, while the detail is not clear yet.

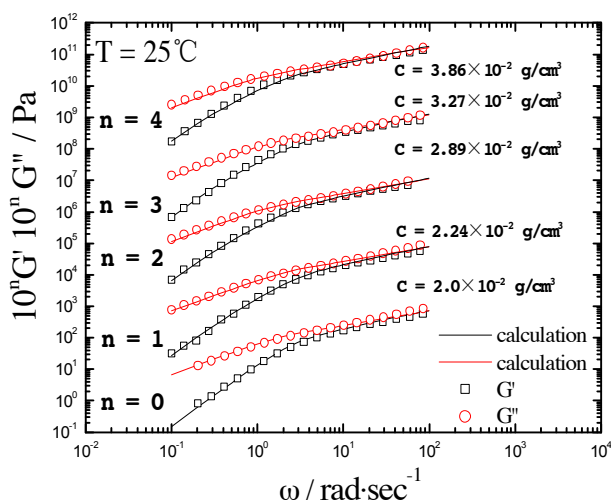


**Fig. 1** Comparison of experimental data and Rouse model of  $M_w = 40.4 \times 10^4$

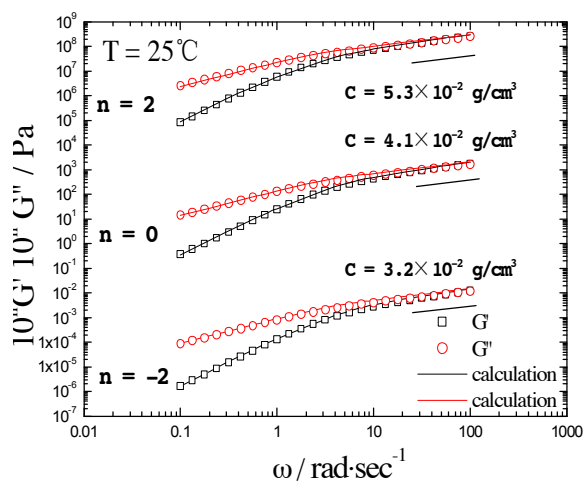


**Fig. 2** Comparison of experimental data and Rouse model of  $M_w = 21.2 \times 10^4$

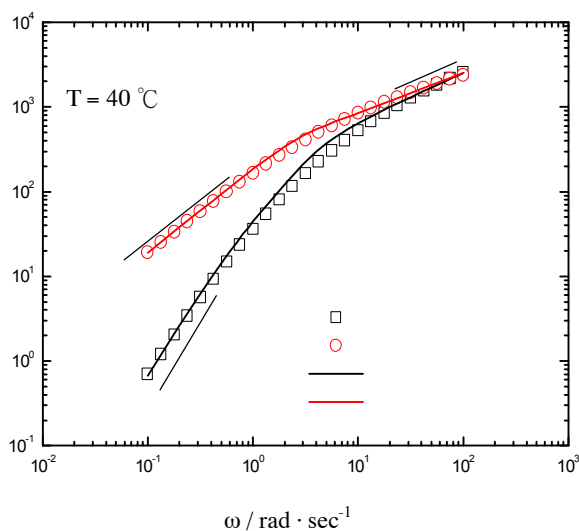


**Fig. 3** Comparison of experimental data and Rouse model of cellulose

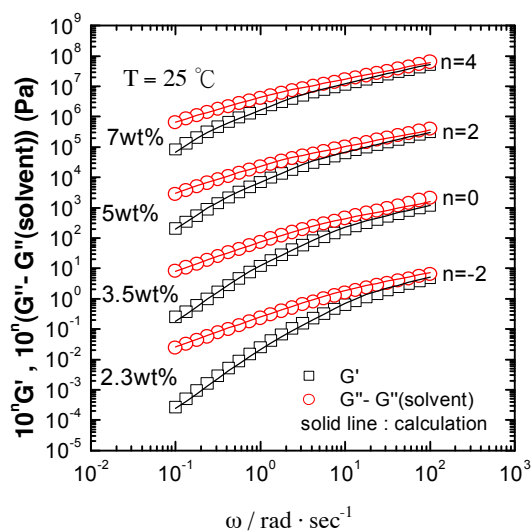


**Fig. 4** Comparison of experimental data and Rouse model of silk [ref. 2]

[1] K. OSAKI, T. INOUE, T. UEMATSU, *Journal of Polymer Science: Part B: Polymer Physics*, **Vol. 39**, 211–217 (2001)

[2] HIROSHI ICHIGAWA, Interdisciplinary Graduate School of Engineering Sciences, Kyushu University, Dissertation For Master Degree (2011)

## Localized Surface Plasmon Resonance properties of mixed monolayers composed of silver and gold nanoparticles

Keisuke Imazu<sup>1,2</sup>, Akihito Yoshida<sup>1</sup>, Koichi Okamoto<sup>1</sup> and Kaoru Tamada<sup>1</sup>

<sup>1</sup> Institute for Materials Chemistry and Engineering, Kyushu University, Japan

<sup>2</sup> Research Institute of Electrical Communication, Tohoku University, Japan

Localized Surface Plasmon Resonance (LSPR) is a phenomenon that metallic nanoparticles (NPs) absorb and scatter the light at a specific range of wavelengths. Interaction between adjacent metal NPs with nano-gap, so called “plasmon coupling”, can change their spectroscopic properties and induces additional enhancement of local electromagnetic field. Our group has been interested in tuning the resonance wavelength of LSPR by changing the metallic NPs 2D array structures by mixing Au and Ag metallic NPs<sup>[1]</sup>. Here we report the plasmonic characteristics of mixed two dimensional NP films fabricated at air-water interface by spreading the mixed NP solutions.

Fig.1 shows UV-vis transmission spectra of the mixed film composed of dodecane(C12) thiol-capped gold NP (AuC12 NP, 6.2 nm in diameter)<sup>[2]</sup> and myristic acid-capped silver NP (AgMy NP, 5 nm in diameter)<sup>[3]</sup> at air-water interface. The positions of LSPR bands of AuC12 NPs and AgMy NPs was appeared at the wavelength of 442.2 nm and 551.8 nm respectively. These band position were red-shifted compared to that of NP dispersions in chloroform (the dashed lines in Fig.1), and didn't change by compression. In my poster, I will discuss the correlation between LSPR bands position and mixing ratio of particles.

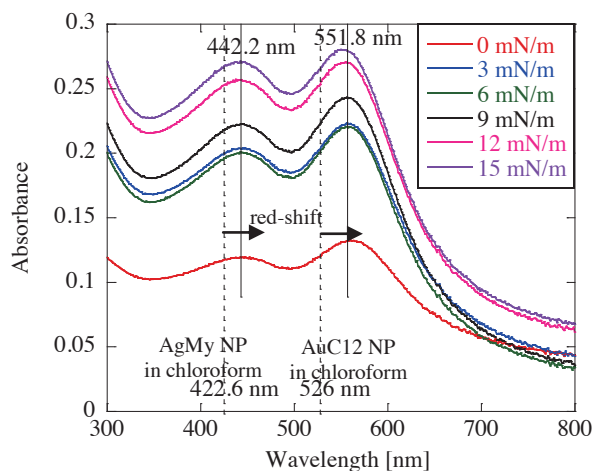


Fig.1 UV-vis transmission spectra of mixed NP film at air-water interface (AuC12 NP : AgMy NP = 1 : 1 )

[1] H. Acharya, et al. Chem. Mater. 21, 4248-4255 (2009).

[2] Jana, et al. J. Am. Chem. Soc. 125, 14280 (2003)

[3] K. Tamada et al. Proc. SPIE. 7213, 7213E (2009)

## Stimuli-Responsive Gels through Complexation of Halide and Anion Receptors

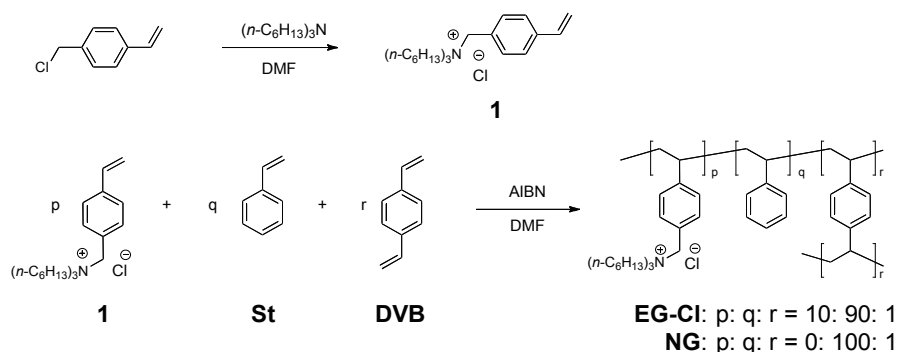
Kazuya Iseda<sup>1)</sup>, Yohei Haketa<sup>4)</sup>, Kenta Kokado<sup>2)</sup>, Hiromitsu Maeda<sup>4),5)</sup>, Hiroyuki Furuta<sup>3)</sup>,  
Kazuki Sada<sup>2)</sup>

<sup>1</sup>Graduate School of Chemical Science and Engineering, <sup>2</sup>Graduate School of Science, Hokkaido University, Sapporo, Japan <sup>3</sup>Graduate School of Engineering, Kyushu University, Fukuoka, Japan <sup>4</sup>Institute of Science and Engineering, Ritsumeikan University, Kyoto, Japan <sup>5</sup>PRESTO, JST

Polyelectrolyte gels are well-known as super-absorbent polymers that swell in water, and their swelling degrees are several hundreds or more. They are used in a wide range of applications such as nappies, separation media, drug delivery systems, biomedical devices and sensors. However, these gels collapse in most of organic solvents except highly polar ones due to aggregation of the ions, and synthesizing super-absorbent polymers that swell with high swelling degrees in nonpolar organic solvents ( $\epsilon < 10$ ) had been never realized. Recently, we reported that lipophilic polyelectrolyte gels based on poly(alkyl acrylate) and poly(styrene) with tetraalkylammonium tetraphenylborate groups had extreme large swelling abilities in such organic solvents<sup>1),2)</sup>. In this presentation, we demonstrate new molecular design of lipophilic polyelectrolyte gels by complexation between the common polyelectrolyte gels and lipophilic molecular receptors (**R1-R3** in Fig. 1). The complexation enhanced the swelling degrees by improvement of the lipophilicity and promotion of ion dissociation.

The styrene-based polyelectrolyte gels with chloride anions (**EG-Cl**) were prepared by copolymerization of an ionic monomer (**1**), styrene (**St**) and divinyl benzene (**DVB**) as a crosslinker in the presence of AIBN, as shown in Scheme 1. The feed ratio was adjusted to **1: St: DVB** = 10: 90: 1. As a reference, nonionic gels (**NG**) were prepared under the same copolymerization conditions (**St: DVB** = 100: 1) without **1**.

**Scheme. 1** Preparation of monomer **1**, ionic polymer gels (**EG-Cl**) and nonionic polymer gels (**NG**).



The swelling behaviors of **EG-Cl** in organic solvents and in the presence of anion receptors **R1-R3** were investigated. The swelling degrees ( $Q$ ) were calculated as the following

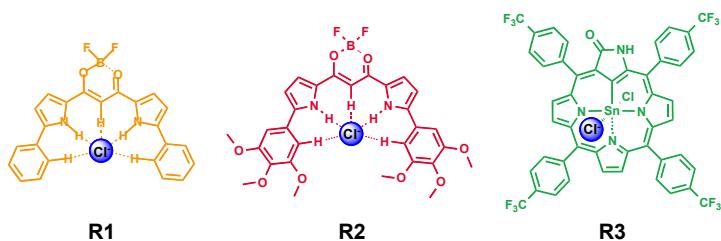


**Figure 1** The structures of anion receptors.

equation;  $Q = (L_{\text{add}} - L_{\text{wet}}) / L_{\text{wet}}$  (mm / mm), where  $L_{\text{add}}$  and  $L_{\text{wet}}$  are the wet length of **EG-Cl** in the presence and absence of the anion receptors, respectively. In acetone ( $\epsilon = 20.6$ ), the swelling degrees of **EG-Cl** increased by addition of the all anion receptors (Fig. 2), but the swelling degrees of **NG** didn't change. This result indicated that the swelling degrees of the **EG-Cl** were enhanced by the complexation between the chloride anions in the polymer network of **EG-Cl**. We further investigated solvent

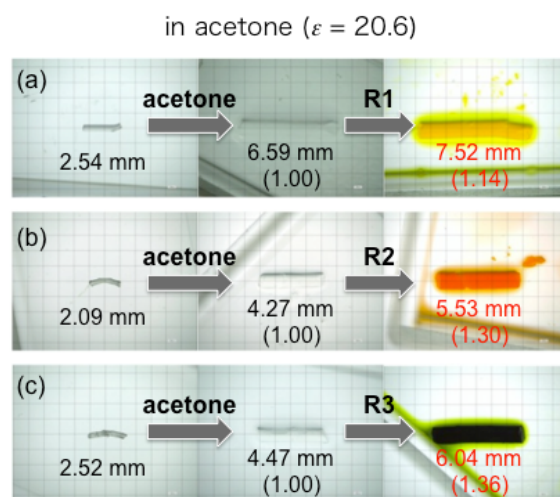


**Figure 2.** Swelling behaviors of **EG-Cl** in acetone in the presence of (a) **R1**, (b) **R2** and (c) **R3**.

dependence of the swelling degrees of **EG-Cl** in the presence of **R2** and **R3** (Figure 3). Starting from the nonpolar solvents, the swelling degrees increased with increasing dielectric constant, and the maximum swelling degree was observed in acetone. On the other hand, in highly polar solvents such as DMF ( $\epsilon = 36.7$ ) and DMSO ( $\epsilon = 46.5$ ), the swelling degrees didn't change by addition of the receptors. These results indicated that ion dissociation was promoted by complexation with the anion receptors in less polar media to increase the swelling degrees.

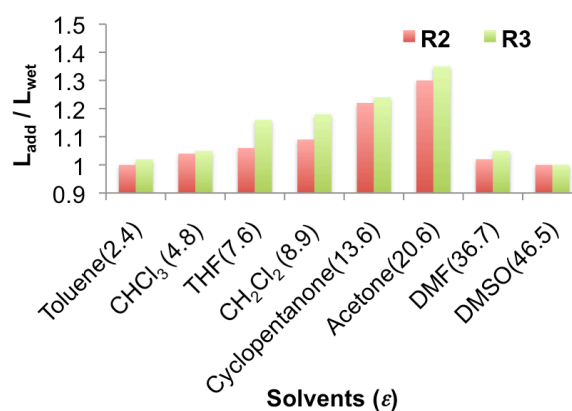


**Figure 3.** Solvent dependence of the swelling degrees of **EG-Cl**.

In summary, we demonstrate enhancement of swelling abilities of the polyelectrolyte gels induced by molecular receptors toward counter ions in the polymer network. They should be regarded as new stimuli-responsive gels that act in nonpolar media.

## References

- 1) T. Ono, T. Sugimoto, S. Shinkai, K. Sada, *Adv. Funct. Mater.* **2008**, *18*, 3836.
- 2) K. Iseda, M. Ohta, T. Ono, K. Sada, *Soft Matter* **2011**, *7*, 5938.

## Preparation and Catalysis of Polysiloxane Gels in which Palladium Nanoparticles are encapsulated

Ai Ishii<sup>2</sup> and Hideo Nagashima<sup>1,2</sup>

Institute for Materials Chemistry and Engineering<sup>1</sup>, and Graduate School of Engineering Sciences<sup>2</sup>, Kyushu University, 6-1 Kasugakoen, Kasuga, Fukuoka, Japan, 816-8580

Immobilized catalysts, in which transition metal species are embedded to polymer supports, have been received considerable attention due to their ability that facile separation of the catalyst from the product is achieved and the catalyst recovered is reusable.<sup>1</sup> We have been concerned with polysiloxane gels encapsulating organotransition metal species, which behaves as unique reusable catalysts for several organic reactions.<sup>2</sup> The conceptual drawing is shown in Fig. 1. During the studies, we are that the polysiloxane gels can encapsulate not only monomethallic species but also monomethal particles.

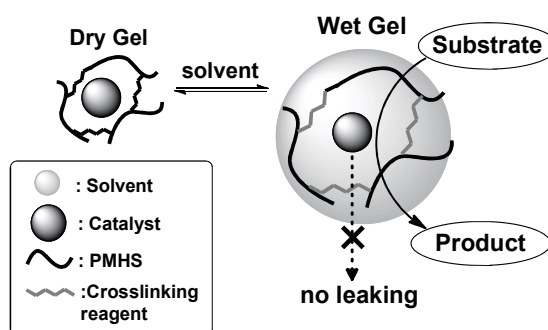
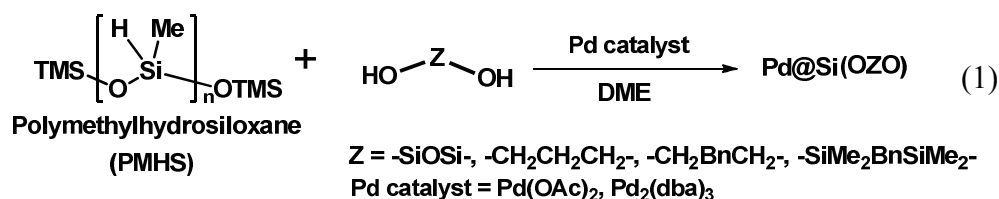
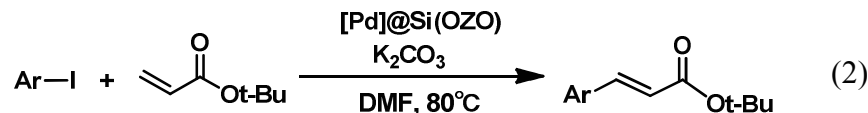


Fig. 1. The conceptual image of transition metal species are encapsulated in to the polysiloxane gel.

In this paper, we wish to report that a treatment of certain palladium compounds with PMHS in the presence of  $\alpha,\omega$ -diols or  $\alpha,\omega$ -silanediols resulted in polysiloxane gel containing well dispersed nano-size palladium particles (eq. 1). The resulting Pd@Si(OZO) are proved to act as reusable catalyst for several palladium-catalyzed coupling reactions; a representative is Mizoroki-Heck reaction<sup>3</sup> shown in eq. 2.



### Mizoroki-Heck reaction



[1] Gladysz, J. A. *Pure Appl. Chem.*, **73**, 1319. (2001)

[2] (a) Nagashima, H. *Chem. Commun.*, **42**, 5321-5323 (2008). (b) Nagashima, H. *Org. Lett.*, **11**, 1345-1348 (2009). (c) Nagashima, H. *Chem. Commun.*, **46**, 2256-2258 (2010)

[3] A.; Meyer, F. E. Jr.; *Angew. Chem. Int. Ed. Engl.*, **33**, 2379. (1994)



## Synthesis of $\alpha,\omega$ -Di-Nitrilotriacetic Acids-End-Functionalized Polystyrenes by Combination of ATRP and Click Coupling

Mohammad Abdul Kadir,<sup>1</sup> Aleya Hasneen,<sup>1</sup> Hyun-jong Paik<sup>1\*</sup>

<sup>1</sup>*Department of Polymer Science & Engineering, Pusan National University  
San 30 Jangjeon 2-dong Geumjeong-gu, Busan 609-735, Republic of Korea*

We report the synthesis of  $\alpha,\omega$ -di-nitrilotriacetic acids end-functionalized polystyrene (NTA-PS-NTA) by combining atom transfer radical polymerization (ATRP) and click chemistry. First,  $\alpha,\omega$ -dibromopolystyrene was synthesized using dimethyl 2,6-dibromoheptanedioate initiator by ATRP for the facile post modification of the polymer chain-end groups. After introduction of azide groups at the chain ends of the polymer by simple nucleophilic substitution, *t*-butyl protected NTA moieties were attached at the  $\alpha,\omega$ -chain-ends by click coupling and subsequently, *t*-butyl groups were removed. The polymer was characterized by <sup>1</sup>H NMR, FT-IR and GPC.

## Networked Polymer-in-salt Electrolyte with Poly(hydroxyethyl methacrylate)

Yu-Jeong Lim, Young-Deok Kim, and Nam-Ju Jo \*

Department of Polymer Science and Engineering, Pusan national University, South Korea

Solid polymer electrolytes (SPEs) have good safety for lithium battery compared to liquid electrolytes because of the non-volatility, low toxicity and higher energy density. Although SPEs have excellent advantages, they could not entirely free from the fault of lower ionic conductivity [1]. To solve the problem, we have introduced polymer-in-salt electrolyte (PISE) with the ion hopping mechanism through percolation path [2]. However, PISE has considerable disadvantages that are poor mechanical properties with increasing salt concentration.

In this study, we prepared networked polymer electrolytes consisting of poly(hydroxyethyl methacrylate) (p(HEMA)), lithium triflate and hydrochloric acid as acid catalyst to improve mechanical properties. Fig. 1 shows the ionic conductivities of networked p(HEMA)-based SPEs with various molecular weight between crosslinking point ( $M_c$ ) and salt concentration. By introduction of networked structure, the ionic conductivity at the low salt concentration decreased since the restriction of segmental motion. Meanwhile, all of networked p(HEMA)-based SPE possessed high ionic conductivity at the high salt concentration since PISE has had ion hopping mechanism regardless of segmental motion. Fig. 2 shows the mechanical properties according to  $M_c$  related to the concentration of acid catalyst. As the concentration of acid catalyst increased, mechanical property increased.

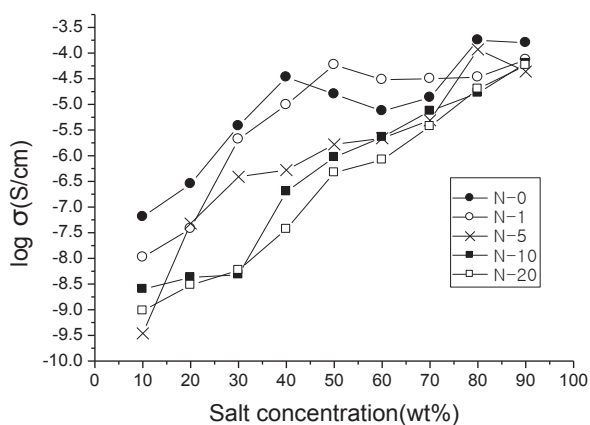


Fig.1. Ionic conductivity of networked p(HEMA)-based SPE according to salt concentration and  $M_c$ .

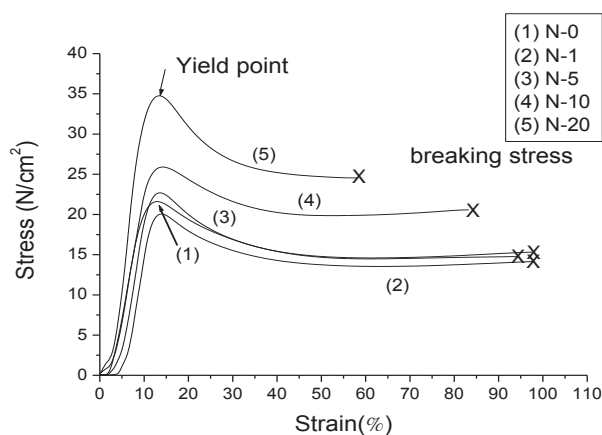


Fig.2. Mechanical property of networked p(HEMA) according to  $M_c$ .

[1] S. Kim, S. J. Park, J. Colloid and Interface Science, **332**, 145 (2009).

[2] 2. C. A. Angell, C. Liu, E. Sanchez, Nature, **362**, 137 (1993)

## Immuno-detection by Hydrogel-modified Field Effect Transistor

Yasuhiro Maeda<sup>1</sup>, Takashi Endo<sup>2</sup>, Akira Matsumoto<sup>1</sup>, Takashi Miyata<sup>3</sup>, Ryo Yoshida<sup>2</sup>, Yuji Miyahara<sup>1</sup>,

<sup>1</sup> Institute of Biomaterials & Bioengineering, Tokyo Medical and Dental University, Japan

<sup>2</sup> Department of Materials Engineering, The University of Tokyo, Japan

<sup>3</sup> Unit of Chemistry, Kansai University, Japan

Stimuli-responsive materials capable of undergoing physicochemical changes in response to environmental signals represent valuable tools for use in a variety of biomedical applications. Miyata et al. and others reported that protein-protein interaction could be used for induction of swelling and deswelling of hydrogel [1,2].

Vinyl-functionalized antigen and antibody were polymerized in the presence of main-chain acrylamide (AAm) and

N,N-methylene-bis-acrylamide (MBA) resulting in the covalently-formed hydrogel bearing variable (reversible) crosslinking points achievable through antigen-antibody complexation. The addition of free antigen, due to competitive binding toward the antibodies, led to decreased pre-formed antigen-antibody crosslinks and thus the swelling of the hydrogel (Fig. 1). In this paper, we demonstrate such a smart immuno-sensitive hydrogel can also provide a functional interface suitable for field effect transistor (FET)-based immune-sensors.

Immuno-sensitive hydrogels were prepared by copolymering N-succinimidylacrylate (NSA)-modified rabbit immunoglobulin G (Rabbit IgG) and goat anti-rabbit IgG in the presence of AAm and MBA. To characterize the antigen-sensitivity of the hydrogel, free rabbit IgG antigen was added and the changes in diameter of the cylindrical hydrogels were investigated. It was confirmed that a replacement of the

gel-immobilized antigens by the free antigens causes swelling of the hydrogel (Fig. 2) due to decreased pre-formed crosslinking density of the gel. The antigen-antibody hydrogel was covalently introduced onto the surface of an extended gate gold electrode, which was then

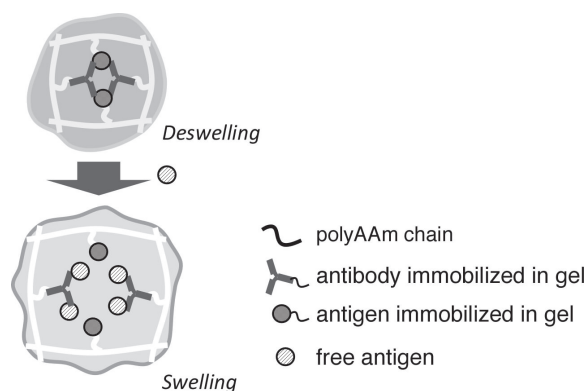


Fig. 1. Mechanism for the swelling of an antigen-antibody hydrogel in response to free antigen.

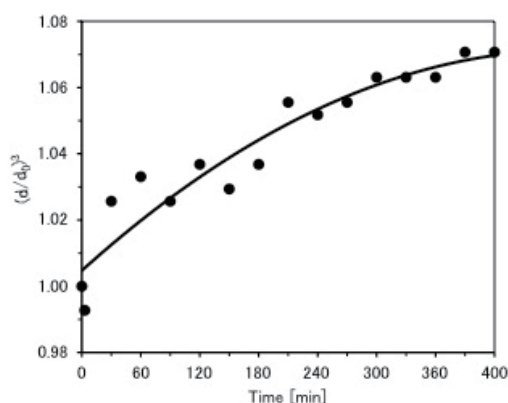


Fig. 2. Antigen recognition by the antigen-antibody hydrogel. The swelling ratio of the antigen-antibody hydrogel is shown, after the addition of rabbit IgG

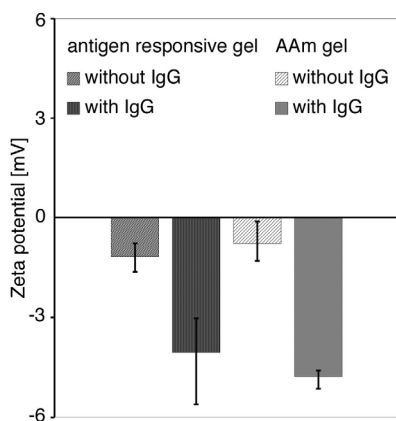


Fig. 3. Zeta potentials of antigen–antibody hydrogel and acrylamide hydrogel with and without rabbit IgG

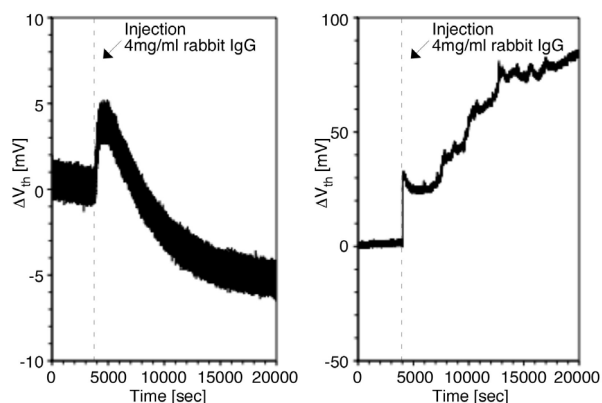


Fig. 4. Antigen recognition by the antigen–antibody hydrogel and acrylamide hydrogel. The threshold voltage ( $V_T$ ) measured by the hydrogel-modified field effect transistor is shown, before and after the addition of rabbit IgG.

electrically lined to an FET gate. Fig. 4 shows time course responses of the threshold voltage ( $V_T$ ) on adding 5 mg/ml rabbit IgG onto the electrode. In the case of the antigen-antibody hydrogel, the  $V_T$  rapidly increased at first, and then decreased gradually but more remarkably. In sharp contrast, in the case of the AAm hydrogel,  $V_T$  continuously (and monotonously) increased. Based on size measurement and zeta potential study (Fig. 3), the initial increase of  $V_T$  observed for both cases were attributed to the increase of negative charges due to the penetration of rabbit IgG, whereas the decrease of  $V_T$  observable only for the antigen-antibody hydrogel could be explained by the swelling of the hydrogel correlated to apparently decreased density of pre-formed antigen–antibody crosslinks.

To summarize, we proposed and demonstrated a unique way of utilization of antigen-sensitive hydrogel as a bio-recognition and signal transduction interface for FET-based immuno-detection. So far, because of the limitation related to Debye's length, only charged small molecules are feasible targets in conventional FET systems [3]. In the configuration herein described, capturing of specific antigen by the hydrogel can trigger changes in other physicochemical properties of the hydrogel such as volume, charge density and permittivity, thus accomplishing a conversion of biochemical signal into electrical signal. This new detection scheme could be extended to a wider range of targets including other proteins, large molecules and even electrically neutral molecules involved in many important bio-recognition events.

- [1] T. Miyata, N. Asami, T. Uragami, *Macromolecules*, **32**, 2082 (1999).; T. Miyata, N. Asami, T. Uragami. *Nature*, **399**, 766 (1999).
- [2] Z. Lu, P. Kopeckova, J. Kopecek, *Macromolecular Bioscience*, **3**, 296 (2003).
- [3] T. Goda and Y. Miyahara, *Analytical Chemistry*, **82**, 8946 (2010).

## Core-Shell Hybrid Particles with Controlled Shell Thickness by Using Nanoparticle Adsorption

Tsuyoshi Morisaki<sup>1</sup>, Takeshi Wakiya<sup>1</sup>, Makoto Takafuji<sup>1,2</sup>, Hiroataka Ihara<sup>1,2</sup>

<sup>1</sup>Department of Applied Chemistry and Biochemistry, Kumamoto University, Japan

<sup>2</sup>Kumamoto Institute for Photo-Electro Organics (Phoenix), Japan

Organic-inorganic core-shell particles have caught extensive attention as useful materials. Monomer adsorption and following polymerization are mostly utilized to synthesize core-shell particles. However this method has difficulties in layer thickness control and creating thicker layer.

In this paper, we introduce a novel method to prepare core-shell particles with controlled shell-thickness through the adsorption of silica nanoparticles as a shell component and the following polymerization of tetraethoxysilane (TEOS) in the particle shell layer.

Poly(divinylbenzene) particles (pDVB,  $d = 7.5 \mu\text{m}$ ) were treated with aminopropyltrimethoxysilane (APS) and stirred with silica nanoparticles for 1 h in water/ethanol (7 / 3). The resultant pDVB-silica composites were gathered by decantation and washed with ethanol and water. The SEM image of Fig. 1a showed that silica nanoparticles were adsorbed on a core. No similar structure was observed without treatment of APS, and therefore it is estimated that the composite is created through electrostatic interaction.

The obtained core-shell particles were stirred for 24 h at room temperature in water/ethanol (3 / 7) with TEOS, cetyltrimethylammoniumbromide, and ammonia as a catalyst. The obtained particles were washed with water and ethanol. The SEM of Fig. 1b showed that the core diameter increased slightly and the surface morphology became smoother. The SEM of Fig. 1c showed that the hollow particle was obtained after removal of a core polymer by burning. On the other hand, Fig. 1d showed the hollow particle obtained by using 200 nm nanoparticles.

In conclusion, we have succeeded to control the shell-thickness of the core-shell particles by using nanoparticles as a shell component. In addition, the hollow silica particles can be obtained from the core-shell particles by burning.

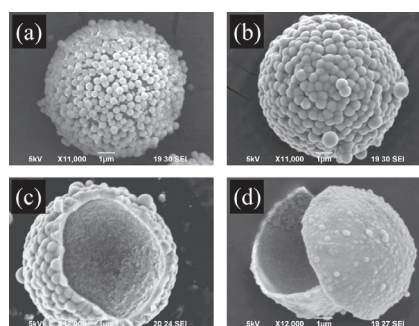


Fig. 1 SEM images of  
 (a) pDVB-silicananoparticle (450 nm) composite,  
 (b) pDVB-silicananoparticle (450 nm) after sol-gel reaction with TEOS,  
 (c) hollow particle in 600 nm thickness,  
 (d) hollow particle in 270 nm thickness.

## Charge Transfer Nanomaterials Self-assembled from Polyoxometalate and Nucleotides

Takao Noguchi<sup>1</sup>, Nobuo Kimizuka<sup>1,2,3</sup>

<sup>1</sup>Graduate School of Engineering, Kyushu University, Japan

<sup>2</sup>International Research Center for Molecular Systems (IRCMS), Kyushu University

<sup>3</sup> Japan Science and Technology (JST), CREST

Polyoxometalates (POMs) have been attracting much interest due to their intrinsic functions such as catalytic and redox properties. The use of POMs to fabricate functional devices such as fuel cells, batteries, and capacitors has been a new frontier in nanomaterials science. It requires directed assembly of POMs on substrates or electrodes and to develop functions unique to these nano-interfaces. Self-assembly of POMs is one of the promising approaches, and it is necessary to impart self-assembling properties to anionic POMs. We have recently developed supramolecular methodologies to cover one-dimensional metal complexes or POMs by using synthetic lipids, which afforded soluble nanowires in organic media. Notably, their electronic and spin states have been controlled on the basis of lipid chemical structures and physical conditions. [1,2,3] Another strategy to integrate anionic molecules is to employ electrostatic assembly with oppositely charged molecules. [4] Self-assembly of nucleotides with lanthanide ions also afforded amorphous nanoparticles which showed inclusion of guest materials via adaptive self-assembly. [5]

Here we present supramolecular self-assembly of anionic POMs by using nucleotides as counter-cations (Fig.1). The complexes of POM/nucleotides form a wide variety of supramolecular morphologies such as cubes, sheets, fibers, and spheres depending on the constituent metal ions in POM and the chemical structure of nucleotides.

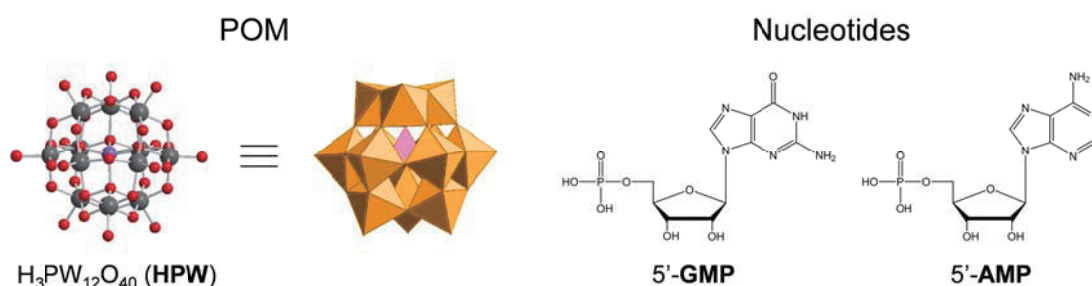


Fig. 1. Chemical structures of polyoxometalate (**HPW**) and nucleotides (**GMP** and **AMP**).

The powdery complexes **PW/AMP** and **PW/GMP** were obtained by mixing aqueous solutions of **HPW** (15 mM, pH 1.5, 10 mL) and the nucleotides (45 mM, pH 1.5, 10 mL), respectively (Fig. 2a). Composition of these two complexes are [PW]<sup>3-</sup>·(H<sup>+</sup>-AMP)<sub>3</sub> and [PW]<sup>3-</sup>·(H<sup>+</sup>-GMP)<sub>3</sub> respectively, as determined by X-ray photoelectron spectroscopy and

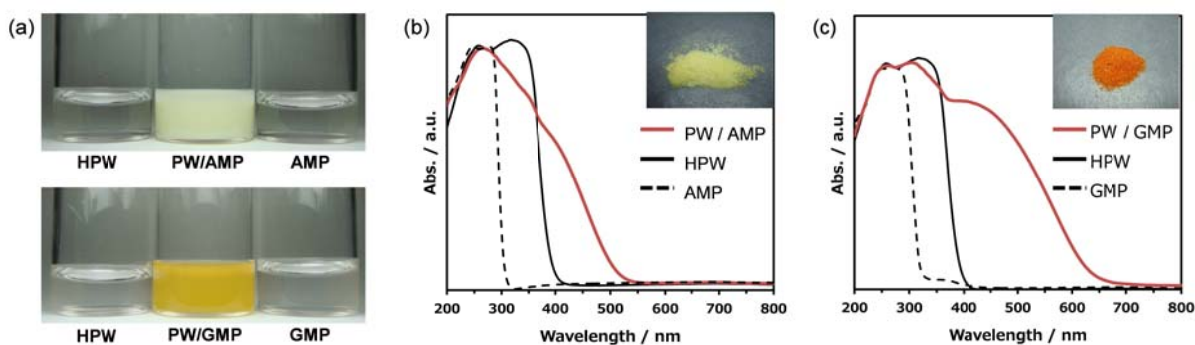


Fig. 2. Photographs of **PW/AMP** and **PW/GMP** dispersions obtained by mixing the starting solution (a), and diffuse reflectance spectra of **PW/AMP** (b) and **PW/GMP** (c). Insets are the photographs of the solid complexes obtained.

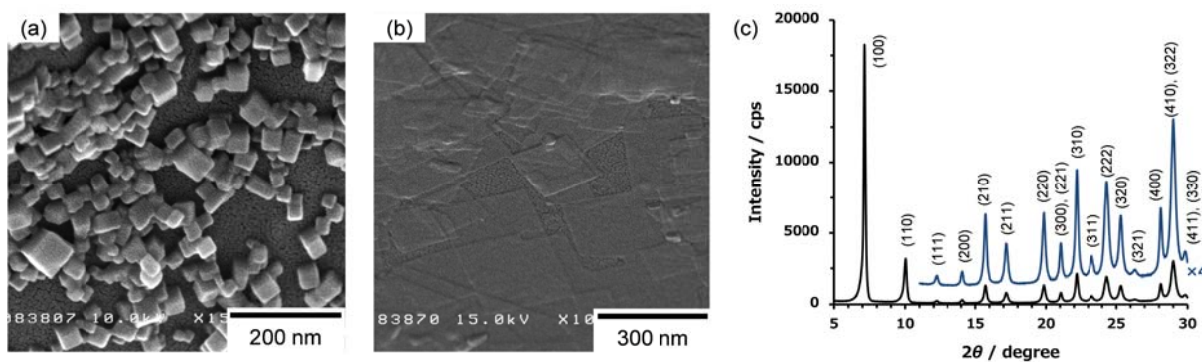


Fig. 3. SEM images of **PW/AMP** (a) and **PW/GMP** (b), and a representative XRD profile of **PW/AMP** (c).

elemental analysis. Notably, the color of solids obtained was yellow for **PW/AMP** and orange for **PW/GMP**, respectively (Fig. 2, insets). Diffuse reflectance spectra show that a new absorption band appeared at the visible wavelength region (Fig. 2b,c). These new absorption bands were also observed for complexes formed from **HPW** and nucleobases such as adenine and guanine. These results suggest that the newly observed absorption band is attributed to charge-transfer (CT) from nucleobases to **HPW**.

Very interestingly, these complexes gave ordered nanostructures as observed by scanning electron microscopy (SEM). Nanocubes were observed for **PW/AMP** (Fig. 3a), while **PW/GMP** formed nanosheets (Fig. 3b). Powder X-ray diffraction (XRD) of **PW/AMP** revealed the packing structure to be primary cubic as can be indexed in Fig. 3c. **PW/GMP** showed similar XRD pattern as observed for **PW/AMP**. Thus, supramolecular self-assembly of POM and nucleotides afforded varied nanostructures depending on the chemical structure of nucleobases. We envisage that CT interactions in these nanostructures may give new photochemical functions.

- [1] N. Kimizuka, *Adv. Mater.*, **12**, 1461 (2000).
- [2] H. Matsukizono, K. Kuroiwa, N. Kimizuka, *J. Am. Chem. Soc.*, **130**, 5622 (2008).
- [3] T. Noguchi, C. Chikara, K. Kuroiwa, K. Kaneko, N. Kimizuka, *Chem. Comm.*, **47**, 6455 (2011).
- [4] M. Morikawa, M. Yoshihara, T. Endo, N. Kimizuka, *J. Am. Chem. Soc.*, **127**, 1358 (2005).
- [5] R. Nishiyabu, C. Aime, R. Gondo, T. Noguchi, N. Kimizuka, *Angew. Chem. Int. Ed.*, **48**, 9465 (2009).

## Synthesis of comb-shaped block copolymer and characterization of its self-assembled structure

Atsushi Sakai<sup>1</sup>, Tomoyasu Hirai<sup>2</sup>, Masahiko Asada<sup>3</sup>, Jun-ichiro Koike<sup>3</sup>, Misao Horigome<sup>3</sup>, Hiroki Ogawa<sup>4</sup>, Hiroyasu Masunaga<sup>4</sup>, and Keiji Tanaka<sup>1,2</sup>

<sup>1</sup>Department of Automotive Science and <sup>2</sup>Department of Applied Chemistry, Kyushu University, Fukuoka 819-0395, Japan, <sup>3</sup>DIC Corporation Central Research Lab., 631 Sakato, Sakura-shi, Chiba 285-8668, Japan, <sup>4</sup>Japan Synchrotron Radiation Research Institute, Hyogo 679-5198, Japan

**Introduction:** Block copolymer (BCP) consists of chemically distinct polymer blocks connected by a covalent bond. Immiscibility of the polymer blocks leads to microphase separation with a size ranging from 50 nm down to 5 nm, depending on the architecture, chemical composition and degree of polymerization [1]. BCP thin films are strongly affected by the presentation of a surface and/or interface. This is mainly because the wetting layer of a component is formed at the surface and substrate interface to minimize the free energy of the system [2]. However, such a structure may not be necessarily desired, depending on what the purpose of using BCP is. Thus, the control of the orientation for microphase-separated domains is still needed. In this study, a comb-shaped BCP was synthesized by a living anionic polymerization to realize the alignment of microphase-separated domains along the direction normal to the surface.

**Experiments:** Figure 1. shows synthetic route for the comb-shaped BCP with hydroxyl end groups. First, the synthesis of macromonomer, polystyrene-*b*-polyisoprene (PS-*b*-PI) with a vinyl group, was carried out. PS was synthesized with *sec*-BuLi as an initiator at 195 K for 10 min. and then PI was connected to it at 233 K for 48 h. Number-average molecular weight ( $M_n$ ) and polydispersity index (PDI) against PS standards were 10,000 and 1.05, respectively. To obtain comb-shaped BCP with *tert*-butyl end group, a living anionic polymerization of macromonomer was carried out again with *sec*-BuLi as an initiator at 195 K for 24 h. The reaction was quenched after a given time by 2-bromoethoxy-*tert*-butyl dimethylsilane. The  $M_n$  and PDI of the comb-shaped BCP with *tert*-butyl end group were 68,000 and 1.08, respectively. A deprotection reaction of *tert*-butyl end group was performed using tetrabutylammonium fluoride. The  $M_n$  and PDI of target comb-shaped BCP with hydroxyl end group were 68,000 and 1.08, respectively. Transmission small-angle X-ray scattering (SAXS)

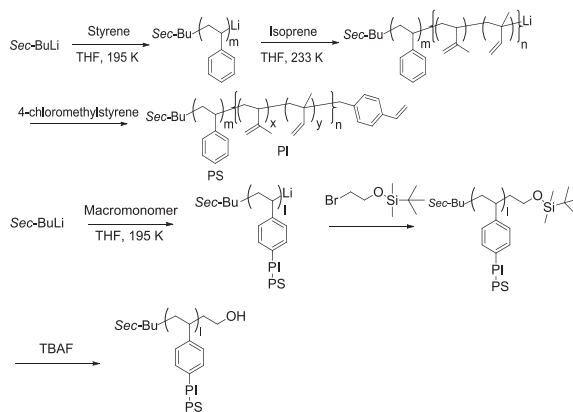


**Figure 1.** Synthesis strategy of comb-shaped BCP with hydroxyl end group.



were performed on the BL03XU beamline at Spring-8. Thin films were prepared onto silicon wafers by a spin-coating method, and then were annealed at 463 K for 24 h. Surface structure in the films was discussed on the basis of atomic force microscopic (AFM) observation.

**Results and discussion:**  $M_n$  and PDI of macromonomer and comb-shaped polymers were summarized in Table 1. Monodisperse comb-shaped BCPs were successfully synthesized by using a living anionic polymerization. However, macromonomers were not polymerized when the molecular weight was higher than 16,000.

**Table 1.**  $M_n$  and PDI of Comb-shaped BCPs

Entry	$M_n$ Macromonomer	$M_n$ Comb-shaped BCPs	PDI
1	8,000	72,000	1.04
2	9,000	24,000	1.14
3	10,000	68,000	1.08
4	11,000	60,000	1.14
5	14,000	54,000	1.09
6	16,000	-	-
7	17,000	-	-
8	21,000	-	-
9	30,000	-	-

This is probably because of an effect of steric hindrance on the reaction becomes remarkable with increasing size of the macromonomer. Molecular weight remained constant before and after the deprotection reaction, meaning that the deprotection proceeded without any side reactions.

As a representative comb-shaped BCP, entry 3 in Table 1 was used for characterization. Chemical structure of the comb-shaped BCP with hydroxyl end groups was characterized by nuclear magnetic resonance ( $^1\text{H}$  NMR) spectroscopy. All signals were assigned indicated that the polymer desired were definitely obtained. Also,  $^1\text{H}$  NMR spectrum revealed that the PS weight fraction in the comb-shaped BCP was 51 %. Bulk morphology of the comb-shaped BCP in a film, which should be closely in a quasi-equilibrium state. Figure 2. shows the SAXS line profile for comb-shaped BCP. Only the first order scattering peak was observed at the scattering vector of  $0.18\text{ nm}^{-1}$ , indicating that the domain identity period for the microphase-separated structure was 35 nm and that the structure did not possess a long-range order. Finally, to

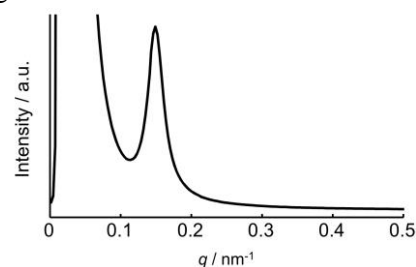


**Figure 2.** SAXS line profile for a comb-shaped BCP with hydroxyl end groups.

study an effect of comb-shape polymer on microphase separation, the thin film was prepared. Figure 3. shows the AFM phase image for the thin film of the comb-shaped BCP. The image was composed of darker and brighter regions without a long-range order. That is implied that the formation of PI wetting layer was regulated using comb-shaped BCP.

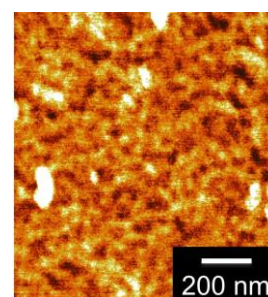


**Figure 3.** AFM phase image of comb-shaped BCP.

## References

- [1] D. Y. Ryu, K. Shin, E. Drockenmuller, C. J. Hawker, T. P. Russell, *Science* **2005**, *308*, 236.
- [2] P. Mansky, T. P. Russell, C. J. Hawker, J. Mays, D.C. Cook, S. K. Satija, *Physical Review Letters* **1997**, *79*, 237.

## Fabrication of Loop Polymer Brushes through Immobilization of Telechelic Polymers on a Solid Surface

Shinichiro Sakurai<sup>1</sup>, Hirohmi Watanabe<sup>1</sup>, and Atsushi Takahara<sup>1,2</sup>

<sup>1</sup>Japan Science Technology Agency, ERATO Takahara Soft Interfaces Project

<sup>2</sup>Institute for Materials Chemistry and Engineering, Kyushu University,  
744 Motooka, Nishi-ku, Fukuoka, 812-0395, Japan.

The physicochemical properties of soft interfaces are strongly influenced by the surface morphology (topology) and the chemical properties of the materials. To introduce molecular-scale topological effects into the interface has attracted great interest for control of the interfacial properties such as wettability, adhesion, and friction. de Gennes [1] and Guiselin [2] predicted that the distribution of looped polymer chains has a large effect on the wettability in the polymer film. In this study, we synthesized loop polymer brushes using telechelic poly(dimethylsiloxane) (PDMS) with various molecular weight (poly-**1** in Figure 1). Both ends of the PDMS polymer were anchored on the substrate surface through a covalent bond, and the chain conformation of the surface-tethered polymer was investigated. Linear PDMS polymer brush with the functional group only at one end was also prepared from a PDMS (poly-**2** in Figure 1). The surface morphology of the telechelic PDMS-immobilized silicon wafer was observed by atomic force microscopy. The observed smooth surface indicated that the loop structure was formed without any cross-linking or gelation of the triethoxysilyl groups. Although the thicknesses of these brushes increased with increasing the molecular weight, the difference between the loop and linear polymer brushes in a dried state was not obvious. It is probably due to the restriction of chain conformation in the dried state. In water and ethylene glycol, however, the thickness of the linear brush was thicker than that of the loop counterpart. Details of the difference between the two will discuss in the presentation.

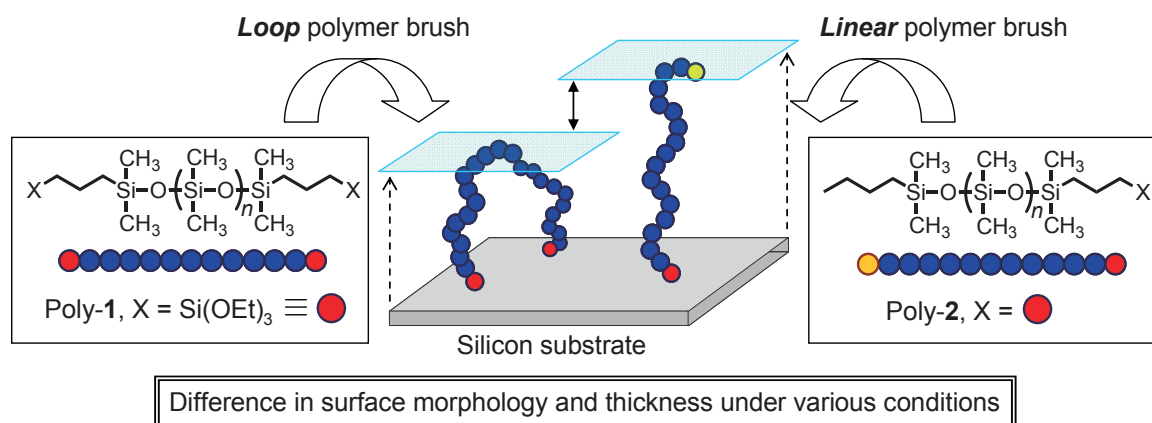


**Figure 1.** Schematic illustration of the structure of loop and linear polymer brushes on silicon surface.

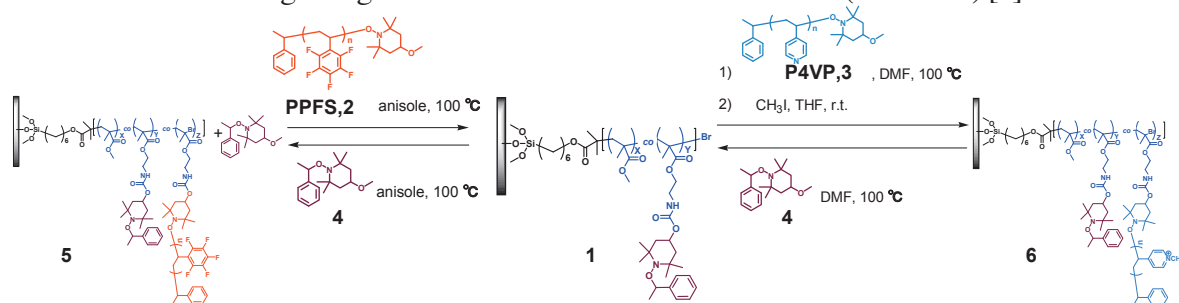
[1] P. G. de Gennes, *Macromolecules* **13**, 1069 (1980).

[2] M. Aubouy, O. Guiselin, E. Raphaël, *Macromolecules* **29**, 7261 (1996).

## Surface Property Control by Radically Exchangeable Reactive Polymer Brushes

Tomoya Sato<sup>1</sup>, Yoshifumi Amamoto<sup>1</sup>, Hiroki Yamaguchi<sup>1</sup>, Hideyuki Otsuka<sup>1,2</sup>, and Atsushi Takahara<sup>1,2</sup>  
<sup>1</sup>Graduate School of Engineering, <sup>2</sup>Institute for Materials Chemistry and Engineering,  
 Kyushu University, 744 Motooka, Nishi-ku, Fukuoka, Japan

High density polymer brushes have been studied intensively to improve the surface properties of solids. The advantage of polymer brushes, particularly surface-initiated approach, over other surface modification methods is their mechanical and chemical robustness, coupled with a high degree of synthetic flexibility towards the introduction of various functional groups. On the other hand, we have reported many types of polymer reactions based on alkoxyamine units [1]. Because of the reactivity of alkoxyamines under heating condition, polymers containing these units can reorganize after structural determination. In this study, we prepared the polymer brushes with alkoxyamine side chains and demonstrated reversible grafting reaction via a radical crossover reaction (**Scheme 1**) [2].



**Scheme 1.** Grafting and de-grafting reaction between PMMA-co-PALMA brush 1 and functional polymers.

Polymer brushes containing alkoxyamine units were prepared by surface-initiated atom transfer radical polymerization, and their surfaces were confirmed by X-ray photoelectron spectroscopy (XPS) and static contact angle measurement. XPS spectra of the polymer brushes showed these brushes contain nitrogen atom derived from alkoxyamine units. In addition, to investigate the reactivity of these brushes, we treated alkoxyamine-containing brush with alkoxyamine-terminated functional polymers. For example, when these brushes (**1**) were treated with poly(2,3,4,5,6-pentafluorostyrene) **2** under heating conditions, they show more hydrophobicity. On the other hand, when **1** was treated with poly(4-vinylpyridine) **3**, the brush surface shows more hydrophilicity after the quaternization reaction. Reversible grafting and de-grafting reaction with functional polymers were also confirmed by XPS as shown in **Figure 1**, **Figure 2** and static contact angle measurements. These results indicated that the polymer brushes including alkoxyamine units can react after structural formation determination and are effective for reversible surface property control.

### References

- [1] T. Maeda, H. Otsuka, and A. Takahara, *Prog. Polym. Sci.*, **34**, 581 (2009).  
 [2] T. Sato, Y. Amamoto, H. Yamaguchi, H. Otsuka, and A. Takahara, *Chem. Lett.*, **39**, 1209 (2010).

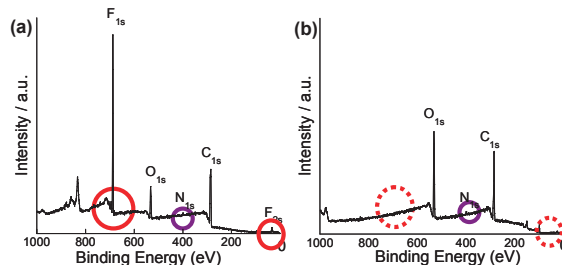


**Figure 1.** Wide-scan XPS spectra of each polymer brushes (a) after grafting **2** (b) after de-grafting.

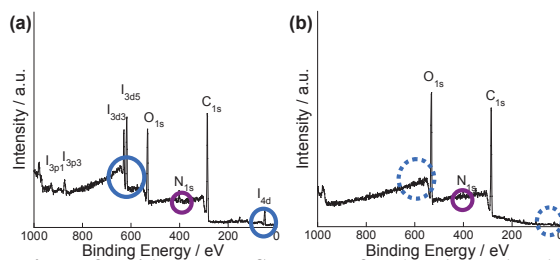


**Figure 2.** Wide-scan XPS spectra of each polymer brushes (a) after grafting **3** and subsequent quaternization (b) after de-grafting.

## Polymeric Ionic Liquid-immobilized Silica for High Molecular Shape-Selective HPLC

Kaori Shingo<sup>1</sup>, Hongdeng Qiu<sup>1</sup>, Makoto Takafuji<sup>1,2</sup>, Hiroataka Ihara<sup>1,2</sup>

<sup>1</sup> Department of Applied Chemistry and Biochemistry, Kumamoto University, Japan

<sup>2</sup> Kumamoto Institute for Photo-Electro Organics (Phoenixes), Kumamoto, Japan

Ionic liquids (ILs) have attracted considerable attention from both the academic and industrial viewpoints because of their unusual chemical and physical properties such as low vapor pressure, low melting point, and high thermal stability [1]. Their physical and chemical properties can be tailored via the modification of counter ions [2]. ILs have played various roles in facilitating chromatographic separation either as mobile-phase additives or as stationary phases [3]. Here a new method to tune the selectivity by simple modifications of the counter anions in the polymerized IL (PIL) phase is introduced. Ultra-high selectivity toward geometrical isomers of polycyclic aromatic hydrocarbons (PAHs) can be realized by using methyl orange (MO) as counter anions in the PIL-immobilized silica phase [4].

In this paper, we introduce two new PIL-grafted silica stationary phases with different counter anions (Sil-PImC<sub>18</sub>-Br and Sil-PImC<sub>18</sub>-MO) prepared according to the following procedure: (1) 1-vinyl-3-octadecylimidazolium bromide was prepared through the reaction of the mixture of 1-vinylimidazole and 1-bromooctadecane. (2) This monomer was polymerized on mercaptopropylated silica (Sil-MPS) through surface radical chain-transfer polymerization. (3) The counter ions in PIL-grafted silica (Sil-PImC<sub>18</sub>-Br) was exchanged from Br to methyl orange (MO) to form Sil-PImC<sub>18</sub>-MO as shown in Fig. 1.

Polymerization was confirmed by elemental analysis and DRIFT spectroscopy. Elemental analysis showed that the amounts of mercaptopropyl and IL moieties attached on the silica surface were calculated as 3.50  $\mu\text{mol m}^{-2}$  and 3.74  $\mu\text{mol m}^{-2}$  for Sil-MPS and Sil-PImC<sub>18</sub>-Br, respectively (Table 1). The carbon percent increased from 9.87% to 13.52% by exchanging of the counter ion from Br to MO for Sil-PImC<sub>18</sub>-Br. The DRIFT spectra showed that the absorption bands around 1562 and 1467  $\text{cm}^{-1}$  were related to an imidazolium group. Additional characteristic

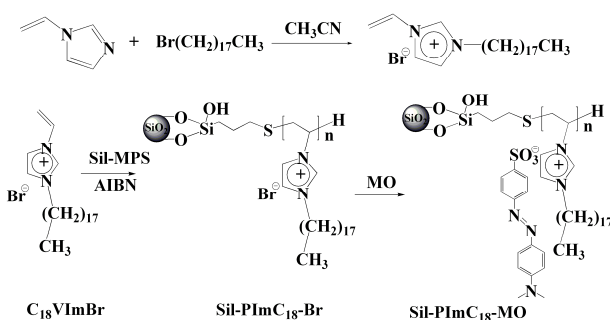


Fig. 1. Synthesis of poly(ionic liquid)-immobilized silica materials *via* polymerization and ionic

Table 1. Elemental analysis

Sample	%C	%H	%N	Coverage ( $\mu\text{mol m}^{-2}$ )
Sil-MPS	1.22	1.00	-	3.50
Sil-PImC <sub>18</sub> -Br	9.87	1.93	0.88	3.74
Sil-PImC <sub>18</sub> -MO	13.52	1.98	2.04	3.57

signals of MO are evident at 1604, 1518, and 1362  $\text{cm}^{-1}$  in Sil-PImC<sub>18</sub>-MO.

Shape-selectivity performance of Sil-PImC<sub>18</sub>-Br and Sil-PImC<sub>18</sub>-MO were assessed by SRM 869b as a column selectivity test mixture for liquid chromatography. This mixture consists of three PAHs with planar and non-planar shapes. In general, the late elution of benzo[*a*]pyrene (BaP) relative to tetrabenzonaphthalene (TBN) indicates enhanced column selectivity towards geometrical isomers. The selectivity coefficient of TBN/BaP can be used as a measure of this property. The chromatogram of the SRM 869b indicated that Sil-PImC<sub>18</sub>-MO ( $\alpha_{\text{TBN/BaP}} = 0.26$ ) could exhibit enhanced polymer-like retention behaviour with ultra-high shape selectivity compared with Sil-PImC<sub>18</sub>-Br ( $\alpha_{\text{TBN/BaP}} = 0.97$ ).

The impact of this phase can be demonstrated by the separation of SRM 1647e (16 priority pollutant PAHs) and several steroids isomers. Furthermore, we know that the 17 $\alpha$ -estradiol and 17 $\beta$ -estradiol pair is one of the most difficult target molecules for chromatographic separation. However, Sil-PImC<sub>18</sub>-MO showed that this pair was readily separated within five minutes even with methanol as the eluent.

In conclusion, we have demonstrated that the polymeric ionic liquid-immobilized silica as a stationary phase for HPLC can be further functionalized by exchanging the counter anions and the selectivity can be tailored by proper selection of the counter anions.

[1] H. Qiu, M. Takafuji, T. Sawada, X. Liu, S. Jiang, H. Ihara, *Chem. Comm.*, **46**, 8740 (2010).

[2] H. Qiu, T. Sawada, S. Jiang, H. Ihara, *Mater. Lett.*, **64**, 1653 (2010).

[3] H. Qiu, M. Takafuji, X. Liu, S. Jiang, H. Ihara, *J. Chromatogr. A*, **1217**, 5190 (2010).

[4] H. Qiu, A. K. Mallik, M. Takafuji, H. Ihara, *Chem. Eur. J.*, **17**, 7288 (2011).

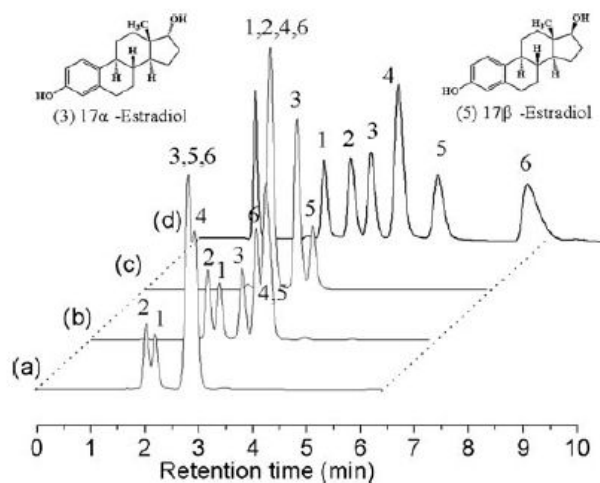


Fig. 2. Separation of six steroids, prednisolone (1), estriol (2), 17 $\alpha$ -estradiol (3), testosterone (4), 17 $\beta$ -estradiol (5), and estrone (6), with a) C<sub>18</sub>, b) C<sub>30</sub>, c) Sil-PImC<sub>18</sub>-Br, and d) Sil-PImC<sub>18</sub>-MO columns with methanol/water (9:1, v/v) as the eluent.

## Non-destructive Characterization of 'Buried' Nano-structure in Polymer Thin Film by Small Angle X-ray Scattering

Takamichi Shinohara<sup>1</sup>, Tomoko Shirahase<sup>2</sup>, Daiki Murakami<sup>2,3</sup>, Taiki Hoshino<sup>2,3</sup>,  
Moriya Kikuchi<sup>2,3</sup>, Hiroyasu Masunaga<sup>4</sup>, Hiroki Ogawa<sup>4</sup>, Jun-ichiro Koike<sup>5</sup>,  
Misao Horigome<sup>5</sup>, Atsushi Takahara<sup>1,2,3,4</sup>

<sup>1</sup> Graduate School of Engineering, Kyushu University, Japan,

<sup>2</sup> Institute for Materials Chemistry and Engineering, Kyushu University, Japan

<sup>3</sup> JST, ERATO, Japan

<sup>4</sup> Japan Synchrotron Radiation Research Institute, Japan

<sup>5</sup> DIC Corporation, Japan

### Introduction

Nano-imprint lithography [1, 2] (NIL) is a simple, low cost and high-resolution patterning method (Fig. 1.). Much attention has been focused on NIL in the various fields, for example, biomedical devices, electro-optical devices and so on. Nano-imprinted structures were used as not only surface, but also inside of device, so called 'buried' structure. The 'buried' structures affect the device properties, such as the increase of light emitting intensity of LED [3]. However non-destructive and precise characterization method of nano-imprinted surface and 'buried' structure is not established. Synchrotron radiation small angle X-ray scattering (SR-SAXS) is non-destructive characterization method. This technique could provide us structural information not only surface, but also 'buried' structure of the sample. In this study, we attempt to characterize surface and 'buried' nano-structure by microscopic and scattering techniques.

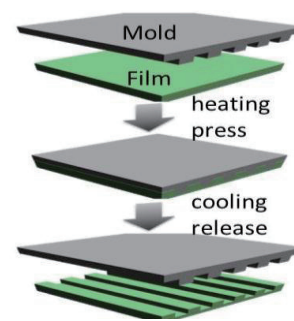


Fig. 1. Schematic diagram of NIL.

### Experimental

Poly (lactic acid) (PLA) was used for molding material. In order to prepare a PLA film, PLA ( $T_g = 331$  K, amorphous) pellets were compression molded at 453 K under normal pressure of 10 MPa for 2 min. The thickness of PLA film was approximately 200  $\mu\text{m}$ . The silicone molds with line/space (LS) pattern was used for NIL. NIL was carried out at 353 K and 20 MPa for 3 min. To prepare 'buried' structure, nano-imprinted PLA film (NIL\_PLA) was covered with spin coated polystyrene film by floating technique (PS/NIL\_PLA). The thickness of spin casted PS film was approximately 600 nm. The prepared nano-structures of polymer films were characterized by scanning electron microscopy (SEM) and SR-SAXS. For SEM observation, polymer films were coated with osmium using a sputter coater. SR-SAXS was carried out at BL03XU [4] beam line of SPring-8 using an incident X-ray with wavelength of 0.1 nm. Scattered X-rays were detected using an imaging palate with a 4289 mm sample-to-detector distance.

### Results and discussions

Fig. 2. shows the SEM images of the NIL\_PLA and PS/NIL\_PLA. The surface nano-structure was

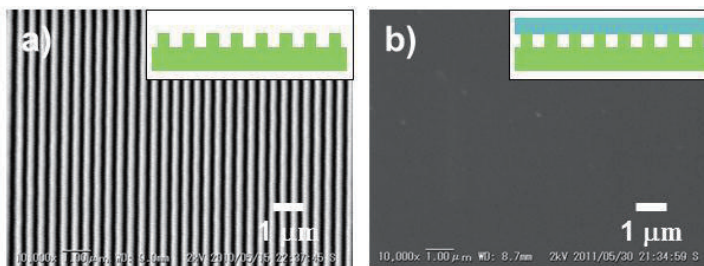


Fig. 2. SEM images of prepared films, a) NIL\_PLA, b)PS/NIL\_PLA.

successfully fabricated on NIL\_PLA (Fig. 2-a.). In contrast, nano-structure was not observed on the surface of PS/NIL\_PLA (Fig. 2-b.). It was confirmed that ‘buried’ structure was fabricated under polymer films.

Fig. 3. shows the two dimensional diffraction patterns of the NIL\_PLA and PS/NIL\_PLA. The anisotropic diffraction spots were clearly observed up to the 20th order peaks, indicating that the nano-structure has the high regularity [5]. These spots were not observed from flat PLA films, so these spots can be attributed by nano-structure. The line and space width of the ‘buried’ structure were estimated by diffraction intensity, assuming the scattering body was rectangular LS model (Fig. 4.). The line intensity profiles of  $q_x$  direction was fitted by eq. 1.:

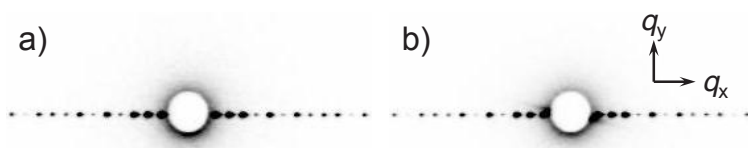


Fig. 3. Two dimensional diffraction pattern, a) NIL\_PLA, b) PS/NIL\_PLA.

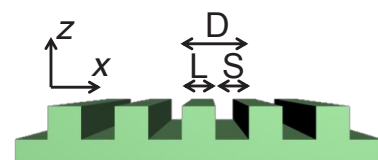


Fig. 4. Rectangular LS model of cross sectional scattering body.

$$I(q_x) = A \frac{\sin^2(q_x \frac{L}{2}) \sin^2(q_x \frac{ND}{2})}{q_x^2 \sin^2(q_x \frac{D}{2})} \quad (1)$$

where A is the scaring factor, L is the line width, D is the pitch and N is the number of lattices.

Fig. 5. shows the  $q_x$ -dependence of diffraction intensity plot and corresponding fitting curves calculated by eq. 1. The diffraction intensity was successfully described by rectangular LS model. The estimated structure size of the NIL\_PLA was  $L = 175$  nm and  $S = 240$  nm. Also, these of PS/NIL\_PLA was  $L = 176$  nm and  $S = 239$  nm. On the other hand, the mold size estimated by SR-SAXS was  $L = 242$  nm,  $S = 174$  nm. These results show the good agreement between mold and ‘buried’ structure size.

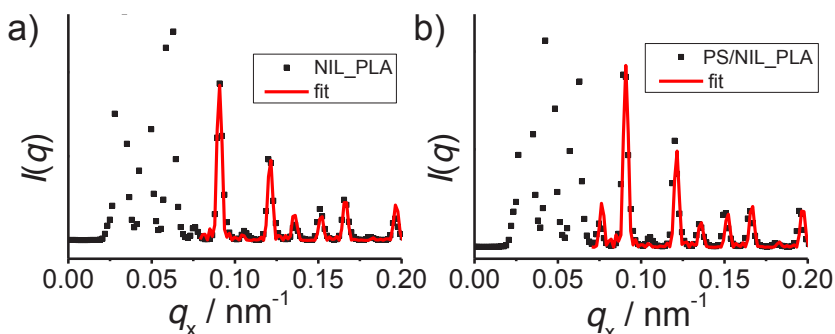


Fig. 5. Line intensity profiles and fitting results of surface and ‘buried’ structure on PLA films. a) NIL\_PLA, b) PS/NIL\_PLA.

These results show the good agreement between mold and ‘buried’ structure size.

These indicate that SR-SAXS could precisely and non-destructively characterize not only the surface, but also ‘buried’ structure.

## References

- [1] M. Kondo, H. Yasuda, K. Kubodera, *JP Patent*, 1979-22389.
- [2] S. Y. Chou, P. R. Krauss, and P. J. Renstrom, *Appl. Phys. Lett.*, **67**, 3114 (1995).
- [3] Y. Li, S. You, M. Zhu, L. Zhao, W.Hou, T.Detchprohm, Y.Taniguchi, N. Tamura, S. Tanaka, and C.Wetzel, *Appl. Phys. Lett.*, **98**,151102 (2011).
- [4] K. Sakurai, *et al.*, *Polymer Journal*, **43**, 471 (2011).
- [5] T. Shinohara, T. Shirahase, D. Murakami, T. Hoshino, M. Kikuchi, J. Koike, M. Horigome, H. Masunaga, H. Ogawa, A. Takahara, *IOP Conference Series: Materials Science and Engineering*, in press.

## Characterization of Nanoimprinted Polyimide Thin Films

Sudu Siqing<sup>1</sup>, Hui Wu<sup>2</sup>, Atsushi Takahara<sup>1,2\*</sup>

<sup>1</sup>Graduate School of Engineering, Kyushu University, Japan

<sup>2</sup>Institute for Materials Chemistry and Engineering, Kyushu University, Japan

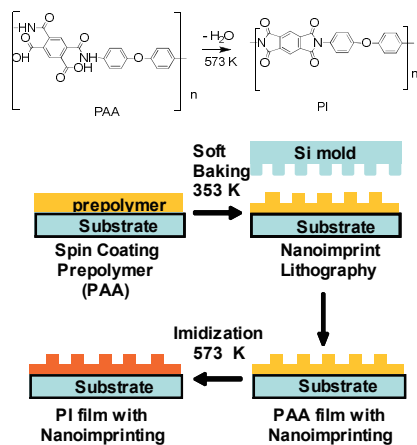


Figure 1. Scheme of nanoimprint lithography on PAA and imidization.

**Introduction.** Nowadays, chemical and physical issues occurring during imidization have been investigated intensively.<sup>[1]</sup> Here, we report that the molecular reorientation of nanoimprinted poly(amic acid) (PAA) and polyimide (PI) could affect the imidization degree.

**Experimental Section.** Pyromellitic dianhydride (PMDA), oxydianiline (ODA) and N-methyl-2-pyrrolidone (NMP) were used to prepare poly(amic acid) (PAA). PAA NMP solution was spin coated on Si wafer. Soft baking was carried out on a hot plate at 353 K for 3 min. Nanoimprint lithography (NIL) on PAA film with Si substrate was

carried out by a commercial nanoimprinter. The imidization of PAA film was performed at 573 K. The Scheme of NIL is shown in Fig. 1. The imidization degree of PI is defined as the ratio of the number of imidized groups to the number of all imidizable groups:

$$\text{Imidization degree} = \frac{\text{Number of imidized groups}}{\text{Total number of imidizable groups}} = \frac{n_i}{n_a} \quad (1)$$

where  $n_i$  is the number of imide groups and  $n_a$  is the number of amide groups.

**Results and Discussion.** AFM image and photo of nanoimprinted PI film are shown in Fig. 2. Two areas, the area with pattern and without pattern, for nanoimprinted PAA and PI film were examined. The area with pattern is ca.  $0.45 \times 0.45 \text{ cm}^2$ . To compare imidization degree at two areas, FTIR measurement was carried out at the area with pattern and that without pattern for nanoimprinted PAA film and nanoimprinted PI film, respectively. In order to compare PAA film before and after NIL, FTIR spectrum of PAA film before nanoimprinting (after soft baking) is shown in the curve (c) of Fig. 3. The curve (b) in Fig. 3 shows the FTIR spectrum of PAA film which was obtained after soft baking and NIL at the area without pattern. FTIR spectrum of PAA film at the area with pattern is shown in curve (c) of Fig. 3. This sample was measured again after imidization at the area without pattern and the area with pattern, then curve (d) and (e) of Fig. 3 was obtained

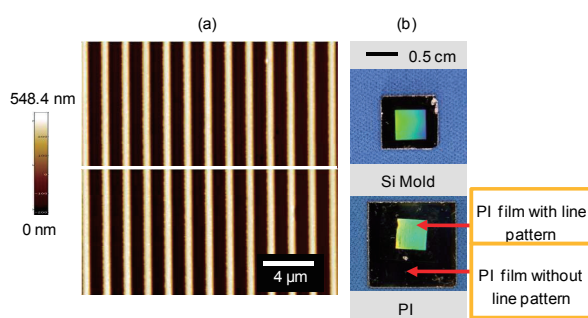


Figure 2. (a) AFM image and (b) photo images of Si mold and nanoimprinted PI film.



respectively.

In curve (a) of Fig. 3, the broad absorption bands at ca. 1650 and 1550  $\text{cm}^{-1}$  correspond to the absorption of C=O (CONH) and C-NH, which means that very little PAA was imidized in PAA film before nanoimprinting. The absorption peaks at 1778  $\text{cm}^{-1}$  and 1728  $\text{cm}^{-1}$  are assigned to the C=O asymmetrical stretching and symmetrical stretching. The peak at 1381  $\text{cm}^{-1}$  is the C-N stretching of the aromatic imide ring. The absorption peak at 1247  $\text{cm}^{-1}$  is associated with the C-O-C asymmetric stretching. The peak at 1500  $\text{cm}^{-1}$ , corresponding to the C=C stretching of *p*-substituted benzene, was used as an internal standard. Therefore, the degree of imidization could be indirectly characterized by the ratio of the absorbance at 1778, 1728 or 1381  $\text{cm}^{-1}$  to that at 1500  $\text{cm}^{-1}$ . Table 1 summarized the absorbance ratio which is extracted from the IR spectra. Compared the PAA film with line pattern to that of PAA film without line pattern, the ratio of the absorbance at 1778, 1728 and 1381  $\text{cm}^{-1}$  to that at 1500  $\text{cm}^{-1}$  was increased in the PAA film with line pattern, although the PAA film with line pattern

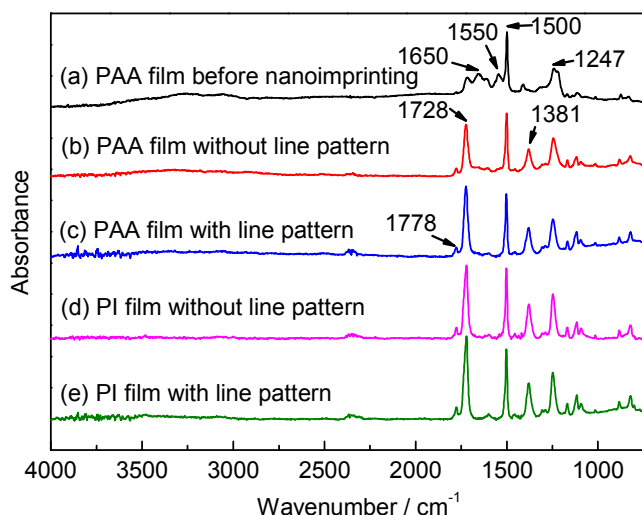


Figure 3. FT-IR spectra of (a) PAA film before nanoimprinting (after soft baking), (b) PAA film without line pattern (after soft baking and NIL ), (c) PAA film with line pattern (after soft baking and NIL ), (d) PI film without line pattern (after soft baking, NIL and imidization ), (e) PI film with line pattern (after soft baking, NIL and imidization ).

was experienced the same heating process and pressure as the PAA film without line pattern. The same result can be observed in PI film with line pattern and PI film without line pattern. According to previous result, C=O stretching has orientation in nanoimprinted films, so it could not be used to determine the imidization degree. However, the C-N stretching is no orientation in PI molecule. The molecular orientation does not affect the intensity of the absorbance of C-N. So, we can confirm the imidization degree in the films with line pattern is higher than that in the films without line pattern.

Table 1. The ratio of the absorbance at 1778, 1728 and 1381  $\text{cm}^{-1}$  to that at 1500  $\text{cm}^{-1}$ .

	C=O (1778)/C=C	C=O (1728)/C=C	C-N/C=C
PAA film before NIL (after soft baking)	0.034	0.275	0.078
PAA film without line pattern (after soft baking and NIL )	0.120	0.824	0.426
PAA film with line pattern (after soft baking and NIL )	0.149	1.130	0.460
PI film without line pattern (after soft baking, NIL and imidization )	0.164	1.160	0.533
PI film with line pattern (after soft baking, NIL and imidization )	0.189	1.326	0.573

## Reference

[1] T. Nishino, M. Kotera, N. Inayoshi, N. Miki, K. Nakamae, *Polymer*, **41**, 6913 (2000).

## Mechanical Properties of Deoxyribonucleic Acid Films

Jie Zhan, Hisao Matsuno, Keiji Tanaka

Department of Applied Chemistry, Kyushu University, Japan

**Introduction:** In the last 15 years, much attention has been focused on deoxyribonucleic acid (DNA) as a generic material instead of just a genetic material. DNA is a biodegradable and non-oil-based product, thus, if the usage of DNA on a large scale is realized, the consumption of polymers originating from oil would be reduced. In fact, we can obtain a huge amount of DNA from nature as an industrial waste in Japan every year. Hence, DNA is a sustainable alternative to conventional synthetic polymers. So far, many groups have reported solid-state DNA films prepared by conjugation with other chemical compounds such as cationic lipids and polymers.[1-3] These films are applied to, for instance, conductive materials, absorbents for removal of a toxic intercalater, and so on. On the other hand, understanding basic physical properties such as thermal molecular motion and mechanical properties of these films are required for further applications, but unfortunately, almost of them have not been revealed yet, because other chemicals which made analyses difficult existed in the films. To overcome this problem, we prepared a DNA solid film without any other organic compounds and revealed its dynamic mechanical property over a wide temperature range.[4] In this study, we investigate mechanical properties of the DNA film.

**Experiments:** Commercially available DNA sodium salt (NaDNA) derived from salmon sperm with molecular weight ranging from 300k to 9M was used. A NaDNA aqueous solution with a concentration of 1 wt% was cast on a dish made of polystyrene. After water evaporation by heating it at 313 K and successive vacuum drying at room temperature, a self-standing and transparent film with a thickness of approximately 100  $\mu\text{m}$  was obtained. Hereafter, a NaDNA film is referred as a DNA film. A water content of the DNA film was regulated by leaving it in water environment for a given time, and its value was determined by thermogravimetry (TG) using SSC5200 (SII Nano Technology, Inc.). TG measurements were carried out at temperatures ranging from 298 K to 473 K with a heating rate of 10 K/min. Mechanical properties of the DNA films were recorded on a standard tensile testing machine TENSILON RTC1250 (A&D Co., Ltd). The tensile tests were carried out at room temperature with a crosshead speed of 5 mm/min.

**Results and discussion:** Fig. 1 shows typical stress-strain curves (S-S curves) of the DNA films at different water contents. In the case of the film at a water content of 16.6 wt%, the film behaved as a brittle material. The initial slope was sharp corresponding to a high modulus and the stress at break was low. When the water content increased to 24.5 wt%, surprisingly, the film showed necking behavior and the strain at break reached to approximately 1.8. As the water content reached 45.7 wt%, the strain at break further increased, but necking behavior was not observed. Detail analyses revealed that the necking

process was observed only at the particular water contents between approximately 22 and 33 wt%. Fig. 2 shows the water content dependencies of Young's modulus and yield stress for the DNA films. Young's modulus decreased with increasing water contents, implying that water played a role of a plasticizer in the DNA film. At a relatively lower water content region, the S-S curve for the DNA film was featureless, similar to typical non-crystalline polymer materials and the Young's modulus value was over 1 GPa. That is, the DNA film mechanically behaves as a glassy polymer.

When the water content went beyond 22 wt%, the DNA film exhibited mechanical properties similar to crystalline polymers. Furthermore, elastomeric behaviors could be also observed at a relatively higher water content region. These results show that DNA films could be used as solid materials that mechanical properties were controllable by regulating water content. Given that a small amount of water molecules are existed in the films, the interaction between DNA molecules would be strong. Interestingly, this interaction would be weakened with increasing water content. This makes it possible that the orientation of molecular chains of DNA would be released in the film. Polarized microscopic observation and X-ray analysis revealed the relationship between aggregation states and mechanical properties for DNA molecules in the film. This will be also discussed in the presentation.

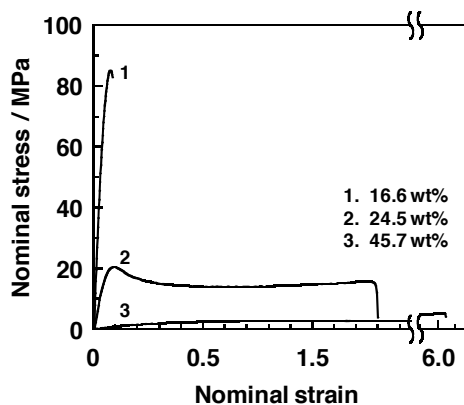


Fig. 1. Typical stress-strain curves for the DNA films with different water contents.

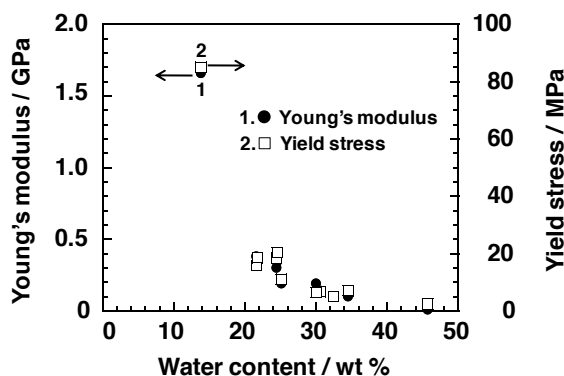


Fig. 2. Water content dependencies of Young's modulus and yield stress for the DNA films, respectively.

## References

- [1] Y. Okahata, T. Kobayashi, K. Tanaka, *Langmuir*, **12**, 1326 (1996).
- [2] L. Wang, J. Yoshida, N. Ogata, S. Sakai, T. Kajiyama, *Chem. Mater.*, **13**, 1273 (2001).
- [3] T. Nagamura, M. Yamamoto, M. Terasawa, K. Shiratori, *Appl. Phys. Lett.*, **83**, 803 (2003).
- [4] H. Matsuno, J. Nakahara, K. Tanaka, *Biomacromolecules*, **12**, 173 (2011).

## Molecular Dynamics Characterization of PS brush films by Lateral Force Microscopy

Hiroshi Arita<sup>1</sup>, Koji Mitamura<sup>2</sup>, Moriya Kikuchi<sup>2</sup>, Motoyasu Kobayashi<sup>2</sup>,  
Atsushi Takahara<sup>1,2,3\*</sup>

<sup>1</sup> Department of Engineering, Kyushu University, Fukuoka, Japan

<sup>2</sup> Japan Science and Technology Agency, ERATO, Takahara Soft Interfaces Project,  
Fukuoka, Japan

<sup>3</sup> Institute for Materials Science and Engineering, Kyushu University, Fukuoka, Japan

Polymer brushes are systems in which chains of polymer molecule are attached through an anchor group to a surface, or to an interface, in such a way that the graft density of the polymers is high enough that the attached chains are stretched away from the surface in a brush-like conformation. Therefore, the activity of a molecular motion of brush should be different from that of polymers in the conventional spin cast films.<sup>1,2)</sup> In this study, the thermal molecular motion of polystyrene (PS) brush and spin cast film around at the surface glass transition temperatures ( $T_g$ ) were investigated by ellipsometry and lateral force microscopy (LFM).

PS brush was prepared by by surface initiated nitroxide-mediated polymerization. The graft density was estimated to be 0.90 chains/nm<sup>2</sup> by the number average molecular weight ( $M_n$ ) and thickness determined by X-ray reflectivity.

Figure 1 shows temperature dependency of optical coefficient  $\Delta$  on ellipsometry of PS brush and PS spin cast film with similar thickness. Both thin films revealed inflection point of  $\Delta$  at the same temperature corresponding to the transition of glassy and rubbery states. No remarkable difference was observed in  $T_g$  of PS brush and spin cast film.

On the other hand, difference in the surface  $T_g$  was observed by LFM of PS brush and spin cast film, as shown in Figure 2. The surface  $T_g$  of spin cast film was observed at 363 K, while that of the brush was observed at 374 K. Thermal molecular motion of PS chains at the outer most surface might be different between the spin cast film and brush state due to the anchoring effect.

In addition, effect of the molecular weight distribution (MWD) should be also considered. In this study, PS with broad MWD was used for ellipsometry and one with narrow MWD was used for LFM. The molecular motion of PS brush chains with uniform chain length might be more regulated than that with broad MWD.

### References

- [1] S. Yamamoto, Y. Tsujii, T. Fukuda, *Macromolecules*, **35**, 6077 (2002).  
[2] K. Tanaka, K. Kojio, R. Kimura, A. Takahara, T. Kajiyama, *Polym. J.*, **35**, 44 (2003).

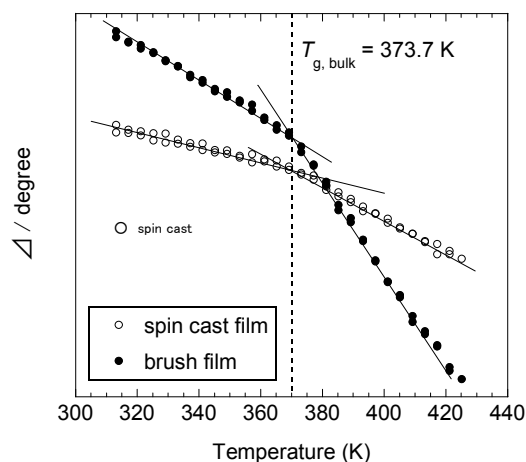


**Figure 1.** Temperature dependency of optical coefficient  $\Delta$  for PS brush ( $M_n = 95k$ ,  $M_w/M_n = 2.01$ , thickness = 144.2 nm) and PS spin cast films (thickness = 142.5 nm).

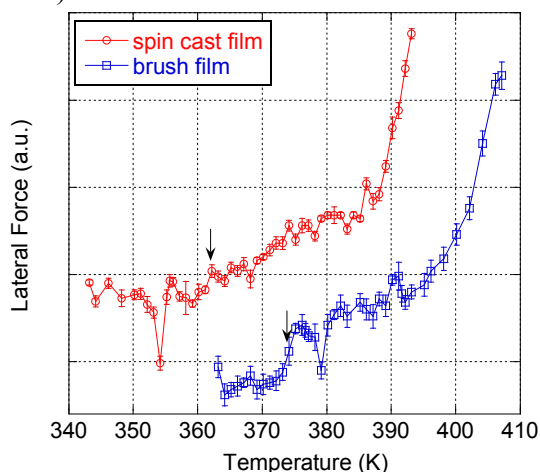


**Figure 2.** Lateral force-temperature curves for PS brush film ( $M_n = 123K$ ,  $M_w/M_n = 1.25$ , thickness = 131 nm) and spin-cast film (thickness = 130.0 nm) at the scanning rate of  $10^3 \text{ nm s}^{-1}$ .

## Structural Stability Control of Liquid Marbles

Daisuke Matsukuma, Hirohmi Watanabe, and Atsushi Takahara\*

JST, ERATO Takahara Soft Interfaces Project,

Kyushu University, 744, Motoooka, Nishi-ku, Fukuoka, 819-0395, JAPAN

E-mail: takahara@cstf.kyushu-u.ac.jp

Liquid marble is a liquid droplet which is stabilized by the adsorption of hydrophobic particles at the liquid-gas interface.[1] Liquid marble behaves like a soft solid, and it works well as a non-wetting system due to their low adhesion to substrates. These unique characteristics offer a variety of applications such as low energy transportation systems, microreactors, and microreservoirs.

For the use of liquid marble as a microreactor, the mixing of individual droplets is an essential process to trigger the chemical reaction. However, a well-stabilized liquid marble cannot perform the mixing due to the prevention of hydrophobic particles at the interface. On the other hand, a less-stabilized liquid marble cannot keep their shape. It is clear that the control of structural stability of liquid marble is indispensable to cause the mixing effectively.

Recently, we have reported that the stability of liquid marble is influenced by the surface energies of components.[2] The spreading coefficient ( $S_{SL}$ ), which represents the factor to determine the spontaneous spreading and dewetting for polymer particles on a liquid droplet, have a strong effect on the formation of stable liquid marble. In this presentation, the difference of the structural stability of liquid marbles on the mixing behavior was evaluated by using liquid marbles with different  $S_{SL}$  value.

Liquid marbles were fabricated by the combination of 1  $\mu\text{m}$  poly(tetrafluoroethylene) (PTFE) particles with various ionic liquids. The calculated  $S_{SL}$  values of the combination and the digital camera views of the obtained liquid marbles were shown in Table 1 and Fig. 1, respectively. There is a good correlation between the apparent stability of liquid

**Table 1** Surface energies of materials and its calculated  $S_{SL}$  value by the combination.

		Surface energy/ $\text{mNm}^{-1}$			$S_{SL}$
		$\gamma^d$	$\gamma^p$	$\gamma$	
Solid	PTFE	18.4	1.6	20.0	-
	[emim][Tf <sub>2</sub> N]	21.9	12.2	34.1	9.0
Liquids	[bmim][Tf <sub>2</sub> N]	21.8	10.4	32.2	8.2
	[hmim][Tf <sub>2</sub> N]	21.7	8.2	29.9	7.2

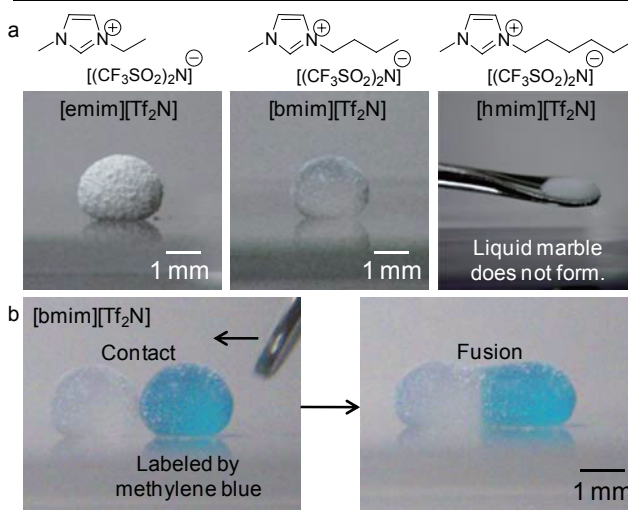


**Fig. 1** a) The digital camera view of liquid marbles with various ionic liquids. b) Fusion of liquid marbles.

marbles and the  $S_{S/L}$  values. Actually, a liquid marble with relatively high  $S_{S/L}$  showed high structural stability. On the other hand, the combination with low  $S_{S/L}$  does not form liquid marbles (Fig. 1a).

It was interesting that coalescence of liquid marbles was observed with the combination of PTFE and [bmim][Tf<sub>2</sub>N] which shows adequate  $S_{S/L}$  value. After the contact of two marbles, liquid marbles were fused each other with maintaining the shape as shown in Fig. 1b. Functional liquid marble which has different structural stability is now designed by the change of surface properties of materials.

[1] P. Aussillous *et al.*, *Nature* **2001**, *411*, 924.

[2] D. Matsukuma *et al.*, *Langmuir* **2011**, *27*, 1269.

## Gelation of Polystyrene Copolymer Containing Catechol Groups in the Presence of Iron (III) Ions

Hang Xu,<sup>1</sup> Motoyasu Kobayashi,<sup>2</sup> Jin Nishida,<sup>2</sup> Hideyuki Otsuka,<sup>1,3</sup> Atsushi Takahara<sup>1,2,3\*</sup>

<sup>1</sup>Graduate School of Engineering, Kyushu University, Japan

<sup>2</sup>JST, ERATO Takahara Soft Interfaces Project, Japan

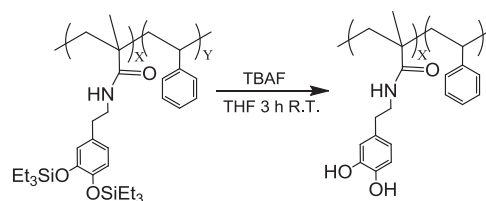
<sup>3</sup>Institute for Materials Chemistry and Engineering, Kyushu University, Japan

### Introduction

Mussel adhesive protein works as an excellent adhesive in nature [1] using the versatile reactivity of catechol groups for oxidative polymerization and strong interaction with metal ions [2] to give an insoluble gel. In this study, effect of the iron ion on the gelation process of catechol functionalized polymer was investigated by using a solution of polystyrene-base copolymer bearing the catechol units in the presence and absence of iron (III) ions.

### Experimental

A copolymer bearing catechol unit was prepared by conventional free radical polymerization of styrene and *N*-2-(3',4'-ditriethylsilyloxyphenyl)ethyl methacrylamide, and successive deprotection reaction catalyzed by tetra-*n*-butylammonium fluoride in THF, as shown in Scheme 1. The molar ratio of methacrylamide and styrene in the copolymer was estimated to be 1/50 by NMR.



Scheme.1 Deprotection and chemical structure of the catechol-containing copolymer

### Results and Discussion

It is well-known that catechol derivatives in the basic solution are slowly polymerized by oxidants, such as oxygen in the air. Actually, the 10wt% toluene solution of copolymer bearing catechol units in the presence of sodium methoxide (2 times molar excess of catechol units) gradually became viscous solution at room temperature to result in a transparent gel with pale yellow color within 8 hours, probably due to the oxidative polymerization of catechol units. In contrast, insoluble black precipitate was quickly formed when the sodium methoxide solution was added to a mixture of 10wt% toluene solution of the copolymer and acetone solution of iron (III) trifluoromethanesulfonate with one third molar of the catechol units. As a control experiment, no reaction took place in the mixture of sodium methoxide and iron (III) ions without copolymer. We supposed that the catechol units of the copolymer partially coordinated with iron (III) ion to promote the oxidative polymerization because of the complex formation of three catechol compounds with iron (III) ions[3]

### REFERENCE

- [1]. H. Lee, S. M. Dellatore, W. M. Miller, P. B. Messersmith, *Science*. **2007**, 318, 426-430.
- [2] Mary J. Sever and Jonathan J. Wilker *Dalton Trans*, **2004**, 1061-1072.
- [3] M. J. Harrington, A. Masic, N. Holten-Andersen, J. H. Waite, and P. Fratzl *Science* **2010**, 328, 216-220.

## **Prolongation of the Active Lifetime of a Biomolecular Motor System for In Vitro Motility Assay**

Arif Md. Rashedul KABIR,<sup>1</sup> Inoue DAISUKE,<sup>2</sup> Akira KAKUGO,<sup>3,4</sup> and Jian Ping GONG<sup>3</sup>

<sup>1</sup>Division of Biological Sciences, Graduate school of Science, Hokkaido University, JAPAN;

<sup>2</sup>Graduate School of Life Science, Hokkaido University, JAPAN; <sup>3</sup>Faculty of Advanced Life Science, Hokkaido University, JAPAN; <sup>4</sup>PRESTO, Japan Science and Technology Agency

(JST)

Over the last few decades, the *in vitro* motility assay has been performed to probe the biophysical and chemo-mechanical properties as well as the self-organization process of biomolecular motor systems like actin-myosin and microtubule-kinesin. However, aggression of the reactive oxygen species (ROS) and concomitant termination of the activity of biomolecular motors during investigation remains a drawback of this assay. Despite enzymatic protection that makes use of a combination of glucose, glucose oxidase and catalase, the active lifetime of biomolecular motors is found to be only a few hours and this short lifetime restricts further study on those systems. We have solved this problem by using a newly developed system of the *in vitro* motility assay that is conducted in an inert nitrogen gas atmosphere free of ROS. Using microtubule-kinesin as a model system we have shown that our system has prolonged the active lifetime of biomolecular motor till several days and even a week by protecting them from oxidative damage.



## Functional hybrid materials based on nanoporous silicas

Makoto Ogawa

*Graduate School of Science and Engineering, and Department of Earth Sciences,  
Waseda University, Nishiwaseda 1-6-1, Shinjuku-ku, Tokyo 169-8050, Japan*

After the successful preparation of mesostructured and mesoporous silica films by the solvent evaporation method,<sup>1,2</sup> the preparation of mesoporous silica films have been extensively investigated partly due to the wide range of applicabilities of mesoporous silica films for low- $k$  material for semiconductor electronics<sup>3</sup>, nano-reactors for photochemical reaction<sup>4</sup>, and membranes<sup>5</sup>.

In addition to the solvent evaporation method, the deposition of mesoporous silica layer from acidic aqueous solution and vapor phase has been reported to prepare mesoporous silica layers on flat substrates toward with high structural regularity or controlled thickness.<sup>6,7</sup>

Here, we report an alternative synthetic way to deposit homogeneous nanoporous silica thin layer on a variety of solids surfaces from flat substrate to micrometer size powders and, as to the materials, from oxide and hydroxides to organic polymers.<sup>8-14</sup> The present reaction is very simple, where substrates (both plate and powder) were put into a homogeneous solution containing tetraethoxysilane, hexadecyltrimethylammonium chloride, methanol, water and ammonia.

The present synthesis is a new and versatile method to prepare nanoporous silica thin layers on solid substrate especially when the reported procedure is not applicable; substrate with complex morphology and/or unstable in acidic solutions such as hydrotalcite and ZnO. Mesoporous silica coating is regarded as a way to modify the surface properties of powders as well as to impart new functions such as molecular sieving one on catalysts and adsorbents.

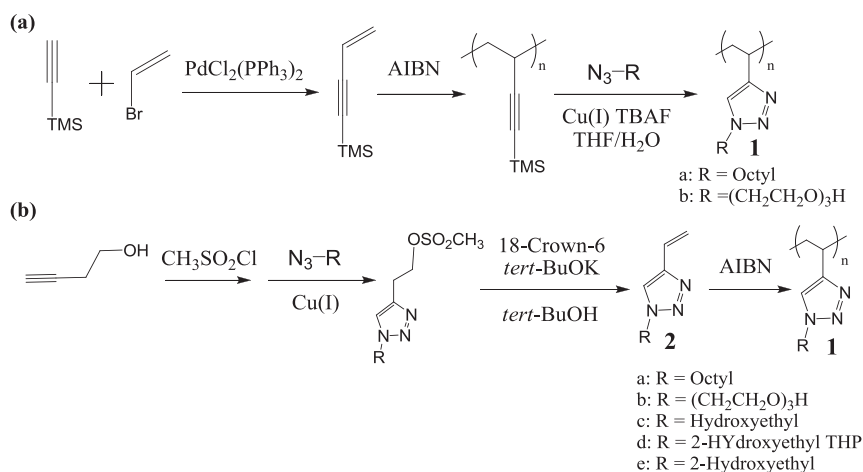
- [1] M. Ogawa, *J. Am. Chem. Soc.*, *116*, 7941(1996).
- [2] M. Ogawa, *Chem. Commun.*, 1149(1996).
- [3] R. J. Pai et al., *Science*, *303*, 507(2004).
- [4] M. Ogawa, *J. Photochem. Photobiol., C Photochem. Rev.* 2002, *3*, 129(2002).
- [5] M. Klotz; A. Ayrál; C. Guizard; L. Cot, *Sep. Purif. Technol.* 2001, *25*, 71(2001).
- [6] H. Miyata; K. Kuroda, *Chem. Mater.* 1999, *11*, 1609(1999).
- [7] N. Nishiyama, S. Tanaka, Y. Egashira; Y. Oku; K. Ueyama, *Chem. Mater.*, *15*, 1006 (2003).
- [8] M. Ogawa; N. Shimura; A. Ayrál, *Chem. Mater.*, *18*, 1715 (2006).
- [9] M. Ogawa; N. Shimura, *J. Colloid Interface Sci.*, *303*, 250 (2006).
- [10] M. Ogawa; N. Shimura, *J. Colloid Interface Sci.*, *317*, 312(2006).
- [11] M. Ogawa; D. Naito, *Chem. Lett.*, *36*, 462 (2007).
- [12] R. Kato; N. Shimura; M. Ogawa, *Chem. Lett.*, *37*, 76 (2008).
- [13] Y. Ide; Y. Koike; M. Ogawa, *J. Colloid Interface Sci.*, *J. Colloid Interface Sci.*, *358*, 245 (2011).
- [14] K. J. Nakamura; Y. Ide; M. Ogawa, *Mater. Lett.*, *65*, 24 (2011).

## Grafting of Poly(1-substituted vinyltriazole), Prepared via Click Reaction, onto Colloidal Silica and Selective Trapping of Transition Metal Ion

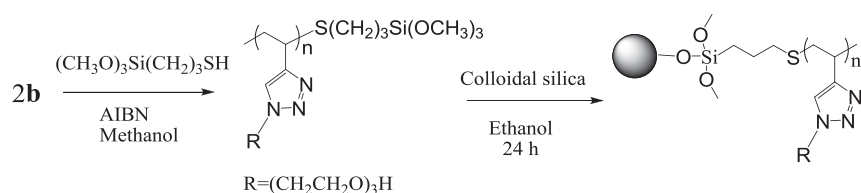
Kohji Yoshinaga<sup>1\*</sup>, Shinya Kawasaki<sup>2</sup>, Emiko Mouri<sup>2</sup>, Suguru Motokuchou<sup>1</sup>, Ken Kojio<sup>1</sup>  
<sup>1</sup> Department of Materials Science, Faculty of Engineering, Nagasaki University, Japan  
<sup>2</sup> Department of Applied Chemistry, Faculty of Engineering, Kyushu Institute of Technology, Japan

Triazole compounds exhibit characteristic properties coming from p-conjugated five-membered ring with lone pair electrons for complex formation with transition metal ion. In this work, synthesis of poly(1-substituted-4-vinyl-1,2,3-triazole) and grafting of hydrophilic poly(vinyltriazole) to colloidal silica for application to selective extraction materials of transition metal ion.

We examined two synthetic routes via (a) 'One Pot' reaction and (b) polymerization of vinyltriazole, as shown in Scheme 1. In Route (a), polymer **1a** was obtained in 58% yield, but 2-(2-(2-hydroxyethoxy)ethoxy)ethyl-substituted polymer **1b** was given in low yield of 4%. Radical polymerization of vinyltriazoles in Route (b) afforded polymer **1a** of molecular weight 24,000 in high yield of 93%, and **2b** and **2c** of molecular weight of 7,000 and 15,000 in relatively high yield, respectively. The reaction of colloidal silica, of 140 nm in diameter, with poly(4-vinyl-1,2,3-triazole)-trimethoxysilane with 2-(2-(2-hydroxyethoxy)ethoxy)ethyl at 1-position gave high disperse polymer-grafted silica in water (Scheme 2). The hybrid particles selectively captured transition metal ion, Ni<sup>2+</sup>, Cu<sup>2+</sup>, Zn<sup>2+</sup>, stability constants of which were in the range from 1.4 x 10<sup>3</sup> to 3.6 x 10<sup>3</sup>, being 10<sup>2</sup> times higher than those of alkali earth metal ion.



**Scheme 1.** Synthesis of poly(1-substituted-4-vinyl-1,2,3-triazole) via (a) 'One Pot' reaction and (b) the polymerization of vinyl monomer.



**Scheme 2.** Grafting of poly(2-(2-(2-(4-vinyl-1,2,3-triazole-1-yl))ethoxy)ethoxyethanol) to colloidal silica.

## Synthesis and Characterization of Silica Based Nanocomposites

Eun Hwa Jung, Ildoo Chung

Department of Polymer Science and Engineering,  
Pusan National University, Busan 609-735, Korea

Novel hybrid organic-inorganic nanocomposites were prepared from colloidal silica (CS) with vinyl trimethoxy silane (VTMS) by sol-gel process. The molar ratios of VTMS to CS were ranged from 1 to 10.

During sol-gel process, hydrogens of hydroxyl groups on silica cluster were replaced by hydrolytically stable  $\equiv\text{Si}-\text{C}_2\text{H}_3$  through  $-\text{O}-\text{SiC}_2\text{H}_3$  bonds on VTMS. After the sol-gel reaction was completed, the aqueous solvent was exchanged to ethoxyethanol (EC). The resultant nano-scaled dispersions were characterized by Fourier Transform Infrared (FT-IR) spectroscopy as shown in Fig. 1.

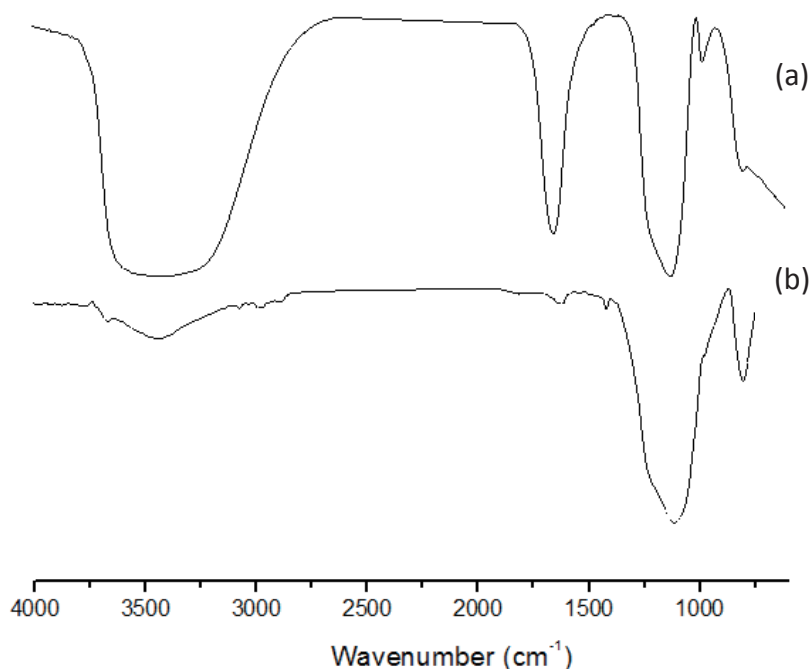


Fig. 1. FT-IR spectra of (a) colloidal silica (CS) and (b) CS modified with VTMS.

- [1] S. S. Latthe, *Porous Mater* **17**, 565–571 (2010).
- [2] Y. G. Lee, J. H. Park, *Langmuir* (2007).

## Functionalization of Periodic Mesoporous Organosilica by Sulphonic Acid Groups for Rare Metal Ions Adsorption

Sang Hyun Lee, Sung Soo Park, M. Santha Moorthy, Chang-Sik Ha\*

Department of Polymer Science and Engineering, Pusan National University, Republic of Korea

Bissilylated urea (BU) bridged periodic mesoporous organosilica (BU-PMO) precursor have been successfully synthesized through co-condensation of 2,6-diaminopyridine and triethoxysilylpropyl isocyanate at 85 °C under N<sub>2</sub> atmosphere for 24 hours. The bissilylated urea precursor has been utilized to prepare BU-PMO with various BU precursor to tetraethylorthosilicate (TEOS) ratios, using triblock copolymer (Pluronic P123) as a structure directing agent in acidic conditions. The surfactant was removed by solvent extraction method using 1% HCl-ethanol at 60 °C. The prepared PMO materials were characterized by powder X-ray diffraction (XRD), transmission electron microscopy (TEM), Fourier-transform infrared spectroscopy (FT-IR), N<sub>2</sub> sorption isotherm, <sup>29</sup>Si and <sup>13</sup>C CP MAS NMR spectroscopic analyses. The morphologies of materials were identified by scanning electron microscopic analysis (SEM). The amine group of the bridged organic functionality was further modified using chlorosulphonic acid in chloroform solvent. Chemically functionalized materials were shown to be suitable for adsorption of metal cations from aqueous solution. The adsorbed metal ion concentration was determined by inductively-coupled plasma-atomic emission spectroscopy (ICP-AES) analysis.

Fig. 1 shows XRD patterns of sulphonic acid modified periodic mesoporous organosilica with different molar ratio. With low ratio (*i.e.*, below 10 %) of the sulphonic acid groups, the XRD patterns of the PMO materials show typical (110) and (200) peaks to be contributed by 2-D hexagonal mesostructure. With the increase of the sulphonic acid groups up to 30 %, the ordering of mesostructure decreased.

Fig.2. shows a SEM image of sulphonic acid modified periodic mesoporous organosilica. The particles have a flat morphology with ca. 700 nm in size.

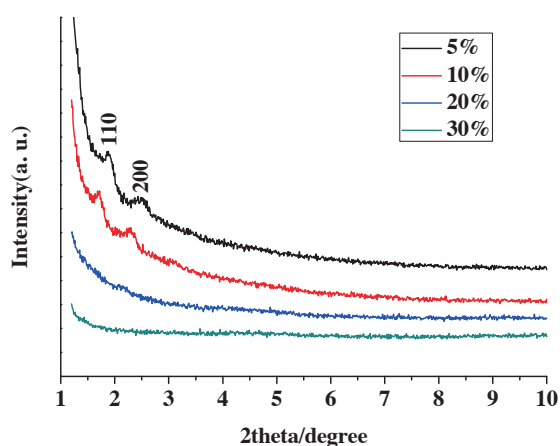


Fig.1. X-ray diffraction of sulphonic acid modified periodic mesoporous organosilica with different content.

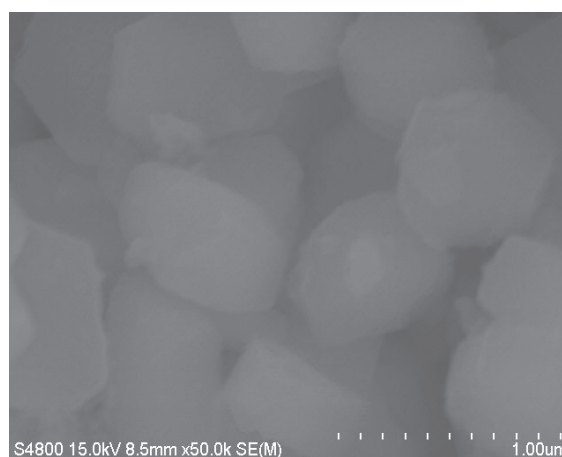


Fig.2. SEM image of sulphonic acid modified periodic mesoporous organosilica with 5 % content.

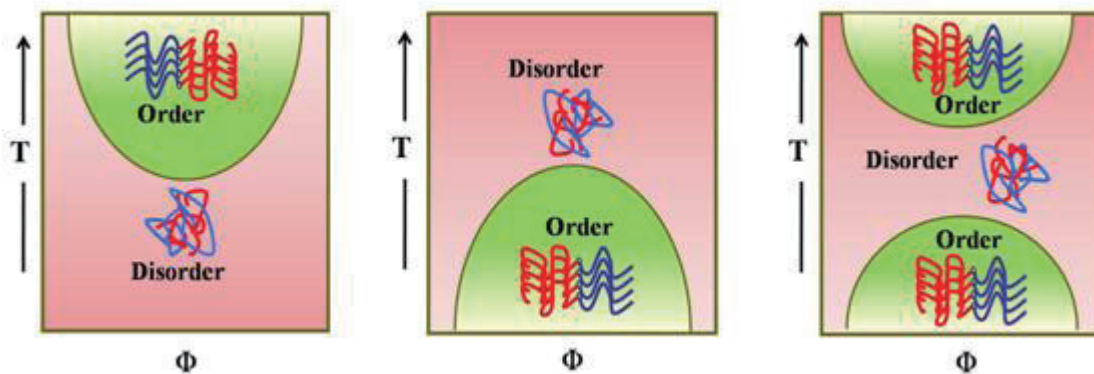
- [1] M. Rat, M. H. Zahedi-Niaki, S. Kaliaguine, T. O. Do, *Microporous Mesoporous Mater.*, **112**, 26 (2008).
- [2] X. Sheng, J. Gao, L. Han, Y. Jia, W. Sheng, *Microporous Mesoporous Mater.*, **143**, 73 (2011).

## Phase Transition Behavior in the Blends of Weakly Interacting Block Copolymers

Yonghoon Lee, Hyungju Ahn, Hoyeon Lee, Du Yeol Ryu,\*

Department of Chemical and Biological Engineering, Yonsei University, Seoul 120-749,  
Korea

The Flory–Huggins interaction parameters ( $\chi$ ) between different components were described by the temperature-dependent function in the homopolymer blends and block copolymers. A blend system undergoes the phase transition with temperature, showing the upper critical solution transition (UCST) behavior as a consequence of weakened non-favorable segmental interactions, whereas in the lower critical solution transition (LCST), an increasing entropy can be correlated to an increase of free volume (or thermal expansion coefficient).



Similar to binary polymer blends, the phase behavior of diblock copolymers has been known to exhibit a microphase separation from an ordered to a disordered state either upon cooling or upon heating, where the latter behavior is called the order-disorder transition (ODT) with enthalpic origin, and the former can be induced by entropic origin, denoted to the lower disorder-order transition (LDOT). In this study, we observed the transition behavior in the blend of weakly-interacting symmetric block copolymers using small angle X-ray scattering (SAXS), small angle neutron scattering (SANS) depolarized light scattering (DLS) and differential Scanning Calorimetry (DSC).

### References

- [1] Ryu et al., *Nat Mater*, **1**, 114-117 (2002)
- [2] Kim et al., *Macromolecules*, **41**, 6793-6799 (2008)

## Preparation of poly(methyl methacrylate) grafted imogolite nanotubes by surface-initiated ARGET ATRP

Wei Ma<sup>1</sup>, Hideyuki Otsuka<sup>1,2</sup>, Atsushi Takahara<sup>1,2</sup>

<sup>1</sup> Graduate School of Engineering, Kyushu University, Japan

<sup>2</sup> Institute for Materials Chemistry and Engineering, Kyushu University, Japan

Clay nanotubes are attracting an increasing research interests in recent years, because they are nature friendly and abundant. Imogolite is an aluminosilicate clay nanotube. It forms a single-walled nanotube by the curling of a gibbsite-like sheet. The external and internal diameters of imogolite nanotube are about 2 and 1 nm, respectively. Imogolite has potential applications in numerous areas, such as, gas storage, building blocks for self-assembly, and fillers for organic/inorganic hybrid materials.[1] However, one challenge involving imogolite application is their homogeneous dispersion in hydrophobic materials.

The surface modification of imogolite at nanotube level has been demonstrated previously.[2] The present study focuses on grafting polymer chains from imogolite surface, in order to achieve homogeneous dispersion in various organic media. For this purpose, a surface-initiated polymerization of methyl methacrylate (MMA) from imogolite surface was carried out. An activators regenerated by electron transfer for atom transfer radical polymerization (ARGET ATRP) process was employed, because it can be carried out in a mild condition, and only needs ppm level of catalyst. Fig. 1 presents the preparation procedure for PMMA grafted imogolite nanotubes. The obtained PMMA grafted imogolite presents excellent dispersibility in various organic solvents.[3]

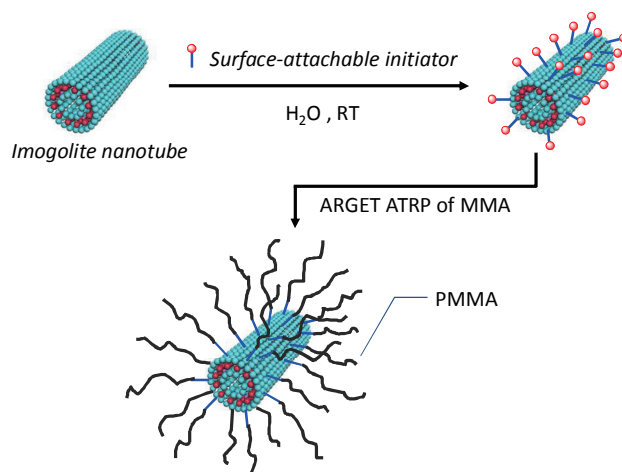


**Fig. 1.** Schematic representation for the preparation of PMMA grafted imogolite nanotube.

- [1] K. Yamamoto, H. Otsuka, S-I. Wada, D. Sohn, A. Takahara, *Soft Matter*, **1**, 372 (2005).  
 [2] W. Ma, J. Kim, H. Otsuka, A. Takahara, *Chem. Lett.*, **40**, 159 (2011).  
 [3] W. Ma, H. Otsuka, A. Takahara, *Chem. Commun.*, **47**, 5813 (2011).

## Flow reactor syntheses of titania-octadecylamine hybrid spherical particles — Variation of particle size and insertion of heteroelements —

Kota Shiba<sup>1</sup> and Makoto Ogawa\*<sup>1,2</sup>

<sup>1</sup> Graduate School of Creative Science and Engineering, Waseda University, Japan

<sup>2</sup> Department of Earth Sciences, Waseda University, Japan

Flow reactor has been used for the synthesis of a variety of particles in wide size range from several nanometers to microns, taking advantage of the fact that chemical reactions in a small size space correlate with the homogeneity of products.[1, 2] Another merit of flow reactor is to design reaction pathways, possibly leading to the formation of products with complex and/or hierarchical texture, structure and organization. On the other hand, flow reactor synthesis is not suitable for long time reactions because of the limitation of reaction set-up such as tube length, flow rate etc. We have recently proposed a sequential reaction combining a flow reactor synthesis with a conventional batch reaction to overcome the limitations; nucleation in the flow reactor and subsequent particle growth by a batch reaction. Using a flow reactor as an initial stage of sol-gel reactions, we successfully prepared uniform-sized spherical particles of titania-octadecylamine (titania-ODA) hybrids with submicron size.[3] We have been examining the two step syntheses for various hybrid particles.

Here, we report the flow reactor syntheses of titania-ODA hybrid spherical particles with uniform size in the range of 70 to 900 nm and the attempt to co-precipitate titanium oxide with other elements such as zirconium and silicon. Due to the homogeneity of the composition and particle size of the spherical particles of nanoporous titania, which we have successfully synthesized,[3] the functionalization and applications of them are worth investigating. Therefore, co-precipitation or doping of a heteroelement into titania and preparation of core-shell type particles was conducted as a way of functionalization.

The titania-ODA with various sizes were synthesized based on the procedure reported previously.[3] The synthetic procedure is schematically shown in Fig. 1. Titanium tetraisopropoxide (TTIP) containing isopropyl alcohol (IPA) and IPA aqueous solution were flowed within a PFA tube by a syringe pump at a constant speed and mixed within the flow reactor made of PTFE and with a flow channel of Y-type junction. The channel cross section was ca. 1 mm<sup>2</sup>. The volume of each solution was 12.5

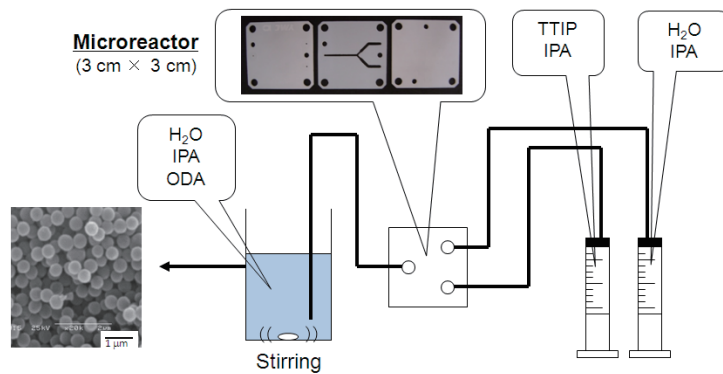


Fig. 1. Flow reactor set-up used in the present study and SEM image of titania-ODA particles.

mL and the molar ratio of TTIP:H<sub>2</sub>O after the mixing was 1:2.7. The mixture was further flowed within a PFA tube of 70 cm in length and then mixed with the solution composed of deionized water, IPA and ODA under magnetic stirring until the addition of the mixture was completed. After the aging at room temperature for 24 h, products were collected by vacuum filtration, washed with IPA, and then dried at 60 °C in air for a day. Titania and silica were co-precipitated by adding a given amount of tetraethoxysilane (TEOS) into TTIP/IPA mixture. Silica coated titania core-shell particles were prepared by dispersing as-synthesized titania-ODA particles into aqueous ammonia/methanol (MeOH) mixture containing hexadecyltrimethylammonium chloride before adding TEOS/H<sub>2</sub>O/MeOH mixture which was prepared within the flow reactor by the same manner as described above in the titania-ODA synthesis.

A variety of titania and silica based hybrid spherical particles were obtained by the present two step syntheses as summarized in Fig. 2. We prepared uniform sized titania-ODA spherical particles with the size range of 70 to 900 nm, which was possible to be transformed to nanoporous titania by ODA removal and subsequent calcination. Co-precipitation of titania and silica led to the formation of spherical particles with the weight SiO<sub>2</sub>/TiO<sub>2</sub> ratio in the range of 0.11 to 0.87. TEM-EDX analyses revealed that Ti, Si and O atoms distributed uniformly in each particle. Silica coated titania particles were also prepared and the thickness of the silica shell varied (from a few nm to ca. 100 nm) depending on the amount of TEOS. Further modification of flow path, e.g. connecting several reactors using tubes with various lengths, is a possible way for the preparation of particles with variable size, composition and structure.

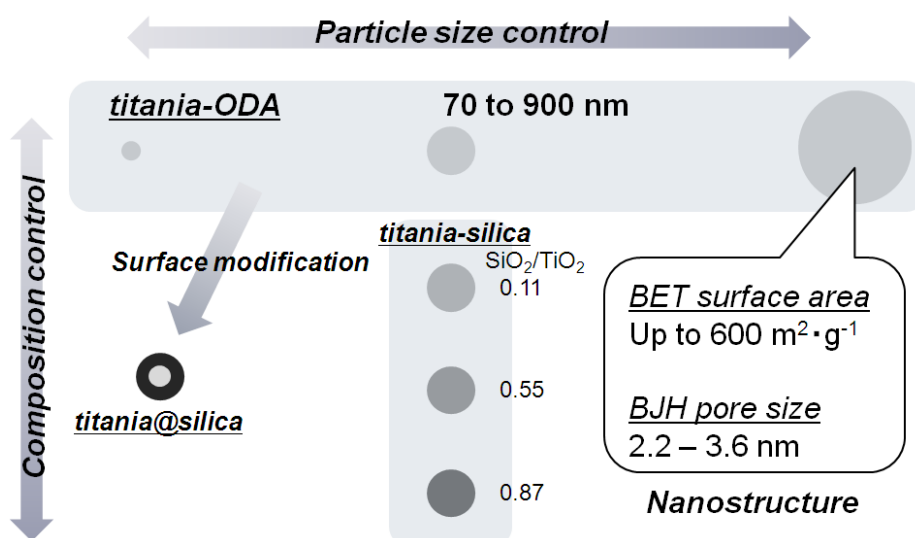


Fig. 2. Summary of a variety of products prepared in the present study.

## References

- [1] P. Watts and C. Wiles, *Chem. Commun.*, 443-467 (2007).
- [2] Y. Song, J. Hormes and C. S. S. R. Kumar, *Small*, **4**, 698-711 (2008).
- [3] K. Shiba and M. Ogawa, *Chem. Commun.*, 6851-6853 (2009).



## Morphology and Mechanical Properties of Jellified Chitosan–Clay Nanocomposite Formed by Means of Regulated Charging of Polysaccharide

Vladimir E. Silantyev<sup>1</sup>, Irina V. Postnova<sup>2</sup>, Yury A. Shchipunov<sup>1</sup>

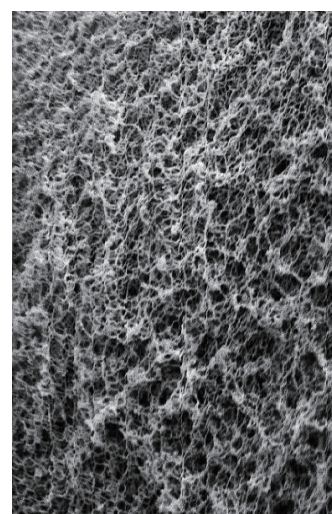
<sup>1</sup>Institute of Chemistry, Far East Department, Russian Academy of Sciences, 690022, Vladivostok, Russia

<sup>2</sup>Far Eastern Federal University, Vladivostok, Russia

Chitosan is the only natural cationic polysaccharide consisting of glucosamine residues. As a typical of weak polyelectrolytes, its charging depends on the pH of aqueous media. This feature is in the basis of a method suggested previously in [1]. As tiny microparticles, the chitosan is dispersed in a solution of exfoliated clay. We used saponite. Its plate nanoparticles attain a thickness of ca. 1 nm and diameter of 20-30 nm. Their surface bears negatively charged silane groups. When pH is gradually shifted in the acidic region, there is charging the polysaccharide that is involved in electrostatic interaction *in situ* with nanoparticles. This results in the jellification of solution. To exclude the precipitation or phase separation, it was suggested in [1] to perform the acidification in a gradual manner. The glucono- $\delta$ -lactone is applied as an acidulating agent. When experiencing the hydrolysis, it generates progressively the gluconic acid that leads to a slow pH decrease. This provides a means for the control on the solution jellification as a result of chitosan regulated charging.

The transition to the gel state took place even at small amount of added chitosan in a solution with dispersed saponite. By using the oscillating rheology, the mechanical properties of chitosan-saponite systems were characterized in sufficient details. It was also used to determine a real transition from a solution to the hydrogel. These data allowed constructing a phase diagram.

To have an insight into structural organization of chitosan with saponite nanoparticles in their hydrogels, scanning electron microscopy was applied. As an example, one can see an image in Fig. 1. There are fibrils that are arranged into a three dimensional network. Its formation explains the jellification of solution. Fibrillar structure is typical of this type of hydrogels. It can be formed through self-organization of chitosan with saponite nanoparticles that is regulated by gradual pH shift.



— 2  $\mu$ m

Fig. 1. An image of hydrogel taken by scanning electron microscopy (EVO 40, Zeiss). A sample for the observation was prepared by exchanging water to ethanol, acetone and then to liquid carbon dioxide that was removed at supercritical conditions. Hydrogel composition: 0.5 wt. % chitosan, 1.0 wt. % saponite

### References

[1] Y. A. Shchipunov, N. A. Ivanova, V. E. Silant'ev, *Green Chemistry*, **11**, 1758 (2009).

## Selective Modification on Lumen of Halloysite: New Inorganic Tubule Micelle

Weng On Yah<sup>1</sup>, Yuri M. Lvov<sup>2</sup>, and Atsushi Takahara<sup>1</sup>

<sup>1</sup> Institute for Materials Chemistry and Engineering, Kyushu University, JAPAN

<sup>2</sup> Institute for Micromanufacturing, Louisiana Tech University, USA

Halloysite (Figure 1, general formula:  $\text{Al}_2\text{Si}_2\text{O}_5(\text{OH})_4 \cdot 2\text{H}_2\text{O}$ , 1:1 layer aluminosilicate), is a type of natural occurring clay mineral with nanotubular structures, narrow lumen of 15 nm, chemically active external and internal surfaces [1]. Halloysite can be an effective nano-adsorbent for removal of cationic dye methylene blue [2] and uranium from aqueous solution [3]. For some applications, properties such as hydrophobicity need to be improved. By grafting octadecylphosphonic acid (ODP) selectively into lumen of halloysite, adsorption capability toward hydrophobic molecule in aqueous solution enhanced significantly.

Halloysite was modified by ODP in EtOH:H<sub>2</sub>O (pH 4) and denoted as halloysite-ODP. Surface chemical compositions measured by XPS showed that the primary mode of attachment to the alumino surface is bidentate and tridentate with a fraction of monodentate configuration. The <sup>29</sup>Si CPMAS NMR spectrum of the halloysite-ODP shows that the binding of phosphoryl groups to the silica surface can be ruled out, as no high-field resonance arising from penta- or hexa-coordinated Si atoms was detected. The time dependent profile of ferrocene adsorption showed that modified halloysite-ODP leads to relatively faster adsorption of ferrocene compared to unmodified halloysite. The release profile (Figure 2) shows that more ferrocene is released from the halloysite-ODP than pristine halloysite, suggesting that large amount hydrophobic molecule had been adsorbed inside the less polar lumen of halloysite-ODP. In conclusion, XPS and solid state NMR confirmed that internal surface of halloysite was modified with ODP. Time dependent adsorption and release profile suggested that adsorption of hydrophobic molecules in aqueous solution of THF/H<sub>2</sub>O was achieved through selective surface modification on the lumen of halloysite.

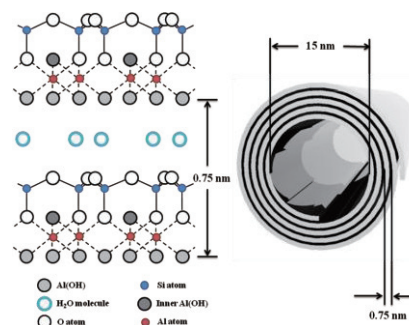


Fig 1. Structure of halloysite

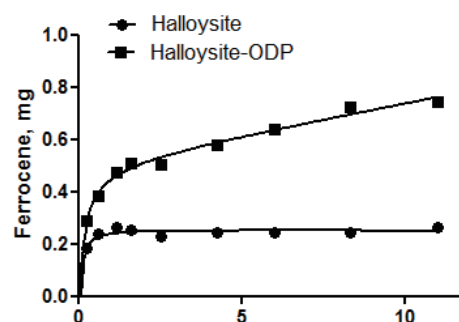


Fig 2. Release profile of the ferrocene from halloysite and halloysite-ODP.

[1] Y. Lvov, *Biomacromolecules*, **11**, 820 (2010).

[2] M. Zhao, *Micropor. Mesopor. Mater.*, **112**, 419 (2008).

[3] A. Kilislioglu, *Radiochimica Acta*, **90**, 155 (2002).

## Environmentally Friendly Low Viscous 4-Arm Star Polymers via Emulsion ATRP

Jieun Yang<sup>1</sup>, Youngsoo Na<sup>2</sup>, Ildoo Chung<sup>1</sup>  
<sup>1</sup>Department of Polymer Science and Engineering,  
 Pusan National University, Busan 609-735, Korea  
<sup>2</sup>Segye Chem Company, Yangsan 626-110, Korea

The preparation of well-defined polymers and copolymers by controlled radical polymerization has recently been an area of high interest. One of these methods is atom transfer radical polymerization (ATRP), which has been used for the successful polymerization of well-defined polymers and copolymers of styrenes, acrylates, methacrylates, and acrylonitrile. It has also been applied to emulsion systems, in which polymers with predetermined molecular weights and low polydispersities were obtained in stable latexes. [1, 2]

In this paper, we discuss the ATRP copolymerization of n-butyl acrylate (n-BA), methyl acrylate (MA), 2-hydroxyethyl methacrylate (HEMA) in emulsion systems using multifunctional ATRP initiator, 4,4'-dinonyl-2,2'-bipyridyl (dNbp) as a ligand and polysorbate 80 (Tween80) as an emulsifier.

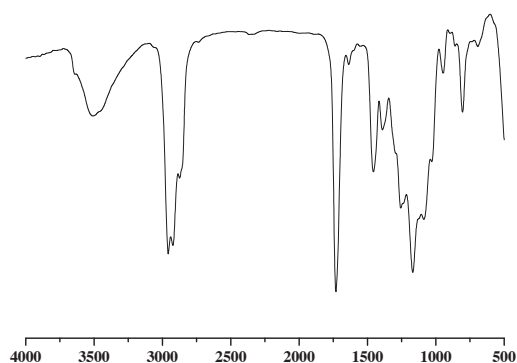


Fig. 1. FT-IR spectrum of 4-arm star

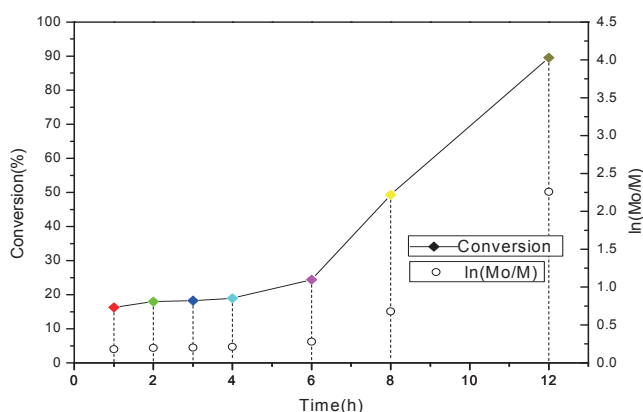


Fig. 2. Kinetic plot of 4-arm star copolymer.

In FT-IR spectrum of the synthesized copolymer (Fig.1), a strong absorbance was observed at  $1720\text{ cm}^{-1}$  related to the carbonyl stretching with disappearance of C=C double bond stretching of the monomer at  $1650\text{ cm}^{-1}$ .

The  $^1\text{H}$  NMR spectrum of 4-arm star copolymer shows that the monomer moieties at 5.90-6.43 ppm had completely disappeared, while correspondingly, new signal of polymer backbone was observed at 1-2 ppm. The kinetic characteristics of the ATRP reaction of copolymer is illustrated in Fig. 2. The plot of  $\ln([M_0]/[M])$  versus reaction time is almost linear, indicating that the radical polymerization follows first order kinetics especially at latter stage of the polymerization. The preliminary results indicate that ATRP in emulsion is very promising and future works will focus on the emulsion ATRP of various acrylate as well as the elimination of emulsifier effectively.

[1] H. Peng, S. Cheng, Z. Fan, *Polymer Engineering and Science*, 291 (2005).

[2] G. Chambard, P. d. Man, B. Klumperman, *Macromol. Symp*, **150**, 45 (2000).

## Characterization of Molecular Aggregation Structure of Poly(vinyl alcohol) Nanofiber Fabricated by Electrospinning

Takahiro Yano<sup>1</sup>, Moriya Kikuchi<sup>2</sup>, Taiki Hoshino<sup>2</sup>, Noboru Ohta<sup>3</sup>, Motoyasu Kobayashi<sup>2</sup>,  
and Atsushi Takahara<sup>1,2,4</sup>

<sup>1</sup>Graduate School of Engineering, Kyushu University, Japan

<sup>2</sup>JST, ERATO, Japan

<sup>3</sup>JASRI/SPring-8, Japan

<sup>4</sup>Institute for Materials Chemistry and Engineering, Kyushu University, Japan

**[Introduction]** Poly(vinyl alcohol) (PVA) nanofibers fabricated by the electrospinning method have attracted much attention due to potential applications in various fields including the environmental, medical, and nanoscience fields. The degree of crystallinity of PVA nanofibers at various annealing temperature was reported by Wan et al.[1], however, the structural changes of the nanofibers during uniaxial stretching have not been clarified yet. In this study, the orientation states of the nanofiber and the crystallite during uniaxial stretching of the non-woven nanofiber mat were analyzed by simultaneous stress-strain/wide-angle X-ray diffraction (WAXD) and stress-strain/small-angle X-ray scattering (SAXS) measurements.

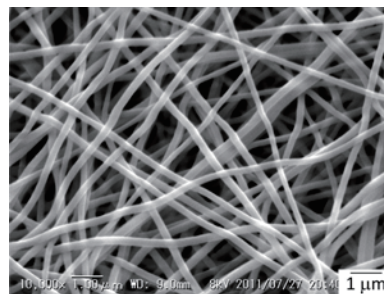


**Figure 1.** SEM image of electrospun PVA nanofibers prepared from 8.0 wt% water/DMF(70/30, wt/wt) solution.

### **[Experimental section]**

PVA (degree of polymerization: 1700, degree of hydrolysis: 87.0-89.0%) was dissolved in water/DMF (70/30, wt/wt) to prepare 8.0 wt% solution, which was discharged from the nozzle at 1.0 mL/h of feed rate with 20 kV of applied voltage to fabricate the PVA non-woven nanofiber mat on the collection target at a distance of 15.0 cm apart from the electrospinning nozzle. The morphology of the obtained nanofiber was observed by scanning electron microscopy (SEM, Figure 1). Simultaneous stress-strain/wide-angle X-ray diffraction (WAXD) measurement using a flat panel detector with 71 mm of camera length and stress-strain/small-angle X-ray scattering (SAXS) using a imaging plate detector with 2230 mm of camera length were performed at BL40B2 beamline of SPring-8 using a X-ray beam with 0.1 nm wavelength. During the non-woven nanofiber mat was elongated by the tensile testing apparatus on the sample stage in the hatch, the simultaneous SAXS/WAXD measurements were conducted. The orientation state of the nanofibers was evaluated based on the Ruland's method.[2] The orientation state of the crystallite was evaluated by the orientation function,[3] which was calculated by 1-D peak intensity distribution of (101) and (111) crystalline diffraction along the azimuthal angle.

## [Results and Discussion]

The misorientation width calculated from SAXS pattern represents the orientation distribution of longitudinal voids in the non-woven nanofiber mat. Therefore, narrow misorientation width stands for higher degree of nanofiber orientation. The misorientation width decreased with an increase in the degree of elongation, as shown in Figure 2. The nanofibers were oriented to the elongation direction with the elongation, but the degree of nanofiber orientation was saturated even after the nanofiber was elongated more than 50% of the initial length of the nanofiber specimen.

Orientation function calculated from WAXD pattern is a parameter representing the average cosine square angle of the crystalline axis against the standard Z axis, which shows the degree of the crystalline orientation. The orientation function value for an isotropic material and fully oriented chain are zero and 1.0, respectively. When the chain is oriented perpendicular to the draw direction, the value will be -0.5. The orientation function at the various elongation states in Figure 3 revealed that the polymer chains were continuously oriented with the elongation process. The standard Z axis was provided to equatorial direction against elongation direction. The orientation function of the b-axis decreased to the negative value with the elongation, indicating that the polymer chain axis (b-axis) in the crystalline was oriented to meridional direction due to the uniaxial stretching. On the other hand, the a-axis and c-axis which are perpendicular to the polymer chain axis (b-axis) were oriented to the equatorial direction with the molecular chain orientation in the crystalline.

In conclusion, we conducted simultaneous SAXS/WAXD measurements during uniaxial stretching process of PVA non-woven nanofiber mat to demonstrate that both the nanofiber and polymer chain were oriented at the beginning of the strain, and the crystallite of PVA oriented to the elongation direction with an increase in the degree of elongation, while the degree of nanofiber orientation was saturated at the elongation of 50%.

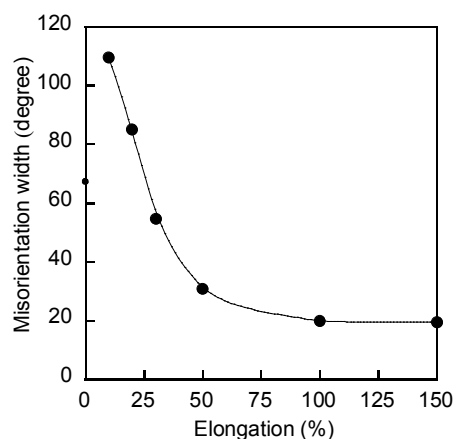


**Figure 2.** The relationship between misorientation width of the nanofiber direction and

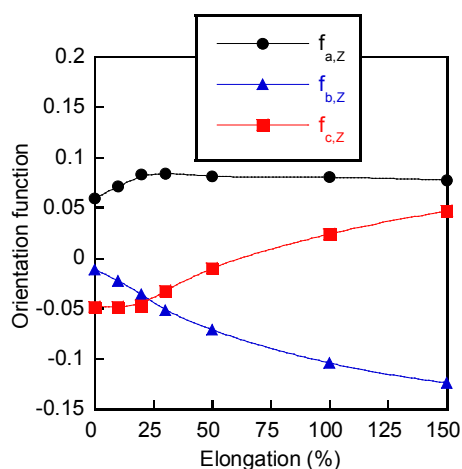


**Figure 3.** Variations of the orientation function with elongation.

[1] K. K. H. Wong, M. Z. Allmang, W. Wan, *J. Mater. Sci.*, **45**, 2456 (2010)

[2] W. Ruland, *J. Polymer Sci.*, **28**, 143 (1969)

[3] Z. W. Wilchinsky, *J. Appl. Phys.*, **30**, 792 (1959)

## Electrical Properties of Transparent Conductive Films Prepared by Dispersed Single-Walled Carbon Nanotubes Using Poly[2-(dimethylamino)ethyl methacrylate]-*co*-Polystyrene

Donghyun Kim<sup>1</sup>, Keonwoo Kim<sup>1</sup>, Bong-Soo Kim<sup>1</sup>, Sangwoo Park<sup>1</sup>,  
Kwonwoo Shin<sup>2</sup>, Jonghun Han<sup>2</sup> and Hyun-jong Paik<sup>1\*</sup>

<sup>1</sup> Department of Polymer Science and Engineering, Pusan National University,  
San 30 Jangjeon2 dong GeumJeong-gu, Busan 609-735, Korea

<sup>2</sup> Green-energy Research Center, Korea Electronics Technology Institute,  
Gyeonggi-do 463-816, Korea

The single-walled carbon nanotubes (SWNTs) coatings on plastic film have been investigated as transparent conductive film (TCF) to alternate indium tin oxide (ITO) electrode. One of important factor that makes TCF more conductive is the dispersion of SWNTs. However, SWNTs exist as a bundle due to a strong intertube van der Waals attraction. In order to obtain well dispersed SWNTs, efficient dispersants are firstly required. In this study, poly[2-(dimethylamino)ethyl methacrylate]-*co*-polystyrene (PDMAEMA-*co*-PS) was synthesized and used as polymeric dispersants for SWNTs in organic solvent. PDMAEMA-*co*-PS with different copolymer composition were prepared by atom transfer radical polymerization (ATRP) and characterized by gel permeation chromatography (GPC) and <sup>1</sup>H NMR. With PDMAEMA-*co*-PS, SWNTs were effectively dispersed through non-covalent functionalization by ultrasonication in tetrahydrofuran (THF). Unbundled structures of SWNTs were observed by transmission electron microscopy (TEM). Using the turbiscan optical analyzer, dispersion stabilities of SWNTs were compared in THF with PDMAEMA-*co*-PS in different copolymer composition. SWNTs coatings on polyethylene terephthalate (PET) film were prepared via spin coating of SWNTs dispersion solution and networks of SWNTs were observed by field emission scanning electron microscope (FE-SEM). Transmittance and sheet resistance of SWNTs coatings were obtained by UV-vis spectroscopy and four point probe measurement, respectively.

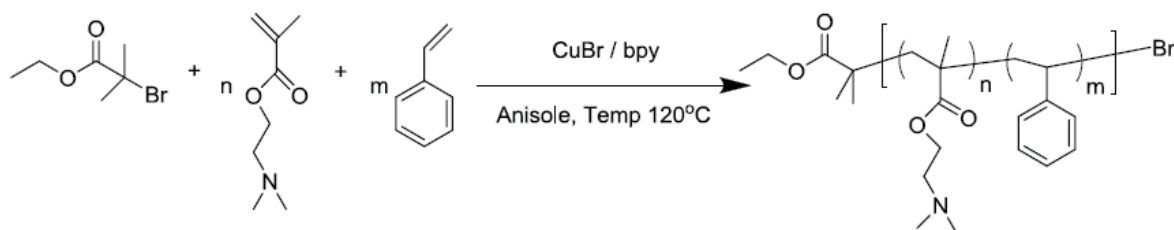


Fig. 1. Synthetic scheme of random copolymer PDMAEMA-*co*-PS.

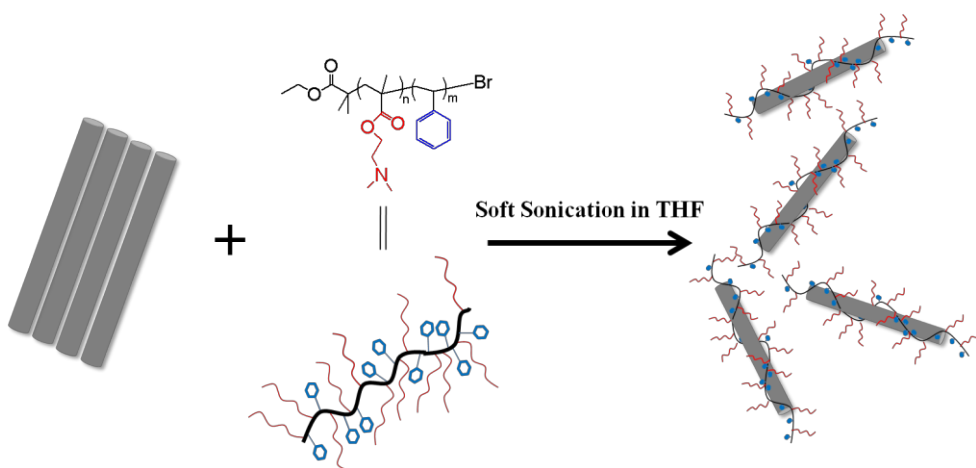


Fig. 2. Schematic illustration of non-covalent functionalization of SWNT with PDMAEMA-co-PS

## Metal-Catalyzed Anisotropic Etching of CVD-Grown Graphene

○Kazuma Yoshida,<sup>1</sup> Hiroki Ago,<sup>\*,1,2</sup> Masaharu Tsuji<sup>1,2</sup>

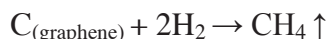
<sup>1</sup>Graduate School of Engineering Sciences, Kyushu University, Kasuga, Fukuoka, Japan

<sup>2</sup>Institute for Materials Chemistry and Engineering, Kasuga, Fukuoka, Japan

\*Correspondence: ago@cm.kyushu-u.ac.jp

Graphene, a monolayer of carbon atoms arranged into a hexagonal lattice, has attracted a great interest because of their unique two-dimensional structure and promising properties [1]. Extraordinary high carrier mobility reaching 200,000 cm<sup>2</sup>/Vs [2] promises the application in electronics, such as field-effect transistors and high-frequency transistors. These applications require the fine control of graphene structure including its edge state, because electronic structure of graphene is strongly influenced by shape and edge structures. In particular, graphene nanoribbons, which are expected to open the band gap of graphene, need precise control of the edge structure.

Recently, metal-catalyzed cutting of a graphene sheet has been demonstrated (Figure 1). The following reaction proceeds in the presence of Ni or Fe nanoparticles under H<sub>2</sub> flow at high temperature [3,4].



Preferential cutting along zigzag edge has been proposed [3,4], and this is useful for the fine control of graphene structure. We applied this method to our large-area, single-layer graphene grown by chemical vapor deposition (CVD).

Single-layer graphene was synthesized by CVD over hetero-epitaxial Cu(111) film. Hetero-epitaxial metal films offer the uniform single-layer graphene, in which orientation of graphene hexagons is well controlled by the underlying single-crystalline metal film [5,6]. This orientation-controlled growth is important for the metal-catalyzed cutting, because the cutting direction is determined by the orientation of hexagons. Note that the conventional CVD over polycrystalline metal film/foils as well as mechanically exfoliated graphene have random orientation of hexagons. Figure 2 shows the Raman spectra of three different points of a graphene film transferred onto SiO<sub>2</sub>(300nm)/Si wafer. The Raman spectra show high I<sub>2D</sub>/I<sub>G</sub> ratio (>2), signifying the formation of single-layer graphene. The absence of defect-related D-band at 1350 cm<sup>-1</sup> indicates that our graphene is of high quality.

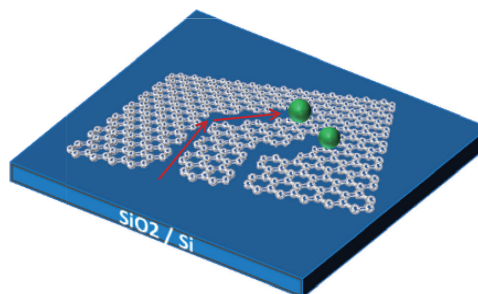


**Fig. 1.** Schematic of metal-catalyzed graphene cutting process.



We studied the metal-catalyzed cutting reaction using three different metals. After dipping the graphene into metal salt solution, the graphene was annealed in the mixed flow of H<sub>2</sub> and Ar at 1000 °C. We found that graphene cutting occurred for our CVD-grown graphene, as shown in Figure 3. It is noteworthy that the cutting for CVD-grown is demonstrated for the first time, since other previous works used mechanically exfoliated graphene which is highly crystalline but size limited. The observation of direction-oriented cutting proves that our graphene film is high quality and the hexagon orientation is well defined. Further study to achieve specific graphene nanostructures, such as nanoribbon and quantum dots with defined crystallographic edges, is necessary for future electronic applications.

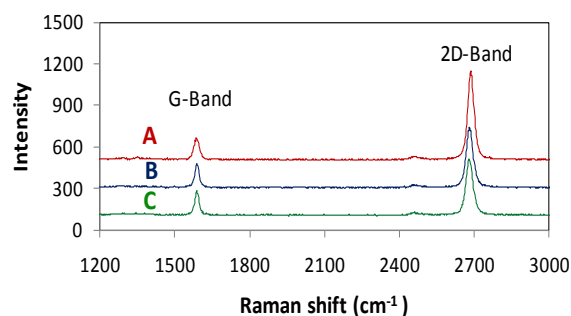


**Fig. 2.** Raman spectra of CVD-grown graphene film. Three different points were measured.

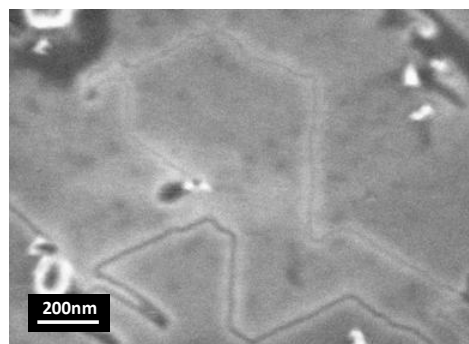


**Fig. 3.** SEM image of the cutting lines observed for single-layer graphene.

## References

- [1] K. S. Novoselov *et al.*, *Science*, **306**, 666 (2004).
- [2] K. I. Bolotin *et al.*, *Solid State Commun.*, **146**, 351 (2008).
- [3] C. Compos *et al.*, *Nano Lett.*, **9**, 2600 (2009).
- [4] S. Datta *et al.*, *Nano Lett.*, **8**, 1912 (2008).
- [5] H. Ago *et al.*, *ACS Nano*, **4**, 4707 (2010).
- [6] B. Hu *et al.*, *Carbon*, submitted.

## Volume change of behavior of poly(L-lysine-alt-terephthalic acid) microcapsules near the transition pH

Hirokazu Takakura, Naoko Ogata, Takayuki Narita, Yushi Oishi

Department of Chemistry and Applied Chemistry, Saga University, Japan

The poly(L-lysine-alt-terephthalic acid) microcapsule, PPL-MC changes its volume in response to pH environment. This volume change occurs at pH 5.6 by the volume phase transition of the gel membrane which is based on an electrostatic interaction change. The volume response of microcapsule in pH change is very faster than that of same size spheres consisting of PPL because microcapsule have no networked polymers in its core, and hence PPL membrane on microcapsules can easily contact with outer environment in which pH change is triggered. The dynamics of volume phase transitions of gel membrane is dominated by some conditions, especially characteristic size, such as membrane thickness, and the quench depth of phase transition. The volume change near transition point, meaning the shallow quench, is very interesting since a volumetric hysteresis is usually observed in the volume phase transition of some hydrogels. At the region near the phase transition point, the volume change in microcapsules therefore, may be different from that for the same-size gel spheres. In this study, we investigated the volume change behavior of PPL-MC near volume phase transition of PPL gel membrane as functions of pH and ion strength, I.S.

The water phase containing L-lysine and  $\text{Na}_2\text{CO}_3$  was mixed with the oil phase consisting of cyclohexane, chloroform and Span85 to obtain a W/O emulsion solution. PPL-MC was prepared by adding cyclohexane/chloroform solution of Terephthaloyl Dichloride in the W/O emulsion. The capsules obtained were washed with distilled water (pH 5.9). To change the outer environment of the capsules, these were immersed in buffer solutions which were adjusted to a given pH (5-9) and I.S. (0.1, 0.01, 0.001 mol/l) by CAPS (N-Cyclohexyl-3-aminopropanesulfonic acid). The time courses of microcapsules after the solution replacement of outer solution were obtained by an optical microscope attached with a CCD camera.

When immersing microcapsules in the buffer solution below pH 5, all capsules shrank monotonically within about 10h. On the contrary, the immersion above pH 9 allowed microcapsules to swell. On the other hand, the microcapsules in a pH range from 6 to 8 oscillated its volume with time after immersing in the buffer solution. The period and amplitude of volume oscillation were about 0.06-10 hours and about tens-millions  $\mu\text{m}$ , respectively, and ceased at 24 hours after the replacement of outer solution. The pH range in which the volume oscillation occurred reduced with an increase in I.S, as shown in Fig. 1. The reduction of pH range for volume oscillation suggests that an osmotic pressure gap between inside and outside of the capsule membrane relates to the driving force for oscillating microcapsule.

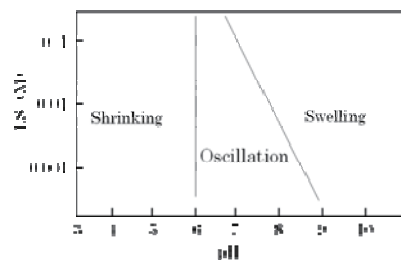


Fig. 1. Phase diagram of volume change behavior.

## Mechanical properties of the acrylonitrile functionalized emulsion SBR/silica compounds

Dongwon Kim<sup>1</sup>, Dong-chul Bae<sup>1</sup>, Byeung-ho Seo<sup>1</sup>, Wonho Kim<sup>1\*</sup>

<sup>1</sup> Chemical and Biomolecular Engineering, Pusan National University, Korea

\*E-mail : whkim@pusan.ac.kr

### 1. Introduction

As EU tire labeling set to be enforced in 2012, in response to demanding requirements for high-performance tires, tire industries for automobiles are striving to find approaches to increase fuel efficiency and reduce road transport emissions[1].

Although silica has started to be used as a reinforcement agent for rubber in the tire industry, its application is still limited because silica has polarity on its surface, which makes it difficult to distribute them into the non-polar rubber matrix due to a weak bonding force between rubber matrix and silica[2]. The major efforts for the development of the terpolymer, which is polymerized with styrene, butadiene, and polar monomers by using the emulsion polymerization, are needed to improve compatibility between filler and rubber. Acrylonitrile is explained as the suitable polar monomer in ESBR for enhancing the interaction with silica.

Therefore, in this study, curing characteristics, mechanical and viscoelastic properties of the rubber compounds were investigated to analyze the properties of acrylonitrile as the functionality in AN-SBR compounds by comparison with SBR 1721 compound and PEG was used to reduced the filler-filler interactions for improving the silica dispersion[3].

### 2. Results and discussion

AN-SBR/silica compound had higher values in minimum torque than SBR 1721/silica compound during the vulcanization because AN-SBR has higher molecular weight than SBR 1721 in the raw material. AN-SBR/silica compounds(A-2, A-4) had faster vulcanization time and higher delta torque values than SBR 1721/silica compounds(A-1, A-3). Because interaction between acrylonitrile group and silica surface prevented adsorption of the accelerator on the hydroxyl groups on the silica surface, which improved the vulcanization reaction efficiency and enhanced the degree of crosslinking. When PEG was applied to the SBR 1721/silica or AN-SBR/silica compound, the accelerator and the ingredients could not be absorbed to the hydroxyl groups on the silica surface, which improved vulcanization time[3]. In the mechanical properties, AN-SBR/silica compounds(A-2, A-4) had higher 100% and 300% modulus values than the SBR/silica compounds(A-1, A-3) owing to the interaction between acrylonitrile group and silica surface, which improved the degree of crosslinking. But, When

PEG was applied to the SBR 1721/silica or AN-SBR/silica compound, 100% and 300% modulus values were not improved. Because PEG did not enhance the degree of crosslinking. AN-SBR/silica compounds(A-2, A-4) had lower values in the swelling ratio than the SBR/silica compounds(A-1, A-3) owing to the interaction between acrylonitrile group and silica surface, which improved the degree of crosslinking that caused great mechanical properties.

### 3. References

- [1] X. Liu and S. H. Zhao, *J Appl Polym Sci.*, **108**, 3038 (2008).  
 [2] Hui, R.; Yixin, Q.; Suhe, Z. *Chinese J Chem Eng.*, **14**, 93 (2006)  
 [3] Valentin, J. L.; Posada, P.; Maros-Fernandez, A.; Ibarra, A.; Rodriguez, A. *J Appl Polym Sci.*, **99**, 3222 (2006)

Table.1. Formulation of the various compounds

	A-1	A-2	A-3	A-4
SBR 1712	100	-	100	-
AN-SBR	-	100	-	100
Silica (zeosli-175)	30			
PEG-4000	-	-	2	2
ZnO	3			
BHT	1			
Stearic acid	1			
Sulfur	2.2			
TBBS	1.5			
DPG	0.8			

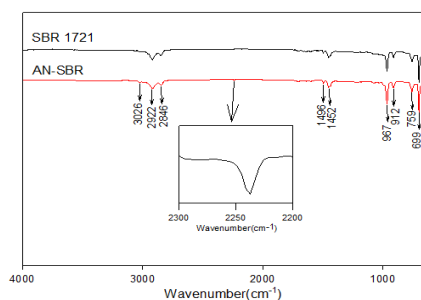


Fig. 1. FTIR spectra of AN-SBR and SBR 1721

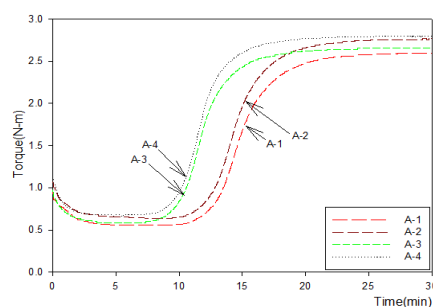


Fig. 2. Cure characteristics of the various compounds.

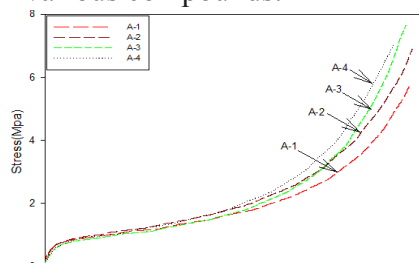


Fig. 3. Tensile properties of the various compounds.

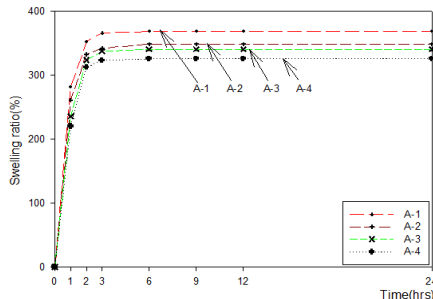


Fig. 4. Swelling ratio of the various compounds.

## Synthesis of sodium methallyl sulfonate-*co*-poly(ethylene glycol) diacrylate ion exchange bead at different molecular weight of PEGDA

Jin Sun Koo, Youngmin Baek, Taek Sung Hwang\*

Department of Chemical Engineering, College of Engineering,  
Chungnam National University, 79 Daehang-no, Yuseong-gu, Daejeon 305-764, South Korea

### Abstract

The copolymer beads (SMS/PEGDA) were synthesized by suspension polymerization based on sodium methallyl sulfonate and poly(ethylene glycol) diacrylate. Their chemical structures and composition were determined by FT-IR and SEM-EDS respectively. The basic properties of SMS/PEGDA beads such as ion exchange capacity, water uptake and yield were measured for preparing ion exchange beads. The water uptake and ion exchange capacity values of beads increased with decreasing amount of PEGDA contents. The surface morphology investigated by scanning electron microscope and optical microscope clearly showed an increase of roughness with increasing molecular weight of PEGDA.

### 1. Introduction

Suspension polymerization has been frequently used in producing polymer bead for various industry[1-3]. In suspension polymerization form droplets of the monomer phase is dispersed into the dispersion medium by agitation. The size and its distribution of the final beads are significantly associated with those of the initial emulsion droplets. Namely the stirring/dispersing condition provides control over the size performance of the final beads [4, 5]. Polyethylene glycol(PEG) is a synthetic polymer that has been informed of the thing of affinitive with human and harmless polymer [1].

Although other derivatives capable of free radical polymerization have been described, commonly, most PEG derivatives are functionalized with methacrylate groups and acrylate at the chain ends.

In this study, the copolymer bead was synthesized by suspension polymerization based on sodium methallyl sulfonate (SMS) and poly(ethylene glycol) diacrylate (PEGDA). Immersing the bead in sulfuric acid was performed to introduce protons instead of sodium ion. The chemical structures of the bead were characterized by their FT-IR. The basic properties of bead such as water uptake, ion exchange capacity

(IEC) were measured for the prepared ion exchange beads. The metal adsorption tests were performed to analyze properties of beads in waste water. The surface morphology obtained by SEM showed the pore and sphere approximately.

### 2. Experimental

Sodium methallyl sulfonate (SMS; 98%), and poly(ethylene glycol) diacrylate (PEGDA) were supplied by Aldrich used as monomer. Toluene (99.5%) was also purchased by Aldrich used as porogen. Benzoyl peroxide was obtained from Lancaster. All of materials were high-purity grades used without further purification

Ion exchange beads were produced in a 500 ml three-necked. Copolymer was synthesized by suspension polymerization in various monomer weight ratios. The distilled water (containing the desired amount of PVA), the solvent, was put into a reactor with reflux condensation. The mixture of monomers was transferred into the dispersion medium, and then the initiator in porogen was added to the flask. The reactor temperature was kept at 70 °C for 4 h. The solution was filtered after polymerization In order to separate pure beads.

The yields of SAS-PEGDA beads after polymerization were determined by

gravimetric analysis. The yields were calculated according to the following equation (1).

$$\text{Yields} = \frac{W_d}{W_m} \times 100 \quad (1)$$

where  $W_d$ =weight of clean and dry polymer beads (g) and  $W_m$ =weight of monomer initially charged to the reactor (g).

The IEC was calculated according to the following equation [6]:

$$\text{Ion exchange capacity} \left( \frac{\text{meq}}{\text{g}} \right) = \frac{(V_{\text{NaOH}} \times N_{\text{NaOH}}) - (V_{\text{HCl}} \times N_{\text{HCl}})}{\text{Weight of sample}} \quad (2)$$

where  $N_{\text{NaOH}}$  and  $N_{\text{HCl}}$  are the concentrations of the NaOH and HCl solutions, respectively, and  $V_{\text{HCl}}$  and  $V_{\text{NaOH}}$  are the volumes of HCl and NaOH solutions, respectively.

### 3. Results and discussion

The yields of the SMS/PEGDA beads determined from Eq.(1) are plotted in Fig. 1. When the beads were weighed, all the beads were individual dried beads not aggregates. The aggregates and initial reactant like monomers were removed in the washing step. Accordingly, all these losses were included in these yields values.

The ion exchange capacities of H-form SMS-PEGDA beads were determined, and the results were shown in the Fig. 2. The ion exchange capacities increased with increasing amount of SMS as expected. The space between the polymer chains was different from each crosslinking density due to PEGDA content at each molecular ratio. Thus, crosslinking density was decreased with decreasing PEGDA content and at that time IEC value showed high property because of permeation of sulfuric acid into

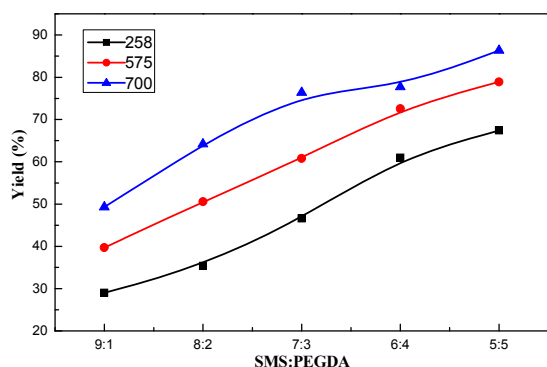


Fig. 1. Yields of SMS/PEGDA copolymer bead.

the SMS-PEGDA well.

### 4. Conclusion

A copolymer bead based on sodium methallyl sulfonate-poly(ethylene glycol) diacrylate (SMS/PEGDA) was synthesized by suspension polymerization.

The yield values of beads increased with increasing amount of PEGDA contents and its molecular weight

The SMS/PEGDA ion exchange beads were characterized by ion exchange capacity, water uptake, yield, adsorption properties. The ion exchange capacity and water uptake values of beads increased with increasing amount of SMS contents due to the increased content of sulfonic groups in the beads. However, ion exchange capacity values of beads increased with decreasing molecular weight of PEGDA while water uptake values of beads increased with increasing molecular weight of PEGDA.

- [1] R. Arshady, *BIOMATER.* 14, 5 (1993).
- [2] F. Amadeo, B. Muirel, B. Dominique, *REACT. FUNCT. POLYM.*, 56, 123 (2003).
- [3] Z. Cheng, P. Werner, H.U. Moritz, P. Jan, H.J. Warnecke, *CHINESE J. CHEM. ENG.* 7, 332 (1999).
- [4] L. Li, J. Cheng, X. Wen, P. Pi, Z. Yang, *CHINESE J. CHEM. ENG.* 14, 471 (2006).
- [5] S.A. Bencherif, A. Srinivasan, J.A. Sheehan, L.M. Walker, C. Gayathri, R. Gil, J.O. Hollinger, K. Matyjaszewski, N.R. Washburn, *ACTA. BIOMATER.* 5, 1872 (2009).
- [6] Y.J. Choi, H.S. Lee, T.S. Hwang, *POLYMER KOREA* 33, 608 (2009).

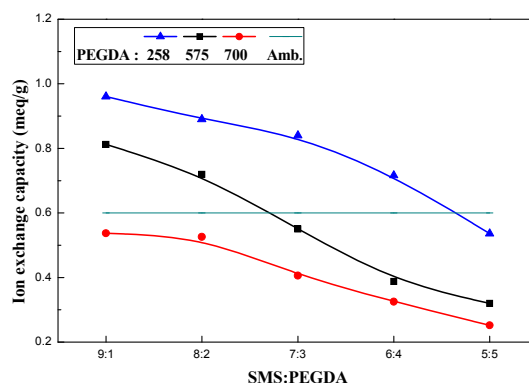


Fig. 2. Ion exchange capacity of SMS/PEGDA copolymer bead.

## Synthesis of phosphonic type micro bead by suspension polymerization and its adsorption properties

Noh-Seok Kwak, Seon-Ho Lee, Taek Sung Hwang\*

Department of Chemical Engineering, College of Engineering,  
Chungnam National University, 79 Daehang-no, Yuseong-gu, Daejeon 305-764, South Korea

### Abstract

The micro beads were synthesized by suspension polymerization based on vinyl phosphonic acid, methacrylic acid and poly(ethylene glycol) diacrylate and its indium adsorption properties were investigated. The micro beads were wrinkled sphere at all components and their sizes ranged from 100-200  $\mu\text{m}$ . The structures of the micro beads were confirmed by Fourier transform infrared (FT-IR) spectroscopy. The strong band at  $1194\text{ cm}^{-1}$  was ascribed to stretching vibrations for P=O and the absorption band at  $965\text{ cm}^{-1}$  was assigned to the P-OH stretching band. The micro beads have a thermal stability up to  $260^\circ\text{C}$ . Synthetic yields and ion exchange capacity decreased as the increase in VPA content and water uptake increased as the increase in VPA content. The maximum amount of adsorption predicted by Langmuir adsorption isotherm model was the highest at the molar ratio of 5:5.

### 1. Introduction

The consumption of indium is increasing with the rapid development of industry. Nevertheless, indium is widely spread in nature and generally in low concentrations in some sulfide ores of zinc, copper and lead. For this reason, indium recovery technology is desirable.

A few researches on metal recovery using an ion exchanger have been reported. M.C.B. Fortes et al. reported on the indium adsorption onto some ion exchangers of different organic functional groups such as iminodiacetic acid, diphosphonic acid and aminophosphonic acid [1]. F.D. Mendes et al reported on the adsorption of nickel and cobalt onto some commercially available chelating ion exchange resins [2]. However most of researches on indium recovery using an ion exchanger have mentioned only about its adsorption properties of commercially available ion exchangers. Therefore, in this study, the micro beads for the use of ion exchange were prepared by the suspension polymerization and their adsorption

properties were investigated.

In this study, the micro bead was synthesized by suspension polymerization based on vinyl phosphonic acid (VPA) and methacrylic acid (MAA) used as a monomer and poly(ethylene glycol) diacrylate (PEGDA) used as a crosslinking agent. The structure and morphology of micro bead were confirmed by Fourier transform infrared (FT-IR) and scanning electron microscope (SEM). And then, adsorption properties of the micro bead were investigated.

### 2. Experimental

Poly (VPA-co-MAA) with different monomer ratio was synthesized by suspension polymerization. The polymerization was conducted in a 500 mL, 3-neck round bottom flask equipped with a stirrer, condenser, nitrogen inlet, thermometer, and dropping funnel. VPA, MAA, and PEGDA were dissolved in the mixture of distilled water and PVA at  $65^\circ\text{C}$ . The solution was under strong agitation

continuously until all the monomers were completely dissolved. And then, BP as an initiator and toluene were put in the solution with a dropping funnel. The polymerization was carried out in an airtight equipment at 65°C for 1~2 hr.

**Table 1-** The synthetic conditions of poly (vinyl phosphonic acid-co-methacrylic acid)

Monomer		C.A	Initiator
VPA	MAc	PEGDA	Toluene
0%	100	30~50%	Same with PEGDA
25%	75%		
50%	50%		
75%	25%		
100%	0%		

### 3. Results and discussion

The synthetic yields of poly (VPA-co-MAA) are shown in Fig 1. The maximum synthetic yield was 82% in the absence of VPA. The synthetic yields, however, were dependent on the VPA content and a decreasing trend in the yield was observed. It shows that conversion of VPA radical is lower than MAA and PEGDA. The synthetic yields were also proportionate to the concentration of crosslinking agent due to the increase in crosslinking agent and the consequential decrease in VPA. The micro bead, meanwhile, was not formed at the 20 wt% crosslinking agent.

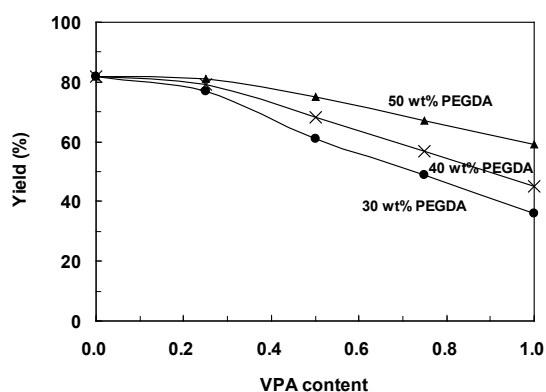


**Fig. 2** – The effect of VPA content and crosslinking agent concentration on the poly(VPA-co-MAA) yields.

The IEC provides an indication of the acid group content in the micro bead. The

experimental IEC values are given in Fig. 2. The IEC values increased as the decrease in VPA and the consequential increase in MAA. This is an indication that a plenty of sodium were adsorbed onto the functional group of –COOH rather than –PO<sub>3</sub>H<sub>2</sub> and the conversion of VPA is lower than MAA and PEGDA. It is the same result with the Fig. 2 and Table 2. The IEC meanwhile was dependent on the amount of crosslinking agent and the values increased to a maximum of 0.822 due to the decrease in the crosslinking density of the micro beads.

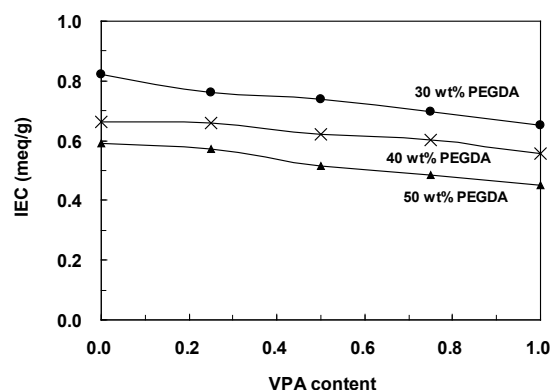


**Fig. 6** – Effect of VPA contents and crosslinking agent concentration on the ion exchange capacity.

### 4. Conclusion

we were able to obtain an optimum condition of preparing micro bead at 30 wt% crosslinking agent and 5:5 molar ratio of monomers. Furthermore, at the optimum condition, adsorption capacity of indium was 0.70 mmol/g resin, the water uptake was 101% and the synthetic yield was 75%.

[1] M. C. B. Fortes, A. H. Martins, J. S. Benedetto, Indium adsorption onto ion exchange resins, *Miner. Eng.* 16 (2003) 659-663.

[2] F. D. Mendes, A. H. Martins, Selective sorption of nickel and cobalt from sulphate solutions using chelating resins, *Int. J. Miner. Process* 74 (2004) 359-371.



## Indium adsorption experiment with continuous electrodeionization System

Seon-Ho LEE<sup>1</sup>, Noh-Seok KWAK<sup>2</sup>, Taek Sung HWANG<sup>2</sup>

<sup>1</sup> Department of Green Energy Technology, Graduate School of Green Energy Technology, Chungnam National University, Daejeon 305-764, Korea

<sup>2</sup> Department of Applied Chemistry and Biological Engineering, College of Engineering, Chungnam National University, Daejeon 305-764, Korea

\* [tshwang@cnu.ac.kr](mailto:tshwang@cnu.ac.kr)

### Abstract

In this research the principle of electrodialysis is described and its advantages and limitations in various applications are pointed out. More recent developments in electrodialysis as well as in related processes such as electroalytic water dissociation or continuous electrodeionization are discussed and their present and potential future applications are indicated. Purolite S930 is Indium adsorption resins. We must recover the Indium with continuous electrodeionization system.

### Introduction

Electrodialysis is a mature process which is applied since more than 50 years on a large industrial scale for the production of potable water from brackish water sources.[1] But more recently electrodialysis in combination with bipolar membranes or with ion-exchange resins has found a large number of new interesting applications in the chemical process industry, in the food and drug industry as well as in waste water treatment and the production of high quality industrial water.[2]

Recent work on the recovery of copper from aqueous solutions via membrane technologies has included the use of liquid membranes to separate indium from ions in chloride solutions.

### Experiment

The studied solution contained indium. Its initial composition is given in Table 1.

Table 1. Initial concentrations in the studied solution.

	Concentration In(III) (g/L)	Current density ( $Am^{-2}$ )
ED01	1.0	200
ED02	1.0	225
ED03	1.0	250

The cell design is as follows (see Fig. 1):

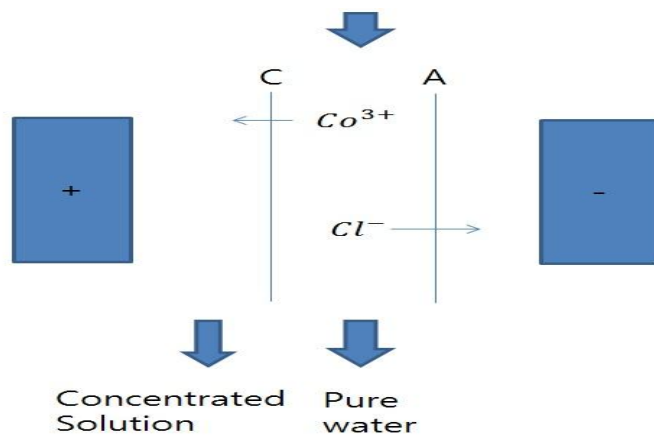
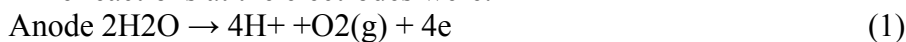


**Fig. 1.** Sketch of a three-compartment cell stack. C and A indicate cation-exchange membranes and anion-exchange membranes, respectively.

The reactions at the electrodes were:



Test times for various experiments were 4 and 24 h. A 24 h test was carried out with the test electrolyte, which was used as working solution in the five-compartment ED cell. The cell current density was  $250\text{Am}^{-2}$ , the temperature was  $25\text{ }^\circ\text{C}$  and the recirculation flowrate was  $17\text{ L h}^{-1}$ .

### Results and discussion

The effect of cell current density is shown in Figs. 2

Fig. 2 shows that the rate of In(III) removal from the working solution towards the cation concentrate clearly increased as the cell current density varied from  $200\text{Am}^{-2}$  to  $250\text{Am}^{-2}$ .

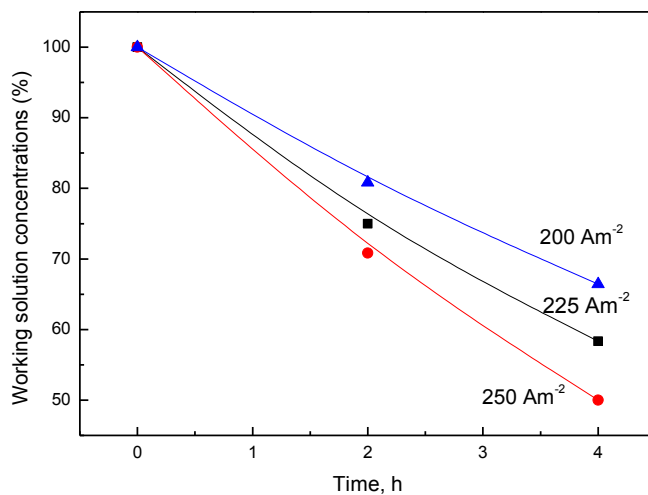


**Fig. 2.** In concentration in the working solution as a function of cell current density and time.

[1] H.Strathmann, *Desalination*, **264**, 268-288 (2010).

[2] Nicoletta Boniardi, Renato Rota, Giuseppe Nano and Bruno Mazza, *Separations Technology*, **6**, 43-54 (1996).

**Withdrawn**

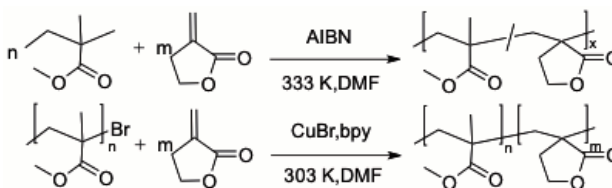
## Preparation and characterization of environmentally friendly polymer materials with $\alpha$ -methylene- $\gamma$ -butyrolactone (MBL) monomer.

Ryosuke OKAZAKI<sup>1</sup>, Yuki TERAYAMA<sup>1</sup>, Hiroe SOEJIMA<sup>2</sup>, Tomoko SHIRAHASE<sup>2</sup>,  
Moriya KIKUCHI<sup>2</sup>, Yuji HIGAKI<sup>1,2</sup>, Atsushi TAKAHARA<sup>1,2</sup>

<sup>1</sup>Graduate School of Engineering, Kyushu University <sup>2</sup>Institute for Materials Chemistry and Engineering, Kyushu University, 744 Motooka, Nishi-ku Fukuoka 819-0395, Japan<sup>1,2</sup>

**Introduction**  $\alpha$ -methylene- $\gamma$ -butyrolactone (MBL), a natural product found in tulip, has the similar chemical structure as methyl methacrylate (MMA). The polymer resulting from radical polymerization of MBL (PMBL), has a remarkably higher glass-transition temperature ( $T_g$ ) of 468 K than a typical  $T_g$  of 378 K for atactic PMMA and exhibits excellent solvent resistance because of the conformational rigidity of the chain incorporating the butyrolactone ring<sup>1</sup>. In this study, we prepared and characterized environmentally friendly novel polymer materials with MBL monomer.

**Experiment** PMMA-*ran*-PMBL copolymers with different MBL/MMA content was synthesized by free radical polymerization. PMMA-*block*-PMBL copolymers with different MBL/MMA content was synthesized by atom transfer radical polymerization<sup>2</sup>. Copolymer films were prepared by solvent cast method with 2,2,2-trifluoroethanol. The glass transition temperature ( $T_g$ ) of MMA/MBL copolymers was measured by differential scanning calorimetry (DSC). The viscoelastic properties were characterized by dynamic viscoelastic analysis. Microphase separated structure of PMMA-*block*-PMBL thin films was characterized by small angle X-ray scattering (SAXS). The thermal stability was measured by thermogravimetry (TG).



Scheme 1. Synthesis of PMMA-*ran*-PMBL and PMMA-*block*-PMBL.

**Result and Discussion** DSC and dynamic viscoelastic measurements revealed that PMMA-*block*-PMBL have two individual  $T_g$  at 400 K and 470 K corresponding to PMMA and PMBL phase, respectively. On the other hands, PMMA-*ran*-PMBL have single  $T_g$  of miscible phase, and the  $T_g$  was improved with an increase of MBL content. SAXS profiles of PMMA-*block*-PMBL film (with PMBL weight fraction of 0.56) were shown in Figure 1. For as cast and annealed sample, the scattering maxima can be detected at relative  $q$  value of 1, 2 or 1, 3, 5, that is assigned to lamella structures. The values of Bragg's spacing  $d$ , which are evaluated from the position of first-order scattering peak, were 22.2 and 31.2 nm, respectively. The annealed sample's domain size is larger than that of as cast sample and 3rd order peak suggesting improvement of the state of phase separation.

### References

- 1) Akkareddi, M. K. *Macromolecules* **1979**, *12*, 546-551.
- 2) Mosnacek J.; Matyjaszewski K. *Macromolecules* **2008**, *41*, 5509-5511.

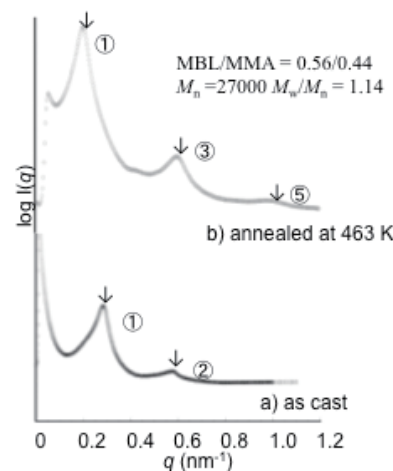


Figure 1. SAXS profiles of PMMA-*block*-PMBL measured at room temperature (a) as-cast and (b) annealed at 463 K for 24h.

## Dual Responsive Triblock Copolymers Based on Polypseudorotaxanes via Atom Transfer Radical Polymerization

Taeyoon Kim, Ildoo Chung

Department of Polymer Science and Engineering,  
Pusan National University, Busan 609-735, Korea

Recently, polymers based on oligo(ethylene glycol) methyl ether methacrylate have been announced as promising thermoresponsive polymers, because these macromolecules with short hydrophilic oligo (ethylene glycol) side chain as well as hydrophobic backbone and terminal methoxy group exhibit a well defined lower critical solution temperature (LCST) in water. Triblok copolymer of 2-(2-methoxyethoxy) ethyl methacrylate (MEO<sub>2</sub>MA) and oligo ethylene glycol ether methyl methacrylate (OEGMA, Mn = 475) were synthesized by atom transfer radical polymerization using the inclusion complex of polyethylene glycol and  $\alpha$ -cyclodextrin macroinitiator. Molecular weights of triblock copolymers were measured by GPC and MALDI-TOF. The ratio of copolymer composition was measured by NMR spectrometer. Their LCST determined by UV-Vis spectrometer and DLS technique were used to evaluate their dual responsivities such as pH and temperature. The resulting triblock copolymers have shown controllable dual reponsivites and may have potential applications for drug delivery system.

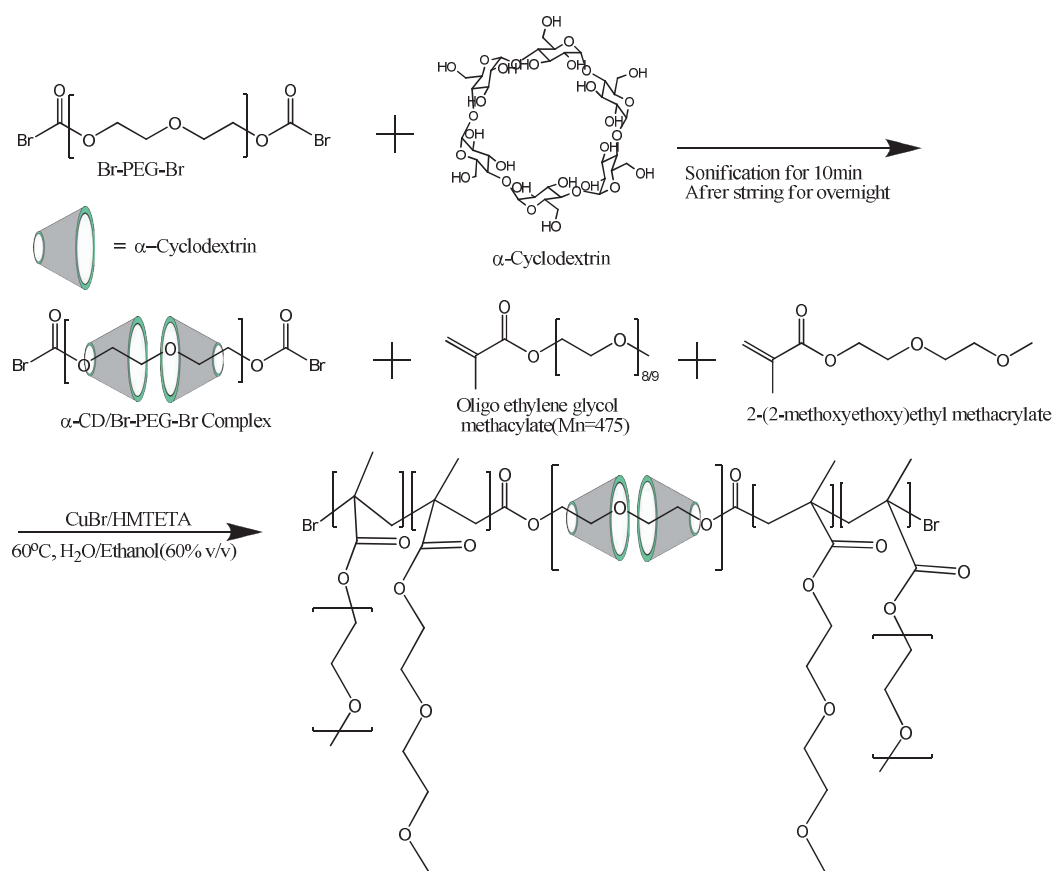


Fig. 1. Synthesis of triblock copolymer.

## References

- [1] Lutz, J.-F.; A. Hoth, *Macromolecules* 2006, 39, 893-896
- [2] Yamamoto, S.-I.; Pietrasik, J.; Matyjaszewski, K., *Macromolecules* 2007, 40, 9348-9353
- [3] Dong, H.; Mantha, V.; Matyjaszewski, K., *Chem. Mater.* 2009, 21, 3965–3972

## Preparation and Characterization of Poly (lactic acid) Hybrids With Polymer Grafted Imogolite

Tomoko SHIRAHASE<sup>1</sup>, Wei MA<sup>2</sup>, Hiroe SOEJIMA<sup>1</sup>, Ryosuke OKAZAKI<sup>2</sup>,  
Atsushi TAKAHARA<sup>1,2,3</sup>

<sup>1</sup> Institute for Materials Chemistry and Engineering, Kyushu University, Japan

<sup>2</sup> Graduate School of Engineering, Kyushu University, Japan <sup>3</sup>JST, ERATO, Japan

### INTRODUCTION

Poly (lactic acid) (PLA) is one of the bio-based polymer produced from renewable resources, and it has been widely used as an environmentally benign material. Over the past decades, many studies on mineral reinforced thermoplastics known as nanocomposite have been reported, such as PLA reinforced with layered silica, clay and montmorillonite. In this research, we focus on using imogolite, which is a natural inorganic mineral, as the filler to improve the mechanical properties of PLA. Imogolite is a hydrous aluminosilicate ( $\text{Al}_2\text{O}_3 \cdot \text{SiO}_2 \cdot \text{H}_2\text{O}$ ) nanotube. Fig. 1 shows the schematic illustration of imogolite. In order to improve the dispersibility of mineral in matrix polymer, grafting polymer chains from mineral surface has been studied [1]. Polymer grafted imogolite has the potential as filler for PLA. In our case, poly( $\alpha$ -methylene- $\gamma$ -butyrolactone) (PMBL) and poly methyl methacrylate (PMMA) were grafted from imogolite. PMBL is also one of the bio-based polymers, which has a similar chemical structure with PMMA. In this research, the mechanical properties of PLA/PMMA-g-imogolite and PLA/PMBL-g-imogolite hybrids were studied.

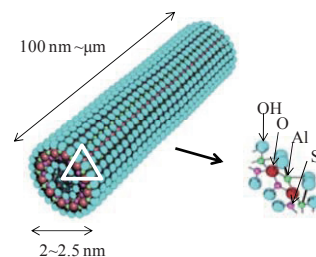


Fig.1. Schematic illustration of imogolite structure.

### EXPERIMENTAL

Imogolite was synthesized by the method of Farmer et al [2]. Fig. 2 shows the steps for the synthesis of PMMA or PMBL grafted imogolite nanotubes. PMMA-g-imogolite or PMBL-g-imogolite was mixed with dried PLA in chloroform or 2,2,2-trifluoroethanol (TFE)

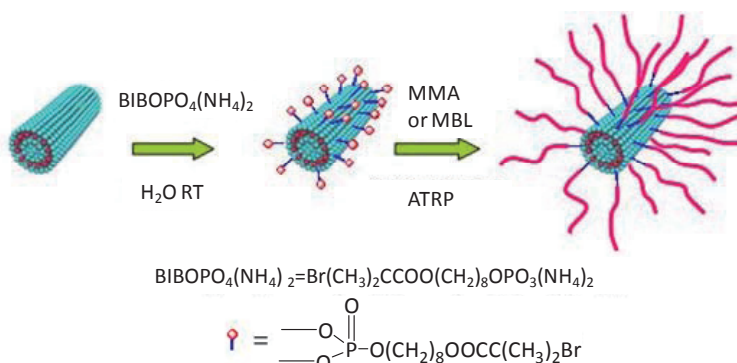


Fig.2. Schematic representation for the synthesis of PMMA grafted imogolite

respectively. The mixture was poured into methanol and PLA/polymer grafted imogolite blend was precipitated. The filtered precipitates were dried and pressed at 453K for 5min, and

then annealed at 383K for 1h. Thermogravimetric analysis (TGA) and dynamic mechanical analysis (DMA) were carried out for the characterization of PLA hybrids.

## RESULTS & DISCUSSION

Fig. 3 shows TGA curves of imogolite and polymer grafted imogolite at the temperature range from 400 to 850K. The weight losses of imogolite, PMMA-*g*-imogolite and PMBL-*g*-imogolite were 19%, 90%, 93%, respectively, indicating that polymer grafted imogolite contained approximately 70% of polymer. PMBL-*g*-imogolite has higher thermal stability compared with PMMA-*g*-imogolite. Fig. 4 shows the temperature dependence of the storage modulus,  $E'$  for PLA and PLA blends. A slight increase in  $E'$  for PLA/PMMA as well as PLA/PMBL blend compared with PLA was observed, because high  $T_g$  component is introduced into PLA. In contrast,  $E'$  of PLA was significantly improved by blending with polymer grafted imogolite. This improvement is ascribed to the fine dispersion of polymer grafted imogolite in PLA

matrix and the physical interactions between PLA matrix and polymer grafted imogolite. The  $E'$  of PLA/PMMA-*g*-imogolite was higher than that of PLA/PMBL-*g*-imogolite. SEM observation revealed that PLA/PMBL-*g*-imogolite contains more aggregates of imogolite than PLA/PMMA-*g*-imogolite. This might be because PLA and PMMA are miscible with weak interaction between components, while PLA and PMBL are immiscible.

## REFERENCES

- [1] W.Ma, H.Otsuka, A.Takahara, *Chem. Commun.*, **47**, 5813 (2011)
- [2] V. C. Farmer, A. R. Fraser and J. M. Tait, *J. Chem. Soc., Chem. Commun.*, 462–463 (1977)
- [3] K. Yamamoto, H. Otsuka, S.-I. Wada, D.-W. Sohn and A. Takahara, *Soft Matter*, **1**, 372–377 (2005)

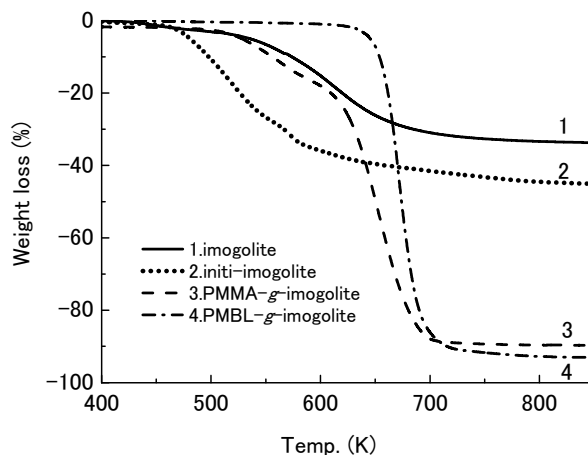


Fig. 3. TGA curves of imogolite and grafted imogolite (10K/min)

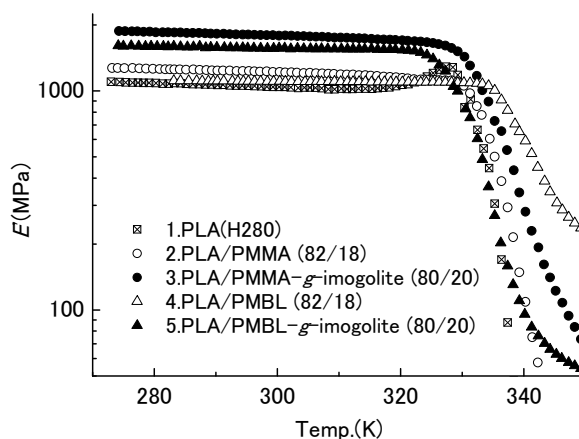


Fig. 4. Temperature dependence of  $E'$  for PLA blends (1K/min at 11Hz)



## Sulfonated polyimide hybrid film through charge-transfer complex formation for proton conductive membrane

Ryohei Watari<sup>1</sup>, Masamichi Nishihara<sup>2,3</sup>, Hideyuki Otsuka<sup>1,2</sup>, Atsushi Takahara<sup>1,2,3</sup>

<sup>1</sup> Graduate School of Engineering, Kyushu University, Japan

<sup>2</sup> Institute for Materials Chemistry and Engineering, Kyushu University, Japan

<sup>3</sup> World Premier International (WPI) Research Center, International Institute for Carbon-Neutral Energy Research (I<sup>2</sup>CNER), Kyushu University, Japan

Sulfonated polyimides (SPIs) are expected to be applied to polymer electrolyte proton membranes for polymer electrolyte fuel cells (PEFCs) [1]. The aromatic polyimides are well known for excellent thermal stability and high mechanical strength. Aromatic SPIs are also expected to have good proton conductivity. However, the stability of the aromatic SPIs against water is poor due to the excessive water uptake. To solve the stability problem, we tried to stabilize SPIs by using charge-transfer (CT) complex formation. Naphthalene diimide (NDI) unit was employed as an electron acceptor. We prepared (SPI/electron donor) hybrid films by mixing proper electron donor molecules such as dialkoxy naphthalenes (DAN). We measured visible spectra of the hybrid films fabricated by solution casting method to confirm that SPIs and DAN formed CT complex in the hybrid films. The mechanical properties of the films were investigated by tensile test. The results showed that Young's modulus and ultimate strength increased with an increase in donor ratio up to 1:1. The mechanical strength, however, gradually decreased with higher molar ratio of the donor molecules because excess amount of donor molecules acted as mechanical defect in the hybrid films. We evaluated their proton conductivities and water uptake. The hybrid film displayed higher proton conductivity than the Nafion film under low humidity condition. It is indicated that we can achieve high proton conductivity films at under low humidity due to the presence of charge-transfer complex.

[1] Y. Yin, *et al.*, *Macromolecules*. **39**, 1189 (2006)

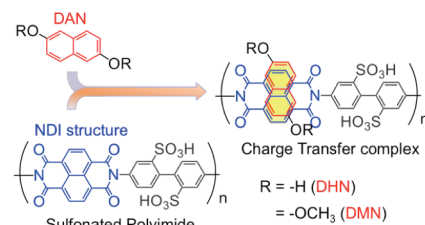


Fig. 1. Charge-transfer complex structure of SPI and DAN

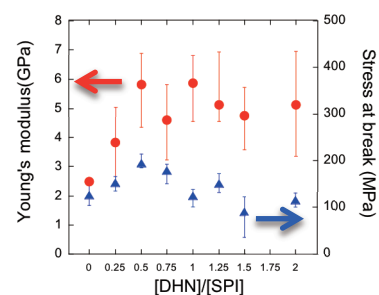


Fig. 2. Relationship of hybrid film compositions and Young's modulus (circle) and stress at break of SPI/DHN complex films (triangle).

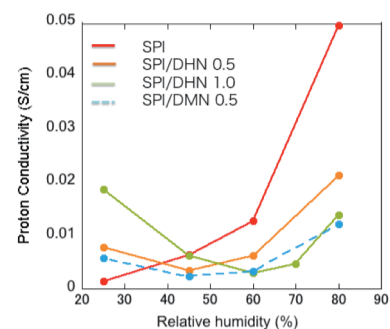


Fig. 3. Relative humidity dependence of proton conductivity of SPI, SPI/DHN and SPI/DMN films at 50 °C.

## Structural Analysis of the Cationic Micelles Made from a Sugar-Bearing and Bromide Cationic Lipid with ASAXS

Takuma Matsuo<sup>1</sup>, Shota Fujii<sup>1</sup>, Yusuke Sanada<sup>1,2</sup> and Kazuo Sakurai<sup>1,2</sup>

<sup>1</sup>The University of Kitakyushu, Japan

<sup>2</sup>JST-CREST, Japan

### [Introduction]

Amphiphilic compounds can aggregate and form the variety of micellar structures in aqueous solutions. Especially cationic lipids can make a complex with DNA, so it is expected as a carrier for drug delivery system (DDS). But it is difficult to control structures of micelles. We synthesized a cationic lipid with C12 alkyl chain (Fig.1), and measured the structure of micelle with anomalous small-angle X-ray scattering (ASAXS) at various pH. The purpose to attach Br is to do ASAXS.

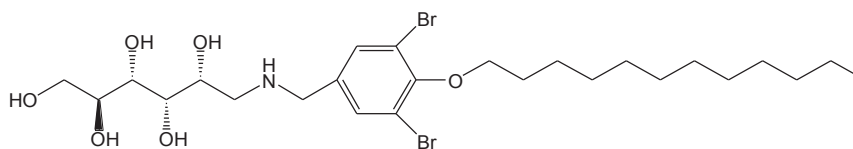


Fig.1 Chemical structure of bromide cationic lipid with sugar-bearing

### [Experimental Section]

We prepared the lipid membrane, and sonicated to disperse in water. The micellar structure of cationic lipid in 50mM NaCl aqueous solution was explored with SAXS. SAXS measurement was performed at the BL40B2 in SPring8, and the incident beam wavelength was tuned at 0.1 nm. The distance between the sample and detector was 1500mm.

### [Results]

Fig.2 shows the SAXS results of the micelle at various pH. For pH 1.9, the micelle formed cylinder. For pH 4.8, it formed vesicle. This result revealed that this lipid undergoes structural transition by pH. ASAXS is in the middle of analysis.

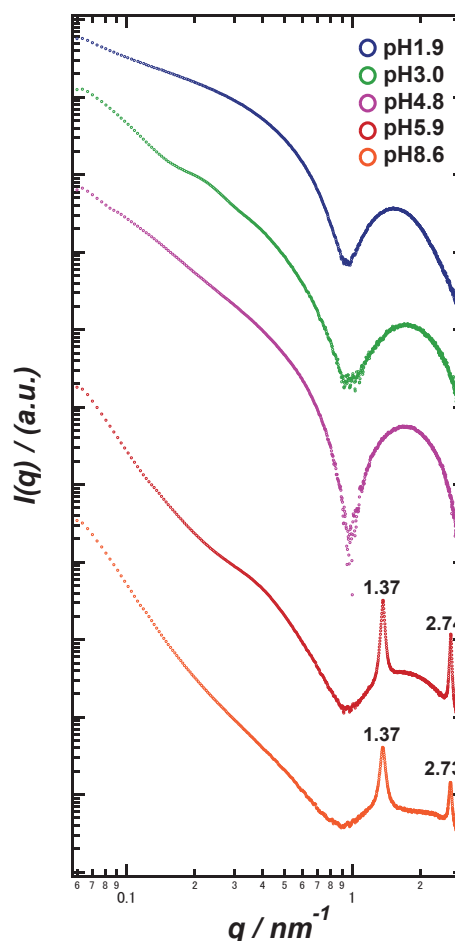


Fig.2 SAXS results at various pH

## Sugar-Bearing Calixarene Lipids to Induce Circular Dichroism and its Structures

Shunsuke Sakamoto<sup>1</sup>, Shota Fujii<sup>1</sup>, Yusuke Sanada<sup>1</sup>, Kazuo Sakurai<sup>1,2</sup>

<sup>1</sup>The University of Kitakyushu

<sup>2</sup>JST-CREST

Amphiphilic compounds bearing rigid structure form stable micelles in aqueous solution. Among of rigid structures, calixarene is useful as building block for amphiphilic compounds because it is easy to be subject to chemical modification to upper and lower rim of calixarene. Although a lot of studies of self-assembled calixarene derivatives have been reported, the structural analysis of micelles formed from amphiphilic calixarene bearing sugar remains unexplored. In addition, sugars have potential to induce helical structure. Here, we reported the synthesis of an amphiphilic calixarene bearing sugar (denoted Gal-CaL3, see Fig.1) and the effect of chirality to micelles structure.

Fig.2 shows CD result of Gal-CaL3 in aqueous solution. This result indicates the structure of micelles is helical structure.

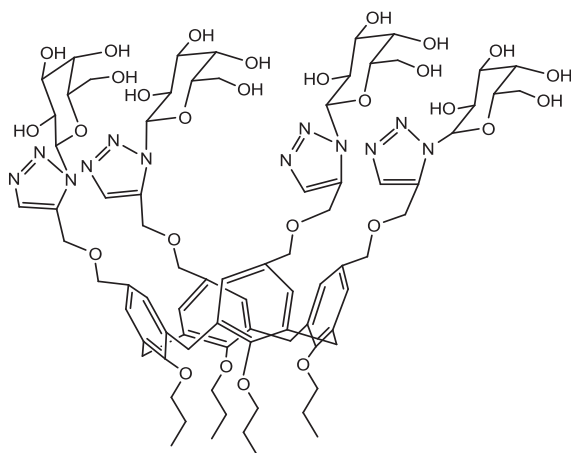


Fig.1 Chemical Structure of Gal-CaL3

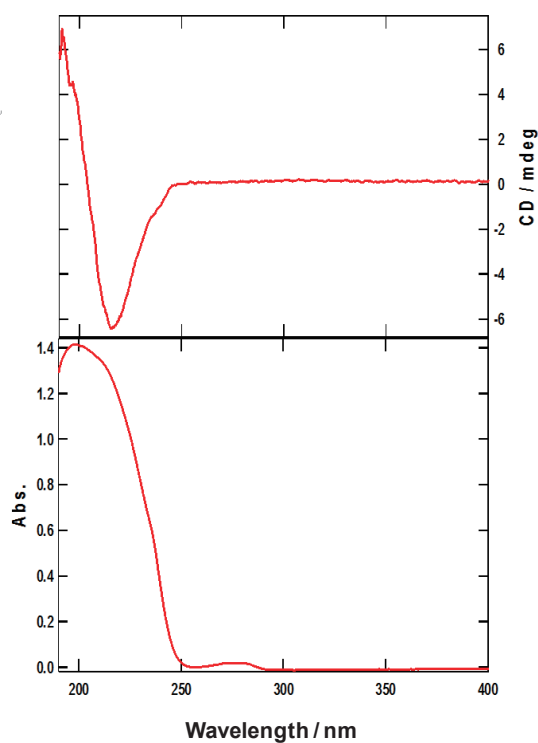


Fig.2 CD and UV Spectra of Gal-CaL3

## Sugar-Bearing Micelle for Targeting DDS and its Structure

Mizuha Sakashita<sup>1</sup>, Shota Fujii<sup>1</sup>, Shinichi Mochizuki<sup>1</sup>, Kazuo Sakurai<sup>1,2</sup>

<sup>1</sup>The University of Kitakyushu

<sup>2</sup>JST-CREST

Micelles are expected as a carrier for DDS (Drug Delivery System). Especially, non ionic lipids bearing sugar are more effective for DDS because the affinity of sugar to body is high and there are a lot of proteins in body which recognize specific a structure of sugars. Among of various sugars, galactose is remarkable because the sugar is recognized by liver parenchyma cell. So we synthesized a new lipid bearing galactose (denoted Gal-lipid, see Fig.1) and study the recognition ability by the cell. In experiment, sample was prepared by mixing cationic lipid (DOTAP) to make complex with DNA and the sample is called D\_Gal-lipid, D\_Glc-lipid which is control sample.

Fig.2 shows QCM results of the interaction between D\_Gal-lipid/DNA complex or D\_Glc-lipid/DNA complex and RCA<sub>120</sub>. This result indicates recognition ability is improved by galactose. Fig.3 shows the transfection efficiency by D\_Gal-lipid and D\_Glc-lipid using HepG2 cell. This result reveals that Gal-lipid helps the recognition by liver parenchyma cell of complex improve.

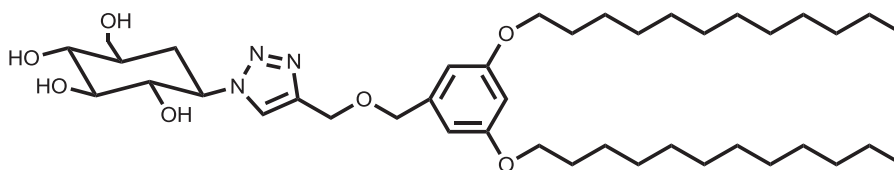


Fig.1 Chemical Structure of Gal-lipid

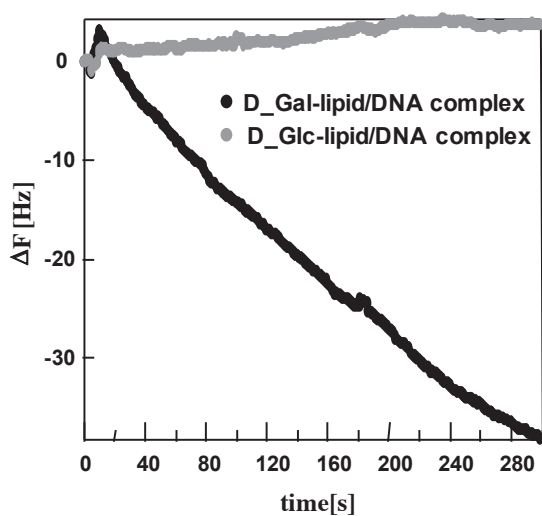


Fig.2 The results of QCM.

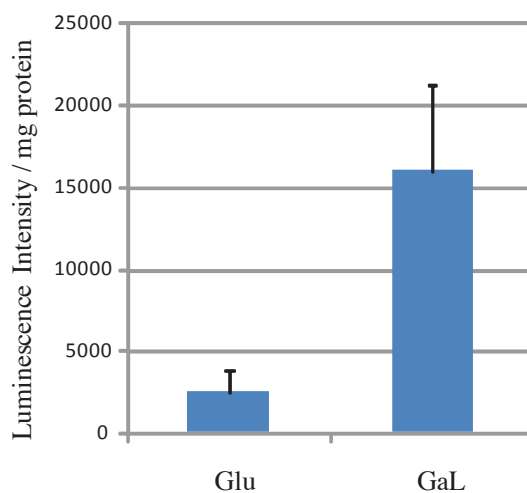


Fig.3 The transfection efficiency by D\_Gal-lipid and D\_Glc-lipid.

## Double Anomalous Small-angle X-ray Scattering Analysis of Poly(4-vinylphenol)-block-Poly(4-bromostyrene) Micelle

Megumi Sakou<sup>1</sup>, Atsuro Takechi<sup>1</sup>, Hiroyasu Masunaga<sup>2</sup>, Kazuo Sakurai<sup>1,3</sup>, Isamu Akiba<sup>1,3</sup>,

<sup>1</sup>Department of Chemistry, The University of Kitakyushu, Japan

<sup>2</sup> Japan Synchrotron Research Institute /Spring-8, Japan, <sup>3</sup> JST-CREST

Anomalous small-angle X-ray scattering (ASAXS) is expected to be a useful method for detail analyses of nano-sized materials. Especially, the ASAXS using the absorption edge of bromine should be useful for the analyses of soft organic materials [1]. In this study, internal structure of polymeric micelle of poly(4-vinylphenol)-*b*-poly(4-bromostyrene) (PVPh-*b*-PBrS) diblock copolymer in alkaline solution was investigated by double anomalous small-angle X-ray scattering (ASAXS) in the vicinities of absorption edges of bromine and rubidium to obtain structure of the micelle of core and shell respectively.

PVPh-*b*-PBrS diblock copolymer was synthesized by sequential nitroxide-mediated radical polymerization (NMRP) by using TEMPO and AIBN. The PVPh-*b*-PBrS was dissolved in RbOH aqueous solution at 10 mg mL<sup>-1</sup>. ASAXS measurements were carried out at BL-40B2 station of SPring-8, Japan.

Fig. 1 shows resonant terms of bromine [panel (a)] and rubidium [panel (b)] obtained from energy-dependences of SAXS intensities near Br and Rb K-edges, respectively. ASAXS analysis revealed that the PVPh-*b*-PBrS micelle had core composed of PBrS chains with 47 nm radius (Fig.1 (a)), and had shell of PVPh chains described with Corona model [2] (Fig.1 (b)). Using the double ASAXS, structure of the micelle of core and shell were calculated respectively, and then whole structure of the micelle was estimated from the fitting analysis.

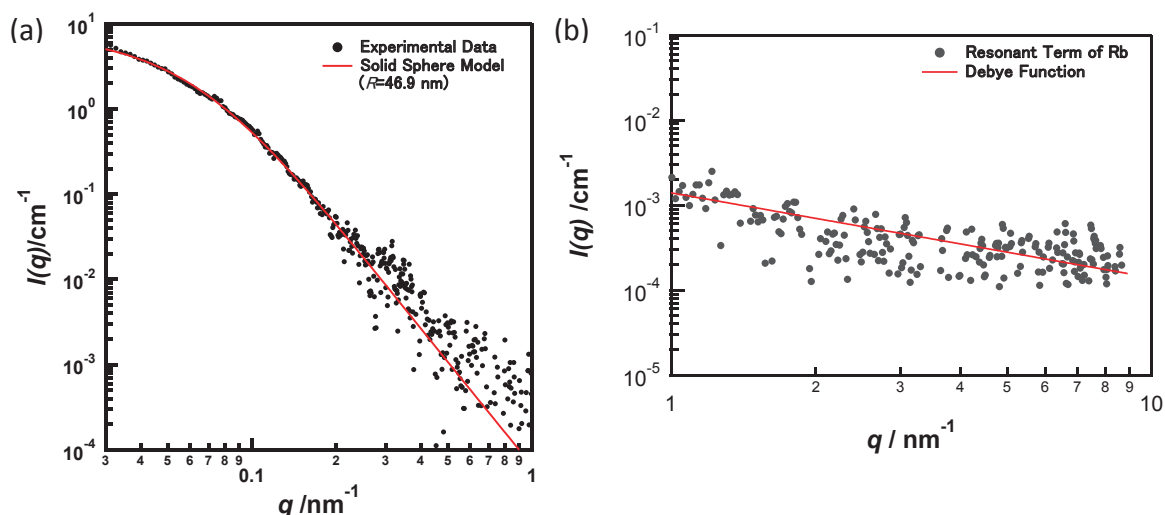


Fig.1. Resonant terms for Br (a) and Rb (b) in SAXS profile from PVPh-*b*-PBrS micelle.

[1] M. Sakou et al, *J. Phys. Conf. Ser.*, 272, 012022 (2010)

[2] N. Dingenouts et al., *Macromolecules*, **37**, 8152 (2004)

## Inverted organic photovoltaic cells having a bulk heterojunction layer and a P3HT layer

Akito Kawanami<sup>1</sup>, Katsuhiko Fujita<sup>1,2</sup>

<sup>1</sup> Department of Applied Science for Electronics and Materials, Graduate School of Engineering Sciences, and

<sup>2</sup> Institute for Materials Chemistry and Engineering, Kyushu University, Japan

### Introduction

Organic photovoltaic cells (OPVs) are attracting much attention due to the light and flexible nature and the potential of low cost production. To improve the device performance, the structure of an active layer should be optimized as well as development of new active materials giving higher optical and electrical properties. Concerning the structural optimization, it is known that p-i-n structure, which is the stacked structure of a donor (p) layer, a donor-acceptor mixture (i) layer and an acceptor (n) layer, gives relatively high performance in small molecule OPVs fabricated by vacuum deposition[1]. We have developed evaporative spray deposition using ultradilute solution (ESDUS) technique which enables layer-by-layer deposition of polymers soluble to a same solvent. It has been reported that the stacked structure of a donor layer and a donor-acceptor mixture (BHJ) layer was successfully constructed to improve the photocurrent[2]. In the present study we fabricated an inverted type BHJ OPVs by ESDUS technique and investigate the effect of the p-layer between the BHJ layer and the hole collecting electrode.

### Experimental

The OPV devices (Figure 1) were fabricated as follows. On a pre-cleaned and 2 mm stripe patterned indium tin oxide (ITO) glass substrate 0.1 wt% solution of cesium carbonate,  $\text{Cs}_2\text{CO}_3$ , in 2-ethoxyethanol was spun at 3000 rpm, followed by thermal treatment in air at 150 °C for 15 min. The 1:1 (w/w) mixture of P3HT and PCBM in *o*-dichlorobenzene at the concentration of 3.0 wt% was spun on the  $\text{Cs}_2\text{CO}_3$  coated substrate in nitrogen atmosphere, followed by thermal treatment at 120 °C for 10 min. The thickness was 200 nm. The P3HT layer was deposited by ESDUS technique using  $6.0 \times 10^{-3}$  wt % solution of P3HT in tetrahydrofuran to obtain the thickness at 10, 20 and 30 nm. The reference device without P3HT layer was also fabricated. Then  $\text{MoO}_3$  (3 nm) and Au (50 nm) electrode were thermally deposited in a vacuum evaporator at less than  $10^{-4}$  Pa through 2 mm striped shadow mask. The active area of each OPV devices was 4 mm<sup>2</sup>. The devices were sealed by cover glasses in nitrogen.

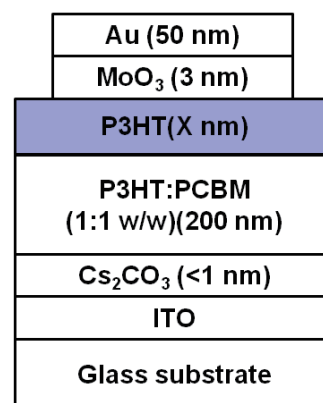


Figure 1. Device structure of the OPV devices (X = 0, 10, 20, 30 nm)

## Results and discussion

The UV-Vis absorption spectra of the OPV devices at the absent position of the electrodes were shown in Figure 2. The absorbance at 510 nm attributed to P3HT was increased corresponding to the P3HT layer thickness while the absorbance at 330 nm attributed to PCBM was almost identical in each device, indicating that P3HT layer was stacked on the BHJ layer.

Figure 3 shows the J-V characteristics of the OPV devices. The open circuit voltage ( $V_{oc}$ ), short circuit current ( $J_{sc}$ ), fill factor (FF), power conversion efficiency (PCE) were listed in Table 1. The device has 10 nm P3HT layer showed improved characteristics compared to the reference device in all parameters. Especially, the increase of  $J_{sc}$  should indicate that the electrons transported through PCBM in the BHJ layer would be blocked at the BHJ/P3HT interface, reducing the carrier elimination at the hole correcting electrode. The devices with the thicker P3HT layer (20, 30 nm) gave relatively lower PCE. It indicated that the P3HT thicker than 10 nm acts as a mere resistance. Although the total thickness of the active layer increased, the exciton generated away from the interface at the thicker P3HT layer could not reach the heterojunction and therefore, cannot contribute to the carrier generation.

### Acknowledgement

This work was financially supported by KAKENHI (B) No.21350102.

### Reference

- [1] T. Taima et al., *Appl. Phys. Lett.*, **85**, 6412 (2004).
- [2] R. Maeda et al., *J. Photopolym. Sci. Technol.*, **22**, 526 (2009).

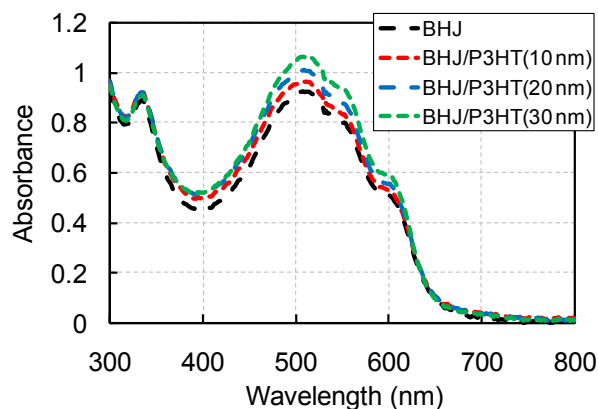


Figure 2. Absorption spectra of the OPV devices

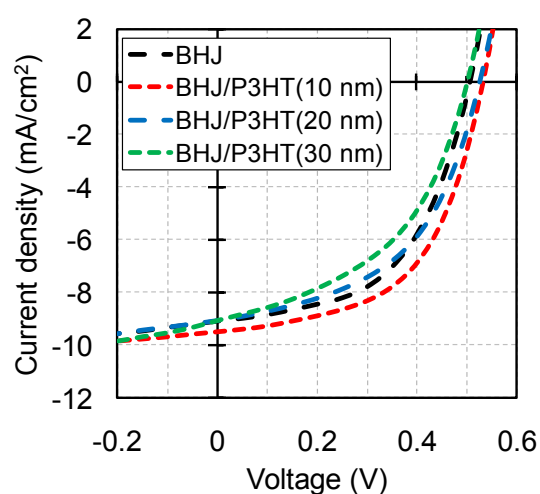


Figure 3. J-V characteristics of the OPV devices under AM1.5 solar simulator at  $100 \text{ mW/cm}^2$

Table 1. Photovoltaic characteristics of the OPV devices

Device	$V_{oc}$ (V)	$J_{sc}$ ( $\text{mA/cm}^2$ )	FF (%)	PCE (%)
BHJ	0.51	9.08	53	2.45
BHJ/P3HT(10 nm)	0.53	9.51	55	2.75
BHJ/P3HT(20 nm)	0.53	9.09	49	2.38
BHJ/P3HT(30 nm)	0.50	9.05	46	2.10

## Influence of interfacial modification by metallic oxide layer in organic resistive memory device

Kimura, M.<sup>1</sup>, Yasui, K.<sup>3</sup>, Ozawa, M.<sup>3</sup>, Odoi, K., Fujita, K.<sup>1,2</sup>

<sup>1</sup>Graduate School of Engineering Science, Kyushu-University, Japan

<sup>2</sup>Institute for Materials Chemistry and Engineering, Kyushu-University, Japan

<sup>3</sup>Nissan chemical Industries, Ltd., Japan

Recently, much attention has been paid to the organic memories for the next-generation nonvolatile memory. However, the driving mechanism has not been clarified yet and the device yield and endurance are poor to practical applications. The devices show two resistive states (ON/OFF states). We have shown that ON state should be caused by the conductive filaments formed by nanoparticles (NPs) in the polymer matrix (filamentary conduction model). Some particle aggregates initially formed at the bottom electrode interface could be the beginning points of filament growth. In this case, a large current locally flows to top electrode through the intermediary of fine filaments. As a result, Al top electrode is oxidized. Therefore, device yield and cycle endurance are poor. It would be important to protect top electrode from oxidation reaction. In this study, we report on the memory characteristics of an organic resistive memory device consisting of composite film with content-varied Au nanoparticles (NPs) in hyper-branched polystyrene (HPS). We fabricated organic memory device which is the interfacial modification at the top electrode. We chose  $\text{TiO}_2$  and  $\text{MoO}_3$  as an interfacial modification layer, because of their thermal stability.

The device structure fabricated is shown Fig. 1. We applied HPS as host polymer and Au NPs which is protected by HPS (HPS-Au) as NPs. HPS-Au was prepared as previously reported [ref.1]. HPS-Au, which contains Au in 4.5 wt.%. Interface-modified device was fabricated by the following procedures. At first, we formed Al bottom electrode by vacuum vapor deposition on glass substrate cleaned by ethanol boiling treatment and UV- $\text{O}_3$  treatment (NL-UV253, Nippon Laser Denshi). And we spincoated o-dichlorobenzene solution of HPS and HPS-Au (4.5 wt.%) mixture (3:1, w/w), followed by thermal treatment in  $\text{N}_2$  atmosphere at 150 °C for 30 min. Then, in  $\text{TiO}_2$  modified case, we spincoated ethanol solution of  $\text{TiO}_2$  NPs (36 mM, 72 mM) followed by thermal treatment in air atmosphere at 80 °C for 15 min.

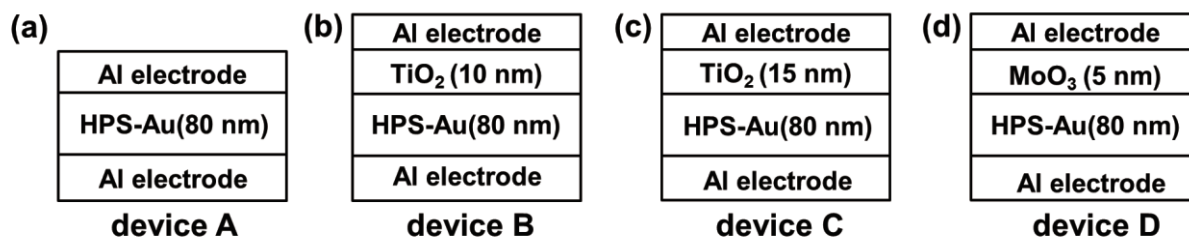


Fig. 1. Device structure:(a)Reference device, (b)Interface-modified device by  $\text{TiO}_2$  (10 nm), (c) Interface-modified device by  $\text{TiO}_2$  (15 nm), (d) Interface-modified device by  $\text{MoO}_3$  (5 nm)



In MoO<sub>3</sub> modified case, we formed MoO<sub>3</sub> layer by vacuum vapor deposition. Finally we formed Al top electrode by vacuum vapor deposition. The cell area was 2×2 mm<sup>2</sup>. We named that reference device is device A, interface modified by TiO<sub>2</sub> (10 nm, 15 nm) is device B, device C, by MoO<sub>3</sub> (5 nm) is device D.

We measured current density-voltage (J-V) characteristics of reference device and interface-modification devices. The result is shown in Fig. 2. Initial conductive state of the devices was low conductive state (OFF state). Current density gradually increased by application of the voltage and abruptly increased and switched to high conductive state (ON state) at ca. 2.0 to 4.0 V. After that, current density decreased by negative differential resistance (NDR). Above NDR region, current density increased monotonously, subsequently, when applied voltage was back to 0 V it exhibited hysteresis without switching to OFF state. After applied voltage turned off, the devices remained ON state. And the devices switched to OFF state when applied voltage swept zero to higher voltage than it of NDR region and instantly cut off. After applied voltage turned off, the devices remained OFF state.

This feature exhibits that our device has non-volatility. As described above, our devices exhibited good electrical bistability. And the statistics of ON and OFF current which was read at 1.8 V is shown in Fig. 4. In Fig. 4, 360 data is included in one plot. The all devices exhibited similar behavior. But current values of interface-modification devices were higher and threshold voltage shift lower than reference device. It is thought that resistance of Al<sub>2</sub>O<sub>3</sub> which is oxidized by local high current is higher than TiO<sub>2</sub> or MoO<sub>3</sub> is a cause in this.

Next, we investigated device yield and cycle endurance. Device yield means the ratio of the device which rightly worked out of fabricated device. And cycle endurance means the number of capable ON/OFF switching. As shown in Fig. 4 interface-modified device showed significantly higher device yield and cycle endurance in comparison with reference device. This would be because interface modified layer effectively protected top electrode from

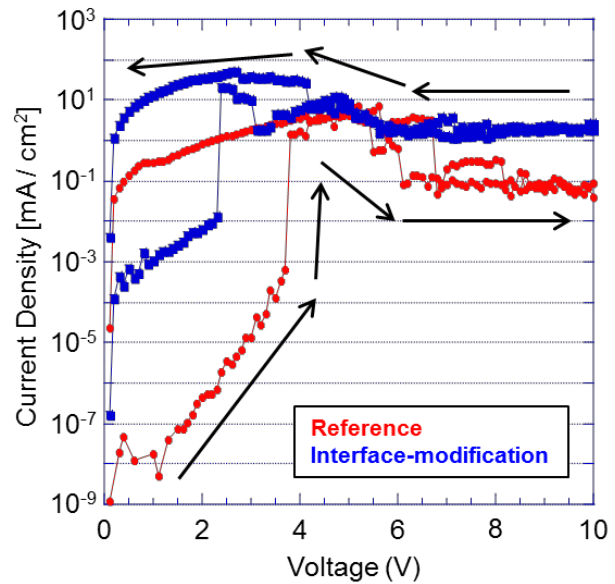


Fig. 2. Current density-voltage characteristics of reference and interface-modification

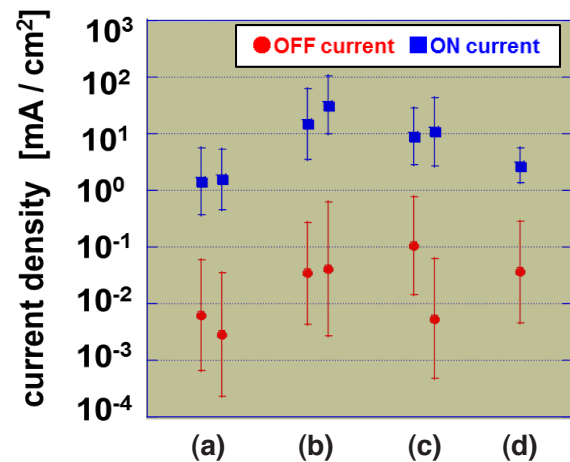


Fig. 3. The statistics of ON and OFF current (a) device A, (b) device B, (c) device C, (d) device D

oxidation reaction which is cause of degredation.

In summary, we fabricated organic memory device of Au nanoparticle/hyper-branched polymer composite film. Our devices exhibited good electrical bistability. And interface modification of the electrode interface by  $\text{TiO}_2$  or  $\text{MoO}_3$  layer could significantly improve reproducibility and performance of device due to protected top electrode from oxidation reaction which is cause of degredation.

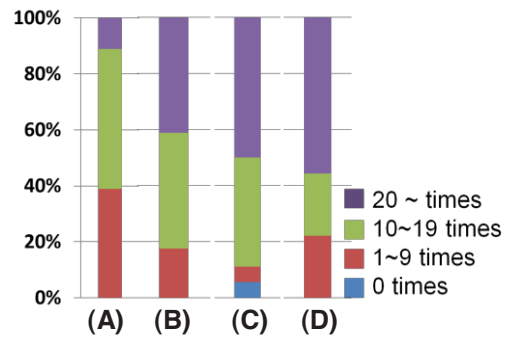


Fig. 4. Device yield and cycle endurance of device A, B, C and D

[1] H. Ichikawa ; K. Yasui ; M. Ozawa ; K. Fujita, *Synth. Met.*, **159** (2009) 973-976

## Electro-Optical Properties of Blue Phase Liquid Crystal by Dual Frequency Driving

Gihwan LIM<sup>1</sup>, Yasushi OKUMURA<sup>2</sup>, Hiroki HIGUCHI<sup>2</sup> and Hirotsugu KIKUCHI<sup>2</sup>

<sup>1</sup> Interdisciplinary Graduate School of Engineering Sciences, Kyushu University, JAPAN

<sup>2</sup>Institute for Materials Chemistry and Engineering, Kyushu University, JAPAN

The narrow temperature range of blue phases (BPs), which had been a crucial issue in practical use, was successfully extended to more than 60 K through polymer-stabilized blue phase (PSBP) [1]. If we use dual frequency liquid crystals (DFLCs), which dielectric anisotropy changes from positive to negative by increasing electric field frequency, as the matrix of blue phases, we will be able to realize novel LC devices with positive and negative birefringence in low and high frequencies, respectively. In this study, we found that the mixtures of the DFLCs and high concentrations of the chiral dopant showed BPs, and confirmed their electro-optical switching.

MJ991526 (Merck) and (s,R)-(R)-1- phenylethane-1, 2-diylbis(4-((1s,4R)-4-pentylcyclohexyl)benzoate)(ZLI4572;Merck) were used as a nematic liquid crystal and a chiral dopant, respectively. Platelet textures of BPs were observed from LC mixture consisting of 81 wt% of MJ991526 and 19 wt% of ZLI4572 filled in ITO-coated glass cells with 4  $\mu\text{m}$  gap over a temperature range of 8 K. Light transmittance of this cell, which changes by intra-cell interference of reflected lights, was controlled by changing optical length of BP through applying electric field (Fig. 1). We compared this electro-optic effect under normal drive by the ON and OFF of the electric field of 1 kHz (Fig. 2a) and dual frequency drive by 10 kHz and 500 kHz of electric field with constant voltage (6.75 V/ $\mu\text{m}$ ) (Fig. 2b). The response times in rise and decay processes from both methods were less than 1 ms.

[1] H. Kikuchi, M. Yokota, Y. Hisakado, H. Yang, and T. Kajiyama, *Nature Materials*, 1, 64-68(2002).

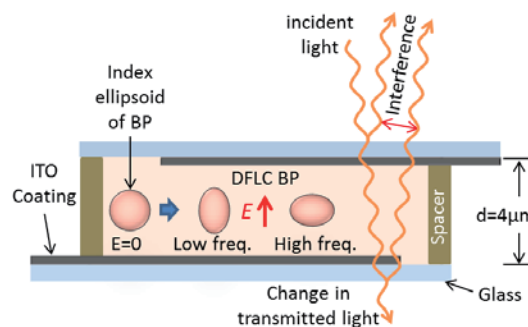


Fig. 1 Structure and principle of transmissive BP device using interference of reflected light controlled by dual frequency electric field.

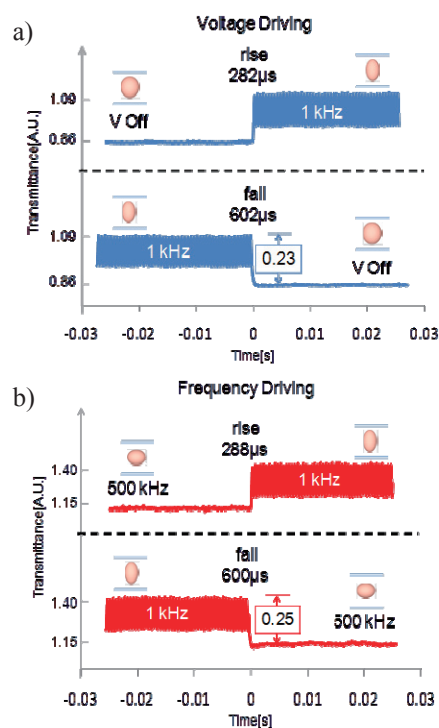


Fig. 2. Response time of transmissive BP device under normal driving and dual frequency driving

## Dye-Sensitized Solar Cells Fabricated with ZnO Nanoparticles for High Conversion Efficiency

Hiroki Yonekawa<sup>1</sup>, Tomohiro Shirosaki<sup>2,3</sup>, Maki Horikawa<sup>2,3</sup>,  
Shoji Nagaoka<sup>2,3</sup>, Makoto Takafuji<sup>1,3</sup>, Hirotaka Ihara<sup>1,3</sup>

<sup>1</sup> Department of Applied Chemistry and Biochemistry, Kumamoto University, Japan

<sup>2</sup> Kumamoto Industrial Research Institute, Japan

<sup>3</sup> Kumamoto Institute for Photo-Electro Organics (Phoenixes), Japan

Among the various oxide semiconductors, ZnO becomes important as an alternative material for dye-sensitized solar cells (DSSCs) because it has not only higher electronic mobility but also bandgap similar to TiO<sub>2</sub> [ref.1]. In addition, ZnO with flat band potential higher than TiO<sub>2</sub> promises enhancing the cell's open-circuit voltage. Therefore, ZnO films have attracted more and more attention in the field of DSSCs. Regardless of these advantages, the highest conversion efficiency of the ZnO-based DSSCs is still less than 7.2% [ref.2], and therefore it cannot even compete with the TiO<sub>2</sub>-based cells [ref.3]. Therefore, it is significant to investigate the effect of fabrication conditions on the performance of ZnO-based DSSCs. In this study, the effect of annealing temperature on the photoelectrochemical properties of DSSCs were explored in order to improve the ZnO-based DSSCs performance.

The ZnO nanoparticles with 15 - 35 nm in average diameter were used in this study to fabricate the ZnO thin film. The ZnO pastes were coated on a conductive glass (FTO, about 13 Ω/sq.) by a squeegee method. The obtained ZnO films were annealed at 100, 200, 300, 400 and 500 °C for 1 h. The dye-sensitized electrodes were prepared by immersing the films in an N719 ethanol solution (0.3 mM) for 3 h at room temperature. The sandwich-type open cells with the obtained ZnO/N719 electrode were fabricated with a spacer film (50 μm), an electrolyte solution and a platinum plate. The electrolyte solution was composed of 0.1 M LiI, 0.6 M 1,2-dimethyl-3-propylimidazolium iodide, 0.05 M I<sub>2</sub> and 0.5 M 4-*tert*-butylpyridine in acetonitrile, and they were filled among both electrodes. The photocurrent (*I*) and photovoltage (*V*) of the cells were measured with an active area of 5 x 5 mm<sup>2</sup> under the AM 1.5 illumination at 100 mW/cm<sup>2</sup>.

Fig. 1 shows the annealing temperature dependencies of conversion efficiency ( $\eta$ ) with each factor obtained from the *I-V* curve of the DSSCs under the present 100 mW/cm<sup>2</sup> light illumination. The  $\eta$  was virtually constant under 200°C, but decreased significantly over 200 °C as shown in Fig. 1(a).

On the other hand, the short-circuit current density (*J*<sub>SC</sub>) decreased gradually with increasing the annealing temperature as shown in Fig. 1(b). The surface area of the ZnO film was virtually constant under 300°C, but it decreased gradually over 300 °C. The amount of adsorbed dye was also decreased along with this changing trend. The decrease of the amount of adsorbed dye led to the decrease of light-harvesting efficiency and *J*<sub>SC</sub> value. However, the

open-circuit voltage ( $V_{OC}$ ) increased slightly with increasing the annealing temperature as shown in Fig. 1(c). Also the fill factor (FF) increased gradually with increasing the annealing temperature at the region of under 200°C, but it decreased gradually at over 200°C as shown in Fig. 1(d). It is known that the FF values are mainly affected by the internal resistances at FTO/TiO<sub>2</sub>, Pt/electrolyte interfaces and the conductive glass substrate [ref.4]. In our experimental condition, the effect of Pt/electrolyte interface could be neglected because the same counter electrode was used for all cells. It is thought that the electron transfer becomes difficult because of the increase of ZnO particles size and the increase of substrate resistance by the annealing at over 300°C, which led to the enhancing of the recombination probability.

In conclusion, the relatively low annealing temperature on the film fabrication is efficient for improvement of ZnO-based DSSCs performance, indicating that possible applications for DSSCs with the ZnO film electrodes would be expanded.

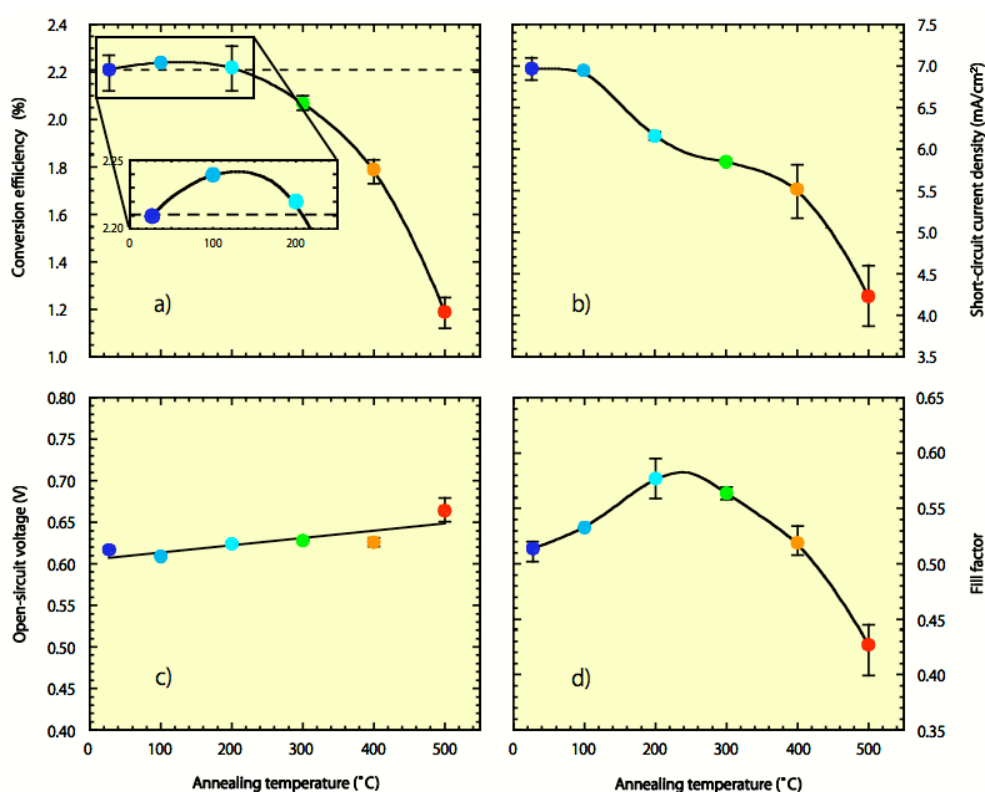


Fig. 1. Annealing temperature dependencies of (a) conversion efficiency, (b) short-circuit current density, (c) open-circuit voltage and (d) fill factor.

## References

- [1] Q. Zhang, C. S. Dandeneau, X. Zhou and G. Cao, *Adv. Mater.*, **21**, 4087 (2009).
- [2] J. B. Xia, F. Y. Li, H. Yang, X. H. Li and C. H. Huang, *J. Mater. Sci.*, **42**, 6412 (2007).
- [3] M. Green, K. Emery, Y. Hishikawa and W. Warta, *Prog. Photovolt: Res. Appl.*, **19**, 84 (2011).
- [4] T. Hoshikawa, M. Yamada, R. Kikuchi and K. Eguchi, *J. Electrochem. Soc.*, **152**, E68 (2005).

## Development of Reversible Cross-Linked Polymeric Micelles with High Durability against Oxygen And Evaluation of Its Function

Masamichi Nishihara<sup>1</sup>, Keiichi Imato<sup>2</sup>, Atsushi Irie<sup>2</sup>, Takeshi Kanehara<sup>2</sup>, Arihiro Kano<sup>2,3</sup>,  
Atsushi Maruyama<sup>2,3</sup>, Hideyuki Otsuka<sup>2,3</sup>, Atsushi Takahara<sup>1,2,3</sup>

<sup>1</sup> World Premier International (WPI) Research Center, International Institute for Carbon-Neutral Energy Research (I<sup>2</sup>CNER), Kyushu University, Japan

<sup>2</sup> Graduate School of Engineering, Kyushu University,

<sup>3</sup> Institute for Materials Chemistry and Engineering, Kyushu University, Japan

Stabilization of polymeric micelles used as drug carriers by various methods such as cross-linking has been investigated<sup>1</sup>. When stimuli-responsive units are employed as cleavable cross-linkers, two conflicting characteristics, the stability of the cross-links under physiological conditions and the cleavability of the cross-links by external stimuli, must be considered. To keep the balance of

these two characteristics, we prepared amphiphilic block copolymer micelles with dynamic covalent bonds as reversible cross-linkers with high tolerance against oxygen (Fig. 1). In this study, diarylbibenzofuranone<sup>2</sup> (DABBF) was employed as a hydrophobic cross-linker owing to its durability to oxygen and autonomous exchange at ambient temperature. The obtained amphiphilic block copolymer containing the DABBF unit has the capability for micellar formation. DABBF was formed using radical dimerization which was conducted in a polymeric micelle aqueous solution. We confirmed the amphiphilic copolymer could form a cross-linking unit with an exchangeable structure by GPC measurement (Fig. 2). Moreover, DABBF could show de-cross-linking behavior in the presence of oxygen by mixing with an excess amount of a de-cross-linker (Fig. 2). This is first example of reversible cross-linked polymeric micelles, formed by dynamic covalent bonding, with high durability against oxygen.

[1] A. Guo, G. Liu, J. Tao, *Macromolecules*, **29**, 2487 (1996).

[2] M. Frenette, C. Aliaga, E. F. Sanchis, J. S. Scaiano, *Org. Lett.* **6**, 2579 (2004).

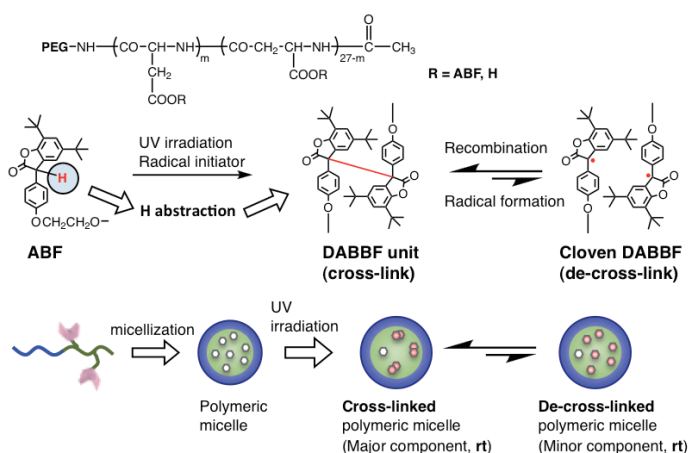


Fig. 1. Chemical structure of DABBF unit and schematic image of reversible cross-linked polymeric micelle.

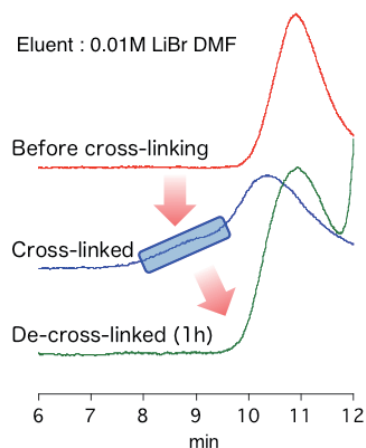


Fig. 2. GPC chromatograms (UV) of lyophilized polymeric micelles. (Top): no cross-linked, (middle): cross-linked and (bottom): de-cross-linked polymer.

## Energy-efficient BTX Separation Using PETLYUK(FTCDC) Column

Minchul Ha, Hosanna Uwitonze, Amit Goyal, Kyu Suk Hwang

Department of Chemical Engineering, Pusan National University, Korea

### INTRODUCTION

In a petrochemical plant, the demand of energy savings for distillation columns to distill multi components has been gradually increasing. Fully thermally coupled distillation columns (FTCDC) which is also known as the Petlyuk column are more efficient than conventional columns. The thermodynamic efficiency of multi components conventional distillation column and the fully coupled column are calculated and compared using the commercial HYSYS software. Simulation study shows that FTCDC can save around 13.4 % of energy cost and requires less investment compared with conventional column.

### BTX SEPARATION PROCESS

In the practical design of distillation columns, an optimum reflux flow is determined first, and the structural importation, such as total number of trays and feed location, is designed later.

Though the commercial design software HYSYS is utilized in the process of 18 components, lack of the structural information may induce lots of computation load in order to find the optimum structural design.

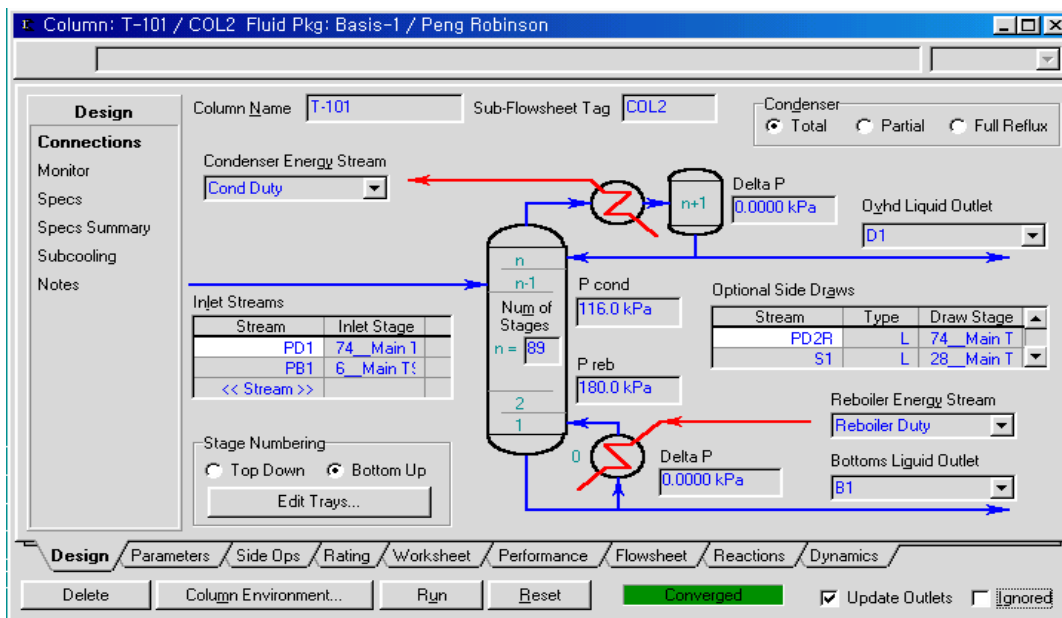
The BTX plant which is one of major processes in a petrochemical plant is composed of four unit processes (hydrotreating, reforming, extraction, fractionation). The products from extraction units are fed to fractionation units, and high purity benzene, toluene, mixed xylene are produced from a series of binary-like columns (benzene column, toluene column and a xylene column). The fractionation units at BTX plants are one of the very complex and the most energy-comsuming process.

Table 1. Compositions of feed and products.

Component	Feed	FTCDC			Conventional 1st		2nd	
		Overhead	Bottom	Side	Overhead	Bottom	Overhead	Bottom
<b>(Light)</b>								
benzene	0.1096	0.9998	0.0000	0.0028	0.9998	0.0030	0.0064	0.0000
dimethyl c-pentane	0.0000	0.0001	0.0000	0.0000	0.0001	0.0000	0.0000	0.0000
<b>(Intermediate)</b>								
methyl c-hexane	0.0000	0.0000	0.0000	0.0000	0.0000	0.0000	0.0000	0.0000
toluene	0.4217	0.0000	0.0087	0.9935	0.0000	0.4721	0.9934	0.0074
n-octane	0.0001	0.0000	0.0000	0.0001	0.0000	0.0001	0.0001	0.0000
<b>(Heavy)</b>								
ethylbenzene	0.0187	0.0000	0.0390	0.0007	0.0000	0.0209	0.0000	0.0396
p-xylene	0.0721	0.0000	0.1520	0.0009	0.0000	0.0807	0.0000	0.1527
m-xylene	0.1603	0.0000	0.3383	0.0018	0.0000	0.1795	0.0000	0.3395
o-xylene	0.0750	0.0000	0.1592	0.0002	0.0000	0.0840	0.0000	0.1589
n-nonane	0.0000	0.0000	0.0000	0.0000	0.0000	0.0000	0.0000	0.0000
n-pentyl benzene	0.0004	0.0000	0.0008	0.0000	0.0000	0.0005	0.0000	0.0009
methyl-ethyl benzene	0.0324	0.0000	0.0689	0.0000	0.0000	0.0363	0.0000	0.0687
tri-methyl benzene	0.0947	0.0000	0.2012	0.0000	0.0000	0.1061	0.0000	0.2006
methyl-n-propyl bz	0.0007	0.0000	0.0015	0.0000	0.0000	0.0008	0.0000	0.0015
di-ethyl benzene	0.0004	0.0000	0.0009	0.0000	0.0000	0.0005	0.0000	0.0009
o-cymen	0.0051	0.0000	0.0109	0.0000	0.0000	0.0058	0.0000	0.0109
tetra-methyl benzene	0.0059	0.0000	0.0126	0.0000	0.0000	0.0066	0.0000	0.0126
penta-methyl benzene	0.0028	0.0000	0.0059	0.0000	0.0000	0.0031	0.0000	0.0059

The structural design procedure is implemented in the design of the industrial FTCDC to replace the first two columns of the conventional fractionation process in BTX plant.

The design outcome and performance comparison with a conventional system indicate that the proposed design procedure is useful to implement the FTCDC for industrial applications. The economics study shows the energy saving of 13.4 % and the investment reduction of 1.7 million dollars from the FTCDC. In addition, a possible extension of the proposed design procedure to industrial application is addressed.



**Fig. 1. Schematic of the Petlyuk column HYSYS simulation**

**Table 2. Structural design and operating condition**

Name	FTCDC		Conventional	
	Prefractionator	Main	1st	2nd
<b>Structural</b>				
number of trays	21(18)	89(82)	60	50
feed/side product	7	28	31	26
interlinking stages		6 74(58)		
<b>Operating</b>				
feed (kg-mol/h)	801.8		801.8	716.1
overhead (kg-mol/h)		86.8	85.70	337.5
bottom (kg-mol/h)		337.7	716.1	378.6
side (kg-mol/h)		377.3		
reflux (kg-mol/h)	290.1	1792	401.3	1106
vapor boilup (kg-mol/h)	492.9	1634	595.2	1315
heat duty (Gcal/h)		14.18	4.95	11.42

## ACKNOWLEDGMENT

Financial support from the Korea Science and Engineering Foundation is gratefully acknowledged.

## REFERENCES

- [1] Y.H. Kim, Chem. Eng. J., 85, (2002) 289
- [2] F. B. Petlyuk, V.M. Platonov, D.M. Slavinskii, Thermodynamically optimal method for separating multi-component mixtures, Int. Chem. Eng. 5 (1965) 555-561



## Au film thickness dependence of Ag particle nanosheet plasmonic coupling

Xinheng Li, Akihito Yoshida, Keisuke Imazu, Koichi Okamoto, and Kaoru Tamada  
 Institute for Materials Chemistry and Engineering, Kyushu University, 6-10-1 Hakozaki,  
 Higashi-ku, Fukuoka 812-8581, Japan

Colloidal metallic nanoparticles (e.g. Ag and Au) have been attractive for their potential applications in biosensors, plasmonic devices etc. due to their size monodispersity, facile surface functionalization, and optical properties in the visible light region, also called localized Plasmon resonance (LPR) absorption<sup>1</sup>. In our previous study, we fabricated highly ordered 2D array of monodisperse Ag particles and interrogated their collective optical properties, e.g. red shifts and sharpened peaks<sup>2</sup>. Recently, we further investigated multilayered Ag nanosheets deposited on the Au thin film with different thickness and observed the gold film thickness dependence of Plasmon peak position and peak width, which are likely to arise from coupling of Ag nanosheets and Au film. In this paper, we describe layer-by-layer structured Ag nanoparticle sheets were deposited by a LB method on Au film with different thickness. As shown in Fig. 1, the surface color after Ag nanosheet deposition on 200 nm Au film changed from yellow to brown to dark red while the color after Ag nanosheet deposition on thinner Au film changed differently. Their absorption spectra of the multilayered Ag nanosheets reveal that plasmon peak and peak width on thick Au film (e.g. 200 nm) varied differently from those on thinner Au film (e.g. 20nm). This strongly suggests a possible interaction between the Ag nanosheets and Au thin film.

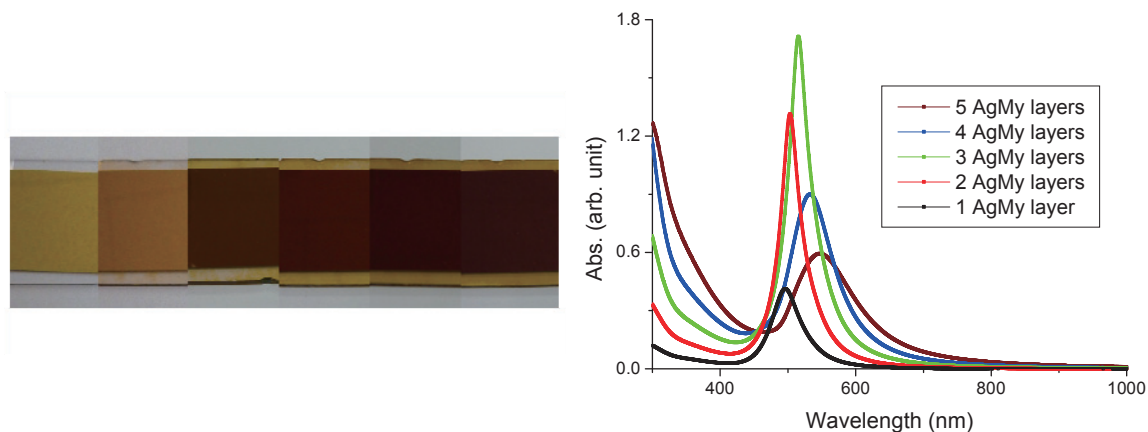


Fig. 1. Optical properties of Ag nanoparticles multilayers on 200 nm Au film. The photos from left to right are 200nm bare Au film, 1-5 Ag nanosheets deposited on 200 nm Au film. The absorption spectra are 1-5 Ag sheets on 200nm Au film, converted from their respective

Ref.

1. E. Prodan; C. Radloff; N. J., Halas; P. Nordlander, *Science* **302**, 419 (2003).

2. M. Toma et al., *Phys. Chem. Chem. Phys.*, **12**, 14749 (2011).

## Catalytic Pyrolysis of Cellulose with ionic liquids

Shinji Kudo<sup>1,2</sup>, Zhenwei Zhou<sup>1</sup>, Koyo Norinaga<sup>1</sup>, Jun-ichiro Hayashi<sup>1</sup>

<sup>1</sup>Institute for Materials Chemistry and Engineering, Kyushu University, Japan

<sup>2</sup>Research and Education Center of Carbon Resources, Kyushu University, Japan

Thermochemical decomposition of cellulosic materials via pyrolysis has been investigated using a variety of techniques to efficiently obtain fuels and fine chemicals. The utilization of chemicals, e.g., mineral acids<sup>[1,2]</sup> and metal ions<sup>[3]</sup>, by impregnating on/in cellulose is effective to reduce the pyrolysis temperature and selectively produce a desired compound. Due to the difficulty of the utilization of solid catalysts, the impregnation method is the most convenient way to catalyze the pyrolysis of cellulose. However, this method is not “catalysis” in a radical meaning because part of the chemicals is consumed during the pyrolysis and therefore cannot be recovered. In the present study, ionic liquids (ILs) were mixed with cellulose at the weight ratio of 1:1 to catalyze the pyrolysis of cellulose. Several types of IL were compared in terms of the influence on the pyrolysis temperature and product distribution, and then a selected IL among them was subjected to a detailed investigation of the potential as a catalyst for cellulose pyrolysis.

Cellulose was simply mixed with ILs, having 1-butyl-2,3-dimethylimidazolium [BMMIM] as a cation and CF<sub>3</sub>SO<sub>3</sub> (OTf), (CF<sub>3</sub>SO<sub>2</sub>)<sub>2</sub>N (NTf<sub>2</sub>), BF<sub>4</sub>, or PF<sub>6</sub> as an anion under ambient conditions. Due to the low content of IL, the samples could be treated as a powder.

Fig. 1. shows the result of Pyrolysis-GC-MS tests (heating rate: ca. 3000 K s<sup>-1</sup>) for each sample. At the pyrolysis temperature of 358°C, [BMMIM]NTf<sub>2</sub> had less or no influence on cellulose pyrolysis, giving a similar

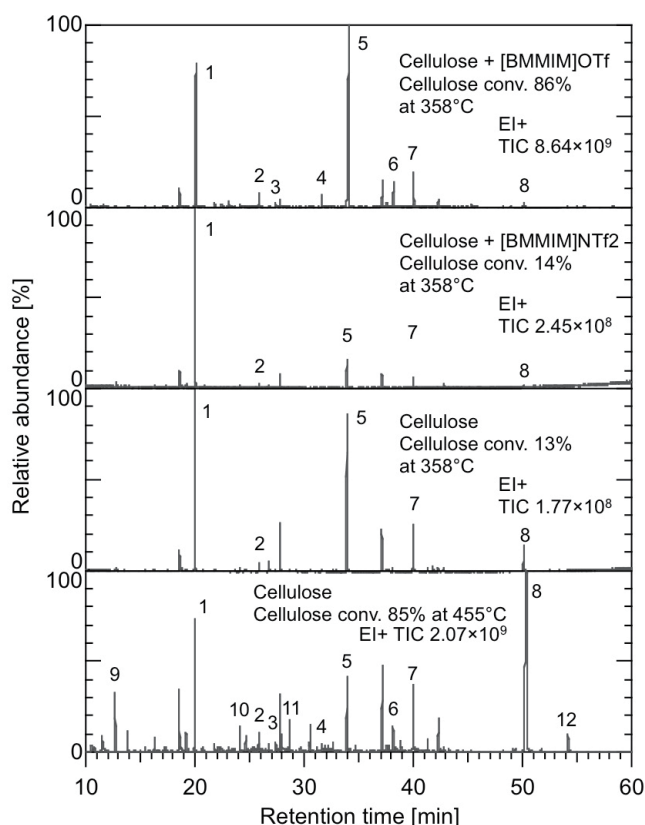


Fig. 1. Pyro-GC-MS chromatograms of cellulose and cellulose mixed with ILs. The main peaks are assigned as follows: 1: Furfural, 2: 2-Furancarboxyaldehyde, 5-methyl-, 3: 2(5H)-Furanone, 5-methyl-, 4: 3-Furancarboxylic acid, methyl ester, 5: Levoglucosenone, 6: 1,4:3,6-Dianhydro- $\alpha$ -D-glucopyranose, 7: 2-Furancarboxyaldehyde, 5-(hydroxymethyl)-, 8: Levoglucosan, 9: Propenone, 1-hydroxy-, 10: 2(3H)-Furanone, dihydro-4-hydroxy-, 11: 1,2-Cyclopentanedione, 3-methyl-, 12: 1,6-anhydro- $\alpha$ -D-galactofuranose.

conversion to that of pure cellulose, while the conversion of cellulose mixed with [BMMIM]OTf was 86%. The same tendency was observed in a thermogravimetric analysis, i.e., [BMMIM]OTf caused a drop in the temperature for the decomposition of cellulose over 100°C compared to that of pure cellulose. As against no influence of [BMMIM]NTf<sub>2</sub>, [BMMIM]BF<sub>4</sub> and PF<sub>6</sub> slightly decreased the pyrolysis temperature, but not significantly. These results indicate that the anion in the ILs has an important role in the catalysis of cellulose pyrolysis.

Principal products from the pyrolysis of cellulose mixed with [BMMIM]OTf were levoglucosenone and furfural, and the yields of the other compounds were very low.

This is very different from the broad product distribution of cellulose pyrolysis at 455°C (cellulose conversion: 85%). Thus, the use of [BMMIM]OTf as a catalyst can not only decrease the pyrolysis temperature, but also contribute to the selective production of these chemicals.

Levoglucosenone is synthetically versatile compound and very expensive since it is not available directly from nature and the chemical synthesis method is limited. In the analysis of the product from slow pyrolysis of cellulose mixed with [BMMIM]OTf (Fig. 2.), the yield of levoglucosenone was 19.0 and 21.4 wt% at 250 and 300°C, respectively. The selectivity of levoglucosenone was more than 70 wt% for condensable organic matters. This yield is far higher than that of the conventionally used acid-catalyzed cellulose pyrolysis method for levoglucosenone production<sup>[4]</sup>. One of the characteristics of the [BMMIM]OTf-catalyzed cellulose pyrolysis is less acceleration of char formation, which is generally found in the use of mineral acids and metal ions for catalysis. Accordingly, it is considered that high reaction selectivity and low char yield resulted in the high yield of levoglucosenone.

Furthermore, [BMMIM]OTf could be fully recovered from the solid residue of pyrolysis by ethanol extraction method, and its reuse for cellulose pyrolysis reproduced the product distribution (Fig. 2. (c) and (d)).

[1] G. Dobelet et al., *J. Appl. Anal. Pyrolysis*, **49**, 307(1997)

[2] D.J. Nowakowski et al., *J. Appl. Anal. Pyrolysis*, **83**, 197(2008)

[3] D.J. Nowakowski et al., *J. Appl. Anal. Pyrolysis*, **83**, 12(2008)

[4] Z. Wang et al., *ChemSusChem*, **4**, 79(2011)

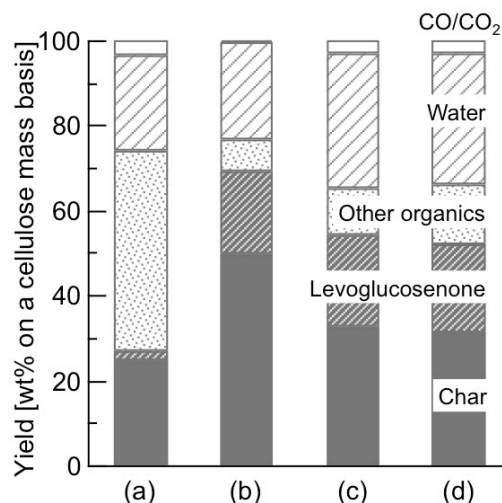


Fig. 2. Products from slow pyrolysis (at 5 K min<sup>-1</sup>) of (a) cellulose at 350°C, cellulose mixed with [BMMIM]OTf at (b) 250°C, (c) 300°C, and (d) reutilization of [BMMIM]OTf at 300°C.

# First Observation of Multi-Step Spin Transition in Fe<sup>III</sup> Complex with One-Dimensional Hydrogen-Bonded Chain

Zhaoyang Li, Shinji Kanegawa, Soonchul Kang, Osamu Sato\*

Institute for Materials Chemistry and Engineering, Kyushu University, 6-1 Ksuga-koen,  
Fukuoka, 816-8580, Japan  
E-mail: sato@cm.kyushu-u.ac.jp

For Fe<sup>III</sup> complexes with appropriate ligand, the Fe<sup>III</sup> center can undergo a thermally induced spin conversion between high-spin (HS,  $S = 5/2$ ) and low-spin (LS,  $S = 1/2$ ) states. But spin transition system with strong cooperative and multi-stepped mechanism is still a great challenge<sup>1-3</sup>. We report here the unprecedented spin transition compound: [Fe(5-Brthsa)<sub>2</sub>]·H<sub>2</sub>O (5-Brthsa = (5-bromo-2-hydroxybenzylidene)hydrazinecarbothioamide), which contains —NH<sub>2</sub> group aimed at forming H-bonding network.

The title compound crystallizes in orthorhombic space group. As seen in Fig. 1, the symmetry unit contains one Fe<sup>III</sup> center, two 5-Brthsa ligands and one free water molecule. The single-crystal structure was determined at 123K, 173K and 283K, respectively. But no phase transition was observed from single-crystal determination under variable temperature. The averaged Fe<sup>III</sup>—N, Fe<sup>III</sup>—O, Fe<sup>III</sup>—S coordination bond lengths are listed in Table 1. The presence of water molecule in the lattice changes the nature of hydrogen bonding but the whole structure always forms infinite one-dimensional hydrogen bonded chain structure (Fig. 2). Owing to the charge balance, herein we propose that the presence of oxonium ion which plays the key role in observing the multi-step spin transitions (Scheme 1).

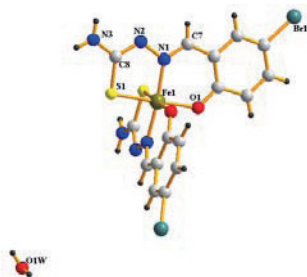


Fig. 1 The symmetry unit of title compound.

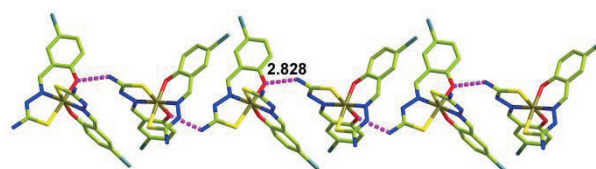


Fig.2 One-dimensional hydrogen-bonded chain connected by N—H···O at 123 K.

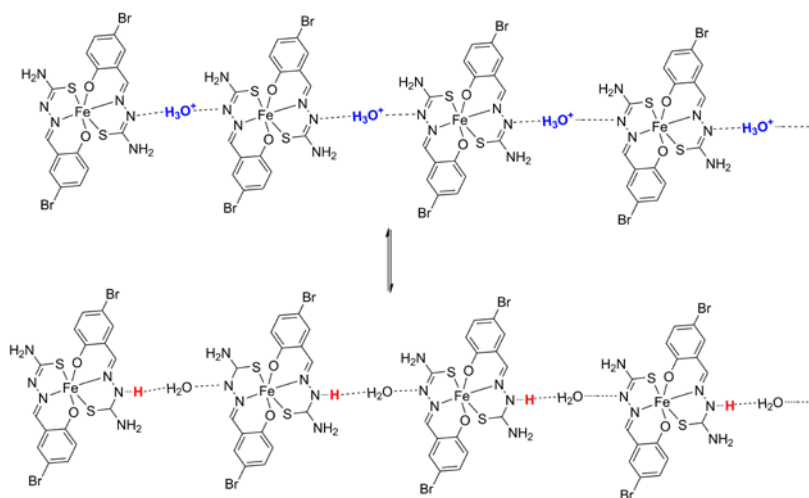
Temperature (K)	123	173	283
Fe <sup>III</sup> —N (Å)	1.963	2.057	2.107
Fe <sup>III</sup> —O (Å)	1.961	1.928	1.944
Fe <sup>III</sup> —S (Å)	2.281	2.359	2.419

Table 1 Fe<sup>III</sup>—N, Fe<sup>III</sup>—O, Fe<sup>III</sup>—S coordination bond lengths at different temperatures (deviation is not given).

Magnetic susceptibility measurements of the title compound were performed in the temperature range of 5-300 K in warming and cooling modes. As shown in Fig. 3, magnetic property shows that the value of  $\chi_m T$  is equal to 4.3 cm<sup>3</sup> K mol<sup>-1</sup>, which corresponds to what is expected for HS state of Fe<sup>III</sup> compound ( $S = 5/2$ ). On further cooling, an

*abrupt-gradual-abrupt* decrease in the  $\chi_m T$  values to  $0.45 \text{ cm}^3 \text{ K mol}^{-1}$  started at 133 K, indicating that the occurrence of spin transition from the HS to LS state. It is worthy to noting that both the warming and cooling modes the  $\chi_m T$  values changed in a five-step manner centered at about 246 K, 216 K, 197 K, 173 K and 148K, respectively. With the hysteresis loop of 5K, the title compound underwent four intermediate phases. As far as we know, five-step spin crossover behavior is firstly observed in monomeric  $\text{Fe}^{\text{III}}$  complex. The variable-temperature  $^{57}\text{Fe}$  Mössbauer spectra and photo-effect measurement is under way.

In summary, the 5-Brthsa ligand has been synthesized to favor intermolecular interactions between mononuclear complex.  $[\text{Fe}(5\text{-Brthsa})_2] \cdot \text{H}_2\text{O}$  is a new multi-step SCO compound with one-dimensional hydrogen bonding chain structure, which plays an important role in observing proton transfer. We hope that the novel feature of the title compound will shine more light on cooperative effects and multiple-stability within SCO materials.



Scheme. 1 The possible mechanism of proton relay in the infinite one-dimensional hydrogen bonded chain.

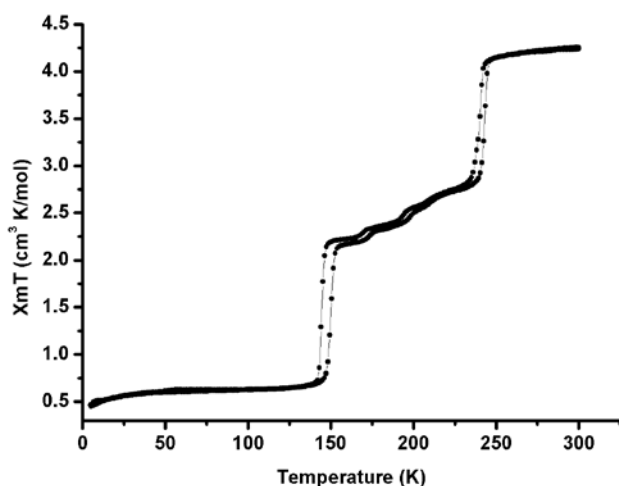


Fig. 3 Temperature-dependent susceptibility of the title compound under 5000 Oe.

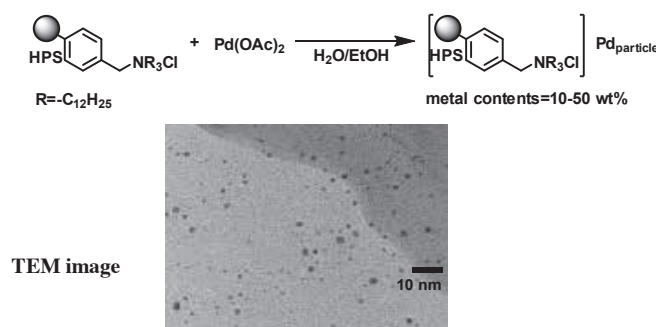
- [1] M. Nihei, *J. Am. Chem. Soc.*, **132**, 3553(2010).
- [2] S. Floquet, *New J. Chem.*, **27**, 341(2003).
- [3] M. D. Timken, *Inorg. Chem.*, **24**, 3450(1985).

## Mizoroki-Heck Reaction and Suzuki-Miyaura Coupling catalyzed by A nano-Pd Particles Embedding to Hyperbranched Polystyrene Ammonium Salt-Catalyzed

Takashi Nishikata<sup>1</sup>, Keisuke Kojima<sup>2</sup>, Hironori Tsutsumi<sup>1</sup>, and Hideo Nagashima<sup>1</sup>  
<sup>1</sup>Institute for Materials Chemistry and Engineering, Kyushu University, Kasuga, Fukuoka, 816-0952 <sup>2</sup>Nissan Chemical Industries, LTD, Funabashi, Chiba, 274-8507,

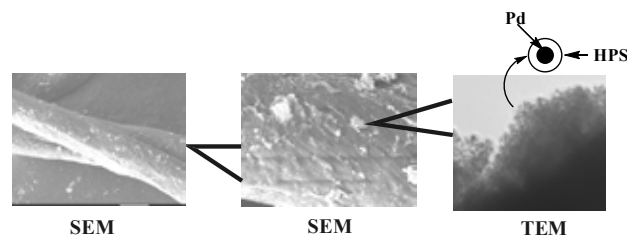
Suzuki-Miyaura coupling<sup>1</sup> and Mizoroki-Heck reaction<sup>2</sup> are one of the most important reactions to construct carbon-carbon bonds mediated by transition metal catalysts. It has been recognized to be problematic that most reactions are carried out in homogeneous systems and metal catalyst wastes have to be removed from the product by distillation or chromatography. One of the promising methods to solve the residual metal problem is immobilization of palladium species onto solid-supports: good immobilized catalysts led to facile separation and recycle of the catalyst from the product without leaching the metallic species.<sup>3</sup> We are interested in the fact that above two reactions are also catalyzed by palladium particles. In the course of our studies on the nano metal particle, we have found that hyperbranched polystyrene(HPS)-ammonium salts turned out to be a good stabilizer for palladium nano-particles. It is important that the well dispersed palladium nanoparticles (2~3 nm) on the HPS-NR<sub>4</sub><sup>+</sup>Cl<sup>-</sup> (Pd@HPS<sub>ammonium</sub>) are good catalyst for hydrogenation of unsaturated molecules in hydrocarbon / water biphasic systems (Scheme 1). Although Pd@HPS<sub>ammonium</sub> is well soluble either in water [R = -(OCH<sub>2</sub>)<sub>3</sub>Me] or hexane [R = octyl or dodecyl even in the recycling experiments, heating with KBr or dicarboxylic acids in the presence of the supports, such as cotton, filter paper, and nylon-6 led to the nano-metal particles surrounding by the hyperbranched polymers which are printed on the surface of the supports. Here, we wish to report that these printed palladium nanoparticles act as reusable catalyst systems for Suzuki-Miyaura coupling and Mizoroki-Heck reaction.

**Scheme 1**



The printing was carried out in DMF at 100 °C for 2 h. As shown in Figure 1, SEM and TEM images showed that Pd nano-particles embedding to HPS-ammonium are immobilized on cotton fibers (Pd@HPS<sub>ammonium</sub>@cotton) (Figure 1).

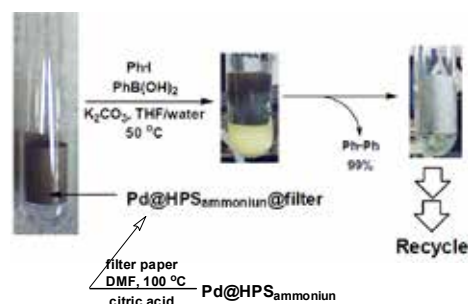
**Figure 1**



The resulting palladium-immobilizing cotton, filter paper and 6-nylon plate were applied to heterogeneous Suzuki-Miyaura coupling (Scheme 2). In a typical example, the coupling was carried out in a glass tube placed Pd@HPS<sub>ammonium</sub>@filter paper, which was produced by treatment with citric acid. The reaction of iodobenzene with PhB(OH)<sub>2</sub> was carried out in THF/water at 50 °C for 24 h. The solid-supported catalyst was removed from the mixture, and was recycled several times. In each run, the desired product was obtained quantitatively, and the metal leaching is 7-15 ppm at the first three runs, whereas below 2 ppm at further runs.

Various combination of aryl iodides and aryl boronic acids can be used for Suzuki-Miyaura coupling. The catalyst is also useful for Mizoroki-Heck reactions (Scheme 3). Details will be discussed at the session.

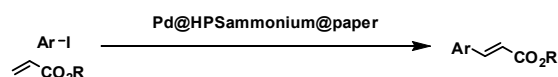
**Scheme 2**



cycle	Ph <sub>2</sub> (%)	leached Pd (ppm)	cycle	Ph <sub>2</sub> (%)	leached Pd (ppm)
1	99	15	4	99	1.5
2	99	7.7	5	99	ND <sup>a</sup>
3	99	13			

<sup>a</sup>Leached Pd was not detected.

**Scheme 3**



## References

- 1 N. Miyaura, A. Suzuki, *Chem. Rev.* **1995**, *95*, 2457.
- 2 A. de Meijere, F. E. Meyer, *Angew. Chem., Int. Ed.*, **1994**, *33*, 2379.
- 3a) J. A. Gladysz, *Pure Appl. Chem.*, **2001**, *73*, 1319. b) C. A. McNamara, M. J. Dixon and M. Bradley, *Chem. Rev.*, **2002**, *102*, 3275. c) D. J. Cole-Hamilton, *Science*, **2003**, *299*, 1702. d) P. McMorn and G. J. Hutchings, *Chem. Soc. Rev.*, **2004**, *33*, 108. e) Catalyst Separation, Recovery and Recycling, ed. D. Cole-Hamilton and R. Tooze, *Catalysis by Metal Complexes Book Series*, No. 30, Springer, The Netherlands, **2006**.

## Self-assembly and luminescent properties of lipophilic BF<sub>2</sub> β-diketone complexes

Shigesaburo Ogawa<sup>1</sup>, Masa-aki Morikawa<sup>1,3</sup>, Nobuo Kimizuka<sup>1,2,3</sup>

<sup>1</sup>Department of Chemistry and Biochemistry, Graduate School of Engineering, Kyushu University, Japan, <sup>2</sup>Kyushu University, IRCMS, <sup>3</sup>JST-CREST

(Dibenzylmethanato)β-diketone–boron difluoride (BF<sub>2</sub>(dbm)) complexes have attracting much attention in recent years because of their intriguing photophysical properties such as large molar absorption coefficients, controllable emission wavelength in visible range and high emission quantum yields [1]. To develop new functionalities of BF<sub>2</sub>(dbm) complexes, it is necessary to control both their self-assembly in solution and that in the solid state. The solution study will serve to understand causal relationships between their chemical structure and physical properties, and to control them. The solid-phase study will allow us to extend their applications in nanodevices. Until now, several self-assembling system of BF<sub>2</sub>(dbm) have been reported for organogels, liquid crystals, nanoparticles and adsorbed monolayers [2-5]. However, molecular design for BF<sub>2</sub>(dbm) complexes to achieve their interfacial self-assembly as homogeneous molecular films has yet-to-be-defined, in spite of its importance in designing functional supramolecular interfaces.

In this study, four types of lipophilic ligands containing multiple β-diketone units **1-4** were developed (Fig. 1). They are linked to a benzene ring in different positions. Self-assembly and luminescence properties of these in organic solutions and solid surfaces were investigated. As a result, a new perspective in designing BF<sub>2</sub>(dbm) assemblies which spontaneously afford homogeneous thin films was obtained.

Four types of ligands were synthesized through Claisen condensation between corresponding methyl ester and ketone materials. Their ligands were further reacted with BF<sub>3</sub>·Et<sub>2</sub>O in mix solvents of toluene and acetic acid to afford compound **1-4**.

Aggregation behavior of compounds **1-4** in chloroform was investigated by <sup>1</sup>H-NMR, dynamic light scattering (DLS) and fluorescence measurements. The morphology and luminescence properties of these complexes in cast films were studied by confocal laser scanning microscopy (CLSM), X-ray diffraction (XRD) and fluorescence measurements.

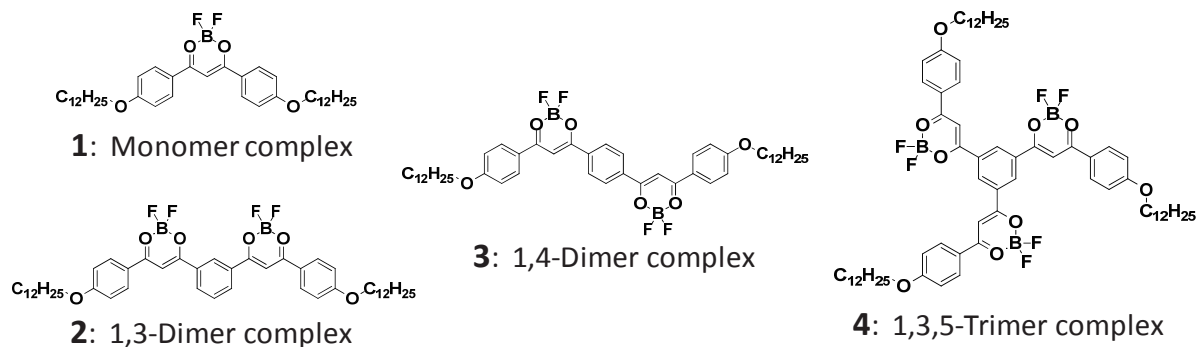


Fig. 1. Chemical structures of lipophilic BF<sub>2</sub> β-diketone complexes.



In  $^1\text{H-NMR}$  spectroscopy, compound **4** showed upfield shifts in the aromatic proton ( $H_a$ ) above the concentration of  $1.0 \times 10^{-3}$  M (Fig. 2). It reflects self-assembly of compound **4** by  $\pi$ - $\pi$  stacking. In contrast, compound **1** showed less tendency to self-aggregate whereas compound **2** and **3** formed precipitates at low concentrations between  $1.0 \times 10^{-3}$  and  $1.0 \times 10^{-4}$  M.

Fig. 3 shows concentration dependence of luminescent spectra observed for **4** in chloroform. A luminescent peak around 460 nm was found for a dilute  $1.0 \times 10^{-4}$  solution, which is ascribed to the  $\text{BF}_2(\text{dbm})$  chromophore in monomeric state. On the other hand, upon increasing the concentration from  $1.0 \times 10^{-4}$  to  $2.5 \times 10^{-2}$  M, a new emission around 560 nm appeared (**b**), which is accompanied by a decrease of the spectral relative intensity around 460 nm (**a**). This is consistent with  $^1\text{H-NMR}$  (Fig. 2) and the observed luminescence spectral red shift is ascribed to self-assembly of **4** at elevated concentrations.

The CLSM images of cast films **1-4** are shown in Fig. 4. Although the complex **1** is monomeric in chloroform, it formed aggregates on a glass plate. Compound **2** and **3** showed needle-like solid, which were formed already in solutions. In contrast, compound **4** exhibited homogeneous cast film with amorphous structure as supported by XRD measurement.

From these results, it is apparent that the trigonal-shaped  $\text{BF}_2(\text{dbm})$  complex **4**, satisfy both the self-assembly in solution and formation of homogeneous cast films. The ability of **4** to spread homogeneously on solid surfaces would be applied to develop functional interfaces which show luminescent properties in response to the physicochemical stimuli.

[1] E. Congé-Laage, *Chem.-Eur. J.* **7**, 974 (2004). [2] X. Zhang, X, *Chem. Comm.*, **46**, 8419 (2010). [3] O. A. Turanova, *Russ. J. Gen. Chem.*, **76**, 730 (2006). [4] Zhang, *Nat. Mater.*, **8**, 747 (2009). [5] R. Rohde, *Langmuir*, **22**, 4750 (2006).

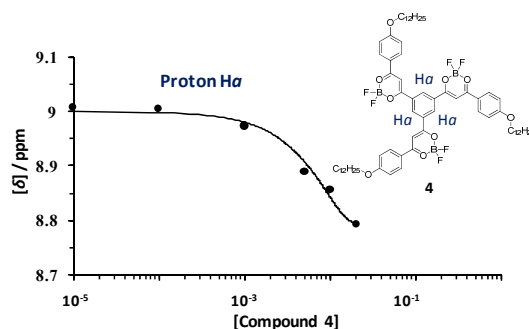


Fig. 2.  $^1\text{H-NMR}$  chemical shifts for complex **4** proton ( $H_a$ ) as a function of its concentration in  $\text{CDCl}_3$  at  $20^\circ\text{C}$ .

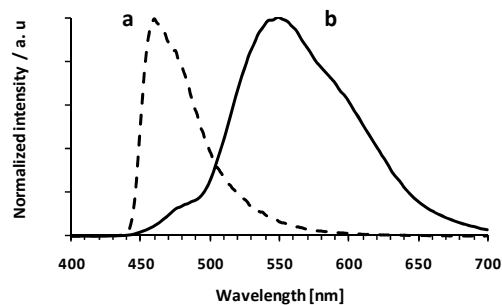


Fig. 3. Concentration dependence of normalized fluorescent spectra observed for complex **4** in  $\text{CHCl}_3$ .  $\lambda_{\text{ex}}$ , 365 nm at  $20^\circ\text{C}$ . (a)  $1.0 \times 10^{-4}$ , (b)  $2.5 \times 10^{-2}$  [M].

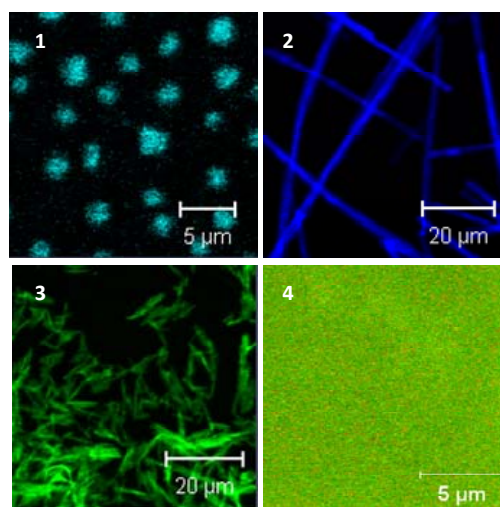


Fig. 4. CLSM images of cast solid films obtained for four  $\text{BF}_2(\text{dbm})$  complexes on glass plates.

## Synthesis of Thermo-responsive Hollow Nanoparticle using Template Micelle

Kazuki Osawa, Masamitsu Noborizato, Shin-ichi Yusa

Department of Materials Science and Chemistry, University of Hyogo, Japan

### Introduction

It is expected that hollow nanoparticles can be used for drug delivery system (DDS), because the hollow nanoparticle can incorporate guest molecules into the hollow core. We have prepared hollow nanoparticles using template micelles [1]. The anionic thermo-responsive diblock copolymer containing the photo-cross-linkable pendants was adsorbed to the surface of the template micelle via hydrogen bonding interaction (Fig. 1). After photo-cross-linking of the thermo-responsive diblock copolymer, the template micelle was removed to prepare the hollow nanoparticles. It is known that poly(*N*-isopropylacrylamide) (PNIPAM) shows the lower critical solution temperature (LCST) in water at 32 °C [2]. PNIPAM was used as a thermo-responsive shell in the hollow nanoparticles. In this paper, we report on preparation of the hollow nanoparticles and their thermo-responsive behavior in water.

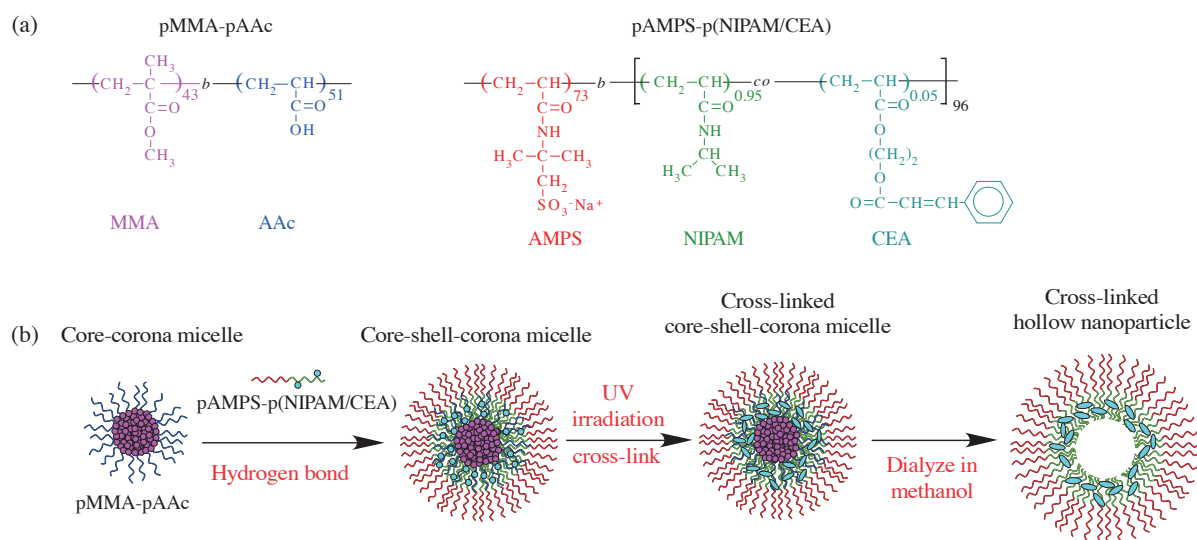


**Fig. 1.** (a) Chemical structures of diblock copolymers and (b) synthetic route of the thermo-responsive hollow nanoparticles.

### Experiment

An amphiphilic diblock copolymer (pMMA-pAAc) was prepared via reversible addition-fragmentation chain transfer (RAFT) controlled radical polymerization. NIPAM and photo-cross-linkable monomer (CEA) were copolymerized via RAFT using a polysulfonate (pAMPS) based macro chain transfer agent to prepare the anionic thermo-responsive diblock copolymer, pAMPS-p(NIPAM/CEA). The p(NIPAM/CEA) block in the diblock polymer can be adsorbed to the pAAc shells in the pMMA-pAAc template polymer micelle by hydrogen

bonding interaction. The shell of the core-shell-corona micelle was cross-linked by UV-irradiation, and the template micelle was removed by dialysis against organic solvent to prepare the thermo-responsive hollow nanoparticle. The polymers were characterized by  $^1\text{H}$  NMR and gel-permeation chromatography (GPC). Photo-cross-linking of cinnamoyl groups was confirmed by UV-vis absorption. The hydrodynamic radius ( $R_h$ ), scattering intensity, and zeta potential ( $\zeta$ ) for each step to prepare the hollow nanoparticle were measured.

## Results and Discussion

$R_h$  and  $\zeta$  for each step to synthesise the hollow nanoparticle are listed in Table 1.  $R_h$  of the template micelle was 22 nm.  $\zeta$  of the template micelle was -3.7 mV because of the pendant carboxylic acid groups in the pAAc shells.  $R_h$  of the hollow nanoparticle at 25 °C was 37 nm.  $\zeta$  of the hollow nanoparticle was -30.8 mV because of sulfonate groups in the pAMPS coronas. As temperature was increased,  $R_h$  of the hollow nanoparticle started to decrease from around 30 °C, reaching a minimum value of 31 nm at 45 °C (Fig. 2). Scattering intensity of the 0.1 M NaCl aqueous solution of the hollow nanoparticle was 190 kHz at 25 °C, which started to increase around 30 °C, reaching a maximum value of 250 kHz at 45 °C. The shrinkage of the cross-linked pNIPAM blocks in the hollow nanoparticles above the LCST ( $\approx 30$  °C) induced a decrease of size and an increase of density for the hollow nanoparticles.

**Table 1.**  $R_h$  and  $\zeta$  for the each step to prepare the hollow nanoparticle

	$R_h$ (nm)	$\zeta$ (mV)
pAMPS-p(NIPAM/CEA)	8	-41.7
Template micelle	22	-3.7
Core-shell-corona micelle	28	-41.3
Hollow nanoparticle (25 °C)	37	-30.8

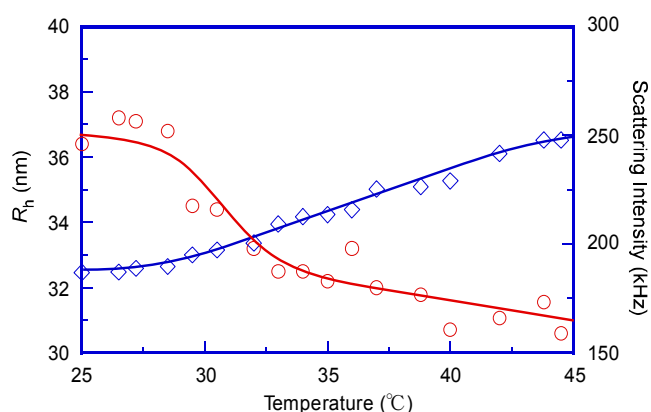


**Fig. 2.** Temperature dependence of hydrodynamic radius,  $R_h$  (○) and scattering intensity (◇) for the hollow nanoparticles in the 0.1M NaCl aqueous solution.

## References

- [1] W. Qui, X. Yan, L. Duan, Y. Cui, Y. Yang, J. Li, *Biomacromolecules*, **10**, 1212 (2009).
- [2] M. Heskins, J. E. Guillet, *J. Macromol. Sci. Chem.*, **A2**, 1441 (1968).

## Reversible Formation of Hydrophilic Chemical Gels Cross-linked by Radically Exchangeable Dynamic Covalent Bonds

Jing Su<sup>1</sup>, Yoshifumi Amamoto<sup>1</sup>, Masamichi Nishihara<sup>2</sup>,

Atsushi Takahara<sup>1,2\*</sup>, Hideyuki Otsuka<sup>1,2\*</sup>

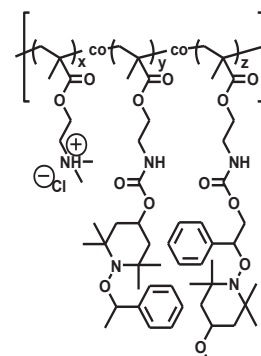
<sup>1</sup> Graduate School of Engineering, Kyushu University, Japan

<sup>2</sup> Institute for Materials Chemistry and Engineering, Kyushu University, Japan

In polymer chemistry, reversible covalent bonds have provided covalently cross-linked polymers with particular abilities such as sol–gel transition and network structure variation. In particular, radical crossover reaction of polymers with dynamic covalent bonds in side chains can allow reorganizability of the chemical gels. [1] Since radical reactions are tolerant of many solvents and functional groups, such reorganizability of water-soluble polymers is expected.

Poly(dimethylaminoethyl methacrylate) with alkoxyamine units in the side chain was synthesized by radical copolymerization in toluene using V-70 as an initiator. The dimethylaminoethyl groups of copolymers were converted into ammonium groups by the treatment with hydrochloric acid to afford the corresponding water-soluble polymer **1**.

Since the obtained water-soluble polymers have complementarily reactive alkoxyamine units in the side chain, the polymers were heated at 100 °C under different concentration conditions. The 10 wt% aqueous solutions of polymer **1** became a gel with heating, as shown in Figure 1. The cross-linking behavior depended remarkably upon the concentration. De-cross-linking reaction was also accomplished by the radical exchange reaction of the cross-linked polymer and hydrophilic alkoxyamine compound to afford soluble polymers after heating and the gel turned into a solution. [2]



**1**

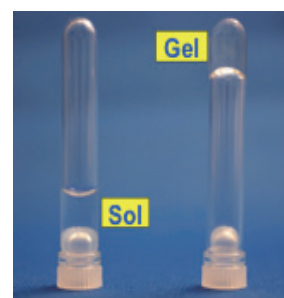


**Figure 1.** Photograph of 10 wt% aqueous solutions of **1** (x:y:z = 18:1:1) after 24 h without (left) and with (right) heating.

### References

- [1] (a) H. Otsuka, Y. Higaki, A. Takahara, *Macromolecules*, **39**, 2121 (2006). (b) Y. Amamoto, M. Kikuchi, H. Masunaga, S. Sasaki, H. Otsuka, A. Takahara, *Macromolecules*, **42**, 8733-8738 (2009). (c) Y. Amamoto, M. Kikuchi, H. Masunaga, H. Ogawa, S. Sasaki, H. Otsuka, A. Takahara, *Polym. Chem.*, **2**, 957 (2011).  
 [2] J. Su, Y. Amamoto, M. Nishihara, A. Takahara, H. Otsuka, *Polym. Chem.*, **2**, (2011), *in press*.

## New Fe(II)-complexes for Atom Transfer Radical Polymerization: The Ligand Design for TACN Results in High Reactivity and Catalyst Performance

Yusuke Sunada<sup>1,2</sup>, Mitsunobu Kawamura<sup>1</sup>, Soichiro Nakanishi<sup>2</sup>, Hidetomo Kai<sup>3</sup>, Nobuyuki Koike<sup>3</sup>, Akane Sasamoto<sup>3</sup>, Hitoshi Hayakawa<sup>3</sup>, Ren-Hua Jin<sup>4</sup>, and Hideo Nagashima<sup>1,2</sup>

<sup>1</sup> Institute for Materials Chemistry and Engineering, Kyushu University, Japan

<sup>2</sup> Graduate School of Engineering Sciences, Kyushu University, Japan

<sup>3</sup> DIC corporation, Japan

<sup>4</sup> Synthetic Chemistry Laboratory, Kawamura Institute of Chemical Research, Japan

Controlled radical polymerization (CRP) is an important method for constructing polymers with fine structure. We have recently reported a trinuclear iron (II) complex (**1**) having a 1,4,7-trimethyl-1,4,7-triazacyclononane (Me<sub>3</sub>TACN) ligand as an effective catalyst for well-controlled ATRP of styrene. The catalyst is easily removable from the polymer by simple washing with methanol, and furthermore, the recovered catalyst is reusable. However, the reaction rate is relatively low and polymerization of methyl methacrylate (MMA) and buthyl acrylate (BA) with **1** gave a polymer with a relatively broad molecular weight distribution. In this paper, we report that the ligand design of TACN realizes the production of a mononuclear complex, (*i*Pr<sub>3</sub>TACN)FeX<sub>2</sub> [*i*Pr<sub>3</sub>TACN = 1,4,7-triisopropyl-1,4,7-triazacyclononane; X = Cl (**2**) or Br (**3**)]. The high reactivity of these catalysts led to well-controlled polymerization and block copolymerization even with lower catalyst concentration

The mononuclear iron complexes **2** and **3** can be synthesized by the reaction of *i*Pr<sub>3</sub>TACN and FeX<sub>2</sub> in acetonitrile in high yield. The molecular structure of **2** and **3** determined by X-ray crystallography showed that **2** and **3** had a mononuclear coordinatively unsaturated 16 valence electron structure (Fig. 1).

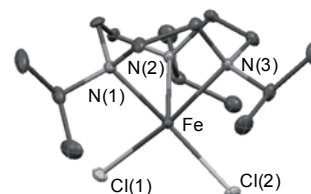


Fig. 1. ORTEP drawing of **2**.

The complexes **2** and **3** were subjected to studies on the catalytic polymerization of styrene, MMA, and BA using halogen initiators. Representative results are summarized in Table 1. Both Cl and Br complexes **2** and **3** are active for well-controlled

Table 1. Polymerization using (tacn)Fe-Catalysts.

entry	cat	monomer	conditions	conv. (%)	$M_n$ (exp.)	$M_n$ (calc.)	$M_w/M_n$
1	<b>1</b>	Styrene	120 °C, 20 h	>95	19,000	25,000	1.17
2	<b>2</b>	Styrene	120 °C, 4 h	>95	25,000	25,000	1.22
3	<b>2</b>	MMA	100 °C, 1 h	85	29,000	21,000	1.49
4	<b>2</b>	BA	100 °C, 20 h	83	28,000	25,000	2.34
5	<b>3</b>	Styrene	120 °C, 4 h	>95	26,000	25,000	1.31
6	<b>3</b>	MMA	100 °C, 1 h	>95	27,000	25,000	1.24
7	<b>3</b>	BA	100 °C, 20 h	82	37,000	26,000	1.22

polymerization of styrene and MMA (entries 2, 3 and 5, 6). The observed  $M_n$  is in accord with the theoretical value calculated from the ratio of monomer to the initiator or the catalyst, whereas  $M_w/M_n$  is around 1.2~1.5. Attempted polymerization of BA catalyzed by **3** in the presence of ethyl dibromoacetate gave the polymer with a broad  $M_w/M_n$  (entry 4). In contrast, that with the bromo-homologue **4** successfully gave polyBA with a narrow molecular weight distribution (entry 7).

## Polymer Scrambling Reactions between Polybutadiene/Polyisoprene and Olefin-containing Polyurethane by Olefin Cross-Metathesis

Kaori Suyama<sup>1</sup>, Shigehisa Kamimura<sup>1</sup>, Keiichi Imato<sup>1</sup>, Atsushi Takahara<sup>1,2</sup>, and Hideyuki Otsuka<sup>1,2</sup>

<sup>1</sup> Graduate School of Engineering, Kyushu University, Japan

<sup>2</sup> Institute for Materials Chemistry and Engineering, Kyushu University, Japan

Main chain exchange reaction based on dynamic covalent chemistry is one of the synthetic methods of novel polymeric materials. The advantage of main chain exchange reaction is that one can manipulate the chemical and physical properties of polymers after polymerization[1]. We previously reported the macromolecular olefin metathesis between 1,4-polybutadiene and olefin-containing polyester. Here, we report scrambling reactions between 1,4-polybutadiene/polyisoprene and olefin-containing polyurethane.

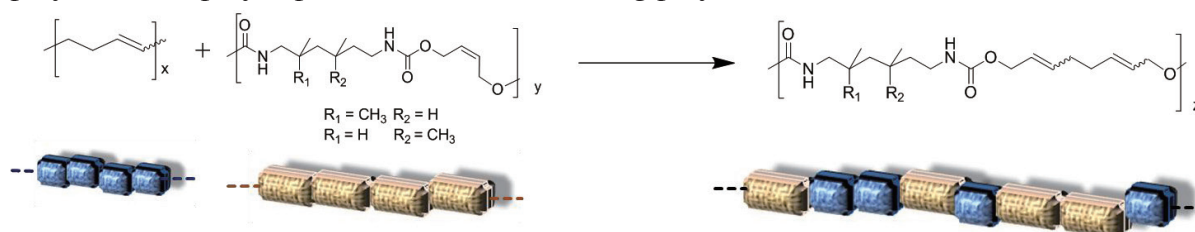


Fig 1. Polymer scrambling reaction between 1,4-polybutadiene and olefin-containing polyurethane via olefin cross-metathesis.

As shown in Fig 1, 1,4-polybutadiene and olefin-containing polyurethane were scrambled in the presence of Grubbs catalysts to afford the corresponding hybrid polymers. In addition, polyisoprene and olefin-containing polyurethane were successfully scrambled. The structures and thermal properties of the hybrid polymers were characterized by NMR, GPC, and DSC measurements. Particularly, in NMR measurement, new peaks appeared with the progress of scrambling reaction. DSC measurement revealed that scrambled polymer has single  $T_g$  in the region between 1,4-polybutadiene and olefin-containing polyurethane (Fig. 2). These results indicate that a hybrid polymer with new properties was formed.

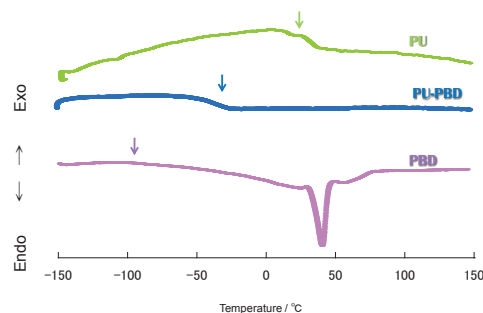


Fig 2. DSC thermograms of polyurethane -1, 4-polybutadiene (PU-PBD) scrambled polymer, polyurethane (PU) and 1,4-polybutadiene (PBD).

The scrambling reactions and the properties of hybrid polymers were well controlled by changing the reaction conditions. To put it more precisely, it allows us to manipulate the degree of hybridization from multiblock copolymers to random copolymers by changing the reaction time and/or the amount of the catalysts for the scrambling reactions.

[1] H. Otsuka, A. Takahara et al., *J. Am. Chem. Soc.*, **125**, 4064 (2003); *Chem. Commun.*, **45**, 1073 (2009); *Prog. Polym. Sci.*, **34**, 581 (2009); *Chem. Commun.*, **46**, 1150 (2010).

## Synthesis and Characterization of Inorganic Polymers with Mixed Cage and Chain Structures

Marie Yoshimatsu<sup>1</sup>, Kunihiro Komori<sup>1</sup>, Yusuke Onagamitsu<sup>1</sup>, Masashi Kunitake<sup>1,3</sup>, Kiyoshi Sakai<sup>2</sup>, Takashi Matsuo<sup>2</sup>

<sup>1</sup>Department of Applied Chemistry & Biochemistry, Graduate School of Science and Technology, Kumamoto University, Japan

<sup>2</sup>JNC Corporation, Japan, <sup>3</sup>JST-CREST, JST, Japan

Polyhedral oligomeric silsesquioxane (POSS), which is a unique cage structure based on siloxane bonds, have attracted attention as novel organic-inorganic hybrid materials. Previously, we have synthesized a series of siloxane polymers consisted of bifunctional “rigid nano-cage” “POSS” and “flexible linear” siloxane chains alternately. The polymers reveal unique properties, such as high heat resistance, flexibility, and small linear expansion. Even though their properties are of interest to various research and industrial fields, very severe synthesis conditions of polycondensation or multiple steps are required in order to synthesize such polymers (Figure 1.).

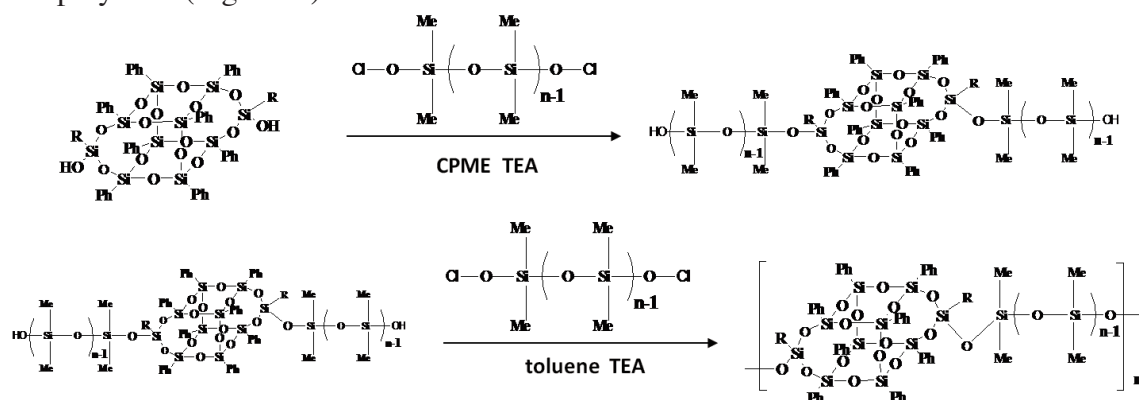


**Figure 1.** Reaction schemes of siloxane polymers alternately bearing POSS cages by polycondensation.

On contrast, many silicone polymers are produced by equilibrium polymerization through ring-opening reaction of cyclic dimethyl silicone such as octamethyl cyclotetrasiloxane (D4) as a general industrially method. Compared with polycondensation, equilibrium polymerization is a simple procedure. In this presentation, we report the synthesis and characterization of polymers consisted of POSS cage and siloxane chain by equilibrium ring-opening polymerization of cyclic dimethyl silicone in the presence of POSS (Figure 2.).

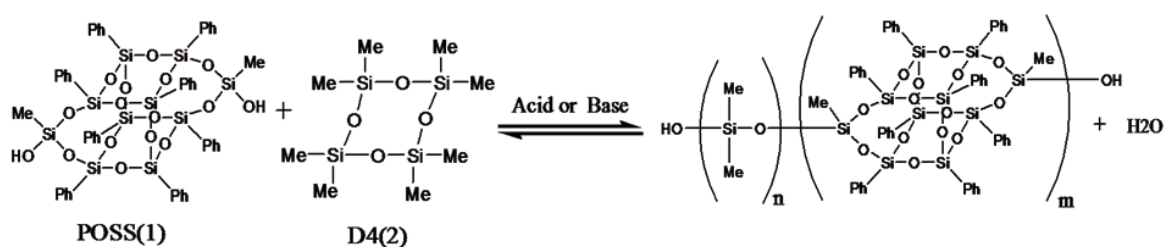


**Figure 2.** Reaction scheme of siloxane polymers alternately bearing POSS cages by equilibrium polymerization.

POSS and D4 were copolymerized with acidic catalyst (*p*-toluenesulfonic acid) under several different reactive conditions. Characterization of the synthesized polymers was carried out by size exclusion chromatography (SEC) and  $^1\text{H-NMR}$ .

The analysis of synthesized siloxane polymers revealed that the polymers consisted of POSS cages and siloxane chains. The dimethyl siloxane chain between POSS cage units was not constant and scattered. The average lengths of siloxane chain segments were decreased with decreasing of molar ratio of D4 to POSS. The cast film of the synthesized polymers revealed good thermal and optical properties, such as high transparency and small linear expansion.

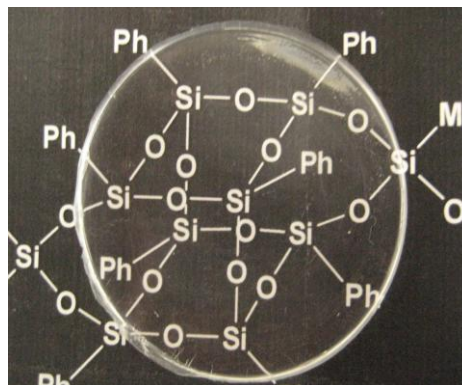


**Figure 3.** A photograph of a cast film of a cage-chain alternated polymer prepared by equilibrium ring-opening polymerization.